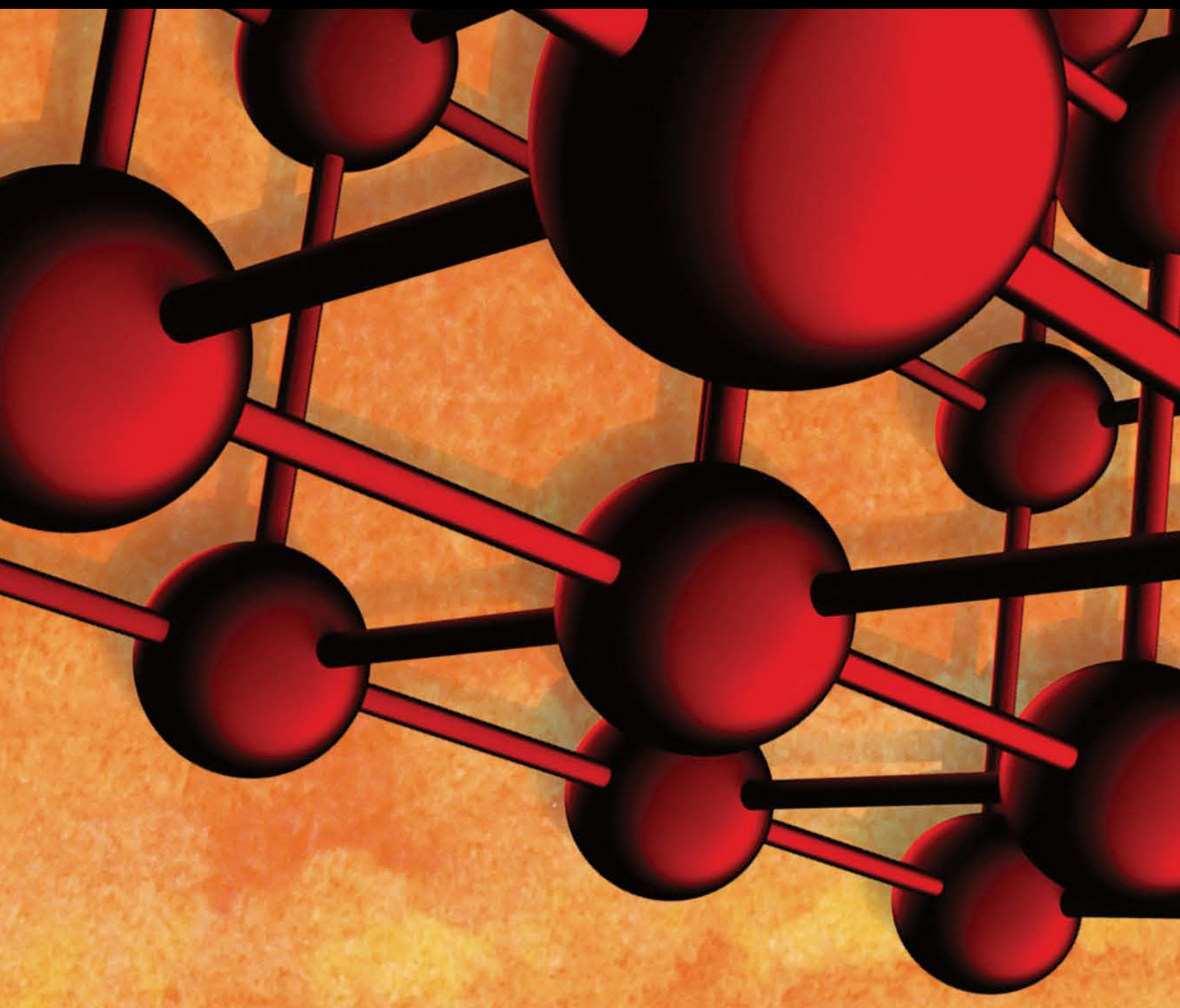


Advances in Materials Science and Engineering

Novel Technologies and Applications for Construction Materials 2016

Guest Editors: Gonzalo Martínez-Barrera, Osman Gencel, João M. L. Dos Reis,
and Juan J. Del Coz Díaz





**Novel Technologies and Applications for
Construction Materials 2016**

Advances in Materials Science and Engineering

**Novel Technologies and Applications for
Construction Materials 2016**

Guest Editors: Gonzalo Martínez-Barrera, Osman Gencel,
João M. L. Dos Reis, and Juan J. Del Coz Díaz



Copyright © 2017 Hindawi Publishing Corporation. All rights reserved.

This is a special issue published in “Advances in Materials Science and Engineering.” All articles are open access articles distributed under the Creative Commons Attribution License, which permits unrestricted use, distribution, and reproduction in any medium, provided the original work is properly cited.

Editorial Board

M. S.A. Abdel-Mottaleb, Egypt
Michael Aizenshtein, Israel
Jarir Aktaa, Germany
K. G. Anthymidis, Greece
Amit Bandyopadhyay, USA
Arun Bansil, USA
M. Barletta, Italy
Mikhael Bechelany, France
Jozef Bednarcik, Germany
Avi Bendavid, Australia
Jamal Berakdar, Germany
Giovanni Berselli, Italy
Patrice Berthod, France
Didier Blanchard, Denmark
Susmita Bose, USA
H.-G. Brokmeier, Germany
Steve Bull, UK
Peter Chang, Canada
Daolun Chen, Canada
Gianluca Cicala, Italy
Gabriel Cuello, France
Narendra B. Dahotre, USA
João P. Davim, Portugal
Angela De Bonis, Italy
Francesco Delogu, Italy
Seshu B. Desu, USA
Guru P. Dinda, USA
Yong Ding, USA
N. Tzankova Dintcheva, Italy
Kaveh Edalati, Japan
Philip Eisenlohr, USA
Paolo Ferro, Italy
Massimo Fresta, Italy
Eric Freysz, France
Sergi Gallego, Spain
S. Garcia-Granda, Spain
Filippo Giannazzo, Italy

Daniel Guay, Canada
Hiroki Habazaki, Japan
Joke Hadermann, Belgium
Satoshi Horikoshi, Japan
David Houivet, France
Rui Huang, USA
Michele Iafisco, Italy
Katsuyuki Kida, Japan
Jae-Ho Kim, Republic of Korea
Akihiko Kimura, Japan
Takayuki Kitamura, Japan
Hongchao Kou, China
Prashant Kumta, USA
Luciano Lamberti, Italy
Heinrich Lang, Germany
Pavel Lejcek, Czech Republic
Cristina Leonelli, Italy
Ying Li, USA
Jun Liu, China
Meilin Liu, Georgia
Wei Liu, France
Yunqi Liu, China
F. Lusquiños, Spain
Peter Majewski, Australia
Philippe Miele, France
Hossein Moayedi, Iran
Paul Munroe, Australia
Rufino M. Navarro, Spain
Luigi Nicolais, Italy
Hiroschi Noguchi, Japan
Chérif Nouar, France
José L. Ocaña, Spain
Tsutomu Ohzuku, Japan
Olanrewaju Ojo, Canada
Gianfranco Palumbo, Italy
A. Maria Paradowska, Australia
Matthew Peel, UK

Gianluca Percoco, Italy
Giorgio Pia, Italy
Jean-Francois Pierson, France
Simon C. Potter, Canada
Manijeh Razeghi, USA
Yuri Ribakov, Israel
Anna Richelli, Italy
Antonio Riveiro, Spain
Pascal Roussel, France
Timo Sajavaara, Finland
Antti Salminen, Finland
F.H. Samuel, Canada
Carlo Santulli, Italy
Franz-Josef Schmitt, Germany
Fridon Shubitidze, USA
Maria A. Signore, Italy
Donato Sorgente, Italy
Charles C. Sorrell, Australia
Costas M. Soukoulis, USA
Sam-Shajing Sun, USA
Kohji Tashiro, Japan
Achim Trampert, Germany
Filip Tuomisto, Finland
Krystyn Van Vliet, USA
Qiang Wang, China
Rong Wang, USA
Rui Wang, China
Lu Wei, China
Jörg M. K. Wieszorek, USA
Wei Wu, USA
Hemmige S. Yathirajan, India
Wenbin Yi, China
Belal F. Yousif, Australia
Jinghuai Zhang, China
Li Zhang, China
Ming-Xing Zhang, Australia
Wei Zhou, China

Contents

Novel Technologies and Applications for Construction Materials 2016

Gonzalo Martínez-Barrera, Osman Gencil, João Marciano Laredo dos Reis, and Juan José del Coz Díaz
Volume 2017, Article ID 9343051, 2 pages

Experimental Study on Autogenous and Drying Shrinkage of Steel Fiber Reinforced Lightweight-Aggregate Concrete

Shunbo Zhao, Changyong Li, Mingshuang Zhao, and Xiaoyan Zhang
Volume 2016, Article ID 2589383, 9 pages

Carbon Nanotubes in Cementitious Composites: Dispersion, Implementation, and Influence on Mechanical Characteristics

Tomas Jarolim, Martin Labaj, Rudolf Hela, and Kamila Michnova
Volume 2016, Article ID 7508904, 6 pages

Study on Strength and Microstructure of Cement-Based Materials Containing Combination Mineral Admixtures

Meijuan Rao, Jianpeng Wei, Zhiyang Gao, Wei Zhou, Qiaoling Li, and Shuhua Liu
Volume 2016, Article ID 7243670, 10 pages

Numerical Studies of the Effects of Water Capsules on Self-Healing Efficiency and Mechanical Properties in Cementitious Materials

Haoliang Huang and Guang Ye
Volume 2016, Article ID 8271214, 10 pages

Compressive Behavior and Mechanical Characteristics and Their Application to Stress-Strain Relationship of Steel Fiber-Reinforced Reactive Powder Concrete

Baek-Il Bae, Hyun-Ki Choi, Bong-Seop Lee, and Chang-Hoon Bang
Volume 2016, Article ID 6465218, 11 pages

In Situ Test of Grouting Reinforcement for Water-Enriched Sandy Gravel Ground in River Floodplain

Jinxing Lai, Zhihua Feng, Junling Qiu, Jianxun Chen, and Haobo Fan
Volume 2016, Article ID 2129659, 12 pages

Off-Axial Tensile Properties of Preconstraint PVDF Coated Polyester Fabrics under Different Tensile Rates

Lanlan Zhang
Volume 2016, Article ID 9856474, 12 pages

Measurement of Surface Damage through Boundary Detection: An Approach to Assess Durability of Cementitious Composites under Tannery Wastewater

Tanvir Manzur, Khaled Mahmood Ehsan, Sinha Lamia Sultana, and Samira Mahmud
Volume 2016, Article ID 5368635, 13 pages

Using Recycled Glass and Zeolite in Concrete Pavement to Mitigate Heat Island and Reduce Thermal Cracks

Erhan Burak Pancar
Volume 2016, Article ID 8526354, 8 pages

Water Vapor Diffusion and Adsorption of Sandstones: Influence of Rock Texture and Composition

Martin Keppert, Jaromír Žumár, Monika Čáčová, Dana Koňáková, Petr Svora, Zbyšek Pavlík, Eva Vejmelková, and Robert Černý
Volume 2016, Article ID 8039748, 7 pages

Energy-Dissipation Performance of Combined Low Yield Point Steel Plate Damper Based on Topology Optimization and Its Application in Structural Control

Haixiang He, Xiaobing Wang, and Xiaofu Zhang

Volume 2016, Article ID 5654619, 16 pages

Experimental Research on High Temperature Resistance of Modified Lightweight Concrete after Exposure to Elevated Temperatures

Ke-cheng He, Rong-xin Guo, Qian-min Ma, Feng Yan,
Zhi-wei Lin, and Yan-Lin Sun

Volume 2016, Article ID 5972570, 6 pages

Experimental Study on the Properties of Concrete Mixed with Iron Ore Tailings

Zhong-xi Tian, Zeng-hui Zhao, Chun-quan Dai, and Shu-jie Liu

Volume 2016, Article ID 8606505, 9 pages

An Analysis of the Thermal Conductivity of Composite Materials (CPC-30R/Charcoal from Sugarcane Bagasse) Using the Hot Insulated Plate Technique

René Salgado-Delgado, Alfredo Olarte-Paredes, Areli Marlen Salgado-Delgado, Zully Vargas-Galarza,
Teresa Lopez-Lara, Juan Bosco Hernández-Zaragoza, Israel Rico-Rodríguez, and Gonzalo Martínez-Barrera

Volume 2016, Article ID 4950576, 5 pages

Characterization of Various Plant-Produced Asphalt Concrete Mixtures Using Dynamic Modulus Test

Muhammad Irfan, Asad S. Waraich, Sarfraz Ahmed, and Yasir Ali

Volume 2016, Article ID 5618427, 12 pages

Utilization of Iron Ore Tailings as Raw Material for Portland Cement Clinker Production

Li Luo, Yimin Zhang, Shenxu Bao, and Tiejun Chen

Volume 2016, Article ID 1596047, 6 pages

Properties of Self-Compacting Concrete with Recycled Coarse Aggregate

W. C. Tang, P. C. Ryan, H. Z. Cui, and W. Liao

Volume 2016, Article ID 2761294, 11 pages

Dye Sensitized Solar Cells with Low Cost Carbon Nanotubes Electrodes

F. M. Al-Marzouki, S. Abdalla, and S. Al-Ameer

Volume 2016, Article ID 4928710, 13 pages

Properties of Reactive Powder Concrete and Its Application in Highway Bridge

Junwei Song and Shuhua Liu

Volume 2016, Article ID 5460241, 7 pages

Cost Optimization of Mortars Containing Different Pigments and Their Freeze-Thaw Resistance Properties

Sadik Alper Yıldız, Gökhan Kaplan, and Ali Uğur Öztürk

Volume 2016, Article ID 5346213, 6 pages

Editorial

Novel Technologies and Applications for Construction Materials 2016

**Gonzalo Martínez-Barrera,¹ Osman Gencel,²
João Marciano Laredo dos Reis,³ and Juan José del Coz Díaz⁴**

¹Laboratorio de Investigación y Desarrollo de Materiales Avanzados (LIDMA), Facultad de Química, Universidad Autónoma del Estado de México, Km. 12 de la Carretera Toluca-Atlacomulco, 50200 San Cayetano, MEX, Mexico

²Civil Engineering Department, Faculty of Engineering, Bartın University, 74100 Bartın, Turkey

³Theoretical and Applied Mechanics Laboratory (LMTA), Universidade Federal Fluminense, 24220 Rio de Janeiro, RJ, Brazil

⁴Departamento de Construcción, Universidad de Oviedo, 33204 Gijón, Spain

Correspondence should be addressed to Gonzalo Martínez-Barrera; gonzomartinez02@yahoo.com.mx

Received 28 December 2016; Accepted 28 December 2016; Published 24 January 2017

Copyright © 2017 Gonzalo Martínez-Barrera et al. This is an open access article distributed under the Creative Commons Attribution License, which permits unrestricted use, distribution, and reproduction in any medium, provided the original work is properly cited.

This second special issue shows recent researches in construction technologies as well as in new construction materials. Such investigations involve important aspects, as the use of easy and novel technologies at low costs for improving of physicochemical properties of construction materials, as well as developing environmental friendly and chemically sustainable materials.

The investigations include several topics, for example, the use of by-products in a cement matrix, where thermal conductivity of such composite is measured; for which charcoal from sugarcane bagasse (CSB) was used; the results show that the composite materials reduce thermal conductivities, mainly for higher CSB concentrations (15% by weight). Other research areas involve recycled materials, including glass and zeolite in concrete pavement to mitigate and reduce thermal cracks, as answer to urban heat island (UHI) effect; as we know it is important to reduce pavement high surface temperature in summer to mitigate UHI effect. Moreover, such temperature also affects slab temperature difference, which induces a high possibility of cracking in concrete roads. Also an investigation is concerned about recycled coarse aggregate (RCA) in self-compacting concrete (SCC), which has the potential to reduce both the environmental impact and financial cost associated with this increasingly popular concrete type.

Another important research area covered in this issue is concerned about cementitious composites, with an

investigation of the effects of carbon nanotubes in such composites, covering dispersion, implementation, and its effects on the mechanical properties. Concrete structures are often subjected to aggressive aqueous environments which consist of several chemical agents that can react with concrete to produce adverse effects; an investigation is focused in assessing durability of such composites through measurement of surface damage when they are exposed to wastewater; the purpose is to reduce the environmental pollution created by wastewater; which consists of several chemicals such as sulfates, chlorides, and ammonium. Another study is concerned about the effects of capsules on the self-healing efficiency and mechanical properties of cementitious materials; the self-healing due to further hydration of unhydrated cement particles and the efficiency of supply of water by using capsules as a function of capsule dosages and sizes are studied. As we know water is an important factor for developing composite materials; a study is concerned about water-enriched sandy gravel ground as grouting reinforcement applied in river floodplain. Other important materials are mineral aggregates; in this issue investigations for rock texture and composition of it are studied to understand the water vapor diffusion, as well as the vapor sorption in composite materials. Sandstones have been used as construction materials due to their good accessibility and workability. Moreover, they are rocks containing quartz class which can be cemented by secondary

precipitated quartz or calcite; since most of sandstones are porous, water vapor can penetrate through sandstone constructions.

Some studies about fiber reinforced concrete are described, for example, steel fiber reinforced reactive powder concrete where compressive behavior and mechanical properties are useful for specific application through to stress-strain relationship studies, or steel fiber reinforced lightweight aggregate concrete (SFRLAC) which have many advantages applied in structural engineering, where autogenous and drying shrinkage are measured, considering the effects of types of coarse and fine aggregates with the changes of water-to-binder ratio and volume fraction of steel fiber, as well as a study of a high-performance reactive powder concrete (RPC) and its application in highway bridges, which was prepared with river sand and under 80°C steam curing condition and tested in terms of strength, uniaxial compressive stress-strain relation, and flexural load deflection relation.

Metals continue to be important materials for construction, for example, studies of iron ore tailings (IOT) as raw material for manufacturing of Portland cement clinker, where the results showed that the raw meal containing IOT had higher reactivity and burnability than the raw meal containing clay, and the use of IOT did not affect the formation of characteristic mineralogical phases of Portland cement clinker, or studies concerned about physicochemical properties of concrete containing iron ore tailings in order to solve the shortage of natural sand and make full use of industrial waste.

Other types of composite materials are studied, for example, cement-based materials containing combination mineral admixtures, in terms of glass powder (GP), limestone powder (LP), and steel slag powder (SP), where both microstructure and mechanical strength are studied. In order to improve the spalling resistance in lightweight aggregate concrete at high temperature, a study shows two types of modified materials by adopting the surface coating modification method. Mass loss and residual axial compressive strength of the modified concrete after exposure to elevated temperatures were tested. The performance of various plant-produced asphalt concrete mixtures was studied by using different dynamic modulus tests. Finally, colored aggregate use, custom colored cement use, or pigment use with white cement are among the options in order to obtain mixtures in different colors for architectural mortar applications; this experimental study covered freeze thaw resistance properties of mortars.

Gonzalo Martínez-Barrera

Osman Gencel

João Marciano Laredo dos Reis

Juan José del Coz Díaz

Research Article

Experimental Study on Autogenous and Drying Shrinkage of Steel Fiber Reinforced Lightweight-Aggregate Concrete

Shunbo Zhao, Changyong Li, Mingshuang Zhao, and Xiaoyan Zhang

School of Civil Engineering and Communication, North China University of Water Resources and Electric Power, No. 36 Beihuan Road, Zhengzhou 450045, China

Correspondence should be addressed to Shunbo Zhao; sbzhao@ncwu.edu.cn

Received 6 April 2016; Accepted 20 October 2016

Academic Editor: Osman Gencel

Copyright © 2016 Shunbo Zhao et al. This is an open access article distributed under the Creative Commons Attribution License, which permits unrestricted use, distribution, and reproduction in any medium, provided the original work is properly cited.

Steel fiber reinforced lightweight-aggregate concrete (SFRLAC) has many advantages applied in structural engineering. In this paper, the autogenous shrinkage and drying shrinkage of SFRLAC for up to 270 days were measured, considering the effects of types of coarse and fine aggregates with the changes of water-to-binder ratio and volume fraction of steel fiber, respectively. The properties of mix workability, apparent density, and compressive strength of SFRLAC were also reported and discussed in relation to above factors. Test results show that the development of autogenous and drying shrinkage of SFRLAC was fast within 28 days and tended to be steady after 90 days. The development of autogenous shrinkage of SFRLAC reduced with the increasing water-to-binder ratio and by using the expanded shale with higher soundness and good water absorption, especially at early age within 28 days; the later drying shrinkage was reduced and the development of drying shrinkage was slowed down with the increasing volume fraction of steel fiber obviously; manufactured sand led to less autogenous shrinkage but greater drying shrinkage than fine lightweight aggregate in SFRLAC. The regularities of autogenous shrinkage and drying shrinkage of SFRLAC expressed as the series of hyperbola are analyzed.

1. Introduction

Shrinkage is a common phenomenon of concrete, which can induce tensile stress when the shrinkage is restrained, and may lead to cracking and finally reduce the service life and durability of concrete structures [1]. With the development of long span, large size, and high rise buildings, the design for considering the influence of concrete shrinkage becomes more and more important [2]. Based on the forming mechanisms, shrinkage can be divided as autogenous shrinkage and drying shrinkage. As the volume of cement hydration products is less than the sum of volumes of water and binders, pores and capillaries formed in the hardened cement paste. Autogenous shrinkage takes place because of the self-desiccation of pores and capillaries, resulting from the continuous hydration of binder materials after initial setting. Drying shrinkage takes place mainly due to the free water evaporated from the pores and capillaries near element surfaces to ambient air. The main factors influencing drying shrinkage are concrete strength, cement type, geometry,

curing condition, and starting age [1–4] as well as some properties of concrete mix such as cement dosage, fine aggregate percentage, air content, and slump [1, 3, 4]. The above properties of concrete mix are also the primary factors influencing the autogenous shrinkage of concrete, which determines the composite microstructure of cement paste in concrete. Meanwhile, the coarse aggregate is the bone of concrete, which constrains the shrinkage of concrete in different degrees depending on the type, grading, maximum size, fine aggregate percentage, and volume ratio of aggregate in concrete [5].

In view of the marked shrinkage of normal weight concrete (NWC), especially of high-strength concrete, the internal curing provided by a partial replacement of normal weight aggregate (NWA) by lightweight aggregate (LWA) has been developed as an effective technique for shrinkage mitigation in recent years [6–15]. In this method, the use of prewetted LWAs as internal water sources of concrete is the key of study, as the unsaturated LWAs may lead to an opposite effect due to the absorption of water from matrix

pores into aggregate pores [7–11]. The saturated LWAs can absorb significant amounts of water before mixing and release the water gradually during concrete hardening. The released water will contribute to restoring part of the water which has been lost through internal self-desiccation or external drying of concrete. However, the efficiency of internal curing by LWAs depends not only on their water absorption but also on their desorption characteristics, as not all kinds of LWA can release a sufficient amount of absorbed water during hardening of concrete, although most of them are able to absorb significant amounts of water because of their high porosity. Generally, the desorption characteristics depend on the microstructures of pores [13], the surface open porosity, and the particle size [14]; a coarse pore structure with a high proportion of well-interconnected pores leads to better desorption behavior for internal curing [15]. Meanwhile, the capability of internal curing of LWAs reduces with the decrease of water-to-binder ratio and the increase of concrete strength [16–18].

Theoretically, if the coarse NWA was fully replaced by the coarse LWA, NWC will become the lightweight aggregate concrete (LAC). As in most cases, structural LAC is made with a LWA as coarse aggregate and normal weight sand (natural river sand or manufactured sand) as the fine aggregate [19]. Therefore, the internal curing of LAC by saturated LWAs should be developed to the best; the difference of shrinkage of LAC to NWC should mainly depend on the difference of properties of coarse aggregates. As reported [20, 21] that with the same strength, LAC with higher moisture content LWAs has smaller shrinkage at early age but is finally larger than NWC; however the shrinkage of LAC with lower moisture content LWAs is always larger than that of NWC. When part of the lower water absorption LWAs was replaced by crushed limestone, the shrinkage of LAC could be reduced. This is because, for the same strength, LAC has larger volume of cement paste, and the modulus of elasticity of LWA is lower than that of NWA. However, with the different compositional parameters such as types of LWA (fly ash based artificial aggregate, sintering expanded clay, pumice aggregate, or oil palm shell), amount and type of binder, water-to-binder ratio, mineral admixture (silica fume, fly ash), and initial prewetting method for LWA, the shrinkage of LAC may be lower or greater than that of NWC [22–27]. Generally, the shrinkage of LACs is reduced by the rigid LWA with higher modulus of elasticity in water saturated condition prewetted and with the greater volume of LWA in the same volume of paste [24–26]. And most importantly, in current standard methods, the shrinkage of LAC is usually estimated from the expressions defined for NWC and always gets higher value than those measured in practice [24, 28]. For the proper prediction of shrinkage, the special characteristics of LAC should be considered.

With the application of fiber reinforced LAC in structure engineering, the effects of steel fibers or hybrid fibers on shrinkage of LAC were also studied. Among them, LACs were made by using cold-bonded fly ash aggregate [29], sintered fly ash aggregate [30], and expanded clay aggregate [31–33] as coarse aggregate and river sand as fine aggregate. Generally, the shrinkage of LACs did not change much at early age;

however it reduced later to some extent. Fibers (carbon fiber, steel fiber, and polypropylene fiber) in LAC could not change the shrinkage behavior of base LAC affected by LWAs and water-to-binder ratio; their effect is mainly on the restraining of drying shrinkage. As the type and content of fibers are new parameters affecting the shrinkage of LAC, the research become complex and should be carried out comprehensively with other parameters changed.

In view of the wide application of sintering expanded shale as a LWA [20, 21] and the inexorable trend of natural sand replaced by manufactured sand [5, 34], this paper is focused on the autogenous and drying shrinkages of SFRLAC (steel fiber reinforced LAC) with the change of expanded shale and fine aggregate. The water-to-binder ratio and the volume fraction of steel fiber are taken into consideration to study their effects on autogenous shrinkage and drying shrinkage, respectively. Meanwhile, the mix workability, apparent density, and compressive strength are also given out. The aim of this study is to quantify the effects of aggregates, water-to-binder ratio, and volume fraction on the shrinkage of SFRLAC and finally gives a reference for the practical analysis of structural design.

2. Experiment

2.1. Raw Materials

Cement: grade P.O. 52.5 ordinary silicate cement produced in accordance with China Standards [35]; the physical and mechanical properties are listed in Table 1.

Admixture: class-II fly ash with physical properties listed in Table 2.

Coarse aggregate: two kinds of ceramsite of sintering expanded shale in continuous gradation with maximum size of 20 mm. They were sieved based on the maximum density principle. The physical and mechanical properties are listed in Table 3.

Fine aggregate: lightweight sand of fine sintering expanded shale and manufactured sand in continuous gradation with size of 1.6–5 mm. The physical properties are listed in Table 4.

Steel fiber: milling type, 36 mm long, 1.35 mm equivalent diameter, and 27.1 aspect ratio.

Water reducer: polycarboxylic acid superplasticizer with water-reducing rate of 19%.

Water: tap water.

The water absorption of lightweight aggregates was measured in accordance with China Standard GB/T 17431.2 [36]; the results are drawn in Figure 1.

2.2. Test Parameters and Mix Proportion of Concrete. Test parameters of this study were considered as volume fraction of steel fiber (ρ_f), water-to-binder ratio (W/B), two kinds of coarse lightweight aggregate, and fine lightweight aggregate and manufactured sand [37, 38]. Their combinations for

TABLE 1: Physical and mechanical properties of cement.

Strength grade	Water requirement of normal consistency (%)	Setting time (min)		Compressive strength (MPa)		Tensile strength (MPa)	
		Initial	Final	3 d	28 d	3 d	28 d
52.5	27.4	150	255	33.6	51.7	6.8	9.2

TABLE 2: Physical properties of fly ash.

Fineness modulus (pass 0.045 mm) (%)	Water demand ratio (%)	Apparent density (kg/m ³)	Water content (%)
26.4	104.2	2049	0.4

TABLE 3: Physical and mechanical properties of expanded shale.

Identifier	Apparent density (kg/m ³)	Bulk density (kg/m ³)	1 h water absorption (%)	Mud content (%)	Cylinder compressive strength (MPa)
H	1444	888	7.65	0.7	8.3
N	1307	816	8.50	0.9	7.3

TABLE 4: Physical properties of lightweight sand and manufactured sand.

Identifier	Grade (mm)	Fineness modulus	Apparent density (kg/m ³)	Bulk density (kg/m ³)	1 h water absorption (%)	Mud content (%)	Stone powder (%)
L	0.16~5	3.60	1350	850	9.02	0.11	—
M	0.16~5	2.82	2730	2320	0.70	2.45	5.0

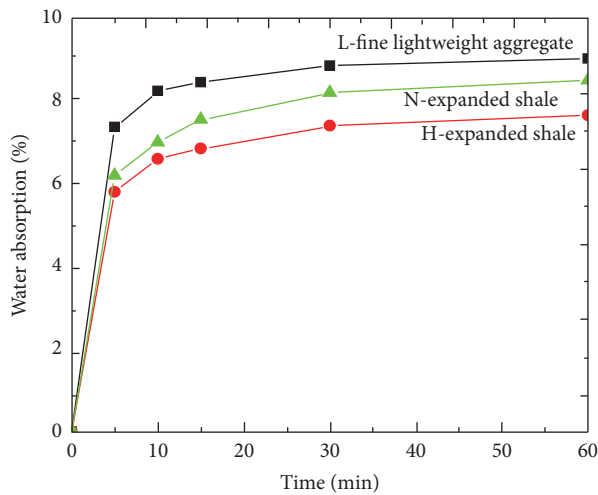


FIGURE 1: Water absorption of lightweight aggregates changing with time.

testing of autogenous shrinkage and drying shrinkage are listed in Table 5, where the double letters of mix number are the identifiers of expanded shale and sand; the following digits represent W/B and ρ_f .

The mix proportion of SFRLAC was designed in accordance with the specifications in China Standard JGJ 51 [19], where the absolute volume method was selected. For all mixes, the dosages of cement and fly ash were 440 kg/m³ and 110 kg/m³; the dosage of water reducer was 5.5% cement.

2.3. Test Methods. From Figure 1, we can know that the water absorption of lightweight sand at 5 min reached 81.7% at 1 hour; the water absorption of ordinary and high-strength expanded shales at 10 min reached 82.4% and 86.3% at 1 hour. Therefore, the lightweight sand was prewetted for 5 min; the expanded shales were prewetted for 10 min, before they were put into concrete mixer. The dosage of prewetted water was calculated by the water absorption at 1 hour.

Test for mix slumps was in accordance with the specification of China Standard GB/T50080 [39], which is identical to British Standard BS EN 12350-2-2009 [40].

The apparent density of SFRLAC was measured in accordance with the specification of China Standard JGJ51 [19]. Three cubes were used as a group for each SFRLAC. They were dried to be a steady weight in drying box at (105~110)°C, and then the apparent density was gotten from the weight divided by the volume of cube.

The cubic compressive strength at 28 d of each group was tested by using the cubes in dimension of 150 mm; each group had three cubes. The cubes were tested on YE-2000A hydraulic compression machine for compressive strength of SFRLAC in accordance with the specifications of China Standard GB/T50081 [41], which is identical to British Standard BS EN 12390-3-2009 [42].

The shrinkage of SFRLAC was measured in accordance with the specification of China Standards GB/T50082 [43], JG/T472 [44], and CECS 13:2009 [45]. As listed in Table 6, six groups of SFRLAC were used to study the autogenous shrinkage; each group had two specimens; eight groups of SFRLAC were used to study the drying shrinkage; each group had three specimens. The measuring device for autogenous

TABLE 5: Parameters of shrinkage tests and mix proportion of concrete.

Mix number	W/B	ρ_f (%)	Mix water (kg/m ³)	Expanded shale (kg/m ³)		Sand (kg/m ³)		Shrinkage test	
				N	H	L	M	Autogenous	Dry
NL0.30/0.8	0.30	0.8	134.8	482.5	0	368.7	0	√	√
NM0.30/0.8	0.30	0.8	134.8	482.5	0	0	745.6	√	√
HM0.30/0.8	0.30	0.8	134.8	0	533.1	0	745.6	√	√
HL0.30/0.4	0.30	0.4	134.8	0	542.2	370.9	0		√
HL0.30/0.8	0.30	0.8	134.8	0	533.0	368.7	0	√	√
HL0.30/1.2	0.30	1.2	134.8	0	523.9	366.4	0		√
HL0.30/1.6	0.30	1.6	134.8	0	514.8	364.1	0		√
HL0.30/2.0	0.30	2.0	134.8	0	505.6	361.9	0		√
HL0.35/0.8	0.35	0.8	157.2	0	514.2	355.9	0	√	
HL0.25/0.8	0.25	0.8	112.3	0	551.8	381.4	0	√	

TABLE 6: Test results of mix slump and apparent density of SFRLAC.

Mix number	Slump (mm)	Apparent density (kg/m ³)		Cubic compressive strength (MPa)
		Wet	Dry	
HL0.3/0.4	165	1754	1695	47.2
HL0.3/0.8	197	1809	1753	49.3
HL0.3/1.2	170	1842	1784	57.6
HL0.3/1.6	98	1843	1787	60.9
HL0.3/2.0	46	1919	1843	64.8
HL0.25/0.8	35	1820	1783	59.3
HL0.35/0.8	175	1796	1696	47.8
HM0.3/0.8	85	2069	1946	51.7
NL0.3/0.8	150	1682	1651	45.0
NM0.3/0.8	75	2000	1869	54.1

shrinkage is shown in Figure 2; the specimen is $\text{Ø}150 \text{ mm} \times 450 \text{ mm}$ cylinder. Two micrometer gauges were fixed symmetrically on the specimen accompanying the copper rods by using the embedded gaging heads with standard datum length of 250 mm. The specimens were placed in the standard curing room with $(20 \pm 2)^\circ\text{C}$ temperature and $(65 \pm 5)\%$ RH. The cast surface was covered by wet cloth. After cast for 12 hours, they were demolded and closely wrapped with polypropylene plastic film. The measuring started at 24 hours after specimen cast.

The prisms in dimension of $100 \text{ mm} \times 100 \text{ mm} \times 550 \text{ mm}$ were used to measure the drying shrinkage. The copper ends were embedded at specimen ends along the longitudinal centroidal axis. The prisms were demolded after casting for 12 hours and placed into the standard curing box shown in Figure 3(a) with $(20 \pm 2)^\circ\text{C}$ temperature and $(60 \pm 5)\%$ RH. The length comparator shown in Figure 3(b) was used to measure the specimen length due to drying shrinkage. The measuring started at 24 hours after specimen cast.

3. Results and Analysis

3.1. Mix Workability. Test results of mix slump are listed in Table 6. As tests reported [37], the mix slump tended to reduce with the increase of volume fraction of steel fiber. This is mainly due to the bridging effect of steel fiber;

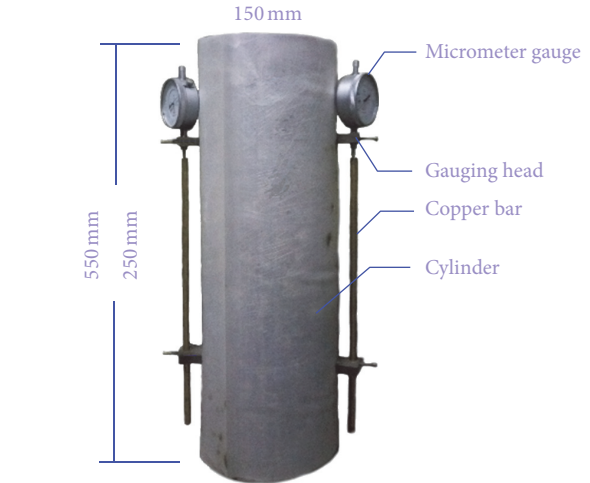


FIGURE 2: Measuring device for autogenous deformation.

the mix flowability increased normally when the mix was vibrated. The mix slump was affected by water-to-binder ratio obviously; the mix with $W/B = 0.25$ did not satisfy the requirement of flowing concrete. Meanwhile, the mixes with manufactured sand had lower slump; this is reasonable because of the peculiarity of manufactured sand with rough

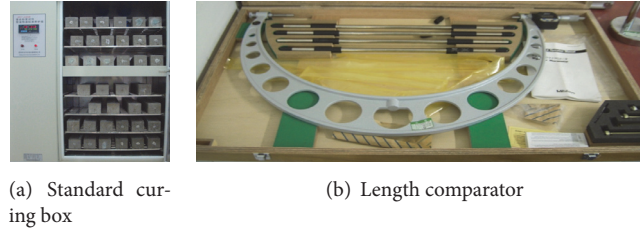


FIGURE 3: Devices for drying shrinkage of specimen.

surface, corner angles, and stone powder [34, 38]. Compared with the mix with H-expanded shale, the mix with N-expanded shale had lower slump. This is because of the larger specific surface area of N-expanded shale with lower density.

3.2. Apparent Density and Compressive Strength. As can be seen from Table 6, due to the high density of steel fiber and design by the absolute volume method, the apparent density of SFRLAC increased with the volume fraction of steel fiber. With the 0.4% increment of volume fraction of steel fiber, the apparent density increased by 1~3% with an average of 2.2%; however the dry apparent density of SFRLAC with lightweight sand was lower than 1850 kg/m³. With the increase of *W/B*, the density of SFRLAC reduced somewhat. The density of SFRLAC with manufactured sand was heavy; fortunately it was also within the specified range of LAC less than 1950 kg/m³ [19].

As tests reported [37], the compressive strength of SFRLAC increased with the volume fraction of steel fiber and decreased with the increase of *W/B*. SFRLAC with manufactured sand had higher compressive strength than that with lightweight sand.

3.3. Autogenous Shrinkage. Test results of autogenous shrinkage of SFRLAC for up to 270 days are listed in Table 7 and shown in Figure 4. As can be seen in this table and figure, the development of autogenous shrinkage of SFRLAC was fast within 28 days and tended to be steady after 90 days. For the SFRLAC with H-expanded shale and L-fine aggregate, the autogenous shrinkage grew slowly with the increasing *W/B*, especially at early age within 28 days; this is because of the cement hydration water supplied by sufficient free water in pores of SFRLAC with larger *W/B*, resulting in the moist pores and capillaries with less pore shrinkage stress. With the same *W/B* and L-fine lightweight aggregate, the autogenous shrinkage of SFRLAC with N-expanded shale developed fast within 28 days and was overall larger than that of SFRLAC with H-expanded shale; this is mainly due to the less compressive strength of N-expanded shale resulting from the weaker particle soundness, resulting in the bad resisting to the shrinkage deformation. Compared to SFRLAC mixed with L-fine lightweight aggregate, SFRLAC mixed with manufactured sand (M-sand) had smaller autogenous shrinkage; this may be due to the higher particle soundness of M-sand filed into the pores of expanded shales to constrain the autogenous deformation and the better interfacial bond property between cement paste and particles

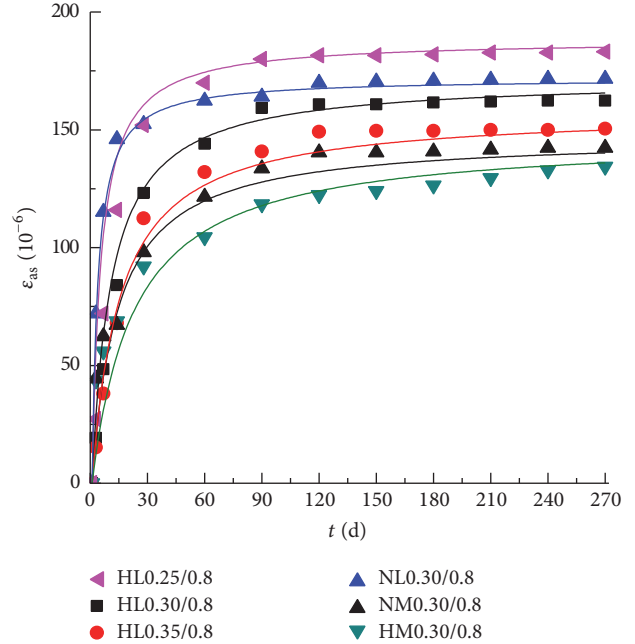


FIGURE 4: Autogenous shrinkage of SFRLAC.

of manufactured sand [5, 38]; all of these are beneficial to reduce the autogenous shrinkage of SFRLAC.

Based on the statistical analysis of test data, the regularity of autogenous shrinkage of SFRLAC can be expressed well as a series of hyperbola:

$$\begin{aligned} \epsilon_{as}(t, t_s) &= \frac{360(t - t_s) \times 10^{-6}}{52.5(\alpha_1 \beta_1 \cdot 4.68(W/B) - 1) + (1 + \alpha_2 \beta_2 \cdot 3.65(W/B))(t - t_s)} \end{aligned} \quad (1)$$

where $\epsilon_{as}(t, t_s)$ is the autogenous shrinkage of SFRLAC at *t* age and *t_s* is the initial age for the testing of autogenous shrinkage, here taken as 1 day after molding. α_1 (α_2) and β_1 (β_2) are the shape factors related to coarse aggregate and fine aggregate, respectively; they are listed in Table 8.

The comparison of formula (1) with test results is also shown in Figure 4, which fitted better with correlation coefficient greater than 0.90.

From formula (1), it can be concluded that *W/B* is a main factor influencing not only the development rate at early age, but also the later developing state of autogenous shrinkage. As can be seen from Table 8, the effects of

TABLE 7: Test results of autogenous shrinkage of SFRLAC.

Mix number	Curing age (days)												
	1	3	7	14	28	60	90	120	150	180	210	240	270
HL0.25/0.8	0	27	72	116	152	170	180	182	182	182	183	183	183
HL0.30/0.8	0	19	48	84	123	144	159	161	161	162	162	162	162
HL0.35/0.8	0	15	38	68	112	132	141	149	150	150	150	150	150
NL0.30/0.8	0	72	115	146	152	162	164	170	170	171	171	172	172
HM0.30/0.8	0	44	56	69	92	104	118	122	124	126	130	133	134
NM0.30/0.8	0	44	62	67	98	121	134	140	140	141	142	142	142

TABLE 8: Values of influencing factors in formula (1).

Aggregate type	Coarse aggregate		Fine aggregate	
	H	N	L	M
α_1 (α_2)	1.0 (1.0)	0.8 (1.0)	—	—
β_1 (β_2)	—	—	1.0 (1.0)	1.45 (1.32)

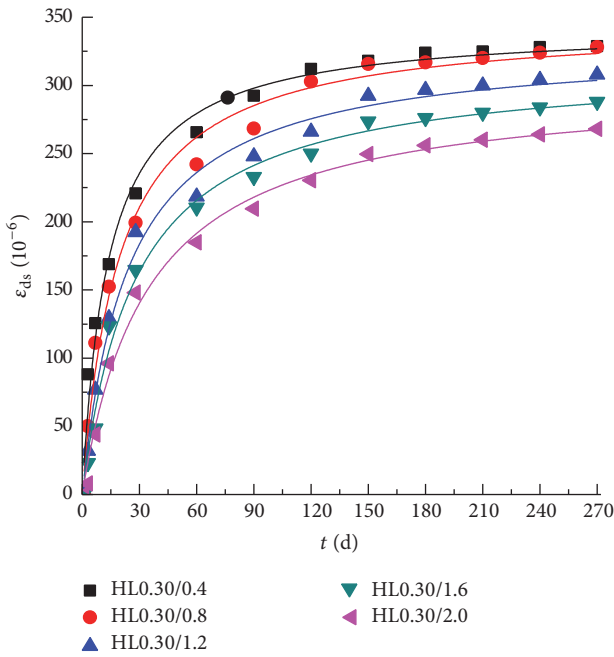


FIGURE 5: Drying shrinkage of SFRLAC with different volume fraction of steel fiber.

different type of aggregate on the autogenous shrinkage of SFRLAC are well reflected by the changes of influencing factors. Under the same condition of other parameters, and compared to the SFRLAC with H-expanded shale and L-fine lightweight aggregate, N-expanded shale increases the development of autogenous shrinkage at early age; M-sand decreases the development rate at early age but prolongs the later developing stage.

3.4. Drying Shrinkage. Test results of drying shrinkage of SFRLAC for up to 270 days are listed in Table 9. As can be seen in this table and Figure 5, the development of drying shrinkage of SFRLAC was slowed down with the increasing volume

fraction of steel fiber. The three-dimensional distribution of steel fibers in concrete builds the frame constraining the shrinkage deformation of concrete; this effect will be stronger with the increasing volume fraction of steel fiber due to the better and better net structure bridged among steel fibers. As the large elastic modulus and tensile strength of steel fibers, the constraining effects of steel fiber on the drying shrinkage of SFRLAC were obvious.

Based on the statistical analysis of test data, the regularity of drying shrinkage of SFRLAC with different volume fraction of steel fiber can be expressed as a series of hyperbola:

$$\varepsilon_{ds}(t, t_s) = \frac{a(t - t_s)}{b + (t - t_s)} \times 10^{-6}, \quad (2)$$

where $\varepsilon_{ds}(t, t_s)$ is the drying shrinkage of SFRLAC at t age and t_s is the initial age for the testing of autogenous shrinkage, here taken as 1 day after molding. a and b are the shape factors related to the volume fraction of steel fiber.

From formula (2), the shape factors a and b can be obtained by the fitting analysis of test data shown in Figure 5. After that, the linear relation of them with volume fraction of steel fiber can be obtained as follows and is shown in Figure 6:

$$a = 5(73.4 - 5.7\rho_f), \quad (3)$$

$$b = 8.91 + 12.53\rho_f. \quad (4)$$

Combined with formula (2), factor a decreases and b increases with the increase of volume fraction of steel fiber. This means that the later drying shrinkage will be reduced and the development of drying shrinkage will be slowed down by the strong restraint effect of steel fibers, respectively. The comparison of formula (2) with test results of SFRLAC with different volume fraction of steel fiber is drawn in Figure 7, which fitted better with correlation coefficient greater than 0.90.

Similar to the development of autogenous shrinkage, with the same water-to-binder ratio and L-fine lightweight aggregate, the drying shrinkage of SFRLAC with N-expanded shale developed fast within 28 days and was overall greater than that of SFRLAC with H-expanded shale. This showed that the constraining effect of steel fibers on shrinkage deformation of SFRLAC could not change the inherent shrinkage of base LAC formed by cement paste and aggregate. Compared to SFRLAC mixed with L-fine lightweight aggregate, SFRLAC mixed with manufactured sand (M-sand) had greater drying

TABLE 9: Test results of drying shrinkage of SFRLAC.

Mix number	Curing age (days)												
	1	3	7	14	28	60	90	120	150	180	210	240	270
HL0.30/0.4	0	88	126	169	221	266	292	312	318	320	325	328	329
HL0.30/0.8	0	50	111	152	199	242	268	303	316	317	320	324	328
HL0.30/1.2	0	32	77	129	192	218	248	266	292	297	300	304	308
HL0.30/1.6	0	23	48	123	165	210	233	250	274	276	280	284	288
HL0.30/2.0	0	8	44	96	148	185	210	230	250	256	260	264	268
NL0.30/0.8	0	109	124	184	225	272	298	323	343	344	345	345	348
HM0.30/0.8	0	84	137	202	283	329	355	376	382	392	400	400	400
NM0.30/0.8	0	129	257	325	361	408	436	464	480	484	488	496	505

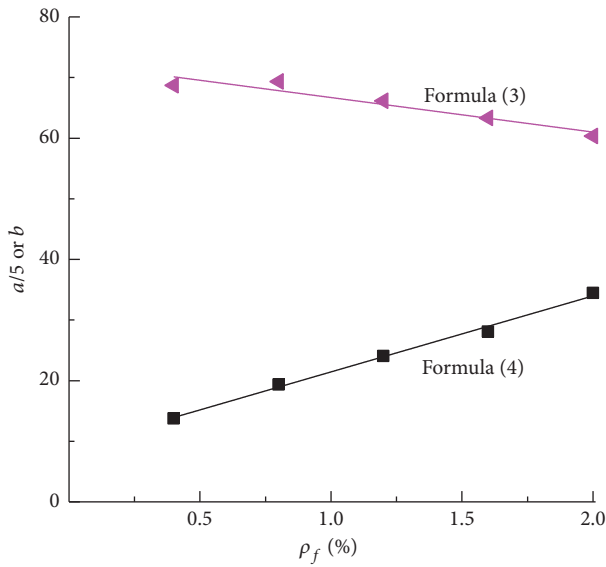


FIGURE 6: Relation of shape factors a and b with volume fraction of steel fiber.

shrinkage. This is because of the larger water absorption of L-fine lightweight aggregate leading to the beneficial internal curing for cement hydration. In this case, the beneficial effects such as the rigid particle of M-sand filling into the pores of expanded shales to constrain the autogenous deformation and the better interfacial bond property between cement paste and particles of M-sand become secondary.

Based on the statistical analysis of test data, the regularity of drying shrinkage of SFRLAC with different aggregates can also be expressed as a series of hyperbola. On the basis of formula (2), it is

$$\epsilon_{ds}(t, t_s) = \frac{\alpha a (t - t_s)}{\beta b + (t - t_s)} \times 10^{-6}, \quad (5)$$

where α and β are the influencing factors related to coarse aggregate and fine aggregate.

Results of statistical analysis for values of influencing factors in formula (5) are listed in Table 10. The comparisons of test data with computation of formula (5) are shown in Figure 8. As can be seen from Table 10, the values of influencing factors α and β for SFRLAC with N-expanded

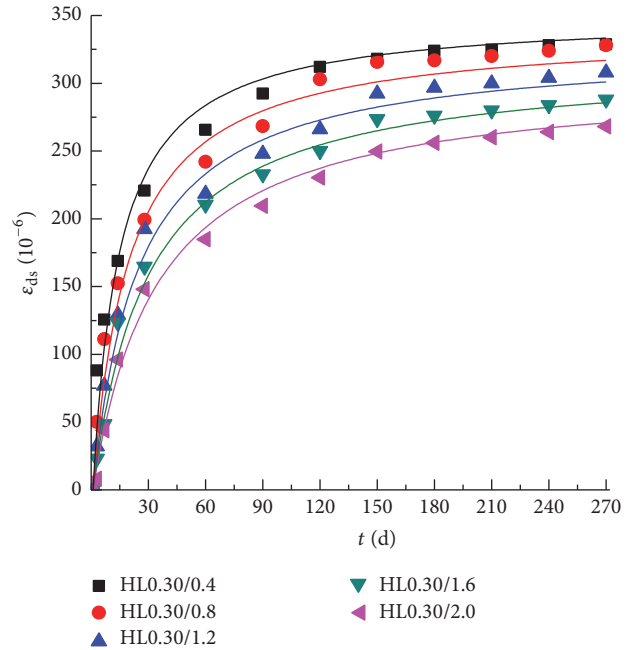


FIGURE 7: Comparison of test data with computation of formula (2).

TABLE 10: Values of influencing factors in formula (5).

Aggregate type	Coarse aggregate * fine aggregate			
	H * L	N * L	H * M	N * M
α	1.0	1.04	1.22	$1.45 > 1.04 \times 1.22 = 1.27$
β	1.0	0.71	0.77	$0.45 < 0.71 \times 0.77 = 0.55$

shale/M-sand are not equal to the product of those for SFRLAC, respectively, with N-expanded shale/L-fine lightweight aggregate and with H-expanded shale/M-sand. This means that the influences of expanded shale and fine aggregate (sand) on drying shrinkage of SFRLAC were correlated. In this study, the drying shrinkage of SFRLAC with N-expanded shale and M-sand was largest.

4. Conclusions

From this study, the main conclusions can be given as follows.

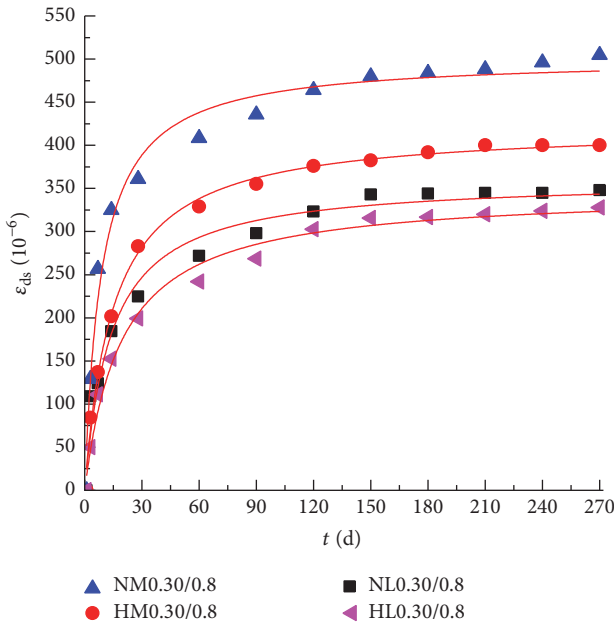


FIGURE 8: Comparison of test data with computation of formula (5).

(1) The mix slump was affected by water-to-binder ratio obviously and tended to reduce with the increase of volume fraction of steel fiber. Mixes with N-expanded shale or manufactured sand had lower slump.

(2) The apparent density of SFRLAC increased with the volume fraction of steel fiber and reduced somewhat with the increase of W/B ; however it was less than 1850 kg/m^3 or 1950 kg/m^3 by using lightweight sand or manufactured sand, respectively. The compressive strength of SFRLAC increased with the volume fraction of steel fiber and decreased with the increasing W/B , while it was higher with manufactured sand than that with lightweight sand.

(3) Test results of autogenous shrinkage of SFRLAC for up to 270 days are given out. The development of autogenous shrinkage of SFRLAC was fast within 28 days and tended to be steady after 90 days. The autogenous shrinkage of SFRLAC with H-expanded shale and L-fine aggregate grew slowly with the increasing W/B , especially at early age within 28 days. With lower compressive strength than that of H-expanded shale, N-expanded shale resulted in the fast development within 28 days and overall greater autogenous shrinkage of SFRLAC. However, L-fine lightweight aggregate led to greater autogenous shrinkage than manufactured sand in SFRLAC.

Based on the test data, the regularity of autogenous shrinkage of SFRLAC can be expressed well as a series of hyperbola, in which the effects of W/B , coarse aggregate, and fine aggregate are independently qualified on the development rate at early age and the later developing state of autogenous shrinkage.

(4) Test results of drying shrinkage of SFRLAC for up to 270 days are presented. The later drying shrinkage was reduced and the development of drying shrinkage was slowed down with the increasing volume fraction of steel fiber obviously. Similar to the development of autogenous

shrinkage, N-expanded shale leads to the fast development within 28 days and overall greater drying shrinkage than H-expanded shale in SFRLAC. But the internal curing of L-fine lightweight aggregate was more beneficial to reduce the drying shrinkage compared with manufactured sand in SFRLAC.

Based on the test data, the regularity of drying shrinkage of SFRLAC can be also expressed as a series of hyperbola in which the shape factors are linear with the volume fraction of steel fiber, and the influencing factors of coarse aggregate and fine aggregate are qualified. The values of influencing factors show that the effects of these two expanded shales, fine lightweight aggregate and manufactured sand, on drying shrinkage of SFRLAC were correlated. In this study, the drying shrinkage of SFRLAC with N-expanded shale and M-sand was largest.

Competing Interests

The authors declare that they have no competing interests.

Acknowledgments

This study was financially supported by the Science and Technology Innovation Team of Eco-Building Material and Structural Engineering in the University of Henan Province, China (13IRTSTHN002), and the Key Research Project of University in Henan Province, China (16A560024).

References

- [1] ACI Committee 209, Prediction of creep, shrinkage and temperature effects in concrete structures, ACI, 209R: Manual of concrete practice, Part 1, 1992.
- [2] GB 50010-2010, *Code for Design of Concrete Structures*, China Building Industry Press, Beijing, China, 2010.
- [3] EN, "Eurocode 2: design of concrete structures—part 1.1: general rules and rules for buildings," EN 1992-1-1, CEN, Brussels, Belgium, 2004.
- [4] CEB-FIP Model Code 2010-Fib Bulletin 55, First Complete Draft, Vol. 1, Fib-International Federation for Structural Concrete, Lausanne, Switzerland, 2010.
- [5] F. L. Li, C. J. Liu, L. Y. Pan, and C. Y. Li, *Machine-Made Sand Concrete*, China Water Power Press, Beijing, China, 2013.
- [6] S. Weber and H. W. Reinhardt, "New generation of high performance concrete: concrete with autogeneous curing," *Advanced Cement Based Materials*, vol. 6, no. 2, pp. 59–68, 1997.
- [7] T. Merikallio, R. Mannonen, and V. Penttala, "Drying of lightweight concrete produced from crushed expanded clay aggregates," *Cement and Concrete Research*, vol. 26, no. 9, pp. 1423–1433, 1996.
- [8] B. Akcay and M. A. Tasdemir, "Effects of distribution of lightweight aggregates on internal curing of concrete," *Cement and Concrete Composites*, vol. 32, no. 8, pp. 611–616, 2010.
- [9] M. Goliias, J. Castro, and J. Weiss, "The influence of the initial moisture content of lightweight aggregate on internal curing," *Construction and Building Materials*, vol. 35, pp. 52–62, 2012.
- [10] A. Bentur, S.-I. Igarashi, and K. Kovler, "Prevention of autogenous shrinkage in high-strength concrete by internal curing using wet lightweight aggregates," *Cement and Concrete Research*, vol. 31, no. 11, pp. 1587–1591, 2001.

- [11] T. Ji, D.-D. Zheng, X.-F. Chen, X.-J. Lin, and H.-C. Wu, "Effect of prewetting degree of ceramsite on the early-age autogenous shrinkage of lightweight aggregate concrete," *Construction and Building Materials*, vol. 98, pp. 102–111, 2015.
- [12] D. Cusson and T. Hoogveen, "Internal curing of high-performance concrete with pre-soaked fine lightweight aggregate for prevention of autogenous shrinkage cracking," *Cement and Concrete Research*, vol. 38, no. 6, pp. 757–765, 2008.
- [13] S. Ghourchian, M. Wyrzykowski, P. Lura, M. Shekarchi, and B. Ahmadi, "An investigation on the use of zeolite aggregates for internal curing of concrete," *Construction and Building Materials*, vol. 40, pp. 135–144, 2013.
- [14] Y. Wei, Y. Xiang, and Q. Zhang, "Internal curing efficiency of prewettted LWFAs on concrete humidity and autogenous shrinkage development," *Journal of Materials in Civil Engineering*, vol. 26, no. 5, pp. 947–954, 2014.
- [15] S.-D. Hwang, K. H. Khayat, and D. Youssef, "Effect of moist curing and use of lightweight sand on characteristics of high-performance concrete," *Materials and Structures*, vol. 46, no. 1-2, pp. 35–46, 2013.
- [16] J. Zhang, Y. D. Han, Y. Gao, and Y. Luosun, "Integrative study on the effect of internal curing on autogenous and drying shrinkage of high-strength concrete," *Drying Technology*, vol. 31, no. 5, pp. 565–575, 2013.
- [17] J. Zhang, J. H. Wang, and Y. D. Han, "Simulation of moisture field of concrete with pre-soaked lightweight aggregate addition," *Construction and Building Materials*, vol. 96, pp. 599–614, 2015.
- [18] I. Maruyama, M. Kanematsu, T. Noguchi, H. Iikura, A. Teramoto, and H. Hayano, "Evaluation of water transfer from saturated lightweight aggregate to cement paste matrix by neutron radiography," *Nuclear Instruments and Methods in Physics Research Section A: Accelerators, Spectrometers, Detectors and Associated Equipment*, vol. 605, no. 1-2, pp. 159–162, 2009.
- [19] JGJ, "Technical specification for lightweight concrete," JGJ 51-2002, China Building Industry Press, Beijing, China, 2002.
- [20] H. Sun, L. Ye, J. Ding, and Y. Guo, "Shrinkage and creep of high-strength lightweight aggregate concrete," *Journal of Tsinghua University*, vol. 47, no. 6, pp. 765–767, 2007.
- [21] P.-J. Song, J.-T. Ding, and Y.-S. Guo, "Shrinkage of high strength lightweight aggregate concrete and factors influencing it," *Journal of Building Materials*, vol. 7, no. 2, pp. 138–144, 2004.
- [22] A. Nilsen and P. C. Aitcin, "Properties of high-strength concrete containing light-, normal-, and heavyweight aggregate," *Cement, Concrete and Aggregates*, vol. 14, no. 1, pp. 8–12, 1992.
- [23] A. Terzić, L. Pezo, V. Mitić, and Z. Radojević, "Artificial fly ash based aggregates properties influence on lightweight concrete performances," *Ceramics International*, vol. 41, no. 2, pp. 2714–2726, 2015.
- [24] J. A. Bogas, R. Nogueira, and N. G. Almeida, "Influence of mineral additions and different compositional parameters on the shrinkage of structural expanded clay lightweight concrete," *Materials and Design*, vol. 56, pp. 1039–1048, 2014.
- [25] P. Shafiqh, H. Ghafari, H. B. Mahmud, and M. Z. Jumaat, "A comparison study of the mechanical properties and drying shrinkage of oil palm shell and expanded clay lightweight aggregate concretes," *Materials and Design*, vol. 60, pp. 320–327, 2014.
- [26] N. Kabay and F. Aköz, "Effect of prewetting methods on some fresh and hardened properties of concrete with pumice aggregate," *Cement and Concrete Composites*, vol. 34, no. 4, pp. 503–507, 2012.
- [27] A. I. M. Ismail, M. S. Elmaghraby, and H. S. Mekky, "Engineering properties, microstructure and strength development of lightweight concrete containing pumice aggregates," *Geotechnical and Geological Engineering*, vol. 31, no. 5, pp. 1465–1476, 2013.
- [28] H. Costa, E. Júlio, and J. Loureno, "New approach for shrinkage prediction of high-strength lightweight aggregate concrete," *Construction and Building Materials*, vol. 35, pp. 84–91, 2012.
- [29] E. Güneyisi, M. Gesoğlu, A. Mohamadameen, R. Alzebaree, Z. Algin, and K. Mermerdaş, "Enhancement of shrinkage behavior of lightweight aggregate concretes by shrinkage reducing admixture and fiber reinforcement," *Construction and Building Materials*, vol. 54, pp. 91–98, 2014.
- [30] L. Domagała, "Modification of properties of structural lightweight concrete with steel fibres," *Journal of Civil Engineering and Management*, vol. 17, no. 1, pp. 36–44, 2011.
- [31] O. Kayali, M. N. Haque, and B. Zhu, "Drying shrinkage of fibre-reinforced lightweight aggregate concrete containing fly ash," *Cement and Concrete Research*, vol. 29, no. 11, pp. 1835–1840, 1999.
- [32] B. Chen and J. Liu, "Contribution of hybrid fibers on the properties of the high-strength lightweight concrete having good workability," *Cement and Concrete Research*, vol. 35, no. 5, pp. 913–917, 2005.
- [33] B. Chen and J. Liu, "Properties of lightweight expanded polystyrene concrete reinforced with steel fiber," *Cement and Concrete Research*, vol. 34, no. 7, pp. 1259–1263, 2004.
- [34] X. X. Ding, C. Y. Li, Y. Y. Xu, F. L. Li, and S. B. Zhao, "Experimental study on long-term compressive strength of concrete with manufactured sand," *Construction and Building Materials*, no. 108, pp. 67–73, 2016.
- [35] SAC, "Common Portland cement," GB 175-2007, Standardization Administration of China, Beijing, China, 2007.
- [36] GB/T, "Test method for lightweight aggregate," GB/T 17431.2-2010, China Standard Press, Beijing, China, 2010.
- [37] Z. Shen, M. H. Chen, M. S. Zhao, and X. K. Li, "Experimental study, "Experimental study on tensile properties of steel fiber reinforced lightweight-aggregate fly-ash flowable concrete," in *Architectural Engineering and New Materials*, pp. 1–8, DESTech, 2015.
- [38] S. Zhao, Y. Xu, and C. Li, "Study on workability of plastic fresh concrete with machine-made sand," in *Proceedings of the International Conference on Transportation, Mechanical, and Electrical Engineering (TMEE '11)*, pp. 2013–2016, Changchun, China, December 2011.
- [39] GB/T, "Standard for test method of performance on ordinary fresh concrete," GB/T 50080-2002, China Building Industry Press, Beijing, China, 2002.
- [40] BS EN, "Testing fresh concrete—slump-test," BS EN 12350-2-2009, 2009.
- [41] CABP, "Standard for test method of mechanical properties on ordinary concrete," GB/T 50081-2002, China Architecture and Building Press, Beijing, China, 2002.
- [42] "Testing hardened concrete—compressive strength of test specimens," BS EN 12390-3-2009, 2009.
- [43] GB/T, "Standard for test method of long-term performance and durability of ordinary concrete," GB/T 50082-2009, China Building Industry Press, Beijing, China, 2010.
- [44] "Steel fiber reinforced concrete," JG/T 472-2015, China Building Industry Press, Beijing, China, 2015.
- [45] CECS, "Standard test methods for fiber reinforced concrete," CECS 13:2009, China Plan Press, Beijing, China, 2010.

Research Article

Carbon Nanotubes in Cementitious Composites: Dispersion, Implementation, and Influence on Mechanical Characteristics

Tomas Jarolim, Martin Labaj, Rudolf Hela, and Kamila Michnova

Faculty of Civil Engineering, Institute of Technology of Building Materials and Components, Brno University of Technology, Veveri 331/95, 602 00 Brno, Czech Republic

Correspondence should be addressed to Tomas Jarolim; jarolim.t@fce.vutbr.cz

Received 18 February 2016; Revised 23 June 2016; Accepted 14 July 2016

Academic Editor: Gonzalo Martínez-Barrera

Copyright © 2016 Tomas Jarolim et al. This is an open access article distributed under the Creative Commons Attribution License, which permits unrestricted use, distribution, and reproduction in any medium, provided the original work is properly cited.

For effective utilization of nanoparticles in cementitious composite materials, their perfect dispersion is necessary. Appropriate quantity of ultrasonic energy (US energy), as well as usage of proper and compatible surfactant, is a prerequisite for carbon nanotubes' (CNT) suitable deagglomeration. US energy was supplied by Bandelin Sonopuls HD 3200 ultrasonic homogenizer. Influence of US energy's amount on CNT's dispersion in aqueous medium was monitored in two steps: at first roughly by an optical microscope and in the next step precisely by the measurement of absorbance via UV/Vis spectrophotometry. After the appropriate amount of US energy was found, cement mortars with CNT were prepared and tested. Their physical and mechanical properties were examined and compared to the reference specimens.

1. Introduction

Nowadays, there are not many new raw materials which could be incorporated into cementitious materials (e.g., concrete) to increase their strength characteristics and durability and decrease their carbon footprint [1–4]. Due to technological progress in a wide spectrum of scientific fields (chemistry, electrical engineering, IT, medicine, optics, etc.), we can now produce nanoparticles using the bottom-up approach. This method means a breakthrough in material engineering because it makes materials' production with accurately defined parameters (and rather interesting ones) possible. Therefore, nanotechnology is one of the fastest developing scientific fields. CNT can be used as a matrix of reinforcement in many industrial sectors like metallurgy [5, 6], polymer industry [7, 8], and, of course, concrete industry [9, 10]. There are other nanomaterials with potentially interesting effects on cementitious composites, for example, nanosilica. Many experiments with nanosilica were performed. Their results confirm that implementation of nanosilica to the cement matrix has positive impact to the cement composites' mechanical characteristics [11, 12]. However, this paper is focused mainly on CNT's implementation into the cementitious composites as a scattered reinforcement of cement

matrix. In the beginning, problems regarding dispersion's stability and potential toxicity as well as financial availability need to be addressed [13, 14].

2. Introduction to the Issue of Carbon Nanotubes

2.1. Carbon Nanotubes (CNT). Carbon nanotubes can be characterized as graphene sheets rolled into a cylindrical tube with a length of 1 to 100 μm . These structures were initially identified in 1991 by Japanese scientist Iijima [15]. Carbon nanotubes can be produced using several methods, for example, electric arc discharge, laser ablation, and chemical vapor deposition. The last mentioned one is currently the most used method. Carbon nanotubes have very good physical-mechanical properties [16, 17]. According to the number of internal layers, CNT are divided into a single-walled carbon nanotubes (SWCNT) and multiwalled carbon nanotubes (MWCNT). SWCNT typically contain one graphene sheet and have an outer diameter of approximately 5–20 nm. MWCNT have an inner diameter of approximately 1.5–15 nm and an outer diameter of up to 100 nm. CNT have exceptional properties which give them potential to become as important

for the development of industry as the discovery of the steam engine. Their typical properties are elastic modulus of approximately 1 TPa, tensile strength in a range of 11–63 GPa, volumetric weight of about $1300 \text{ kg}\cdot\text{m}^{-3}$, and surface area of $70\text{--}400 \text{ m}^2\cdot\text{g}^{-1}$ [18, 19].

2.2. Dispersing Carbon Nanotubes. CNT tends to form bundles; thus, for perfect implementation to the cement matrix, the flawless dispersion and uniform distribution are essential factors [16]. Currently, there are two main approaches for dispersing nanotubes: mechanical methods and chemical methods that modify the surface energy of solids. Mechanical methods include high shear mixing and cavitation, namely, either hydrodynamic cavitation (i.e., cavitation caused by high speed liquid flow) or acoustic/ultrasonic cavitation induced by passing of high energy acoustic waves through liquid medium. Literature mentions the possibility of combining methods for dispersing CNT, for example, ultrasonic method and suitable surfactant. Surface-active substances are capable of preventing carbon nanotubes' reagglomeration after the ultrasonication treatment and make their disentanglement easier as well [20–22]. It is necessary to ensure that the added surfactant does not impact the setting and hardening of concrete or cement mortar. CNT's optimal dispersion is one of the key factors for preparation of enhanced cement based composite materials. CNT possess an enormous surface energy and an extremely high aspect ratio and are attracted to each other with van der Waals forces. These facts result in their strong tendency to form agglomerates/bundles. Bundles reduce the material's overall strength, because they create weak spots in the matrix, in which the initial cracks are developing after loading [23].

A relatively new phenomenon is CNT with surfactants incorporated in their structure. When CNT are dispersed in aqueous medium via ultrasonication, it is important to make sure that the supplied acoustic energy is not exceeded, because otherwise (depending on the CNT's concentration) the structure of graphene sheets could be damaged or even broken. CNT's deformation reduces expected positive impact on physicochemical properties of specimens enhanced with CNT [25, 26].

3. Experimental Part

The main goal of the experiment was to create stable dispersion of CNT, water, and appropriate surfactant and then use it to enhance the cement mortar's properties. Research's structure was designed with consideration of previous experimental work, as well as scientific papers [19–23, 25–27]. The level of CNT's deagglomeration in dispersion was measured via the optical microscope (Jenoptik ProgRes CF) and also (mainly) UV/Vis Spectrophotometer (LAMBDA 1050 UV/Vis/NIR Spectrophotometer made by PerkinElmer). Once the optimal amount of ultrasonic energy was determined, the next step was to incorporate said dispersions to cement mortars and observe the CNT's influence on their flexural and compressive strengths. Mixture of water, CNT, and surfactant was initially homogenized by a magnetic stirrer Variomag Monotherm. Subsequently, the suspension was treated by ultrasonic

TABLE 1: Properties of carbon nanotubes.

Internal diameter	Approximately 5–12 nm
Outer diameter	Approximately 30–50 nm
Length	10–20 μm
Bulk density	$0.22 \text{ g}\cdot\text{cm}^{-3}$
True density	$2.1 \text{ g}\cdot\text{cm}^{-3}$

TABLE 2: OPC's chemical composition [17].

CaO (%)	65.000
SiO ₂ (%)	19.000
Al ₂ O ₃ (%)	4.000
Fe ₂ O ₃ (%)	3.000
MgO (%)	1.000
SO ₃ (%)	3.000
S ^{-II} (%)	0.040
Cl ⁻ (%)	0.051
K ₂ O (%)	0.750
Na ₂ O (%)	0.150
MgO (%)	1.400
Loss on ignition (%)	3.100
Content of insoluble residue (%)	0.700

TABLE 3: Clinker's composition [17].

C ₃ S (%)	67
C ₂ S (%)	11
C ₃ A (%)	7
C ₄ AF (%)	11

homogenizer Badelin Sonopuls HD 3200, which should ensure CNT's flawless disentanglement and distribution. UV/Vis spectroscopy's principle is the measurement of the absorption of electromagnetic radiation of wavelength from about 200 to 800 nm. Measured variable is called absorbance-negative transmittance's logarithm (the ratio of luminous flux passing through the environment and the luminous flux incident on the environment). At zero absorption, the absorbance is zero and vice versa [28].

3.1. Materials. The carbon nanotubes used were supplied by Chinese producer Yurui (Shanghai) Chemical Co., Ltd. These were MWCNT with a purity of more than 95% and were produced by chemical vapor deposition method. For other properties, see Table 1. All information was taken from the supplier's product data sheet.

For CNT's stabilization, naphthalene based superplasticizer was used. As a binder, Ordinary Portland Cement (OPC) class CEM I 42.5 R produced by the Mokra cement plant (HeidelbergCement, Czech Republic) was used. Its composition can be seen in Tables 2 and 3 [29].

CEN (from French *Comité Européen de Normalisation*) standardized quartz sand (with accordance to EN 196-1 [30]) was used; for its particle distribution, see Table 4 [24].

TABLE 4: CEN standardized sand's particle size distribution [24].

Square mesh Size (mm)	Cumulative (%) retained
0.08	99 ± 1
0.16	87 ± 5
0.50	67 ± 5
1.00	33 ± 5
1.60	7 ± 5
2.00	0

TABLE 5: Composition of CNT dispersions.

Component	Dosage (g)
Carbon nanotubes	0.0225
Water	99.0600
Surfactant (naphthalene based superplasticizer)	0.9000

TABLE 6: Material composition of cement mortars with CNT.

Component	Dosage
CNT dispersion (distilled water, MWCNT, surfactant) (g)	225
OPC 42.5 R, Mokra (g)	450
Normalized sand CEN (g)	1350

3.2. *Methods.* The suspension of carbon nanotubes was prepared by mixing all the components (CNT, distilled water and superplasticizer; see in Table 5) while being stirred with a magnetic mixer (600 rpm). The mixture was homogenized for 5 minutes. After 5 minutes of homogenization (and probably partial dispersion), the mixture was transferred to a reaction rosette vessel and ultrasonicated for the total amount of 2000 J/mL of acoustic energy. After each 200 J/mL, a small amount of dispersion was taken as a sample for UV/Vis spectroscopy measurement. Also a drop of dispersion was observed under the optical microscope for bundles presence (or their nonpresence). Those two methods determined the optimal acoustic energy for samples' preparation.

It is important to mention that the sonicated dispersion had to be diluted and the dilution itself is one of the most critical steps because of rapid pH leaps that can lead to CNT's reagglomeration. CNT's dispersion had to be diluted to the required volume of 225 mL for cement mortar samples preparation [19]. Around pH of 7, the shift in particles' zeta potential occurs. This phenomenon leads to dispersion's instability and subsequently results in CNT's reagglomeration [31].

Cement mortar specimens with dimensions of 40 × 40 × 160 mm were casted according to EN 196-1. Cement mortars' material composition is referred to in Table 6 [30]. After 24 hours, the specimens were demolded and placed in a curing environment (20°C, 100% relative humidity).

The specimens' flexural and compressive strengths were tested after 7 and 28 days of curing according to EN 196-1 [30]. Results are discussed below. A small fragment of mortar was taken and prepared for SEM microscopy observation to evaluate the possible presence CNT bundles in the matrix (as can

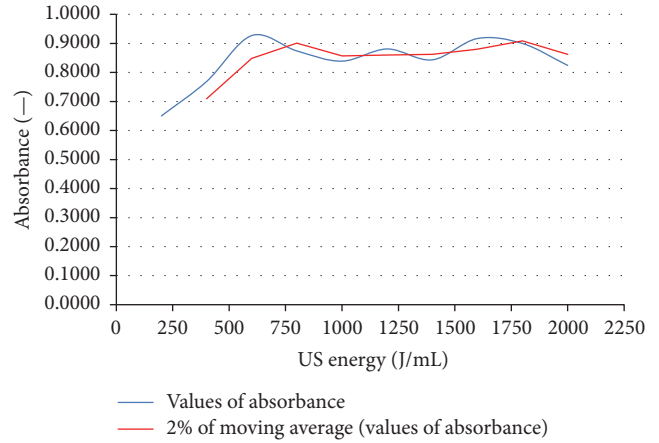


FIGURE 1: Results of absorbance measurement. The optimal value of US energy was determined by finding the curve's inflection point—800 J/mL. At this point, the absorbance (CNT's dispersion) is at its peak value and further ultrasonication is unnecessary.

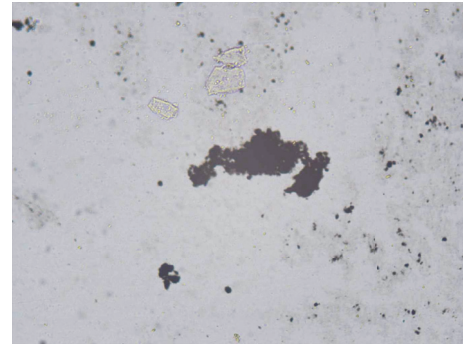


FIGURE 2: Optical microscope image of CNT dispersion after the treatment with 400 J/mL of US energy, magnified 20 times.

be seen in Figures 8(a) and 8(b)). These pictures were taken using Tescan MIRA3 LM scanning electron microscope.

3.3. *Results and Discussion.* Optimal acoustic energy learned from optical microscopy and UV/Vis spectroscopy observation was determined as 800 J/mL as can be seen in Figure 1. The optimal energy was determined by finding the absorbance curve's inflexion point. The absorbance itself represents the quantity of electromagnetic energy absorbed by dispersion. Generally, the darker the suspension, the higher the absorbance. The final dispersion was once more examined via UV/Vis spectroscopy for its absorbance's verification. The moving average trend curve was chosen as the most accurate in this case.

In Figures 2–5, both effectively dispersed nanotubes and bundled ones can be observed. In Figure 2 (400 J/mL of US energy), massive bundles are present. In Figure 3 (800 J/mL of US energy), the well dispersed suspension of nanotubes can be noticed.

As can be seen in Figures 6 and 7, the addition of carbon nanotubes causes an improvement in both flexural and compressive strength in order of percent. In this paper,

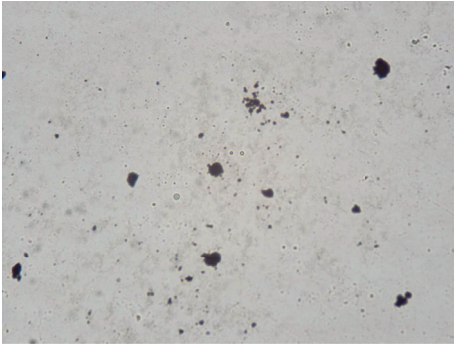


FIGURE 3: Optical microscope image of CNT dispersion after the treatment with 800 J/mL of US energy, magnified 20 times.

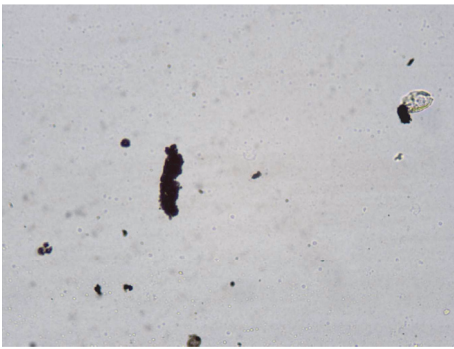


FIGURE 4: Optical microscope image of CNT dispersion after the treatment with 1400 J/mL of US energy, magnified 20 times.

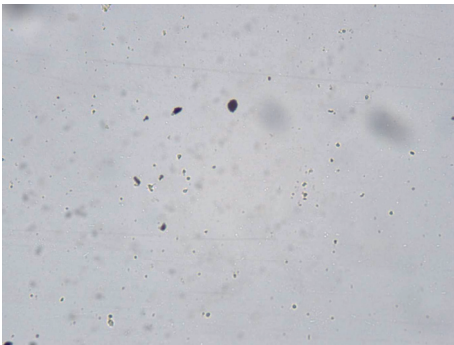


FIGURE 5: Optical microscope image of CNT dispersion after the treatment with 2000 J/mL of US energy, magnified 20 times.

relatively low dosage of CNT was used. The reasoning behind this decision was to prove that even with quantity this low, increase in physicomechanical properties could be achieved, if CNT's deagglomeration is sufficient. The results clearly show that even with 0.005% of CNT (by the weight of cement) it is enough to increase mortar's both flexural and compressive strength. After 7 and 28 days, the 10.4% and 6.1% increase in flexural strength was observed, compared to reference specimens. Compressive strength was increased by 5.5% and 8.6%, respectively.

The reason of strengths (both flexural and compressive) improvement is, according to authors [32–35], the cement

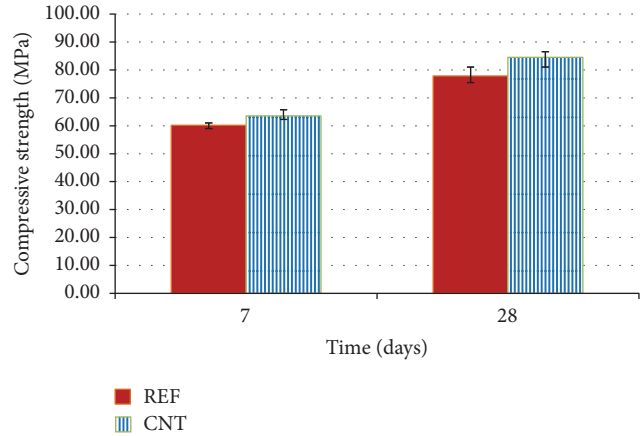


FIGURE 6: Compressive strength of cement mortars with and without CNT after 7 and 28 days. There is obvious increase in mortars' strength with CNT's addition.

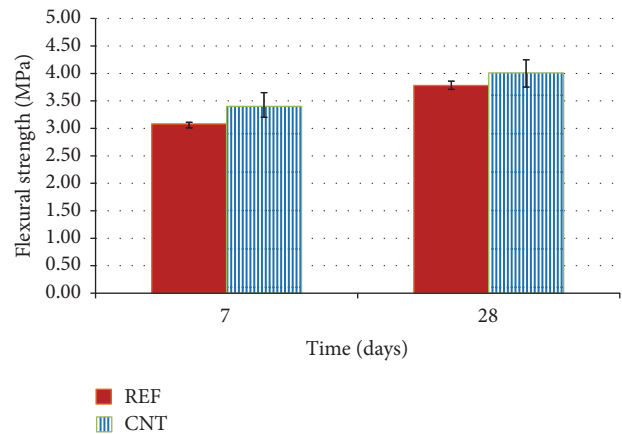


FIGURE 7: Flexural strength of cement mortars with and without CNT after 7 and 28 days. There is obvious increase in mortars' strength with CNT's addition.

matrix's reinforcement with nanotubes. It works on a similar principle, only in macroscale, as reinforcing concrete with steel fibers.

Figures 8(a) and 8(b) show the images of cement mortar's microstructure with CNT addition taken by SEM.

4. Conclusion

As in many industrial fields, nanotechnology is slowly becoming the construction industry's "next big thing." There are many potentially usable nanoparticles, but probably the most promising ones are carbon nanotubes. These extremely small fibers present both benefits and problems, and one of which was examined in this paper, their dispersion and stability:

- (i) With advanced methods like UV/Vis spectroscopy and optical microscopy, the optimal acoustic energy for CNT's effective dispersion was determined, 800 J/mL.

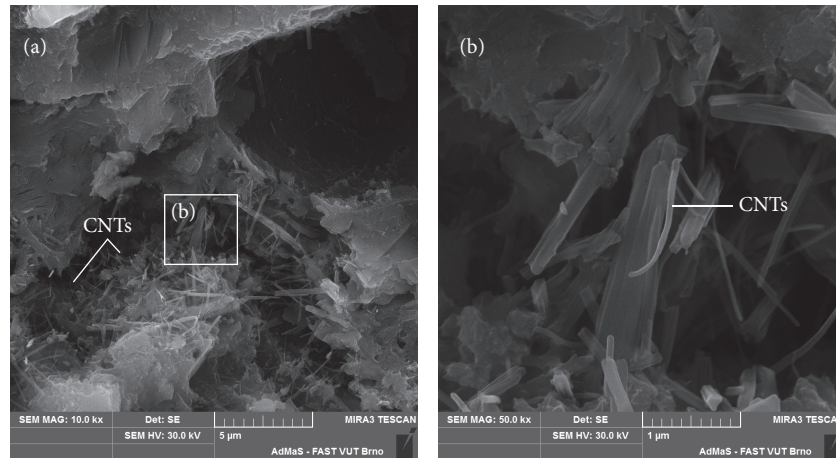


FIGURE 8: (a) SEM images of CNT enhanced cement mortar's microstructure, magnified 10,000 times. (b) SEM images of CNT enhanced cement mortar's microstructure, magnified 50,000 times.

- (ii) The CNT mixture was then added to standardized cement mortar and its effect on mechanical properties was tested after 7 and 28 days, respectively.
- (iii) The increase in observed physicomaterial properties was from 5.5 to 10.4%.
- (iv) An appropriate preparation process of CNT dispersion was specified. The method is, however, not generally applicable. When CNT's parameters (e.g., dimensions, concentration, and purity) change, the whole procedure needs to be repeated [36].

In past decades, research in this area has grown exponentially, and even though we are learning new things every day, there is still plenty of work to do and discoveries to discover.

Competing Interests

The authors declare that there are no competing interests regarding the publication of this paper.

Acknowledgments

This paper has been worked out under Project no. LO1408 "AdMaS UP-Advanced Materials, Structures and Technologies," supported by Ministry of Education, Youth and Sports under the "National Sustainability Program I" and under Project GACR P104/15-23219S "Study of methods of nanoparticles dispersion, determination of conditions for preventing their re-agglomeration for application in cement composites" supported by Czech Science Foundation.

References

- [1] R. Hela, J. Marsalova, and L. Bodnarova, "Fly ashes thermal modification and their utilization in concrete," in *System-Based Vision For Strategic and Creative Design*, F. Bontempi, Ed., vol. 1-3, pp. 1649-1653, 2003.
- [2] L. Bodnarova, T. Jarolim, and R. Hela, "Study of effect of various types of cement on properties of cement pastes," *Advanced Materials Research*, vol. 897, pp. 224-229, 2014.
- [3] A. Karaşin and M. Doğruyol, "An experimental study on strength and durability for utilization of fly ash in concrete mix," *Advances in Materials Science and Engineering*, vol. 2014, Article ID 417514, 6 pages, 2014.
- [4] D. Zhang, S. Shi, C. Wang, X. Yang, L. Guo, and S. Xue, "Preparation of cementitious material using smelting slag and tailings and the solidification and leaching of Pb^{2+} ," *Advances in Materials Science and Engineering*, vol. 2015, Article ID 352567, 7 pages, 2015.
- [5] K. S. Munir, P. Kingshott, and C. Wen, "Carbon nanotube reinforced titanium metal matrix composites prepared by powder metallurgy—a review," *Critical Reviews in Solid State and Materials Sciences*, vol. 40, no. 1, pp. 38-55, 2015.
- [6] L. Jiang, Z. Li, G. Fan, L. Cao, and D. Zhang, "Strong and ductile carbon nanotube/aluminum bulk nanolaminated composites with two-dimensional alignment of carbon nanotubes," *Scripta Materialia*, vol. 66, no. 6, pp. 331-334, 2012.
- [7] B. Arash, Q. Wang, and V. K. Varadan, "Mechanical properties of carbon nanotube/polymer composites," *Scientific Reports*, vol. 4, article 6479, 2014.
- [8] M. Yoonessi, M. Lebroin-Coloïn, D. Scheiman, and M. A. Meador, "Carbon nanotube epoxy nanocomposites: the effects of interfacial modifications on the dynamic mechanical properties of the nanocomposites," *ACS Applied Materials & Interfaces*, vol. 6, no. 19, pp. 16621-16630, 2014.
- [9] P. A. Danoglidis, M. S. Konsta-Gdoutos, E. E. Gdoutos, and S. P. Shah, "Strength, energy absorption capability and self-sensing properties of multifunctional carbon nanotube reinforced mortars," *Construction and Building Materials*, vol. 120, pp. 265-274, 2016.
- [10] S. Parveen, S. Rana, and R. Figueiro, "A review on nano-material dispersion, microstructure, and mechanical properties of carbon nanotube and nanofiber reinforced cementitious composites," *Journal of Nanomaterials*, vol. 2013, Article ID 710175, 19 pages, 2013.
- [11] M. Bastami, M. Baghbadrani, and F. Aslani, "Performance of nano-Silica modified high strength concrete at elevated

- temperatures," *Construction and Building Materials*, vol. 68, pp. 402–408, 2014.
- [12] A. G. Pérez-Luna, A. L. Martínez-Hernández, G. Martínez-Barrera, and C. Velasco-Santos, "Nanoreinforced concrete: effect of gamma-irradiated SiO₂ nanoparticles," *Advanced Materials Letters*, vol. 7, no. 2, pp. 156–162, 2016.
- [13] P. Bartos, *Nanotechnology of Concrete, Recent Developments and Future Perspectives: Nanotechnology in Construction: A Roadmap for Development*, SP-254, American Concrete Institute, Farmington Hills, Mich, USA, 1st edition, 2008.
- [14] F. Sanchez and K. Sobolev, "Nanotechnology in concrete—a review," *Construction and Building Materials*, vol. 24, no. 11, pp. 2060–2071, 2010.
- [15] S. Iijima, "Helical microtubules of graphitic carbon," *Nature*, vol. 354, no. 6348, pp. 56–58, 1991.
- [16] N. M. Mubarak, E. C. Abdullah, N. S. Jayakumara, and J. N. Saha, "An overview on methods for the production of carbon nanotubes," *Journal of Industrial and Engineering Chemistry*, vol. 20, no. 4, pp. 1186–1197, 2014.
- [17] J. Yu, N. Grossiord, C. E. Koning, and J. Loos, "Controlling the dispersion of multi-wall carbon nanotubes in aqueous surfactant solution," *Carbon*, vol. 45, no. 3, pp. 618–623, 2007.
- [18] E. N. Ganesh, "Single walled and multi walled carbon nanotube structure, synthesis and applications," *International Journal of Innovative Technology and Exploring Engineering*, vol. 2, no. 4, pp. 311–320, 2013.
- [19] M. Labaj, *Supervisor: R. Hela [Ph.D. thesis]*, Brno University of Technology, Faculty of Civil Engineering, 2014.
- [20] J. Hilding, E. A. Grulke, Z. G. Zhang, and F. Lockwood, "Dispersion of carbon nanotubes in liquids," *Journal of Dispersion Science and Technology*, vol. 24, no. 1, pp. 1–41, 2003.
- [21] J. B. Bai and A. Allaoui, "Effect of the length and the aggregate size of MWNTs on the improvement efficiency of the mechanical and electrical properties of nanocomposites—experimental investigation," *Composites Part A: Applied Science and Manufacturing*, vol. 34, no. 8, pp. 689–694, 2003.
- [22] S. Azoubel and S. Magdassi, "The formation of carbon nanotube dispersions by high pressure homogenization and their rapid characterization by analytical centrifuge," *Carbon*, vol. 48, no. 12, pp. 3346–3352, 2010.
- [23] F. Collins, J. Lambert, and W. H. Duan, "The influences of admixtures on the dispersion, workability, and strength of carbon nanotube-OPC paste mixtures," *Cement and Concrete Composites*, vol. 34, no. 2, pp. 201–207, 2012.
- [24] Technical certificate of normalized sand CEN. According to EN 196-1 Methods of testing cement—part 1: determination of strength, European Committee for Standardization, 2005.
- [25] O. Mendoza, G. Sierra, and J. I. Tobón, "Influence of super plasticizer and Ca(OH)₂ on the stability of functionalized multi-walled carbon nanotubes dispersions for cement composites applications," *Construction and Building Materials*, vol. 47, pp. 771–778, 2013.
- [26] S. Chuah, Z. Pan, J. G. Sanjayan, C. M. Wang, and W. H. Duan, "Nano reinforced cement and concrete composites and new perspective from graphene oxide," *Construction and Building Materials*, vol. 73, pp. 113–124, 2014.
- [27] T. Jarolím, R. Hela, and M. Labaj, "Influence of the amount of dispersed suspension of carbon nano-tubes on physico-mechanical properties of cement mortar," *Advanced Materials Research*, vol. 1106, pp. 65–68, 2015.
- [28] H. Förster, "UV/VIS spectroscopy," in *Characterization I*, H. G. Karge and J. Weitkamp, Eds., vol. 4 of *Molecular Sieves—Science and Technology*, pp. 337–426, Springer, Berlin, Germany, 2004.
- [29] "Technical certificate of CEM I 42.5 R, Mokra (Heidelberg, Cement Czech Republic)," <http://www.heidelbergcement.cz/cs/cement/volne-lozeny-cement/cemi425r>.
- [30] EN 196-1 Methods of testing cement—Part 1: Determination of strength, European Committee for Standardization, 2005.
- [31] L. Gao, H. Yin, H. Zhu, X. Mao, F. Gan, and D. Wang, "Separation of dispersed carbon nanotubes from water: effect of pH and surfactants on the aggregation at oil/water interface," *Separation and Purification Technology*, vol. 129, pp. 113–120, 2014.
- [32] T. Nochaiya and A. Chaipanich, "Behavior of multi-walled carbon nanotubes on the porosity and microstructure of cement-based materials," *Applied Surface Science*, vol. 257, no. 6, pp. 1941–1945, 2011.
- [33] S. Xu, J. Liu, and Q. Li, "Mechanical properties and microstructure of multi-walled carbon nanotube-reinforced cement paste," *Construction and Building Materials*, vol. 76, pp. 16–23, 2015.
- [34] J. M. Makar, J. C. Margeson, and J. Luh, "Carbon nanotube/cement composites—early results and potential applications," in *Proceedings of the 3rd International Conference of Construction Materials*, pp. 1–10, Vancouver, Canada, August 2005.
- [35] J. M. Makar and G. W. Chan, "Growth of cement hydration products on single-walled carbon nanotubes," *Journal of the American Ceramic Society*, vol. 92, no. 6, pp. 1303–1310, 2009.
- [36] M. S. Konsta-Gdoutos, Z. S. Metaxaa, and S. P. Shabb, "Highly dispersed carbon nanotube reinforced cement based materials," *Cement and Concrete Research*, vol. 40, no. 7, pp. 1052–1059, 2010.

Research Article

Study on Strength and Microstructure of Cement-Based Materials Containing Combination Mineral Admixtures

Meijuan Rao,^{1,2} Jianpeng Wei,³ Zhiyang Gao,² Wei Zhou,³ Qiaoling Li,³ and Shuhua Liu³

¹State Key Laboratory of Silicate Materials for Architectures, Wuhan University of Technology, Wuhan 430070, China

²Changjiang River Scientific Research Institute, Wuhan 430010, China

³State Key Laboratory of Water Resources and Hydropower Engineering Science, Wuhan University, Wuhan 430072, China

Correspondence should be addressed to Shuhua Liu; shliu@whu.edu.cn

Received 17 March 2016; Accepted 26 June 2016

Academic Editor: Osman Gencel

Copyright © 2016 Meijuan Rao et al. This is an open access article distributed under the Creative Commons Attribution License, which permits unrestricted use, distribution, and reproduction in any medium, provided the original work is properly cited.

The compressive strength of complex binders containing two or three blended mineral admixtures in terms of glass powder (GP), limestone powder (LP), and steel slag powder (SP) was determined by a battery solution type compressive testing machine. The morphology and microstructure characteristics of complex binder hydration products were also studied by microscopic analysis methods, such as XRD, TG-DTA, and SEM. The mechanical properties of the cement-based materials were analyzed to reveal the most appropriate mineral admixture type and content. The early sample strength development with GP was very slow, but it rapidly grew at later stages. The micro aggregate effect and pozzolanic reaction mutually occurred in the mineral admixture. In the early stage, the micro aggregate effect reduced paste porosity and the small particles connected with the cement hydration products to enhance its strength. In the later stage, the pozzolanic reaction of some components in the complex powder occurred and consumed part of the calcium hydroxide to form C-S-H gel, thus improving the hydration environment. Also, the produced C-S-H gel made the structure more compact, which improved the structure's strength.

1. Introduction

Cement in modern civil engineering is the most versatile and commonly used construction material [1–3]; unfortunately, cement production is energy-consuming and results in large quantities of CO₂ emissions [4]. In China, industrial production and everyday life produce large amounts of solid waste, such as steel slag generated by steel production, limestone chips, and powder derived from stone processing, mining, and waste glass produced from human's urban construction [3–6]. These materials occupy numerous valuable land resources and pollute the environment. Therefore, incorporating these three admixtures into cement or concrete could reduce waste products and save expenses related to cement production [7–9].

National and international studies have shown that adding finely ground glass powder (GP), limestone powder (LP), and steel slag powder (SP) to concrete will improve the

concrete's mechanical properties, performance, and durability in varying degrees by improving the hydration environment, the micro aggregate effect, and the pozzolanic effect [6, 10–12]. As we know from previous studies, glass powder, because of its high (SiO₂ + Al₂O₃)/CaO ratio rate, promotes pozzolanic activity at late stage [13–17]. On the contrary, limestone powder is an inert material; its main component, CaCO₃, manifests itself by improving early compressive strength by filling pores and by accelerating the hydration process of the complex binder in the early curing ages. Steel slag powder, composed mainly of C₂A and C₃A, is similar to clinkers; it has potential hydraulic properties and reaction activity that is significantly lower than that of clinkers [18–21].

As civil engineering materials science research has progressed, scholars have found that concrete and cement with combined admixtures could achieve even more favorable performance compared with single-admixture concrete [22, 23]. However, no literature has systematically studied composite

TABLE 1: Physical properties of cement (wt.%).

Materials	Density (g/cm ³)	Standard water consumption (%)	Fineness		Stability	Setting time (h : min)	
			80 μ m sieving residue (%)	Specific surface (m ² /kg)		Primary setting	Final setting
Cement	3.1	25.6	1.4	437	Qualified	3 : 25	5 : 51

TABLE 2: Physical properties of limestone powder.

45 μ m sieving residue (%)	Specific surface (m ² /kg)	Water demand ratio (%)	Density (g/cm ³)	Activity index	
				7 d	28 d
16.0	457.9	98	2.69	64.1	69.0

TABLE 3: Physical properties of glass powder and steel powder.

Materials	Density (g/cm ³)	Fineness	
		80 μ m sieving residue (%)	Specific surface (m ² /kg)
Glass powder	2.35	75	230
Steel powder	3.29	90	265

cementitious materials with the combined admixtures of GP, LP, and SP.

Therefore, to improve the utilization of concrete with the above admixtures, this paper studies the influence of complex mineral admixtures on the macro and micro performances of complex binders, as well as the mineral activity index material evaluation method to characterize the contribution of the hydration activity of mineral admixture to paste strength.

2. Experimental Materials and Methods

2.1. Materials. Ordinary Portland Cement (NPC) P.O 42.5 from Huaxin Cement Co. Ltd. (Hubei Province, China) was used. The physical properties of cement and admixtures are shown in Tables 1, 2, and 3. And the chemical compositions of cement and admixtures are shown in Table 4.

2.2. Testing Methods. Group GL, Group GS, Group LS, and Group GLS with the same cement replacement ratios (15, 30, and 45%) were established to analyze the influence of the composite mineral admixtures on the mechanical and hydration characteristics of cement-based materials compared with a pure cement control sample. Table 5 lists the paste mix proportions.

Paste specimens with 40 mm \times 40 mm \times 40 mm dimensions and a 0.4 water-to-solid ratio (W/C) were molded and cured with higher than 90% relative humidity and $20 \pm 2^\circ\text{C}$ temperature until the stipulated age of 7, 28, and 90 days. Determining the compressive strength of paste specimens of different ages was conducted by WAY-2000 (i.e., a battery solution type compressive testing machine). Clean, bean-size samples were taken from the center of the broken specimens and packed into ampere bottles filled up with absolute ethanol to terminate the hydration process before the XRD, TG-DTA, and SEM microcosmic analysis. Sample pieces were held in a dry environment at 60°C for 2 or 3 hours before SEM tests. The other samples were ground in an agate mortar and dried

at 60°C for 2 hours to reduce carbonation before the XRD test and then dried in vacuum condition before the TG-DTA test.

The XRD analysis was made by X-ray diffraction using a copper target and a continuous scan machine produced by RIGAKU, a Japanese company. The TG-DTA in N_2 atmosphere up to a temperature of 1200°C adopted the diamond TG/DTA analysis produced by Perkin Elmer Instruments Plant, and the morphology of the products was investigated using scanning electron microscopy (JSM-5610LV, Japan).

3. Results and Discussion

3.1. Paste Strength. In Figure 1(a), the influence of combined admixture of GP and LP on the compressive strength of cement-based materials involved the characteristics of both GP and LP. When the content of GP and LP reached 15%, the incorporation of GP and LP compensated for the shortcomings of each other because GP has high pozzolanic activity, which causes high latter compressive strength but low strength at the early stage because of its deficient hydration. The effect of LP on complex binder compressive strength shows just the opposite. For Groups GL2 and GL1, compressive strength was higher at 90 d than at 28 d. The reason is that, in a certain range, LP incorporation promoted early hydration in the cement, which increased paste strength. When the content reached 45%, the paste's compressive strength rapidly reduced due to the relative amount of decreased cement, which weakened the hydration products. As a result, the paste's compressive strength was not improved.

From Figure 1(b), the compressive strength of samples GP and SP decrease with the increasing of GP and SP content. When the content is 15%, the compressive strength of 7 d and 90 d is close to that of the NPC group. The reason may be that, at the early stage, the ground steel slag powder can fill the pore system and integrate with the product so the system becomes dense and the strength

TABLE 4: Chemical compositions of cement and admixtures (wt.%).

Materials	SiO ₂	Al ₂ O ₃	CaO	Fe ₂ O ₃	MgO	BaO	F	SO ₃	K ₂ O	Na ₂ O	P ₂ O ₅	MnO	Cl	CeO ₂	ZnO	Loss
Cement	21.25	2.91	63.09	3.24	0.68	—	—	3.36	1.12	0.31	0.17	0.04	—	—	—	3.52
Glass powder	55.75	10.64	6.60	0.28	1.01	0.43	0.94	0.27	0.54	9.92	0.03	0.29	0.31	1.10	0.30	11.9
Limestone powder	0.73	0.20	30.08	0.06	19.38	—	—	0.01	0.05	—	0.03	—	0.01	—	—	49.47
Steel slag powder	14.11	3.51	42.39	17.45	6.60	0.10	—	0.50	0.13	0.22	1.63	2.96	0.06	—	0.03	8.72

TABLE 5: Mix proportion of pastes and compressive strength of paste/MPa.

Samples	Mineral admixture content (%)	Cement (g)	Glass powder (g)	Limestone powder (g)	Steel slag powder (g)	Compressive strength (MPa)		
						7 d	28 d	90 d
NPC	0	1.00	—	—	—	31.5	55.3	58.0
GL1	15	0.85	0.075	0.075	—	23.5	40.6	50.6
GL2	30	0.7	0.15	0.15	—	18.8	28.8	41.9
GL3	45	0.55	0.225	0.225	—	12.4	26.2	38.2
GS1	15	0.85	0.075	—	0.075	29.1	44.4	52.2
GS2	30	0.7	0.15	—	0.15	19.5	32.7	41.7
GS3	45	0.55	0.225	—	0.225	13.9	27.0	33.9
LS1	15	0.85	—	0.075	0.075	32.2	48.4	58.9
LS2	30	0.7	—	0.15	0.15	31.8	39.0	49.6
LS3	45	0.55	—	0.225	0.225	19.8	29.3	36.1
GLS1	15	0.85	0.05	0.05	0.05	32.6	50.2	56.6
GLS2	30	0.7	0.1	0.1	0.1	23.2	40.9	44.7
GLS3	45	0.55	0.15	0.15	0.15	17.2	28.9	32.0

Notes. G: glass; L: limestone; S: steel slag.

improves eventually. However, the late hydration of the steel slag powder will produce calcium hydroxide and release it into the pore solution to increase the alkalinity. The volcanic ash reaction of the glass powder needs some basic excitation and the hydration process consumes a portion of calcium hydroxide which will promote the hydrate of steel slag. Again, when the content is 30% or above, the cement content is relatively smaller and the hydration products are insufficient. As a result, there is no promotion in the hydration of the GP and SP at the later stage. The compressive strength of Group GS at each age is significantly lower than that of NPC group and, thus, there is no improvement of the early and late strength.

From Figure 1(c), the compressive strength of each specimen containing LP and SP increased over time. The compressive strength at 7 days changed based on content; it increased initially and then decreased. Furthermore, at 30%, the intensity reached its maximum and it showed high strength in the early stages. The strength increased with age; however, the compressive strength of the paste at 90 days was similar to that at 7 days, which increased initially and then decreased. The compressive strength at 28 days gradually decreased with the increase of content. The reason is that the finely ground SP and LP at the early stage promoted cement and micro material hydration, which enhanced paste strength. Moreover, the slow hydration of the steel slag powder was favorable for enhancing strength at the latter stage.

From Figure 1(d), the strength increased with age. For the trimix with GP, LP, and SP, 15% of the content of the specimens in the early and late stages showed good strength performance, and the strength was greater than that of the NPC at 7 days. Due to the slower hydration of glass powder and steel powder, the compressive strength at 28 days is lower than that with NPC. Moreover, the strength at 90 days was basically the same as the NPC. The reason is that the

quaternary system of NPC, GP, LP, and SP becomes perfect. Thus, the micro aggregate effect of the micro powder was fully exerted, so the hardened paste porosity was reduced. The volcanic ash interaction effect promoted further cement hydration, causing the system to become more compact.

3.2. *Contribution Rates of the Hydration Activity Effect.* Figure 1 shows the compressive strength of cement pastes with bi- or trimixed admixtures at different ages.

An evaluation methodology of the activity index of the mineral materials is adopted to evaluate the activity of the glass powder. The calculation steps of this methodology are as follows. The contribution of unit cement consumption (meaning 1% cement consumption) to concrete strength is called concrete-cement consumption ratio strength or concrete ratio strength for short [18–20]. Hence,

$$R_{sa} = \frac{R_a}{q_0}. \quad (1)$$

R_a is the absolute value of concrete strength mixed with auxiliary gel materials. q_0 is the mass fraction of cement in a system mixed with auxiliary gel materials.

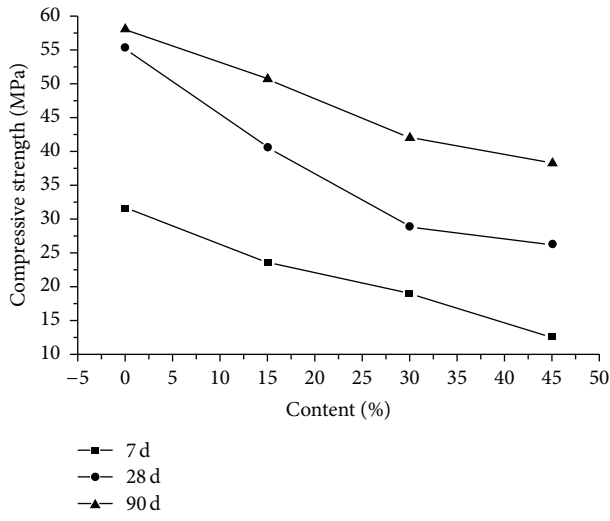
In contrast, the benchmark concrete has a mass fraction of cement q_0 of 100%. The ratio strength is calculated via

$$R_{sc} = \frac{R_c}{100}, \quad (2)$$

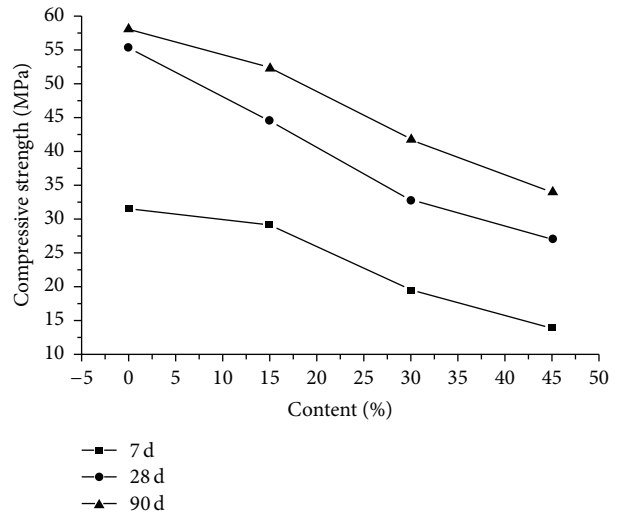
where R_c is the absolute value of benchmark concrete.

Although the cement consumption of concrete mixed with auxiliary gel materials decreases, the potentiation effect due to hydration activity effect often makes R_a greater than R_c and also R_{sa} greater than R_{sc} [21, 22]. The difference between R_{sa} and R_{sc} is called the hydration activity effect ratio strength and the formula is expressed as follows:

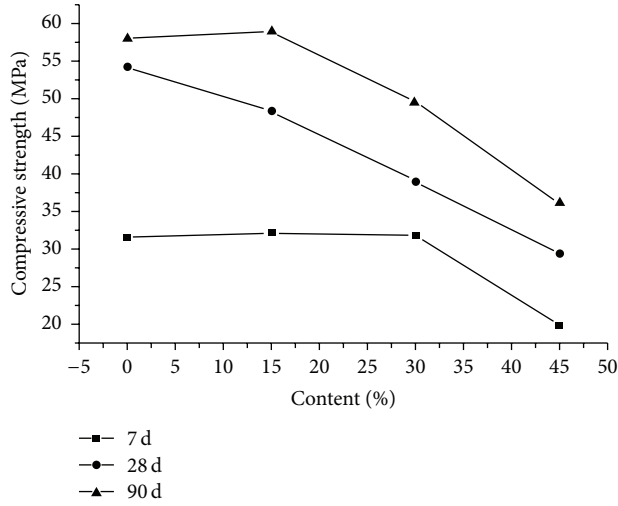
$$R_{sp} = R_{sa} - R_{sc}. \quad (3)$$



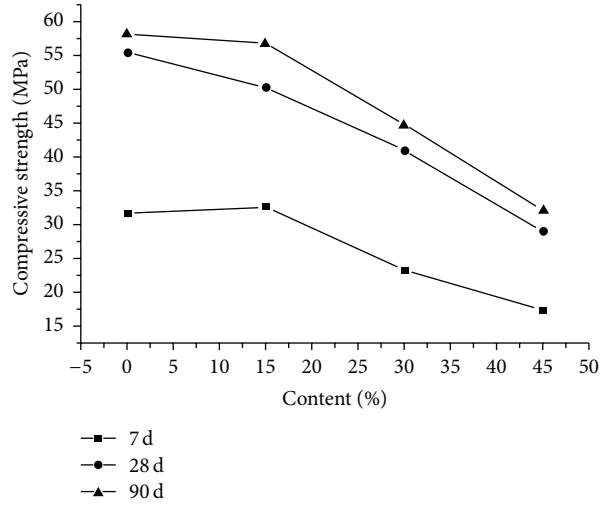
(a) Compressive strength of Group GL



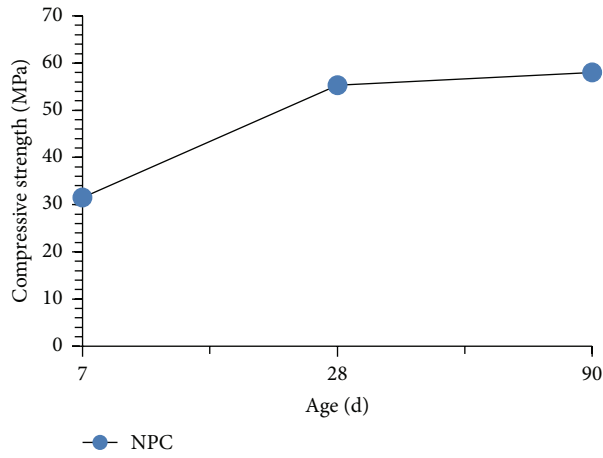
(b) Compressive strength of Group GS



(c) Compressive strength of Group LS



(d) Compressive strength of Group GLS



(e) Compressive strength of Group NPC

FIGURE 1: Compressive strength of pastes with different admixtures.

TABLE 6: Contribution rates of the hydration activity effect.

Samples	3 d	7 d	28 d	90 d
GL1	-0.15	-0.14	-0.16	-0.03
GL2	-0.25	-0.17	-0.34	0.03
GL3	-0.21	-0.40	-0.16	0.17
GS1	-0.03	0.08	-0.06	0.06
GS2	-0.12	-0.13	-0.18	0.03
GS3	-0.15	-0.25	-0.12	0.06
LS1	0.26	0.17	0.03	0.16
LS2	0.18	0.31	0.01	0.18
LS3	0.10	0.13	-0.03	0.12
GLS1	0.15	0.18	0.06	0.13
GLS2	0.04	0.05	0.05	0.09
GLS3	0.05	-0.01	-0.05	0.00

Therefore, a relative index is obtained which is called the hydration activity contribution rate (P_a). P_a can be used to represent the degree of contribution of the hydration activity effect of gel materials. The calculation formula is

$$P_a = \frac{R_{sp}}{R_{sa}} = \frac{R_{sa} - R_{sc}}{R_{sa}} = 1 - \frac{R_{sc}}{R_{sa}} = 1 - \frac{R_c * q_0}{R_a * 100}. \quad (4)$$

The contribution rates of the hydration activity effect of the test sample mineral admixture of all groups were calculated according to the methodology above. Table 6 shows the calculated results. From Table 6, it is obvious that, for GP, LP, and SP, the cured age and the combined methods all significantly affected hydration activity and strength.

For the trimixed groups, GL and GS mixed with glass powder had a low contribution rate to hydration activity at the early stage. The LS group multimixed with limestone powder and steel slag powder and the GLS group trimixed with glass powder, limestone powder, and steel slag powder showed optimal contribution rate of hydration activity at the early and late stages. This trend was more obvious at 15% content.

According to the methodology above, the contribution rates of the hydration activity effect of mineral admixture in the test samples of all groups are calculated. Table 3 shows the calculated results. From Table 3, it is obvious that, for GP, LP, and SP, the cured age and the combined methods all have great importance to hydration activity effect on strength.

For the trimixed groups, GL and GS mixed with glass powder have a low contribution rate of hydration activity at the early age. Group LS multimixed with limestone powder and steel slag powder and Group GLS trimixed with glass powder, limestone powder, and steel slag powder have optimal contribution rate of hydration activity both at the early age and at the late age. This rule is more obvious at content of 15%.

3.3. XRD Analysis. Figures 2 and 3 show the details of the measured XRD patterns. The combined content of glass powder and limestone powder, glass powder and steel slag powder, or limestone powder and steel slag powder had identical diffraction peak positions but different peak values.

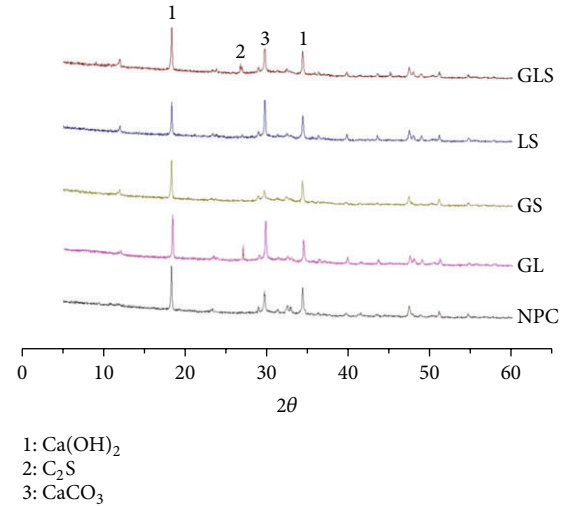


FIGURE 2: XRD results of samples at 28 d.

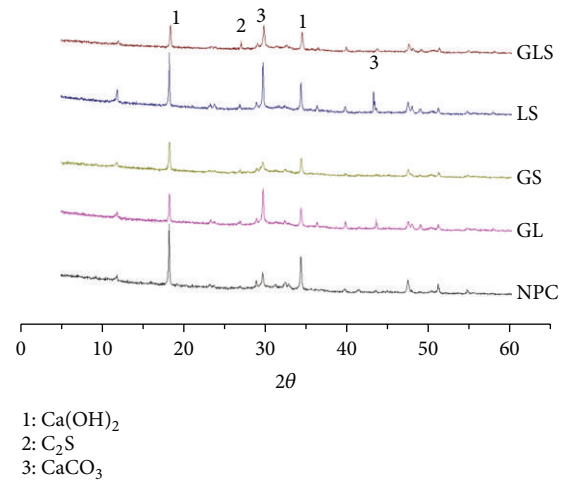


FIGURE 3: XRD results of samples at 90 d.

This shows that the constitutions (i.e., mainly Ca(OH)_2 , unhydrated clinker, and a small amount of CaCO_3 generated via carbonization) of all the groups with different mineral admixtures were basically the same. It can be observed from the graphs that the Ca(OH)_2 diffraction peaks at 28 days were evident. This shows that cement at 28 days hydrated fully and showed good crystallinity under combined content conditions. The C_2S and C_3S diffraction peaks were low at 90 days and also lower than those at 28 days. The implication is that the dicalcium silicate and tricalcium silicate hydrated over time, while the cement at 90 days had not fully hydrated.

For the trimixed cement with glass powder, limestone powder, and slag powder, the Ca(OH)_2 content at 28 days had the highest diffraction peak. This is due to two reasons: first, cement hydration was sufficient under trimixed conditions because the triple-mixed mineral admixture enhanced cement hydration at the early stage, generating more Ca(OH)_2 ; this agrees with the strength test results. Second, glass powder was activated under certain alkaline

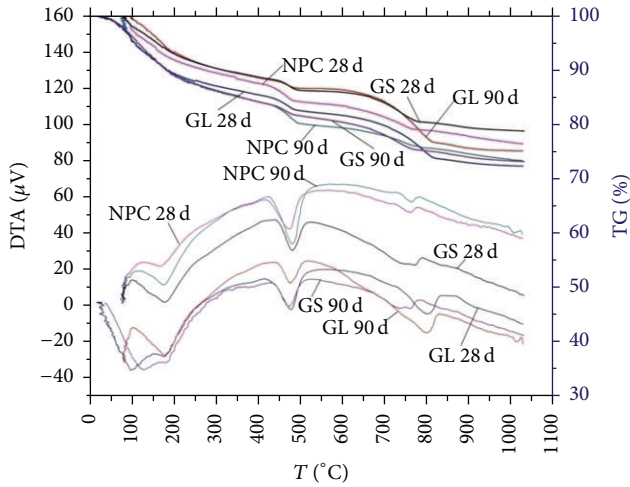


FIGURE 4: TG-DTA curves of samples.

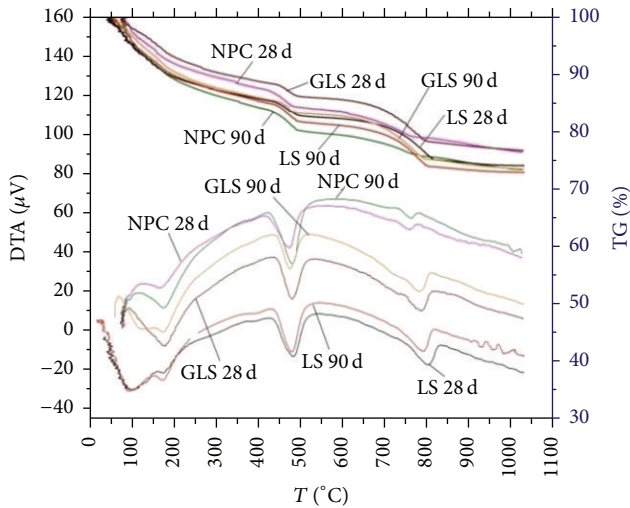


FIGURE 5: TG-DTA curves of samples.

environments, so glass powder activity at the early stage was low and Ca(OH)_2 consumption was very limited.

At the early hydration stage (before 28 d), incorporating different mineral admixtures did not significantly change the kinds of systematic hydration products; however, the number of hydration products changed obviously. Over time, groups mixed with glass powder impressively dropped Ca(OH)_2 content at 90 d. This is because, at the later hydration stage, the alkali concentration of the pore solution gradually increased, which promoted pozzolanic activity and consumed partial Ca(OH)_2 . In these test samples, the unhydrated clinkers such as dicalcium silicate and tricalcium silicate had lower diffraction peaks compared to the other groups, showing that the cement hydration was relatively sufficient.

3.4. TG-DTA. Ca(OH)_2 contents would be quantitatively calculated from TG-DTA results (Figures 5 and 6). The different systems had different Ca(OH)_2 contents and different weight loss ratios. Figure 4 shows the calculated results.

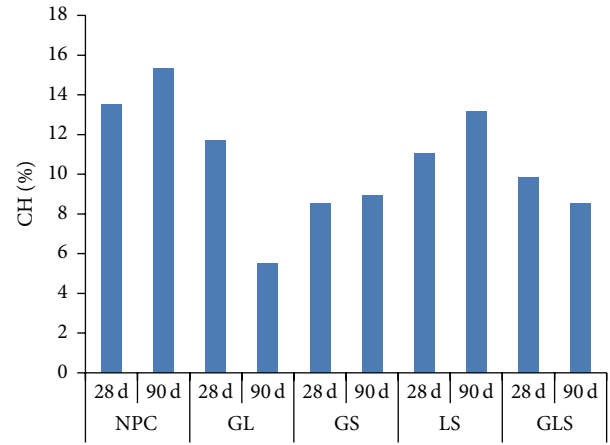


FIGURE 6: Ca(OH)_2 content of samples.

Take a comparison of multimixed admixture and complex admixtures; it could be seen that the amount of calcium hydroxide would be decreased by adding glass powder. At the same time, the amount of calcium hydroxide would be increased by adding limestone powder or steel powder.

3.5. SEM Analysis. 30% content from each group was taken as characteristic specimens of the group. As can be seen from Figure 7 (NPC group), all kinds of slurry are lapped from each other in the cement paste at the age of 28 d, not as dense as the pores which exist at the joint parts of the crystal making the structure appear loose. In addition, the formed calcium hydroxide crystal in the loose holes crossed between the various gels with enough developmental space and seemed significantly larger under an electron microscope. Cement hydration increased significantly, and the constantly generated hydration products filled into the original loose holes over time. The hexagonal calcium hydroxide crystal in slurry was mostly combined with the hydrated calcium silicate (CSH) gel to form a dense structure as a whole. The results are consistent with those of XRD and TG-DTA.

There are a large number of hexagonal layered calcium hydroxide crystals with mesh and granular CSH gel in slurry multimixed with glass powder and limestone powder (Figures 7(c) and 7(d)) (Group GL). It can also be observed that CSH gel filled each pore. The surface of the glass powder began to be eroded with hydration product enrichment on its surface, indicating the occurrence of the pozzolanic reaction. The hydrated structure was relatively dense compared with the pure cement test block at the same age, which closely related to the fine gradation of the multivariate gelling system. From the morphology at 90 d, the constantly generated hydration products filled the pores over time to form a more solid product. Calcium hydroxide crystals were not a single crystal structure but showed laminated cross direction with the CSH gel. Various hydration products alternated to form a denser structure due to the late hydration products of the glass powder, steel slag, and limestone powder reaction filling the pores; this is consistent with the XRD analysis.

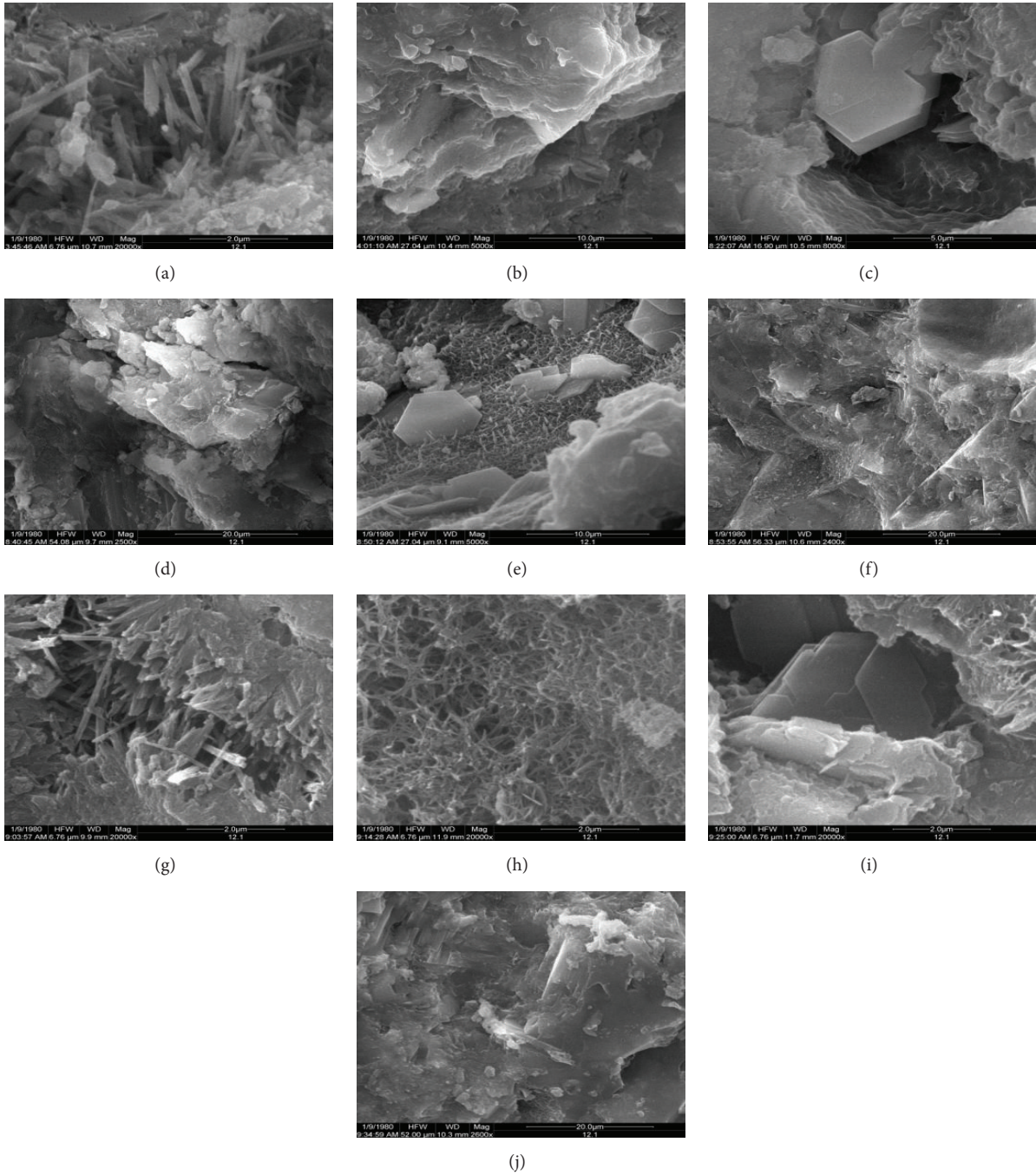


FIGURE 7: SEM images of each sample ((a) NPC 28 d, (b) NPC 90 d, (c) GL 28 d, (d) GL 90 d, (e) GS 28 d, (f) GS 90 d, (g) LS 28 d, (h) LS 90 d, (i) GLS 28 d, and (j) GLS 90 d).

The morphology of Figures 7(e) and 7(f) (Group GS) was similar to that of the bimixed specimen with glass and steel slag powder under the electron microscope. There were a large number of mesh CSH gel and calcium hydroxide crystals at the early stage. The calcium hydroxide crystal was basically submerged in CSH as various hydration products mutually alternated. The hydrate was denser at 28 days.

From Figures 7(g) and 7(h) (Group LS), there were a large number of mesh or cone-shaped clusters of CSH gel

and hydration products that lapped from each other to form a skeletal structure at the early stage. The limestone powder and steel slag powder had a filling effect at the early stage to promote better strength development. Calcium hydroxide crystals were basically submerged in CSH as various hydration products alternated mutually at the late stage. The hydrate was denser than that at 28 d. There were some dense CSH gels at the late stage without complete unhydrated limestone powder and steel slag. The reason may

be that limestone powder and steel slag powder underwent hydration at the late stage, leading to changes in the original morphology, or that the development of the surrounding hydration products caused them to be wrapped in CSH gel.

Figures 7(i) and 7(j) (Group GLS) show the microscopic hydration morphology of specimens trimixed with glass powder, limestone powder, and steel slag powder at 28 and 90 d, respectively. From Figure 7(i), there existed a large number of CSH gels, calcium hydroxide, and hydration products that mutually alternated as a whole. In contrast to the microscopic morphology of other groups at 28 d, the early stage structure was denser with less pore distribution. The reason is that the gradation of the four-element gelling system (i.e., the cement, glass powder, lime stone powder, and steel slag powder) was further optimized to act as a micro aggregate fully and enhanced the compressive strength of the slurry; this is consistent with the strength test results. At 90 d, the hydration degree of the four kinds of cement-based materials increased with various constantly generated hydration products, which filled the pores. As a result, the system formed a dense structure and it was thus difficult to observe the hydration products with distinct morphology.

4. Conclusions

Therefore, we conclude the following:

- (1) The early strength development of glass powder incorporated into the GL and GS specimens was poor but grew rapidly at later stages. The trimixed specimens with glass powder, limestone powder, and slag powder showed the ideal ratio. Also, the strength development of the system showed a good developmental trend from the early to the late stage due to the four-element gelling system, which was further optimized. When the content reached 45%, the pore solution alkalinity could not arouse the high hydration degree of the glass powder for the insufficient cement content and the lack of hydration products.
- (2) The multiple gelling systems with multi- or trimixing mineral admixtures further improved the coarse aggregate grading diameter. The micro aggregate acted fully to make nonhydrated particles and aggregates fill the pores, which reduced slurry porosity and closely connected with the cement hydration products to enhance its early strength. The pozzolanic reaction occurred in the late components of the composite powder to consume part of the calcium hydroxide produced by cement hydration and also improved its hydration environment. At the same time, the generated CSH gels made the structure denser, thereby improving the structure strength.
- (3) Based on this research, the optimal composite institution and the mineral admixture content proportions were obtained, which could provide a new way of using mineral admixtures in concrete.

Competing Interests

The authors declare that they have no competing interests.

Acknowledgments

This project is funded by the National Natural Science Foundation of China (51208391 and 51539002), the Opening Funds of Guangxi Key Laboratory of New Energy and Building Energy Saving (11-03-21-13), and China Postdoctoral Science Foundation (no. 2015M582213).

References

- [1] C. D. Johnston, "Waste glass as coarse aggregate for concrete," *Journal of Testing and Evaluation*, vol. 2, no. 5, pp. 344–350, 1974.
- [2] W. Jin, C. Meyer, and S. Baxter, "Glascrete—concrete with glass aggregates," *ACI Materials Journal*, vol. 97, pp. 208–213, 2000.
- [3] Z. P. Bažant, G. Zi, and C. Meyer, "Fracture mechanics of ASR in concretes with waste glass particles of different sizes," *Journal of Engineering Mechanics*, vol. 126, no. 3, pp. 226–232, 2000.
- [4] Entec Consulting Ltd, *Report on Ontario Blue Box Material Recovery Facilities*, 2007.
- [5] H.-Y. Wang and W.-L. Huang, "Durability of self-consolidating concrete using waste LCD glass," *Construction and Building Materials*, vol. 24, no. 6, pp. 1008–1013, 2010.
- [6] A. Shayan and A. Xu, "Value-added utilisation of waste glass in concrete," *Cement and Concrete Research*, vol. 34, no. 1, pp. 81–89, 2004.
- [7] S. K. Das, A. K. Sharma, F. C. Parida, and N. Kasinathan, "Experimental study on thermo-chemical phenomena during interaction of limestone concrete with liquid sodium under inert atmosphere," *Construction and Building Materials*, vol. 23, no. 11, pp. 3375–3381, 2009.
- [8] T. Schmidt, B. Lothenbach, M. Romer, K. Scrivener, D. Rentsch, and R. Figi, "A thermodynamic and experimental study of the conditions of thaumasite formation," *Cement and Concrete Research*, vol. 38, no. 3, pp. 337–349, 2008.
- [9] P. Pipilikaki, D. Papageorgiou, M. Dimitroula, E. Chaniotakis, and M. Katsioti, "Microstructure changes in mortars attacked by sulphates at 5°C," *Construction and Building Materials*, vol. 23, no. 6, pp. 2259–2264, 2009.
- [10] F. Girardi, W. Vaona, and R. Di Maggio, "Resistance of different types of concretes to cyclic sulfuric acid and sodium sulfate attack," *Cement and Concrete Composites*, vol. 32, no. 8, pp. 595–602, 2010.
- [11] N. Schwarz and N. Neithalath, "Influence of a fine glass powder on cement hydration: comparison to fly ash and modeling the degree of hydration," *Cement and Concrete Research*, vol. 38, no. 4, pp. 429–436, 2008.
- [12] O. Hajime and O. Masahiro, "Self-coMPacting concrete: development, present use and future," in *Proceedings of the 1st International RILEM Symposium on Self-CoMPacting Concrete*, pp. 3–14, Stockholm, Sweden, 1999.
- [13] M. Sonebi, "Medium strength self-compacting concrete containing fly ash: modelling using factorial experimental plans," *Cement and Concrete Research*, vol. 34, no. 7, pp. 1199–1208, 2004.
- [14] G. Kakali, S. Tsivilis, E. Aggeli, and M. Bati, "Hydration products of C₃A, C₃S and Portland cement in the presence of

- CaCO₃,” *Cement and Concrete Research*, vol. 30, no. 7, pp. 1073–1077, 2000.
- [15] New Slag Association, “Cement Americas,” May 2001.
- [16] R. S. Kalyoncu, “Iron and steel slag,” in *Mineral Commodity Summaries*, pp. 92–93, U.S. Geological Survey, 2003.
- [17] H. Motz and J. Geiseler, “Products of steel slags an opportunity to save natural resources,” *Waste Management*, vol. 21, no. 3, pp. 285–293, 2001.
- [18] J. N. Murphy, T. R. Meadowcroft, and P. V. Barr, “Enhancement of the cementitious properties of steelmaking slag,” *Canadian Metallurgical Quarterly*, vol. 36, no. 5, pp. 315–331, 1997.
- [19] D. Niu, L. Jiang, and Q. Fei, “Deterioration mechanism of sulfate attack on concrete under freeze-thaw cycles,” *Journal Wuhan University of Technology, Materials Science Edition*, vol. 28, no. 6, pp. 1172–1176, 2013.
- [20] S. Zhang, L. Li, and A. Kumar, *Materials Characterization Techniques*, CRC Press, Boca Raton, Fla, USA, 2008.
- [21] Q. B. Yang, S. Zhang, S. Huang, and Y. He, “Effect of ground quartz sand on properties of high-strength concrete in the steam-autoclaved curing,” *Cement and Concrete Research*, vol. 30, no. 12, pp. 1993–1998, 2000.
- [22] M.-C. Chen, K. Wang, and L. Xie, “Deterioration mechanism of cementitious materials under acid rain attack,” *Engineering Failure Analysis*, vol. 27, pp. 272–285, 2013.
- [23] C. Shi, A. F. Jiménez, and A. Palomo, “New cements for the 21st century: the pursuit of an alternative to Portland cement,” *Cement and Concrete Research*, vol. 41, no. 7, pp. 750–763, 2011.

Research Article

Numerical Studies of the Effects of Water Capsules on Self-Healing Efficiency and Mechanical Properties in Cementitious Materials

Haoliang Huang¹ and Guang Ye²

¹*School of Materials Science and Engineering, Southeast University, Nanjing 211189, China*

²*Microlab, Faculty of Civil Engineering and Geoscience, Delft University of Technology, 2628 CN Delft, Netherlands*

Correspondence should be addressed to Haoliang Huang; h.l.huang@msn.com

Received 12 March 2016; Revised 18 July 2016; Accepted 19 July 2016

Academic Editor: Joao M. L. Reis

Copyright © 2016 H. Huang and G. Ye. This is an open access article distributed under the Creative Commons Attribution License, which permits unrestricted use, distribution, and reproduction in any medium, provided the original work is properly cited.

In this research, self-healing due to further hydration of unhydrated cement particles is taken as an example for investigating the effects of capsules on the self-healing efficiency and mechanical properties of cementitious materials. The efficiency of supply of water by using capsules as a function of capsule dosages and sizes was determined numerically. By knowing the amount of water supplied via capsules, the efficiency of self-healing due to further hydration of unhydrated cement was quantified. In addition, the impact of capsules on mechanical properties was investigated numerically. The amount of released water increases with the dosage of capsules at different slopes as the size of capsules varies. Concerning the best efficiency of self-healing, the optimizing size of capsules is 6.5 mm for capsule dosages of 3%, 5%, and 7%, respectively. Both elastic modulus and tensile strength of cementitious materials decrease with the increase of capsule. The decreasing tendency of tensile strength is larger than that of elastic modulus. However, it was found that the increase of positive effect (the capacity of inducing self-healing) of capsules is larger than that of negative effects (decreasing mechanical properties) when the dosage of capsules increases.

1. Introduction

Cracking, caused by shrinkage and external loadings, is inherent in reinforced concrete structures. The cracks in reinforced concrete structures facilitate the ingress of aggressive agents and reduce service life of concrete structures. Man-made repair is a traditional solution for the aforementioned problem. However, it is recognized that man-made repair can not last for a long time [1]. Moreover, the cracks in concrete under water or underground are usually inaccessible for man-made repair. Compared to man-made repair, self-healing of cracks, defined as autonomous repairs of cracks [2], can be beneficial [3–6]. Self-healing of cracks has attracted much attention in recent years [7–10]. For instance, capsules storing various adhesive agents are being manufactured in laboratory for self-healing of cracks in cementitious materials [11–13]. Mineral admixtures are used to develop self-healing concrete as well [14–19]. Bacteria are also applied as self-healing agent in concrete structures [17, 20–24]. Even without

these aforementioned healing agents, cementitious materials have the ability of self-healing, that is, autogenous self-healing [7, 25–28]. It has been reported that the availability of water is essential for autogenous self-healing and self-healing based on mineral admixtures and bacteria [9, 10]. Therefore, it is necessary to supply water into cracks in order to promote self-healing based on these mechanisms in concrete structures when concrete structures serve in a dry environment. To do this, water can be stored in capsules and then added into concrete. However, the efficiency of water supply via capsules and its effect on self-healing capacity are insufficiently studied. The impacts of capsules on mechanical properties of cementitious materials as a function of capsule dosages are still unclear either.

In this research, self-healing due to further hydration of unhydrated cement particles is taken as an example for investigating the effects of capsules on the self-healing efficiency and mechanical properties of cementitious materials. It is well known that a substantial amount of cement

remains unhydrated over time due to the lack of water, especially in high performance concrete, as shown in Figure 1 [29]. To promote further hydration, extra water is stored in capsules which are premixed in matrix. When cement matrix cracks, some capsules are broken and the water stored in the capsules is released into the cracks. Thus, further hydration of unhydrated cement particles is promoted. The cracks are expected to be healed by the products of further hydration which are formed in the cracks.

Previous studies [12, 23, 30] have shown that the capsules storing liquid healing agents can be strong enough to resist forces during mixing of concrete but weak enough to be easily broken when hit by cracks. In this study, it was supposed that such capsules can be used to store water. In order to evaluate the feasibility of self-healing by using water capsules, the efficiency of supply of water by using capsules as a function of capsule dosages and sizes will be determined numerically. By knowing the amount of water supplied via capsules, the efficiency of self-healing due to further hydration of unhydrated cement can be quantified by modeling. In addition, the impact of capsules on mechanical properties is also investigated numerically.

2. Reviews of Self-Healing Efficiency versus the Amount of Released Water

In order to determine the efficiency of self-healing due to further hydration of unhydrated cement as a function of capsule dosage and size, the relationship between the self-healing efficiency and the amount of released water should be determined first. This relationship had been investigated in previous study [31]. It was reviewed in this section in order to provide a clearer image of this paper.

2.1. Mechanism of Self-Healing by Further Hydration. As shown in Figure 2, the encapsulated water is embedded in concrete matrix. Because of the low strength of capsules, the capsules are assumed to be broken when they are hit by cracks. The water stored in capsules is released immediately and the cracks are filled with water. When the unhydrated cement particles on the crack surfaces contact with water, the clinker phases of unhydrated cement dissolve instantly. Ca^{2+} begins to diffuse out from unhydrated cement particles immediately and then the silicate starts to diffuse out as well [31]. Consequently, the concentrations of various ions in the crack solution increase gradually. Once the concentrations of ions reach the equilibrium criteria for the precipitation, the further hydration products are formed in the crack. Along with the further hydration products formed around the unhydrated cement, the rate of further hydration slows down and gradually becomes more and more diffusion-controlled [34, 35]. During this period, some parts of the ions are consumed to form the hydration products while other parts of ions may diffuse into the crack solution. Therefore, the formation of healing products in the crack keeps going on but becomes slower and slower.

In addition to the unhydrated cement exposed on the crack surfaces, some ions also diffuse into the solution in

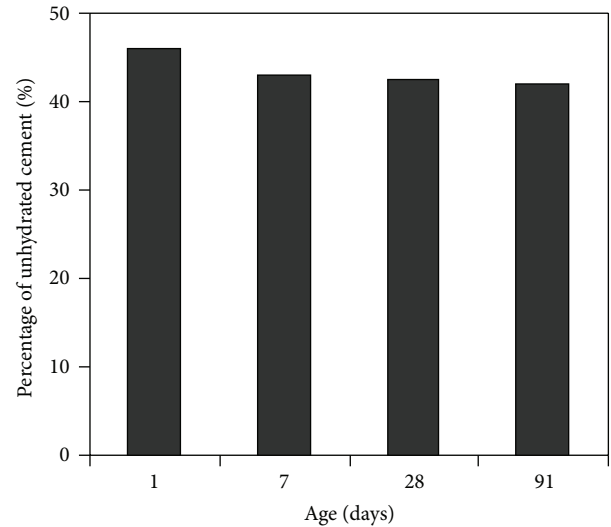


FIGURE 1: The percentage of unhydrated cement in paste (water to binder ratio: 0.18; sand to binder ratio: 1.0; superplasticizer, solid% by weight of binder: 0.9) [29].

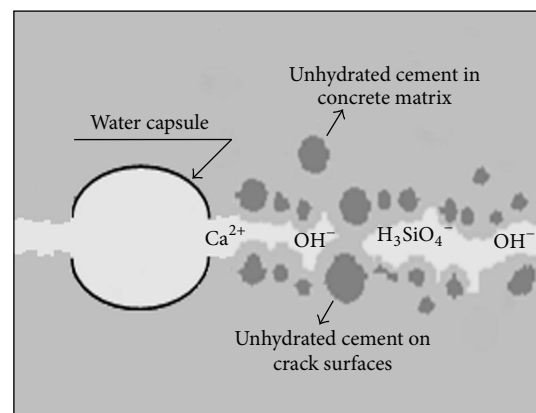


FIGURE 2: Schematic diagram of further hydration [31].

the crack from the unhydrated cement embedded inside the concrete matrix (not on the crack surfaces). These ions also facilitate the formation of healing products in the crack.

What should be mentioned is that the released water in cracks will be absorbed by the concrete matrix due to capillary action. Therefore, the section of crack filled with water will decrease. However, the fact is that the precipitation of further hydration products only takes place in the section of cracks filled with water. When the water in the cracks is absorbed entirely, further hydration in cracks will stop.

2.2. Simulation of Self-Healing by Further Hydration. The processes of self-healing by further hydration mentioned above were simulated in previous study [31]. As shown in Figure 3, a crack with the size of 40 mm (length) \times 40 mm (depth) \times 10 μm (width) is supposed to pass through a capsule. Because the hydration products formed in the cement paste with low w/c ratio are very dense, some unhydrated cement particles can be also passed through by the crack. Assuming

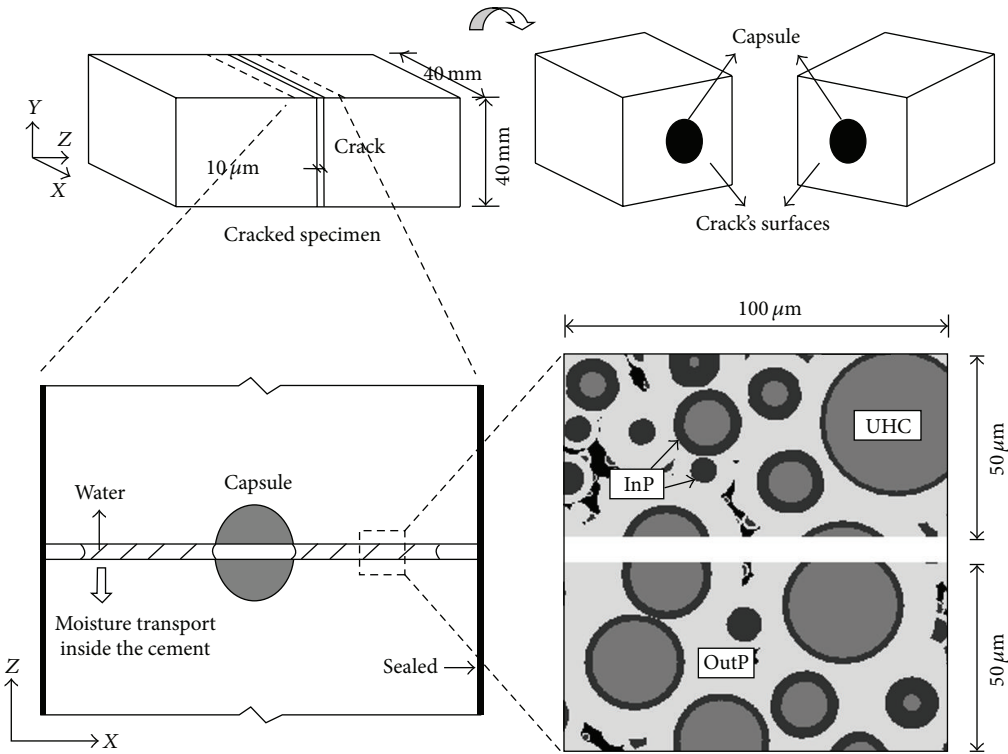


FIGURE 3: Schematic diagram of modeling system for further hydration (InP represents inner products, OutP represents outer products, and UHC represents unhydrated cement particles) [31].

the surrounding surfaces of the cracked specimen are sealed, the water evaporation will not happen and the carbonation of calcite is also prevented.

In the simulation, it was assumed that when the capsules are broken by the crack, all the water stored in the broken capsules can be released into the cracks due to the capillary action. As mentioned, the water in the crack can be absorbed by concrete matrix. The amount of water existing in the crack can be calculated with a water transport model, which is based on mass balance [36–38].

The further hydration processes in water-bearing section of the cracks were simulated in micro level. A tiny square with the size of $100 \mu\text{m} \times 100 \mu\text{m}$ (excluding the crack width) as simulation system from the water-bearing section of crack is shown in Figure 3. The distribution of unhydrated cement particles was simulated by HYMOSTRUC3D [34, 39, 40]. The tiny square was discretized into micropixels with the size of $2 \mu\text{m} \times 2 \mu\text{m}$. The ion concentrations in each micropixel were calculated by the ion diffusion model based on Fick's law. Meanwhile, a thermodynamics model based on chemistry equilibrium, mass balance, and ion charge balance was utilized to simulate the further hydration taking place in the micropixels. At each time step, the ion concentrations calculated by the diffusion model in each micropixel were input into the thermodynamics model. Through the thermodynamics model, the amount of further hydration products was calculated, as well as the ion concentrations after the chemical reaction. The outputs of concentration from the thermodynamics model were input into the diffusion model

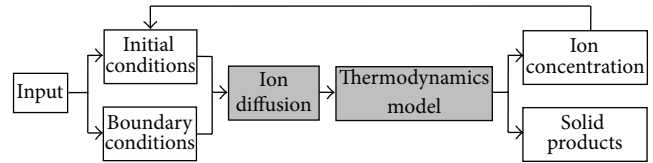


FIGURE 4: Flowchart of the model for further hydration [31].

again as the initial conditions for the next step of calculation. The condensed flowchart of the model for further hydration is shown in Figure 4.

The self-healing efficiency, defined as the volume ratio of the further hydration products to the crack, can be determined by coupling the water transport and further hydration of cement particles.

2.3. Self-Healing Efficiency versus Amount of Available Water. Based on the method in Section 2.2, the relationship between self-healing efficiency and the amount of water released from broken capsules was determined. As shown in Figure 5, self-healing efficiency rises with the increase of released water at two different slopes. When 100 mm^3 of water is provided into the crack, of which the size is 40 mm (length) \times 40 mm (depth) \times $10 \mu\text{m}$ (width), the final self-healing efficiency is about 9.5%. While the broken capsules provide 150 mm^3 of water, the final self-healing efficiency increases to 15.3%. With this slope, the final self-healing efficiency rises to 22.9% when

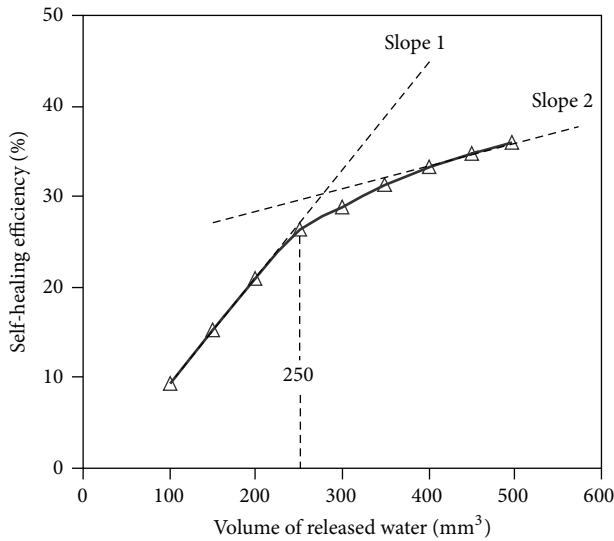


FIGURE 5: Efficiency of self-healing of a crack with the size of 40 mm (length) \times 40 mm (depth) \times 10 μ m (width) versus different amount of extra water supplied to the crack via capsules [31].

the extra water increases to 250 mm³. However, the increase of healing efficiency becomes less significant after this point (the slope of this curve is decreasing). The reason is that when the released water contacts with the unhydrated cement on the crack surfaces, further hydration products increase dramatically. Along with the further hydration products formed around the unhydrated cement, further hydration slows down gradually.

3. Probability of a Crack Hitting Capsules

As discussed in Section 2, self-healing efficiency depends on the amount of released water from the broken capsules. In the simulation, it is assumed that the capsules can be broken when they are hit by the crack. It is easy to imagine that only some parts of capsules are hit by cracks since the capsules randomly distribute in the whole structure. The hitting probability is dominated by the dosage, the size, and the shape of capsules. By now, there are several analytical models [41, 42] for calculating the probability of a crack hitting capsules. In this study, random experiments with the help of computers were performed to calculate the probability of a crack hitting capsules. The effect of capsule size was also taken into account. All the capsules are supposed to be sphere.

3.1. Method for Calculating the Probability of a Crack Hitting Capsules. Corresponding to the simulation in Section 2, the modeling system here is a beam with the size of 40 mm \times 40 mm \times 160 mm. As shown in Figure 6, all capsules with identical radius are uniformly dispersed inside the beam and do not overlap or contact with each other. In addition, the capsules can not cross with the surfaces of the beam.

In this study, the cement paste is simplified as homogeneous material. Capsules are assumed to be intersected if they were hit by cracks. In this case, the crack is planar and can

be simplified as a plane. Therefore, the hitting probability is equal to the probability of the capsules' centers dispersing inside the "influence zone" of the planar crack, which is shown in Figure 6(b). To obtain the probability of capsules centers dispersing inside the "influence zone" of the planar crack, 1000 random experiments were carried out. Statistical analysis on the amount of capsules passed through by the planar crack was performed. According to the statistical analysis, 1000 experiments can guarantee that the average amount of capsules hit by the crack is within 10% of the true value in a 95% degree of confidence.

3.2. Results and Discussion. The probability of the planar crack hitting different amounts of capsules is shown in Figure 7. When the dosage of capsules is 5% and the diameter of the capsules is 5 mm, the probability is 1 for the event that 0.5% of the capsules in the sample are hit by the crack. When the fraction of capsules broken by the crack increases, the corresponding probability decreases. It is impossible for the crack to break all the capsules mixed in the sample. As shown in Figure 7, the probability is almost 0 for the event that more than 6% of the capsules in the sample are hit by the planar crack. In other cases of diameter, the hitting probability varies in similar tendency.

As mentioned before, because of the low strength of the capsules, the capsules are assumed to be broken when they are hit by the crack and the water is released into the crack from the broken capsules. The amount of released water, corresponding to different dosage of capsules, is shown in Figure 8. For this calculation, the degree of confidence is 95% (the probability is 0.95). It is found that the amount of released water is influenced by the size of capsules. When the size of capsules is small enough, that is, 1.5 mm and 3 mm, the amount of released water linearly increases with the increase of capsules. This increasing tendency varies when the size of capsules ranges from 5 mm to 7.5 mm. From Figure 8, it can be learned that, concerning the maximum amount of released water, there is an optimizing size of capsules in each case of dosage of capsules. For example, the optimizing size of capsules is 3.0 mm when the dosage of capsules is 1%. In comparison, the optimizing size of capsules increases to 6.5 mm while the dosage of capsules in the sample is 3%, 5%, and 7%, respectively. This suggestion is also demonstrated in Figure 9. When the dosage of capsules mixed in the sample is 5%, the fraction of broken capsules varies with the size of capsules while the probability is at the same level. In this study, the degree of confidence is expected to be 95%, which means that the probability of the event should be 0.95. With this probability, the fraction of capsules broken by the crack ranges from 0.84% to 2.3% when the diameter of capsules changes from 1.5 mm to 7.5 mm. What should be mentioned is that when the size of capsules is 6.5 mm, the amount of broken capsules is the largest.

From this modeling, the amount of released water as the function of the dosage of capsules premixed is determined, which is essential for self-healing efficiency by further hydration. Moreover, the optimizing capsule sizes for different dosage of capsules premixed are suggested. This optimization

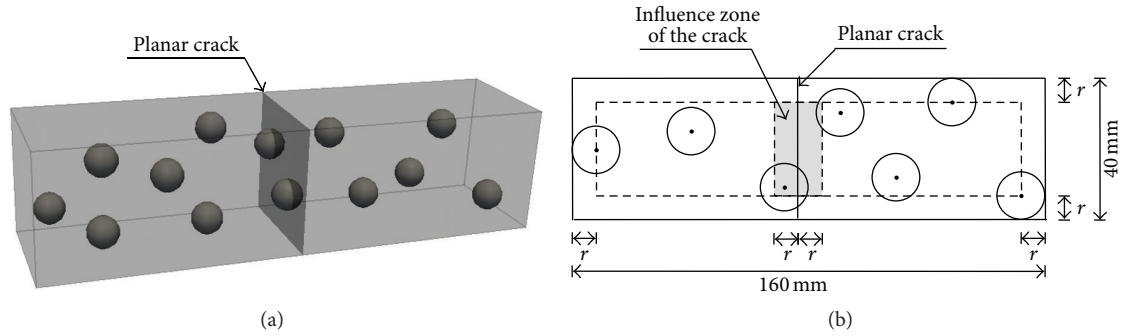


FIGURE 6: Schematic diagram of a planar crack hitting capsules (a). Planform for the capsule distribution in the sample and the influence zone of the planar crack (b).

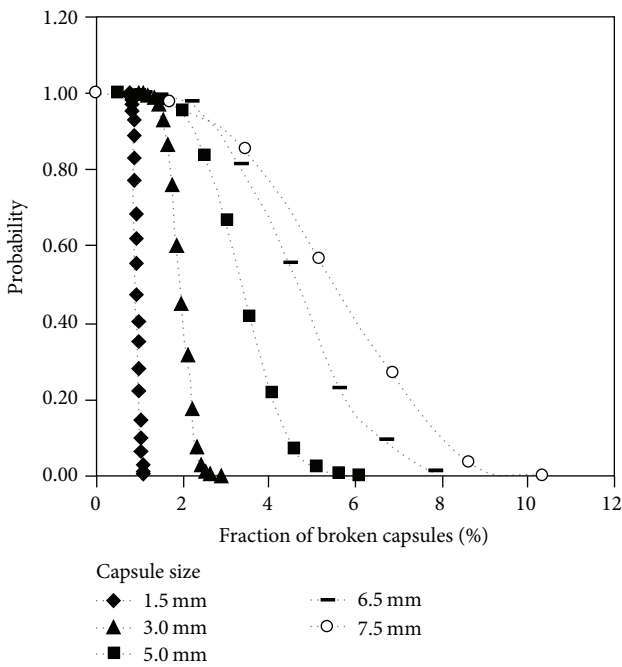


FIGURE 7: Probability of a crack hitting capsules with different size (the dosage of capsules is 5%).

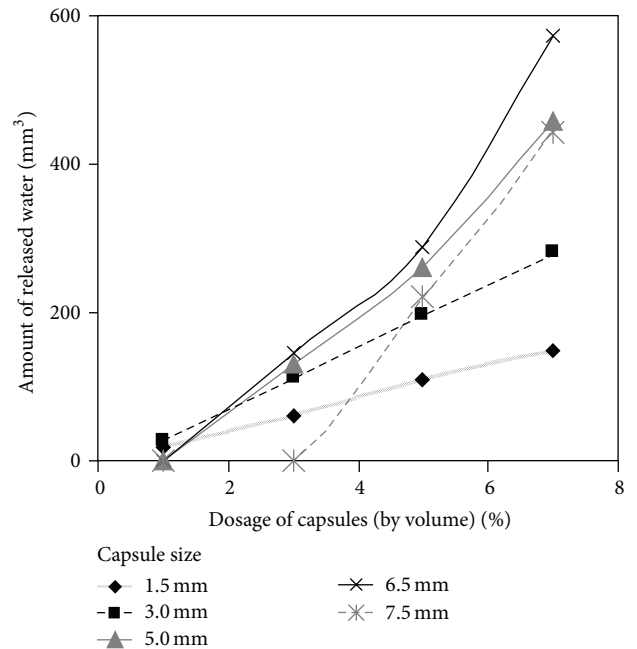


FIGURE 8: Amount of water released from broken capsule with different size (the degree of confidence is 95%).

on capsule size can significantly improve self-healing of cracks by further hydration in cementitious materials.

4. The Effects of Capsules on Mechanical Properties

As mentioned before, since the strength of the capsules is low, the mechanical properties of the structures decrease when some capsules are embedded in the cement matrix. The more the capsules mixed, the lower the mechanical properties. Therefore, the quantified relationship between the mechanical properties and the amount of capsules mixed with cement is essential for the optimization of self-healing. In this section, a 3D lattice model was used to simulate the fracture of the cement paste with capsules.

4.1. 3D Lattice Model

4.1.1. Basics of the Model. Lattice model was proposed to describe a material on a macro scale by means of a network of truss elements in 1941 [43]. However, the network of truss elements can not describe the rotation of material in crack face bridge, which usually occurs during the fracture process of concrete [44]. A lattice model with beam elements was proposed by Schlangen and van Mier [32, 45–47]. A triangular shape of lattice is shown in Figure 10(a). The beam elements have fixed connections in the nodes, which can transfer axial force, shear force, and bending moments, as shown in Figure 10(b). The beam is supposed to behave linearly under tensile stress, which is shown in Figure 10(c). In the simulation, first the stress in the beam elements should

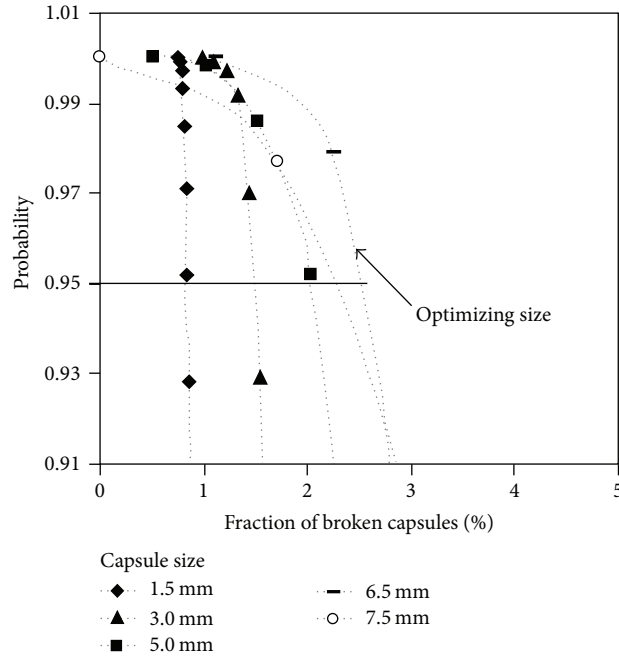


FIGURE 9: Probability of a crack hitting capsules with different size (volume fraction of capsules mixed: 5%).

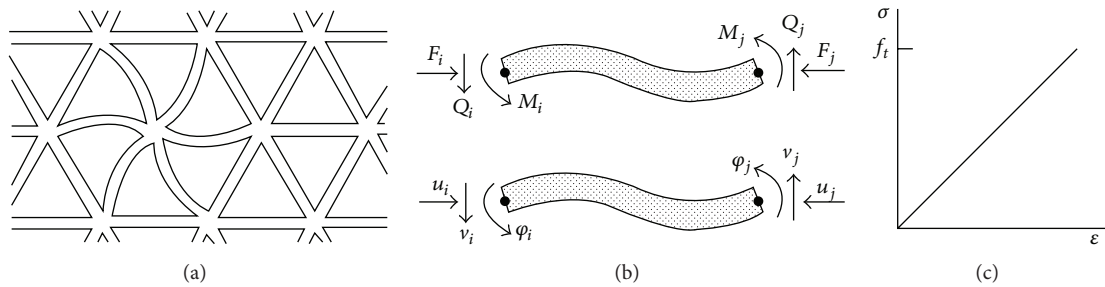


FIGURE 10: Triangular lattice of beam elements (a); external forces on a single beam element (b); stress-strain relation of a single beam element (c). After Schlangen [32].

be analyzed. The tensile stress of the beam elements can be calculated by the following formula:

$$\sigma_t = \frac{N}{A} + \alpha \cdot \frac{(|M_i|, |M_j|)_{\max}}{W}, \quad (1)$$

where N is the normal force, $|M_i|$, $|M_j|$ refer to the bending moments in nodes i and j , respectively, $A = b \times h$, which represents the cross section of the beams and $W = b \cdot h^2/6$, and α is introduced to select a failure mode where it plays either a dominant or a restricted role.

After the stress analysis, fracturing of material takes place by removing the beam element with the highest stress σ_t relative to its tensile strength f_t . The stiffness matrix of the removed beam element will be deleted in the next step of calculation. By multiplying the scale factor, the relationship between the reaction and the displacement can be derived. Following this procedure in each step, an exact solution is obtained.

This lattice model was extended to a 3D model by Qian [33, 48]. In order to obtain more accurate results, the 3D version of lattice model was used in this research.

4.1.2. Construction of Lattice Beam. In order to investigate the effects of capsules on the mechanical properties of the structures, the fracture processes of standard beams ($40 \text{ mm} \times 40 \text{ mm} \times 160 \text{ mm}$) under tensile loading were simulated by 3D lattice model. As shown in Figure 11, the capsules randomly distribute inside the sample. In this modeling, the cement paste is assumed to be homogeneous. In addition, since the strength of the liquid inside the capsules is much lower than that of cement paste, the capsules are simplified as holes. It means that the capsule shell and the interface transition zone (ITZ) between capsule shell and concrete matrix are ignored. In order to guarantee that capsules can be intersected by cracks, the fracture energies of capsule shell and ITZ must be lower than that of concrete matrix. In addition, the capsule shell usually is thin. Therefore, the

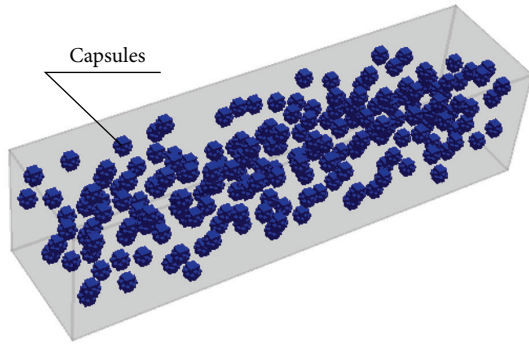


FIGURE 11: Standard beam (40 mm × 40 mm × 160 mm) containing capsules (the dosage of capsules is 5%).

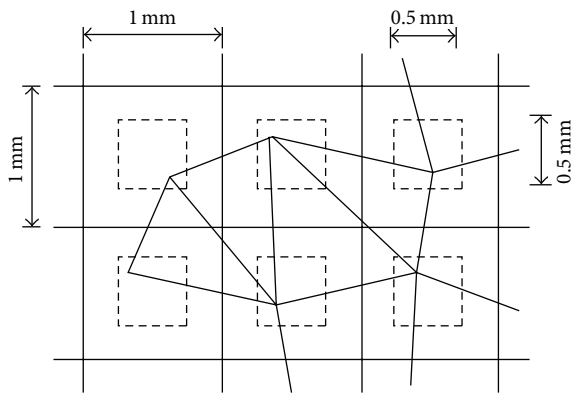


FIGURE 12: Schematic diagram of random lattice from 2D direction. After Schlangen [32].

simplification of capsules as holes has few influences on the calculating strength of concrete with capsules.

Based on these assumptions, the structure of the sample for the lattice model can be generated. This structure for lattice is composed of voxels with the size of 1 mm × 1 mm × 1 mm. As shown in Figure 12, a point is selected at random in the smaller cube (0.5 mm × 0.5 mm × 0.5 mm) in each voxel for cement paste. The random lattice is defined by connecting these points with beam elements. In this way, the disorder of cement paste is implemented by the difference in beam length. The lattice constructed by beam elements for the sample with capsules is shown in Figure 13. The properties of beam elements are assigned according to the properties of cement paste, which are shown in Table 1 [33].

4.2. Results and Discussion. As shown in Figures 14 and 15, the mechanical properties decrease with the increase of capsules mixed in the sample. From Figure 15, it can be found that the decreasing rate of elastic modulus is smaller than that of tensile strength. When the volume of capsules mixed in the sample is 7%, the elastic modulus of the sample drops by almost 17%, while the tensile strength decreases by more than 50%. For the tensile strength, the tendency of decrease is most obvious when the volume fraction of capsules ranges from 0% to 3%.

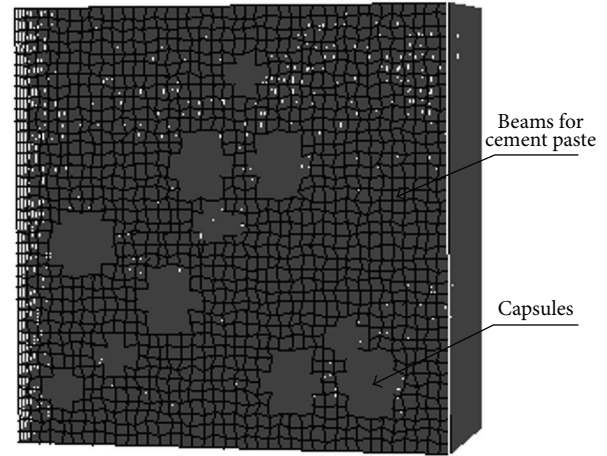


FIGURE 13: Cross section of the lattice constructed by beam elements for the sample with capsules.

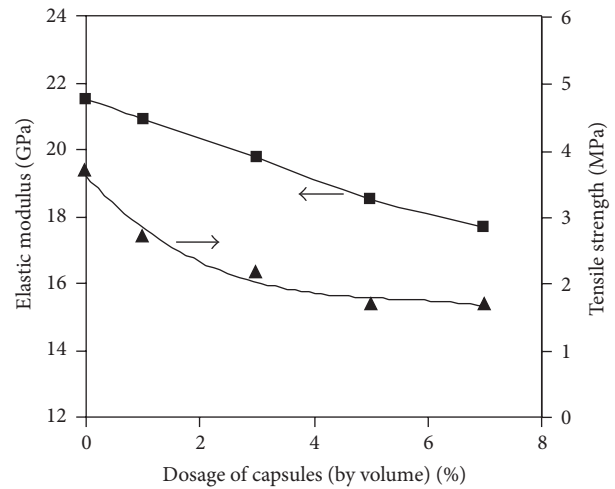


FIGURE 14: The elastic modulus and tensile strength of the samples with different amount of capsules.

From these results, it can be learned that the negative effects of capsules on the mechanical properties are significant, especially for the tensile strength. These negative effects should be taken into account while designing the mixture of cementitious materials with self-healing capacity.

5. Analysis on the Dosage of Capsules

Based on Figures 5 and 8, the relationship between self-healing efficiency and the dosage of capsules with different size can be determined, which is shown in Figure 16. It is clear that the self-healing efficiency increases with the increase of capsules. As discussed in Section 3.2, the amount of water released from the broken capsules is the largest when the diameter of capsules is 6.5 mm (the dosage of capsules is more than 3%). Therefore, as shown in Figure 16, the self-healing efficiency is the highest when the capsules size is 6.5 mm and the dosage of capsules is more than 3%.

TABLE 1: Mechanical properties of cement paste [33].

Tensile strength (MPa)	Compressive strength (MPa)	Elastic modulus (GPa)	Elastic shear modulus (GPa)
4.7	120	23	11

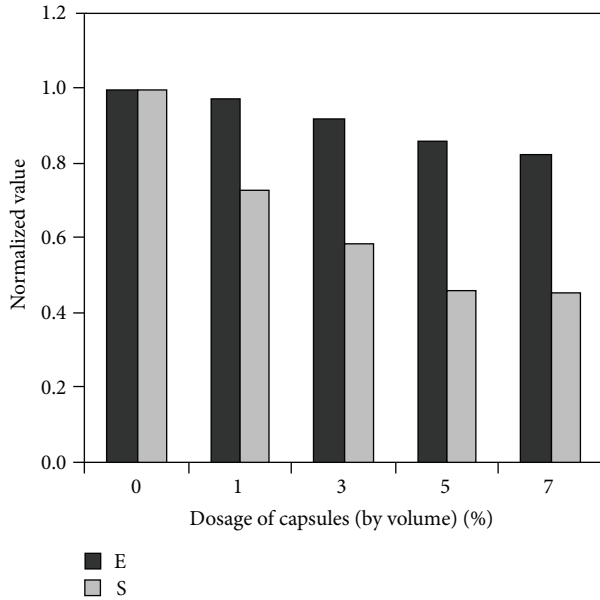


FIGURE 15: The decrease of mechanical properties with the increase of capsules (E: elastic modulus; S: tensile strength).

However, as mentioned in Section 4.2, the mechanical properties decrease with the increase of capsules mixed in the sample. Figure 17 shows the comparison of self-healing efficiency and the decrease of tensile strength when different amounts of capsules are mixed. In order to compare the positive effects with the negative effects of the capsules, the ratio of self-healing efficiency to the decrease of normalized tensile strength was defined. In this study, the positive effect of the capsules refers to the capacity of inducing self-healing by providing extra water. The negative effect refers to the decrease of mechanical properties caused by the addition of capsules.

For capsule dosage of 3%, the tensile strength of concrete containing capsules is about 59% of that without capsules. It can be found that self-healing efficiency increases by 15% while the tensile strength decreases by 41%, when the dosage of capsules is 3%. Therefore, the ratio of self-healing efficiency to the decrease of tensile strength is about 0.36. This ratio increases to 0.70, when the dosage of capsules rises to 7%. It means that the increase of positive effect of the capsules is larger than that of the negative effect when the dosage of capsules goes up.

However, it is obvious that the decrease of more than 30% of the tensile strength is too much for the engineering practice. Therefore, strategies such as increasing reinforced bars or fibers in the mixture should be proposed while applying capsules to realize self-healing in cementitious materials.

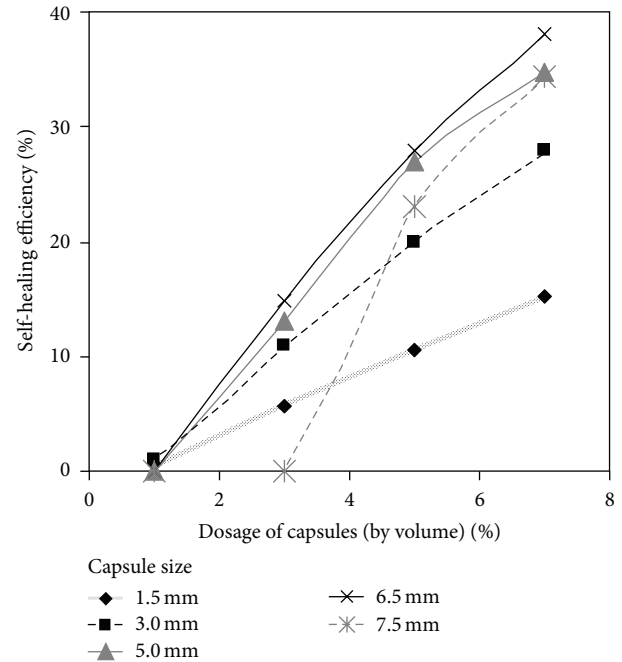


FIGURE 16: The self-healing efficiency with different amount of capsules.

6. Conclusions

The effects of the dosage and size of capsules on self-healing and mechanical properties in cementitious materials were investigated in this paper. The probability of a crack hitting capsules was determined by performing random experiments with the help of computers. In this way, the relationship between the amount of released water and the dosage of capsules was determined. The effects of the capsule size on the amount of released water were also explored. By knowing the amount of water supplied via capsules, the efficiency of self-healing due to further hydration of unhydrated cement was quantified by modeling. In addition, the impact of capsules on mechanical properties was investigated numerically.

From the results, it can be learned that the increase rate of the amount of released water to the dosage of capsules changes with the size of capsules. Concerning the maximum amount of released water, the optimizing size of capsules is 6.5 mm while the dosage of capsules is 3%, 5%, and 7%, respectively. Based on the relationship between self-healing efficiency and the amount of released water from the broken capsules, self-healing efficiency as the function of the dosage of capsules was determined. Regarding the mechanical properties, both elastic modulus and tensile strength of the samples decrease with the increase of capsule. The decreasing tendency of tensile strength is larger than that of elastic modulus. Comparing the effects of capsules

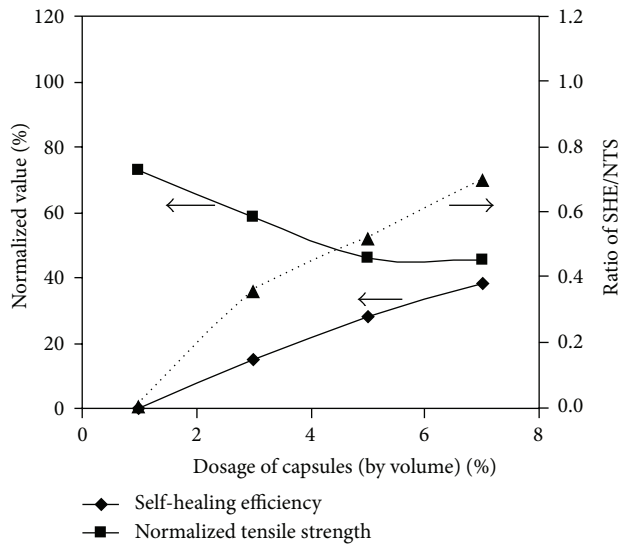


FIGURE 17: Comparison of self-healing efficiency and decrease of tensile strength (SHE/DTS is the ratio of self-healing efficiency to the decrease of normalized tensile strength). The triangles and the dotted curve refer to ratio of SHE/NTS of the vertical axis on the right side.

on self-healing with that on mechanical properties, it can be found that the increase of positive effect (the capacity of inducing self-healing) of capsules is larger than that of negative effects (decreasing mechanical properties) when the dosage of capsules increases. However, the negative effects of capsules on mechanical properties are not ignored. It must be emphasized that self-healing based on mineral admixtures and bacteria proceeds faster than self-healing due to further hydration of unhydrated cement [15, 18, 23]. Therefore, the efficiency of self-healing based on mineral admixtures and bacteria should be higher than that of self-healing due to further hydration of unhydrated cement when the dosages and sizes of capsules are the same.

Competing Interests

The authors declare that they have no competing interests.

Acknowledgments

The authors would like to thank the “Nature Science Fund of Jiangsu” (BK20150601), “Fundamental Research Funds for the Central Universities” (2242016K40014), and the “Open Fund of State Key Laboratory of High Performance Civil Engineering Materials” (2015CEM002) for the financial support. Prof. Erik Schlangen and Dr. Zhiwei Qian are highly appreciated for their help with the use of 3D Lattice Model.

References

- [1] K. van Breugel, “Is there a market for self-healing cement-based materials?” in *Proceedings of the 1st International Conference on Self-Healing Materials*, Noordwijk, The Netherlands, 2007.
- [2] M. de Rooij, K. van Tittelboom, N. De Belie, and E. Schlangen, Eds., *Self-Healing Phenomena in Cement-Based Materials: State-of-the-Art Report of RILEM Technical Committee 221-SHC: Self-Healing Phenomena in Cement-Based Materials*, Springer, New York, NY, USA, 2013.
- [3] C. Edvardsen, “Water permeability and autogenous healing of cracks in concrete,” *ACI Materials Journal*, vol. 96, no. 4, pp. 448–454, 1999.
- [4] H.-W. Reinhardt and M. Jooss, “Permeability and self-healing of cracked concrete as a function of temperature and crack width,” *Cement and Concrete Research*, vol. 33, no. 7, pp. 981–985, 2003.
- [5] S. Granger, A. Loukili, G. Pijaudier-Cabot, and G. Chanvillard, “Experimental characterization of the self-healing of cracks in an ultra high performance cementitious material: mechanical tests and acoustic emission analysis,” *Cement and Concrete Research*, vol. 37, no. 4, pp. 519–527, 2007.
- [6] D. Homma, H. Mihashi, and T. Nishiwaki, “Self-healing capability of fibre reinforced cementitious composites,” *Journal of Advanced Concrete Technology*, vol. 7, no. 2, pp. 217–228, 2009.
- [7] Y. Yang, M. D. Lepech, E.-H. Yang, and V. C. Li, “Autogenous healing of engineered cementitious composites under wet-dry cycles,” *Cement and Concrete Research*, vol. 39, no. 5, pp. 382–390, 2009.
- [8] S. Granger, G. Pijaudier Cabot, A. Loukili, D. Marlot, and J. C. Lenain, “Monitoring of cracking and healing in an ultra high performance cementitious material using the time reversal technique,” *Cement and Concrete Research*, vol. 39, no. 4, pp. 296–302, 2009.
- [9] H. Huang, G. Ye, C. Qian, and E. Schlangen, “Self-healing in cementitious materials: materials, methods and service conditions,” *Materials & Design*, vol. 92, pp. 499–511, 2016.
- [10] V. C. Li and E. Herbert, “Robust self-healing concrete for sustainable infrastructure,” *Journal of Advanced Concrete Technology*, vol. 10, no. 6, pp. 207–218, 2012.
- [11] B. Dong, Y. Wang, G. Fang, N. Han, F. Xing, and Y. Lu, “Smart releasing behavior of a chemical self-healing microcapsule in the stimulated concrete pore solution,” *Cement and Concrete Composites*, vol. 56, pp. 46–50, 2015.
- [12] B. Hilloulin, K. Van Tittelboom, E. Gruyaert, N. De Belie, and A. Loukili, “Design of polymeric capsules for self-healing concrete,” *Cement and Concrete Composites*, vol. 55, pp. 298–307, 2015.
- [13] K. Van Tittelboom, N. De Belie, D. Van Loo, and P. Jacobs, “Self-healing efficiency of cementitious materials containing tubular capsules filled with healing agent,” *Cement and Concrete Composites*, vol. 33, no. 4, pp. 497–505, 2011.
- [14] T.-H. Ahn and T. Kishi, “Crack self-healing behavior of cementitious composites incorporating various mineral admixtures,” *Journal of Advanced Concrete Technology*, vol. 8, no. 2, pp. 171–186, 2010.
- [15] M. Roig-Flores, S. Moscato, P. Serna, and L. Ferrara, “Self-healing capability of concrete with crystalline admixtures in different environments,” *Construction and Building Materials*, vol. 86, pp. 1–11, 2015.
- [16] Y.-S. Lee and J.-S. Ryou, “Self healing behavior for crack closing of expansive agent via granulation/film coating method,” *Construction and Building Materials*, vol. 71, pp. 188–193, 2014.
- [17] C. Stuckrath, R. Serpell, L. M. Valenzuela, and M. Lopez, “Quantification of chemical and biological calcium carbonate precipitation: performance of self-healing in reinforced mortar containing chemical admixtures,” *Cement and Concrete Composites*, vol. 50, pp. 10–15, 2014.

- [18] Z. Jiang, W. Li, and Z. Yuan, "Influence of mineral additives and environmental conditions on the self-healing capabilities of cementitious materials," *Cement and Concrete Composites*, vol. 57, pp. 116–127, 2015.
- [19] K. Sisomphon, O. Copuroglu, and E. A. B. Koenders, "Self-healing of surface cracks in mortars with expansive additive and crystalline additive," *Cement and Concrete Composites*, vol. 34, no. 4, pp. 566–574, 2012.
- [20] H. M. Jonkers, A. Thijssen, G. Muyzer, O. Copuroglu, and E. Schlangen, "Application of bacteria as self-healing agent for the development of sustainable concrete," *Ecological Engineering*, vol. 36, no. 2, pp. 230–235, 2010.
- [21] V. Wiktor and H. M. Jonkers, "Quantification of crack-healing in novel bacteria-based self-healing concrete," *Cement and Concrete Composites*, vol. 33, no. 7, pp. 763–770, 2011.
- [22] M. Luo, C.-X. Qian, and R.-Y. Li, "Factors affecting crack repairing capacity of bacteria-based self-healing concrete," *Construction and Building Materials*, vol. 87, pp. 1–7, 2015.
- [23] J. Y. Wang, H. Soens, W. Verstraete, and N. De Belie, "Self-healing concrete by use of microencapsulated bacterial spores," *Cement and Concrete Research*, vol. 56, pp. 139–152, 2014.
- [24] J. Xu and W. Yao, "Multiscale mechanical quantification of self-healing concrete incorporating non-ureolytic bacteria-based healing agent," *Cement and Concrete Research*, vol. 64, pp. 1–10, 2014.
- [25] N. Hearn, "Self-sealing, autogenous healing and continued hydration: what is the difference?" *Materials and Structures*, vol. 31, no. 212, pp. 563–567, 1998.
- [26] H. Huang, G. Ye, and L. Pel, "New insights into autogenous self-healing in cement paste based on nuclear magnetic resonance (NMR) tests," *Materials and Structures*, vol. 49, no. 7, pp. 2509–2524, 2016.
- [27] H. Huang, G. Ye, and D. Damidot, "Characterization and quantification of self-healing behaviors of microcracks due to further hydration in cement paste," *Cement and Concrete Research*, vol. 52, pp. 71–81, 2013.
- [28] S. Z. Qian, J. Zhou, and E. Schlangen, "Influence of curing condition and precracking time on the self-healing behavior of Engineered Cementitious Composites," *Cement and Concrete Composites*, vol. 32, no. 9, pp. 686–693, 2010.
- [29] N. Van Tuan, G. Ye, K. van Breugel, and O. Copuroglu, "Hydration and microstructure of ultra high performance concrete incorporating rice husk ash," *Cement and Concrete Research*, vol. 41, no. 11, pp. 1104–1111, 2011.
- [30] Z. Yang, J. Hollar, X. He, and X. Shi, "A self-healing cementitious composite using oil core/silica gel shell microcapsules," *Cement and Concrete Composites*, vol. 33, no. 4, pp. 506–512, 2011.
- [31] H. Huang and G. Ye, "Simulation of self-healing by further hydration in cementitious materials," *Cement and Concrete Composites*, vol. 34, no. 4, pp. 460–467, 2012.
- [32] E. Schlangen, *Experimental and Numerical Analysis of Fracture Processes in Concrete*, Delft University of Technology, Delft, Netherlands, 1993.
- [33] Z. Qian, *Multiscale Modeling of Fracture Processes in Cementitious Materials*, Delft University of Technology, 2012.
- [34] K. van Breugel, *Simulation of Hydration and Formation of Structure in Hardening Cement-Based Materials*, Delft University of Technology, Delft, Netherlands, 1991.
- [35] H. F. W. Taylor, *Cement Chemistry*, Thomas Telford Publishing, London, UK, 1997.
- [36] K. Maekawa, R. Chaube, and T. Kishi, *Modeling of Concrete Performance: Hydration, Microstructure and Mass Transport*, E & FN Spon, London, UK, 1999.
- [37] R. Cerny and P. Rovnanikova, *Transport Process in Concrete*, Taylor & Francis, London, UK, 2002.
- [38] H. Huang, G. Ye, and K. Van Breugel, "Numerical simulation on moisture transport in cracked cement-based materials in view of self-healing of crack," *Journal Wuhan University of Technology, Materials Science Edition*, vol. 25, no. 6, pp. 1077–1081, 2010.
- [39] E. A. B. Koenders, *Simulation of Volume Changes in Hardening Cement-Based Materials*, Delft University of Technology, 1997.
- [40] G. Ye, *Experimental Study and Numerical Simulation of the Development of the Microstructure and Permeability of Cementitious Materials*, Delft University of Technology, Delft, The Netherlands, 2003.
- [41] Z. Lv, H. Chen, and H. Yuan, "Quantitative solution on dosage of repair-agent for healing of 3D simplified cracks in materials: short capsule model," *Materials and Structures*, vol. 44, no. 5, pp. 987–995, 2011.
- [42] S. V. Zemskov, H. M. Jonkers, and F. J. Vermolen, "Two analytical models for the probability characteristics of a crack hitting encapsulated particles: application to self-healing materials," *Computational Materials Science*, vol. 50, no. 12, pp. 3323–3333, 2011.
- [43] A. Hrennikoff, "Solution of problems of elasticity by the framework method," *Journal of Applied Mechanics*, vol. 8, pp. 169–175, 1941.
- [44] J. G. M. van Mier, "Mode I fracture of concrete: discontinuous crack growth and crack interface grain bridging," *Cement and Concrete Research*, vol. 21, no. 1, pp. 1–15, 1991.
- [45] E. Schlangen and E. J. Garboczi, "Fracture simulations of concrete using lattice models: computational aspects," *Engineering Fracture Mechanics*, vol. 57, no. 2-3, pp. 319–332, 1997.
- [46] E. Schlangen and J. G. M. van Mier, "Simple lattice model for numerical simulation of fracture of concrete materials and structures," *Materials and Structures*, vol. 25, no. 9, pp. 534–542, 1992.
- [47] E. Schlangen and J. G. M. van Mier, "Experimental and numerical analysis of micromechanisms of fracture of cement-based composites," *Cement and Concrete Composites*, vol. 14, no. 2, pp. 105–118, 1992.
- [48] Z. Qian, *3D Lattice Analysis of Cement Paste*, Delft University of Technology, 2008.

Research Article

Compressive Behavior and Mechanical Characteristics and Their Application to Stress-Strain Relationship of Steel Fiber-Reinforced Reactive Powder Concrete

Baek-II Bae,¹ Hyun-Ki Choi,² Bong-Seop Lee,² and Chang-Hoon Bang²

¹Research Institute of Industrial Science, Hanyang University, 17 Haengdang-Dong, Seongdong-Gu, Seoul 04763, Republic of Korea

²Department of Fire and Disaster Prevention Engineering, Kyungnam University, Gyeongsangnam-do 51767, Republic of Korea

Correspondence should be addressed to Hyun-Ki Choi; chk7796@kyungnam.ac.kr

Received 21 April 2016; Revised 26 May 2016; Accepted 7 June 2016

Academic Editor: Juan J. Del Coz Díaz

Copyright © 2016 Baek-II Bae et al. This is an open access article distributed under the Creative Commons Attribution License, which permits unrestricted use, distribution, and reproduction in any medium, provided the original work is properly cited.

Although mechanical properties of concrete under uniaxial compression are important to design concrete structure, current design codes or other empirical equations have clear limitation on the prediction of mechanical properties. Various types of fiber-reinforced reactive powder concrete matrix were tested for making more usable and accurate estimation equations for mechanical properties for ultra high strength concrete. Investigated matrix has compressive strength ranged from 30 MPa to 200 MPa. Ultra high strength concrete was made by means of reactive powder concrete. Preventing brittle failure of this type of matrix, steel fibers were used. The volume fraction of steel fiber ranged from 0 to 2%. From the test results, steel fibers significantly increase the ductility, strength and stiffness of ultra high strength matrix. They are quantified with previously conducted researches about material properties of concrete under uniaxial loading. Applicability of estimation equations for mechanical properties of concrete was evaluated with test results of this study. From the evaluation, regression analysis was carried out, and new estimation equations were proposed. And these proposed equations were applied into stress-strain relation which was developed by previous research. Ascending part, which was affected by proposed equations of this study directly, well fitted into experimental results.

1. Introduction

The compressive strength of concrete is an important parameter in the design of reinforced concrete structures according to current design criteria [1]. In recent years, performance-based designs have been increasingly used, with accompanying increases in the diversity of types and strengths of concrete and reinforcement used. As a result, prediction of the compressive strength and other mechanical properties of concrete have become important to use various types of materials, because these parameters control the stress-strain behavior of concrete. The concrete stress-strain models developed in previous studies [2–11] and used extensively are based on coefficients determined from experiments. These stress-strain relations cannot be used without additional investigation because many coefficients for stress-strain relation of concrete are determined by limited number of experiments. The reason for this is that there are limits to the strength

ranges to which such models are applicable, depending on the conditions of the tests conducted to develop these models. Therefore, an equation for use in estimating the mechanical properties of ultrahigh strength fiber-reinforced concrete was derived. These equations can serve as a basis for describing the stress-strain relationships for such materials, even beyond the limits of the currently used empirical formulas or code provisions.

Usually, normal strength concrete members are designed using rectangular stress block parameters under flexure. Current design codes provide the rectangular stress block parameters for simplified design methodology. However, these stress blocks are semiempirical parameters. They are determined by tests of reinforced concrete columns and they have apparent limitations. Rectangular stress block can be used because the shape of stress-strain relation of concrete is similar to the trapezoid. However, shape of stress-strain relationship of concrete changed into triangle as increase of

TABLE 1: Mix proportions.

ID	w/b	Weight (kg/m ³)				Steel fiber**	Super-plasticizer	f_{ck} [MPa]	
		Cement	Water	Silica fume	Sand				
30-0 and f series*	0.43 [†]	344	172	—	635	1180 ^{††}	0, 37, 74, 147	0.0	30
80-0 and f series*	0.30	780	255	60	1097	114	0, 37, 74, 147	0.5	80
100-0 and f series	0.25	809	222	80	1052	162	0, 37, 74, 147	1	100
150-0 and f series	0.20	820	190	112	918	186	0, 37, 74, 147	1.04	150
200-0 and f series	0.17	830	176	207	912	246	0, 37, 74, 147	1.08	200

*f series means fiber-reinforced mix.

**0 means no fiber, 37 for 0.5% volume fraction of fiber contents, 74 means 1% volume fraction of fiber contents, and 147 means 2% volume fraction of fiber contents.

[†]Water-cement ratio was used for normal strength concrete.

^{††}Coarse aggregates were used for normal strength concrete.

compressive strength of concrete. For this reason, rectangular stress block parameters depend on the compressive strength of concrete. For the compressive strength of concrete, higher than 76 MPa, rectangular stress block parameters α_1 and β_1 of ACI318 [1] are limited by 0.85 and 0.65, respectively. However, in this case, relation between ultimate strain of concrete and peak stress should be checked again. Because high strength concrete failed with brittle manner usually, they cannot experience the slight and gradual decrease of compressive stress. It may cause the unexpected failure under flexure, especially for ultrahigh strength concrete member.

Making brittle and unexpected failure of ultrahigh strength concrete matrix under compression more ductile, steel fiber can be included in the matrix. Inclusion of steel fiber can change explosive failure of ultrahigh strength concrete and provide more tensile strength and deformability [12]. So steel fiber can usually be used for ultrahigh strength concrete matrix.

Ultrahigh performance concrete usually has much higher compressive strength and tensile strength than normal strength concrete [13, 14]. Shape of stress distribution under compression and effect of tensile strength of concrete shall be considered in design of section. Many related design guidelines were suggested the design methodologies for ultrahigh performance concrete flexural member but their safety should be investigated and more easy way to design the section shall be found. Therefore, in this study, various types of stress block and distribution combinations were evaluated with experimental result and previous research results.

2. Compression Testing of Ultrahigh Strength Steel Fiber-Reinforced Concrete

In this study, compression tests of cylindrical concrete specimens with compressive strengths in the range of 30–200 MPa were carried out to derive equations that can be safely used to estimate the mechanical properties of concrete even beyond the strength limits given in the design criteria. The test results were analyzed to determine the stress-strain relationship of concrete over a range of design concrete strengths and compare the relationship to others described by existing equations. The important mechanical properties related to the stress-strain relationship of concrete under compressive

loading that were considered in this study were the elastic modulus, the stress-to-matrix strength ratio, and the strain at the maximum stress.

2.1. Experiment Design. According to the previous researches on mechanical properties of concrete and fiber-reinforced concrete [2–11], the mechanical properties that determine the stress-strain relationship of fiber-reinforced concrete depend on the proportion of fibers contents and matrix strength of concrete. Therefore, the compressive strength of the concrete matrix and the contents of steel fiber are important parameters in this study. The compressive strength range considered was 30–200 MPa. Because it is hard to make compressive strength exceeding 100 MPa, we use reactive powder concrete (RPC) as steel fiber-reinforced concrete matrix.

Steel fibers were mixed into concrete batches at volumetric ratios of 0.5% to 2% to ensure both improvement of the structural performance of the concrete and workability of the concrete after addition of the fibers. Five cylindrical specimens ($\phi 100 \times 200$ mm in size) were produced for each mix. Loading was performed using KS F 2405 [15]. The strain rate of the specimen was measured using a compressor meter. Table 1 lists the mixes used in the testing.

2.2. Experimental Results for the Mechanical Properties of Steel Fiber-Reinforced Reactive Powder Concrete. Figure 1 shows typical stress-strain relation of steel fiber-reinforced powder concrete cylinder specimens. According to Figure 1, steel fiber can increase ductility and strength of brittle matrix. Therefore, the most important investigation shall be the increase rate of ductility and strength of matrix according to the inclusion of steel fiber. So we listed the test results for the elastic modulus, the maximum stress, and the strain at the maximum stress which show the ductility and strength of material in Table 2.

The values shown are the average values for the five specimens from each mix. The test results indicate that steel fiber significantly affects the properties related to the ductility of material. Figure 2 shows the trends in the parameters of elastic modulus and strain at peak strength with respect to the steel fiber content.

The mixes with design strengths of 30, 80, 100, 150, and 200 MPa that were reinforced with fibers at a volume

TABLE 2: Test results (mean value of test specimens).

ID	V_f [%]	E_c [MPa]	f_{co} [MPa]	ϵ_{co} [%]
C30-0	0	26,756	32.54	2.65
C30-f0.5	0.5	27,659	33.32	2.98
C30-f1.0	1.0	28,751	34.72	3.32
C30-f2.0	2.0	31,221	34.98	3.43
C80-0	0	32,970	80.79	3.16
C80-f0.5	0.5	33,597	82.60	3.55
C80-f1.0	1.0	34,097	85.17	3.64
C80-f2.0	2.0	34,768	89.01	4.04
C100-f0	0	36,233	104.86	3.39
C100-f0.5	0.5	37,376	107.39	3.71
C100-f1.0	1.0	38,732	111.93	3.95
C100-f2.0	2.0	38,099	116.92	4.09
C150-0	0	42,023	149.40	3.97
C150-f0.5	0.5	41,203	154.96	4.47
C150-f1.0	1.0	42,365	159.60	4.77
C150-f2.0	2.0	43,222	162.40	4.79
C200-0	0	45,512	198.21	4.87
C200-f0.5	0.5	45,019	202.70	4.97
C200-f1.0	1.0	46,734	210.40	5.26
C200-f2.0	2.0	47,515	216.52	5.39

V_f : volume fraction of steel fiber (%), E_c : elastic modulus (MPa), f_{co} : compressive strength of concrete (tested value, MPa), ϵ_{co} : strain corresponding peak stress.

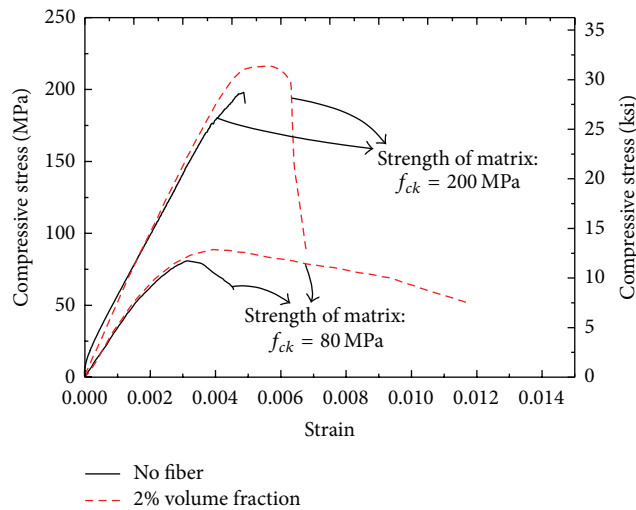


FIGURE 1: Typical uniaxial compressive stress-strain relation of steel fiber-reinforced powder reactive concrete.

of 2% exhibited compressive strength increases of 7.5%, 10.2%, 11.5%, 8.7%, and 9.2%, respectively. The strains at the maximum stress increased by 29.4%, 27.8%, 23.5%, 20.6%, and 10.6%, respectively, with 2% fiber volume fraction. The increases of strain at peak stress are significant in comparison to the increases in strength. Significant increase of strain at peak stress would be caused by the confinement effect of

steel fiber to the formation of cracks along the specimen axis, as shown in Figure 3, the failure aspects of fiber-reinforced specimen.

This reinforcing effect on the strain at peak stress was shown in all the cases of compressive strength of matrix. However, the ductility increase of the concrete specimens with strengths greater than 100 MPa was smaller than the increase of the ductility of the 30 and 80 MPa concrete. That is, at higher compressive strengths, the effect of reinforcing effect of steel fibers on improving the ductility decreases.

3. Estimation of the Mechanical Properties of Steel Fiber-Reinforced Reactive Powder Concrete

We collected concrete material test results from a number of studies [30–44] and analyzed them together with the test results obtained in this study to estimate the important parameters needed to derive a stress-strain relationship that can be easily applied over a wider range of concrete strengths than the range encompassed by previous studies. The data collected included 295 results for compressive strength increase, 134 results for the strain at the maximum stress, and 1486 results for the elastic modulus. In this study, the reinforcing effect of the fiber was characterized using a reinforcing index (RI) associated with the aspect ratio and other physical properties of the fiber. The value of RI for a particular type of fiber is determined using (1). The aspect ratio of the fibers, the fiber end shape, and the amount of fiber reinforcement are important parameters in this equation. Consider

$$RI = \frac{V_f L_f d_f}{D_f}, \quad (1)$$

where RI is reinforcing index, V_f is volume fraction of steel fiber, L_f is length of steel fiber, and D_f is diameter of steel fiber.

The term d_f in (1) is a correction factor for the end shape of the fiber. In this study, we used correction factors of 1, 2.0, and 1.5 for straight fibers, hooked fibers, and crimped fibers, respectively, to correct for the effect of fiber shape, as suggested in the literature [45].

In order to compare the proposed estimation methods and find the important parameters on mechanical characteristics on steel fiber-reinforced reactive powder concrete we also collect the empirical equations about mechanical characteristic estimation equations for concrete under uniaxial compression.

Table 3 shows an equation for estimating the strain at the maximum stress as a function of the reinforcing effect of the steel fibers and the compressive strength of the concrete. Table 4 shows an equation for estimating the elastic modulus. When examining equations about compressive mechanical characteristics on concrete and fiber-reinforced concrete, the most important parameter is compressive strength of concrete and (1), reinforcing index. Most of the equations consider the effect of steel fiber as additional value independent of compressive strength of concrete. However, as

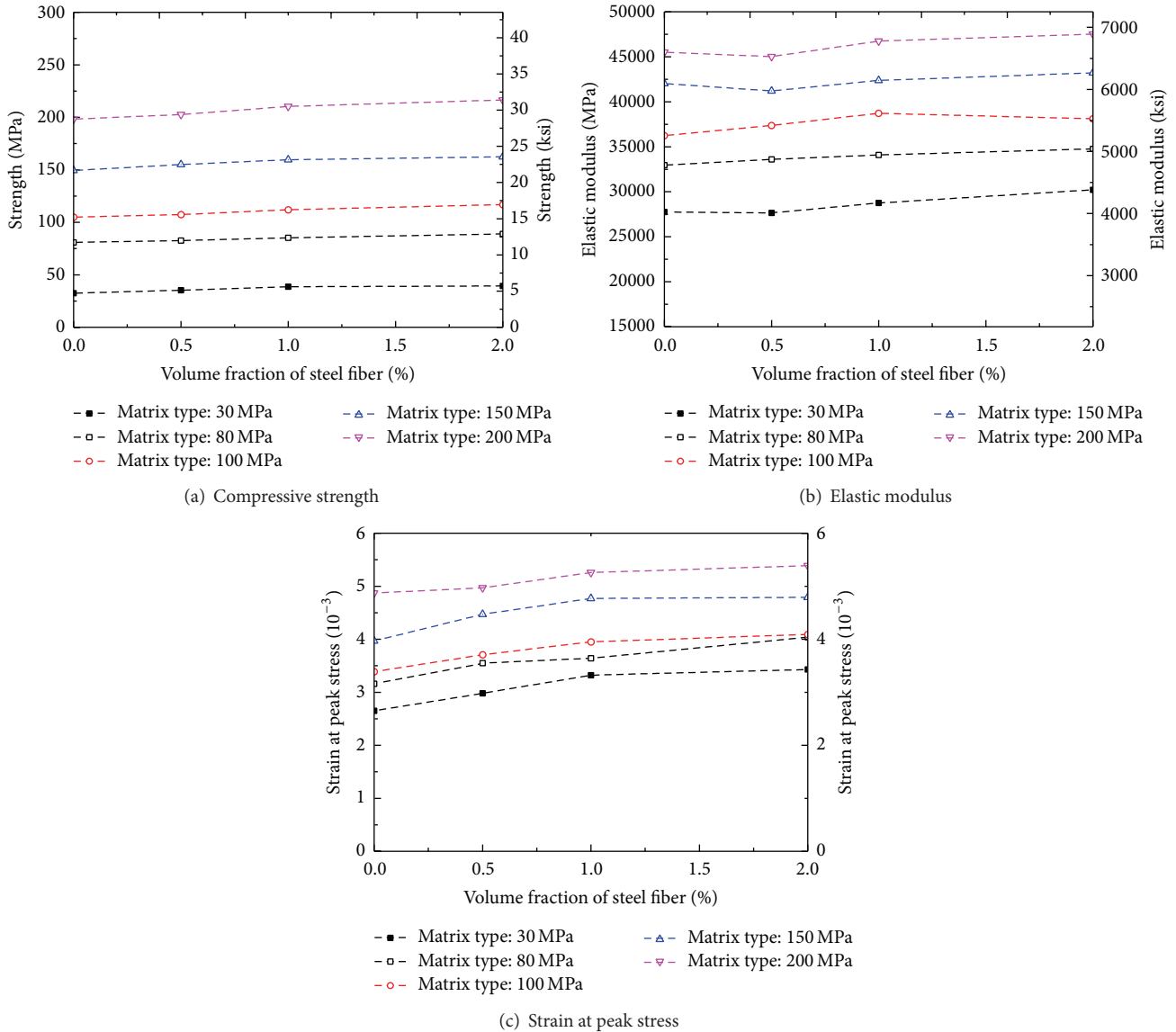


FIGURE 2: Mechanical characteristics of fiber-reinforced reactive powder concrete under uniaxial compression.



FIGURE 3: Failure of specimens under uniaxial compression.

shown in test results, increase rate of mechanical properties of steel fiber-reinforced reactive powder concrete is affected by compressive strength of concrete. In this section we quantify

the increase rate of mechanical properties of concrete considering combination of compressive strength of matrix and steel fiber contents.

3.1. Mechanical Properties of Reactive Powder Concrete Matrix.

For fiber-reinforced concrete, the elastic modulus and the strain at the maximum stress are often determined from equations that are based on test results for nonreinforced mixes. The accuracy of such estimates is significantly affected by the strength ranges of the specimens used to derive the equations. Elastic modulus and ϵ_{co} values derived from the results of material testing conducted in previous studies [30–44] and in the present study are shown in Figures 4 and 5, respectively. The associated equations are also shown. Tables 5 and 6 list the statistical parameters of the equations.

As shown in Table 5 and Figure 4, the current code provisions show the highest accuracy in the estimation of the

TABLE 3: Prediction equations for strain at peak stress (previous researches).

Researcher	Equation	Limitation [MPa]
Collins et al. [6]	$\epsilon_{co} = \frac{f_{ck}}{E_c} \frac{n}{n-1}$, $n = 0.8 + \frac{f_{ck}}{17}$, $E_c = 3320 f_{ck}^{0.5} + 6900$	$f_{ck} \leq 100$
Wee et al. [7]	$\epsilon_{co} = \frac{180 (f_{ck})^{0.25}}{10^6}$	$f_{ck} \leq 120$
Ros [16]	$\epsilon_{co} = \frac{(0.0546 + 0.003713 f_{ck})}{100}$	$f_{ck} \leq 43$
Fafitis and Shah [17]	$\epsilon_{co} = 1.491 \times 10^{-5} f_{ck} + 0.00195$	$f_{ck} \leq 66$
De Nicolo et al. [18]	$\epsilon_{co} = 0.00076 + [(0.626 f_{ck} - 4.33) \times 10^{-7}]^{0.5}$	$f_{ck} \leq 90$
CEB-fip 228 [9]	$\epsilon_{co} = \frac{0.7 (f_{ck})^{0.31}}{1000}$	$f_{ck} \leq 100$
EC2 [19]	$\epsilon_{co} = \frac{(2.0 + 0.085 (f_{ck} - 50)^{0.53})}{1000}$, for $f_{ck} \geq 50$ MPa; otherwise $\epsilon_{co} = 0.002$	$f_{ck} \leq 90$
Soroushian and Lee [20]	$\epsilon_{cof} = 0.007RI + 0.0021$, $RI = \frac{V_f L_f}{D_f}$	—
Nataraja et al. [21]	$\epsilon_{cof} = 0.002 + 0.006(RI)$, $RI = \frac{W_f L_f}{D_f}$	$f_{ck} \leq 50$
Dhakar et al. [22]	$\epsilon_{cof} = 0.002 + 2000\alpha_c V_f^2$, $\alpha_f = 1.0$ (flat), $\alpha_f = 2.4$ (hooked)	$f_{ck} \leq 40$

E_c : secant elastic modulus of concrete at $0.45 f_{ck}$ (MPa), ϵ_{co} : strain corresponding to peak stress (normal concrete), f_{ck} : compressive strength of concrete (MPa), RI: reinforcing index, D_f : diameter of steel fiber (mm), L_f : length of steel fiber (mm), V_f : volume fraction of steel fiber, W_f : weight fraction of steel fiber.

TABLE 4: Prediction equations for modulus of elasticity (previous researches).

Researcher	Equation	Limitation
KCI2007 [23]	$E_c = 8,500 \sqrt[3]{f_{cu}}$, $E_c = 0.077 w_c^{1.5} \sqrt[3]{f_{cu}}$, $f_{cu} = f_{ck} + 8$	Did not specify but $\sqrt{f_{ck}}$ cannot exceed 8.4 MPa
KCI2012 [24]	$E_c = 8,500 \sqrt[3]{f_{cu}}$, $E_c = 0.077 w_c^{1.5} \sqrt[3]{f_{cu}}$, $f_{cu} = f_{ck} + \Delta f$, where $\Delta f = 4$ when $f_{ck} \leq 40$ MPa and $\Delta f = 6$ when $f_{ck} > 60$ MPa. Interpolate between 40 MPa and 60 MPa	
ACI318-11 [1]	$E_c = 4,700 \sqrt{f_{ck}}$ (normal weight concrete), $E_c = w_c^{1.5} 0.043 \sqrt{f_{ck}}$	
CEB-fip 228 [9]	$E_{ci} = E_{co} \left[\frac{(f_{ck} + \Delta f)}{f_{cmo}} \right]^{1/3}$, $\Delta f = 8$, $f_{cmo} = 10$, $E_{co} = 22$ GPa	$f_{ck} \leq 90$
Martinez et al. [25]	$E_c = 3,320 \sqrt{f_{ck}} + 6,900$	$21 \text{ MPa} < f_{ck} < 83 \text{ MPa}$
Cook [26]	$E_c = 3.385 \times 10^{-5} w_c^{2.55} (f_{ck})^{0.315}$	—
Ahmad and Shah [27]	$E_c = 3.385 \times 10^{-5} w_c^{2.55} (f_{ck})^{0.325}$	$f_{ck} < 84 \text{ MPa}$
Graybeal [11]	$E_c = 3,840 \sqrt{f_{ck}}$	$f_{ck} < 200 \text{ MPa}$
Gao et al. [28]	$E_{cf} = E_c (1 + 0.173(RI))$	$70 \text{ MPa} < f_{ck} < 85 \text{ MPa}$
Padmarajaiah [29]	$E_{cf} = E_c + 2440(RI)$	$f_{ck} < 69 \text{ MPa}$

E_c : secant elastic modulus of concrete at $0.45 f_{ck}$ (MPa), w_c : unit weight of concrete (kg/m^3), f_{ck} : compressive strength of concrete (MPa), RI: reinforcing index, $RI = V_f L_f / D_f$.

elastic modulus. As shown in statistical values for KCI2012, current Korean design code provision, a standard deviation is not the lowest among other estimation methods.

However, mean value, coefficient of variation, and IAE (integrated absolute error) values for KCI2012 have lowest value among other prediction methods. In general, the estimation equation for the elastic modulus tends to underestimate the modulus of elasticity for normal strength concrete and overestimate the modulus of elasticity for high strength concrete. However, highest accuracy of KCI2012 occurs because the estimation equation was developed to provide relatively safe estimates for both normal strength and high strength concrete, using different value of Δf according to the compressive strength of concrete. Therefore, even for an ultrahigh strength concrete, there should be no significant

problems associated with using the estimation equation presented in the current design standards to estimate the elastic modulus of the concrete.

Because ϵ_{co} , the strain at the maximum stress, is an important boundary condition in defining the stress-strain relationship and important design parameter, we also compared the results of previous studies and the results of this study with respect to this parameter. In previous studies on the stress-strain relationship of concrete, the typical value used for the strain at the maximum stress is 0.002. However, Figure 5 confirms that the strain at the maximum stress tends to increase with the compressive strength of the concrete. It was confirmed that equations from previous studies for estimation of ϵ_{co} , which take the form of an exponential function of the compressive strength, underestimate the

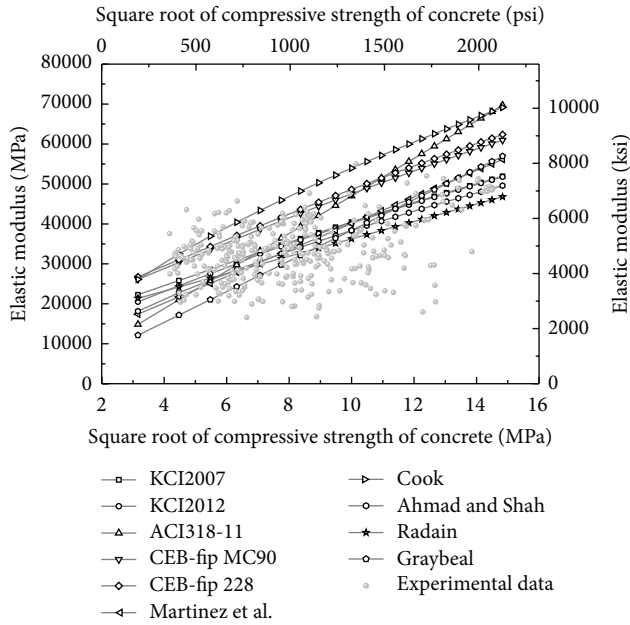


FIGURE 4: Elastic modulus: test results and prediction equations.

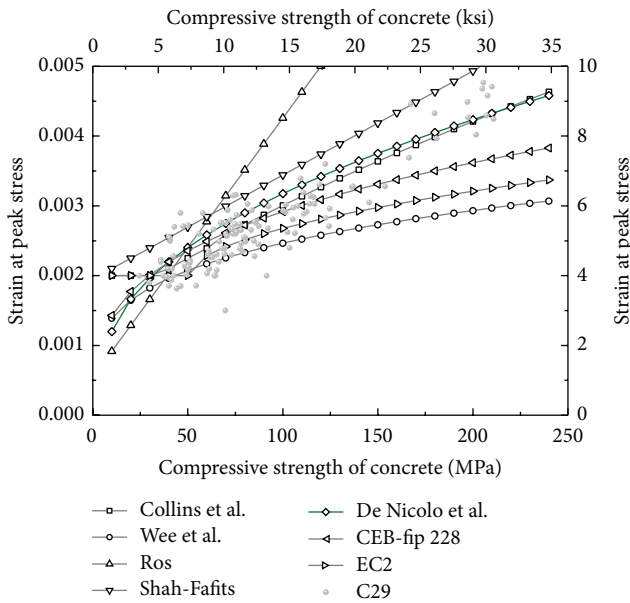


FIGURE 5: Strain at peak stress: test results and prediction equations.

increase in ε_{co} with increasing compressive strength. Table 6 confirms that the accuracy of these equations increases as the compressive strength range considered increases. Given that the equation proposed by Collins et al. [6] has the lowest IAE and average value, Collins et al. [6] equation for ε_{co} was concluded to be suitable for use with high strength mixes. Collins et al. [6] equation, shown in Table 1, reflects the effect of the elastic modulus. Because our analysis confirmed that the equation presented in the current design standards yields the highest accuracy in the estimation of the elastic modulus, this equation was used with Collins et al. [6] equation to

TABLE 5: Statistics on the prediction methods for modulus of elasticity.

Researcher	Mean	SD	CV	IAE
KCI2007 [23]	0.99	0.12	0.12	8.52
KCI2012 [24]	1.01	0.12	0.12	8.42
ACI318-11 [1]	0.93	0.13	0.14	13.72
CEB-fip 228 [9]	0.83	0.10	0.12	20.65
Martinez et al. [25]	1.05	0.13	0.12	9.45
Cook [26]	0.75	0.09	0.12	32.44
Ahmad and Shah [27]	1.07	0.12	0.12	9.83
Graybeal [11]	1.14	0.16	0.14	13.54

SD: standard deviation, CV: coefficient of variation, IAE: integrated absolute error (%).

TABLE 6: Statistics on the prediction methods for strain at peak stress under uniaxial compression.

Researcher	Mean	SD	CV	IAE (%)
Collins et al. [6]	0.99	0.12	0.12	8.74
Wee et al. [7]	1.16	0.17	0.15	16.37
Ros [16]	0.78	0.19	0.25	42.04
Fafitis and Shah [17]	0.84	0.09	0.11	19.49
De Nicolo et al. [18]	0.93	0.11	0.12	11.58
CEB-fip 228 [9]	0.99	0.13	0.13	10.56
EC2 [19]	1.09	0.15	0.14	12.52

SD: standard deviation, CV: coefficient of variation, IAE: integrated absolute error (%).

estimate ε_{co} . As a result, the IAE decreased by 8.67%, and the average of the ratios of experimental values to estimated values was found to be 1.02, indicating that the estimated values were on the safe side.

3.2. Effect of Steel Fiber Contents on Compressive Strength Increase. Figure 6 shows test results from previous studies [30–44] and from this study on the effect of the steel fiber contents on the increase in concrete compressive. The increase of maximum stress of test results was expressed as the ratio of the compressive strength of fiber-reinforced specimens to the compressive strength of non-fiber-reinforced specimens. The average compressive strength increase due to fiber reinforcement was 9.7%. However, for specimens of the same design compressive strength, the compressive strength tended to increase linearly with increasing proportions of fiber. Examination of the results classified by the design compressive strength of the concrete indicated that the increase achieved in compressive strength with increasing fiber content tended to decrease with increasing design compressive strength. However, it is difficult to confirm that a clear correlation exists because of the high degree of variation in the test results. In particular, the correlation between compressive strength increase and fiber content tended to decrease with increasing design compressive strength. The results of our study suggest that the increases achieved in compressive strength with increasing fiber content were comparable over the range of

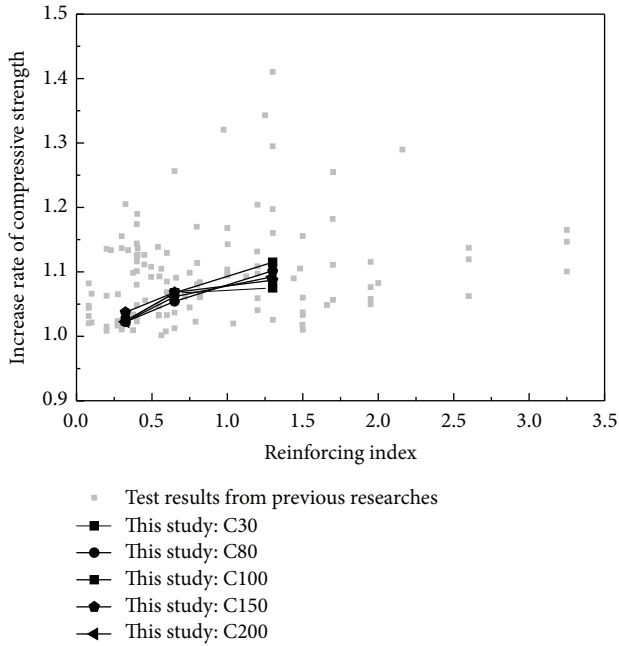


FIGURE 6: Compressive strength increase rate according to reinforcing index.

compressive strengths considered. A maximum compressive strength increase of 10% was verified.

3.3. Effect of Steel Fiber Contents on Strain at Peak Stress. Figure 7 illustrates the effect of the steel fiber contents on the change in the strain at the maximum stress, as indicated by the results of previous studies and by the results of this study. The change in the strain at the maximum stress exhibited a higher correlation to the contents of steel fibers than did the increase with compressive strength of matrix. The results of the experiments conducted in our study are shown in Figure 7 along with the results from previous studies. The test results indicate that, for mixes with design compressive strengths of 80 MPa, ϵ_{co} increases with increasing steel fiber content but, for mixes with strengths of more than 100 MPa, ϵ_{co} decreases with increasing fiber content. This phenomenon was particularly significant for the specimens with design compressive strengths of 200 MPa. Normal strength concrete has shown similar change according to the steel fiber inclusion.

3.4. Effect of Steel Fiber Contents on Elastic Modulus of Concrete. Higher compressive strength of concrete is achieved by homogenization of the constituent materials and of their strengths. Accordingly, the elastic modulus of concrete tends to increase with increasing concrete strength. The elastic modulus derived from test results obtained in previous studies and in our study was examined to assess the trend in the elastic modulus of fiber-reinforced reactive powder concrete with respect to the previously defined reinforcing index. Figure 8 shows the distribution of elastic modulus of concrete test results according to the reinforcing index. Because the elastic modulus is affected by the strength and strain simultaneously, the increases in strength and

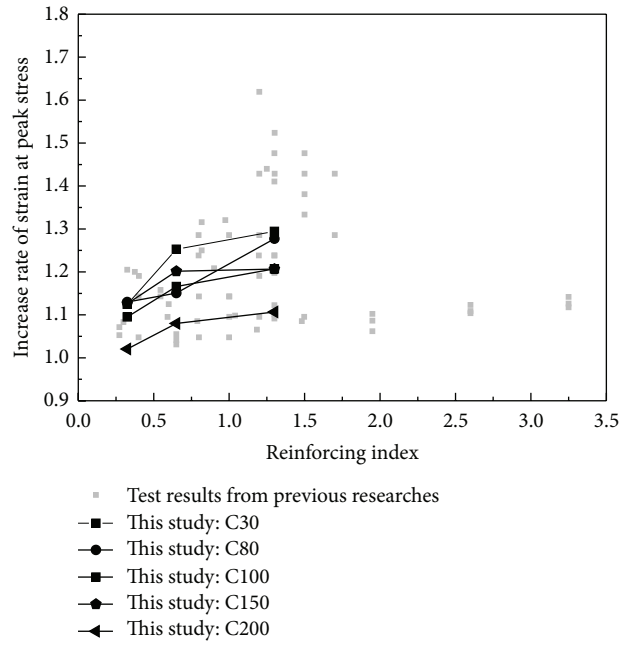


FIGURE 7: Strain at peak stress increase rate according to reinforcing index.

stress exhibit similar trends. The degree to which the elastic modulus increased with the fiber reinforcing index decreased with increasing concrete compressive strength. However, the average increase was 6.5% which is lesser than that for the strength or strain. Our test results revealed similar trends. Specimens in the C80 test group (with design compressive strengths of 80 MPa) exhibited the greatest increases among high strength concrete mixes. Specimens in test groups with design compressive strength greater than 100 MPa exhibited smaller increases and trends similar to those observed in the results from previous studies.

4. Equation for Estimating the Effect of the Steel Fiber Contents on the Mechanical Properties of Steel Fiber-Reinforced Reactive Powder Concrete under Uniaxial Compression

The effects of steel fiber on concrete strength improvement observed in the test results obtained in this study and in previous studies [30–44] were quantified for compressive strength ranges in increments of 20 MPa, as shown in Figure 9. The magnitude of the improvement within each range was determined from linear regression analysis of the data for the specimens within that range. The regression analysis was performed using the model form shown as

$$\frac{k_{cf}}{k_{co}} = 1 + RI \times \alpha, \tag{2}$$

where k_{cf} is mechanical properties for steel fiber-reinforced concrete, k_{co} is mechanical properties on nonreinforced concrete, RI is reinforcing index, and α is regression coefficient.

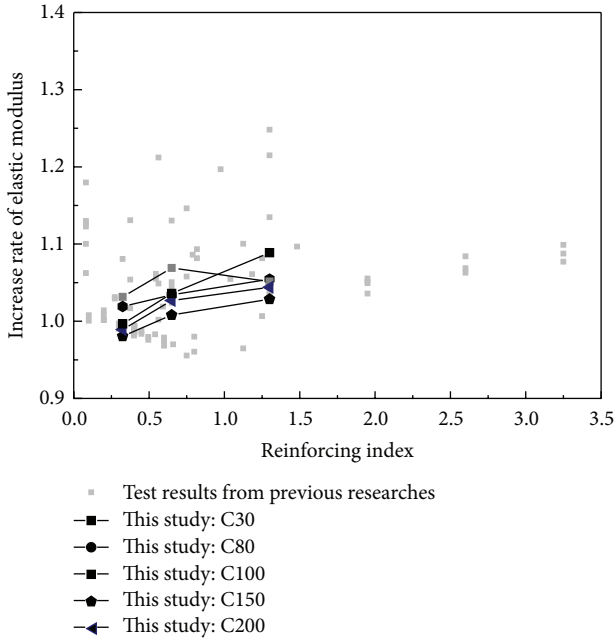


FIGURE 8: Elastic modulus increase rate according to reinforcing index.

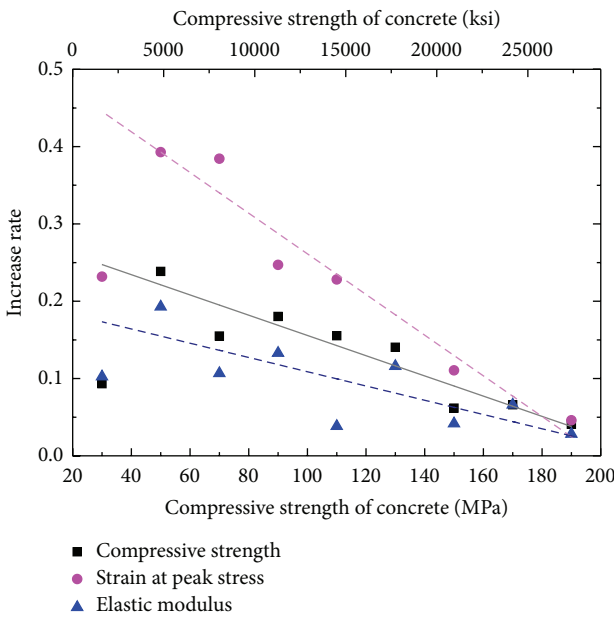


FIGURE 9: Change of statistical values and trend lines on mechanical characteristics of steel fiber-reinforced reactive powder concrete under uniaxial compression.

The increase in compressive strength with inclusion of steel fiber exhibited a clear decreasing trend with increasing concrete compressive strength. The results of the regression analysis suggest that the magnitude of the improvement in the compressive strength, which depends on the elastic modulus, the strain at the maximum stress, and the compressive strength of concrete, can be expressed by

$$\frac{k_{cf}}{k_{co}} = 1 + RI (a_1 - b_1 f_{ck}). \quad (3)$$

In the above equation, a_1 and b_1 are regression coefficients. The values of a_1 and b_1 were determined to be 0.29 and 0.0013, respectively, for change in the compressive strength; 0.52 and 0.0026, respectively, for change in ϵ_{co} ; and 0.20 and 0.00092, respectively, for change in elastic modulus.

In order to verify the applicability of proposed equations predicting mechanical properties of steel fiber-reinforced reactive powder concrete under uniaxial compression, we apply these equations to the stress-strain relation of concrete under uniaxial compression.

Most of the stress-strain relation of concrete are determined by the important mechanical properties, elastic modulus of concrete, and strain at peak stress. Stress-strain relations proposed by previous researches were investigated. There are several types of stress-strain relation of concrete. But in this study, we investigated the way to use the elastic modulus for predicting stress-strain relation of concrete, because stress-strain relations of high strength or ultrahigh strength concrete depend on the elastic modulus as we investigated in this study. The first one of stress-strain relation of concrete we investigated is suggested by Collins et al. [6] and the other is suggested by Attard and Setunge [10]. Collins et al. use the differential of plasticity as base model and Attard and Setunge [10] use the mathematical model to predict stress-strain relationship. Both of them use the elastic modulus of concrete as main variable for prediction of stress-strain relation. However, mathematical model which was suggested by Attard and Setunge [10] needs more boundary conditions such as inflection points after experiencing peak stress. Inflection points of descending curve of stress-strain relation are highly dependent on the experimental equipment. Therefore, in this study, stress-strain relation suggested by Collins et al. [6] is used for prediction of stress-strain relation by using proposed equation of main variables such as elastic modulus and strain at peak stress. The stress-strain relation suggested by Collins et al. [6] can be described using

$$\frac{f_c}{f'_c} = \frac{n(\epsilon_{cf}/\epsilon'_c)}{n-1 + (\epsilon_{cf}/\epsilon'_c)^{nk}}, \quad (4)$$

where f'_c is peak stress obtained from cylinder test, ϵ'_c is strain when f_c reaches f'_c , n is curve fitting factor equal to $E_c/(E_c - E'_c)$, E_c is tangent stiffness when ϵ_{cf} is zero, E'_c is secant stiffness when ϵ_{cf} is ϵ'_c , and k model the strain decay before and after experiencing peak stress. n and k are suggested by using data of high strength concrete and we decided to use these two variables without change. n and k can be calculated by using

$$n = 0.8 + \frac{f'_c}{17}, \quad (5)$$

$$k = 0.67 + \frac{f'_c}{62}.$$

For the verification of the applicability of suggested equations, stress-strain relationships of concrete were constructed and compared with experimental results. As can be seen in Figure 10, predicted stress-strain relationship

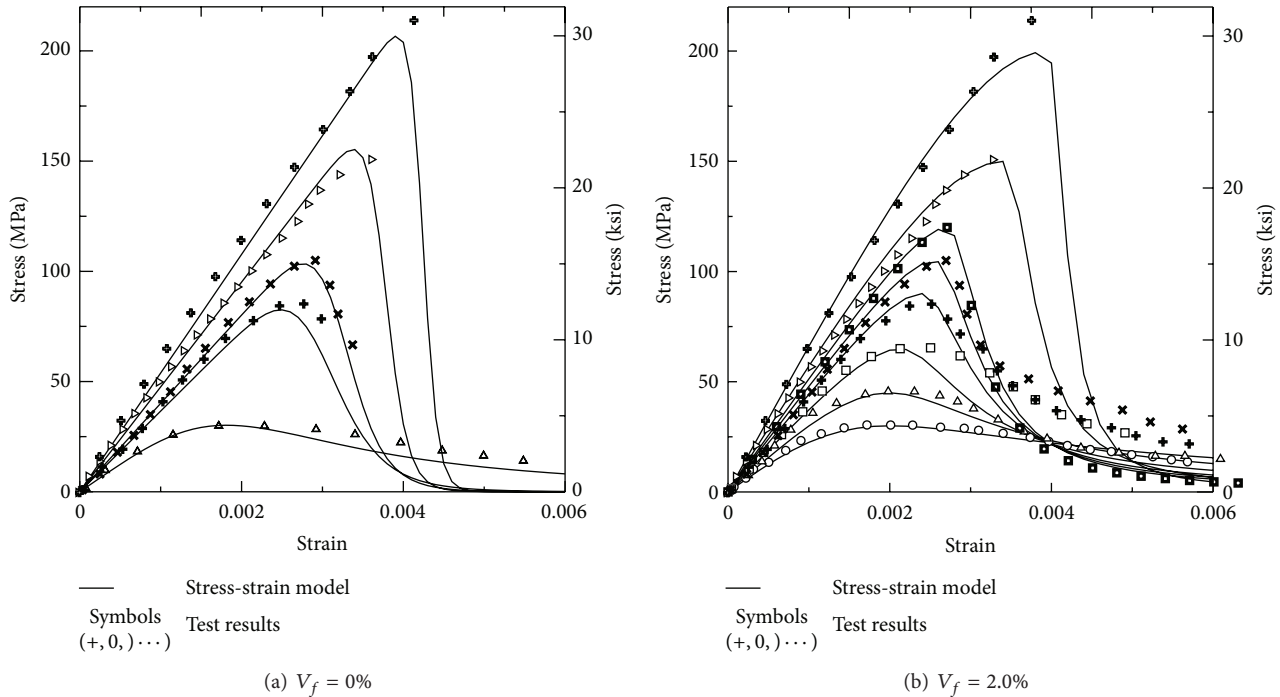


FIGURE 10: Applicability for stress-strain relationship: prediction and experimental results.

of ascending curve was well fitted into the experimental results. However, descending curve of prediction shows less accuracy in descending part of the total stress-strain relation. The inaccuracy of descending curve of stress-strain relation prediction might be caused by the difference of stiffness of experiencing equipment. Making more exact solution, energy absorption capacity under compression shall be investigated.

5. Conclusion

In this study, we conducted material testing to evaluate the properties of ultrahigh strength concrete which was made from reactive powder concrete reinforced with steel fibers under compressive loading, and we evaluated the suitability of equations developed in previous studies for use in estimating material properties of ultrahigh strength concrete. The results of this study are summarized as follows.

- (1) The compression test results for non-fiber-reinforced and fiber-reinforced ultrahigh strength concrete specimens indicated that non-fiber-reinforced concrete specimens exhibited brittle fractures, whereas fiber-reinforced concrete specimens did not. The test results suggest that reinforcing fibers resisted the horizontal tensile forces induced by vertical compressive loading.
- (2) The test results confirmed that the effects of steel fiber on the concrete compressive strength, strain at maximum stress, and elastic modulus exhibited linear trends regardless of the compressive strength of the mix. Compressive strength and elastic modulus were not significantly affected by the amount of reinforcing

fiber in the mix. However, a relatively strong effect on the strain at the maximum stress was confirmed.

- (3) The mechanical properties of the concrete, such as the elastic modulus and the strain at the peak stress, were estimated with a high degree of accuracy using the secant modulus estimation equation presented in the current design standards and by Collins et al.'s equation, respectively. Thus, the applicability of these equations to concrete in the ultrahigh strength range was confirmed.
- (4) Regression analyses were performed on the test results from this study and previous studies to describe the effects of fiber reinforcement on the material properties of interest. The analysis results showed that the reinforcing effects of steel fiber can be expressed in terms of the fiber reinforcing index.
- (5) Analysis of the test results confirmed that the relevant mechanical properties of concrete mix at a given strength level improve in proportion to the fiber reinforcement index. Linear regression analyses were performed for the mechanical properties using equations of the same form for all strength levels. The equation form was chosen so that different values of the regression coefficients were obtained for each strength level.
- (6) Proposed equations for mechanical properties under uniaxial compression on concrete can be used as main variables of stress-strain relation. According to comparison, ascending curve of stress-strain relation can be well fitted into experimental results. However, descending part of stress-strain relation

cannot be well fitted because prediction method did not consider the energy dissipation capacity after experiencing peak stress. In order to construct full range of stress-strain relation of fiber-reinforced concrete, boundary conditions after peak stress shall be considered.

Competing Interests

The authors declare that there is no conflict of interests regarding the publication of this paper.

Acknowledgments

This research was supported by Basic Science Research Program through the National Research Foundation of Korea (NRF) funded by the Ministry of Science, ICT & Future Planning (15CTAP-C097470-01 and NRF-2014R1A1A1005444).

References

- [1] ACI Committee 318, *Building Code Requirements for Structural Concrete (ACI 318-11) and Commentary*, American Concrete Institute, Farmington Hills, Mich, USA, 2011.
- [2] S. Popovics, "A numerical approach to the complete stress-strain curve of concrete," *Cement and Concrete Research*, vol. 3, no. 5, pp. 583–599, 1973.
- [3] M. Sargin, *Stress-Strain Relationship for Concrete and the Analysis of Structural Concrete Sections, Study 4*, Solid Mechanics Division, University of Waterloo, Waterloo, Canada, 1971.
- [4] A. Tomaszewicz, *Betongens Arbejdsdiagram, SINTEF, STF65, A84065*, Trondheim, 1984.
- [5] D. J. Carreira and K.-H. Chu, "Stress-strain relationship for plain concrete in compression," *Journal of the American Concrete Institute*, vol. 82, no. 6, pp. 797–804, 1985.
- [6] M. P. Collins, D. Mitchell, and J. G. MacGregor, "Structural design considerations for high-strength concrete," *Concrete International*, vol. 15, no. 5, pp. 27–34, 1993.
- [7] T. H. Wee, M. S. Chin, and M. A. Mansur, "Stress-strain relationship of high-strength concrete in compression," *Journal of Materials in Civil Engineering*, vol. 8, no. 2, pp. 70–76, 1996.
- [8] P. T. Wang, S. P. Shah, and A. E. Naaman, "Stress-strain curves of normal and lightweight concrete in compression," *ACI Journal Proceedings*, vol. 75, pp. 603–611, 1978.
- [9] Comité Euro-International du Béton-Fédération Internationale de la Précontrainte, "High performance concrete—recommended extensions to the model code 90, research needs," *CEB Bulletin*, no. 228, p. 60, 1995.
- [10] M. M. Attard and S. Setunge, "Stress-strain relationship of confined and unconfined concrete," *ACI Materials Journal*, vol. 93, no. 5, pp. 432–442, 1996.
- [11] B. A. Graybeal, "Compressive behavior of ultra-high-performance fiber-reinforced concrete," *ACI Materials Journal*, vol. 104, no. 2, pp. 146–152, 2007.
- [12] A. K. H. Kwan and L. G. Li, "Combined effects of water film thickness and paste film thickness on rheology of mortar," *Materials and Structures/Materiaux et Constructions*, vol. 45, no. 9, pp. 1359–1374, 2012.
- [13] F. de Larrard and T. Sedran, "Optimization of ultra-high-performance concrete by the use of a packing model," *Cement and Concrete Research*, vol. 24, no. 6, pp. 997–1009, 1994.
- [14] L. G. Li and A. K. H. Kwan, "Packing density of concrete mix under dry and wet conditions," *Powder Technology*, vol. 253, pp. 514–521, 2014.
- [15] KS F 2405, *Standard Test Method for Compressive Strength of Concrete*, Korean Agency for Technology and Standards, 2010.
- [16] M. Ros, *Material-Technological Foundation and Problems of Reinforced Concrete*, Bericht no. 162, Eidgenössische Materialprüfungs- und Versuchsanstalt für Industrie, Bauwesen und Gewerbe, Zurich, Switzerland, 1950.
- [17] A. Fafitis and S. P. Shah, "Predictions of ultimate behavior of confined columns subjected to large deformations," *Journal of the American Concrete Institute*, vol. 82, no. 4, pp. 423–433, 1985.
- [18] B. De Nicolo, L. Pani, and E. Pozzo, "Strain of concrete at peak compressive stress for a wide range of compressive strengths," *Materials and Structures*, vol. 27, no. 4, pp. 206–210, 1994.
- [19] European Committee for Standardization (CEN), *Design of Concrete Structures—Part 1-1: General Rules and Rules for Buildings*, Eurocode 2, Brussels, Belgium, 2004.
- [20] P. Soroushian and C. H. Lee, "Constitutive modeling of steel fiber reinforced concrete under direct tension and compression. fibre reinforced cements and concretes : recent developments," in *Proceedings of the International Conference held at the University of Wales, Collige of Cardiff, School of Engineering, United Kingdom*, London, UK, September 1989.
- [21] M. C. Nataraja, N. Dhang, and A. P. Gupta, "Stress-strain curves for steel-fiber reinforced concrete under compression," *Cement and Concrete Composites*, vol. 21, no. 5-6, pp. 383–390, 1999.
- [22] R. P. Dhakal, C. Wang, and J. B. Mander, "Behavior of steel fibre reinforced concrete in compression," in *Proceedings of the Nanjing: International Symposium on Innovation & Sustainability of Structures in Civil Engineering*, 2005.
- [23] Korea Concrete Institute, *Concrete Design Code and Commentary*, Kimoondang Publishing Company, Seoul, Republic of Korea, 2007.
- [24] Korea Concrete Institute, *Concrete Design Code and Commentary*, Kimoondang Publishing Company, Seoul, Korea, 2012.
- [25] S. Martinez, A. H. Nilson, and F. Slate, "Spirally reinforced high-strength concrete columns," *ACI Journal*, vol. 81, no. 5, pp. 431–442, 1984.
- [26] J. E. Cook, "10,000 PSI concrete," *Concrete International: Design and Construction*, vol. 11, no. 10, pp. 67–75, 1989.
- [27] S. H. Ahmad and S. P. Shah, "Complete triaxial stress-strain curves for concrete," *Journal of the Structural Division*, vol. 108, no. 4, pp. 728–742, 1982.
- [28] J. Gao, W. Sun, and K. Morino, "Mechanical properties of steel fiber-reinforced, high-strength, lightweight concrete," *Cement and Concrete Composites*, vol. 19, no. 4, pp. 307–313, 1997.
- [29] S. K. Padmarajaiah, *Influence of fibers on the behavior of high strength concrete in fully/partially prestressed beams: an experimental and analytical study [Ph.D. thesis]*, Indian Institute of Science, Bangalore, India, 1999.
- [30] H.-K. Choi, B.-I. Bae, and C.-S. Choi, "Mechanical characteristics of ultra high strength concrete with steel fiber under uniaxial compressive stress," *Journal of the Korea Concrete Institute*, vol. 27, no. 5, pp. 521–530, 2015.
- [31] S. V. T. J. Perera, H. Mutsuyoshi, and S. Asamoto, "Properties of high-strength concrete," in *Proceedings of the 12th International Summer Symposium of Japan Society of Civil Engineers (JSCE '10)*, Funabashi, Japan, 2010.

- [32] K. F. Sarsam, I. A. S. Al-Shaarbaf, and M. M. S. Ridha, "Experimental investigation of shear-critical reactive powder concrete beams without web reinforcement," *Engineering & Technology Journal*, vol. 30, no. 17, pp. 2999–3022, 2012.
- [33] D. A. Pandor, *Behavior of high strength fiber reinforced concrete beams in shear [M.S. thesis]*, Massachusetts Institute of Technology, 1994.
- [34] J. Thomas and A. Ramaswamy, "Mechanical properties of steel fiber-reinforced concrete," *Journal of Materials in Civil Engineering*, vol. 19, no. 5, pp. 385–392, 2007.
- [35] S. Kang and G. Ryu, "The effect of steel-fiber contents on the compressive stress-strain relation of Ultra High Performance Cementitious Composites (UHPCC)," *Journal of the Korea Concrete Institute*, vol. 23, no. 1, pp. 67–75, 2011.
- [36] P. Bhargava, U. K. Sharma, and S. K. Kaushik, "Compressive stress-strain behavior of small scale steel fibre reinforced high strength concrete cylinders," *Journal of Advanced Concrete Technology*, vol. 4, no. 1, pp. 109–121, 2006.
- [37] Y.-C. Ou, M.-S. Tsai, K.-Y. Liu, and K.-C. Chang, "Compressive behavior of steel-fiber-reinforced concrete with a high reinforcing index," *Journal of Materials in Civil Engineering*, vol. 24, no. 2, pp. 207–215, 2012.
- [38] A. Samer Ezeldin and P. N. Balaguru, "Normal- and high-strength fiber reinforced concrete under compression," *Journal of Materials in Civil Engineering*, vol. 4, no. 4, pp. 415–429, 1992.
- [39] B.-W. Jo, Y.-H. Shon, and Y.-J. Kim, "The evaluation of elastic modulus for steel fiber reinforced concrete," *Russian Journal of Nondestructive Testing*, vol. 37, no. 2, pp. 152–161, 2001.
- [40] O. Kazuhiro, S. Shunsuke, A. Hideo et al., *An Experimental Study on the Compressive Properties of the Super-High Strength Concrete*, vol. 25, Architectural Institute of Japan, China Branch, Research Report Collection, 2002.
- [41] A. R. Murthy, N. R. Iyer, and B. K. R. Prasad, "Evaluation of mechanical properties for high strength and ultrahigh strength concretes," *Advances in Concrete Construction*, vol. 1, no. 4, pp. 341–358, 2013.
- [42] N. N. Meleka, A. A. Bashandy, and M. A. Arab, "Ultra high strength concrete using economical materials," *International Journal of Current Engineering and Technology*, vol. 3, no. 2, pp. 393–402, 2013.
- [43] D. Moldovan and C. Măgureanu, "Stress-strain diagram for high strength concrete elements in flexure," in *Proceedings of the 3rd International Conference Advanced Composite Materials Engineering (COMAT '10)*, pp. 137–142, Transilvania University Press of Brasov, Brasov, Romania, 2010.
- [44] W. I. Khalil and Y. R. Tayfur, "Flexural strength of fibrous ultra high performance reinforced concrete beams," *ARPJ Journal of Engineering and Applied Sciences*, vol. 8, no. 3, pp. 200–214, 2013.
- [45] R. Narayanan and I. Y. S. Darwish, "Use of steel fibers as shear reinforcement," *ACI Structural Journal*, vol. 84, no. 3, pp. 216–227, 1987.

Research Article

In Situ Test of Grouting Reinforcement for Water-Enriched Sandy Gravel Ground in River Floodplain

Jinxing Lai, Zhihua Feng, Junling Qiu, Jianxun Chen, and Haobo Fan

School of Highway, Chang'an University, Xi'an 710064, China

Correspondence should be addressed to Jinxing Lai; 373159626@qq.com and Junling Qiu; 870133597@qq.com

Received 23 March 2016; Revised 5 June 2016; Accepted 28 June 2016

Academic Editor: Juan J. Del Coz Díaz

Copyright © 2016 Jinxing Lai et al. This is an open access article distributed under the Creative Commons Attribution License, which permits unrestricted use, distribution, and reproduction in any medium, provided the original work is properly cited.

The performance of the ground treatment is always critical for a tunnel excavated in unstable stratum. Laodongnanlu Xiangjiang Tunnel (Changsha, China) across the Xiangjiang River will be constructed in a sandy gravel ground which is characterized by loose structure, extensive porosity, elevated sensitivity, poor stability, and a high groundwater table. Permeation grouting will be employed to improve the bearing capacity and mitigate groundwater movement into the excavation. In order to seek suitable injection parameters and grouting method, a field trial of vertical grouting was conducted in the sandy gravel stratum in river floodplain. A series of tests focusing on grout material, grouting sequence of boreholes, injection pressure, and grouting volume were performed to improve the sandy gravel mass strength and reduce water permeability. The examination of the results obtained during water pressure testing and core drilling on completion of the grouting trial successfully demonstrated that the specified injection criteria had led to an expected effect. Grouting control method of this saturated sandy gravel stratum was concluded after the test, which would contribute to the future pregrouting work during the tunnelling.

1. Introduction

Civil engineering designed in natural ground or stratum often encounters soft, broken, or loose strata, in which effective reinforcement is necessary when the ground bearing capacity, strength, and permeability cannot meet the requirements. A universal and effective method for ground treatment is grouting [1, 2], which is initially invented in France during the 19th century and gradually utilized to improve soil/rock quality along with the invention of cement grout. In the 20th century, grouting technology has been widely applied to dam waterproofing, treatment of weak strata, and reinforcement of tunnel surrounding rock. Different grouting methodologies, including permeation grouting, jet grouting, compaction grouting, and fracture grouting, are applicable for different geotechnical situations. Compared with other stratum reinforcement methods such as dynamic compaction, drainage consolidation method, and vibration compaction, grouting is superior in flexibility, equipment design, efficient application, and less overall strata disturbance [3]. Grout equipment configuration and construction methods have been gradually improved and become much more sophisticated [4–10].

Grouting reinforcement may occur in rock formation, general soil stratum, and sandy gravel stratum. Grouting in the rock strata penetrates cracks for directional filling, providing reinforcement and water plugging, which has been widely developed in engineering application. With good homogeneity in soil strata, the ground strength can be easily improved by grouting methods and many relevant studies have been conducted on the soil strata grouting [11–14]. Generally, permeation grouting is applied to reinforce sandy gravel stratum, in which the grout can easily diffuse and is difficult to control. The sandy gravel stratum is a type of quaternary accumulation consisting of fine sand, gravel, pebble, and boulders, with a loose structure, poor cemented performance, high porosity, elevated sensitivity, and richness in groundwater sometimes. And grouting is the main way to improve the stratum strength [15, 16].

Dano and Tsukamoto et al. [17, 18] studied the reinforcement mechanism and mechanical variation law of grouted sands through laboratory testing; Yang and Yu et al. [19, 20] conducted a laboratory grouting test in typical sandy pebble, regressing some equations about the relations of diffusion



FIGURE 1: The aerial view of project place.

radius, injection pressure, and grouting parameters. Song and Bezuijen et al. [21–24] made a research related to shield tunnelling through gravel stratum and an effective grouting scheme for stabilizing stratum and reducing grout settlement was carried out. Teng and Zhang [25] fabricated new grout materials with the ability to uniformly diffuse as a columnar shape. However, those researches are usually focused on laboratory experiment and the small local scope reinforcement of shield tunnel; few studies have been conducted on grouting parameters and control methods in natural water-enriched sandy gravel stratum. An in situ test of vertical grouting in the typical river floodplain sandy gravel strata was designed to explore suitable grouting parameters and control rules, which will guide the excavation of the underwater tunnel project of Laodongnanlu Xiangjiang Tunnel.

2. Engineering Overview

2.1. Tunnel Situations. Laodongnanlu Xiangjiang Tunnel, designed as an important urban road connecting the Yuelu District and the Tianxin District, will cross the Xiangjiang River and the Orange Islands according to the urban planning of Changsha City. The tunnel is designed to be an urban trunk road with two independent tunnel chambers at an average distance of 35 m, a scale of 4-lane double-way, and 4.01 km length. Design speed is 50 km/h and the maximum longitudinal slope is 5.5%. The river is divided into 2 branches at the site with a width of 1.3 km and a depth of 8.5 m (Figure 1). Geological investigation indicated that this site features complicate stratum structure with exceptionally diverse quaternary strata [26]. The underlying bedrock contains Cretaceous system conglomerate and Devonian system dolomite with relatively stable contact faces. Overlying strata mainly consist of the floodplain accumulation horizon and terrace with a thickness of 9–40 m. The floodplain at the west bank is obviously thick. The unconsolidated formation of quaternary system consists of plain fill, muddy silty clay, fine sand, sandy gravel, pebble, and so forth, while the grade of surrounding rock preliminarily planned for tunnel installation is nearly all V and IV. Figure 2 provides a geological section [27].

2.2. Characterizations of Sandy Gravel Stratum. This floodplain sandy gravel stratum with nearly no cement material,

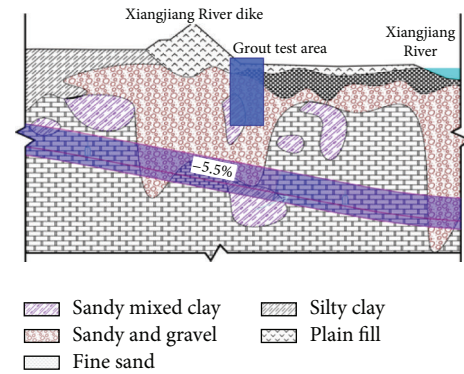


FIGURE 2: West part longitudinal geological profile of north line (vertical scale 1 : 500 and horizontal scale 1 : 1000) [26].

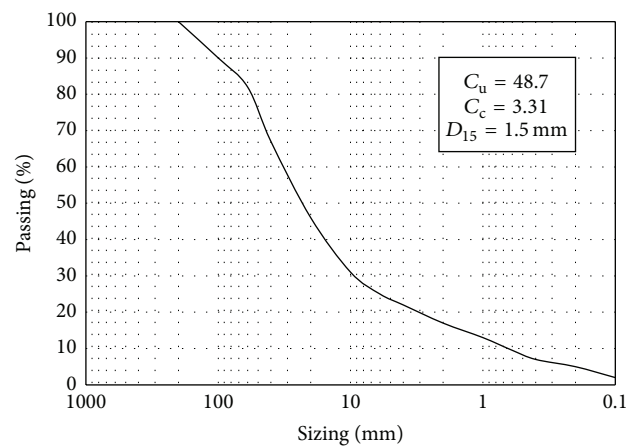


FIGURE 3: Grading curve of typical core sample.

however, is quite different from the normal gravel strata in related codes. Grain diameter composition is mainly 5–60 mm gravel and filled with 0.5–2 mm in the gap. There are almost no complete core samples in the geological investigation. Grading curve and typical core sample are shown in Figures 3 and 4. This sandy gravel stratum is caused by a combination of alluvial effects and diluvial actions and is widely distributed in the west bank with a thickness varying from 7 to 28 m, contacting bedrock at the bottom. The ground permeability coefficient is 2.3×10^{-4} m/s and its groundwater connects with the river water. The tunnel section with a length of 220 m will be constructed in sandy gravel stratum by drilling and blasting method, which should be well treated before excavation in consideration of the risks of sudden geological disasters such as water ingress and collapse.

3. Experimental Design and Implementation

3.1. Test Aims. Because of the safety issues associated with tunnelling crews working in unstable ground conditions, the performance of the ground treatment is critical. The pre-grouting is an effective way to improve the stability and reduce water permeability prior to excavation, but specific



FIGURE 4: Core sample of sandy and gravel stratum.

injection parameters and grouting sequence must be determined first. To obtain the grouting parameters in sandy gravel ground, a test could always work. For this purpose, in situ testing is necessary to determine the required grouting parameters and the control technology for this ground. A program of field trials was designed to address the following:

- (1) Selecting the appropriate grout for the ground conditions.
- (2) The volume of grout required per m^3 of treated ground.
- (3) The grouting volume and grouting pressure in the designed diffusion radius.
- (4) Injection sequence for the grouting boreholes in the zone.

The treated ground should meet the general requirements of engineering construction; the ground bearing capacity must meet the design requirements of over 400 kPa; meanwhile the permeability coefficient of stratum should be lower than 1×10^{-6} m/s [28–30]. Vertical grouting was applied in the grouting test, and an evaluation of treated ground obtained by core drilling and water testing will be provided after completion.

3.2. Test Site and Injection Methodology. The test site is located at the west bank floodplain of Xiangjiang River, directly above the north-line tunnel position of XK1 + 180, and its plane position and section position are shown in Figures 1 and 2. The field is covered with typical sandy gravel except the shallow upper layer. This site is within close proximity to the flood control dike, offering a convenient and rapid path for material transport and evacuation in the event of a flood. A platform (Figure 5), with a plane size of 16 m \times 14 m, was built on the original ground surface of the test site to prevent potential inundation resulting from rising river levels since the rainy season was coming when the grouting work started. High grouting pressure may lead to stratum expansion and dam structure damage, so deformation monitoring was performed during grouting. There are totally 85 boreholes with a depth of 24 m and a diameter of 91 mm.

All the boreholes were spilt into 2 groups according to their locations, a peripheral group with 68 boreholes and an



FIGURE 5: The platform for grouting work.

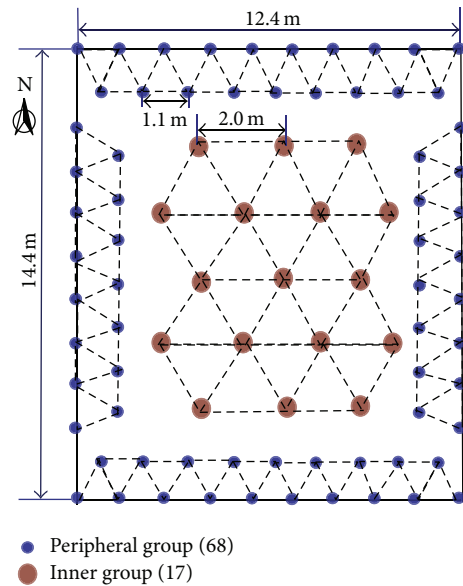


FIGURE 6: Distribution of boreholes.

inner group with 17 boreholes, distributed following equilateral triangles (Figure 6). The peripheral group boreholes would be injected first to compose a reinforced curtain, and then the inner group boreholes would be injected to form a unified entity.

The sleeve valve tube grouting method has been extensively applied in loose stratum reinforcement [31–34] and is also adopted in this test. The sleeve valve tube is comprised of sleeve tube and core tube. The sleeve tube is divided into 50 sections, and the core tube will be lifted up from the bottom of sleeve tube until the ground surface, drawing back when the section is injected into target grout volume, and this cycle will be repeated until the whole sections of a borehole are injected. Figure 8 shows the process and details. Hole collapse happened frequently at the beginning because of the loose structure of sandy gravel, which was solved after taking the Italy Casa C6 drill equipment. The grouting pump type was KBY-50/70, which could mix two kinds of slurry.

3.3. The Optimum Grout Mix Formulation. Cement slurry, composite slurry, cement, and sodium silicate mixed slurry are often employed to grout the sandy and gravel ground.

TABLE 1: Experiment results of grout with different mixture ratio.

Number	Water cement ratio (mass ratio)	Concentration of water glass (Be)	Average gelation time (s)	Opinion
1	W : C = 1 : 1	45	74.4	Not applicable
2		40	62.5	Applicable
3		35	56	Applicable
4		30	47.5	Applicable
5	W : C = 0.8 : 1	45	52.6	Applicable
6		40	46.5	Applicable
7		35	41.1	Not applicable
8		30	36.2	Not applicable

However, the grout should have a good ability of dispersion resistance and a short gelation time because the sandy gravel stratum in the test field is rich in groundwater. Cement slurry features a high stone rate but a long gelation time and poor antidispersion properties. Composite slurry possesses high viscosity but the configuration processes are complex, and it is expensive. Cement and sodium silicate mixed grout is cost saving and satisfies operating requirements of viscosity, gelation time, and good consolidation strength; thus it is selected in this field test based on the overall consideration of factors and the grout optimum mix formulation will be determined in the laboratory experiments.

A grout gelation time with a range of 45–70 s is appropriate based on the theory that gelation occurs when slurry diffuses to the expected position [34]. Raw materials are P42.5# composite Portland cement, 51 Be sodium silicate (diluted to different concentrations later, $M = 1.7\text{--}3.1$), and drinking water. Material proportion is as follows: cement-to-water quality ratio $W : C = 0.8 : 1\text{--}1 : 1$ and cement-to-sodium silicate volume ratio $C : S = 1 : 1$. There were 8 groups in experiment with different mix formulation being conducted and the gelation time of each group would be obtained after repeating the same experiment 3 times. Experimental results were displayed in Table 1.

The experiment demonstrated that reaction speed increases with the decrease of water-cement ratio and the decrease of water glass density. Several groups achieved the specified criteria and group number 3 was selected for the field trial due to its lower cost. Mix proportions in the remaining groups were stored for reserve purposes.

3.4. Grouting Calculation

3.4.1. Grout Volume Calculation. Permeation grouting was adopted to fill gaps of particles with slurry, cementing the particles to a whole entity without damaging the original arrangement conditions [35–37]. Permeation grouting has a series of calculation formulas; one of them is the Maag equation for the globe symmetry diffusion [35], but they are hardly helpful in practical engineering. The injection parameters are usually selected on the basis of empirical formulas or previous experience in China, and one empirical formula [36] is employed to estimate the target grout volume:

$$Q = K\alpha\beta V, \quad (1)$$

where Q is grout volume (m^3), K is shrinkage factor whose value is in the range 1.1–1.3 in sandy gravel ground, α is formation porosity (%), β is filling rate whose value is between 70% and 90% in sandy gravel ground, and V is the treated ground volume (m^3).

Considering all factors in the field test, K is 1.1, α is 0.3, and β is 0.8. To realize the reinforcement of entire designed test zone, the target grout volume is

$$Q = K\alpha\beta V = 1.1 \times 0.3 \times 0.8 \times 3789 \text{ m}^3 = 1000.3 \text{ m}^3. \quad (2)$$

3.4.2. Injection Pressure. The hydrostatic pressure, pipe friction loss pressure, pore resistance, and so forth should be considered in the grouting pressure setting in this trial. No accurate calculation results can be used, but an empirical formula is available for sandy gravel grouting pressure as follows [38]:

$$P = P_W + P_L + (0.5 \sim 1 \text{ MPa}), \quad (3)$$

where P_W is hydrostatic pressure, P_L is pipe friction loss pressure along grout pipe, and (0.5–1 MPa) are the other combined pressures.

In this test, P_W was 0.2 MPa, P_L was 0.2 MPa, and grouting pressure was between 0.9 and 1.4 MPa, so the grouting pressure between 0.5 and 1.5 MPa would be adopted. The spacing of holes is fixed before grouting, so the grouting pressure and grouting volume would be adjusted to achieve more uniform spreading around borehole. Preliminary grouting parameters are outlined in Table 2.

3.5. In Situ Grouting Test

3.5.1. The Injection of Peripheral Group. Prior to the formal grouting, all the boreholes were named as shown in Figure 9. Several boreholes were injected first according to the designed parameters. The injection pressure and grouting volume for each section were adjusted to the site conditions and all information was recorded to help find the best grouting control method.

Four boreholes of peripheral group were injected first, following a sequence of $C1 \rightarrow A1 \rightarrow C2 \rightarrow C11$. In different sections of a borehole, an increasing grouting pressure and a constant injection pressure had been tried independently. The adjacent holes were selected as observation points during

TABLE 2: Preliminary grouting parameters.

Number	Parameters name	Value
1	Diffusion diameter	1.6 m (D_1), 2.6 m (D_2)
2	Depth of treated ground	4~24 m
3	Reinforced length	20 m
4	Grout gelation time	56 s
5	Grout pressure	0.5~1.5 MPa
6	Grout volume of each section of peripheral group holes	212 L
7	Grout volume of each section of inner group holes	560 L

the grouting process. Analyzing data collected during grouting, C1 and A1 had a similar process of change under two kinds of grouting pressures as shown in Figures 10(a) and 10(b), while the holes of C2 and C11 had a similar process of change under two kinds of grouting pressures as shown in Figures 11(a) and 11(b). The following results were gathered:

- (1) The sandy and gravel ground can be easily injected under a low injection pressure. The grouting rate decreased with time at a constant grouting pressure.
- (2) The adjacent boreholes are affected by each other. The former borehole has a greater grouting volume than the adjacent boreholes.
- (3) When the grout leaking occurred frequently in the adjacent holes, the grouting pressure decreased and grouting work should be stopped. Boreholes of C1 and A1 have an average grouting volume of 280 L in each section, and boreholes of C1 and A1 have an average grouting volume of 220 L in each section.
- (4) The time that grout diffuses to the expected position is quite different under the different grouting pressure, and time spent under constant pressure is more than 1.5~2 times as much as an increasing grouting pressure spent. Therefore, grouting at an increasing injection pressure is much more effective.

As information from the 4 boreholes, the grouting sequence should be well arranged due to the interaction effects of adjacent boreholes. Additionally, if one hole was grouted, the adjacent hole could not be injected with the same volume due to the diffusion effect from the previous holes; thus the adjacent holes of peripheral group should be injected separately. The remaining holes of peripheral group were divided into two groups: peripheral group A and peripheral group B (Figure 12), which were injected in different control orders.

Peripheral group A would be injected first at a principle of low injection pressure whose value was between 0.5 and 0.8 MPa and a constant grout volume of 280 L. Total grouting orders were as the following: C1 → A1 → C2 → C11 → A2 → A4 → A6 → A8 → B10 → B12 → B14 → B16 → B18 → B19 → D8 → D6 → D4 → D2 → D1 → C10 → C8 → C6 → C4 → C3.

Peripheral group B would be started after all of the boreholes of peripheral group A were all injected. It was to be

injected at a constant volume or a certain end pressure; that is, if the grout volume reached 220 L in every section, grouting was discontinued and the upper section was initiated and if volume had not reached 220 L but grouting pressure had reached 1 MPa, the grouting was also discontinued and the upper section was to be initiated. Total grouting sequence was as follows: A9 → A3 → A11 → A10 → A5 → A7 → B1 → B11 → B13 → B15 → B17 → D7 → D5 → D3 → C9 → C7 → C5 → A12 → A13 → A14 → A15 → B2 → B3 → B4 → B5 → B6 → B7 → B8 → B9 → D15 → D14 → D13 → D12 → D11 → D10 → D9 → C19 → C18 → C17 → C16 → C15 → C14 → C13 → C12.

3.5.2. The Injection of Inner Group. The grouting curtain was created in the surrounding area of the site before the inner group was injected, so a high injection pressure was necessary to ensure effective filling. The typical injection process of hole E1 was recorded and the changes were displayed in Figure 13. It was obvious that the inner group had a bigger injection pressure and grouting volume than the peripheral group. These results indicated that an increasing injected pressure and a grouting volume of 400 L were suitable for each section. However, considering the location and time, grouting with an increasing grouting pressure and discontinuing at an end pressure of 2 MPa was the best control method. So the rest holes of inner group were injected in the biggest end pressure of 2 MPa. Final grouting sequence was the following: E1 → E2 → E3 → E4 → E5 → E6 → E7 → E8 → E9 → E10 → E11 → E12 → E13 → E14 → E15 → E16 → E17.

3.5.3. The Preliminary Summary of Grouting Work. The test was initiated on April 10 and finished on May 11, and a total of 85 holes were injected. The relative performance of grouting volume and injection pressure in different diffusion diameters was established at the beginning to facilitate effective grouting in each group. The total slurry consumption was 1085 m³, which fitted well with the computed amount. Grouting information of the 3 groups was detailed in Table 3. Peripheral group A featured a moderate grouting volume and smallest grouting pressure among 3 groups due to large porosity and loose structure of sandy gravel ground. Peripheral group B was conducted at a constant grout volume or a fixed end pressure, with the smallest average grouting amount and bigger grouting pressure than the first group. The inner group featured larger borehole spacing and a maximum hole

TABLE 3: Grouting overview for 3 groups.

Group	Control principles	Specified injection criteria	Hole number	Volume of each hole (m ³)
Peripheral group A	Constant grout volume	280 L/section	24	15.3
Peripheral group B	Constant grout volume or pressure	200 L/section or 0.8 MPa	44	9.6
Inner group	Fixed end pressure	2 MPa	17	18.0

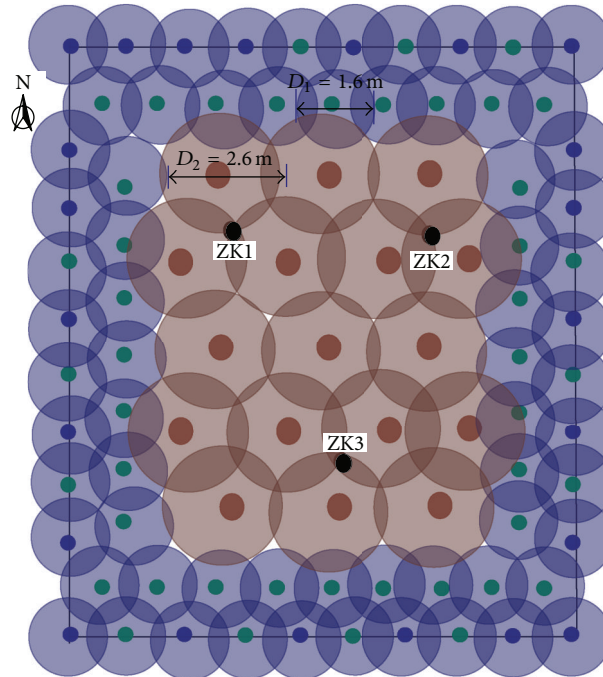


FIGURE 7: The designed diffusion diameter.

grouting volume under the biggest end injection pressure. Oozing slurry occurred near the end of grouting work and the platform had an obvious ground heave in the last grouted holes, which indicated that the slurry had achieved significant filling under the design pressure.

4. Test Results Examination

4.1. Core Boring Check. Core boring check, including core integrity rate, slurry filling rate, and core strength, was used to evaluate the treated ground. It was difficult to obtain intact core samples from the treated gravel due to the existence of large grain-sized pebbles, and core sample only allowed a qualitative evaluation by observation rather than strength test. There were 3 drill holes, located in the middle of 3 grouted holes in which place the grout is relatively difficult to reach, named ZK1, ZK2, and ZK3 (Figure 7). The ground in the test area mainly consists of sandy and gravel, little silty-fine sand. Figures 4 and 14 represent the typical core samples of sandy gravel strata and fine gravel strata prior to grouting and Figures 15 and 16 represent core samples after injection.

The structure of gravel exhibits a loose state prior to grouting, without gelled material, mainly composed of 2–4 mm round gravel (Figure 14). After grouting the core

sample is exceptionally firm with an integrated rate over 80% (Figure 15). The typical sandy and gravel core sample displayed a wide particle size distribution and larger pebbles (Figure 4); then the rate of coring completeness reached approximately 45% ~60% with a grout filling rate of 40% ~45% after injection (Figure 16). These results indicated the grout diffusion radius has achieved a desired requirement and the stratum integrity and bearing capacity are significantly improved.

4.2. Water Pressure Test. An in situ permeability test is another important index to evaluate the treated ground. Water pressure testing is applied to determine the stratum permeability coefficient k . This test can get specific water absorption levels by forcing water to permeate the surrounding rock from the cracks in the borehole walls via a pressure pump. The calculation formula is as follows [39]:

$$k = \frac{Q}{2\pi LH} \lg \frac{L}{r}, \quad (4)$$

where L is the length of test section (m), H refers to the head elevation (m), r is the radius of borehole (m), and Q is steady flow (m³).

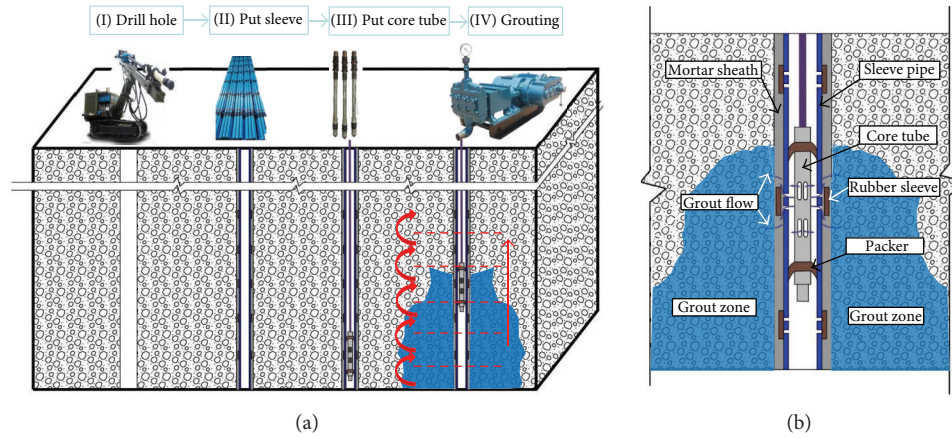


FIGURE 8: The grouting procedure of sleeve valve tube grouting method and its detailed composition.

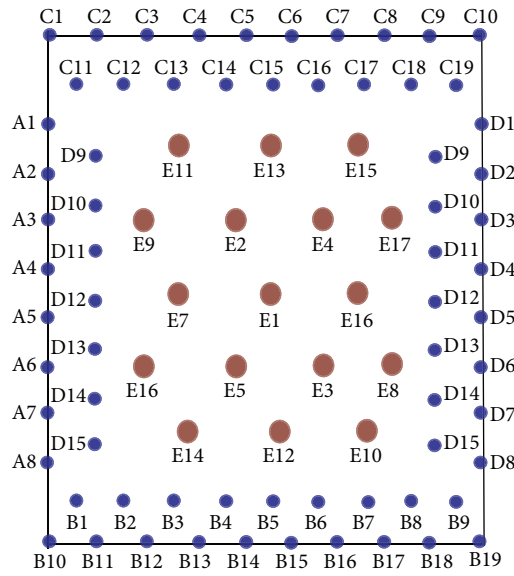


FIGURE 9: Distribution of 2 groups of boreholes.

Water pressure test was conducted at a depth of 12–22 m. The permeability coefficient obtained was between 1.22×10^{-8} m/s and 5.21×10^{-7} m/s after grouting [40], which was significantly reduced and considerably lower than the specified median of 1×10^{-6} m/s for underground construction.

4.3. Monitoring for Flood Protection Dike. Improper grouting often leads to expansion of the stratum and threatens the safety of surrounding buildings [41]. Settlement monitoring of dike was arranged to avoid structural damage resulting from stratum uplift during the grouting. No obvious ground uplift was observed until the final phase, May 7–10, when the last several holes of the inner group were being injected (Figure 17). The maximum settlement of ground surface was +7.1 mm and a local crack appeared in the dike on May 8. Things went on well after the grouting speed was slowed down in the remaining holes. Most monitoring points presented

a maximum vertical settlement less than 5 mm, which indicated that the dike just stayed in safe state.

5. Conclusions

The final results demonstrated that the specified injection criteria for different group holes could meet the reinforced and water ingress requirements. To summarize this in situ test of vertical grouting in typical river floodplain sandy gravel stratum, the following results are obtained:

- (1) Permeation grouting method and sleeve valve pipe grouting technology can be applied to treat sandy gravel ground. The cement-sodium silicate binary slurry, with a mix grout proportion of W:C (mass ratio) of 1:1, C:S (volume ratio) of 1:1, PC 42.5 cement, Baume degree of water glass 30 Be, and

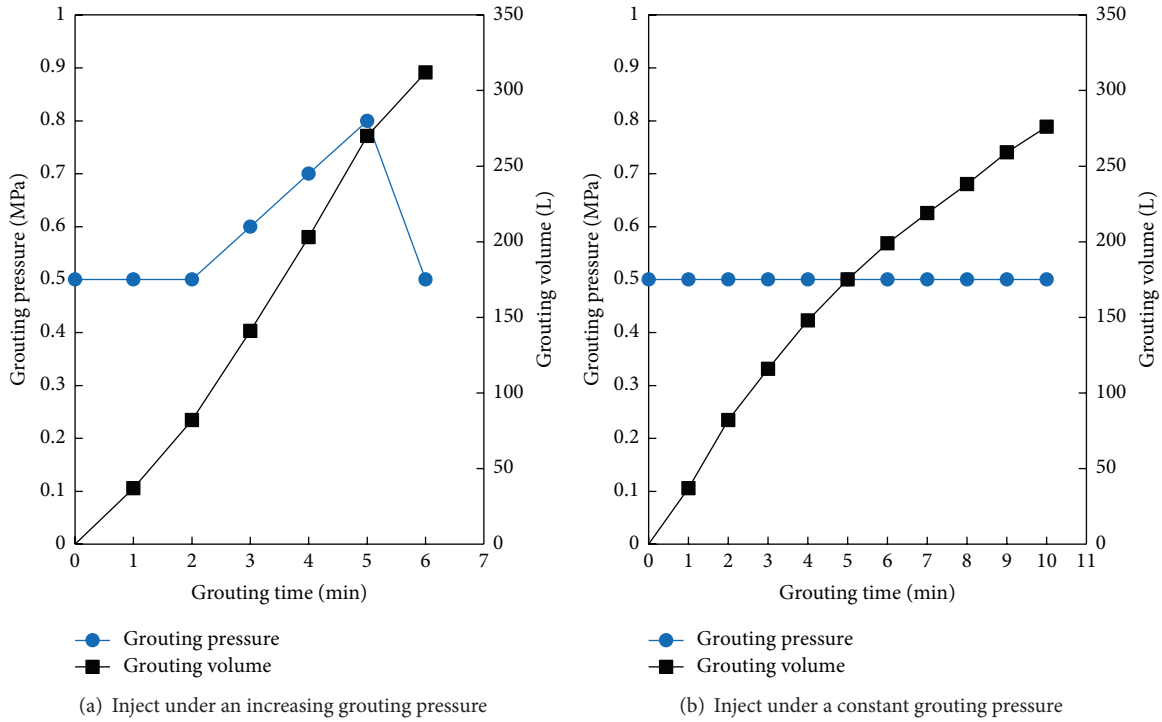


FIGURE 10: The typical grouting process of C1 and A1.

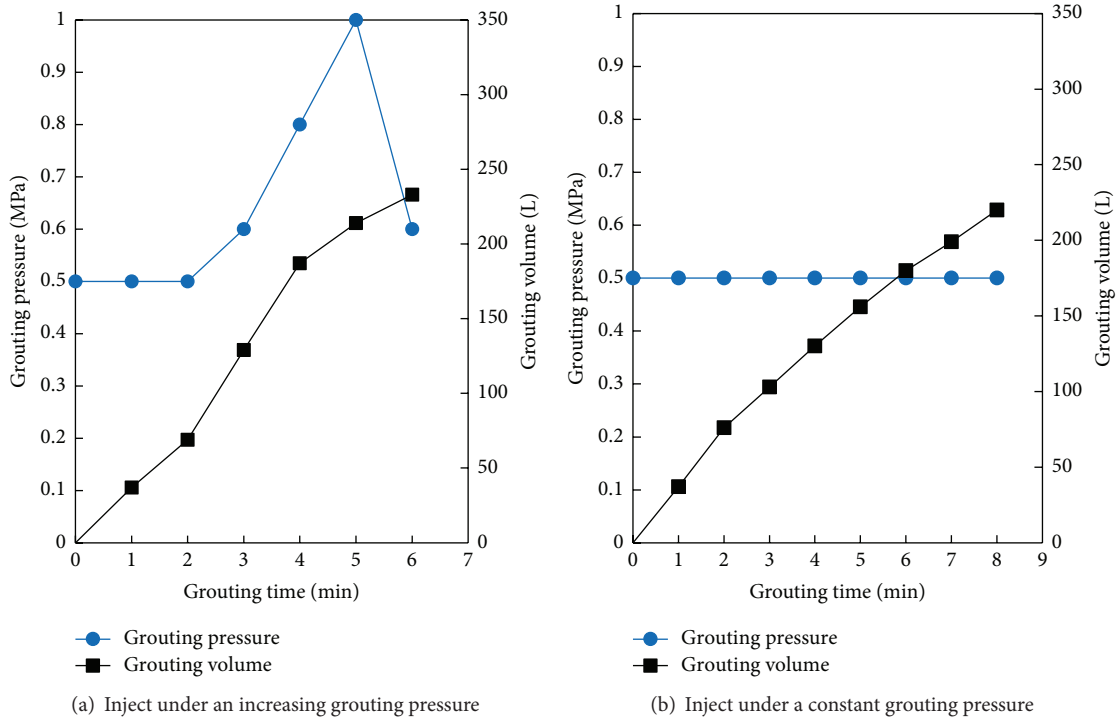


FIGURE 11: The typical grouting process of C2 and C11.

gelation time 47.5 s, can be well applied to inject the saturated sandy gravel ground.

- (2) The designed ground treatment program: injecting the surrounding holes first and the inner holes next

proved to be right. Typical injection process of peripheral group holes demonstrated that this sandy and gravel ground can be easily injected under a low injection pressure and grout leaking occurred

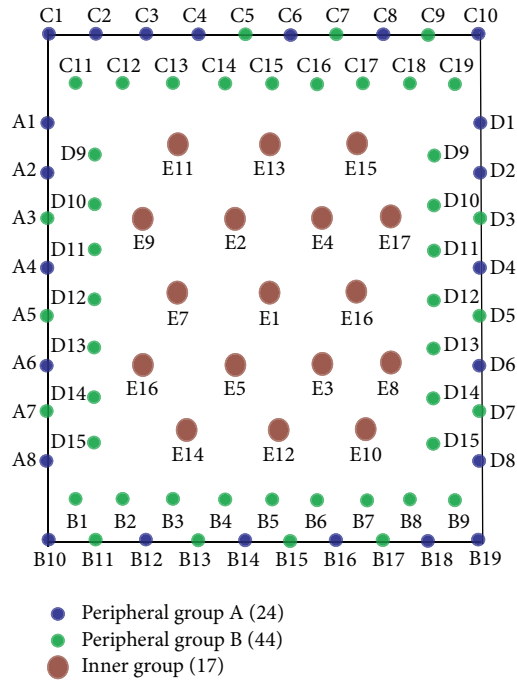


FIGURE 12: Distribution of 3 groups of boreholes.

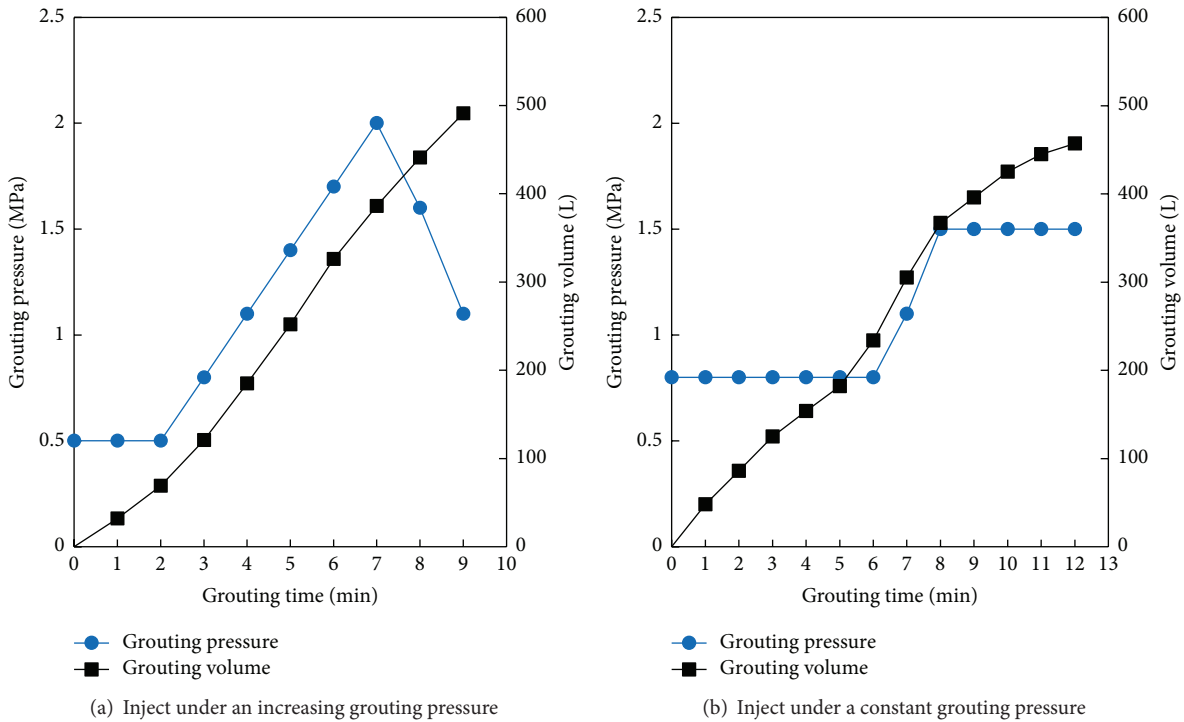


FIGURE 13: The typical grouting process of E1.

frequently in the adjacent holes when the injection pressure was increased over 0.8 MPa. The holes of inner group were injected later; a high injection pressure was more appropriate considering the grouting

curtain had been created. Taking the factors of time saving and effectiveness of grouting into account, the specified injection criteria in this test are as follows: the holes in peripheral group A were injected first at a



FIGURE 14: Core sample of fine gravel before grouting.



FIGURE 15: Core sample of fine gravel after grouting.

principle of low injection pressure whose value was in the range 0.5~0.8 MPa and a constant grout volume of 280 L. The holes in peripheral group B were injected at a constant volume of 220 L or a certain end pressure of 1 MPa. The inner group holes were grouted with an increasing grouting pressure and ended at pressure of 2 MPa.

- (3) Core boring check results indicated that the strata integrity and stability are significantly improved, and the coefficient permeability on completion of grouting trial is lower than 1×10^{-6} m/s, which could meet the underground construction requirements of waterproofing and subgrade bearing capacity, and the protection dike was in a safe state during grouting.
- (4) The empirical formulas chosen to predict the demanded grout volume fit well with the actual situations. The specified injection criteria which contain injection pressure, grout volume, and grout sequence and obtained from the frond holes for three groups contribute to sufficient strength of the entire field. Additionally, these effective injection criteria and control methods will provide valuable references for pregrouting work during the tunnel construction stage.



(a)



(b)

FIGURE 16: Core sample of sandy gravel after injection.



FIGURE 17: The surface uplift in the dike caused by grouting.

Competing Interests

The authors declare that there are no competing interests regarding the publication of this paper.

Acknowledgments

This work is financially supported by the Special Fund for Basic Scientific Research of Central Colleges of Chang'an University (Grant no. 310821165011), the Brainstorm Project on Social Development of Shaanxi Provincial Science and Technology Department (no. 2016SF-412), and the Key

Industrial Research Project of Shaanxi Provincial Science and Technology Department (Grant no. 2015GY185).

References

- [1] E. D. Graf, "Compaction grouting technique and observations," *ASCE, Journal of Soil Mechanics and Foundation Engineering*, vol. 95, pp. 1151–1158, 1969.
- [2] R. Widmann, "International society for rock mechanics commission on rock grouting," *International Journal of Rock Mechanics and Mining Sciences*, vol. 33, no. 8, pp. 803–847, 1996.
- [3] E. Nonveiller, *Grouting Theory and Practice*, Elsevier, Amsterdam, The Netherlands, 1989.
- [4] J. N. Shirlaw, K. Hayata, G. Berry, and S. Tan, "A review of grouting techniques utilised for bored tunnelling with emphasis on the jet grouting method," *Construction and Building Materials*, vol. 2, no. 1, pp. 34–41, 1988.
- [5] H. Lisa, G. Gunnar, F. Åsa, and N. Tommy, "A statistical grouting decision method based on water pressure tests for the tunnel construction stage—a case study," *Tunnelling and Underground Space Technology*, vol. 33, no. 1, pp. 54–62, 2013.
- [6] J. X. Lai, S. Mao, J. L. Qiu et al., "Investigation progresses and applications of fractional derivative model in geotechnical engineering," *Mathematical Problems in Engineering*, vol. 2016, Article ID 9183296, 15 pages, 2016.
- [7] A. Zolfaghari, A. S. Bidar, M. R. M. Javan, M. Haftani, and A. Mehinrad, "Evaluation of rock mass improvement due to cement grouting by Q-system at Bakhtiary dam site," *International Journal of Rock Mechanics and Mining Sciences*, vol. 74, pp. 38–44, 2015.
- [8] L. Hu, J. Hao, and L. Wang, "Laboratory evaluation of cement treated aggregate containing crushed clay brick," *Journal of Traffic and Transportation Engineering (English Edition)*, vol. 1, no. 5, pp. 371–382, 2014.
- [9] J. M. Soler, M. Vuorio, and A. Hautojärvi, "Reactive transport modeling of the interaction between water and a cementitious grout in a fractured rock. Application to ONKALO (Finland)," *Applied Geochemistry*, vol. 26, no. 7, pp. 1115–1129, 2011.
- [10] W. J. Xue, E. Weaver, L. B. Wang, and Y. Wang, "Influence of tyre inflation pressure on measured pavement strain responses and predicted distresses," *Road Materials and Pavement Design*, vol. 17, no. 2, pp. 328–344, 2016.
- [11] L. Hernqvist, Å. Fransson, G. Gustafson, A. Emmelin, M. Eriksson, and H. Stille, "Analyses of the grouting results for a section of the APSE tunnel at Äspö Hard Rock Laboratory," *International Journal of Rock Mechanics and Mining Sciences*, vol. 46, no. 3, pp. 439–449, 2009.
- [12] M. Shimoda and H. Ohmori, "Ultra fine grouting material," in *Proceedings of the Conference on Grouting in Geotechnical Engineering*, pp. 77–91, ASCE, New Orleans, La, USA, February 1982.
- [13] Z.-M. Zhang, J. Zou, J.-Y. He, and H.-Q. Wang, "Laboratory tests on compaction grouting and fracture grouting of clay," *Chinese Journal of Geotechnical Engineering*, vol. 31, no. 12, pp. 1818–1824, 2009.
- [14] H. Güllü, "On the viscous behavior of cement mixtures with clay, sand, lime and bottom ash for jet grouting," *Construction and Building Materials*, vol. 93, pp. 891–910, 2015.
- [15] K. Komiya, K. Soga, H. Akagi, M. R. Jafari, and M. D. Bolton, "Soil consolidation associated with grouting during shield tunnelling in soft clayey ground," *Geotechnique*, vol. 51, no. 10, pp. 835–846, 2001.
- [16] P. Vincent and A. Sadah, "Fabric analyses of some Saudi Arabian pediment gravels," *Journal of Arid Environments*, vol. 30, no. 4, pp. 371–384, 1995.
- [17] J. W. Kim and S. K. Chough, "A gravel lobe deposit in the prodelta of the Doumsan fan delta (Miocene), SE Korea," *Sedimentary Geology*, vol. 130, no. 3–4, pp. 183–203, 2000.
- [18] C. Dano, P.-Y. Hicher, and S. Tailliez, "Engineering properties of grouted sands," *Journal of Geotechnical and Geoenvironmental Engineering*, vol. 130, no. 3, pp. 328–338, 2004.
- [19] Y. Tsukamoto, K. Ishihara, K. Umeda, and T. Enomoto, "Cyclic resistance of clean sand improved by silicate-based permeation grouting," *Soils and Foundations*, vol. 46, no. 2, pp. 233–245, 2006.
- [20] P. Yang, Z.-B. Peng, Y.-Q. Tang, W.-X. Peng, and Z.-M. He, "Penetration grouting reinforcement of sandy gravel," *Journal of Central South University of Technology*, vol. 15, no. 2, pp. 280–284, 2008.
- [21] C. R. Yu, *Research on grouting influence and Mechanism of shield tunneling in the sand-gravel stratum [Ph.D. thesis]*, Shanghai Jiao Tong University, Shanghai, China, 2011.
- [22] X. Y. Song, "Analysis on deep hole grouting consolidation for tunnels in water-rich sandy gravel stratum," *Modern Tunnelling Technology*, vol. 48, no. 3, pp. 132–135, 2011.
- [23] F. Yong, W. Jun, H. Chuan et al., "Impact of shield tunneling on adjacent spread foundation on sandy cobble strata," *Chinese Journal of Modern Transport*, vol. 22, no. 4, pp. 244–255, 2014.
- [24] A. Bezuijen, R. T. Grotenhuis, A. F. V. Tol, J. W. Bosch, and J. K. Haasnoot, "Analytical model for fracture grouting in sand," *Journal of Geotechnical & Geoenvironmental Engineering*, vol. 137, no. 6, pp. 611–620, 2011.
- [25] L. Teng and H. Zhang, "Meso-macro analysis of surface settlement characteristics during shield tunneling in sandy cobble ground," *Rock and Soil Mechanics*, vol. 33, no. 4, pp. 1141–1160, 2012.
- [26] J. Cui, S. H. Liu, W. Z. Wang et al., "Experimental study on selection and grouting effect of new grouting materials applied in thick water-rich sandy gravel strata," *Tunnel Construction*, vol. 35, no. 8, pp. 778–786, 2015.
- [27] Shanghai Municipal Engineering Design General Institute, *The Plane and Section Blueprint of the Preliminary Design of Xiangjiang River Municipal Road Tunnel in Laodonglu*, Shanghai Municipal Engineering Design General Institute, Shanghai, China, 2009.
- [28] "Code for design of building foundation," Tech. Rep. GB50007-2011, China Architecture and Building Press, Beijing, China, 2011.
- [29] Z. B. Peng, *Calculation and Construction of Grouting Projection Design*, China University of Geosciences Press, Wuhan, China, 1997.
- [30] JT/G/T F60-2009, *Technical Guidelines for Construction of Highway Tunnel*, China Communications Press, Beijing, China, 2009.
- [31] S.-C. Wu, A.-B. Jin, and Y.-T. Gao, "Studies of sleeve-valve-pipe grouting technique and its effect on soil reinforcement," *Rock and Soil Mechanics*, vol. 28, no. 7, pp. 1353–1358, 2007.
- [32] G. H. Ren, "Case study on consolidation of water-rich cobble/gravel strata in nanning by means of soletanche grouting," *Tunnel Construction*, vol. 34, no. 12, pp. 1183–1190, 2014.
- [33] Y. Luo, J. Chen, W. Xi et al., "Analysis of tunnel displacement accuracy with total station," *Measurement*, vol. 83, pp. 29–37, 2016.

- [34] J. X. Lai, J. L. Qiu, H. B. Fan et al., "Fiber bragg grating sensors-based in-situ monitoring and safety assessment of loess tunnel," *Journal of Sensors*, In press.
- [35] E. Nonveiller, *Grouting Theory and Practice*, Elsevier, Zagreb, Croatia, 1989.
- [36] C. A. Anagnostopoulos, "Laboratory study of an injected granular soil with polymer grouts," *Tunnelling and Underground Space Technology*, vol. 20, no. 6, pp. 525–533, 2005.
- [37] J. X. Lai, K. Y. Wang, J. L. Qiu et al., "Vibration response characteristics of the cross tunnel structure," *Shock and Vibration*, vol. 2016, Article ID 9524206, 16 pages, 2016.
- [38] J. J. Cui and X. Q. Cui, *Grouting Technology of Tunnel and Underground Engineering*, China Architecture & Building Press, Beijing, China, 2011.
- [39] W. Z. Zhang, *Groundwater and Soil Water Dynamics*, China Water Resources and Hydropower Publishing House, Beijing, China, 1999.
- [40] China Railway Tunnel Group, "Water injecting test report of Xiangjiang river sand and gravel stratum after grouting reinforcement," Research Report, China Railway Tunnel Group, 2013.
- [41] A. B. Padura, J. B. Sevilla, J. G. Navarro, E. Y. Bustamante, and E. P. Crego, "Study of the soil consolidation using reinforced jet grouting by geophysical and geotechnical techniques: 'La Normal' building complex (Granada)," *Construction and Building Materials*, vol. 23, no. 3, pp. 1389–1400, 2009.

Research Article

Off-Axial Tensile Properties of Preconstraint PVDF Coated Polyester Fabrics under Different Tensile Rates

Lanlan Zhang

College of Construction Management, Jiangsu Vocational Institute of Architectural Technology, Xuzhou 221116, China

Correspondence should be addressed to Lanlan Zhang; zhanglanlan007@163.com

Received 30 March 2016; Revised 2 June 2016; Accepted 19 June 2016

Academic Editor: Gonzalo Martínez-Barrera

Copyright © 2016 Lanlan Zhang. This is an open access article distributed under the Creative Commons Attribution License, which permits unrestricted use, distribution, and reproduction in any medium, provided the original work is properly cited.

Two types of Preconstraint PVDF coated polyester are taken as the research objects. A series of uniaxial tensile tests were carried out to study the tensile performances of the specimens in eleven in-plane directions including 0° , 5° , 15° , 25° , 35° , 45° , 55° , 65° , 75° , 85° , and 90° , and six tensile rates (10 mm/min, 25 mm/min, 50 mm/min, 100 mm/min, 200 mm/min, and 500 mm/min) were also considered. The corresponding failure modes and fracture mechanisms were discussed, and the relationships between tensile strength and strain at break and tensile rate and off-axial angles were obtained. Results show that the Preconstraint PVDF coated woven fabrics are typically anisotropic. With off-axial angle increasing, the tensile strength decreases while the strain at break increases. Three failure modes can be observed, including failure of yarns pulled out, yarns fracture, and mixture failure. With tensile rate increasing, the tensile strength increases slightly while the strain at break decreases. The tensile strength and strain at break show good linear relationship with tensile rate's logarithm.

1. Introduction

Membrane structure is a new structural system developed in the middle of 20th century. It is welcomed by the architects, engineers, and others, due to complex architectural forms and special mechanical properties [1–3]. Its structural stiffness can be obtained by tensioning the membrane surface, together with the curvature forms. The design membrane prestress is strongly related to the curvature forms of membrane surface. Whether the accuracy of membrane prestress can satisfy the design requirements may directly affect the construction accuracy, even the structure safety [4].

Coated fabric is a principal material used in membrane structures. It can only resist tensions, almost without any flexural resistance. As shown in many existing literatures, for plain woven polyester coated with PVDF, the differences between the mechanical properties of the warp and the weft are significant. The unbalanced woven structure of the materials results in the unbalanced deformations of membrane materials. When the warp stress is less than the weft stress, negative strain in the warp direction may reduce the application efficiency of the material. However, it is often beneficial for installation for a fabric to be unbalanced so

that it can be tensioned in the weft direction and prestress is induced in the warp direction by interaction of the yarns. Then, the Preconstraint woven technology was proposed by the Serge Ferrari Company. A more stable fabric can be obtained by applying tension to warp and weft of a plain woven fabric, in order to obtain more consistent and more balanced warp and weft stiffness through the cloth. Until now, there are only a few of references about the mechanical properties of PVDF coated polyester with the Preconstraint technology. Ambroziak carried out series of tests on the mechanical behaviors under different loading protocols, such as monotonous loading, cyclic loading, and others [5–8]. The main mechanical parameters including tensile strength, elastic modulus, and Poisson ratio are obtained. However, there are few literatures about the failure mechanisms and strength criterion of Preconstraint coated fabrics. Zhang et al. conducted the off-axial tensile tests on the Preconstraint PVDF coated polyester with the tensile rate of 100 mm/min and analyzed the corresponding failure mechanisms [9].

As we know, the failure mechanisms and strength criteria are important for the design and analysis of membrane structures. Considering the stress states in practical engineering, the biaxial tests may be the best method to solve

this question. However, it is difficult to find the suitable specimens for the tests. There are some previous references about the failure tests of the coated fabrics [10–13]. However, until now, the failure strength obtained in those references is only the failure strength of biaxial specimens, not the failure strength of this material. Nowadays, the off-axial test may be the most suitable method to analyze the failure mechanism of coated fabrics, although it can only produce some simple stress states. Some researchers have used the off-axial tests to analyze the failure mechanisms and strength criteria of coated fabrics. The off-axial tests always contain seven bias angles, including 0° , 15° , 30° , 45° , 60° , 75° , and 90° [13–15]. The results indicate that the material strength decreases significantly under the interaction of shear and tensile, especially for the bias angles from 0° to 15° or 90° to 75° . This phenomenon cannot be accurately described by the current strength criteria, in which the shear stress plays an important role in this aspect [16–18]. Therefore, it is necessary to reduce the angle gap of off-axial tests to study the failure mechanism of coated fabrics further.

Just as shown in previous references, the current researches are mainly on the mechanical properties of coated fabrics under the standard test conditions recommended in the codes or the specifications. However, as anisotropic polymer composites, the loading protocols may have significant effects on the mechanical properties of coated fabrics [4–6, 8, 19–21].

The wind-borne debris always hits the surface of membrane structures and the microcrack may appear in the membrane surface. Under harsh environments, the microcrack can easily propagate and lead to the overall failure of membrane structures due to low tear strength. The membrane structures are always the landmark and their failure will bring economic loss and huge social impacts. The rate-dependent mechanical properties of coated fabrics are an important basis of design and analysis of membrane structures. There are a lot of references about the viscoelastic properties of coated fabrics under low strain rates [22–28]. Some classical viscoelastic models are proposed for the construction analysis and the determination of shrinkage ratio in the pattern cutting analysis [29–31]. Meanwhile, there are fewer references about the material response under dynamic loading. However, the structural response under dynamic loading with high rates is also very important for the design, for example, the analysis of wind-induced disasters. Therefore, it is necessary to study the mechanical properties and failure mechanisms of coated fabrics under different tensile rates.

This paper presented the off-axial tensile behaviors and failure mechanisms of Preconstraint PVDF coated polyester, in which the effects of tensile rate on the mechanical parameters and failure modes are discussed.

2. Materials and Methods

The Preconstraint PVDF coated polyester Ferrari 1002 T2 and 702 T2 are taken as the research objects, as shown in Table 1. They are plain woven by the Preconstraint technology with PVDF top coats in both sides. The Preconstraint technology holds the textile under tension in both warp and weft

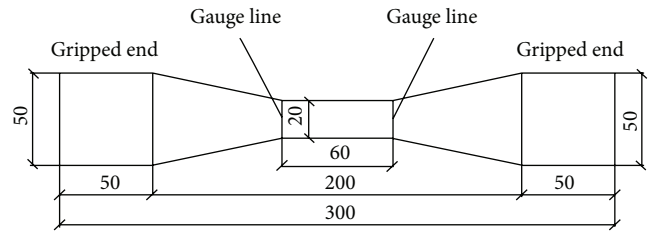


FIGURE 1: Dimensions of dumbbell specimens.

directions throughout the manufacturing process to ensure higher levels of dimensional stability and tensile strength, less elongation, and a flatter base cloth. This enables a more substantial protective coating to be placed on top of the yarn without increasing overall thickness, creating a flatter, lighter textile subject to less deformation under tension. It is with good durability and self-cleaning, which can be used in permanent structures.

The uniaxial tests are carried out using the electromechanical universal testing machine with temperature box. The strip specimens are always used in the off-axial tests. However, the failure always appears in the gripped ends, for example, fracture or slippage, and then the test data is invalid. Therefore, the dumbbell specimens are used in this test, as shown in Figure 1. The stress is got by dividing the tensile forces by the area of cross-section in the middle. The strain is got by the displacement measurement.

3. Results and Discussions

3.1. Comparisons of Strip Specimens and Dumbbell Specimens. Here, this part also presents the comparisons of dumbbell and strip specimens under the off-axial tensile tests by the finite element analysis. In the finite element analysis, the orthotropic constitutive relation is used and the elastic modulus in warp and weft is 600 MPa and 400 MPa, respectively. The strip specimens are prepared according to German codes DIN 53334 [32]. The width is 50 mm, the length is 300 mm, and the original gage length is 200 mm. The pattern equality of samples is important for the test results.

The comparisons of the stress distributions of dumbbell and strip specimens are shown in Figure 2. For strip specimens, it can be observed that the stress in the gripped ends is high and the slippage always appears before the fracture of materials. This is also related to the smooth surface of PVDF coating. This phenomenon is consistent with the tensile tests. For dumbbell specimens, in the effective area, the stress distribution is consistent with that of strip specimens. The width of gripped ends is larger than that of the effective area. It can afford enough fractional force to avoid the slippage of specimens. The maximum stress always appears in the effective area and the test data is valid. If the failure does not appear in the effective area, the test data can be considered as invalid.

3.2. Uniaxial Tensile Curves. Due to the same woven method, the variation trends of tensile behaviors of two materials (702

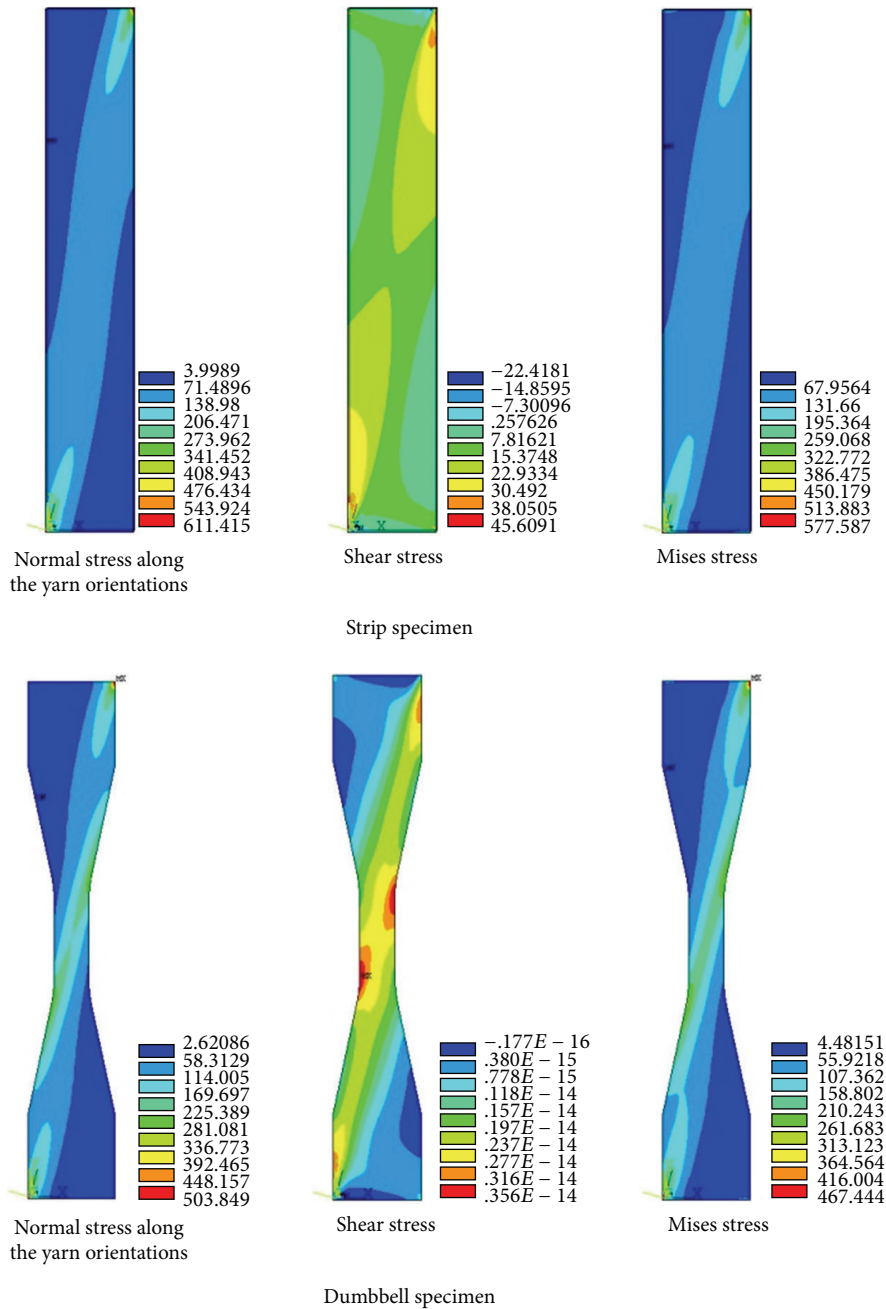


FIGURE 2: Stress distribution of 15-degree specimens.

T2 and 1002 T2) are similar. Therefore, limited by the layout, this part only presents the test results of Preconstraint 702 T2, as shown in Table 2.

First, the tensile behaviors under the tensile rate of 100 mm/min are taken as the research object, because 100 mm/min is the recommended tensile rate in current codes/specifications [1]. The angles 0° and 90° are the weft and the warp, respectively. Figure 3 shows that the Preconstraint PVDF coated polyester performs typically orthotropic. The differences between the tensile strength in the warp and in the weft are not so significant as those of the plain weave fabrics, which is related to the woven densities and woven methods

[33]. Then, for Preconstraint coated fabrics, the pretension is applied to the warp and weft of yarns and a more consistent and more balanced warp and weft stiffness through the cloth are obtained. For the on-axial specimens, part of yarns fracture first and the unloading will be transferred to the adjacent yarns. Due to high adhesive strength, the yarns are difficult to be pulled out from the coating/substrate interface, and most of yarns fracture at the same section. Then, the main failure modes are even failure, which is “yarn fracture” (Figure 4). When the bias angle is 85° and 5°, there will be a significant decrease compared with those of on-axial specimens. Although the number of yarns in the effective

TABLE 1: Specifications of test materials.

Type	Manufacturer	Weight g/m ²	Thickness mm	Yarn density dtex PES HT		Tensile strength kN/m		Tear strength N	
				Warp	Weft	Warp	Weft	Warp	Weft
Ferrari 1002 T2	Serge Ferrari	1050	0.78	1100	1100	84.0	80.0	500	460
Ferrari 702 T2		750	0.56	1100	1670	60.0	56.0	300	280

TABLE 2: Off-axial test results of Preconstraint 702 T2 (100 mm/min).

Angle	Tensile strength/(kN·m ⁻¹)		Strain at break/%	
	Average value	Standard deviation	Average value	Standard deviation
0°	58.051	3.444	13.541	0.154
5°	50.542	1.633	12.662	0.061
15°	44.834	0.864	18.072	0.760
25°	39.271	1.664	32.556	0.363
35°	38.081	1.827	38.992	0.338
45°	37.709	0.733	40.416	0.189
55°	37.981	0.198	39.101	0.348
65°	40.771	0.908	32.662	0.144
75°	45.934	0.945	21.441	0.201
85°	51.339	2.345	14.100	0.126
90°	58.699	0.966	14.446	0.125

area remains almost unchanged, the application ratio of yarns decreases significantly under the tensile-shear interaction. In the fracture section, most of the yarns fracture even and part of yarns are pulled from the adjacent yarn-coating interface. Additionally, the strain at break may be lower than that of the on-axial specimens.

When the bias angle increases, for example, the specimens with bias angles of 75°, 15°, 65°, and 25°, the tensile strength decreases and the strain at break increases. The failure modes are the mid-section fracture and part of adjacent yarns are pulled out. Compared with the specimens with smaller bias angles (85° and 5°), the number of pulled-out yarns increases and the number of fractured yarns decreases. Therefore, the strain at break increases significantly and the fracture section is uneven. When the bias angles are 55, 35, and 45, the tensile strength is the lowest and the strain at break is the highest. Then, the failure mode is “interface failure,” as shown in Figure 4(b). The coating can constrain the deformation of yarns, which is in favor for the loading capacity of coated fabrics. The shear force plays a dominant role in the material failure. The “yarns pulled out” is the main failure mode.

In the off-axial tests, there are two types of yarns, complete ones and incomplete ones. With bias angle increasing, the number of incomplete yarns remains unchanged, while the number of complete ones decreases. From Figure 5, due to high shear force, the incomplete yarns are easily pulled out and then the tensile strength decreases significantly. When the bias angle increases from 15° to 25° (or 75° to 65°), the number of complete yarns decreases to 0. Then, the tensile stress decreases and the shear stress increases, but the decreasing of tensile strength is not very obvious. When the bias angle increases from 25° to 45° (or 65° to 45°), the shear

stress gradually becomes the dominant and the shear failure is observed.

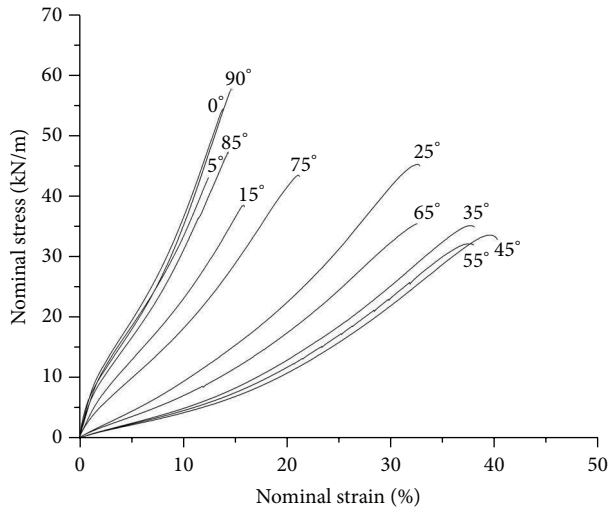
According to the SEM image shown in Figure 6(a), the fracture cross-section is even fracture in the failure mode “yarns even fracture.” The fiber bundles parallel to the loading direction show even fracture. Figure 6(b) is typically mixed failure. The middle part of the fiber bundles perform uneven fracture, while the sides are pulled out, accompanied by the damage of a small amount of coating. For the failure mode “yarns pulled out” (Figure 6(c)), the fiber bundles are completely pulled out, and then the coating is serious damage.

3.3. Loading Rate. Figure 7 shows that the effect of tensile rate on the material tensile strength is obvious and the tensile strength increases with tensile rate increasing. The least square method is used to fit the mechanical parameters (tensile strength and strain at break) under different tensile rates. The black points are experiment data, and the line is the fitting results. As shown in Figure 8, with tensile rate increasing, the tensile strength increases about 5%–15%, and the strain at break decreases about 5%–10%. Figure 8 shows the material tensile strength and strain at break shows a good linear correlation with the tensile rate’s logarithm.

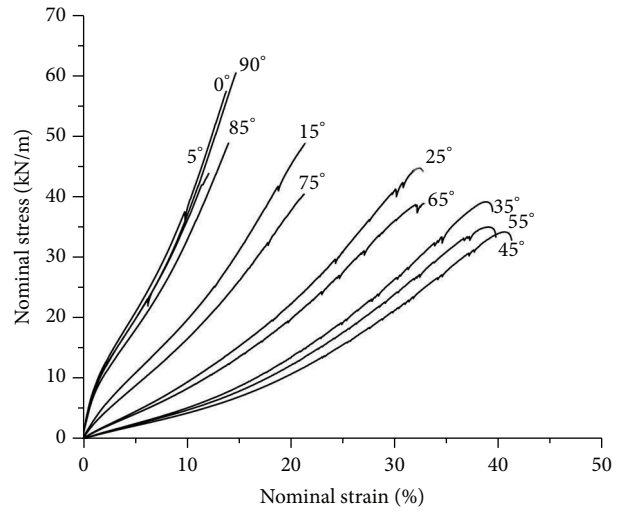
As shown in Figure 8, the relationship between tensile strength, strain at break, and tensile rate is as follows:

$$\begin{aligned} f_u &= a + b \lg v_\varepsilon, \\ \varepsilon_u &= c + d \lg v_\varepsilon, \end{aligned} \quad (1)$$

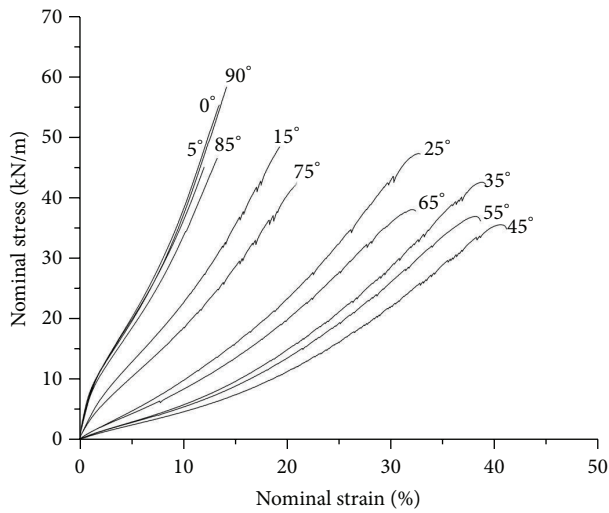
where f_u is material tensile strength, kN·m⁻¹, ε_u is strain at break, %; v_ε is tensile rate, mm/min; a , b , c , and d are the parameters that have no physical meanings. The parameters



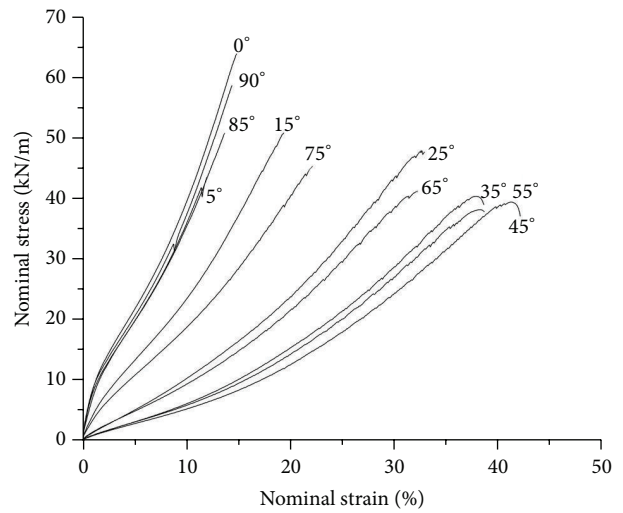
(a) 10 mm/min



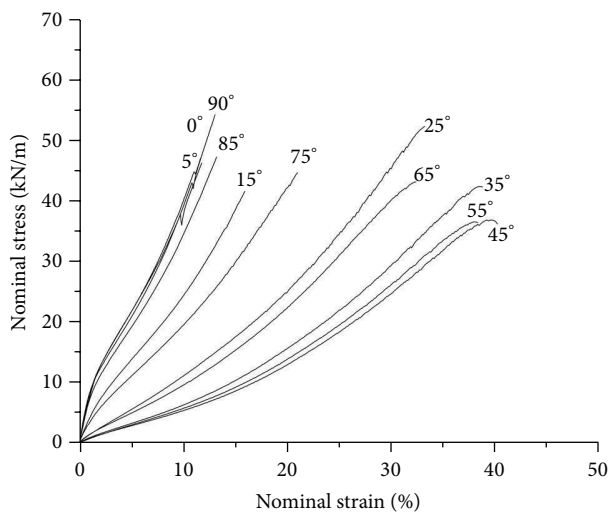
(b) 25 mm/min



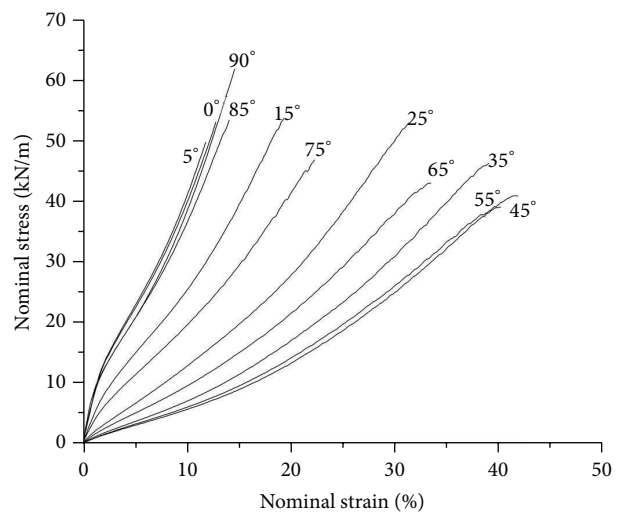
(c) 50 mm/min



(d) 100 mm/min



(e) 200 mm/min



(f) 500 mm/min

FIGURE 3: Off-axial tensile curves of Preconstraint 702 T2 under different loading rates.

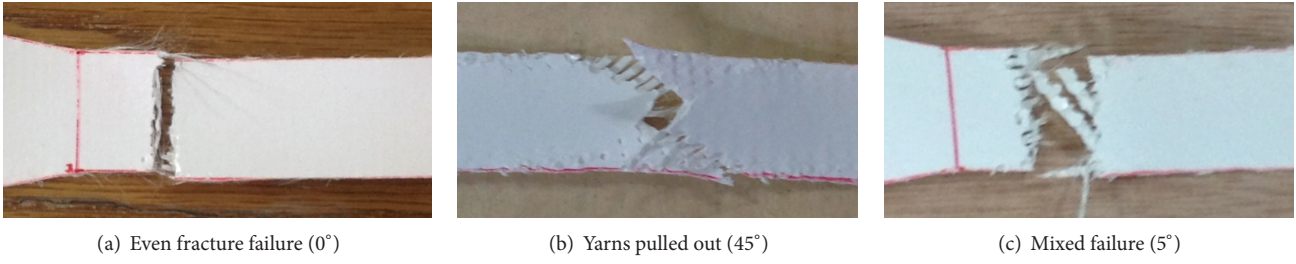


FIGURE 4: Failure modes of Preconstraint 702 T2.

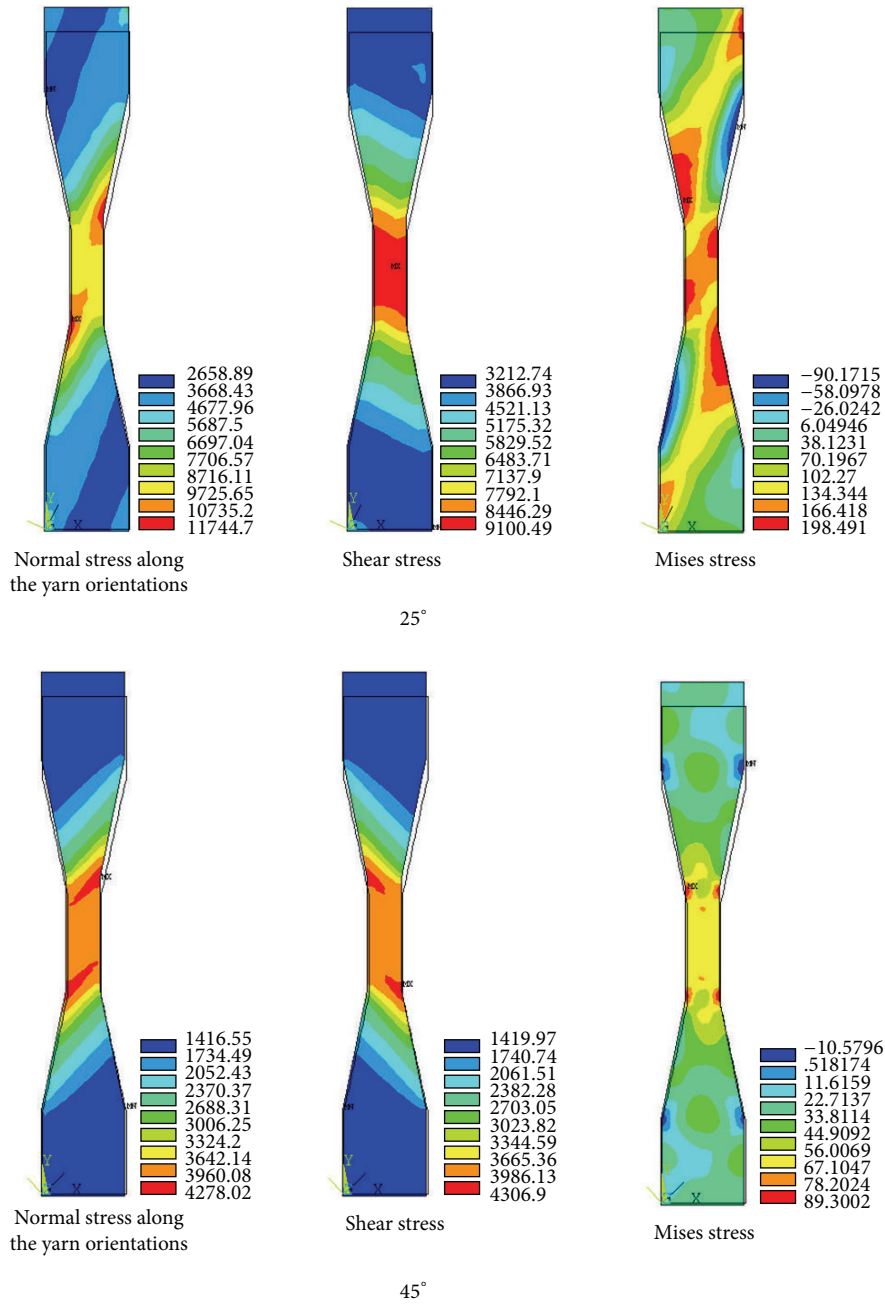


FIGURE 5: Finite element analysis of off-axial tensile test (Preconstraint 702 T2).

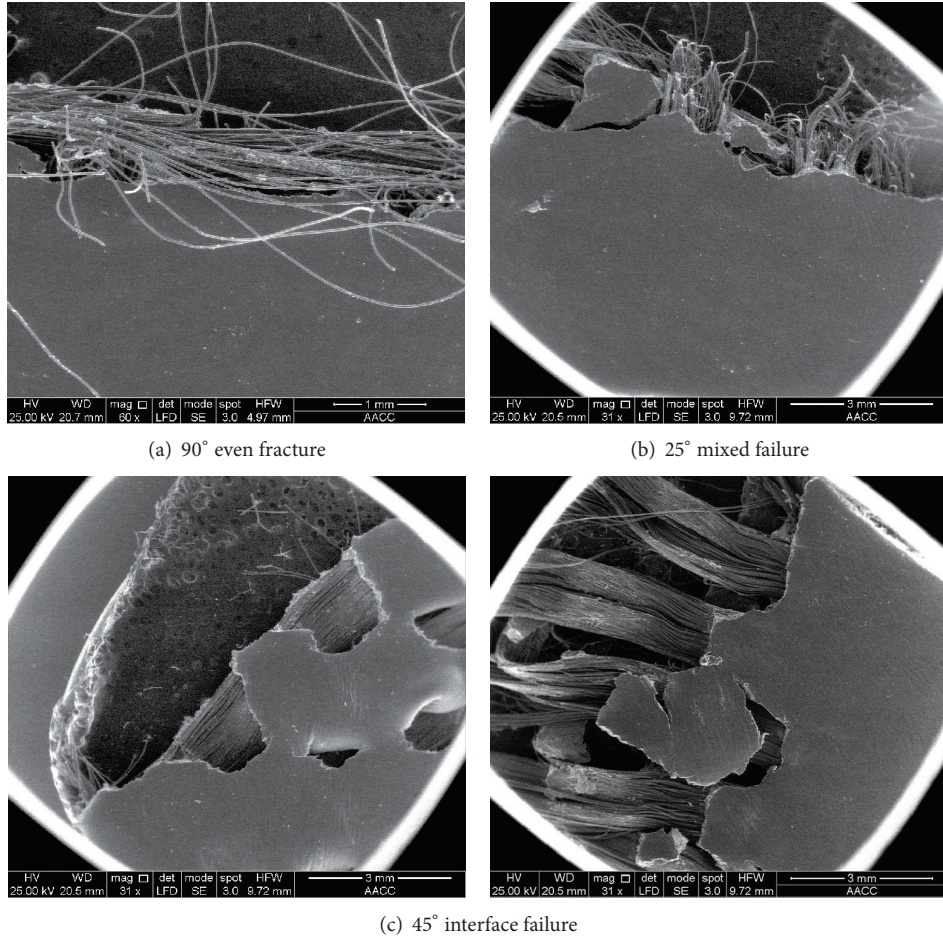


FIGURE 6: SEM images of fractographies of off-axis specimens.

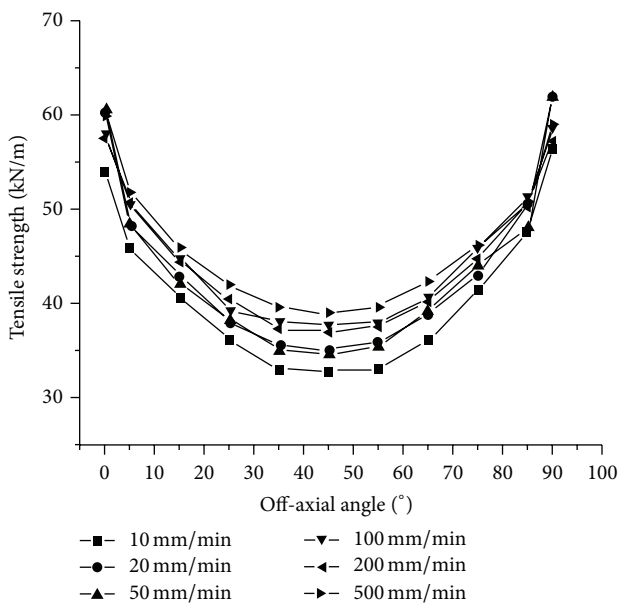


FIGURE 7: Off-axis tensile strength of Preconstraint 702 T2 under different loading rates.

can be obtained by fitting the experimental data, as shown in Table 3. The tensile strength and strain at break under different tensile rates can be predicted by using the above equations, which can be used for the mechanical behaviors of membrane structures under different tensile rates. Besides, the wind-induced disasters are the main reason for the failure of membrane structures. The tensile strength increases with tensile rate increasing, which is favorable for the safety of membrane structures under high rate winds, for example, typhoon. Using the tensile strength obtained by the standard inspection method with the tensile rate of 100 mm/min is conservative and can increase the safety reliability of membrane structures.

As shown in Figure 8, for the specimens with the same bias angles, the failure modes regarding different loading rates are almost the same. With bias angle increasing, the failure modes change from “even fracture” to “mixed failure.” Finally, the main failure mode is yarns pulled out, when the bias angle is 45 degrees. With tensile rate increasing, the deformation energy of membrane materials increases and the rate of energy absorption increases. Therefore, the material fracture toughness increases and the ultimate total

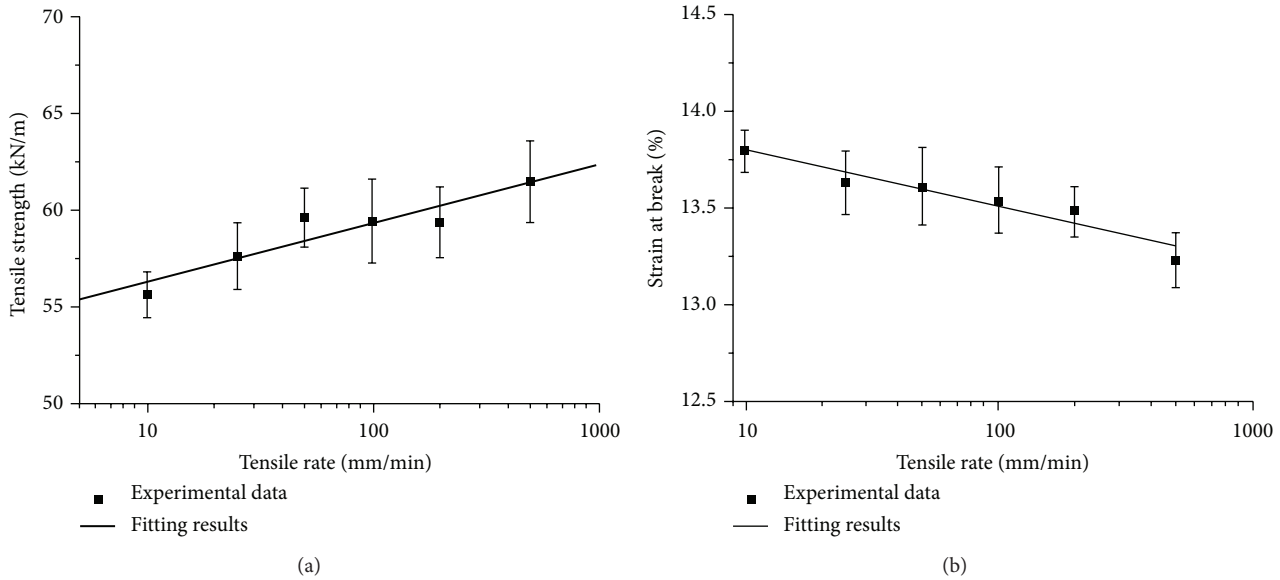


FIGURE 8: Relationship between tensile strength and strain at break and tensile rate.

TABLE 3: Relationship between tensile strength & strain at break and tensile rate.

Bias angle/ $^{\circ}$	<i>a</i>	<i>b</i>	<i>c</i>	<i>d</i>
0	55.113	1.779	14.092	-0.293
5	46.188	1.941	12.812	-0.068
15	38.001	2.976	19.490	-0.654
25	32.978	3.256	33.107	-0.401
35	29.863	3.288	39.739	-0.335
45	29.553	3.488	41.608	-0.621
55	30.042	3.546	39.302	-0.181
65	32.402	4.147	33.462	-0.386
75	39.338	2.654	22.206	-0.409
85	48.87	0.674	14.792	-0.397
90	58.496	0.189	14.903	-0.253

energy of membrane fracture increases, which will lead to the increasing of membrane tensile strength. Meanwhile, with tensile rate increasing, the material resistance to crack propagation increases, while the strain at break decreases slightly [14]. It can be observed that when the tensile rate is low, the effect of microflaws on material tensile strength is significant. Here, the “mixed failure” is taken as the example. When the tensile rate is low, the side yarns are easily pulled out from the adjacent yarns or the coating/yarn interface. The failure always appears in the boundary, part of yarns are pulled out, and the mid-section of membrane materials fractures finally. With tensile rate increasing, fewer yarns are pulled out and more yarns fracture. Then, most of the mid-section fractures and fewer of yarns are pulled out. During the failure process, the coating plays an important role in the failure mechanisms. The coated fabric is composed of the coating and the substrate, while the stress wave may pass with different rates in the coating and the substrate. The

substrate carries most of the force and the coating carries less. Then, the coating may restrain the deformation of substrates, due to smaller deformation. Therefore, when the tensile rate is low, the material fracture toughness and the resistance to crack propagation are low. Then, the microcrack can easily propagate and lead to the failure of materials. When the tensile rate is high, the resistance to crack propagation provided by the coating increases, while there is not enough time to achieve the ultimate deformation. Then, the crack propagates slowly and the tensile strength increases, because the limit strain energy remains almost unchanged. This is also why the strain at break decreases.

It should be noted that there are slight differences on the failure modes under different loading rates. As shown in Figure 9, when the tensile rate is low, it can be seen that some of yarns fracture while the other yarns are pulled out. When the tensile rate is high, more yarns fracture while fewer yarns are pulled out. This is mainly related to the interface strength, which is associated with the frictions between the longitudinal yarns and the transverse yarns and the frictions between the substrate and the coating [34, 35]. Besides, it may be related to the microdefects in the coated fabrics due to the manufacture and construction process. The failure modes are related to the distributions of microdefects. When the tensile rate is low, the microscopic defects can easily develop to macroscopic slits/cracks under tensile loading. It may lead to the interactions of many slits, which is a complex failure mode. This cannot be predicted by the macroscopic strength criteria. It can only be described by the damage mechanics based on the microscopic structures of coated fabrics.

4. Strength Criterion

As the expansion of the failure criterion for homogeneous materials, the macroscopic strength criteria of composites are

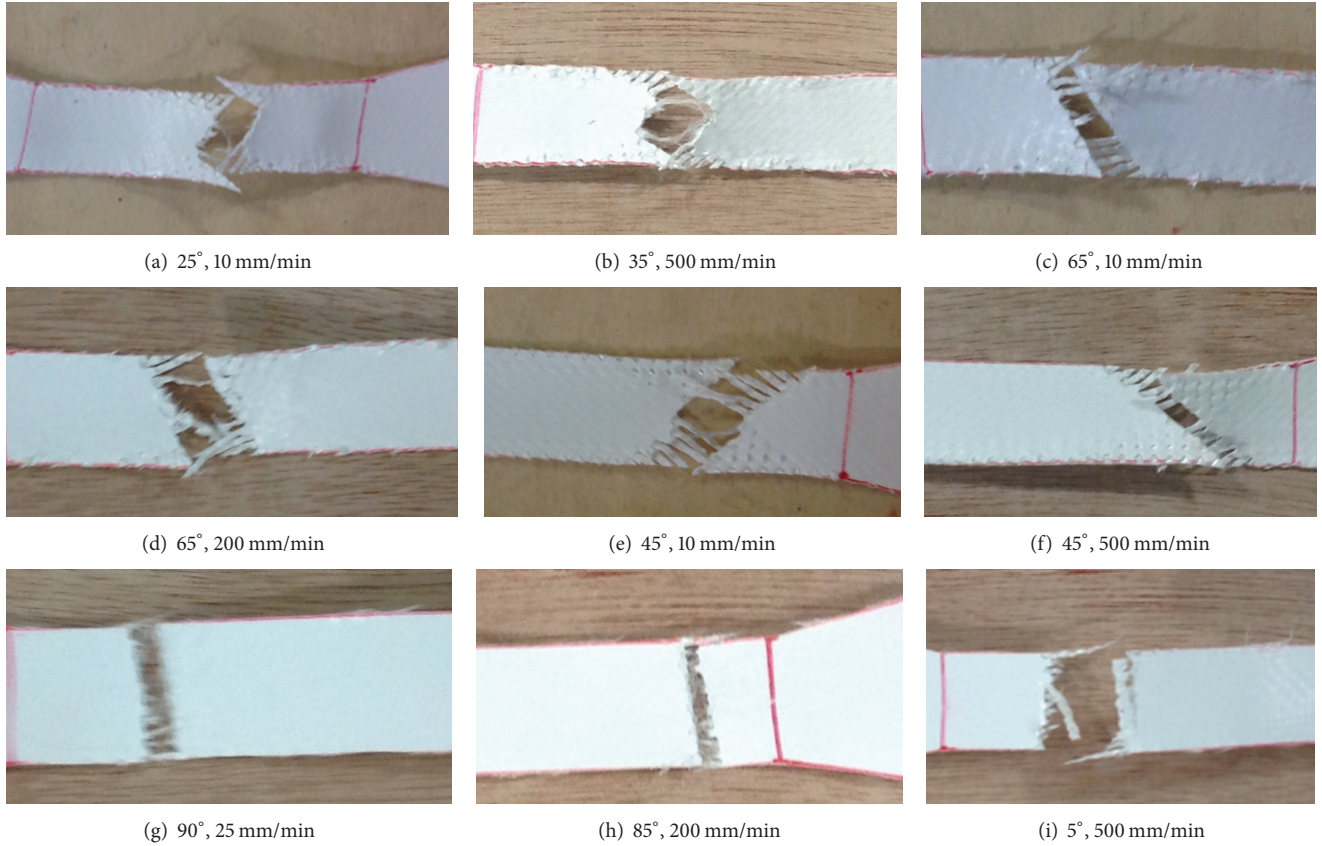


FIGURE 9: Failure modes of PVDF coated woven fabrics under different tensile rates.

popular due to operationally simple expressions. For engineering design, prediction accuracy and simple expressions are two important aspects of failure criteria. Among the current strength criteria, the quadratic criteria are recommended by many researchers, because they are single valued functions with smooth and continuous failure envelope, particularly suitable for the numerical solution [36–40].

For building coated fabric, it is similar to a plane anisotropic material, of which the mechanical properties in the Z direction (thickness) are always ignored. When predicting the failure strength of building coated fabrics, the failure criteria for three-dimensional composites materials should be degenerated into a two-dimensional criterion.

Here, several classical strength criteria are chosen to predict the tensile strength of off-axial samples, including Tsai-Hill criterion, Yeh-Stratton criterion, Hashin criterion, and Zhang criterion [13, 37, 41, 42]. They are shown as follows:

Tsai-Hill criterion is

$$\frac{\sigma_x^2}{X^2} + \frac{\sigma_y^2}{Y^2} - \frac{\sigma_x \sigma_y}{X^2} + \frac{\tau_{xy}^2}{S^2} = 1. \quad (2)$$

Yeh-Stratton criterion is

$$\frac{\sigma_x}{X} + \frac{\sigma_y}{Y} - \frac{\sigma_x \sigma_y}{X^2} + \frac{\tau_{xy}^2}{S^2} = 1. \quad (3)$$

Hashin criterion is

$$\left(\frac{\sigma_{11}}{X}\right)^2 + \left(\frac{\tau}{S}\right)^2 = 1. \quad (4)$$

Zhang criterion is

$$\frac{\sigma_x}{X} + \frac{\sigma_y}{Y} + \frac{\tau_{xy}}{S} + F_{12} \frac{\sigma_x \sigma_y}{XY} + F_{16} \frac{\sigma_x \tau_{xy}}{XS} = 1, \quad (5)$$

where σ_x and σ_y are the normal stress in weft and warp, τ is the shear stress, X and Y are the tensile strength in weft and warp, and S is the shear strength.

Figure 10 shows the comparison between experiment results and the predictions of several existing strength criteria. In most cases, the current strength criteria can make a good prediction of the failure strength of Preconstraint PVDF coated fabric. However, slight deviations appear in the tests of small off-axial angles, such as 15° and 75° . This is perhaps because of the crimp interchange in the weaving and coating processes.

In the Tsai-Hill criterion and the Yeh-Stratton criterion, the parameter F_{12} (the interaction item of σ_x and σ_y) is only associated with longitudinal strength X . Meanwhile, in the Norris criterion, it is related to the longitudinal strength X and the transverse strength Y . For plain woven fabrics, the differences between them are not as significant as that in unidirectional reinforced fabrics. It is an important,

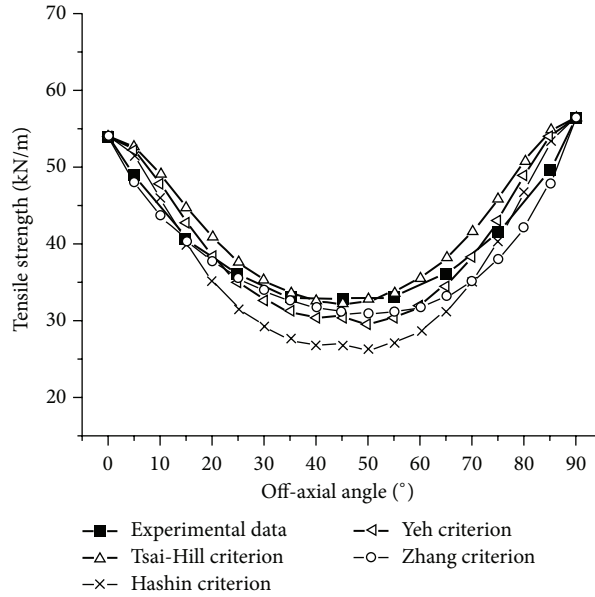


FIGURE 10: Comparison of experiment data and predictions of several existing strength criteria.

independent but constrained strength component. It is very sensitive in biaxial tests and can be approximately got in such biaxial tests. The determination of the value of F_{12} can be achieved through infinite number of combined-stress states. Comparisons are made with optimum values obtained from least-squares analyses. The value of F_{12} is always small but not ignored. Besides, the parameter F_{16} (the interaction term of normal stress and shear stress) cannot be ignored, especially for the samples with small off-axial angles.

As orthotropic materials, the mechanical properties of the coated fabrics are affected by the bias angles, just as shown in Figure 10. The tensile strength of the on-axial specimens (0 and 90 degrees) is the highest, while that of 45° specimen is the lowest. Therefore, the warp and weft yarns should be located along the principal stress. If not, the ultimate loading capacity of the membrane structure will decrease and the wrinkling may appear under extreme loadings. This should be considered in the form-finding analysis and the cutting pattern design. Under harsh environments, the microcrack in the coated fabrics can easily propagate and lead to the overall failure of membrane structures due to low tear strength. From the above analysis, the tensile strength will increase slightly under high loading rates, which is favorable for the design of membrane structures under high loading rates, for example, the analysis of wind-induced disasters.

Finally, coated fabric is not a continuous homogeneous material in meso- or microscales. In the process of weaving and coating, the yarns and coating are aligned regularly depending on the weaving method. Therefore, in the macroscale, it can be taken into account as a homogeneous material. This is why most of the data can agree well with the predictions of current macroscopic strength criteria. The transfer of force in coated fabrics is mainly through the yarns. The failure always appears at the weakest point and propagates quickly through the yarns. Therefore, the

traditional quadratic criteria may not reflect the failure mechanisms of coated fabrics. Further research should be carried out to obtain a simplified equation, which is based on the microscopic structural analysis.

5. Conclusions

(1) The Preconstraint PVDF coated polyester is typically anisotropic. With bias angle increasing, the tensile strength decreases and the strain at break increases. The warp tensile strength is slightly higher than that in weft, while the strain at break is lower than that in weft. There are not significant differences between the warp and the weft, which is different from the plain woven materials. This is related to the Preconstraint woven methods and the woven densities.

(2) The tensile strength is mainly related to failure modes and substrate structure. When the bias angle is 0° and 90°, the tensile stress is the dominant, and the main failure mode is “yarns even fracture.” Then, the tensile strength is the highest and the application ratios of yarns are the highest. When the bias angles are close to 45°, the material failure is yarns pulled out, which is the interface failure. The shear stress is dominant and the tensile strength is the lowest. In the intermediate angles, the main failure mode is mixed failure, including yarns fracture and interface failure.

(3) With tensile rate increasing, the tensile strength increases while the strain at break decreases. The tensile strength shows good linear relationship between tensile rate's logarithms. With tensile rate increasing, the deformation energy of coated fabrics increases quickly, while the constraint of coating on material deformation increases. There are slightly differences on the failure modes under different loading rates. Besides, it may be related to the microdefects in the coated fabrics due to the manufacture and construction process.

(4) Most of the current strength criterion can make a better prediction of the material off-axial strength, except for the specimens of 15° and 75°. This is perhaps related to complex failure modes and woven structures. The traditional strength criteria are always based on the homogeneous materials, while the coated fabrics are actually the composition of yarns and substrate.

Competing Interests

The author declares that there is no conflict of interests regarding the publication of this paper.

Acknowledgments

This work is supported by Research Program of Jiangsu Vocational Institute of Architectural Technology (Grant no. JYA14-09).

References

- [1] B. Forster and M. Mollaert, *European Design Guide for Tensile Surface Structures*, TensiNet, 2004.
- [2] T. D. Dinh, A. Rezaei, W. Punurai et al., "A shape optimization approach to integrated design and nonlinear analysis of tensioned fabric membrane structures with boundary cables," *International Journal of Solids and Structures*, vol. 83, pp. 114–125, 2016.
- [3] B. N. Bridgens and M. J. S. Birchall, "Form and function: the significance of material properties in the design of tensile fabric structures," *Engineering Structures*, vol. 44, pp. 1–12, 2012.
- [4] Y. Zhang, Q. Zhang, Z. Yang, L. Chen, and Y. Cao, "Load-dependent mechanical behavior of membrane materials and its effect on the static behaviors of membrane structures," *Journal of Materials in Civil Engineering*, vol. 27, no. 11, Article ID 04015018, 2015.
- [5] A. Ambroziak, "Mechanical properties of PVDF-coated fabric under tensile tests," *Journal of Polymer Engineering*, vol. 35, no. 4, pp. 377–390, 2015.
- [6] A. Ambroziak, "Mechanical properties of Preconstraint 1202S coated fabric under biaxial tensile test with different load ratios," *Construction and Building Materials*, vol. 80, no. 1, pp. 210–224, 2015.
- [7] A. Ambroziak and P. Kłosowski, "Mechanical properties for preliminary design of structures made from PVC coated fabric," *Construction and Building Materials*, vol. 50, pp. 74–81, 2014.
- [8] A. Ambroziak, "Mechanical properties of polyester coated fabric subjected to biaxial loading," *Journal of Materials in Civil Engineering*, vol. 27, no. 11, Article ID 04015012, 2015.
- [9] Y. Zhang, Q. Zhang, and H. Lv, "Mechanical properties of polyvinylchloride-coated fabrics processed with Preconstraint® technology," *Journal of Reinforced Plastics & Composites*, vol. 31, no. 23, pp. 1670–1684, 2012.
- [10] H. W. Reinhardt, "On the biaxial testing and strength of coated fabrics," *Experimental Mechanics*, vol. 16, no. 2, pp. 71–74, 1976.
- [11] S. H. Chen, X. Ding, R. Fanguero, H. Yi, and X. Yang, "Tensile performance and crack propagation of coated woven fabrics under multiaxial loads," *Journal of Applied Polymer Science*, vol. 113, no. 5, pp. 3388–3396, 2009.
- [12] J. W. Chen and W. J. Chen, "Central crack tearing testing of laminated fabric uretek3216LV under uniaxial and biaxial static tensile loads," *Journal of Materials in Civil Engineering*, vol. 28, no. 7, Article ID 04016028, 2016.
- [13] Z. Yingying, S. Xiaoguang, Z. Qilin, and L. V. Henglin, "Fracture failure analysis and strength criterion for PTFE-coated woven fabrics," *Journal of Composite Materials*, vol. 49, no. 12, pp. 1409–1421, 2015.
- [14] S. H. Chen, X. Ding, and H. L. Yi, "On the anisotropic tensile behaviors of flexible polyvinyl chloride-coated fabrics," *Textile Research Journal*, vol. 77, no. 6, pp. 369–374, 2007.
- [15] Z. Zou, J. Han, H. Liu et al., "Orthotropic behavior of PVC architectural membrane materials under tensile loading," *Journal of Zhejiang Sci-Tech University*, vol. 27, no. 2, pp. 186–190, 2010.
- [16] J. Cao, R. Akkerman, P. Boisse et al., "Characterization of mechanical behavior of woven fabrics: experimental methods and benchmark results," *Composites Part A: Applied Science and Manufacturing*, vol. 39, no. 6, pp. 1037–1053, 2008.
- [17] A. G. Colman, B. N. Bridgens, P. D. Gosling, G.-T. Jou, and X.-Y. Hsu, "Shear behaviour of architectural fabrics subjected to biaxial tensile loads," *Composites Part A: Applied Science and Manufacturing*, vol. 66, pp. 163–174, 2014.
- [18] J. Launay, G. Hivet, A. V. Duong, and P. Boisse, "Experimental analysis of the influence of tensions on in plane shear behaviour of woven composite reinforcements," *Composites Science and Technology*, vol. 68, no. 2, pp. 506–515, 2008.
- [19] A. Gilat, R. K. Goldberg, and G. D. Roberts, "Experimental study of strain-rate-dependent behavior of carbon/epoxy composite," *Composites Science and Technology*, vol. 62, no. 10–11, pp. 1469–1476, 2002.
- [20] A. Martin, R. Othman, and P. Rozycki, "Experimental investigation of quasi-static and intermediate strain rate behaviour of polypropylene glass fibre (PPGF) woven composite," *Plastics, Rubber and Composites*, vol. 44, no. 1, pp. 1–10, 2015.
- [21] B. C. Ray, "Effects of changing environment and loading speed on mechanical behavior of FRP composites," *Journal of Reinforced Plastics and Composites*, vol. 25, no. 12, pp. 1227–1240, 2006.
- [22] S. Kato, H. Minami, T. Yoshino et al., "Visco-inelastic constitutive equations for fabric membranes based on fabric lattice model-simulations for creep and relaxation compared with experiments," in *Research Report on Membrane Structures*, pp. 29–43, The Membrane Structures Association of Japan, Tokyo, Japan, 1996.
- [23] L. Meng and M.-E. Wu, "Study on stress relaxation and creep properties of PTFE membrane," *Journal of Building Materials*, vol. 15, no. 2, pp. 206–210, 2012.
- [24] W.-R. Yu, M. S. Kim, and J. S. Lee, "Modeling of anisotropic creep behavior of coated textile membranes," *Fibers and Polymers*, vol. 7, no. 2, pp. 123–128, 2006.
- [25] K. J. Kim, W.-R. Yu, and M. S. Kim, "Anisotropic creep modeling of coated textile membrane using finite element analysis," *Composites Science and Technology*, vol. 68, no. 7–8, pp. 1688–1696, 2008.
- [26] M. Lei, *Stress Analysis of the Equilibrium Surface for Membrane Structures by Considering Viscoelastic Properties of Coated Fabrics*, Tongji University, Shanghai, China, 2013.
- [27] Y. Li and M. Wu, "Uniaxial creep property and viscoelastic-plastic modelling of ethylene tetrafluoroethylene (ETFE) foil," *Mechanics of Time-Dependent Materials*, vol. 19, no. 1, pp. 21–34, 2015.

- [28] Y. Zhang, S. Xu, Q. Zhang, and Y. Zhou, "Experimental and theoretical research on the stress-relaxation behaviors of PTFE coated fabrics under different temperatures," *Advances in Materials Science and Engineering*, vol. 2015, Article ID 319473, 12 pages, 2015.
- [29] J. Fujiwara, M. Ohsaki, and K. Uetani, "Cutting pattern design of membrane structures considering viscoelasticity of material," in *Proceedings of the IASS Symposium*, pp. 112–113, Nagoy, Japan, October 2001.
- [30] H. Nakajima, M. Saitoh, and A. Okada, "Structure analytical study on stress relaxation in tensile membrane structures-structural principle on tensile membrane structure with spring-strut system," in *Research Report on Membrane Structures '07*, pp. 15–25, The Membrane Structures Association of Japan, Tokyo, Japan, 2007.
- [31] S. Kato and T. Yoshino, "Simulation for introducing tensions into curved membranes considering both of the cutting pattern method and visco-elasto-plastic characteristics of the fabrics," in *Proceedings of the IASS Symposium*, pp. 110–111, International Association for Shell and Spatial Structures, Nagoya, Japan, 2001.
- [32] DIN, "Testing of artificial leather-tensile test," DIN 53354, 1981.
- [33] A. K. Sen, *Coated Textiles: Principles and Applications*, CRC Press, 2nd edition, 2007.
- [34] Y. Wang, X. G. Chen, R. Young, and I. Kinloch, "Finite element analysis of effect of inter-yarn friction on ballistic impact response of woven fabrics," *Composite Structures*, vol. 135, pp. 8–16, 2016.
- [35] H. Wang and Z.-W. Wang, "Quantification of effects of stochastic feature parameters of yarn on elastic properties of plain-weave composite. Part I: theoretical modeling," *Composites Part A: Applied Science and Manufacturing*, vol. 78, pp. 84–94, 2015.
- [36] H. Y. Yeh and L. T. Kilfoy, "A simple comparison of macroscopic failure criteria for advanced fiber reinforced composites," *Journal of Reinforced Plastics and Composites*, vol. 17, no. 5, pp. 406–445, 1998.
- [37] S. W. Tsai, "Survey of macroscopic failure criteria for composite materials," *Journal of Reinforced Plastics and Composites*, vol. 3, no. 1, pp. 40–62, 1984.
- [38] C. C. Chamis, "Polymer composite mechanics review—1965 to 2006," *Journal of Reinforced Plastics & Composites*, vol. 26, no. 10, pp. 987–1019, 2007.
- [39] F. Paris, "A study of failure criteria of fibrous composite materials," Tech. Rep. NASA/CR-2001-210661, NASA Langley Research Center, Hampton, Va, USA, 2001.
- [40] J. Echaabi, F. Trochu, and R. Gauvin, "Review of failure criteria of fibrous composite materials," *Polymer Composites*, vol. 17, no. 6, pp. 786–796, 1996.
- [41] H.-Y. Yeh and C. H. Kim, "The Yeh-Stratton criterion for composite materials," *Journal of Composite Materials*, vol. 28, no. 10, pp. 926–939, 1994.
- [42] Z. Hashin, "Failure criteria for unidirectional fiber composites," *Journal of Applied Mechanics*, vol. 48, no. 4, pp. 846–852, 1981.

Research Article

Measurement of Surface Damage through Boundary Detection: An Approach to Assess Durability of Cementitious Composites under Tannery Wastewater

Tanvir Manzur, Khaled Mahmood Ehsan, Sinha Lamia Sultana, and Samira Mahmud

Department of Civil Engineering, BUET, Dhaka 1000, Bangladesh

Correspondence should be addressed to Tanvir Manzur; tmanzur.buet@gmail.com

Received 22 April 2016; Revised 19 June 2016; Accepted 28 June 2016

Academic Editor: Gonzalo Martínez-Barrera

Copyright © 2016 Tanvir Manzur et al. This is an open access article distributed under the Creative Commons Attribution License, which permits unrestricted use, distribution, and reproduction in any medium, provided the original work is properly cited.

Concrete structures are often subjected to aggressive aqueous environments which consist of several chemical agents that can react with concrete to produce adverse effects. A Central Effluent Treatment Plant consisting of reinforced concrete structures which is being constructed at Savar, Bangladesh, is an example of such a case. The purpose of this treatment facility is to reduce the environmental pollution created by tannery wastewater. However, tannery wastewater consists of several chemicals such as sulfates, chlorides, and ammonium, which, from the literature, are known to generate detrimental effects on concrete. Evaluation of durability of concrete structures in such environments is therefore imperative. This paper highlights a technique of boundary detection developed through image processing performed using MATLAB. Cement mortar cubes were submerged in simulated tannery wastewater and the images of the surface of cubes were taken at several time intervals. In addition, readings for compressive strength and weight were also taken on the same days. In this paper, an attempt is made to correlate the results from image processing with that of strength and weight loss. It was found, within the scope of this study, that the specimens which suffered greater strength and weight loss also underwent greater loss of surface area.

1. Introduction

Durability of concrete structures is a matter of concern when the structure is exposed to harsh environmental conditions. Assessing the durability of an existing concrete structure in such conditions is neither a very straightforward nor a simple task. It is rather complex, as several factors have a controlling effect on the behavior of concrete and also because no direct measurement of durability can be acquired. Therefore, this paper aims to provide a directive regarding the durability of concrete in tannery wastewater. Simulated water having different proportions of eight primary constituents of tannery waste that have a significant effect on cement composites has been used in this study. The proportions of constituents were determined from the analysis of collected field samples of tannery wastewater. Field samples were collected from the largest tannery industrial site of the country. The findings of this study therefore depict the behavior of concrete when exposed to tannery wastewater composed of

these constituents. However, the practical application of the analysis described in this paper lies in the fact that it enables the engineer to perform a study using images of the damaged portion of the structure without the need to be present at the location of the structure itself, which may be beneficial particularly in the case of remote or less easily accessible areas. Also, the use of this technique could be useful when a prompt analysis is required to get a primary idea about the extent of degradation, before pursuing a more detailed study based on which mitigation measures may be employed.

Tannery effluent consists of several chemicals such as high amount of sulfides, lime, ammonium salts, chlorides, sulfate, and protein, which are discharged into the effluent from the beam house operations soaking, liming, and deliming as discussed by Ramasami et al. [1]. It is well known that cement composites undergo deterioration in sulfate rich environments. The extent and kinetics of this deterioration depend on factors as discussed by Skalny et al. [2] and Brown [3] such as the sulfate content in the water,

wet-dry cycle, and pH of the solution. There are three chemical reactions between sulfate ions and hardened cement pastes, which are recrystallization of ettringite, formation of gypsum, and decalcification of the main cementitious phase (C-S-H). The effects of sulfate attack can be summarized as expansion leading to spalling and disintegration, loss of strength, and loss of mass. Ammonium salts are the most aggressive among the factors which can degrade concrete as discussed by Lea [4] and Biczok [5]. A very soluble calcium nitrate, a slightly soluble calcium nitroaluminate, and ammonia gas are produced during chemical attack on concrete by ammonium nitrate, inducing total leaching of calcium hydroxide and rapid decalcification of C-S-H. The effects of ammonium nitrate attack can be summarized as very large increase in porosity and notable swelling with the occurrence of cracks due to the formation of expansive crystals. Therefore, it is evident that concrete in contact with tannery waste is susceptible to high degree of deterioration. So, study is necessary to assess the durability of concrete structures constructed in waste prone facilities like Central Effluent Treatment Plant at Savar, Bangladesh.

In this paper, an image processing technique used to calculate the percentage loss of surface area of cement mortar cubes due to being immersed in simulated tannery wastewater has been discussed. This percentage loss of surface area cannot alone give an adequate assessment of the total damage that the specimens underwent. For this study to have a broader scope, more parameters needed to be considered. Correlating the results of image processing with those of strength and weight loss thus enabled a more comprehensive analysis to be performed on the extent of damage. Several difficulties were faced during image processing. For instance, grey level range of the images was very small, which made it difficult to detect the actual boundary line from the binary image. Contrast stretching was applied as a preprocessing technique as a result of which the boundary line detection from the image became easier and precise. Also, during the retrieval of the images, it was noticed that a certain region around the image formed shadow of the mortar cube. As a result, only thresholding would have included shadow when trying to locate the boundary from binary image, which would have been a source of error. The use of standard deviation filter for boundary detection after contrast stretching enabled avoiding the shadow of low contrast and detecting the main boundary. Finally, an efficient boundary detection technique has been developed to evaluate the surface loss of cement composites subjected to tannery wastewater.

2. Materials and Methods

The materials used, the preparation of test specimens, and the tests conducted are all discussed in detail in this section.

2.1. *Materials.* The materials used are as follows:

- (i) Graded standard sand: natural silica sand conforming to the requirements for graded standard sand in ASTM Specification C778 [6].
- (ii) Ordinary Portland Cement (OPC).

TABLE 1: Mass % of different elements in OPC cement sample.

Analyte	Mass %
CaO	65.98
SiO ₂	16.83
Al ₂ O ₃	7.02
Fe ₂ O ₃	3.03
MgO	3.11
SO ₃	2.67
Na ₂ O	0.18
K ₂ O	0.44
TiO ₂	0.38
P ₂ O ₅	0.14
MnO	0.097
Cr ₂ O ₃	0.023
SrO	0.059
ZnO	0.051
Cl	0.00

TABLE 2: Chemical parameters of the collected field tannery wastewater sample.

Parameters	Units	Raw sample	Filtered sample
Total hardness	mg/L as CaCO ₃	5900	7200
Alkalinity	mg/L	3540	7030
Cl ⁻	mg/L	660	900
SO ₄ ²⁻	mg/L	3100	3700
PO ₄ ³⁻	mg/L	97	61
NH ₃ -N	mg/L	2300	2175
NO ₃ -N	mg/L	40	—
CO ₃ ²⁻	mg/L	0.026	0.082
HCO ₃ ⁻	mg/L	4270	8540
COD	mg/L	56,600	67,600
BOD ₅	mg/L	22,000	24,000

Composition of cement was determined by X-ray fluorescence (XRF) analysis which was conducted using LAB CENTER XRF-1800. The cement composition is provided in Table 1.

2.2. *Simulated Tannery Wastewater.* Tannery wastewater samples were collected from Hazaribagh Area in Dhaka, Bangladesh. Table 2 shows chemical parameters of this field sample [7]. Wastewater samples, resembling the composition of tannery wastewater, were then simulated in the laboratory. The dominant constituents of tannery wastewater that can make concrete susceptible to degradation were identified from previous studies [8, 9]. The following ions were selected for this study:

- (i) Anions: chloride and sulfate.
- (ii) Cation: ammonium.

Total concentrations of these anions and cation in tannery wastewater were determined from laboratory testing and,

TABLE 3: Concentration of the prepared stock solutions.

Stock solution	Concentration (mg/L)	Stock solution	Concentration (mg/L)
NaCl	100,000	Na ₂ S·5H ₂ O	100,000
NaNO ₃	10,000	Na ₂ SO ₄	100,000
Na ₂ CO ₃	100	Na ₃ PO ₄	10,000
NaHCO ₃	100,000	NH ₄ NO ₃	100,000

TABLE 4: Different types of tannery wastewater used in the study.

Notation	Wastewater type	Constituents
T1	Tannery wastewater with all primary constituents	NaCl, Na ₃ PO ₄ /Na ₂ HPO ₄ ·2H ₂ O, NaNO ₃ , Na ₂ CO ₃ , NaHCO ₃ , Na ₂ S·5H ₂ O, NH ₄ NO ₃ , Na ₂ SO ₄
T2	Tannery wastewater without chloride	Na ₃ PO ₄ /Na ₂ HPO ₄ ·2H ₂ O, NaNO ₃ , Na ₂ CO ₃ , NaHCO ₃ , Na ₂ S·5H ₂ O, NH ₄ NO ₃ , Na ₂ SO ₄
T3	Tannery wastewater without sulfate	NaCl, Na ₃ PO ₄ /Na ₂ HPO ₄ ·2H ₂ O, NaNO ₃ , Na ₂ CO ₃ , NaHCO ₃ , NH ₄ NO ₃
T4	Tannery wastewater without ammonium	NaCl, Na ₃ PO ₄ /Na ₂ HPO ₄ ·2H ₂ O, NaNO ₃ , Na ₂ CO ₃ , NaHCO ₃ , Na ₂ S·5H ₂ O, Na ₂ SO ₄

eventually, stock solution was prepared. The concentrations of different constituents of stock solution are shown in Table 3. The first simulated sample had all selected primary tannery wastewater constituents in it. The other three simulated samples were prepared such that chloride was excluded from one, sulfate from another, and ammonium from the third. Table 4 shows the description of different types of simulated water samples used in the study.

2.3. Compressive Strength Test and Weight Loss Measurement.

The strength test was conducted in accordance with ASTM C109 [10]. Three samples were taken for each type of water condition on each day of testing, that is, 90 days and 180 days. The cement mortar cubes were prepared as per ASTM C109 Code [10]. The mortar used consisted of 1 part of cement and 2.75 parts of sand proportioned by mass. Fifty-millimeter (2-inch) test cubes were compacted by tamping in two layers. The cubes were cured for one day in the molds and stripped and immersed in lime water. A water-cement ratio of 0.485 was used for all the specimens. For measuring weight loss of samples, cubes were first cured in lime water for 28 days. After curing, cubes were then oven dried for 3 hours at 110°C and initial weight was measured. A similar process was followed to calculate the weight at 90 and 180 days. The mortar cubes were removed from the trays and dried in the oven for 3-4 hours at 110°C and then the final weight was determined. Weight loss (%) was calculated from the initial and final weights.

2.4. Image Capturing. Large trays were filled with the water samples, each tray containing a single type of water as described in Table 4. Samples were submerged in simulated water of each type as shown in Figure 1. Images of surface were taken for each cube using a DSLR camera before submergence using an image capturing setup. The setup consisted of a black cylindrical object made of nylon. An LED source was fitted to the upper end which emitted LED light

when connected to a power supply. The specimen was placed inside the cylindrical setup such that it was at the bottom end of the cylinder. Image was captured from the light source end. The camera was placed at the same position for every image, so a fixed focal distance was maintained for every image. After the submergence period of 90 days and 180 days, cubes were dried in the oven and images were taken. The initial and final pictures were taken on the same particular exposed surface to ensure appropriate comparison between the initial and final conditions.

3. Image Processing

This section describes the methodology employed to obtain the percentage of surface area loss through image processing. First, the RGB image (True Color Image) was taken which consists of three independent planes where every pixel color is a combination of red, green, and blue intensity values, the primary components of colors. After that, contrast stretching was done as an enhancement technique for boundary detection as discussed by Casado [11]. Using a filter, the standard deviation of every pixel was calculated. Then, the image was converted into binary image. However, it showed noise along the boundary line. Median filter was used to remove noise, followed by "bwareaopen," a function of MATLAB [12] to remove small objects. In order to get final boundary line by connecting the segmented pixels, dilation followed by erosion was done. Figure 2 shows the flow diagram of the image processing technique used in the study. Details of every step are described in the following sections.

3.1. Contrast Stretching (CS). Contrast is the difference in pixel intensity which can provide details about boundary of an object. The visibility of an object from its surroundings depends mostly on its boundary features. Adjustment of contrast is needed before extracting features from images having areas of low contrast or homogeneous intensity across



FIGURE 1: Specimens submerged in different types of water.

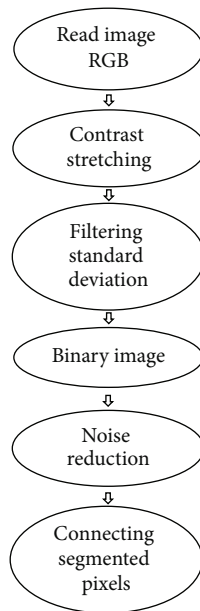


FIGURE 2: Methodology flow chart.

the same boundary line. Homogeneity means statistical consistency where pixel intensities have close values. Weak homogeneity leads to local spatial dissimilarity and breaks the continuation of arrangements which results in segmented pixel output along the boundary. Such homogeneity creates very low range of grey levels. Besides, low-contrast images may generate from poor illumination or wrong settings of lens aperture during image acquisition [13]. Surface texture conditions of the object itself may also generate low-contrast images. To overcome such problems, contrast stretching technique can be followed. Contrast stretching is a simple image enhancement technique which increases the dynamic range of the grey levels. In the current study, the accuracy of detecting the boundary was mostly dependent on the surface conditions of the mortar cubes; that is, the intensity variations of the image mostly depend on the extent of precipitation on the surface of the cubes under different water conditions.

The general form of contrast stretching as discussed by Casado [11] is

$$s = \frac{1}{1 + (m/r)^e}, \quad (1)$$

where s is the output image value, r is the input image value, m is the thresholding value, and e is the slope.

Initially, histogram equalization technique was used to detect exact boundary. Histogram equalization distributes the frequency of greyscale values to a wider range which effectively adjusts the global contrast of an image. However, from Figure 3, it is apparent that histogram equalization failed to retrieve exact boundary. This is due to the fact that histogram technique is capable of enhancing black and white areas rather than middle grey levels [11]. Contrast stretching is thus used to identify the boundary of the damaged surface of the samples. It is evident from Figure 4 that, before contrast stretching, pixels of the concrete block were of close grey level ranges, approximately within 150–250. But, after contrast stretching, grey level ranges significantly changed to a wider range of 50–220 by enhancing middle grey levels. It was clearly visible from the image that after contrast stretching it was darker in the dark areas and lighter in the light areas as shown in Figure 4(a) indicating the increased difference between intensities of the pixels.

3.2. Boundary Detection Using Local Standard Deviation Filter. Standard deviation is a statistical measure which is used to express variability in data set. In case of image processing, as discussed by Kumar and Gupta [13], standard deviation means the deviation of intensity of a pixel from mean in a specified neighborhood. Low standard deviation indicates that data set values are close to mean value. Higher standard deviation means significant dispersion of the values from the mean. Standard deviation enables measuring dispersion, which makes boundary detection possible, as the level of intensity changes at the boundary of an object by a significant amount. Calculation details of local standard deviation using filter are described in the following sections.

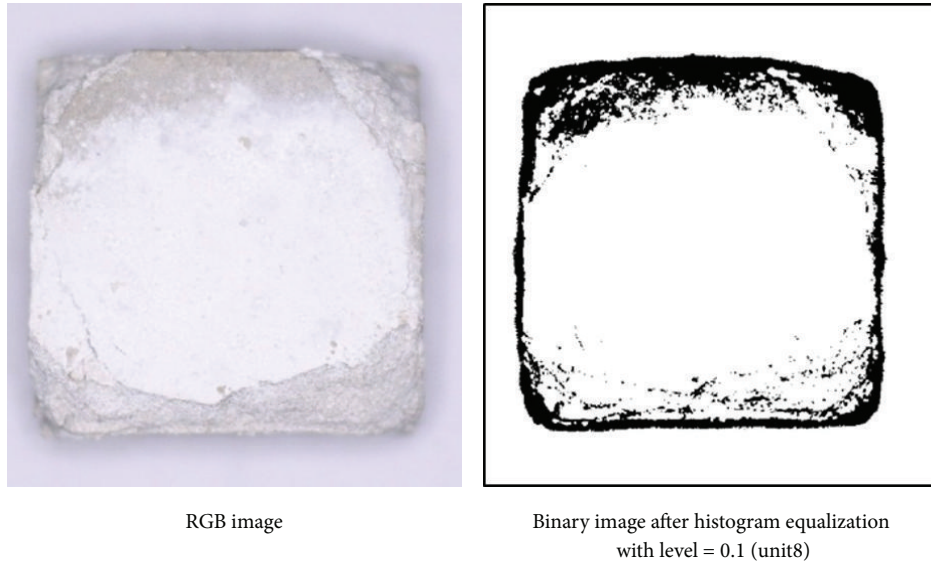


FIGURE 3: Failure in detecting boundary line without contrast stretching.

3.3. Filter for Local Standard Deviation. Local standard deviation of the input image was calculated using “stdfilt,” a built-in function in MATLAB [12]. The images were converted from unit8 to double-precision floating point data type which ranges from 0 to 1. Each output pixel represents standard deviation by 3×3 neighborhood around the corresponding pixel in the input image [12]. The texture boundaries can be detected effectively by calculating standard deviation as discussed by Hidayat and Green [14]. If only one texture is present in the local neighborhood, the output only represents intraclass variations. When both textures across boundary line are present, the output represents interclass along with intraclass variations [14]. Besides, standard deviation filters work well in case of pattern recognition in noisy image [13, 15]. After filtering, two types of output images were obtained in this study:

Type 1. Output showing the undamaged portion.

Type 2. Output showing the damaged portion.

Accuracy in detecting boundary line depends on the intensity variations and uniformity of a region. Nonuniform intensity variations, in other words weak homogeneity, occurred due to variations of depth which eventually resulted in segmented and noisy boundary lines after transformation into binary image. Similar phenomena were also observed by Ito et al. [16].

3.4. Conversion to Binary Image. Resizing of image was needed as the output image after filtering contained segmented pixel because of nonuniform variations in intensity. The output image showed only the pixels with higher standard deviation, which included both the boundary and the noise around the boundary. Resizing was important in designing filters and structuring element for noise removal. Using MATLAB function “imresize” [12], the images were

resized into $[512 \times 512]$. Conversion to binary image was done by using MATLAB [12] built-in function “im2bw” with changing the levels within certain ranges. It was found that conversion worked well within the range from 0.01 to 0.03 in class double.

3.5. Shadow Removal Technique. As image contrast was increased by contrast stretching (CS), it made the dark zones darker as highlighted in Figure 5(a). As a result, when the image was converted into binary image (Figure 5(b)), it also detected shadow as boundary line with higher level value. Different points within the shadow zone were of close intensity variations. Using standard deviation filter, the shadow was significantly removed. As a result, only the pixels within the specified level appeared in the binary image, as shown in Figure 6.

3.6. Filtering for Noise Reduction. Noise is described as the random fluctuations of pixel intensity value. “salt-pepper” noise is impulse valued noise. For an 8-bit image, the typical value for pepper noise is 0 and that for salt noise is 255. In this study, nonuniform precipitation created maximum value impulse noise on the surface, that is, “salt noise.” Therefore, such pixels containing noise interfered with a small number of pixels surrounding it [17]. For these pixels, the mean differed significantly, as a result of which, standard deviation filter showed them as an output. Conventional low pulse filtering was not effective for impulse noise [17]. Median filter is often used since it is capable of preserving the edges and small details in the image [18]. Hence, median filter was used for effective removal of “salt-pepper” noise in this study. MATLAB [12] function “bwareaopen” was then used for further removal of small objects which could not be removed by median filter [12]. After noise removal, the output images were found to consist of segmented pixels. Therefore, in order to get continuous boundary line, dilation followed by

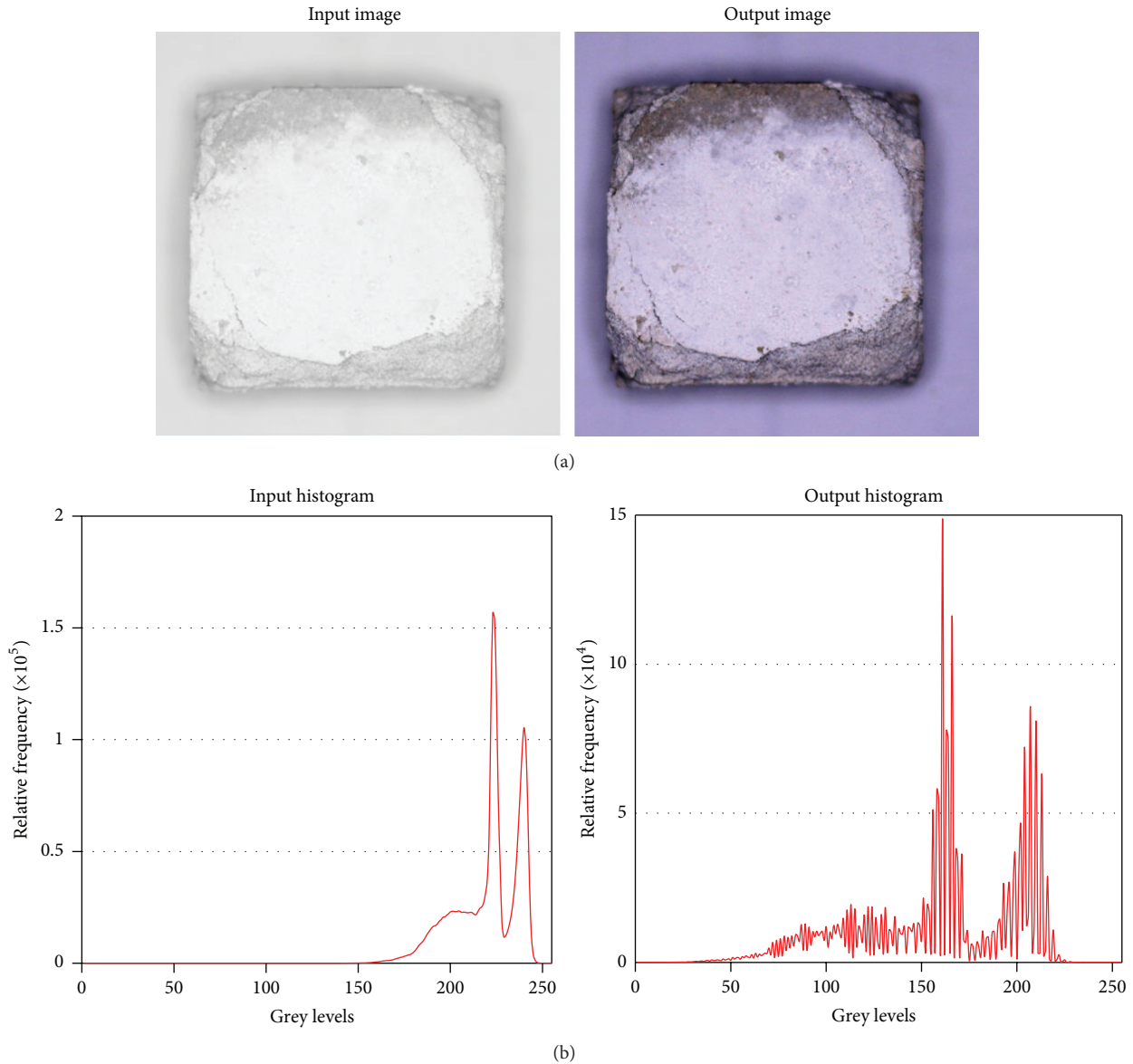


FIGURE 4: Histogram before and after contrast stretching.

erosion was done. As discussed by Gonzalez and Woods [19], dilation can be defined as the morphological operation which expresses vector addition between an image or point set and the structuring element. After dilation operation, object areas expand. Therefore, reduction of object area is required which is done by erosion technique. Erosion is defined as the operation where output points are from vector subtraction between a set of points and the structuring element. For Type 1, the size of “disk shaped” structuring element varied within the range of 3–15 and for Type 2 image it varied between 1 and 9. When the segmented pixels were connected, “infill” function of MATLAB [12] was used to fill the closed boundary foreground pixels with white color [12]. Figures 7 and 8 show the images after noise removal and after connecting segmented pixels, respectively.

3.7. Calculation of Percent Surface Damage. In case of images having low standard deviations, the segmented pixels were not connected. As a result, the size of the structuring element for dilation was much greater than for erosion. This process resulted in error as dilation increased object boundary compared with the actual one. To minimize this error, the same structuring element was designed for dilation and erosion to retrieve the initial images. In calculating initial pixel quantity, the same image was used by changing level value for thresholding. This process was followed due to the occurrence of damage at different depths of mortar block which preserved almost the original square shape of the boundary. While adjusting level value above a certain range, shadow may also be included depending on the presence of shadow. For this case, a slope value and a threshold value were

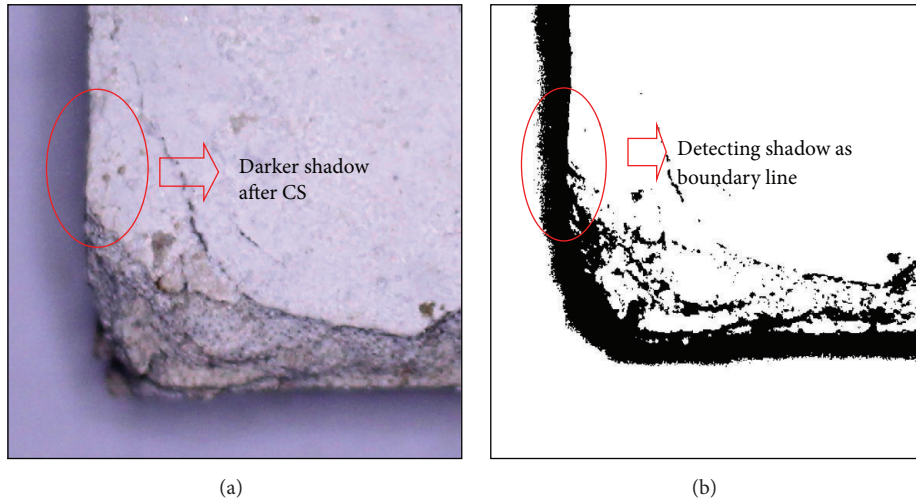


FIGURE 5: Problems related to shadow.

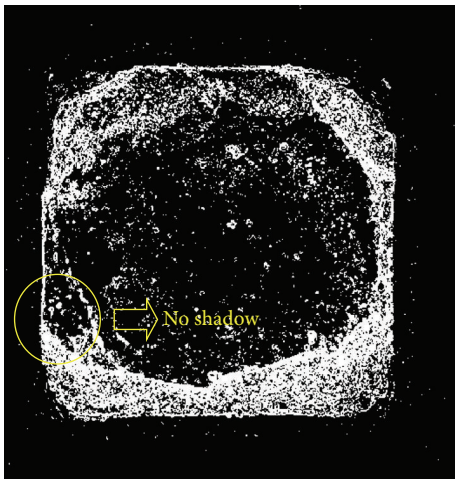


FIGURE 6: Shadow removal of Type 2 output by standard deviation filter.

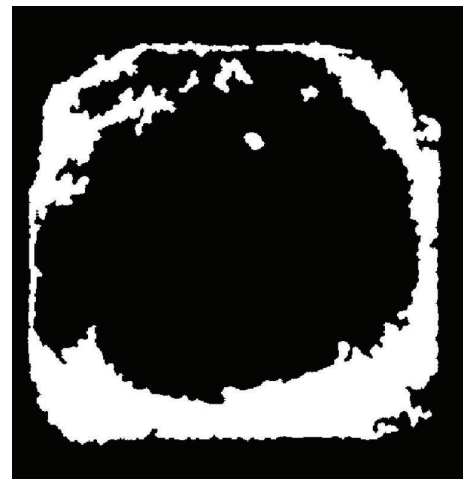


FIGURE 8: Connecting the segmented pixels.

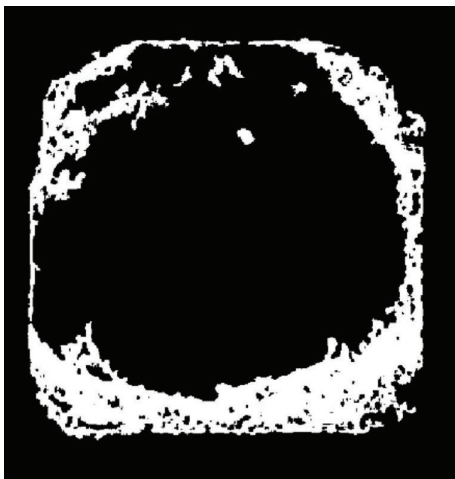


FIGURE 7: Output after noise removal.

adjusted to avoid shadow for getting initial pixels. Finally, the following equation was used for calculating the percentage of damage:

$$\% \text{ of damage} = \frac{\text{total damaged pixels counted}}{\text{total initial pixels}} \times 100\% \quad (2)$$

4. Results and Discussion

In this section, surface area loss determined by the proposed image processing technique is presented. The relations between surface area loss and strength and weight loss are also discussed. Figures 9 and 10 show the images of the cube surfaces taken after submergence in different water conditions for 90 days and 180 days, respectively. Both figures (Figures 9 and 10) show the initial images and the final images after image processing. Corresponding threshold value (m)

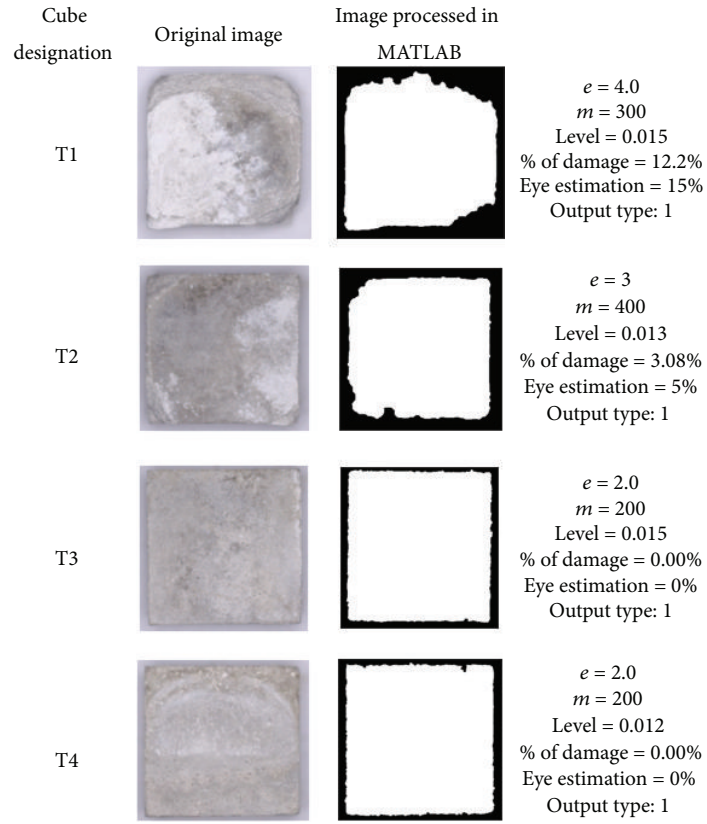


FIGURE 9: Surface area damage after submergence for 90 days.

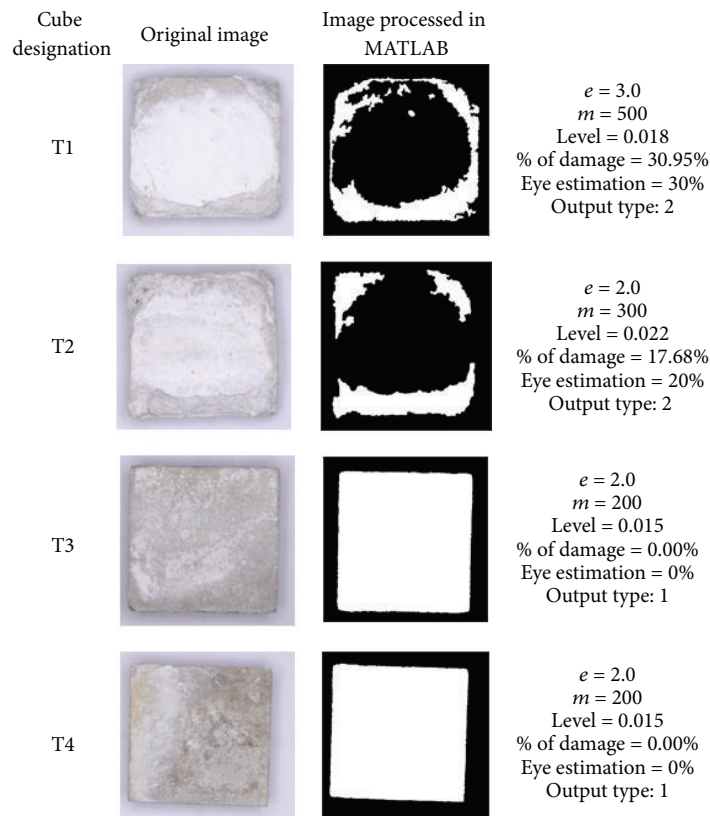


FIGURE 10: Surface area damage after submergence for 180 days.

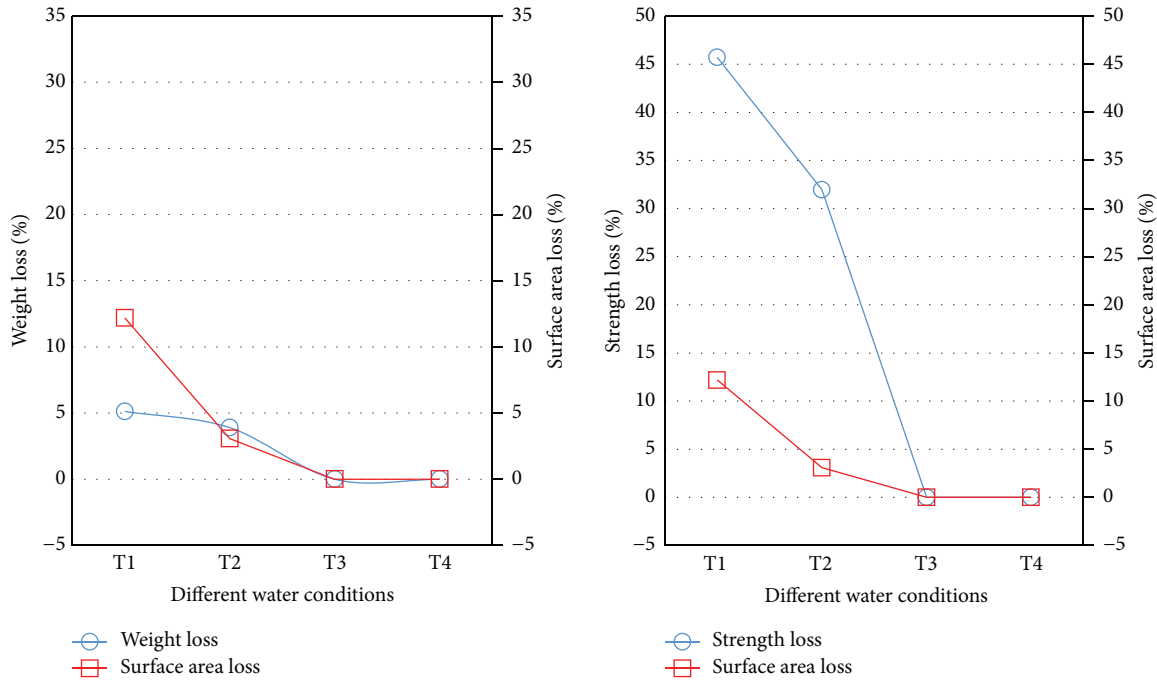


FIGURE 11: Comparison of surface area loss with weight loss and strength loss at 90 days.

and slope value (e) for contrast stretching and level for binary image transformations are also given. In addition, calculated percent damage using (2) is provided. It is found that cubes under T1 and T2 tannery water conditions lost about 12% and 3% surface area, respectively, at 90 days as shown in Figure 9. Cubes under T3 and T4 conditions show no damage. These values, therefore, indicate that, after 90 days of submergence, cement composites under T1 and T2 conditions suffer significant area loss whereas cubes under T3 and T4 conditions experience no damage at all. At 180 days, surface area losses of cubes under T1 and T2 conditions were found to be about 31% and 17.5%, respectively. Similar to the case at 90 days, cubes under T3 and T4 conditions show no surface damage. Hence, it is evident that cement composites under T1 and T2 tannery water conditions lost significant surface area at 180 days. On the contrary, T3 and T4 water conditions appear to have no detrimental effect on cement cubes. However, the efficiency of the proposed image processing technique depends on existence of a good correlation between the calculated surface area loss and the actual strength and weight loss of the cement cubes. Figures 11 and 12 show the comparison of the strength loss, weight loss, and surface area loss of different samples subjected to various combinations (T1, T2, T3, and T4) of tannery wastewater considered in the study. The aforementioned image processing has been developed to trace two types of conditions: one was damaged cubes with a certain percentage of surface area lost and the other was cubes without any loss of surface area. It is, therefore, not required to calculate the percentage gain in surface area for cubes which had expanded. Also, these expanded samples do not fall within the damaged category. This is why gains in strength or weight are ignored for this particular study and any percentage

gain in strength or weight is instead regarded as “zero loss.” Moreover, percent gains in weight of cubes in all cases are found to be insignificant (in the range between 0.5% and 1.5%).

As it can be observed from Figures 11 and 12, both T1 and T2 cubes have undergone significant strength loss and weight loss whereas T3 and T4 cubes show little or no strength loss and weight loss. What is interesting is that consistency is observed between the test results of strength and weight and that of image processing; that is, for the cases where surface area loss occurred, strength and weight loss also occurred, and, for the cases where surface area loss was zero, strength and weight losses were also zero. It also appears that the relations between surface area loss by image processing method and weight and strength loss are not linear and will require a range of surface loss values to identify particular durability criteria, that is, actual strength loss. Therefore, in order to develop a statistically significant relationship between the proposed image processing outcome and the actual durability measurements, more experiments will be needed to be conducted with large sample size. Nevertheless, it is evident that the proposed image processing technique is in harmony with the experimental results and proves its potential to provide reliable durability information on cement composites.

5. Comparison between Conventional Edge Detection Techniques and the Proposed Method

In this section, the effectiveness of the proposed method in comparison with some commonly used boundary detection

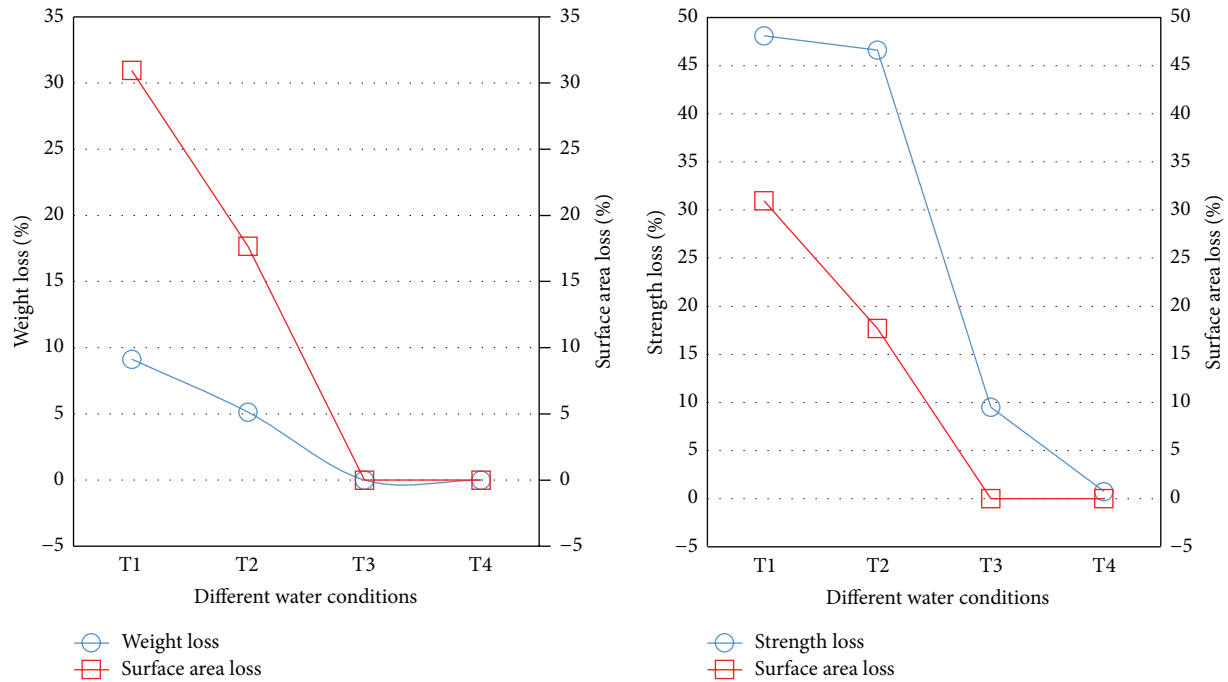


FIGURE 12: Comparison of surface area loss with weight loss and strength loss at 180 days.

functions of MATLAB is discussed. Sobel, Prewitt, LoG, and Canny operators were used to detect edges of T1 sample after 180 days of submergence. The outcomes of these methods are then compared with the proposed technique.

In Sobel operator, 3×3 convolution mask is applied both horizontally and vertically in X and Y directions and the magnitude values are combined to find the absolute magnitude of the whole image [20–22]. Sobel creates good results for high frequency variations as discussed by Rana and Dalai [21]. Sobel method returns edges at those points where the gradient magnitude values of the image are maximum as described by Juneja and Sandhu [23]. Figure 13(a), displaying the output of Sobel operator, shows maximum gradient along with missing edges. Prewitt operator is a first-order derivative operator and uses eight possible orientations to estimate gradient of image intensity function in the 3×3 neighbourhood [24, 25]. The entire set of eight masks are computed and the largest module is selected. Therefore, both Sobel and Prewitt operators result in similar edge detection output which is also evident from Figures 13(a) and 13(b). Laplacian of Gaussian (LoG) operator combines Gaussian filtering with Laplacian for edge detection. Gaussian filter smoothens the image as 2nd derivative is sensitive to noise. Detection is done by finding the zero crossing which produces double edges. According to Sharma and Kaur [26], LoG does not properly detect boundary at the corners and curves where the intensity changes abruptly. It can be seen from Figure 13(c) that this operator fails to locate the actual boundary and instead detects false boundary lines. Smoothing for noise reduction in such a case might lead to reduction of magnitude

of image gradients as the gradient would be much lower because of low grey level range. Canny operator calculates gradient using the derivative of a Gaussian filter [26]. Using double thresholding, Canny is less sensitive to noise and can detect true weak edges because of double thresholding. For noise reduction, Gaussian 2D smoothing kernel with specified standard deviation is used as a blurring operation [27]. For Canny, edge detection results become erroneous for values of σ greater than 0.35 as discussed by Kumar and Singh [28]. For determination of boundary line of surface damaged cement composites, it is necessary to locate weak lines, that is, fine edges, as actual areas appear to have homogeneity on both sides of the line. Figure 13(d) shows how Canny operator is detecting boundaries with false boundary lines along with missing portions as described by Dhankhar and Sahu [29]. But it is clearly visible that this operator better performs detection in noise conditions [29].

In the proposed method, as described earlier, it was found that grey level ranges of the images were small. Then, contrast stretching was done as an enhancement technique to increase grey level ranges which also included darker shadow zones. Then, standard deviation filter was used to locate intensity variations as well as boundary lines. Noise reduction was done using filter and, eventually, segmented pixels were found as an output. It is evident from the output of the proposed method that, compared to conventional edge detection techniques, the proposed method yielded better results along with much less false boundary lines as shown in Figure 13(e). As the output of the images consisted of intensity irregularities as shown in Figure 13(e), general morphological operations were adopted for image restoration as discussed

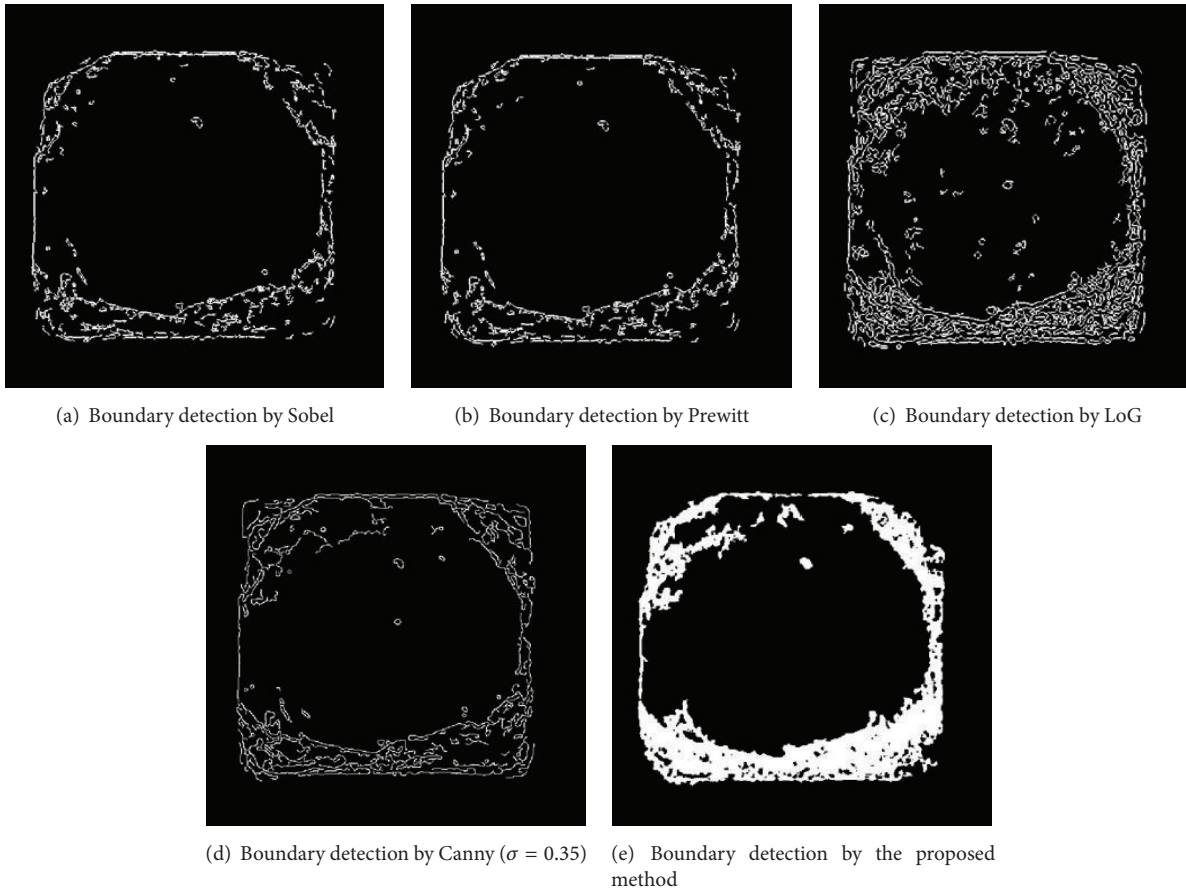


FIGURE 13: Comparison between conventional edge detection techniques and the proposed method for cube T1 (submerged for 180 days).

by Raid et al. [30]. To overcome intensity discontinuities, dilation followed by erosion was done. As a result, images with defined boundary lines were obtained. Then, the final pixel percentage was calculated using (2).

Figure 14 shows the edge detection of T1 samples after 90 days by various conventional boundary detection techniques and the proposed method. The superior efficiency of the proposed method as compared to traditional boundary detection techniques is also evident from Figure 14.

6. Conclusion

This paper has described a method for evaluation of concrete degradation under tannery wastewater by employing an image processing technique. Some key findings of this study are as follows:

- (a) An edge detection technique has been developed in MATLAB which can effectively detect boundaries of mortar cubes where different areas show homogeneity or weak homogeneity along the same boundary line.
- (b) The effectiveness in using standard deviation for boundary detection has also been presented along with its ability to avoid shadow of low contrast by adjusting contrast.

- (c) Quantification of percentage of surface area loss was obtained once the boundary was detected.
- (d) An effective correlation between surface area loss and experimental strength and weight loss has been observed.
- (e) It was found that cubes which underwent greater loss of surface area also suffered greater loss of strength.
- (f) In addition, cubes which experienced greater loss of surface area were also the ones which lost more weight.
- (g) A comparison of the proposed method with available conventional techniques reveals the superior effectiveness of the proposed technique for boundary detection.

When the results from image processing (surface area loss), strength loss, and weight loss were studied together, it could be inferred qualitatively that the cubes which faced greater loss of surface area are the ones which also suffered greater loss of strength and weight. However, whether or not quantification of this correlation is possible is a question which can only be answered through further research, preferably with a larger sample size. This study establishes a cornerstone for undertaking an extensive study regarding the patterns of

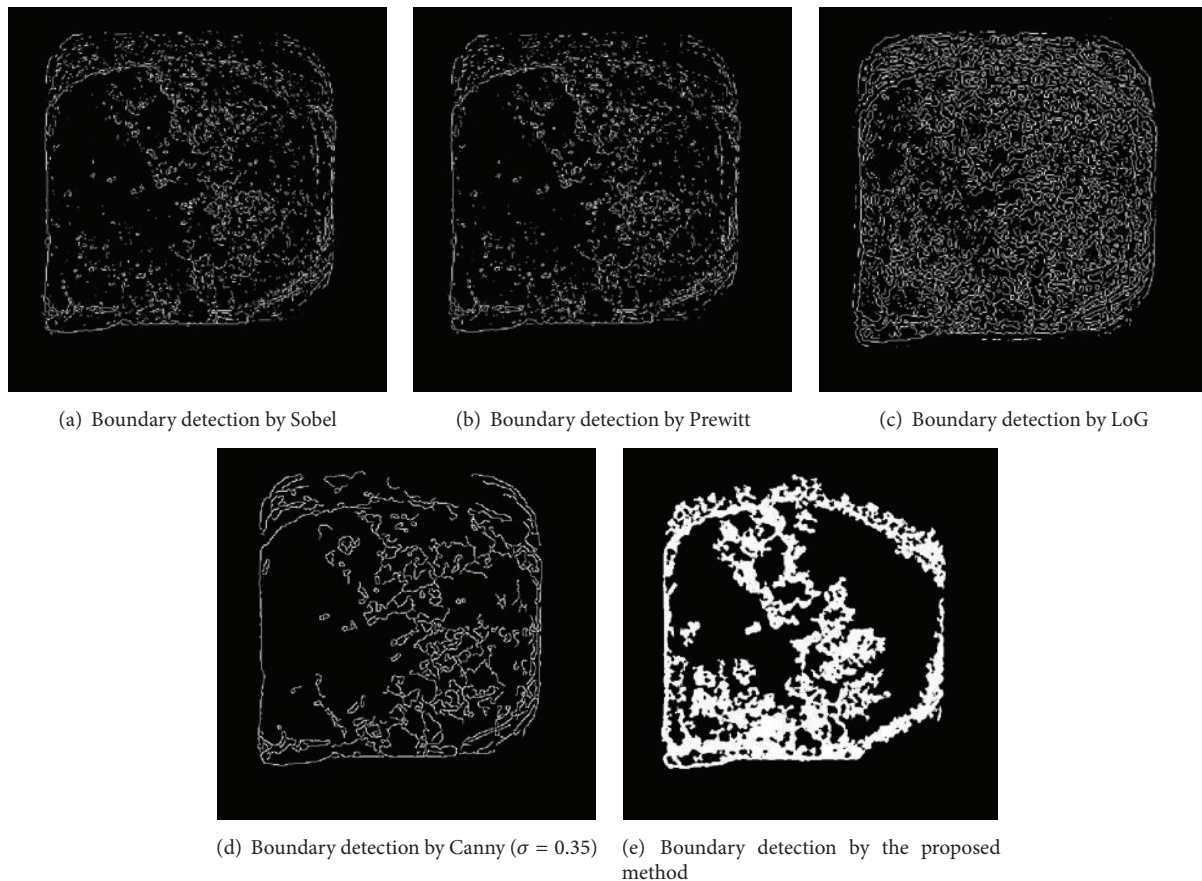


FIGURE 14: Comparison between conventional edge detection techniques and the proposed method for cube T1 (submerged for 90 days).

surface area loss, weight loss, and strength loss to explore the correlation more elaborately.

Competing Interests

The authors declare that they have no competing interests.

Acknowledgments

The authors are grateful to the personnel of the Concrete Laboratory, Department of Civil Engineering, Bangladesh University of Engineering and Technology (BUET), for their assistance and cooperation for successful execution of the experiments.

References

- [1] T. Ramasami, S. Rajamani, and J. Raghavarao, "Pollution control in leather industry: emerging technological options," in *Proceedings of the International Symposium on Surface and Colloidal Science and Its Relevance to Soil Pollution*, Madras, India, March 1994.
- [2] J. Skalny, J. Marchard, and I. Odler, *Sulfate Attack on Concrete*, Spon Press, Taylor & Francis Group, London, UK, 2002.
- [3] P. W. Brown, "An evaluation of the sulfate resistance of cements in a controlled environment," *Cement and Concrete Research*, vol. 11, no. 5-6, pp. 719–727, 1981.
- [4] F. M. Lea, "The action of ammonium salts on concrete," *Magazine of Concrete Research*, vol. 17, no. 52, pp. 115–116, 1965.
- [5] I. Biczok, *Concrete Corrosion and Concrete Protection*, Akademiai Kiado, Budapest, Hungary, 1972.
- [6] "Standard specification for standard sand," Tech. Rep. ASTM C778-13, ASTM International, West Conshohocken, Pa, USA, 2013.
- [7] S. Saha and S. A. Papry, *Assessment of cement mortar degradation when exposed to tannery wastewater [Undergraduate thesis]*, Bangladesh University of Engineering and Technology, 2016.
- [8] M. Bosnic, J. Buljan, and R. P. Daniles, *Pollutants in Tannery Effluents*, UNIDO, Vienna, Austria, 2000.
- [9] S. L. Sultana, S. Mahmud, and T. Manzur, "Review on possible detrimental effects of tannery wastewater constituents on concrete," in *Proceedings of the International Conference on Advances in Civil Infrastructure and Construction Materials (CICM '15)*, MIST, Dhaka, Bangladesh, December 2015.
- [10] "Standard test method for compressive strength of hydraulic cement mortars," Tech. Rep. ASTM C109/C109M-13e1, ASTM International, West Conshohocken, Pa, USA, 2013.
- [11] C. O. Casado, *Image Contrast Enhancement Methods*, Research Project, Faculty of Telecommunications, Department of Radio Communications and Video Technologies, Technical University, Sofia, Bulgaria, 2010.
- [12] Mathworks, January 2016, <http://www.mathworks.com/help/images>.

- [13] V. Kumar and P. Gupta, "Importance of statistical measures in digital image processing," *International Journal of Emerging Technology and Advanced Engineering*, vol. 2, no. 8, pp. 56–62, 2012.
- [14] R. Hidayat and R. Green, *Real-Time Texture Boundary Detection from Ridges in the Standard Deviation Space*, Computer Science and Software Engineering Department, University of Canterbury, Christchurch, New Zealand, 2009.
- [15] M. Mastriani and A. E. Giraldez, "Enhanced directional smoothing algorithm for edge-preserving smoothing of synthetic-aperture radar images," *Journal of Measurement Science Review*, vol. 4, no. 3, pp. 1–11, 2004.
- [16] A. Ito, Y. Aoki, and S. Hashimoto, "Accurate extraction and measurement of fine cracks from concrete block surface image," in *Proceedings of the 28th Annual Conference of the IEEE Industrial Electronics Society*, pp. 2202–2207, Sevilla, Spain, November 2002.
- [17] R. Garg and A. Kumar, "Comparision of various noise removals using bayesian framework," *International Journal of Modern Engineering Research*, vol. 2, no. 1, pp. 265–270, 2012.
- [18] F. A. Jassim, "Semi-optimal edge detector based on simple standard deviation with adjusted thresholding," *International Journal of Computer Applications*, vol. 68, no. 2, pp. 43–48, 2013.
- [19] R. C. Gonzalez and R. E. Woods, *Digital Image Processing*, Prentice Hall, New York, NY, USA, 2002.
- [20] I. Sobel, "An isotropic 3×3 gradient operator," in *Machine Vision for Three-Dimensional Scenes*, H. Freeman, Ed., pp. 376–379, Academic Press, New York, NY, USA, 1990.
- [21] D. Rana and S. Dalai, "Review on traditional methods of edge detection to morphological based techniques," *International Journal of Computer Science and Information Technologies*, vol. 5, no. 4, pp. 5915–5920, 2014.
- [22] K. Wang and W. Dai, "Approach of image edge detection based on Sobel operators and grey relation," *Computer Applications*, vol. 26, no. 5, pp. 1035–1036, 2006.
- [23] M. Juneja and P. S. Sandhu, "Performance evaluation of edge detection techniques for images in spatial domain," *International Journal of Computer Theory and Engineering*, vol. 1, no. 5, pp. 614–621, 2009.
- [24] M. S. Sri and M. Narayana, "Edge detection by using lookup table," *International Journal of Research in Engineering and Technology*, vol. 2, no. 1, pp. 483–488, 2013.
- [25] N. Senthilkumaran and R. Rajesh, "A study on edge detection methods for image segmentation," in *Proceedings of the International Conference on Mathematics and Computer Science (ICMCS '09)*, vol. 1, pp. 255–259, 2009.
- [26] K. Sharma and N. Kaur, "Comparative analysis of various edge detection techniques," *International Journal of Advanced Research in Computer Science and Software Engineering*, vol. 3, no. 12, pp. 617–621, 2013.
- [27] J. Canny, "A computational approach to edge detection," *IEEE Transactions on Pattern Analysis and Machine Intelligence*, vol. 8, no. 6, pp. 679–698, 1986.
- [28] M. Kumar and S. Singh, "Edge detection and denoising medical image using morphology," *International Journal of Engineering Sciences & Emerging Technologies*, vol. 2, no. 2, pp. 66–72, 2012.
- [29] P. Dhankhar and N. Sahu, "A review and research of edge detection techniques for image segmentation," *International Journal of Computer Science and Mobile Computing*, vol. 2, no. 7, pp. 86–92, 2013.
- [30] A. M. Raid, W. M. Khedr, M. A. El-dosuky, and M. Aoud, "Image restoration based on morphological operations," *International Journal of Computer Science, Engineering and Information Technology*, vol. 4, no. 3, pp. 9–21, 2014.

Research Article

Using Recycled Glass and Zeolite in Concrete Pavement to Mitigate Heat Island and Reduce Thermal Cracks

Erhan Burak Pancar

Department of Architecture, Ondokuz Mayıs University, 55100 Samsun, Turkey

Correspondence should be addressed to Erhan Burak Pancar; erhanpancar@hotmail.com

Received 22 April 2016; Accepted 15 June 2016

Academic Editor: Joao M. L. Reis

Copyright © 2016 Erhan Burak Pancar. This is an open access article distributed under the Creative Commons Attribution License, which permits unrestricted use, distribution, and reproduction in any medium, provided the original work is properly cited.

Urban heat island (UHI) effect is built environmental issue related to pavements. It is desired to reduce pavement high surface temperature in summer to mitigate UHI effect. High surface temperature also affects slab temperature difference (the top surface temperature minus the bottom surface temperature of the slab). The increased slab temperature difference induces a high possibility of cracking in concrete roads. The prime aim of this study was to reduce the slab surface temperature by using recycled glass as a fine aggregate and zeolite as cement in concrete. Recycled glass was used to replace fine aggregate in proportions of 10%, 20%, and 30% by total weight of aggregate. Zeolite replaced Portland cement in proportions of 10% and 30% for three different proportions of recycled glass concrete mixtures. Optimum proportions were determined by examining mechanical properties of samples and alkali-silica reactions. It was noticed that using recycled glass and zeolite together in concrete reduces pavement surface temperature and temperature gradient in summer.

1. Introduction

Built environmental issue related to pavements is the urban heat island (UHI) effect. Heat islands can be considered as surface and atmospheric heat islands [1, 2]. Hot pavements contribute to the heat island effect. Surface heat islands can affect human thermal comfort and air quality. 70–80°C surface temperatures on pavements have been measured on hot summer days in Phoenix, Arizona [3]. As one major thermal characteristic, solar reflectivity or albedo (1-solar absorptivity) is an indicator of the reflecting power of a surface. It is defined as the ratio of the reflected solar radiation to the incident solar radiation at the surface. It is dimensionless fraction and is measured on a scale from 0 to 1. Albedo of 0 means no reflecting power and albedo of 1 means perfect reflection [4]. Increasing the solar reflectivity of a pavement surface by using surfacing materials of light colour or applying light colour coating on dark surfacing materials can lower the pavement surface temperature [5–8]. Solar reflective materials can be identified as one of the most promising solutions to counteract urban heat island [9].

Portland cement concrete (PCC) pavements are affected by temperature differences. The temperature at the top

surface of the slab is higher than that of the bottom during the day. The top tends to expand while the bottom tends to contract. The temperature at the top surface of the slab is lower than that of the bottom at night and the top tends to contract. Kuo [10] recommended using loading at the centre of the slab during the daytime and loading at the edge of the slab at nighttime in analysing of concrete pavement. Negative temperature gradient (nighttime) is not taken into account especially at concrete road design in Germany. This is because negative gradient is less than positive gradient (daytime) [11].

Thermal conductivity is used to estimate the temperature gradient of concrete pavement [12]. Temperature gradient is the uniform flow of heat in a specific sample from one side to the other. Temperature gradients throughout the slab thickness play a key role in calculating thermal stresses in PCC pavements, known as curling [13]. Decreasing the thermal conductivity of concrete also decreases the temperature gradient of concrete road and reduces thermal cracks in concrete slab. It is necessary to decrease the curling stresses resulting from the fluctuation of temperature gradients.

Aggregate type, percent of cement paste, coarse aggregate, fine aggregate, porosity, supplementary cementitious materials (SCMs), moisture, and temperature of local environment

are some of the factors that affect the thermal conductivity of concrete [13–16]. Researches done before investigated that mixes with a high fine aggregate proportion had a higher thermal conductivity compared to a high proportion of coarse aggregate [14, 17]. The use of structures with high thermal resistance has become of great importance in hot weather countries where temperature can reach high levels especially in summer [18]. The low value of thermal conductivity is desirable due to the associated ability to provide thermal insulation [19].

This study mainly focuses on reducing the temperature gradient that causes thermal cracks in concrete road and also mitigates heat island. The effects of different proportions of recycled glass and zeolite used as a fine aggregate and Portland cement, respectively, were investigated. Compressive strength, flexural strength, and alkali-silica reaction (ASR) for the determined proportion of materials were investigated. The slab temperatures were measured at various depths of three different types of pavements to control the effects of recycled glass and zeolite on temperature gradient of concrete road. Pavement surface temperatures were measured in summer for different types of concrete mixtures. Ideal concrete mixture which had lower surface temperature was determined.

2. Glass and Zeolite in Concrete

Water absorption capacity of glass is almost zero and when it is used as an aggregate in concrete, it decreases the water absorption and drying shrinkage values which is a desired property for concrete [20]. ASR occurs in concrete when alkalis from cement react with free silica presented in certain aggregates to form alkali-silica gels [21]. This phenomenon reduces the service life of the affected structure. Glass has a higher value of SiO_2 and Lam et al. [20] observed whether ASR expansion would be seen or not in concrete with glass in its mix design when there is enough moisture. It was observed that if the proportion of the glass is lower than 25% weight of the aggregate in concrete, ASR expansions are in negligible level. Byars et al. [22] determined that the reactivity of glass particles generally increases with particle size from around 1-2 mm. Glass particles below this size appear to reduce the propensity for ASR in larger glass particles. Ready-mixed concrete made with glass pozzolan and/or glass sand showed increasing in strength development to 1 year, indicating a pozzolanic contribution from the fine glass particles. Krishnamoorthy and Zujip [23] determined that using recycled glass as fine aggregate decreases thermal conductivity of concrete.

Zeolite is a natural or synthetic hydrated aluminosilicate mineral of alkali and alkaline earth metal with an open three-dimensional crystal structure. Zeolite concrete is much less frequent subject of investigation as compared with fly ash, silica fume, or ground granulated blast furnace slag as SCMs. The most significant effects of using zeolite as cement in concrete are reduction in expansion due to alkali-silica reaction, resistance to acid and sulfate attacks, and pozzolanic consumption of calcium hydroxide component of Portland cement hydration in the paste. The performance of natural

zeolite in mortar/concrete has been compared with performance of other pozzolanic materials [24–26]. Poon et al. [25] determined that the degree of reaction of natural zeolite in a paste with a higher percentage of replacement is lower than in a paste with a lower percentage of replacement. Chan and Ji [26] noticed that pozzolanic reactivity of natural zeolite is between pulverized fuel ash and silica fume. Kılınçarslan [27] determined that using zeolite as Portland cement decreases the thermal conductivity of concrete.

3. Pavement Surface Temperature

Li et al. [4] investigated the effect of albedo on concrete pavement surface temperature and they determined that surface temperatures were 44°C, 50°C, and 59°C for concrete mixtures with an albedo of 0.29, 0.26, and 0.18, respectively. The effects of thermal conductivity and heat capacity were assumed identical in that study. Qin and Hiller determined that maximum thermal tensile stress of a slab can increase up to 0.3 MPa when the pavement surface's solar absorptivity rises from 0.65 to 0.85 [28]. Although this stress value can be assumed as small, after combining with external loadings from traffic, it makes the total stress of a slab close to the flexure tensile strength.

When the albedo of the concrete surface is high and the thermal conductivity of the concrete is low, the temperature fluctuations of the pavement surface will be in minimum during a day and temperature gradient will be reduced. This will also reduce thermal cracks on concrete road and lower surface temperature will mitigate heat island.

Sand as a fine aggregate has a good thermal conductivity and if the material used as sand in concrete does not cause ASR and if that material has a lower thermal conductivity than the sand, curling stress will reduce at the concrete pavement slab. Also, this reduction can be obtained by replacing Portland cement with a material which has a lower thermal conductivity. Pancar and Akpınar [29] used glass beads as a fine aggregate in concrete road and they obtained lower surface temperature in summer while the albedo was the same. The concrete pavement surface temperature decreased 12.5°C by using glass bead in their study. If the alternative materials used as fine aggregate and Portland cement have lighter colour than fine aggregate and Portland cement used in control mixture, the albedo will also increase and this property will also help to decrease the pavement surface temperature in summer.

4. Methods

Ten different types of mixtures were designed to study the effects of recycled glass and natural zeolite on compressive strength, flexural strength, and ASR of the concrete. One of these mixtures was a control mixture and three of the mixtures had 10%, 20%, and 30% proportions of recycled glass by total weight of aggregates. Six different mixtures with different proportions (10% and 30%) of zeolite for each recycled glass sample proportion were also prepared. All coarse and fine aggregates were limestone in control mix design. Fine aggregates are more effective in thermal conductivity

TABLE 1: Mixture design of concrete samples.

Mixtures	Cement PC 42.5 (Kg)	Water (lt)	Recycled glass (Kg)	Zeolite (Kg)	0–5 mm fine aggregate (Kg)	5–12 mm coarse aggregate (Kg)	13–22 coarse aggregate (Kg)	Admixture (gr)
Standard mixture	7.70	3.85	0	0	20.22	8.80	12.32	80
G10Z0	7.70	3.85	4.13	0	16.09	8.80	12.32	80
G10Z10	6.93	3.85	4.13	0.77	16.09	8.80	12.32	80
G10Z30	5.39	3.85	4.13	2.31	16.09	8.80	12.32	80
G20Z0	7.70	3.85	8.27	0	11.95	8.80	12.32	80
G20Z10	6.93	3.85	8.27	0.77	11.95	8.80	12.32	80
G20Z30	5.39	3.85	8.27	2.31	11.95	8.80	12.32	80
G30Z0	7.70	3.85	12.40	0	7.82	8.80	12.32	80
G30Z10	6.93	3.85	12.40	0.77	7.82	8.80	12.32	80
G30Z30	5.39	3.85	12.40	2.31	7.82	8.80	12.32	80

TABLE 2: Sieve analysis of recycled glass as a fine aggregate.

Sieve size (mm)	Percentage passing by weight (%)
<0.125	0.0
0.125	1.7
0.160	3.8
0.250	14.7
0.315	23.1
0.500	63.0
0.630	86.6
1.000	100.0

TABLE 3: Sieve analysis of standard fine aggregate.

Sieve size (mm)	Percentage passing by weight (%)
<0.063	0.0
0.063	11.5
0.250	32.6
0.500	41.0
1.000	52.8
2.000	72.7
4.000	100.0

than coarse aggregates. Due to this reason, recycled glass was used as a fine aggregate to obtain lower slab temperatures in this study. Aggregates used in this study were limestone and Portland cement 42.5 R was used in all mixtures. The mixtures were named using the type and percentage of recycled glass and zeolite in the concrete mixtures. For example, G10Z0 represents the concrete mixture that consists of 10% proportion of recycled glass by total weight of aggregate and 0% proportion of zeolite in cement. Water/cement ratio was 0.50 in all blends. Standard 15 cm × 15 cm × 15 cm cube C30/37 strength class concrete specimens were prepared for the testing program. Mixture designs of the concrete samples are in Table 1. Sieve analysis of recycled glass, used as a fine aggregate, and standard fine aggregate are in Tables 2 and 3, respectively. Chemical properties of fine aggregate, recycled glass, zeolite, and Portland cement are in Table 4.

The potential ASR expansion of the prepared mortar bars (25 × 25 × 285 mm) with a water to cement ratio of 0.47 was assessed in accordance with ASTM C1260 [30]. Ten series of mortar bars were prepared in total. In these series, three different proportions (10%, 20%, and 30%) of recycled glass and two different proportions (10% and 30%) of zeolite for each recycled glass sample were prepared with control mixture. The test period was 28 days. The result of mortar bars test is shown in Figure 1. ASR expansion needs to meet the requirements prescribed in ASTM C1260 (<0.1% within 14 days). Mixture proportions of mortar bars are in Table 5.

Compressive and flexural strength measurements were done for all samples at 28 and 90 days. The compressive strength values need to be at least 37 MPa at 28-day measurement for C30/37 type of concrete. After ASR and compressive strength measurements, some mixture samples were eliminated and temperature measurements of concrete road were made for ideal mixtures. In order to monitor the temperature profiles during the day, temperature sensors were installed at every 5 cm depth of 3 different types of 25 cm thick concrete slabs. The length and width of the slabs were 1 m and 1.5 m, respectively.

5. Results

It was observed that all samples used in this study were able to meet the ASR expansion requirements. Using recycled glass, smaller than 1 mm, as fine aggregate increases the expansions after 14 days and using zeolite as Portland cement significantly decreases the expansions of mixtures with recycled glass. ASR test results for ten different types of mixtures are in Figure 1.

Compressive and flexural strength of ten different types of mixtures for 28 and 90 days are in Table 6. G30Z0, G30Z10, and G30Z30 mixtures did not meet the compressive strength requirements of C30/37 type of concrete and these mixtures were eliminated for the temperature gradient measurements.

After ASR and compressive strength measurements, it was observed that the standard mixture, G20Z0 mixture, and G20Z30 mixture were suitable for temperature gradient measurements and these measurements were done on these samples. Before measuring temperature gradients on the site, thermal conductivities of standard mixture, G20Z0 mixture,

TABLE 4: Chemical properties of fine aggregate, recycled glass, zeolite, and Portland cement.

Oxide	Fine aggregate	Recycled glass	Zeolite	Portland cement 42.5 R
SiO ₂ (%)	2.59	71.72	68.81	22.55
Al ₂ O ₃ (%)	1.09	0.92	14.17	7.12
CaO (%)	95.09	8.50	1.91	61
MgO (%)	—	4.22	1.10	3.56
Fe ₂ O ₃ (%)	0.92	0.11	1.84	3.81
K ₂ O (%)	0.17	0.45	3.40	0.12
Na ₂ O (%)	—	13.78	—	—

TABLE 5: Mixture proportions of mortar bars.

Mixtures	Cement (gr)	Water (gr)	Fine aggregate (gr)	Zeolite (gr)	Recycled glass (gr)
Control mixture	440	207	990	—	—
G10Z0	440	207	900	—	90
G10Z10	396	207	900	44	90
G10Z30	308	207	900	132	90
G20Z0	440	207	800	—	200
G20Z10	396	207	800	44	200
G20Z30	308	207	800	132	200
G30Z0	440	207	600	—	300
G30Z10	396	207	600	44	300
G30Z30	308	207	600	132	300

and G20Z30 mixture concrete were measured by using the Testo-635 product. Thermal conductivities were determined as 2.57 W/m·K, 2.2 W/m·K, and 2.08 W/m·K for standard mixture, G20Z0 mixture, and G20Z30 mixture, respectively. One of the slabs was standard concrete mixture type and the others were G20Z0 and G20Z30 types of concrete. The sensors were installed at the middle of the slabs and the slabs were on 25 cm thick crushed limestone base course layer. The slab temperatures at various depths were measured between 08:00 AM and 6:00 PM in August. Temperature measurements are in Figures 2, 3, and 4 for three different types of concrete slabs.

It is observed from Figure 2 that the highest temperature measurement of the top surface of the control mixture slab was at 2:00 PM and it was 50.0°C. The biggest temperature difference on top surface of the slab was 20.0°C during the testing time. The biggest temperature difference on bottom of the slab was 4.0°C during the testing time. The biggest temperature difference between the top and bottom surface of the slab was 14.0°C at 2:00 PM. The bottom surface temperatures changed in the range of 34°C–38°C during the measurement time.

It is observed from Figure 3 that the highest temperature measurement of the top surface of the G20Z0 mixture slab was at 2:00 PM and it was 41.0°C. The biggest temperature difference on top surface of the slab was 13.0°C during the testing time. The biggest temperature difference on bottom of the slab was 4.0°C during the testing time. The biggest temperature difference between the top and bottom surface of the slab was 7.0°C at 2:00 PM. The bottom surface temperatures changed in the range of 30°C–34°C during the measurement time.

It is observed from Figure 4 that the highest temperature measurement of the top surface of the G20Z30 mixture slab was at 2:00 PM and it was 38.0°C. The biggest temperature difference on top surface of the slab was 10.0°C during the testing time. The biggest temperature difference on bottom of the slab was 3.0°C during the testing time. The biggest temperature difference between the top and bottom surface of the slab was 5.0°C at 2:00 PM. The bottom surface temperatures changed in the range of 30°C–33°C during the measurement time.

6. Discussion

It is observed from Figure 5 that the surface temperature of standard mixture is higher than G20Z0 mixture between 8:00 AM and 6:00 PM and the surface temperature of G20Z0 mixture is higher than G20Z30 mixture between 10:00 AM and 6:00 PM. Using recycled glass in proportion of 20% by total weight of aggregate decreases the biggest surface temperature of concrete pavement from 50°C to 41°C at 2:00 PM. Replacing zeolite with Portland cement in proportion of 30% in this type of recycled concrete mixture decreases the biggest surface temperature 3°C more.

Top and bottom surface temperature differences measured for three concrete samples are in Figure 6. It is observed that these differences are very close to 0°C at 10:00 AM and 5:00 PM. Top and bottom surface temperature differences are increasing between these hours and come to the highest point at 2:00 PM for three samples. The biggest top and bottom surface temperature difference is 14°C, 7°C, and 5°C for standard sample and G20Z0 and G20Z30 samples, respectively.

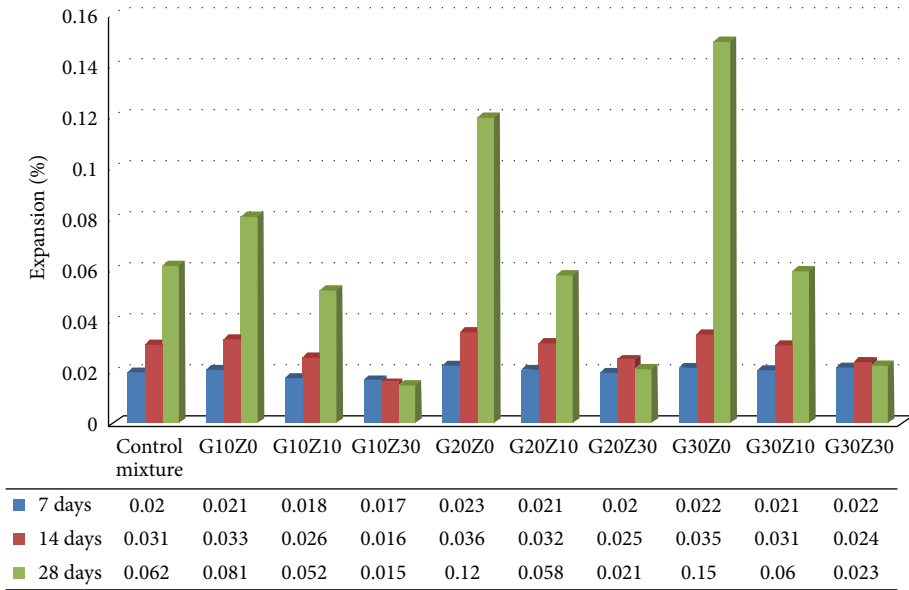


FIGURE 1: ASR test results for samples.

TABLE 6: Compressive and flexural strength of samples.

Mixtures	28-day compressive strength (MPa)	90-day compressive strength (MPa)	28-day flexural strength (MPa)	90-day flexural strength (MPa)
Standard mixture	38.8	48.4	4.26	5.35
G10Z0	38.25	47.86	4.53	5.36
G10Z10	40.15	49.56	4.65	5.45
G10Z30	37.11	47.92	4.51	5.28
G20Z0	40.28	53.72	4.98	5.75
G20Z10	41.06	55.13	5.07	5.88
G20Z30	38.22	54.01	4.89	5.72
G30Z0	30.72	40.63	3.94	4.48
G30Z10	30.61	42.06	3.96	4.47
G30Z30	28.12	40.62	3.78	4.44

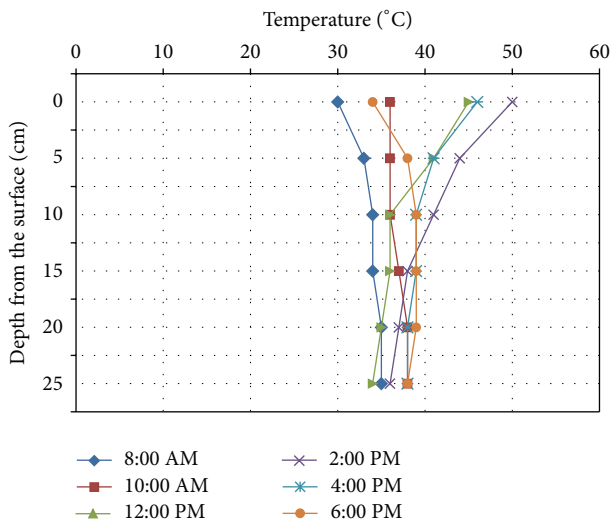


FIGURE 2: Temperature gradients for standard mixture.

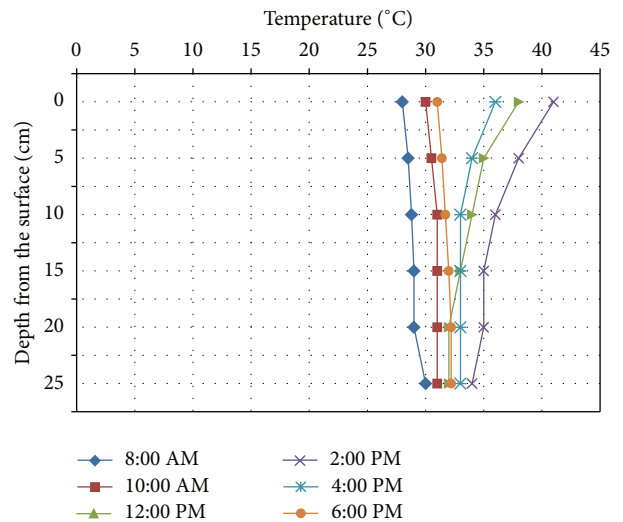


FIGURE 3: Temperature gradients for G20Z0 mixture.

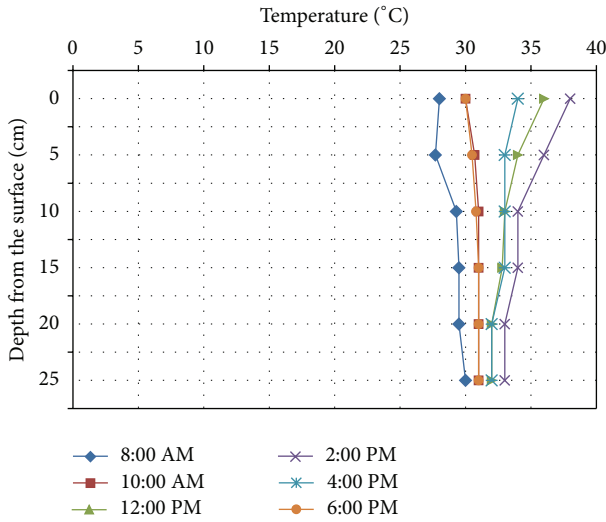


FIGURE 4: Temperature gradients for G20Z30 mixture.

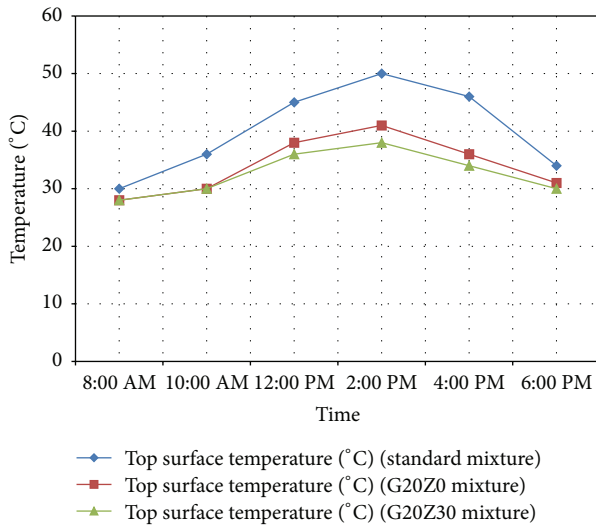


FIGURE 5: Top surface temperatures of standard mixture, G20Z0 mixture, and G20Z30 mixture.

The reflection coefficient or albedo was not measured by a device in this study. However based on visual observation it was determined that G20Z0 mixture and standard mixture have almost the same surface colour and G20Z30 mixture had a slightly lighter colour than these mixtures (Figure 7). At the end of this study, it was determined that the concrete pavement surface temperature can decrease from 50°C to 38°C by using G20Z30 type of concrete mixture instead of control mixture and the biggest top and bottom surface temperature difference may decrease from 14°C to 5°C by this method.

7. Conclusion

If the temperature gradient value is high, it is probable to see cracks in concrete roads. Temperature gradients also need to be decreased. This can be done by reducing the pavement surface temperature and thermal conductivity of concrete.

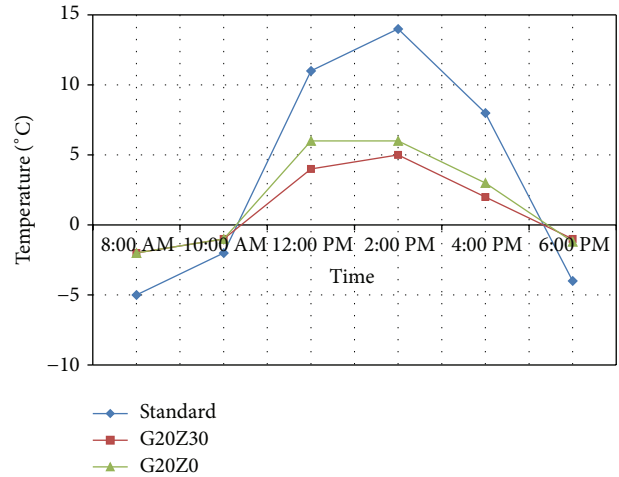


FIGURE 6: Top and bottom surface temperature differences for three samples.



FIGURE 7: Standard mixture sample, G20Z0 sample, and G20Z30 sample, respectively (from left to right).

Reducing the surface temperature also helps to mitigate heat island effect. The first concern of this study was to reduce concrete pavement surface temperature and temperature gradients in concrete while maintaining the concrete strength in the necessary limit during the day in summer.

Aggregates used in this study were limestone. Recycled glass (smaller than 1 mm) was used to replace fine aggregate in proportions of 10%, 20%, and 30% by total weight of aggregate. Zeolite replaced Portland cement in proportions of 10% and 30% for three different proportions of recycled glass concrete mixtures. ASR measurements were done and all samples met the ASR expansion requirements. Using recycled glass increased the ASR expansions but replacing Portland cement with zeolite in proportion of 30% decreased these expansions significantly. Compressive strength and flexural strength of all samples were measured at 28 and 90 days. The sample in proportion of 30% recycled glass as a fine aggregate did not meet the compressive strength requirements whether zeolite was added or not. G30Z0, G30Z10, and G30Z30 mixtures were eliminated for temperature gradient measurements. Temperature gradient measurements were done on concrete slabs for standard mixture, G20Z0 mixture, and G20Z30 mixture between 08:00 AM and 6:00 PM in summer. At the end of this study it was observed that recycled glass (smaller than 1 mm) can be used as a fine aggregate up to proportion of 20% by total weight of aggregate in concrete

mixtures. Using recycled glass in proportion of 20% by total weight of aggregate decreases the biggest surface temperature of concrete pavement from 50°C to 41°C. Replacing zeolite with Portland cement in proportion of 30% in this type of recycled concrete mixture decreases the biggest surface temperature 3°C more. Using G20Z0 and G20Z30 mixtures mitigates heat island effect by decreasing surface temperature. The biggest temperature differences between top and bottom surfaces of concrete slab occur at 2:00 PM in summer. These differences are 14°C, 7°C, and 5°C for standard mixture, G20Z0 mixture, and G20Z30 mixture, respectively. G20Z0 and G20Z30 mixtures have smaller temperature gradients in summer and they are good alternative mixtures to prevent thermal cracks.

Recycled glass (smaller than 1 mm), which is needed to be used in sustainability, as a fine aggregate and zeolite, which decreases the emission of carbon dioxide released during the production of cement, as Portland cement in concrete, can be used with zeolite in concrete mixture and this mixture is very effective in mitigating heat island and decreasing temperature gradient of concrete pavement.

Competing Interests

The author declares that there are no competing interests.

Acknowledgments

This research has been supported by Ondokuz Mayıs University, under Project no. PYO.MİM.1902.15.001.

References

- [1] H. Akbari and H. D. Matthews, "Global cooling updates: reflective roofs and pavements," *Energy and Buildings*, vol. 55, pp. 2–6, 2012.
- [2] H. Akbari, H. D. Matthews, and D. Seto, "The long-term effect of increasing the albedo of urban areas," *Environmental Research Letters*, vol. 7, no. 2, Article ID 024004, pp. 1–10, 2012.
- [3] H. Li, *Evaluation of Cool Pavement Strategies for Heat Island Mitigation in Civil and Environmental Engineering*, University of California, Davis, Calif, USA, 2012.
- [4] H. Li, J. T. Harvey, T. J. Holland, and M. Kayhanian, "Corrigendum: the use of reflective and permeable pavements as a potential practice for heat island mitigation and stormwater management," *Environmental Research Letters*, vol. 8, Article ID 015023, pp. 1–14, 2013.
- [5] A. Synnefa, T. Karlessi, N. Gaitani, M. Santamouris, D. N. Assimakopoulos, and C. Papakatsikas, "Experimental testing of cool colored thin layer asphalt and estimation of its potential to improve the urban microclimate," *Building and Environment*, vol. 46, no. 1, pp. 38–44, 2011.
- [6] M. Santamouris, A. Synnefa, and T. Karlessi, "Using advanced cool materials in the urban built environment to mitigate heat islands and improve thermal comfort conditions," *Solar Energy*, vol. 85, no. 12, pp. 3085–3102, 2011.
- [7] D. Kolokotsa, P. Maravelaki-Kalaitzaki, S. Papantoniou et al., "Development and analysis of mineral based coatings for buildings and urban structures," *Solar Energy*, vol. 86, no. 5, pp. 1648–1659, 2012.
- [8] A. Deluka-Tibljaš, S. Šurdonja, S. Babić, and M. Cuculić, "Analyses of urban pavement surface temperatures," *The Baltic Journal of Road and Bridge Engineering*, vol. 10, no. 3, pp. 239–246, 2015.
- [9] C. Ferrari, A. Muscio, C. Siligardi, and T. Manfredini, "Design of a cool color glaze for solar reflective tile application," *Ceramics International*, vol. 41, no. 9, pp. 11106–11116, 2015.
- [10] C.-M. Kuo, "Effective temperature differential in concrete pavements," *Journal of Transportation Engineering*, vol. 124, no. 2, pp. 112–122, 1998.
- [11] L. J. M. Houben, C. R. Braam, A. J. V. Leest, M. J. A. Stet, J. W. Fréney, and G. Bouquet, "Backgrounds of VENCON2.0 software for the structural design of plain and continuously reinforced pavements," in *Proceedings of the 10th International DUT-Workshop on Fundamental Modelling of Design and Performance of Concrete Pavements*, pp. 1–20, Old-Turnhout, Belgium, September 2006.
- [12] A. G. Heydinger, "Monitoring seasonal instrumentation and modelling climatic effects on pavements at the Ohio/SHRP test road," ODOT Project No. 14704(0), FHWA/OH Report 2003/018, The University of Toledo, Toledo, Ohio, USA, 2003.
- [13] Y. H. Huang, *Pavement Analysis and Design*, Prentice Hall, Upper Saddle River, NJ, USA, 2nd edition, 2004.
- [14] K.-H. Kim, S.-E. Jeon, J.-K. Kim, and S. Yang, "An experimental study on thermal conductivity of concrete," *Cement and Concrete Research*, vol. 33, no. 3, pp. 363–371, 2003.
- [15] H. Uysal, R. Demirboga, R. Şahin, and R. Gül, "The effects of different cement dosages, slumps, and pumice aggregate ratios on the thermal conductivity and density of concrete," *Cement and Concrete Research*, vol. 34, no. 5, pp. 845–848, 2004.
- [16] R. Demirboğa and R. Gül, "The effects of expanded perlite aggregate, silica fume and fly ash on the thermal conductivity of lightweight concrete," *Cement and Concrete Research*, vol. 33, no. 5, pp. 723–727, 2003.
- [17] A. H.-C. Shin and U. Kodide, "Thermal conductivity of ternary mixtures for concrete pavements," *Cement and Concrete Composites*, vol. 34, no. 4, pp. 575–582, 2012.
- [18] K. S. Al-Jabri, A. W. Hago, A. S. Al-Nuaimi, and A. H. Al-Saidy, "Concrete blocks for thermal insulation in hot climate," *Cement and Concrete Research*, vol. 35, no. 8, pp. 1472–1479, 2005.
- [19] Y. Xu and D. D. L. Chung, "Effect of sand addition on the specific heat and thermal conductivity of cement," *Cement and Concrete Research*, vol. 30, no. 1, pp. 59–61, 2000.
- [20] C. S. Lam, C. S. Poon, and D. Chan, "Enhancing the performance of pre-cast concrete blocks by incorporating waste glass—ASR consideration," *Cement and Concrete Composites*, vol. 29, no. 8, pp. 616–625, 2007.
- [21] C. Meyer and S. Baxter, "Use of recycled glass for concrete masonry blocks," Final Report 97-15, New York State Energy Research and Development Authority, Albany, NY, USA, 1997.
- [22] E. A. Byars, B. Morales-Hernandez, and Z. HuiYing, "Waste glass as concrete aggregate and pozzolan Laboratory and industrial projects," *Concrete*, vol. 38, no. 1, pp. 41–44, 2004.
- [23] R. R. Krishnamoorthy and J. A. Zujip, "Thermal conductivity and microstructure of concrete using recycle glass as a fine aggregate replacement," *International Journal of Emerging Technology and Advanced Engineering*, vol. 3, no. 8, pp. 463–471, 2013.
- [24] M. Najimi, J. Sobhani, B. Ahmadi, and M. Shekarchi, "An experimental study on durability properties of concrete containing zeolite as a highly reactive natural pozzolan," *Construction and Building Materials*, vol. 35, pp. 1023–1033, 2012.

- [25] C. S. Poon, L. Lam, S. C. Kou, and Z. S. Lin, "A study on the hydration rate of natural zeolite blended cement pastes," *Construction and Building Materials*, vol. 13, no. 8, pp. 427–432, 1999.
- [26] S. Y. N. Chan and X. Ji, "Comparative study of the initial surface absorption and chloride diffusion of high performance zeolite, silica fume and PFA concretes," *Cement and Concrete Composites*, vol. 21, no. 4, pp. 293–300, 1999.
- [27] Ş. Kılıncarslan, "Thermo-mechanical properties of concrete containing zeolite," *Suleyman Demirel Universitesi Fen Bilimleri Enstitusu Dergisi*, vol. 11, no. 3, pp. 262–267, 2007.
- [28] Y. Qin and J. E. Hiller, "Modeling the temperature and stress distributions in rigid pavements: impact of solar radiation absorption and heat history development," *KSCE Journal of Civil Engineering*, vol. 15, no. 8, pp. 1361–1371, 2011.
- [29] E. B. Pancar and M. V. Akpınar, "Temperature reduction of concrete pavement using glass bead materials," *International Journal of Concrete Structures and Materials*, vol. 10, no. 1, pp. 39–46, 2016.
- [30] ASTM C1260, *Standard Test Method for Potential Alkali Reactivity of Aggregates (Mortar-Bar Method)*, Annual Books of ASTM Standards, West Conshohocken, Pa, USA, 2001.

Research Article

Water Vapor Diffusion and Adsorption of Sandstones: Influence of Rock Texture and Composition

Martin Keppert, Jaromír Žumár, Monika Čáchová, Dana Koňáková, Petr Svora, Zbyšek Pavlík, Eva Vejmelková, and Robert Černý

Department of Materials Engineering and Chemistry, Faculty of Civil Engineering, Czech Technical University in Prague, Thákurova 7, 166 29 Prague 6, Czech Republic

Correspondence should be addressed to Martin Keppert; martin.keppert@fsv.cvut.cz

Received 22 April 2016; Accepted 12 June 2016

Academic Editor: Osman Gencel

Copyright © 2016 Martin Keppert et al. This is an open access article distributed under the Creative Commons Attribution License, which permits unrestricted use, distribution, and reproduction in any medium, provided the original work is properly cited.

The term sandstone is used for wide range of rocks containing quartz clasts which can be cemented by secondary precipitated quartz or calcite; moreover the space between clasts can be filled by matrix. These facts result in existence of numerous rocks having highly various properties. Sandstones have been used as construction materials due to their good accessibility and workability. Since most of sandstones are porous, water vapor can penetrate through sandstone constructions. The rate of water vapor diffusion, as well as the vapor sorption isotherm, was determined for range of sandstone types. The diffusion resistance factor was found to be dependent on the total porosity of sandstone but the sorption behavior was strongly influenced by nature of the particular sandstone; the specific surface area of stone and presence of clay matrix are determining its sorption isotherm. The published data enable estimating (i) diffusion resistance factor of a sandstone via knowledge of its total porosity and (ii) the sorption isotherm via knowledge of the stone's nature and specific surface area. This approach can significantly reduce the time necessary to acquire vapor-related properties of a sandstone.

1. Introduction

Ability of a building material to transport and store water vapor is influencing durability and performance of a building structure. Water vapor is one of sources of moisture content in materials and structures; it is entering the structure from the surrounding air of certain relative humidity, and then it is transported by diffusion through the pore system of the material and adsorbed on the surface of material. The water vapor-related material's parameters are significantly influencing indoor climate, performance of building envelopes, or drying of moist structures [1–4]. These parameters are also crucial for modeling of coupled heat and moisture transport in constructions [5–7] which is nowadays necessary tool in design of new constructions as well as in rehabilitation of older structures for new purposes or for improvement of their performance. Sandstones have been used as construction material for centuries; today their importance lies mainly in decorative applications, for example, cladding. Regardless, sandstone is used as load bearing or decorative material and

its ability to transport and store water vapor is crucial for the construction durability and performance.

The rate of transport of water vapor in a porous body is usually quantified by means of water vapor diffusion coefficient D ($\text{m}^2 \text{s}^{-1}$) which is defined by (1), where j ($\text{kg m}^{-2} \text{s}^{-1}$) is flux of water vapor and ρ_v (kg m^{-3}) partial density of water vapor per unit volume of porous body. Water vapor diffusion resistance factor μ (see (2)) is frequently used in building practice; D_a is diffusion coefficient of water vapor in air. It describes the water vapor diffusion resistance of the material in comparison to air at normal pressure:

$$j = -D \text{grad } \rho_v, \quad (1)$$

$$\mu = \frac{D_a}{D}. \quad (2)$$

The rate of water vapor diffusion through a material is conventionally measured by a standard (dry/wet) cup method, for example, [8, 9], where specimen of a known dimensions is separating two environments of different values of relative

humidity (RH) and amount of diffused water vapor is measured gravimetrically in time. The diffusion coefficient D is then calculated according to (3), where Δm is mass of transported water in time τ , d and S are dimensions of specimen, T is temperature, R is gas constant, M is molar mass of water, and Δp is difference of water partial pressure between the two environments. Fast transient method for D determination was developed in order to reduce the experimental duration [10]. Values of water vapor diffusion resistance factors of various sandstones were published elsewhere [11–13]:

$$D = \frac{\Delta m \cdot d \cdot R \cdot T}{\tau \cdot S \cdot \Delta p \cdot M} \quad (3)$$

The ability of a material to store water vapor is described by sorption isotherm, dependence of equilibrium amount of adsorbed moisture upon relative pressure of water vapor in surrounding air. There are several experimental methods of sorption isotherm determination [14, 15] but most frequently the specimen is subjected to air of a given constant value of relative humidity and let to reach equilibrium moisture content which is determined gravimetrically. The shape of a sorption isotherm is influenced by mechanism of adsorption prevailing on the given surface; sorption isotherms are conventionally classified according to IUPAC recommendation [16] which has been subject of several proposed modifications [17, 18]. The experimental sorption data can be fitted with a model, equation describing the sorption isotherm. This approach provides useful information about mechanism of sorption in the studied sorbate-sorbent system and enables generalizing the experimental results on similar systems. Numerous semiempirical and theoretical sorption models were proposed in recent years [19]; applicability of selected models on building materials was tested as well [20]. The Generalized D'Arcy and Watt (GDW) model [19, 21] was used to fit the experimental data in this work. This model assumes that surface of a sorbent contains certain amount of primarily sorption centers where Langmuir monolayer sorption is taking place. The water molecules sorbed at these primary sorption centers act as secondary sorption centers where further water sorption takes place due to cluster formation (Dubinin-Sierpinski theory). The GDW model [21] is expressed by (4), where M is the sorbed amount of water vapor and φ is the relative pressure of water vapor. The model involves four parameters: m is the maximum sorbed amount on primary centers; K and k are kinetic constants of sorption on primary and secondary sorption sites; and w is ratio of molecules sorbed on primary centers and converted to secondary centers:

$$M = \frac{m \cdot K \cdot \varphi}{1 + K \cdot \varphi} \cdot \frac{1 - k(1 - w) \cdot \varphi}{1 - k \cdot \varphi} \quad (4)$$

The importance of study of water vapor sorption isotherm of building materials, besides the problems mentioned above, lies also in the field of materials durability and, when one is talking specifically about rocks, the water vapor sorption is influencing also deterioration of sculptures and natural monuments [12, 13, 22]. The moisture sorption can be

significantly influenced also by present salts what is frequent case in buildings and natural monuments [23].

Water vapor diffusion and sorption properties of sandstones were so far measured and published with respect to behavior of individual rocks; the intention of the present paper is to relate these parameters to fundamental properties and composition of sandstones.

2. Methods

The phase composition of stones was studied by X-ray diffraction analysis (diffractometer PANalytical X'PertPRO MPD with $\text{Cu}_{K\alpha}$ radiation source); the quantification was performed by Rietveld analysis. The SEM images were acquired by help of SEM JEOL JSM-6510; observed particles were characterized by help of EDS detector SDD x-act 10 mm² INCA. The compressive strength of rocks was evaluated by means of 100 mm cubes; the bending strength was measured by help of 100 × 100 × 300 mm prisms. Pore size distribution and specific surface area were measured by mercury intrusion porosimetry device Pascal 140 + 440 (Thermo). Water vapor sorption was measured gravimetrically by help of device DVS Advantage (Surface Measurement Systems). The water vapor diffusion coefficient and diffusion resistance factor was determined in isothermal conditions (20°C) according standard [8]; the dry cup arrangement was used in order to avoid overestimation of vapor diffusion coefficient due to simultaneous partial transport of liquid water.

3. Results

3.1. Properties of Materials. Six types of sandstones quarried in Czech Republic were selected with respect to various porosity, composition, and diagenesis processes. Stones were sorted and signed according to the increasing porosity (Table 1). Sandstone S 1 (quarry Tešín-Řeka) contains mainly quartz clasts accompanied by smaller amount of feldspar (microcline, albite) and muscovite. Its matrix is formed by calcite and chlorite; muscovite and feldspars are present both as clasts and in matrix (Figure 1). Weak silicification is contributing to very high strength of this stone as well (Table 2). Stone S 2 (Úpice) contains silicified quartz clasts; it contains high amount of matrix composing of kaolinite (23 wt.% of the whole stone) and muscovite. In contrary stone S 3 (Kocbeře) contains quartz clasts and just limited amount (ca 1%) of kaolinite. The clasts are highly silicified and the silicification is responsible for very high strength of this stone even though its porosity is ca 15%. Sandstone S 4 (Záměl) is very complicated stone where quartz clasts are accompanied with glauconite, chlorite, and kaolinite. These minerals are present as clasts as well as in the stone matrix. Stone S 5 (Hořice) is similar to S 2 but with lower content of kaolinite matrix (14%) and higher porosity. The highest porosity was exhibited by stone S 6 (Mšené) with just very small amount of kaolinite matrix (ca 1%) and weak silicification.

The composition and diagenesis of studied stones obviously determine their fundamental physical properties (Table 2). The compressive and bending strength of porous stones are generally inversely dependent on porosity [24, 25];

TABLE 1: Composition and porosity of studied sandstones.

		Clasts		Matrix and cement		Porosity (%)
		Nature	Content (%)	Nature	Content (%)	
S 1	Tessin	Quartz	65	Calcite	7	7.2
		Muscovite		Muscovite	Total 10	
		Feldspars		Feldspars	Total 10	
				Chlorite	5	
				weak silicification		
S 2	Upice	Quartz	71	Kaolinite	23	10.4
				Muscovite	5	
				silicification		
S 3	Kocbere	Quartz	99	Kaolinite	1	14.8
				intensive silicification		
S 4	Zamel	Quartz	86	Chlorite		19.5
		Microcline		Glaucanite		
		Glaucanite		Kaolinite		
				weak silicification		
S 5	Horice	Quartz	84	Kaolinite	14	27.3
				Illite	2	
				variable silicification		
S 6	Msene	Quartz	99	Kaolinite	1	28.2
				weak silicification		

the studied sandstones obey this rule with one exception: stone S 4 has unexpectedly high strength due to intensive silicification. The composition of sandstones is reflected also in their pore size distribution (Figure 2). Pore system of the stone S 6 is formed mainly by large pores, voids between quartz grains (mean pore diameter $37 \mu\text{m}$, Table 2). The porosity of stone S 5 is nearly the same but an important difference lies in its pore size distribution; S 5 contains relatively high amount of clays and thus its pore system is bimodal; it is formed by capillaries and in addition also by smaller pores ($0.1\text{--}1 \mu\text{m}$) in clay matrix. Sandstone S 4 is similar to S 5 but the total porosity is smaller due to lower volume of capillary pores. S 3 is sort of analogy of S 6; there is very small amount of kaolinite and thus the pore size distribution is unimodal, and pore system contains nearly uniquely capillaries between 10 and $100 \mu\text{m}$. The mean pore diameters of S 3 and S 6 are roughly equal. Stones S 1 and S 2 do not contain the large interparticular capillaries but their pore system is composed just from pores in their matrices. Consequently their values of mean pore diameter are of one and two orders of magnitude lower. Specific surface area (SSA) of stones is an important parameter with respect to their ability to adsorb water vapor. The highest values were obtained in case of stones S 4 and S 1 due to presence of high amount of small pores in their matrices; smaller pores obviously contribute to specific surface area more than large pores of the same specific volume. It is obvious that "sandstone" cannot be regarded as a single material but one has to consider its original character and composition when properties of a sandstone are discussed.

3.2. Diffusion of Water Vapor in Sandstones. The dependence of vapor diffusion coefficient (measured by dry cup) of studied sandstones on their porosity P (%) is shown in Figure 3. The diffusion coefficient D ($\text{m}^2 \text{s}^{-1}$) is increasing linearly upon porosity. When the same results are expressed in form of water vapor diffusion resistance factor μ , one obtains inversely proportional function (Figure 4). The corresponding equations are as follows:

$$D = 6.37 \cdot 10^{-5} \cdot P - 1.72 \cdot 10^{-7},$$

$$\mu = \frac{2.3 \cdot 10^{-5}}{6.37 \cdot 10^{-5} \cdot P - 1.72 \cdot 10^{-7}}. \quad (5)$$

3.3. Sorption of Water Vapor on Sandstones. Primary water vapor sorption isotherms where mass of adsorbed water is related to mass of sorbent (stone) are shown in Figure 5. Hysteresis between adsorption and desorption isotherms indicates occurrence of condensation of water vapor in pores. The present data feature wide range of adsorbed vapor amounts on a "single" type of rock (i.e., sandstone). The highest sorption was measured in case of sample S 4 while the lowest in S 6. These two materials are also the extremes (among of the studied stones) regarding the specific surface area; S 4 achieved the highest value of SSA while S 6 the lowest. The sorption values of S 3 were found to be similar to S 6.

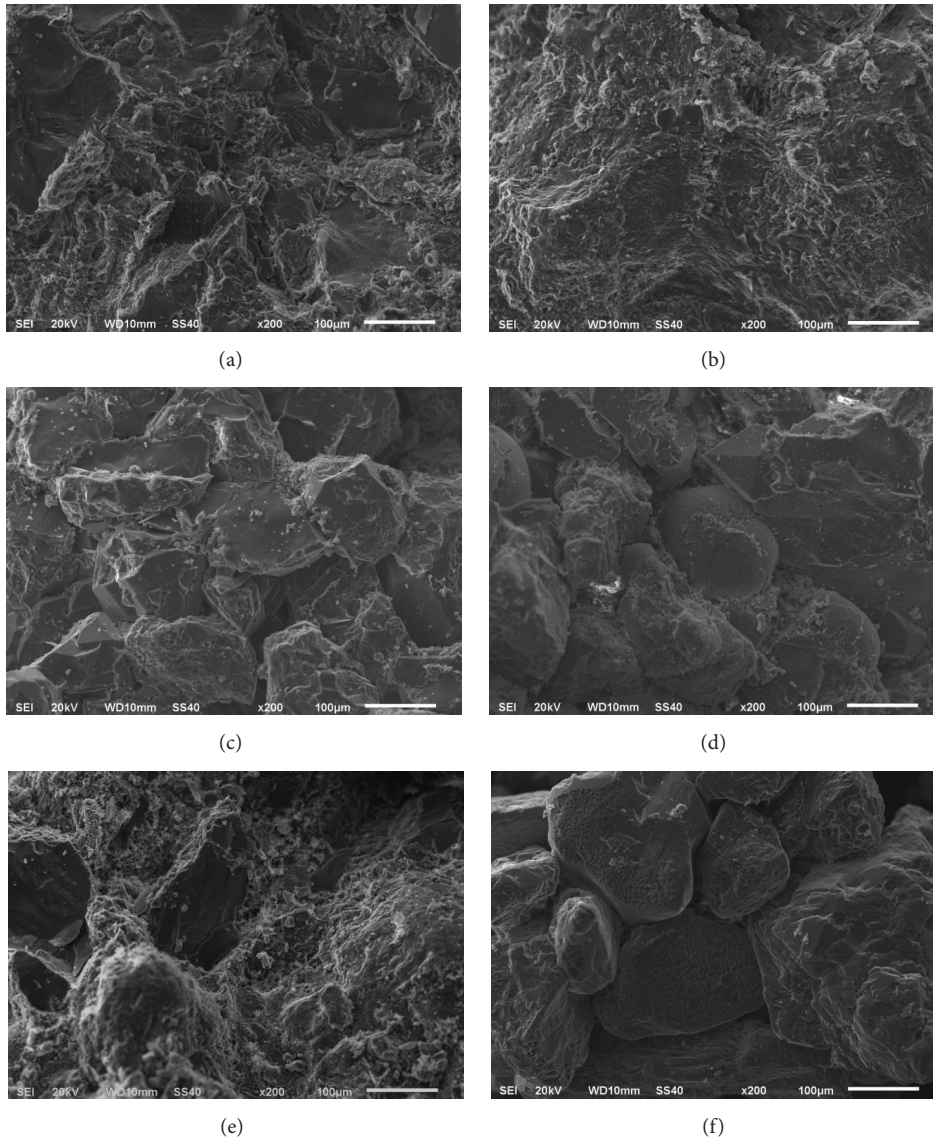


FIGURE 1: SEM of studied sandstones ((a) S 1, (f) S 6).

TABLE 2: Fundamental properties of studied sandstones.

	Porosity %	Specific pore volume $\text{cm}^3 \text{g}^{-1}$	Mean pore diameter Micrometer	Specific surface area $\text{m}^2 \text{g}^{-1}$	Compressive strength MPa	Bending strength MPa
S 1	7.2	0.027	0.11	2.014	82.8	14.2
S 2	10.4	0.040	1.53	0.679	63.5	7.6
S 3	14.8	0.061	32.73	0.67	85.4	15.4
S 4	19.5	0.088	18.60	3.303	25.6	5.1
S 5	27.3	0.133	38.37	0.754	21.1	3.8
S 6	28.2	0.139	36.51	0.44	8.7	1.6

4. Discussion

The experimentally determined water vapor diffusion resistance factors, when being plotted upon total porosity (Figure 4), are in very good agreement with data published in studies [11–13]. The total porosity can be regarded as

the crucial factor controlling the rate of vapor diffusion in sandstones; influence of any other parameter was not observed. The explanation of identified different sorption behavior of individual sandstones has to be searched in different composition and pore size distribution of the stones; clearly these two factors are associated. Since the water vapor

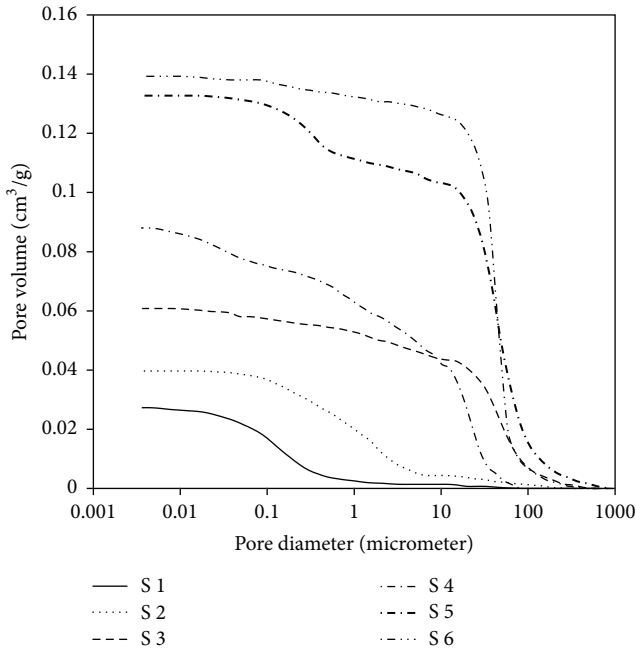


FIGURE 2: Pore size distribution.

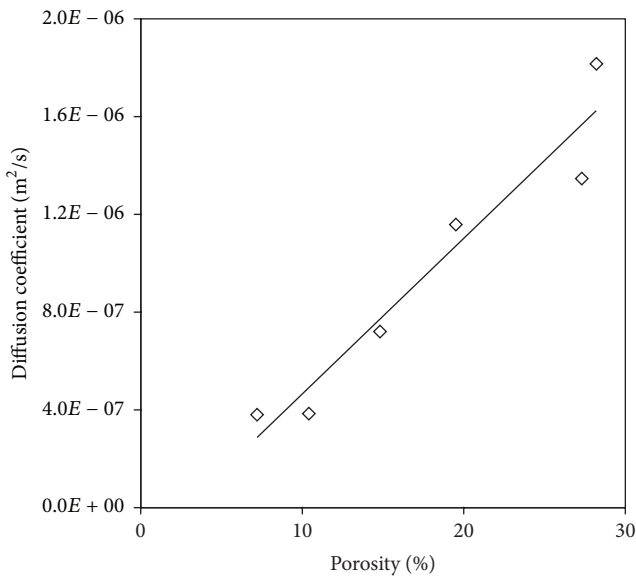


FIGURE 3: Dependence of water vapor diffusion coefficients of sandstones on porosity.

adsorption is a surface process the experimental sorption data were replotted as mass of adsorbed vapor-related to unit of surface area of a given stone (Figure 6). There, the range of acquired values is somewhat smaller; the experimental data of S 1, S 2, S 4, and S 5 relatively well collapse to a similar values. The remaining stones (S 3 and S 6) reached somewhat lower sorption per m^2 of surface. The difference between these two groups of sandstones lies in their nature; stones S 3 and S 6 contain just negligible amount of matrix while quartz clasts (and quartz cement) are their dominant components; the other stones contain significant amount of matrix. One

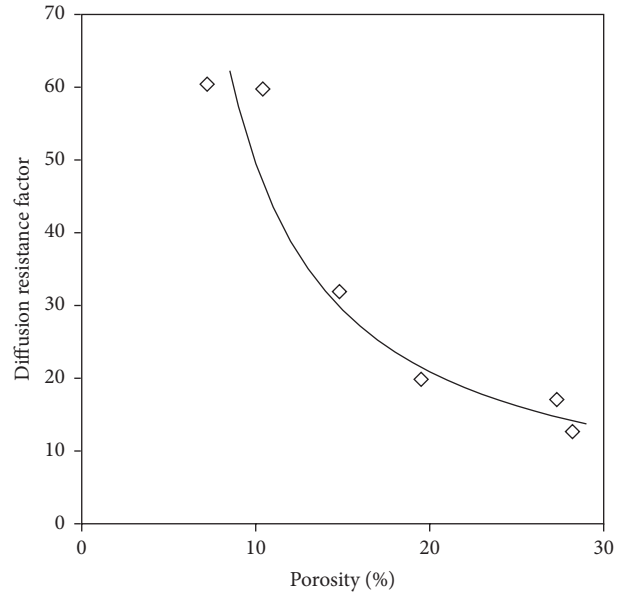


FIGURE 4: Diffusion resistance factor of sandstones as function of porosity.

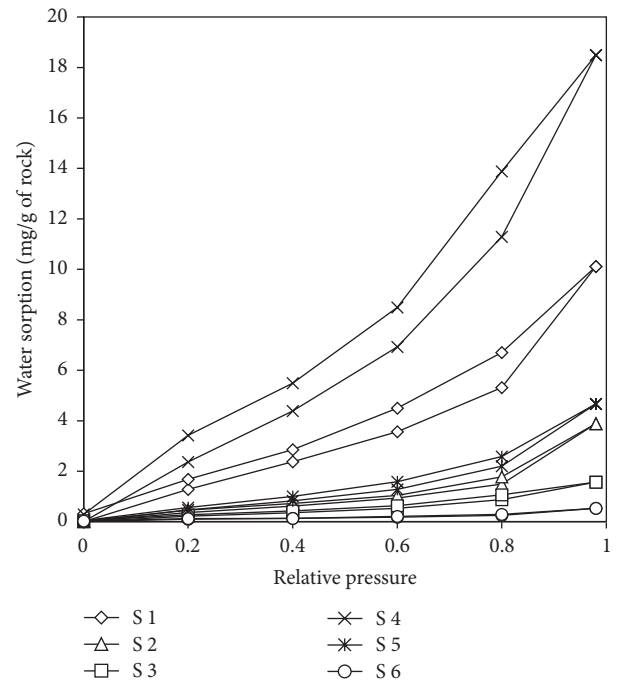


FIGURE 5: Sorption/desorption isotherms of sandstones expressed by mg of water adsorbed per 1 g of sample.

observes that presence of matrix in stones clearly increases SSA and also ability of water vapor sorption. Nevertheless this link is not straightforward; in such case all isotherms in Figure 4 would collapse together. In fact nature of surface is important as well; samples S 2 and S 3 have similar specific surface area but adsorbed amount is higher in S 2 where high amount of kaolinite is present. The adsorbed maximum amount of water on quartz or calcite is about 1 mg/g [26],

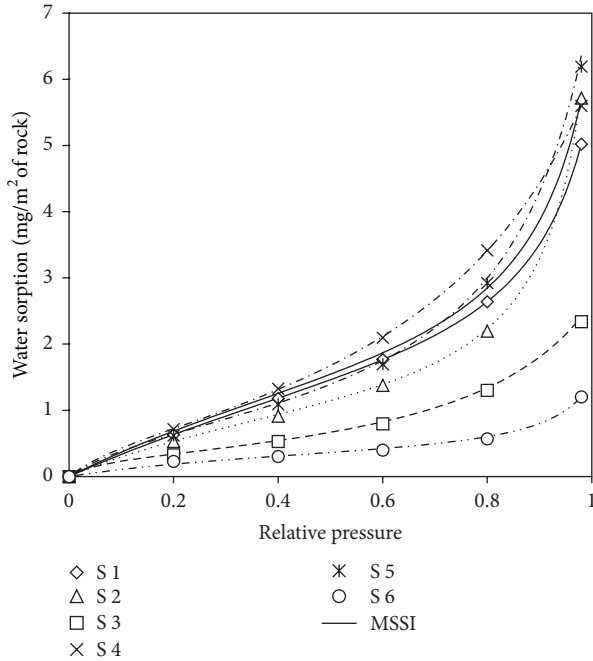


FIGURE 6: Sorption isotherms where mass of adsorbed water is expressed per unit specific surface area (m^2 of rock). Points: experimental data; lines: fitted GDW isotherms.

TABLE 3: Coefficients of GDW sorption isotherms (see (4)) of studied stones.

	m	K	k	w
S 1	4.004	0.8864	0.8984	0.23
S 2	1.802	1.8803	0.9365	0.36
S 3	0.480	7.3457	0.8547	0.93
S 4	4.723	0.9514	0.9264	0.25
S 5	4.608	0.7285	0.8597	0.35
S 6	0.441	2.1500	0.8200	0.75
MSSI	3.336	1.2185	0.9028	0.29

similarly to values obtained for S 3 and S 6 samples (Figure 5) where quartz is nearly the sole component. On the other hand, clay minerals, which are present in other samples, are generally able to adsorb tens to hundreds of mg of water per g [27, 28].

In order to find a general relationship between adsorbed water amount and properties of stones, the experimental sorption data (expressed per unit specific surface area) were fitted by GDW isotherm (see (4)); the regression coefficients are provided in Table 3 (adsorbed amount in mg/m^2 , dimensionless relative pressure). Since the experimental data for samples S 1, S 2, S 4, and S 5 are close to each other and these four stones contain significant amount of (mostly) clayey matrix, an overall fitting for these four samples was performed as well; the obtained isotherm MSSI (matrix sandstone sorption isotherm) is shown in Figure 4. The values of m parameter (adsorbed amount on primary centers) are lower for “quartz-only sandstones” S 3 and S 6 compared to the “matrix-containing” materials. The value of parameter w ,

expressing the amount of secondary adsorption centers, is significantly higher in case of S 3 and S 6 which correspond to lower adsorbed amount on primary centers on quartz compared to clay minerals and thus the effort on adsorption on secondary sites is higher.

5. Conclusions

The water vapor diffusion and storage parameters of six different sandstones were determined. While the diffusion resistance factor was found to be simply dependent on the total porosity (studied range 7–28%) the adsorption behavior was more complicated. The sorption isotherms acquired on studied sandstones were influenced by (i) specific surface area of the stone and (ii) its composition, specifically by content of clay minerals. When the adsorbed amount is related to m^2 of stone, the data acquired on sandstones with clay matrix collapsed to a single line while adsorbed amounts on “quartz-only” sandstones are lower. The regression coefficients of GDW sorption isotherm indicate different mechanism as well; the stones without matrix contain higher amount of secondary sorption centers than stones with matrix where Langmuir sorption is prevailing. The acquired data enable estimating (i) diffusion resistance factor of a sandstone via knowledge of its total porosity and (ii) the sorption isotherm via knowledge of the stone’s nature and specific surface area.

Competing Interests

The authors declare that there are no competing interests regarding the publication of this paper.

Acknowledgments

This research has been supported by the Czech Science Foundation under Project no. 14-17207S “Transport Parameters and Durability of Porous Rocks.”

References

- [1] A. H. Holm and H. M. Kuenzel, “Practical application of an uncertainty approach for hygrothermal building simulations—drying of an AAC flat roof,” *Building and Environment*, vol. 37, no. 8-9, pp. 883–889, 2002.
- [2] V. Kočí, J. Maděra, and R. Černý, “Exterior thermal insulation systems for AAC building envelopes: computational analysis aimed at increasing service life,” *Energy and Buildings*, vol. 47, pp. 84–90, 2012.
- [3] Z. Pavlík and R. Černý, “Hygrothermal performance study of an innovative interior thermal insulation system,” *Applied Thermal Engineering*, vol. 29, no. 10, pp. 1941–1946, 2009.
- [4] V. Kočí, J. Maděra, and R. Černý, “Computer aided design of interior thermal insulation system suitable for autoclaved aerated concrete structures,” *Applied Thermal Engineering*, vol. 58, no. 1-2, pp. 165–172, 2013.
- [5] M. Qin, R. Belarbi, A. Ait-Mokhtar, and L.-O. Nilsson, “Coupled heat and moisture transfer in multi-layer building materials,” *Construction and Building Materials*, vol. 23, no. 2, pp. 967–975, 2009.

- [6] H. L. S. C. Hens, "Combined heat, air, moisture modelling: a look back, how, of help?" *Building and Environment*, vol. 91, pp. 138–151, 2015.
- [7] J. Carmeliet and S. Roels, "Determination of the isothermal moisture transport properties of porous building materials," *Journal of Thermal Envelope and Building Science*, vol. 24, no. 3, pp. 183–210, 2001.
- [8] ISO, "Hygrothermal performance of building materials and products," Tech. Rep. EN ISO 12572, Determination of Water Vapour Transmission Properties, 2001.
- [9] ASTM E96-95, Standard test methods for water vapor transmission of materials, 2001.
- [10] Z. Pavlík, J. Žumár, M. Pavlíková, and R. Černý, "A Boltzmann transformation method for investigation of water vapor transport in building materials," *Journal of Building Physics*, vol. 35, no. 3, pp. 213–223, 2012.
- [11] J. Ruedrich, T. Bartelsen, R. Dohrmann, and S. Siegesmund, "Moisture expansion as a deterioration factor for sandstone used in buildings," *Environmental Earth Sciences*, vol. 63, no. 7, pp. 1545–1564, 2011.
- [12] H. Stück, S. Siegesmund, and J. Rüdrieh, "Weathering behaviour and construction suitability of dimension stones from the Drei Gleichen area (Thuringia, Germany)," *Environmental Earth Sciences*, vol. 63, no. 7, pp. 1763–1786, 2011.
- [13] H. Stück, R. Plagge, and S. Siegesmund, "Numerical modeling of moisture transport in sandstone: the influence of pore space, fabric and clay content," *Environmental Earth Sciences*, vol. 69, no. 4, pp. 1161–1187, 2013.
- [14] B. Johannesson and M. Janz, "Test of four different experimental methods to determine sorption isotherms," *Journal of Materials in Civil Engineering*, vol. 14, no. 6, pp. 471–477, 2002.
- [15] C. Franzen and P. W. Mirwald, "Moisture content of natural stone: static and dynamic equilibrium with atmospheric humidity," *Environmental Geology*, vol. 46, no. 3-4, pp. 391–401, 2004.
- [16] IUPAC, "Reporting physisorption data for gas/solid systems with special reference to the determination of surface area and porosity," *Pure & Applied Chemistry*, vol. 57, pp. 603–619, 1985.
- [17] M. D. Donohue and G. L. Aranovich, "Classification of Gibbs adsorption isotherms," *Advances in Colloid and Interface Science*, vol. 76-77, pp. 137–152, 1998.
- [18] J. Blahovec and S. Yanniotis, "Modified classification of sorption isotherms," *Journal of Food Engineering*, vol. 91, no. 1, pp. 72–77, 2009.
- [19] S. Furmaniak, P. A. Gauden, A. P. Terzyk, and G. Rychlicki, "Water adsorption on carbons—critical review of the most popular analytical approaches," *Advances in Colloid and Interface Science*, vol. 137, no. 2, pp. 82–143, 2008.
- [20] Z. Pavlík, J. Žumár, I. Medved, and R. Černý, "Water vapor adsorption in porous building materials: experimental measurement and theoretical analysis," *Transport in Porous Media*, vol. 91, no. 3, pp. 939–954, 2012.
- [21] S. Furmaniak, A. P. Terzyk, R. Gołembiewski, P. A. Gauden, and L. Czepirski, "Searching the most optimal model of water sorption on foodstuffs in the whole range of relative humidity," *Food Research International*, vol. 42, no. 8, pp. 1203–1214, 2009.
- [22] Z. Pavlík, P. Michálek, M. Pavlíková, I. Kopecká, I. Maxová, and R. Černý, "Water and salt transport and storage properties of Mšené sandstone," *Construction and Building Materials*, vol. 22, no. 8, pp. 1736–1748, 2008.
- [23] C. Franzen and P. W. Mirwald, "Moisture sorption behaviour of salt mixtures in porous stone," *Chemie der Erde*, vol. 69, no. 1, pp. 91–98, 2009.
- [24] C. Chang, M. D. Zoback, and A. Khaksar, "Empirical relations between rock strength and physical properties in sedimentary rocks," *Journal of Petroleum Science and Engineering*, vol. 51, no. 3-4, pp. 223–237, 2006.
- [25] N. K. Tamrakar, S. Yokota, and S. D. Shrestha, "Relationships among mechanical, physical and petrographic properties of Siwalik sandstones, Central Nepal Sub-Himalayas," *Engineering Geology*, vol. 90, no. 3-4, pp. 105–123, 2007.
- [26] N. Hackerman and A. C. Hall, "The adsorption of water vapor on quartz and calcite," *The Journal of Physical Chemistry*, vol. 62, no. 10, pp. 1212–1214, 1958.
- [27] M. S. Gruszkiewicz, J. Horita, J. M. Simonson, R. E. Mesmer, and J. B. Hulen, "Water adsorption at high temperature on core samples from The Geysers geothermal field, California, USA," *Geothermics*, vol. 30, no. 2-3, pp. 269–302, 2001.
- [28] P. Mokrejs, A. Zikanova, D. Hradil et al., "The influence of heat pre-treatment on the sorption of water vapour on bentonite," *Adsorption*, vol. 11, no. 1, pp. 57–63, 2005.

Research Article

Energy-Dissipation Performance of Combined Low Yield Point Steel Plate Damper Based on Topology Optimization and Its Application in Structural Control

Haoxiang He,^{1,2} Xiaobing Wang,¹ and Xiaofu Zhang¹

¹Beijing Key Laboratory of Earthquake Engineering and Structural Retrofit, Beijing University of Technology, Beijing 100124, China

²Beijing Collaborative Innovation Center for Metropolitan Transportation, Beijing 100124, China

Correspondence should be addressed to Haoxiang He; hxx7856@163.com

Received 14 April 2016; Revised 31 May 2016; Accepted 1 June 2016

Academic Editor: Juan J. Del Coz Díaz

Copyright © 2016 Haoxiang He et al. This is an open access article distributed under the Creative Commons Attribution License, which permits unrestricted use, distribution, and reproduction in any medium, provided the original work is properly cited.

In view of the disadvantages such as higher yield stress and inadequate adjustability, a combined low yield point steel plate damper involving low yield point steel plates and common steel plates is proposed. Three types of combined plate dampers with new hollow shapes are proposed, and the specific forms include interior hollow, boundary hollow, and ellipse hollow. The “maximum stiffness” and “full stress state” are used as the optimization objectives, and the topology optimization of different hollow forms by alternating optimization method is to obtain the optimal shape. Various combined steel plate dampers are calculated by finite element simulation, the results indicate that the initial stiffness of the boundary optimized damper and interior optimized damper is larger, the hysteresis curves are full, and there is no stress concentration. These two types of optimization models made in different materials ratios are studied by numerical simulation, and the adjustability of yield stress of these combined dampers is verified. The nonlinear dynamic responses, seismic capacity, and damping effect of steel frame structures with different combined dampers are analyzed. The results show that the boundary optimized damper has better energy-dissipation capacity and is suitable for engineering application.

1. Introduction

In order to resist the dynamic action of strong earthquakes and hurricanes, building structures should have enough capacities to dissipate energy and avoid severe damage. The seismic performance of the traditional buildings is improved by enhancing the mechanical parameter such as strength, stiffness, and ductility; that is, the structure can reserve and dissipate the input energy by self-resistance. Therefore, the structure designed by normal methods does not have the capability of self-adjustment, which may lead to unacceptable damage and even collapse during earthquakes and the safety requirements are hard to meet. Hence, the traditional seismic design methods need to be improved by inducing new energy-dissipation technology. Structural control provides a safe and effective way to enhance the aseismic capacity of structures. Structural seismic control is to change or adjust the dynamic characteristic or dynamic action by installing

devices (such as seismic isolation bearing), some mechanisms (such as energy-dissipation braces and joints, fluid viscous damper, and metallic damper), some substructure (such as tuned mass damper), or external force (such as external energy input) in a certain part of structure. Under small earthquake and wind, the structure itself has enough lateral resistance to meet the operating requirement, and structure is in the elastic state. Under severe earthquake and strong wind, the lateral deformation of the structure will continuously increase, and the energy-dissipation devices firstly enter the inelastic state, provide enough damping, dissipate the vibration energy, and rapidly attenuate the vibration responses of the main body structure so as to reduce the damage degree. The realization of structural seismic control mainly depends on the application of simple and effective dampers and energy-dissipation devices. In recent years, a large number of dampers, such as mild steel damper, friction damper, viscous fluid damper, and smart damper, are developed and

utilized in practical engineering, and the damping effect is very obvious.

Low yield point metal damper is a kind of passive energy-dissipation device, which has a wide range of applications, and the advantages include simple conformation, stable hysteretic performance, low cost, and explicit mechanism. By using plastic hysteresis deformation of different forms of metals to dissipate energy, low yield point metal damper has superior hysteretic characteristics during plastic stage and absorbs a large amount of energy in the process of elastic-plastic hysteresis. Thus, it is used as energy-dissipation dampers in civil engineering with diverse types [1]. Since Kelly et al. [2] put forward the concept of energy dissipation with metal energy-dissipation devices and carried out the relevant experimental study in 1972, many theoretical and experimental researches on metal dampers are carried out. Various forms of low yield point metal dampers are studied, such as U-shaped steel plate damper, conical steel damper, shear yielding type steel damper, and axial yield damper. Kajima Company proposed a honeycomb metallic yield damper, which can be installed in walls or beams. Whittaker et al. [3] and Tsai et al. [4] firstly proposed displacement bending type of dampers with X shape and triangle shape. Tirca et al. [5] proposed a kind of steel damper which only generates in-plane deformation and the corresponding high-rise structure with such dampers was analyzed, and it is verified that the dampers have excellent energy-dissipation capacity. Zhou and Liu [6, 7] developed several new metal energy-dissipation devices, such as the circular ring damper and double circular ring mild steel damper. Zhang et al. [8] presented a mild steel damper with a diamond shape hollow in-plane, and this kind of damper has the advantages of large plastic deformation and full hysteresis curve, but its initial stiffness is small and the total amount of steel is large. In order to improve the initial stiffness of dampers, Mito et al. [9] put forward a shear panel damper with rectangle shape, but the plane stress of the four corners on the plate can prematurely concentrate and the energy dissipation capacity is inadequate, and G. Li and H. Li [10] proposed the mild steel dampers with a single circular hole and double X shape. The initial stiffness of these dampers is relatively large and hysteretic curve is full, but there are still some disadvantages such as obvious stress concentration, limited yield area, and low utilization ratio.

Although the research and application on energy-dissipation technology of low yield point steel dampers have achieved great progress, there are still many problems to be studied and solved: (1) the existing low yield point steel dampers are usually packaged structures, which are not convenient for installation and adjustment, and the maintenance cost is high. (2) The damping performance of the dampers cannot be fully embodied in the small and medium earthquakes but only works in strong earthquakes and hurricanes due to the high yield strength; thus, the ultralow-yield point dampers are highly required especially for low and medium level vibration. In order to maximize the effect of the energy dissipation, the damper should have the capability of both large initial stiffness and good deformation energy-dissipation capacity after yield. (3) The adjustability of the current dampers is deficient, and the research on seismic

strengthening and repair of existing building structures with combined low yield point steel dampers should be enhanced. (4) The resilient function and replaceability of the low yield point steel damper are insufficient, and it needs to develop new type of damper to fulfill the requirements of earthquake resilient structure. Therefore, it is significant to develop novel dampers with low cost and low yield strength. In view of this, a combined low yield point steel plate damper is presented in this study, the yield stress is low, and it can be adjusted according to engineering demand. At the same time, the "maximum stiffness" and "full stress state" are both used as optimization objectives to achieve the topology optimization of damper shape in order to make the damper have ideal deformation capacity and energy-dissipation capacity. During an earthquake, low yield materials firstly deform and reach the yield stage to fully dissipate the energy, and there is no serious plastic deformation in the original main structure, so the overall seismic performance and safety are guaranteed. After the main earthquake, the combined steel plate with low yield point material can be quickly replaced to restore the global seismic performance, which makes the main elements and frame structure have the ability to resist the aftershocks.

2. Composition and Characteristics of Composite Low Yield Point Steel Damper

2.1. Material Property Test of Low Yield Point Steel. The material in the low yield point damper is different from the normal steel in traditional steel structures, its yield strength is low, plastic deformation may occur under small strain, it has sufficient ductility and bearing capacity, and the low cycle fatigue performance is superior. Hence, one of the key technologies of low yield point steel damper production is to select the metal with lower yield strength and larger extensibility. For the conventional low yield point metal including mild steel or low yield point steel, lead, aluminum, and zinc-aluminum alloy the common characteristics of these materials are that the plastic deformation capability is strong, the low cycle fatigue property is superior, and the hysteretic performance is stable and can be recycled. At present, there are many theoretical studies on the shock absorption of low yield point metal, but the studies on the steel product which has high stability and safety and simultaneously meets the requirements of engineering applications are still rare [11].

In this study, the new developed low yield point steel LY160 (yield stress is about 160 MPa), which is made in China, is selected as the energy-dissipation material and the corresponding experimental study is carried out. In order to achieve low yield point performance, the original material of LY160 mainly consists of the composition of industrial pure iron, and a small amount of Ti and Al is added to retain carbon and nitrogen atoms, so as to reduce the hindrance of the dislocation motion. In addition, the rolling technique is adjusted to realize grain growth coursing and obtain the single ferrite organization. Finally, the special steel has excellent plasticity, low yield strength ratio, and good low cycle fatigue performance. In order to obtain and compare the performance parameters of different steel materials,

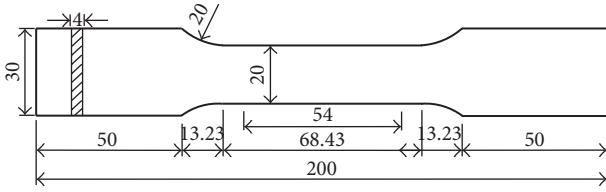


FIGURE 1: Diagram of specimen size (unit: mm).



FIGURE 2: Specimens with tensile fracture.

the comparative research on Q345 steel (yield point is about 345 MPa), Q235 steel (yield point is about 235 MPa), and LY160 steel (yield stress is about 160 MPa) is carried out. The specimens are sheet tensile components, and they are processed in accordance with the relevant provisions of guidelines [12]. The diagram of specimen size is shown in Figure 1.

Three specimens made in each kind of material are produced and different types of specimens are shown in Figure 2. The quasistatic tensile test of the specimens is performed on a normal stretching testing machine, as shown in Figure 3. The longitudinal extensometer is placed on the specimens to measure the longitudinal strain, and the stretching rate is 3 mm/min. The experimental results are shown in Figure 4 and Table 1. It is evident that the low yield point steel has expected yield stress and super ductility. According to the comparison between the yield strength and the nominal yield strength in Table 1, it can be seen that the yield point of LY160 is relatively stable, and the difference between the yield point and the nominal value is about 2%. In summary, LY160 steel has the ideal low yield point, excellent ductility, and toughness to dissipate energy, so it can be used as the material of the low yield point damper.

2.2. Composition of Combined Low Yield Point Steel Plate Damper. In view of the limitation of the yield point of the traditional metal damper, a new type of combined low yield point steel plate damper is proposed. This damper includes the upper and lower horizontal connecting steel plates connected with the structure and the metal plates with the hollow parts arranged between upper and lower horizontal connecting plate. The metal plates are composed of low yield point steel plate (such as Q160) and ordinary steel plate (such as Q345) with different combined ratio, and the thickness is the same, so the equivalent yield strength is lower and can be adjusted or controlled. Two types of metal plates are arranged



FIGURE 3: Stretching testing machine.

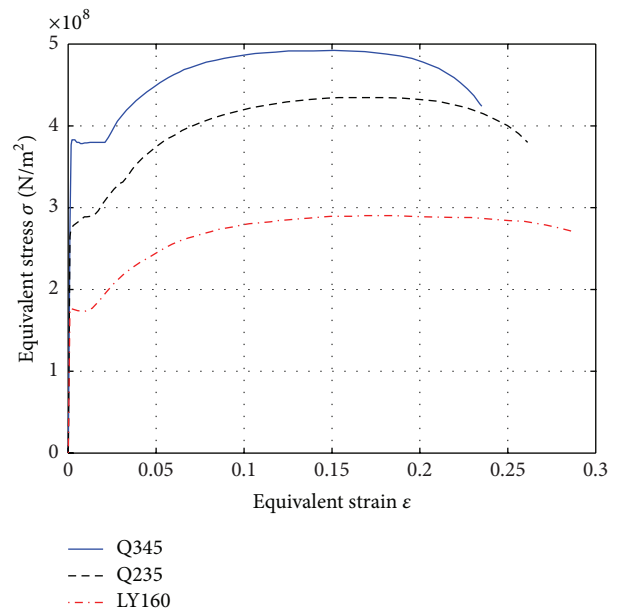


FIGURE 4: Stress-strain curve of different steels.

alternately between the fixed connections and connected by high strength bolts, and the specific construction detail is shown in Figure 5. The number, size, and hollow form of the energy-dissipation metal plates should be determined based on the anticipated yield strength and fixed effect between metal plates, so as to ensure adequate deformation capacity.

The combined low yield point steel plate damper can be installed in the structure beams or the infill walls with the cooperation of braces. During earthquakes, the damper firstly enters the plastic state to dissipate the earthquake energy and ensure the safety of the main structure.

Compared with other steel shear dampers, the advantages of this novel damper are as follows: (1) the energy-dissipation steel plates with different yield points are assembled, so the yield stress of this damper is lower, and the combined steels can fully work in small and moderate earthquakes, and the hysteretic behavior is fulfilling. (2) Compared with the damper only using Q160 steel, the combined damper has better controllability, the best damping performance and energy-dissipation effect can be obtained by modulating

TABLE 1: Results of monotonic tensile test.

Strength grade	Sample number	Yield stress (MPa)	Tensile stress (MPa)	Elongation (%)	Difference between yield point and nominal value (%)
Q345	Number 1	387.2	496.6	22.2	12.2
	Number 2	383.3	485.5	24.4	11.1
	Number 3	385.5	492.6	23.5	11.7
	Mean	385.3	491.6	23.4	11.7
Q235	Number 1	279.2	435.5	30.4	18.8
	Number 2	276.5	433.0	26.3	17.7
	Number 3	273.6	434.5	25.4	16.4
	Mean	276.4	434.3	27.4	17.6
LY160	Number 1	160.2	262.2	30.9	0.0
	Number 2	165.1	266.1	33.4	3.2
	Number 3	164.5	260.4	30.6	2.8
	Mean	163.3	262.9	31.6	2.0

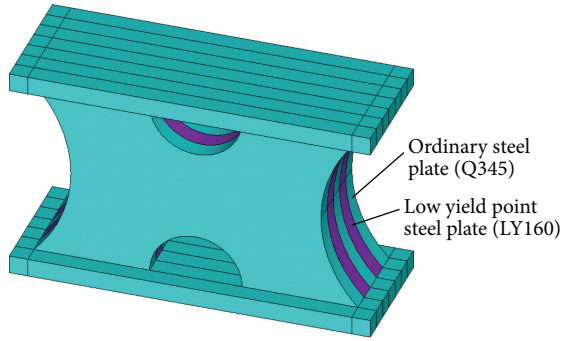


FIGURE 5: Composition of combined low yield point steel plate damper.

the thickness ratio of two types of steel plates, and it is convenient to install, upgrade, and maintain. (3) The construction of this damper is simple and the materials are low cost, so it has wide prospect in application.

3. Double Topology Optimization Design of Damper

3.1. Shape Optimization Design of Damper. The normal low yield point steel plate damper consists of rectangular steel plates or local hollow steel plates. The rectangular steel plates usually just yield in the limited area of central part, so the material utilization ratio is low and the global deformation is small. The local hollow plate can yield at each point of the same thickness along the direction of length side, which will significantly improve the energy-dissipation capacity and deformation capacity [13]. In addition, some low yield point plate dampers resist the external forces in the form of out-of-plane style, and the energy dissipation is realized through the obvious plastic deformation after the plates yield due to bending. However, the initial stiffness and the load capacity of the damper are both small. If the steel plates dissipate energy by shear deformation in the plane, the damper will

have a larger initial stiffness but the damage due to stress concentration or local buckling is prone to occur. Hence, deformation capacity and energy-dissipation capacity of the damper may not reach the expected requirement if there are no optimizations for the hollow form of steel plates.

In view of the above problems, Deng et al. [14] used the finite element analysis to simulate the traditional shear type steel plate damper and obtained the optimal shapes of plates with various sizes, as shown in Figure 6(a). After the shape optimization, the low cycle fatigue capacity of shear type steel plate damper is significantly improved, but the improvement of the dissipation capacity is not obvious. Wang and An [15] presented a new steel plate damper, as shown in Figure 6(b). The initial stiffness and the yield stress are both larger, the stress distribution is uniform, and no obvious stress concentration occurs under cyclic loading, but it is easy to appear as out-of-plane buckling. G. Li and H. Li [10] presented a double X type steel damper by changing the geometry of the steel plates, as shown in Figure 6(c). The multiple point yields will occur in the plates, and better energy-dissipation effect can be achieved, but the stress concentration is obvious and the yield area is small; the utilization ratio of steel is not high enough.

The main reason for the shortage of the above steel plate dampers is that the determination of the hollow forms mainly depends on engineering experience, but the explicit optimization objectives and solid theoretical support are not adequately studied, so the corresponding hollow forms are not optimal. Therefore, it is necessary to carry out a comprehensive optimization for external shape and hollow form under the guidance of the topology optimization theory.

Structural topology optimization mainly refers to the optimization of structural form, also known as the shape optimization. The goal of topology optimization is to find the optimal material distribution scheme of the structure under the given design domain, constraint condition, and loading. In the traditional topology optimization method, the optimization criterion method is generally used as the basic solution method, and the "maximum stiffness" is selected as

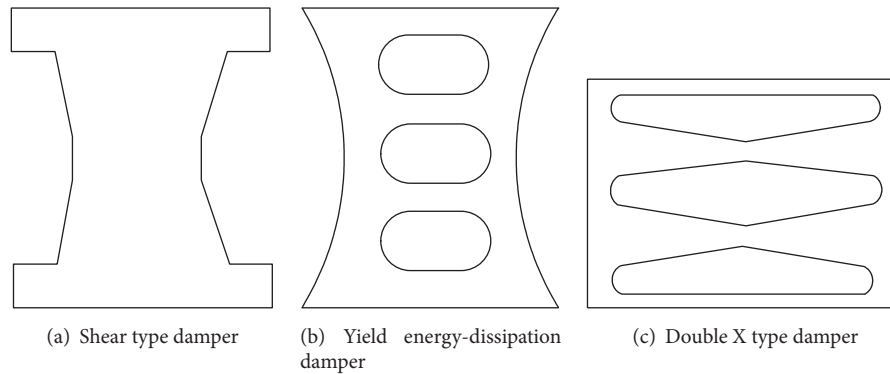


FIGURE 6: The hollow form of steel plate.

the optimization objective to obtain the maximum stiffness under the designated volume constraint. However, only the structural elastic analysis can be carried out in the process of the optimization for “maximum stiffness,” and the stress state of the material is not fully considered, so the stress distribution is not uniform even in the optimal solution. Hence, the actual energy-dissipation capacity of the damper scheme obtained by the above topology optimization method may not be optimal, and it is significant to realize comprehensive optimization by combining other optimization objectives [16–21].

As a kind of basic structural optimization design method, full stress design is widely accepted and used in the structural optimization analysis. The stress of most parts of the material can reach the allowable value under designated load by the full stress design method, so the material is fully utilized and the full stress state can be used as the optimization objective of the structural topology optimization design. The full stress design method can solve the problem of elastic-plastic analysis, but the disadvantage is that it is usually applied to the optimal design of statically determinate structure under static load, so it is not a perfect method also [22–24]. In conclusion, if “maximum stiffness” and “full stress state” are both used as the optimization objectives, after a number of iterations and modifications, the performance of the material can be fully utilized under the condition of large stiffness and the optimum balance of stiffness and full stress can be achieved, so that a more comprehensive optimization scheme can be obtained. Therefore, a topology optimization method based on full stress is proposed and applied to the shape optimization of steel plate in order to enable the low yield point steel plate damper that has the optimal hysteretic behavior and energy-dissipation capacity.

For general topology optimization analysis software, the “maximum stiffness” and “full stress state” can be used as the optimization objective alternately, and the double optimization results for specified volume reduction ratio are obtained, and then the optimization results of different volume reduction rates are compared to determine the final optimization scheme. The specific optimization process is shown in Figure 7.

3.2. Optimization Model and Results. In this study, shape optimization of the combined low yield point steel plate is executed according to the design flow of shape topology optimization and optimization philosophy based on the full stress. Based on the double X model proposed in paper [10] and the deficiency of its shear capacity, an interior optimized damper form is presented, as shown in Figure 8(a). In addition, since the material utilization rate of the unilateral optimization model in paper [14] is not the maximum, a boundary optimized damper model is presented, as shown in Figure 8(b). Furthermore, the model proposed in paper [15] is improved and the ellipse optimized model is proposed to overcome the deficiency of easy buckling out of the plane, as shown in Figure 8(c). The double optimization on the initial shape of three types of dampers in Figure 8 is carried out. The length of each model is 350 mm, the width is 200 mm, and the thickness is 20 cm.

At first, the finite element model of the interior optimized damper is established, as shown in Figure 8(a), and the bottom of the model is fixed and horizontal load is applied on the top end. Secondly, the model shape topology optimization design for the specified volume reduction rate is carried out, and the final stress nephogram is obtained, as shown in Figure 9(a). If the maximum stress distribution is uniform or the colors of the stress nephogram are close, it can be considered that the model is close to the full stress state and the current model is determined as the final optimization scheme for the specified volume reduction rate. Otherwise, the region or the volume of lowest stress should be weakened appropriately and the damper model should be modified, as shown in Figure 9(b). Then the topology optimization is carried out again, until the stress distribution of the model reaches full stress state, namely, the optimal size is obtained for this volume reduction ratio, as shown in Figure 9(c). Finally, the optimization results and the overall effect of the model under various volume reduction conditions are generally considered, and the final optimization scheme is determined, as shown in Figure 9(d).

According to the flow chart in Figure 5 and the double optimization process of interior optimized damper, the final scheme of the boundary optimized damper model can be

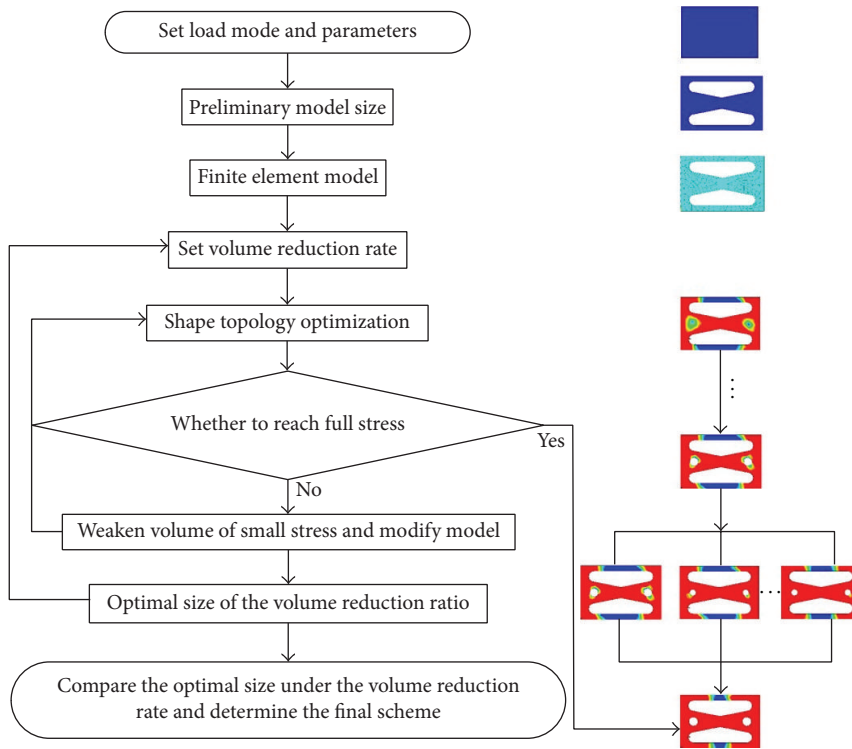


FIGURE 7: Optimization process.

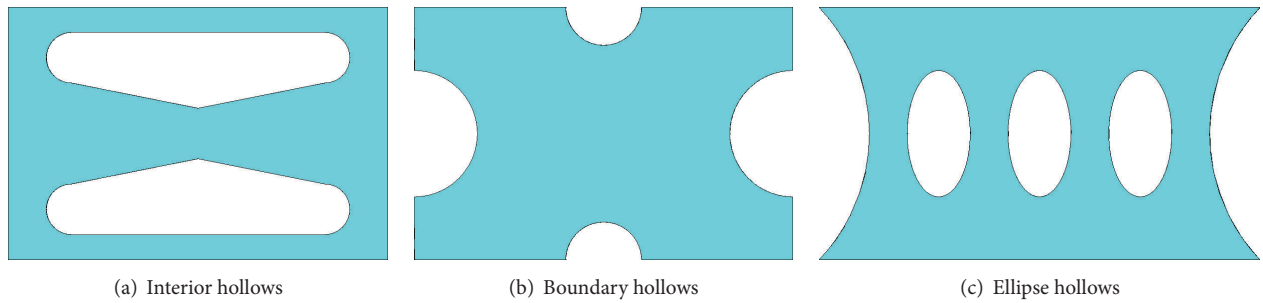


FIGURE 8: The initial form of damper.

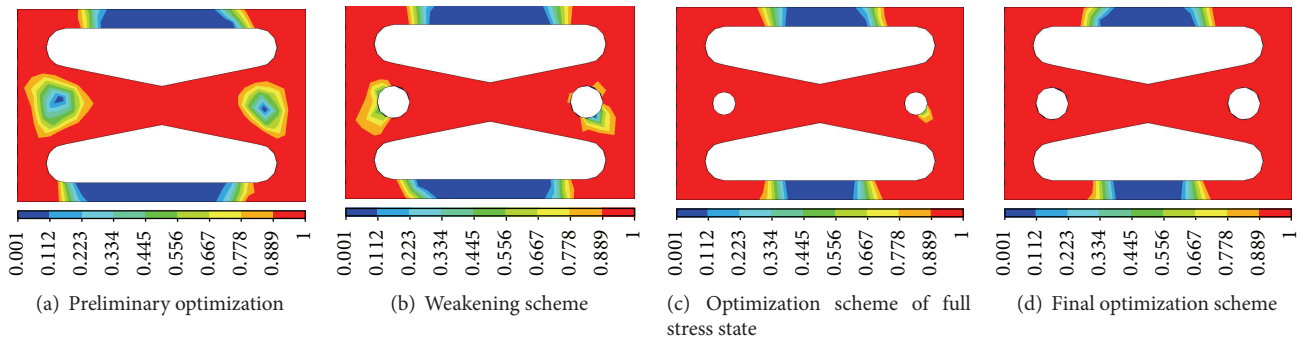


FIGURE 9: Optimization process of interior optimized model.

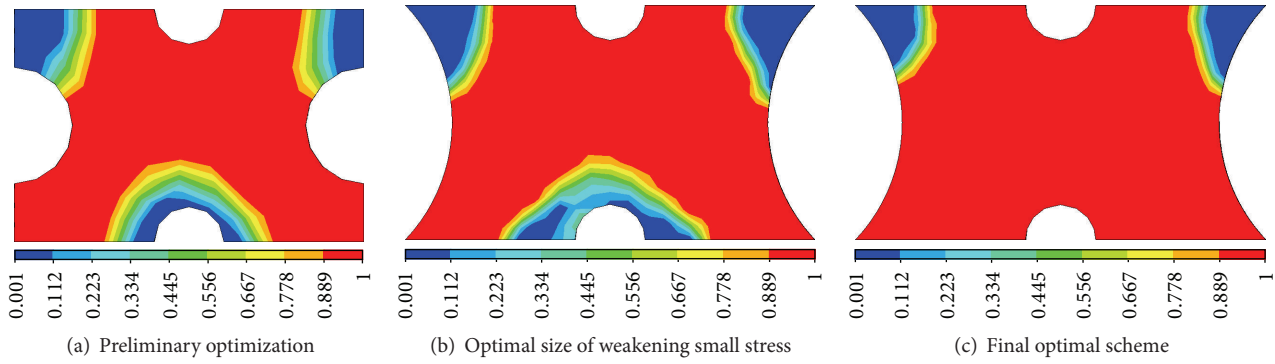


FIGURE 10: Optimization process of boundary optimized model.

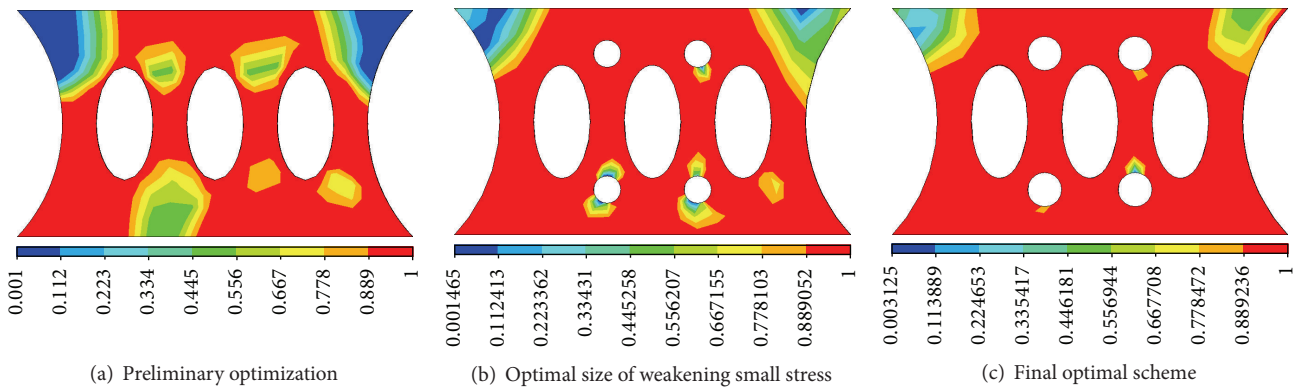


FIGURE 11: Optimization process of ellipse optimized model.

obtained, as shown in Figure 10. In addition, the optimal result of the ellipse optimized model is shown in Figure 11. The final dimension charts of all the optimized dampers are shown in Figure 12.

4. Performance Simulation of Combined Dampers

4.1. Performance Comparison of Different Shape Dampers. After the optimal forms of these dampers are determined, it is necessary to carry out a more intensive elastic-plastic analysis to further verify the energy-dissipation performance of the dampers. The finite element models of different types of combined low yield point steel plate dampers are established, as shown in Figure 5. The first kind of plate is made in Q345 steel, and the second kind of plate is made in LY160 steel. The top end of the model is fixed, and the low cyclic loading is applied to the bottom. The loading mode is variable amplitude loading according to displacement, as shown in Figure 13. The overall hysteretic curves of the three models are shown in Figure 14. The stress nephograms of Q345 steel plate and Q160 steel plate with different forms are shown in Figures 15 and 16, respectively.

It can be seen from the simulation results and hysteresis curves that the yield shearing force of the interior optimized damper is smaller and the deformability is outstanding.

Furthermore, the hysteretic curve of the boundary optimized damper model is fullest, and the initial stiffness is maximum, so this model has excellent energy-dissipation capacity.

It can be seen from the stress nephograms that the stress distribution of the interior optimized damper is relatively homogeneous but the stress level is rather low. On the contrary, the stress level of boundary optimized damper is high and the stress distribution is also homogeneous, so the full stress design criteria are ideally realized. In addition, the stress concentration of the ellipse optimized model is obvious, and the utilization rate of material is lowest.

The skeleton curves of different combined low yield point steel plate dampers under cyclic loading are shown in Figure 17. Three kinds of dampers are in the elastic stage before the displacement is less than 0.05 mm. After the displacement increases to 0.1 mm, all the dampers entered into the yield stage. Under the action of the same force, the displacement of the boundary optimized damper is minimum, and its initial stiffness is significantly larger than that of the other two dampers. It is obvious that the ductility and the aseismic capability of the boundary optimized damper is superior and the bearing capacity and the initial stiffness of main structure can be effectively improved if this damper is applied.

In conclusion, the interior optimized damper is suitable for the engineering structures such as large-span spatial structure and workshop structures, which needs the dampers to resist large deformation. Because the energy-dissipation

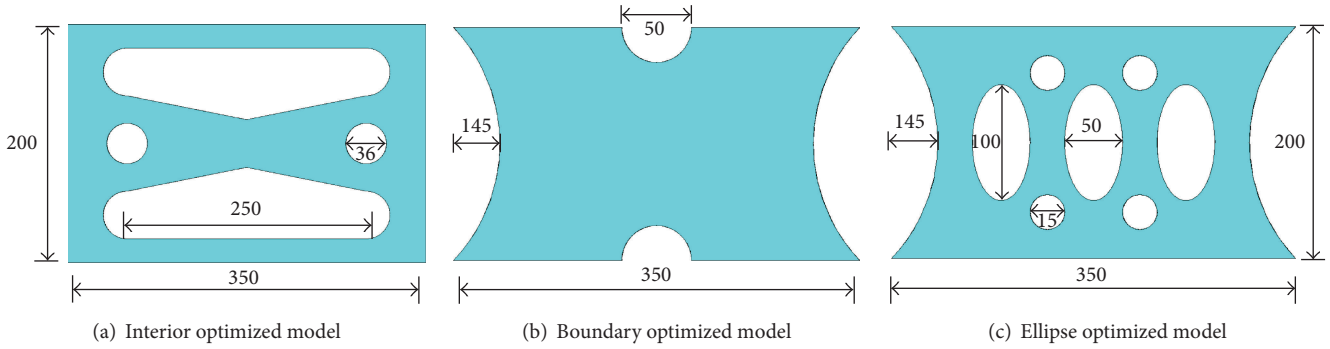


FIGURE 12: Final optimized size (unit: mm).

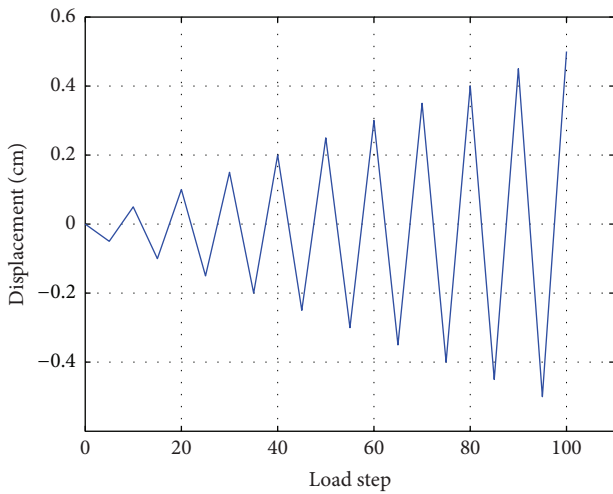


FIGURE 13: Loading mode.

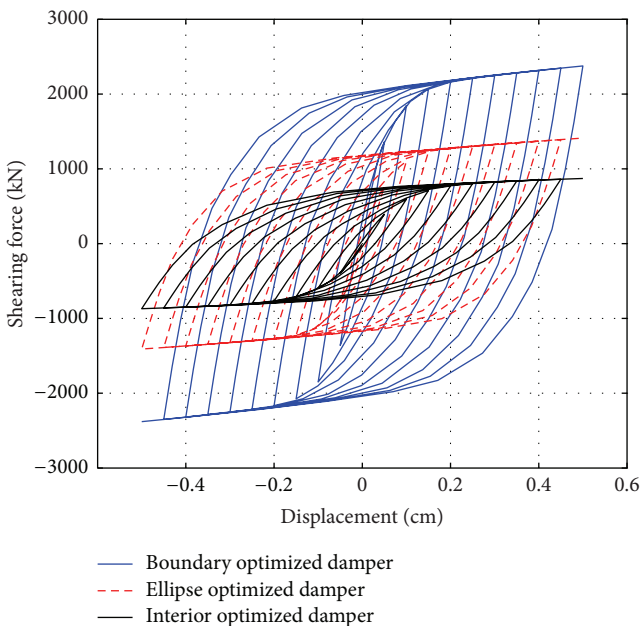


FIGURE 14: Comparison of hysteresis curves.

capacity of the boundary optimized damper is strong and the comprehensive performance is optimal, it is applicable for common structures. Since the ellipse optimized damper may lead to device failure due to stress concentration, it is not recommended for normal structures.

To compare the energy-dissipation capacity of different types of dampers in more explicit parameters, Park-Ang damage index [25] and the equivalent hysteretic damping ratio calculation model are used to evaluate the performance under low cyclic loading.

As a classic damage index, Park-Ang index can be calculated as follows:

$$DI = \frac{x_m}{x_{cu}} + \beta \frac{E_h}{F_y x_{cu}}, \quad (1)$$

where x_{cu} is the limit displacement under monotonic loading; F_y is the yield strength; x_m and E_h are the actual maximum deformation and cumulative hysteretic energy dissipation, respectively. β is the energy-dissipation factor of component, and the value is set as 0.15 in this study.

The equivalent hysteretic damping ratio ξ can be calculated as follows [26, 27]:

$$\xi = \frac{E_D}{4\pi E_S}, \quad (2)$$

where E_D is the hysteretic dissipated energy under structural single cycle motion, which is equal to the envelope area of the hysteresis loop, and E_S is maximum strain energy.

The Park-Ang damage index curves and the equivalent hysteretic damping ratios of each damper under different displacement are calculated, as shown in Figures 18 and 19, respectively. It can be seen that the energy-dissipation capacity of each damper is close at the initial stage, and the energy-dissipation capacity gradually enlarges with the increase of deformation. At the later stage of loading, the equivalent damping ratio of the boundary optimized damper and the ellipse optimized model grows faster, which indicates that the corresponding energy-dissipation capacity rises rapidly, and the growth rate of the energy-dissipation capacity of the interior optimized damper is slightly lower.

4.2. Adjustability Verification of Combined Dampers. From the above analysis, it is assumed that the boundary optimized

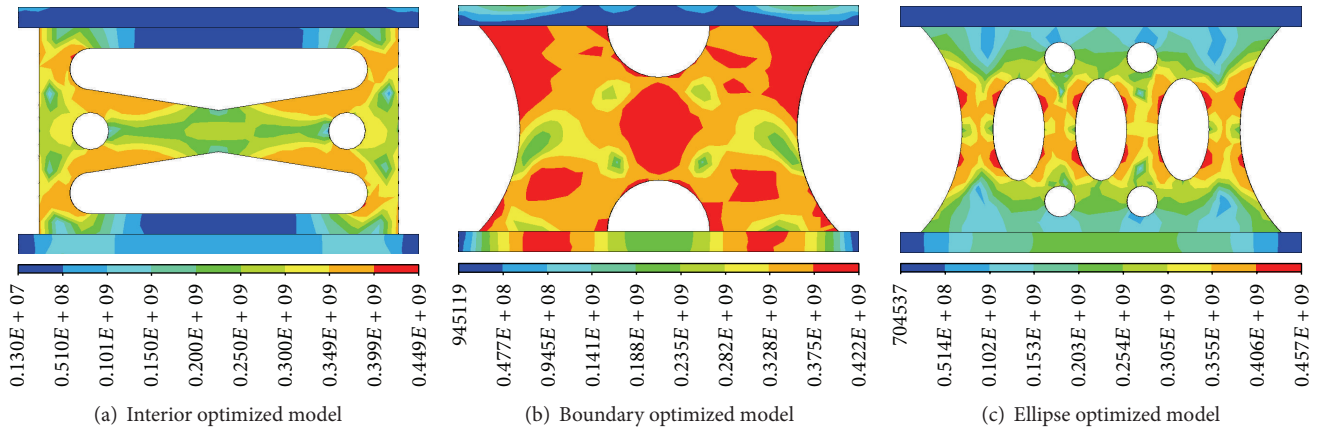


FIGURE 15: Stress nephogram of Q345 steel plate.

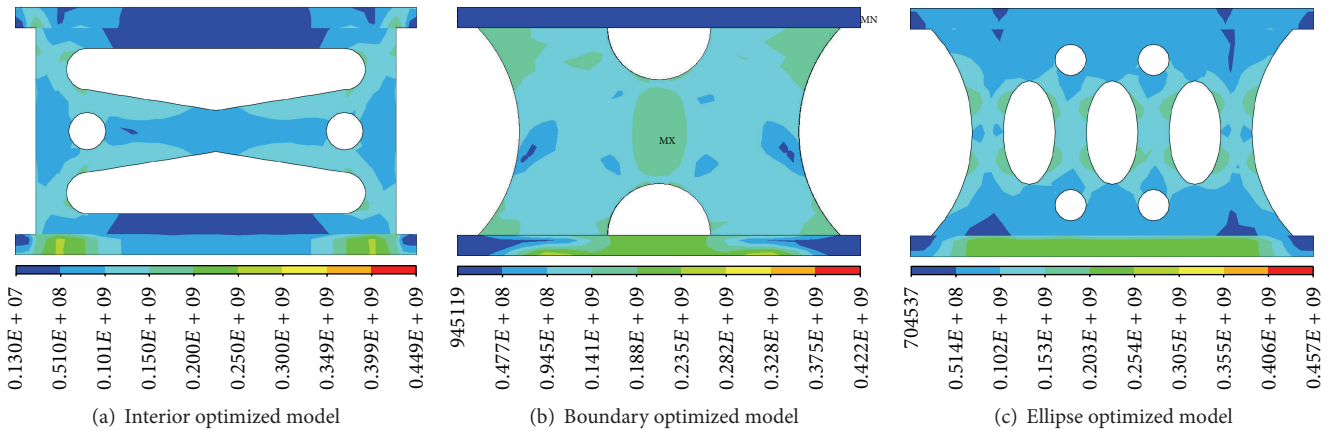


FIGURE 16: Stress nephogram of LY160 steel plate.

damper and the interior optimized damper have excellent energy-dissipation capacity and stability. In order to verify the adjustability of these combined dampers, the effect of different materials ratio on the performance of the damper is studied.

Three schemes are designed to analyze the performance of the combined dampers, and 5 steel plates with the same thickness are adopted to assemble the dampers; only the material properties and the proportion of steel plates are different. For the first scheme, all the 5 steel plates are made in LY160, and Q345 steel plates are used for the second scheme. In the third scheme, the damper is alternatively assembled by 3 pieces of Q345 plates and 2 pieces of LY160 plates. The finite element software is used to simulate the damper models, and the dampers are applied to low cyclic loading. The hysteresis curves of the interior optimized damper and the boundary optimized damper is shown in Figures 20 and 21, respectively. From the comparison of the hysteresis curves, it is evident that the yield stress of the third scheme is between the corresponding values of the first scheme and the second scheme. Hence, the yield stresses of the combined dampers can be adjusted by changing the combination proportion of different materials.

5. Energy-Dissipation Effect of Combined Dampers on Frame Structure

The characteristics such as large initial stiffness and strong energy dissipation of the boundary optimized damper and the interior optimized damper are validated by the simulated quasistatic test, but the integrated performance is necessary to be verified if the two types of dampers are used in the engineering structures. In this following study, the finite element software ANSYS is used for simulation analysis, and the simulation models are established by parametric language APDL. The combined damper is installed on a steel frame with one story and one span, as shown in Figure 22.

The height of the frame is 1.5 m and the span is 3.0 m. The dimension of the column section is 200 mm × 200 mm, the dimension of the beam section is 200 mm × 180 mm, and the dimension of the diagonal brace is 100 mm × 200 mm. The dimensions of the dampers are the same as sizes shown in Figure 12, and the compositions of the combined dampers are alternatively assembled by 3 pieces of Q345 plates and 2 pieces of LY160 plates. In order to ensure the accuracy of analysis and simplify the analysis process, the beam, the columns, and the dampers are modeled by solid element, and

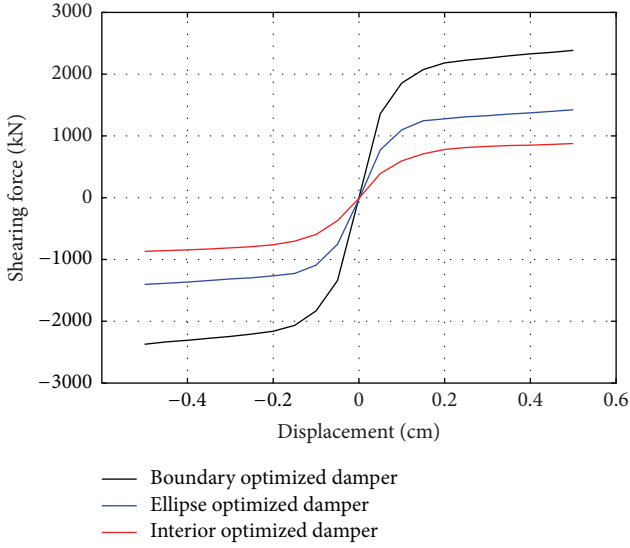


FIGURE 17: Skeleton curves of different dampers.

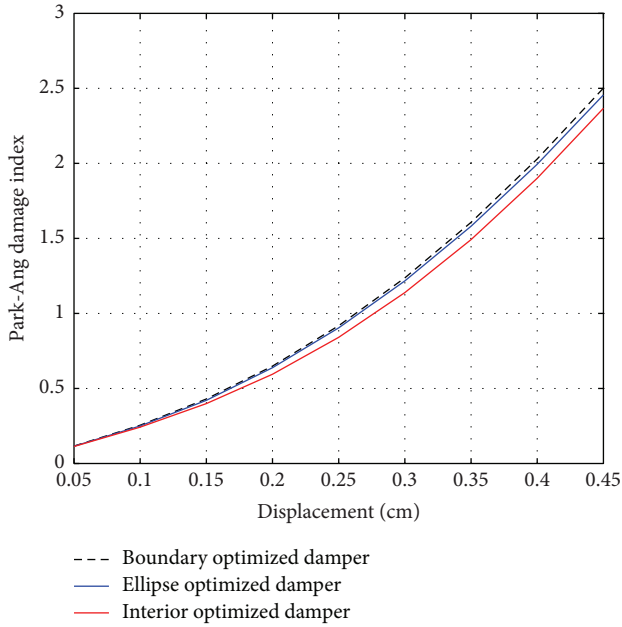


FIGURE 18: Comparison of damage index.

the diagonal braces are simulated by beam element. In the process of model building, the column bottoms have fixed constraints and the cyclic displacement loading is applied on the column top, as shown in Figure 12. The detailed models of the dampers in the frame and the connection connected with the beam and the damper are shown in Figure 23.

The displacement response of the damper under each loading step is extracted and the displacement history is obtained, as shown in Figure 24. The displacements of the two types of dampers are equal in the loading steps 0–130 because the structures are still in the elastic state and the equivalent stiffness of the dampers is identical. After

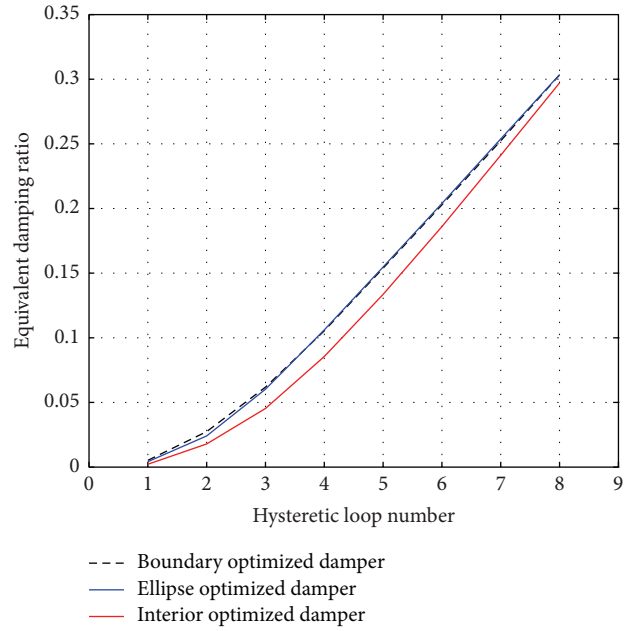


FIGURE 19: Comparison of equivalent damping ratio.

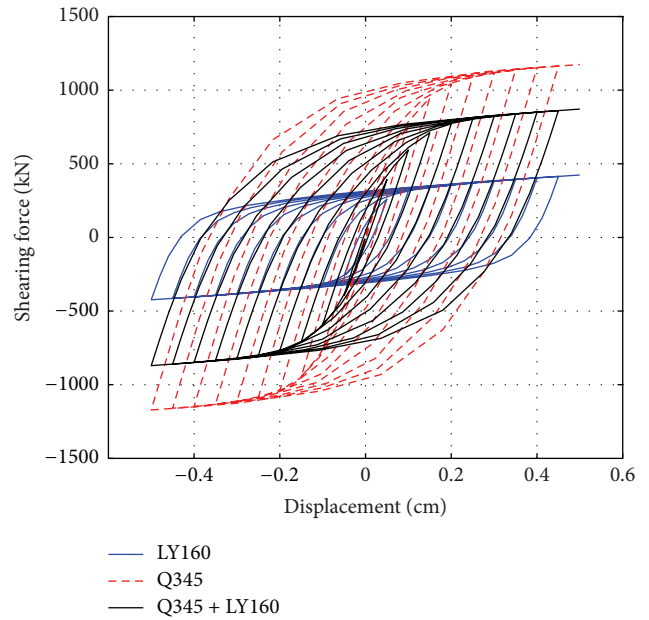


FIGURE 20: Hysteresis curves of interior optimized damper.

loading step 130, the boundary optimized damper can reduce the structural displacement more effectively because damping starts to work.

The base shear of the frame structure is extracted and the force history is obtained, as shown in Figure 25. It can be seen that the base shear of the frame structure with boundary optimized damper is significantly greater than the corresponding values of structure with interior optimized damper or

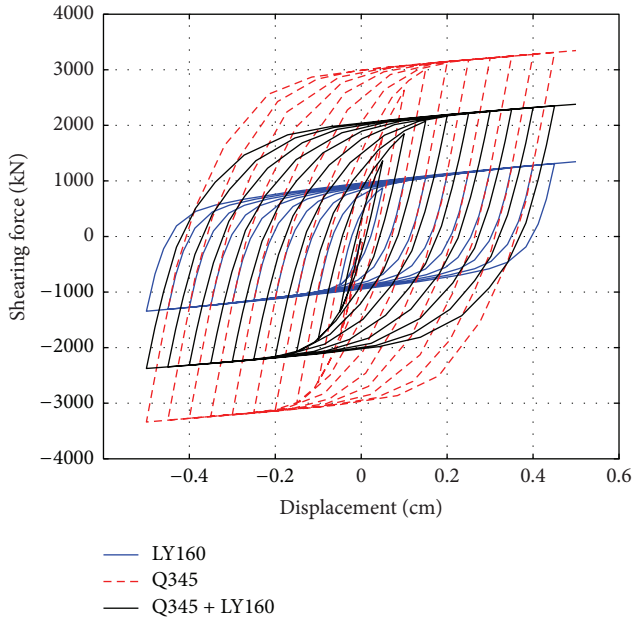


FIGURE 21: Hysteresis curves of boundary optimized damper.

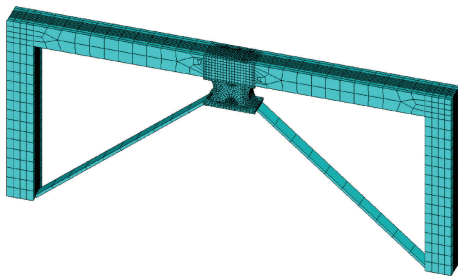


FIGURE 22: Damper model in the frame.

the uncontrolled structure, which indicates that the boundary optimized damper has better energy-dissipation capacity and obviously improves the structural resistance.

The strain nephogram and hysteretic curves of the dampers are shown in Figures 26 and 27, respectively.

It indicates that the nephogram color of the boundary optimized damper is homogeneous and the hysteretic curve is fuller, and the effect of energy dissipation is obvious. The comparison of dissipated energy of each hysteretic loop is shown in Figure 28, and the actual dissipated energy of the boundary optimized damper and the interior optimized damper is 1.349×10^{10} N·m and 9.383×10^9 N·m, respectively. All the results indicate that the energy-dissipation capacity of the boundary optimized damper is more prominent. Hence, the combined low yield point steel plate damper with boundary optimized shape is recommended in practical engineering applications.

It indicates that the nephogram color of the boundary optimized damper is homogeneous and the hysteretic curve

is fuller, and the effect of energy dissipation is obvious. The comparison of dissipated energy of each hysteretic loop is shown in Figure 28, and the actual dissipated energy of the boundary optimized damper and the interior optimized damper is 1.349×10^{10} N·m and 9.383×10^9 N·m, respectively. All the results indicate that the energy-dissipation capacity of the boundary optimized damper is more prominent.

Though it is verified that the optimized dampers have the superior performances such as large initial stiffness and strong energy-dissipation capacity by quasistatic simulation, the integrated performance is still necessary to be verified if the two types of dampers are used in multilayer frame structures which are subjected to earthquakes. Since the computational efficiency of ANSYS for nonlinear time-history analysis is lower, finite element analysis software ETABS is used to simulate the structural nonlinear responses under earthquake. At first, the same one-layer frame as the previous model of ANSYS is established by ETABS, and the damper element is adopted as the brace connection in the model. By appropriately setting the property parameters of the connection element, the hysteresis curve of the connection element under low cyclic loading is close to that of ANSYS, and the results are shown in Figure 29, so the damping parameter in ETABS is assumed to be accurate. For the final optimal results, the damping exponent of the edge optimized damper is 2.00, and the damping is 3000 kN·s/m. The damping exponent of the interior optimized damper is 1.85, and the damping is 3500 kN·s/m.

In order to study the damping performance of the multilayer structure with optimized dampers, a one-dimensional and three-layer steel frame with boundary optimized dampers or interior optimized dampers is established by ETABS, respectively. Besides, the uncontrolled frame model is established as a reference structure, and there are no dampers but only the same braces on it. The corresponding plane graphs of the frame structure are shown in Figure 30. The height of the steel frame is 3.6 m, and the span is 6.0 m. The frame column cross section is H400 × 300 × 25 × 25 (mm) and the beam section size is H250 × 150 × 20 × 12 (mm). The diagonal brace section size is H150 × 150 × 12 × 8 (mm). The yield strength of all the components is 235 MPa. The dampers are simulated according to the previous parameters. The site type is soft rock and the seismic fortification intensity is 8.0. The fundamental period of the uncontrolled frame and controlled frame is 0.194 s and 0.197 s, respectively.

In order to study and compare the seismic performance of these three kinds of structures, a series of typical one-dimensional earthquake waves which include El Centro earthquake, Taft earthquake, and Michoacán earthquake are selected because these ground motion records were collected from hard soil and the predominant periods are close to the structural period; then nonlinear time-history analysis are carried out. To consider the effect of ground motion amplitude on the damage degree, the peak ground motion in the horizontal direction is separately adjusted to 0.11 m/s², 0.22 m/s², and 0.51 m/s², so as to adjust the earthquake waves as the excitation for small earthquake, moderate earthquake, and severe earthquake, respectively.

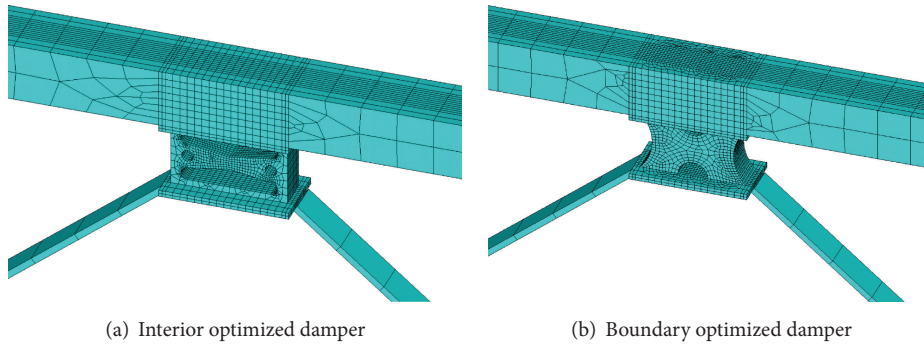


FIGURE 23: Optimized damper connected with beam.

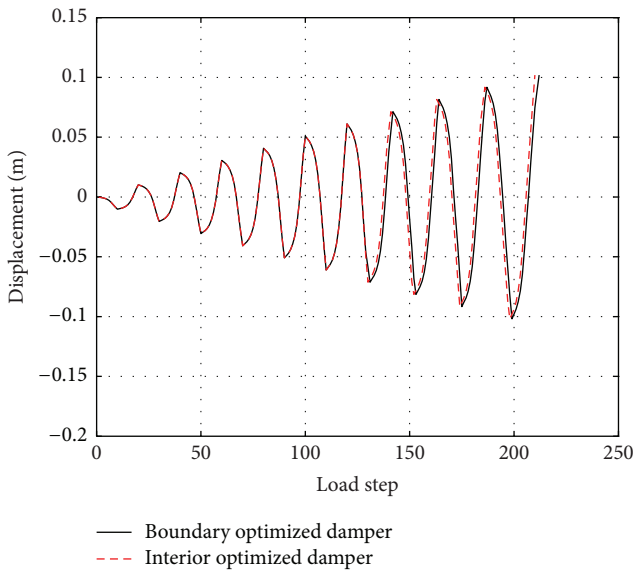


FIGURE 24: Comparison of displacement history in frame.

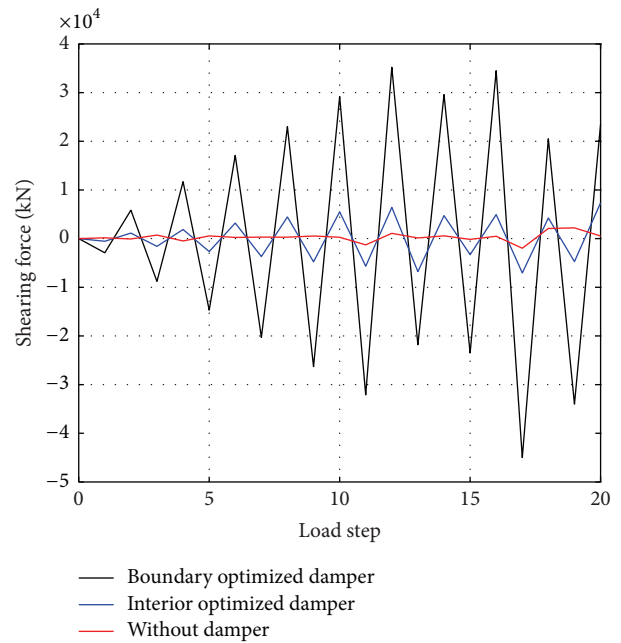


FIGURE 25: Comparison of force history.

The top displacements and the top accelerations of various structures which are subjected to earthquakes with different amplitudes are extracted and analyzed. The specific results are shown in Table 2. In this study, the peak damping ratio (PDR) refers to the ratio between the differences of the absolute maximum responses before and after vibration control and the absolute maximum structural response before control. The envelope damping ratio (EDR) refers to the ratio between the differences of the sum of absolute responses before and after vibration control and the sum of absolute response before control. It should be noted that plan A means the structure with edge optimized dampers and plan B means the structure with interior optimized dampers. In addition, the top displacement history curves of various structures which are subjected to El Centro wave with different amplitudes are shown in Figures 31–33.

It can be seen from Table 2 and Figures 31–33 that the damping effects of the edge optimized damper and

the interior optimized damper are both superior, and the former has a stronger damping capacity. Furthermore, the inelastic energy-dissipation capacity of the damper is gradually highlighted with the increase of peak ground acceleration, and the damping effect is more obvious. In summary, the damping performance of the low yield point metal damper is excellent and stable, and it can significantly improve the structural seismic capacity. In practical engineering applications, the boundary optimized damper is still the preferred option.

In view of the adoption for practical applications, a design procedure of the combined low yield point steel plate damper is finally proposed based on the above analysis. According to the concept of performance based seismic

TABLE 2: Results of damping effect.

Earthquake	Damping effect							
	PDR of top displacement (%)		PDR of top acceleration (%)		EDR of top displacement (%)		EDR of top acceleration (%)	
	Plan A	Plan B						
El Centro								
Small	23.50	13.83	55.17	42.39	20.69	14.99	81.30	76.57
Medium	29.43	21.31	61.50	49.93	30.76	21.82	85.31	81.19
Large	66.88	48.98	67.23	58.13	62.53	42.48	88.29	84.90
Taft								
Small	49.37	32.74	69.64	68.78	52.34	47.30	71.00	65.07
Medium	49.56	43.04	84.78	74.76	54.46	51.61	87.67	80.71
Large	74.63	60.68	89.96	82.26	78.14	66.64	91.84	85.60
Michoacán								
Small	68.29	64.63	61.18	51.29	60.52	55.82	78.10	73.24
Medium	74.39	70.43	66.87	58.19	68.74	64.67	83.11	76.91
Large	79.95	75.23	80.74	61.49	77.21	65.09	91.23	84.46

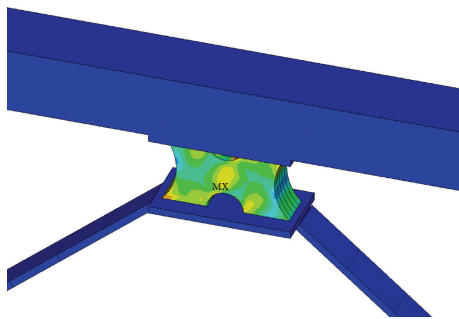
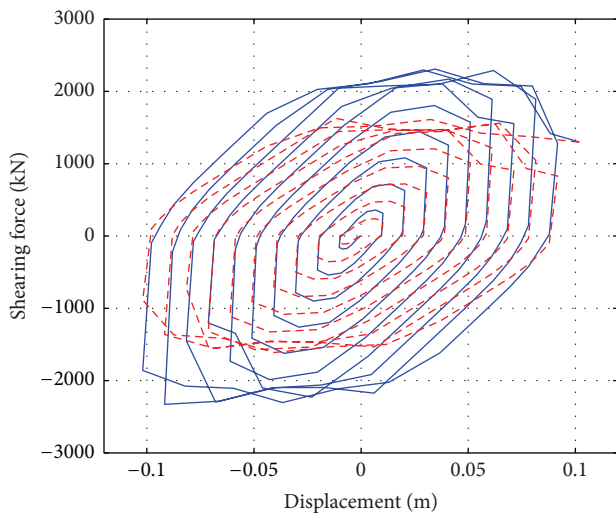


FIGURE 26: Strain nephogram of boundary optimized damper.



— Boundary optimized damper
 - - - Interior optimized damper

FIGURE 27: Hysteretic curves of damper.

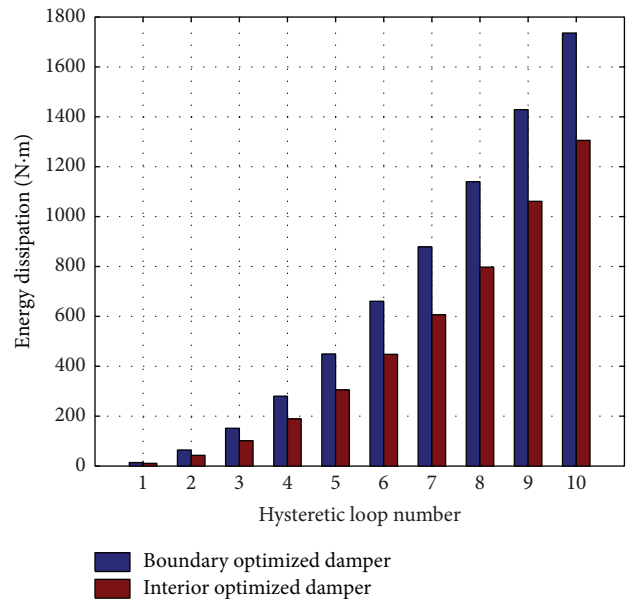


FIGURE 28: Comparison of energy dissipation of different dampers.

design, a generalized displacement-based design procedure of hysteretic damped braces has been proposed by Mazza and Vulcano [28, 29], which proportions hysteretic damped braces to attain a designated performance level of an existing framed structure. On the basis of this research, the main steps of the proposed design procedure of frame with combined steel plate damper are summarized below:

- (1) Carry out pushover analysis of the unbraced frame and definition of an equivalent single degree of freedom system to evaluate the equivalent viscous damping due to hysteresis loading.

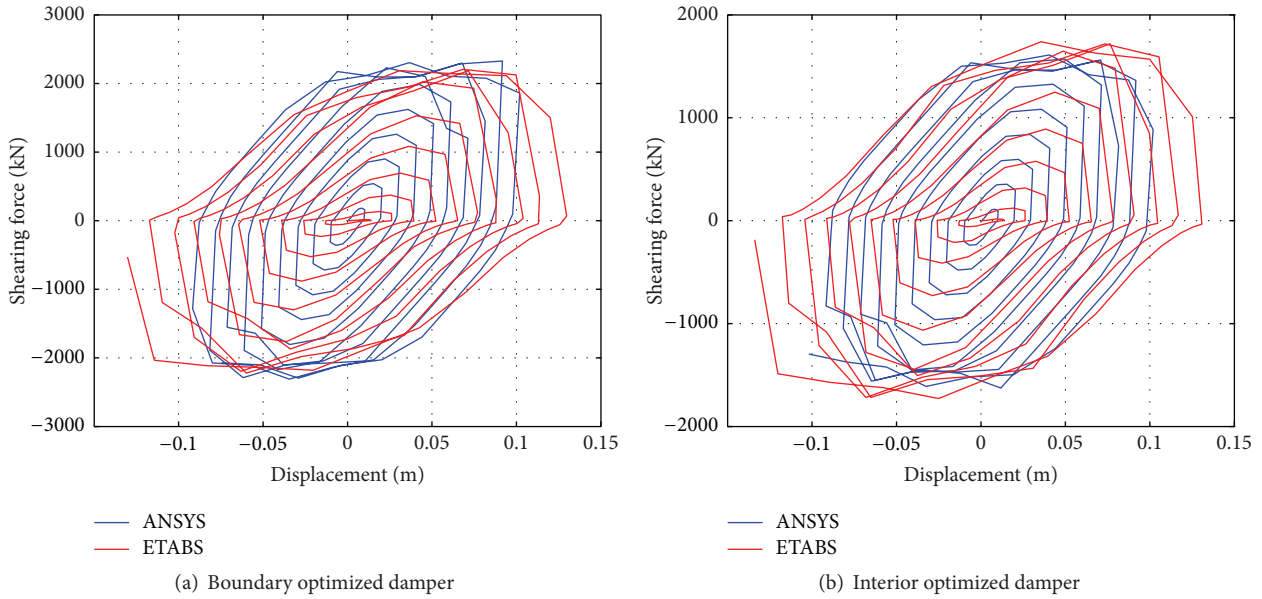


FIGURE 29: Comparison of hysteresis curves using ANSYS and ETABS.

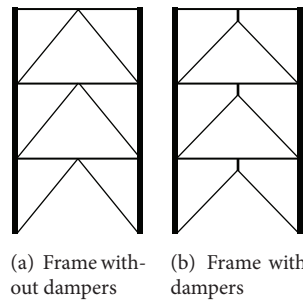


FIGURE 30: Plane graph of uncontrolled frame and controlled frame.

- (2) Determine the equivalent viscous damping due to hysteresis loading of the damped braces according to the integral ductility demand.
- (3) Determine the shape of the dampers based on topology optimization, and both “maximum stiffness” and “full stress state” are used as the optimization objectives.
- (4) Determine the equivalent viscous damping of the frame with damped braces.
- (5) Determine the effective stiffness of the equivalent damped brace based on effective period.
- (6) Determine the effective strength properties of the equivalent damped brace based on effective yield base shear.
- (7) Carry out design of the hysteretic damped braces of the controlled frame considering special demands.

6. Conclusion

In order to solve the deficiencies such as high yield point and low adjustability of the traditional low yield point plate steel damper, three kinds of combined low yield point plate steel dampers which consist of low yield point steel plates and common steel plates in different proportions are proposed. Based on the concept of “maximum stiffness” and “full stress state,” the dampers with interior hollows, boundary hollows, and ellipse hollows are optimized by alternating topology optimization method, and three types of combined low yield point steel plate dampers are obtained, which at the same time meet the optimization objectives “maximum stiffness” and “full stress state.”

Finite element models of the optimized various combined steel plate dampers are analyzed. The results show that the interior optimized damper is suitable for the structure with large deformation, and the energy-dissipation capacity of the boundary optimized damper is excellent and

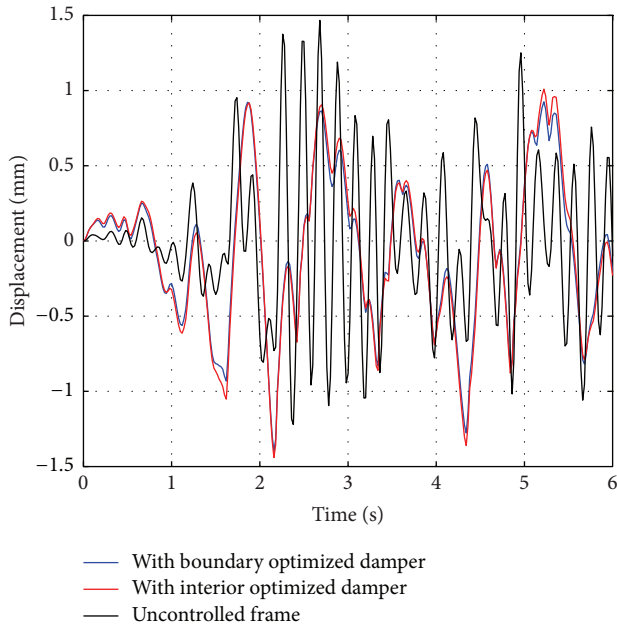


FIGURE 31: Time-history curve under small earthquake.

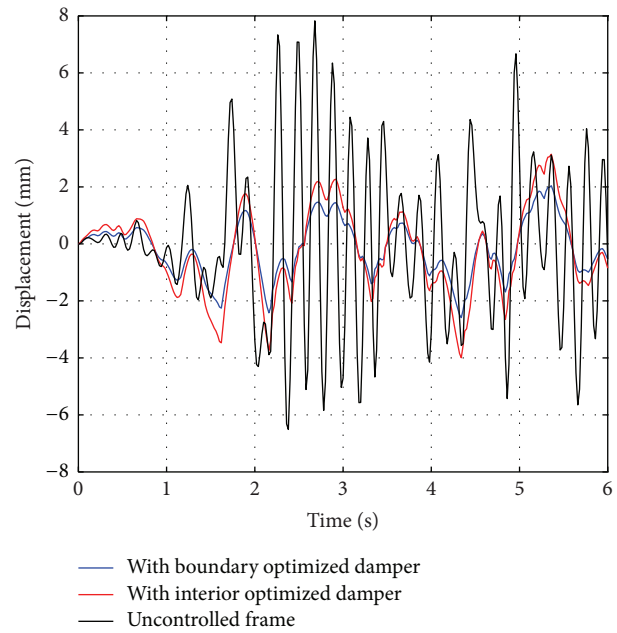


FIGURE 33: Time-history curve under large earthquake.

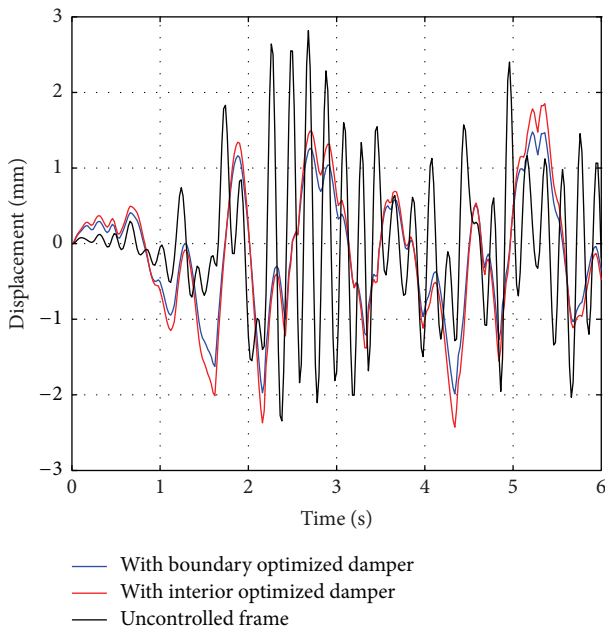


FIGURE 32: Time-history curve under medium earthquake.

the comprehensive performance is optimal. Two kinds of optimization models with different material ratios are studied by numerical simulation, and it is verified that the yield stress of combined dampers can be regulated through changing material proportion.

In order to verify the actual damping effect on the structure installed combined dampers, the seismic capacity of a steel frame structure with different types of dampers is studied by simulation analysis. The results indicate that the boundary optimized damper has better energy-dissipation

capacity than the interior optimized damper. In practical engineering applications, the boundary optimized damper is recommended.

Competing Interests

The authors declare that there are no competing interests regarding the publication of this paper.

Acknowledgments

This work is partially supported by Natural Science Foundation of China under Grants nos. 51478024 and 51108009 and Foundation of Beijing Key Lab of Earthquake Engineering and Structural Retrofit under Grant no. USDE201403.

References

- [1] C. J. Zhang, A. Q. Li, and M. Zhao, "Summary of research on and applications of passive energy dissipation systems of mild steel damper," *Industrial Construction*, vol. 36, no. 9, pp. 17–21, 2006.
- [2] J. M. Kelly, R. I. Skinner, and A. J. Heine, "Mechanisms of energy absorption in special devices for use in earthquake-resistant structures," *Bulletin of the New Zealand Society for Earthquake Engineering*, vol. 5, no. 3, pp. 63–88, 1972.
- [3] A. S. Whittaker, V. V. Bertero, C. L. Thompson, and L. J. Alonso, "Seismic testing of steel plate energy dissipation devices," *Earthquake Spectra*, vol. 7, no. 4, pp. 563–604, 1991.
- [4] K.-C. Tsai, H.-W. Chen, C.-P. Hong, and Y.-F. Su, "Design of steel triangular plate energy absorbers for seismic-resistant construction," *Earthquake Spectra*, vol. 9, no. 3, pp. 505–528, 1993.
- [5] L.-D. Tirca, D. Foti, and M. Diaferio, "Response of middle-rise steel frames with and without passive dampers to near-field

- ground motions," *Engineering Structures*, vol. 25, no. 2, pp. 169–179, 2003.
- [6] Y. Zhou and J. Liu, "Experimental study on the behavior of circular ring energy dissipator," *World Information on Earthquake Engineering*, vol. 11, no. 4, pp. 1–7, 1996.
- [7] Y. Zhou and J. Liu, "Experimental study on double circular ring mild steel energy dissipator," *Journal of Earthquake Engineering & Engineering Vibration*, vol. 18, no. 2, pp. 117–123, 1998.
- [8] W.-Y. Zhang, M.-Z. Zhang, and D.-W. Li, "An experimental research on performance and application of a new type of mild steel damper added damping and stiffness (ADAS)," *Journal of Harbin Institute of Technology*, vol. 40, no. 12, pp. 1888–1894, 2008.
- [9] M. Mito, R. Tamura, and K. Shimizu, "Study on seismic design method for building with steel damper (part1)," in *Proceedings of the AIJ Annual Meeting*, 1997.
- [10] G. Li and H. Li, "Study on vibration reduction of structure with a new type of mild metallic dampers," *Journal of Vibration and Shock*, vol. 25, no. 3, pp. 66–72, 2006.
- [11] J. Tian, Z. C. Yan, and J. L. Lu, "Seismic control research of the multi-ribbed slab structure using the ultra-low yield strength steel," *Journal of Vibration and Shock*, vol. 33, no. 5, pp. 160–164, 2014.
- [12] *GB/T 228.1-2010 Metallic Materials Tensile Testing Part 1: Method of Test at Room Temperature*, China Standards Press, Beijing, China, 2011.
- [13] S.-T. Xing and X. Guo, "Study on mechanical behavior and effectiveness of a new type of mild steel damper," *Journal of Earthquake Engineering and Engineering Vibration*, vol. 23, no. 6, pp. 179–186, 2003.
- [14] K. Deng, P. Pan, J. Sun, J. Liu, and Y. Xue, "Shape optimization design of steel shear panel dampers," *Journal of Constructional Steel Research*, vol. 99, pp. 187–193, 2014.
- [15] Q. Wang and L. G. An, "Analysis on vibration suppression of a new type of planar steel damper," *China Civil Engineering Journal*, vol. 43, pp. 341–344, 2010.
- [16] Y. Liu and M. Shimoda, "Shape optimization of shear panel damper for improving the deformation ability under cyclic loading," *Structural and Multidisciplinary Optimization*, vol. 48, no. 2, pp. 427–435, 2013.
- [17] M. Ohsaki, *Optimization of Finite Dimensional Structures*, CRC Press, 2010.
- [18] P. Pan, M. Ohsaki, and H. Tagawa, "Shape optimization of H-beam flange for maximum plastic energy dissipation," *Journal of Structural Engineering*, vol. 133, no. 8, pp. 1176–1179, 2007.
- [19] G. N. Vanderplaats, "Multidiscipline design optimization," *Applied Mechanics Reviews*, vol. 41, no. 6, pp. 257–262, 1988.
- [20] U. Kirsch, M. Bogomolni, and I. Sheinman, "Efficient procedures for repeated calculations of the structural response using combined approximations," *Structural and Multidisciplinary Optimization*, vol. 32, no. 6, pp. 435–446, 2006.
- [21] Y. Liu and M. Shimoda, "Shape optimization of shear panel damper for improving the deformation ability under cyclic loading," *Structural & Multidisciplinary Optimization*, vol. 48, no. 2, pp. 427–435, 2013.
- [22] X. Huang and Y. M. Xie, "A new look at ESO and BESO optimization methods," *Structural & Multidisciplinary Optimization*, vol. 35, no. 1, pp. 89–92, 2008.
- [23] Q. M. Liu, "A design method of rib distribution for thin plate structure based on the full stress rule," *Machinery Design & Manufacture*, vol. 1, no. 1, pp. 23–24, 2007.
- [24] X. H. Ding and L. Cheng, "Topology optimization of full-stressed structures based on SKO method," *China Mechanical Engineering*, vol. 20, no. 15, pp. 1765–1770, 2009.
- [25] Y.-J. Park, A. H.-S. Ang, and Y. K. Wen, "Seismic damage analysis of reinforced concrete buildings," *Journal of Structural Engineering*, vol. 111, no. 4, pp. 740–757, 1985.
- [26] FEMA274, *NEHRP Commentary on the Guidelines for the Seismic Rehabilitation of Buildings*, Federal Emergency Management Agency, Washington, DC, USA, 1997.
- [27] ATC40, *Seismic Evaluation and Retrofit of Concrete Buildings*, ATC, Redwood City, Calif, USA, 1996.
- [28] F. Mazza, "Nonlinear seismic analysis of unsymmetric-plan structures retrofitted by hysteretic damped braces," *Bulletin of Earthquake Engineering*, vol. 14, no. 6, pp. 1311–1331, 2016.
- [29] F. Mazza, M. Mazza, and A. Vulcano, "Displacement-based seismic design of hysteretic damped braces for retrofitting in-elevation irregular r.c. framed structures," *Soil Dynamics and Earthquake Engineering*, vol. 69, no. 2, pp. 115–124, 2015.

Research Article

Experimental Research on High Temperature Resistance of Modified Lightweight Concrete after Exposure to Elevated Temperatures

Ke-cheng He,^{1,2} Rong-xin Guo,^{1,2} Qian-min Ma,^{1,2} Feng Yan,^{1,2}
Zhi-wei Lin,^{1,2} and Yan-Lin Sun³

¹Faculty of Civil Engineering and Mechanics, Kunming University of Science and Technology, Kunming 650500, China

²Key Lab of Yunnan Higher Education Institutes for Mechanical Behavior and Microstructure Design of Advanced Materials, Kunming University of Science and Technology, Kunming 650500, China

³Faculty of Chemical Engineering, Kunming University of Science and Technology, Kunming 650500, China

Correspondence should be addressed to Rong-xin Guo; guorx@kmust.edu.cn

Received 20 February 2016; Accepted 4 May 2016

Academic Editor: Osman Gencel

Copyright © 2016 Ke-cheng He et al. This is an open access article distributed under the Creative Commons Attribution License, which permits unrestricted use, distribution, and reproduction in any medium, provided the original work is properly cited.

In order to improve the spalling resistance of lightweight aggregate concrete at high temperature, two types of modified materials were used to modify clay ceramsite lightweight aggregates by adopting the surface coating modification method. Spalling of the concrete specimens manufactured by using the modified aggregates was observed during a temperature elevation. Mass loss and residual axial compressive strength of the modified concrete specimens after exposure to elevated temperatures were also tested. Concrete specimens consisting of ordinary clay ceramsites and crushed limestone were manufactured as references for comparison. The results showed that the ordinary lightweight concrete specimens and the crushed limestone concrete specimens were completely spalled after exposure to target temperatures above 400°C and 1000°C, respectively, whereas the modified concrete specimens remained intact at 1200°C, at which approximately 25% to 38% of the residual compressive strength was retained. The results indicated that the modified lightweight concrete specimens have exhibited superior mechanical properties and resistance to thermal spalling after exposure to elevated temperatures.

1. Introduction

Lightweight aggregate concrete types are well known for their advantages of being lightweight and fire-resistant and for having high strength. They have wide use in high-rise buildings and large span bridges. Lightweight aggregates, such as pumice, expanded perlite, and clay ceramsite, which are made by burning, naturally have excellent resistance to high temperature [1]. Thus, it is expected that lightweight aggregate concrete types also have high application potential in chimneys, high temperature furnaces, tunnel fireproof layers, and other fire-resistant constructions. Several references claim that the residual mechanical properties of lightweight aggregate concrete types after exposure to high temperatures of 800°C or 1000°C were considerably higher than those of ordinary concrete types [2–7].

However, the spalling resistance of lightweight aggregate concrete types often behaves worse than that of ordinary concrete types in a fire due to the ability of lightweight aggregates to act as water reservoirs for evaporable water [8, 9]. The water in the lightweight aggregates either comes from prewetting of the aggregates, absorption from the fresh concrete, or penetration from the environment [10]. The increased moisture content will lead to both increased pore pressure and an increased temperature gradient during a fire [11]. The higher the moisture content, the higher the spalling probability as the moisture content is greater than a threshold value [12]. Thus, moisture content is the direct factor for the explosive spalling of lightweight aggregate concrete types. If the lightweight aggregate concrete types undergo explosive spalling in fire, their high temperature resistance cannot be fully effective

TABLE 1: Chemical composition and physical properties of slag cement.

Slag cement	Chemical composition: %						Physical properties		
	SiO ₂	CaO	Al ₂ O ₃	Fe ₂ O ₃	MgO	SO ₃	Loss on ignition	Specific gravity	Fineness (45 μm): %
PSA	17.9	54.03	5.26	3.44	1.78	1.7	4.30	3.04	11

TABLE 2: Physical properties of coarse aggregates.

Aggregate type	Bulk density (kg/m ³)	1 h water absorption: %	Cylinder compressive strength (MPa)	Crushing value (2.5 mm): %
LS	1430	0.5	16.57	7.8
LWA	407	14.5	3.07	47.5
PLWA	410	10.8	2.74	/
GLWA	485	9.2	3.19	/

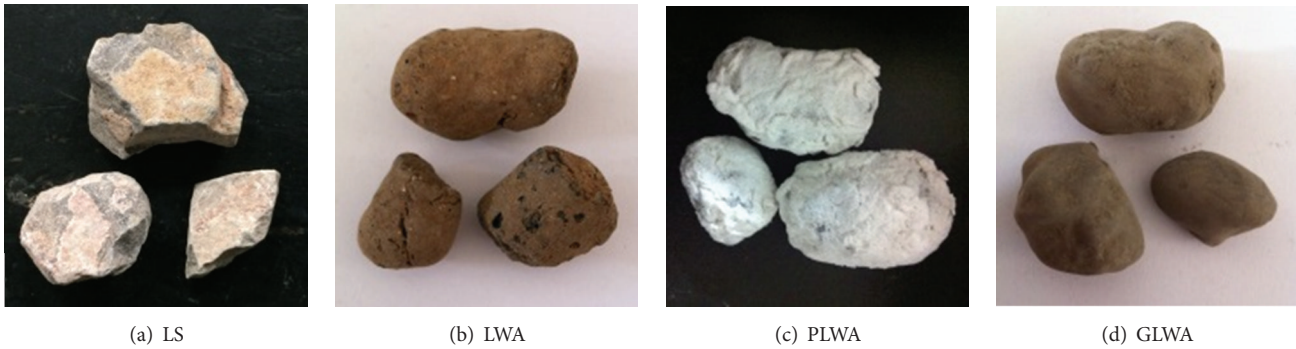


FIGURE 1: Different types of coarse aggregates.

in fire protection, thus limiting their application in the fire protection of the building structure.

In light of the unstable high temperature behavior of lightweight aggregate concrete types, in this study, two types of materials were used to modify clay ceramsite. The modified clay ceramsites were used to manufacture lightweight concrete types. The spalling characteristics, mass loss, and residual axial compressive strength of the concrete types after high temperature exposure were examined, and the results were compared to those of concrete types manufactured using normal clay ceramsites and crushed limestone.

2. Experimental Programmes

2.1. Raw Materials. The cement used in this study was slag Portland cement (PSA 32.5), provided by Hongshi Cements Ltd., Yiliang, Kunming, Yunnan, China. Its chemical composition and physical properties are given in Table 1. Sand with a fineness modulus of 2.54 was used as fine aggregate. Limestones (LS) and clay ceramsite lightweight aggregates (LWA) were used as coarse aggregates. Both the LS and the LWA had particle size ranges of 5 mm to 30 mm and were under continuous grading. Both fine aggregate and coarse aggregates were provided by Chengwei Chemical Building Materials Ltd., Kunming, Yunnan, China.

2.2. Modifications of the Lightweight Aggregates. By adopting the surface coating modification method, two types of materials were used to modify clay ceramsites, that is,

modification material I [13] and modification material II [14]. The LS, LWA, modification material I modified lightweight aggregates (PLWA), and modification material II modified lightweight aggregates (GLWA) are shown in Figure 1. The physical properties of the different types of coarse aggregates are given in Table 2.

2.3. Preparation of Specimens. In order to investigate spalling and the compressive performance of the concrete types after exposure to high temperatures, four concrete mixes were prepared, including normal concrete (NC), lightweight aggregate concrete (LWAC), modification material I modified lightweight aggregate concrete (PLWAC), and modification material II modified lightweight aggregate concrete (GLWAC). A water/binder ratio (W/B) of 0.49 was used, and the total volume of aggregates was kept constant for all four mixes. The W/B used can allow the slump of all the mixes to meet the requirement of S2 [15]. The mix proportions of the concrete specimens are given in Table 3. Before mixing, oven-dried LS, LWA, PLWA, and GLWA were presaturated with the water required for their 1 h water absorption and half of the mixing water. The rest of the mixing water was added during the mixing.

After mixing, concrete types were cast into 100 mm × 100 mm × 300 mm prism mould. After demoulding, concrete specimens were cured in a standard curing room at a temperature of 20 ± 2 °C and relative humidity above 95% for 28 days. Before the exposure to high temperatures, the extra water on the surface of the specimens was wiped off with a damp cloth.

TABLE 3: Mix proportions.

Mix	Per cubic meter (kg/m ³)				28 d compressive strength (MPa)
	Cement	Water	Coarse aggregate	Sand	
NC	370	180	1222	658	28.3
LWAC	370	180	317	693	12.6
PLWAC	370	180	318	693	12.8
GLWAC	370	180	378	693	13.2

TABLE 4: Appearance and spalling statistics of the concrete specimens after exposure to elevated temperatures.

Mix	Temperatures: °C	Appearance			Spalling statistics <i>R</i> ⁽¹⁾ : %
		Colors	Cracks	Spalling	
NC	20	Slight gray	—	—	66.7
	400	Slight red	Scarce and local	Slight	
	600	Dark red	A small amount of fine cracks	Medium	
	800	Cinereous	Long and wide	Medium	
	1000	Straw white	A large amount of long cracks	Heavy	
	1200	Slight yellow	Numerous and random	Heavy	
LWAC	20	Dark gray	—	—	100
	400	Dark red	Local microcracks	Slight	
	600	Slight red	A certain amount of fine cracks	Medium	
	800	Straw white	Long and wide	Medium	
	1000	Slight yellow	A large amount of long cracks	Heavy	
	1200	Soil yellow	Numerous and random	Heavy	
PLWAC	20	Dark gray	—	—	25
	400	Dark red	Scarce and local	—	
	600	Slight red	Few small shallow cracks	Slight	
	800	Straw white	A certain amount of fine cracks	Slight	
	1000	Slight yellow	Long and wide cracks at edges	Medium	
	1200	Soil yellow	Large amount and located at edges	Medium	
GLWAC	20	Dark gray	—	—	16.7
	400	Dark red	Unclear	—	
	600	Slight red	Scarce and local	Slight	
	800	Straw white	A small amount of fine cracks	Slight	
	1000	Soil yellow	Long and wide cracks at edges	Medium	
	1200	Brownish Yellow	Large amount and located at edges	Medium	

⁽¹⁾ *R* represents the percentage of the specimens spalled when the target temperature was above 400°C.

2.4. Heating Regime and Test Procedure. Before heating, the specimens in saturated-surface-dry condition were weighed at room temperature. Then, the specimens were placed in an electric furnace under unstressed condition and were heated to 200°C, 400°C, 600°C, 800°C, 1000°C, and 1200°C, respectively, with an increasing rate of 10°C/min. The elevation of temperature was controlled by a programming instrument with precision of 10°C. When the target temperatures were achieved, the temperatures were maintained as constant for 3 h to allow the specimens to reach a thermal steady state. Then, the heated specimens were cooled down slowly to room temperature in the furnace.

During the temperature elevation, the temperatures when spalling occurred were recorded. When the specimens were cooled, they were taken out from the furnace, and any surface changes (i.e., colors, cracks, spalling, etc.) of the specimens

due to the high temperatures were recorded as well. The specimens that were still intact (i.e., without spalling) were weighed again followed by crushing for compressive strength test [16].

3. Results and Discussion

3.1. Appearance and Spalling. The appearance and spalling statistics of the specimens after exposure to elevated temperatures are reported in Table 4, and the spalling of the specimens after heating is shown in Figure 2. From Table 4 and Figure 2, it can be observed that no spalling occurred for the concrete specimens when the temperature was below 400°C. When the temperature increased to approximately 450°C, spalling occurred for the concrete specimens to different extents. Based on a statistical calculation, 66.7% of the NC specimens

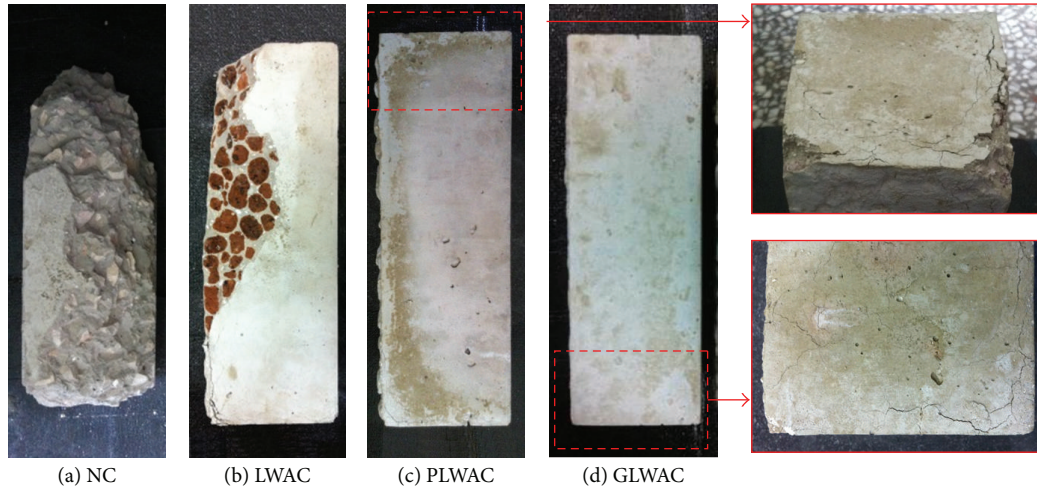


FIGURE 2: Spalling of the concrete specimens.

were spalled when the temperature was above 400°C; these values for the LWAC, the PLWAC, and the GLWAC specimens were 100%, 25%, and 16.7%, respectively. In general, the extent of the damage caused by spalling was most serious for the NC specimens. Spalling mainly occurred at the edges and corners of the specimens, and a considerable volume of the specimens was broken off from the prisms, as shown in Figure 2(a). The spalling mode for the LWAC specimens was tangential damage at the edges of the specimens, with cracks throughout the lightweight aggregates (refer to Figure 2(b)). However, for the PLWAC and the GLWAC concrete specimens, only mild damage was observed at the corners of the specimens, as shown in Figures 2(c) and 2(d).

From Table 4, it can be observed that, due to the prewetting treatment of the lightweight aggregates, the moisture content of the LWAC specimens should be higher than that of the NC ones, and the LWAC specimens were more prone to spall. However, the extent of the damage caused by spalling was smaller for the LWAC specimens. The modifications of the lightweight aggregates greatly reduced the risk of thermal spalling. This may be attributed to the following reasons: (1) the water absorption of the lightweight aggregates was reduced after the modifications (refer to Table 2), as well, leading to a lower moisture content in the concrete specimens, thereby reducing the spalling risk of the modified lightweight concrete types during heating; (2) with the increase of temperature, parts of modification material I could be melted gradually below 400°C to form microcracks, connecting the existing capillary pores to provide a channel for the escaping of water vapor, thus reducing the risk of the PLWAC specimens to spall [13]; (3) modification material II exhibited a superior performance at high temperature [14]. Therefore, the aggregates in the GLWAC specimens were enhanced, and the performance of the GLWAC specimens at high temperature was improved.

3.2. Mass Loss. Figure 3 shows the mass loss of the concrete specimens at different temperatures. Due to the spalling of the LWAC specimens after 400°C and of the NC specimens after

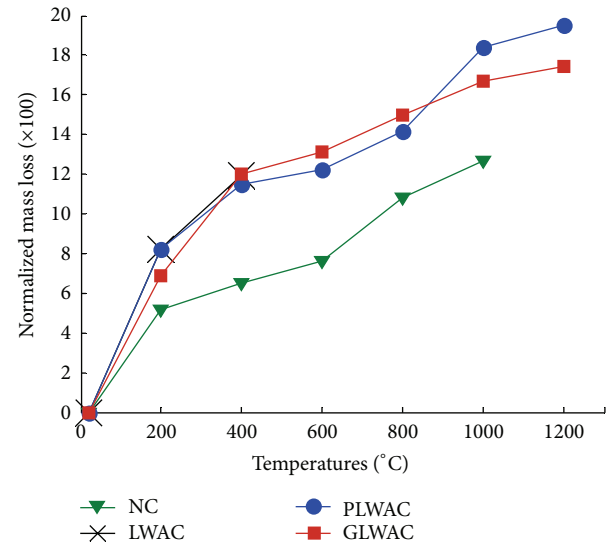


FIGURE 3: Mass loss of the specimens after being heated.

1000°C, the mass loss test could not be conducted for these two mixes above these temperatures. Normalized mass loss was calculated by using the following equation:

$$N_{ml} = \frac{M_o - M_t}{M_o} \times 100, \quad (1)$$

where N_{ml} is normalized mass loss; M_o is the original weight at room temperature; M_t is the weight at a given temperature.

From Figure 3, it can be observed that the mass losses of the concrete specimens increased to different extents with the increase of temperature. Furthermore, the mass losses of the concrete specimens manufactured using lightweight aggregates were much larger than those of the NC specimens at all the temperatures. Therefore, it is considered that evaporation of water may be the main cause for the mass loss of the concrete specimens as more water could have been introduced into the lightweight concrete types at the beginning of

TABLE 5: Compressive strength of the concrete specimens after exposure to elevated temperatures.

Mix	Compressive strength (MPa)						
	20°C	200°C	400°C	600°C	800°C	1000°C	1200°C
NC	28.3	24.2	22.3	14.1	12.8	11.7	/
LWAC	12.6	12.4	11.4	/	/	/	/
PLWAC	12.8	11.8	10.7	8.9	8.0	5.3	3.3
GLWAC	13.2	11.9	12.1	8.8	7.8	6.2	4.9

the mixing. Due to the modifications of the lightweight aggregates, the water absorption of the PLWA and the GLWA was lower than that of the reference lightweight aggregates (refer to Table 2). Therefore, it was expected that the mass losses of the modified concrete types should be lower than that of the reference lightweight concrete. This was true for the GLWAC specimens. However, the mass loss of the PLWAC specimens was similar to that of the LWAC specimens. The reason for this could be attributed to the melting of modification material I at approximately 200°C–400°C to increase the mass loss of the PLWAC specimens. When the temperature increased to approximately 400°C, although a larger amount of water was involved in the LWAC specimens, the escape of water was much difficult (which may be the reason why the LWAC specimens spalled completely at such temperature). Therefore certain amount of water could be still retained in the specimens, which reduced their mass loss. Compared to the PLWAC specimens, the greater mass losses of the GLWAC specimens at both 600°C and 800°C may be the result of the solidification of the matrix of modification material II [14]. The higher mass loss of the PLWAC specimens after 800°C could be due to the decomposition of modification material I.

3.3. Relative Residual Compressive Strength. Compressive strengths of the concrete specimens at room temperature and the elevated temperatures were reported in Table 5, and the relative results were plotted in Figure 4. The relative residual compressive strength is defined as the ratio between the residual compressive strength at a given temperature and the compressive strength at room temperature. Due to the occurrence of spalling, the compressive strength tests were not conducted for the LWAC specimens after 400°C and for the NC specimens after 1000°C, respectively. From Figure 4, it can be observed that, with the increase of temperature, the residual compressive strength of all the specimens declined. When the temperature was below 400°C, more than 80% of the compressive strength was retained for the concrete specimens. When the temperature was above 400°C, the LWAC specimens spalled completely, and the residual compressive strength for the other concrete specimens began to dramatically decrease. When the temperature further increased to 1200°C, the NC specimens spalled completely, whereas the PLWAC and the GLWAC specimens still had 25% and 38% of the compressive strength retained, respectively.

From Figure 4, it also can be seen that the lightweight concrete specimens always had higher residual compressive strength than the NC specimens after exposure to the elevated temperatures. It is known that the heat conductivity of

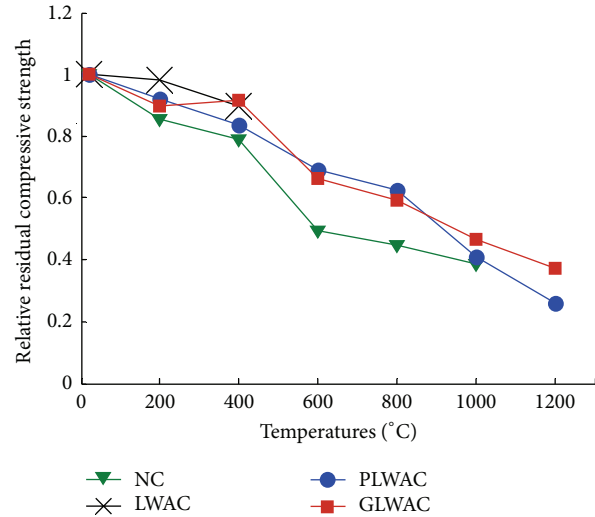


FIGURE 4: Relative residual compressive strength of the concrete specimens after exposure to elevated temperatures.

lightweight aggregates is lower than that of limestone aggregates [17, 18]. As a result, the temperature rise in lightweight aggregate concrete specimens is at least 15%–20% lower than that of ordinary concrete specimens at high temperature [19]. In this context, compared to the NC specimens, the influence of high temperature on the compressive performance was smaller for the concrete specimens with lightweight aggregates. Furthermore, the materials used to modify the lightweight aggregates may have changed the bonding properties between the cement matrix and the lightweight aggregates. Compared to the reference lightweight concrete specimens, such changing would likely have resulted in different mechanical behavior for the modified concrete specimens. This issue will be explored and detailed in further work.

When the temperature was above approximately 800°C, the decrease in the compressive strength of the PLWAC specimens was clearer than that of the GLWAC specimens. The reason for this may be attributed to the decomposition of modification material I in the former, whereas the solidification of modification material II at high temperature could allow the strength of the latter to remain at a relatively high level.

4. Conclusions

Based on the experimental programme adopted in this study, the following conclusions could be drawn:

- (i) The modified lightweight aggregate concrete specimens had much lower risks and extents of spalling after exposure to elevated temperatures. The reasons for this could be attributed to the reduced water absorption, the melting of parts of modification material I in PLWAC specimens, and the improved high temperature resistance of modification material II in GLWAC specimens.

- (ii) After 1200°C, the PLWAC and the GLWAC specimens still had 26% and 38% of the compressive strength retained, respectively, exhibiting superior resistance to high temperature.

Competing Interests

The authors declare that there are no competing interests regarding the publication of this paper.

Acknowledgments

The authors gratefully acknowledge the financial supports from the National Science Foundation of China (Grant no. 11562010), the China Postdoctoral Science Foundation (Postdoctoral no. 150039 and Grant no. 2015M572646XB), and the Talent Introduction Project of Kunming University of Science and Technology (Grant no. KKSJ201406112).

References

- [1] ACI Committee 213R-14, *Guide for Structural Lightweight Aggregate Concrete*, chapter 2, American Concrete Institute, 2014.
- [2] E. Sancak, Y. Dursun Sari, and O. Simsek, "Effects of elevated temperature on compressive strength and weight loss of the light-weight concrete with silica fume and superplasticizer," *Cement and Concrete Composites*, vol. 30, no. 8, pp. 715–721, 2008.
- [3] H. Tanyildizi and A. Coskun, "Performance of lightweight concrete with silica fume after high temperature," *Construction and Building Materials*, vol. 22, no. 10, pp. 2124–2129, 2008.
- [4] H. Tanyildizi and A. Coskun, "The effect of high temperature on compressive strength and splitting tensile strength of structural lightweight concrete containing fly ash," *Construction and Building Materials*, vol. 22, no. 11, pp. 2269–2275, 2008.
- [5] X. Wu, Z.-M. Wu, J.-J. Zheng, T. Ueda, and S.-H. Yi, "An experimental study on the performance of self-compacting lightweight concrete exposed to elevated temperature," *Magazine of Concrete Research*, vol. 65, no. 13, pp. 780–786, 2013.
- [6] Q. M. Ma, R. X. Guo, Z. M. Zhao, Z. W. Lin, and K. C. He, "Mechanical properties of concrete at high temperature—a review," *Construction and Building Materials*, vol. 93, pp. 371–383, 2015.
- [7] F. Koksal, O. Gencel, W. Brostow, and H. E. Hagg Lobland, "Effect of high temperature on mechanical and physical properties of lightweight cement based refractory including expanded vermiculite," *Materials Research Innovations*, vol. 16, no. 1, pp. 7–13, 2012.
- [8] H. Justnes and P. A. Hansen, "Lightweight aggregate concrete for floaters, SP4 hydrocarbon fire resistance. Report 4.1—a theoretical evaluation based on material technology," SINTEF Report STF65 F90009, SINTEF, Trondheim, Norway, 1990.
- [9] T. A. Hammer, "Spalling reduction through material design," Trondheim: report 6.2, HSC Phase 3. SINTEF-report nr STF70 A95024, 1995.
- [10] J. Lindgård and T. A. Hammer, "Fire resistance of structural lightweight aggregate concrete a literature review survey with focus on spalling, supplementary papers," in *Proceedings of 4th CANMET/ACI/JCI International Conference on Recent Advances in Concrete Technology*, pp. 25–39, Tokushima, Japan, 1998.
- [11] W. J. Copier, "The spalling of normal and lightweight concrete exposed to fire," in *Proceedings published in Fire Safety of Concrete Structures*, pp. 219–236, Fall Convention of the American Concrete Institute, Detroit MI, USA, 1983.
- [12] S. Y. N. Chan, G.-F. Peng, and M. Anson, "Fire behavior of high-performance concrete made with silica fume at various moisture contents," *ACI Materials Journal*, vol. 96, no. 3, pp. 405–411, 1999.
- [13] R. X. Guo, Q. M. Ma, Y. L. Sun et al., "Coated light-weight aggregate, and preparation method and application thereof," China, Patent CN104529212A, patent pending, April 2015.
- [14] R. X. Guo, Q. M. Ma, Y. L. Sun et al., "Coated light-weight aggregate, and preparation method and application thereof," China, Patent CN104556767A, patent pending, April 2015.
- [15] China Standard, *JBJ 51 Technical Specification for Lightweight Aggregate Concrete*, China Standard, Beijing, China, 2002.
- [16] China Standard, *GBJ50081 Method for Testing Mechanical Properties of Normal Concrete*, China Standard, Beijing, China, 2002.
- [17] *FIP Manual of Lightweight Aggregate Concrete*, Kapitlene 5.8.2 og 6.3, Surrey University Press, London, UK, 2nd edition, 1983.
- [18] R. Felicetti, P. G. Gambarova, and P. Bamonte, "Thermal and mechanical properties of light-weight concrete exposed to high temperature," *Fire and Materials*, vol. 37, no. 3, pp. 200–216, 2013.
- [19] R. I. Zwiers and B. J. Morgan, "Performance of concrete members subjected to large hydrocarbon pool fires," *PCI Journal*, vol. 34, no. 1, pp. 120–136, 1989.

Research Article

Experimental Study on the Properties of Concrete Mixed with Iron Ore Tailings

Zhong-xi Tian,^{1,2} Zeng-hui Zhao,^{3,4} Chun-quan Dai,^{1,4} and Shu-jie Liu^{1,4}

¹College of Civil Engineering and Architecture, Shandong University of Science and Technology, Qingdao 266590, China

²College of Architecture and Civil Engineering, Liaocheng University, Liaocheng 252000, China

³State Key Laboratory of Mining Disaster Prevention and Control Cofounded by Shandong Province and the Ministry of Science and Technology, Shandong University of Science and Technology, Qingdao 266590, China

⁴Shandong Province Key Laboratory of Civil Engineering Disaster Prevention and Mitigation, Shandong University of Science and Technology, Qingdao 266590, China

Correspondence should be addressed to Zeng-hui Zhao; tgzyzzh@163.com

Received 4 December 2015; Revised 13 March 2016; Accepted 28 March 2016

Academic Editor: Juan J. Del Coz Díaz

Copyright © 2016 Zhong-xi Tian et al. This is an open access article distributed under the Creative Commons Attribution License, which permits unrestricted use, distribution, and reproduction in any medium, provided the original work is properly cited.

The objective of this study is to evaluate the modified performance of concrete with mixing of iron ore tailings in order to solve the shortage of natural sand and make full use of industrial waste. Firstly, the raw materials of mixing were analyzed, and the test ratio was determined. Secondly, the workability and mechanical property of concrete specimens with different amounts of iron ore tailings as replacement were tested. Results show that 35% replacement of natural aggregate by iron ore tailings is optimal. Finally, tests of impermeability, frost resistance, and carbonation resistance were further performed for the concrete specimens with optimal amount of iron ore tailings. The compression performance of the specimens after a durability test was determined. The change in the mechanical properties of the specimens was obtained after seepage, freezing-thawing, and carbonation. Findings showed that the performance of the concrete with 35% replacement of iron ore tailings is basically equivalent to that of natural sand concrete. Hence, it can be utilized in engineering applications.

1. Introduction

With China continuing to increase the investment in the infrastructure construction, the demand for concrete has increased sharply. This results in a shortage of natural sand in some areas and a series of environmental problems due to irrational overexploitation. On the other hand, mining activities not only destroy and occupy lots of land resources but also bring about many serious environmental and social problems, and a lot of waste such as tailings requires disposal [1–5]. It is urgent to solve the shortage of natural sand and make full use of industrial waste. Thus, it is quite significant to vigorously develop the iron ore tailings concrete for the construction.

In recent years, the domestic and oversea scholars have achieved some progress on the preparation and performance testing of concrete with iron mine tailings. Zhao

et al. [6] carried out indoor experiments to study the working performance and mechanical behavior of concrete with iron ore tailings and analyzed the test results from micro aspect. Experimental results established by Alwaeli and Nadziakiewicz [7] proved that the shielding effect of concrete with different proportions of scrap steel chips on gamma rays is superior to the ordinary concrete with natural sand. Onoue et al. [8] investigated the fatigue properties of slag concrete and derived the equations for calculating its fatigue life by the theory of fatigue mechanics. A series of laboratory experiments on the mechanical behavior of concrete prepared by abandoned iron ore tailings in Iraq was carried out by Ismail and AL-Hashmi [9], and results revealed that its performance was superior to ordinary concrete and exhibited higher compressive strength and flexural strength. Zhang et al. [10] comprehensively analyzed the disposal and utility circumstance of iron ore tailings in China. Tian [11]



FIGURE 1: Comparison between iron ore tailings and natural sand.

TABLE 1: Chemical composition of iron ore tailings.

SiO ₂	Al ₂ O ₃	Fe ₂ O ₃	CaO	MgO	K ₂ O	Na ₂ O	SO ₃	Cl ⁻	Loss amount
70.32	5.1	10.93	4.71	4.51	1.14	1.3	0.26	0.016	1.1

experimentally determined the basic performance of the concrete with iron ore tailings and listed a large number of successful applications of prepared concrete in city construction. He et al. [12] and Davraz and Gunduz [13] prepared the C60 high-strength concrete using iron ore tailings whose performance is superior to the normal concrete.

Many achievements have been made in the research on the utilization of iron ore tailings. However, results of mixing amount of iron ore tailings on the mechanical performance of concrete are not abundant. Thus, the modified performance of concrete with different mixing amounts of iron ore tailings was tested in this study in order to find the optimum one.

2. Raw Material Property

2.1. Iron Ore Tailings. The iron ore tailings were collected from a copper-iron mine in Zibo city. The particles appear as fine gray granular, and the fineness modulus was within 1.9~2.3. Comparison of particle size between the collected iron ore tailings and natural sand from Wen River was shown in Figure 1.

The chemical components of the collected iron ore tailings obtained from phase analysis were shown in Table 1. Obviously, the main components of iron ore tailings are basically the same as natural sand. This indicates that it can be used to prepare concrete.

2.2. Cement. The ordinary Portland cement P.O 42.5 produced from Tai'an was adopted, and its chemical components and property indexes are shown in Table 2.

2.3. Coarse and Fine Aggregate. The coarse and fine aggregate used in this test are the gravel with a dimension within 5~25 mm in Tai'an area and medium sand collected from Wen River. From particle-size analysis, the grading curves of crushed stone and medium sand are shown in Figure 2.

2.4. Mineral Admixture. Adding admixture, fly ash into raw materials, is an important way to get high-performance concrete. Amorphous active substance of Al₂O₃ in fossil waste of

fly ash can react chemically with Ca(OH)₂. This form of attack directly leads to the formation of gel component and reduction of the porosity in concrete [14]. As a result, the characteristics of adhesiveness, liquidity, water retention, and pumpability of fresh concrete can be improved. Besides, the choice of commonly available fly ash can also protect the environment and make secondary use of the chemical waste. In this test, Primary grade fly ash provided by power plant in Shandong was adopted, and its chemical composition is listed in Table 3.

2.5. Water Reducer. Polycarboxylic high-performance water-reducing agent of SM-IV was introduced, and its technical indicators were listed in Table 4. This water reducer can reduce levels of chloride iron and is an environmentally friendly additive [15]. Besides, it can also improve the concrete contracting rate.

3. Test to Find the Optimum Mixing Amount of Iron Ore Tailings

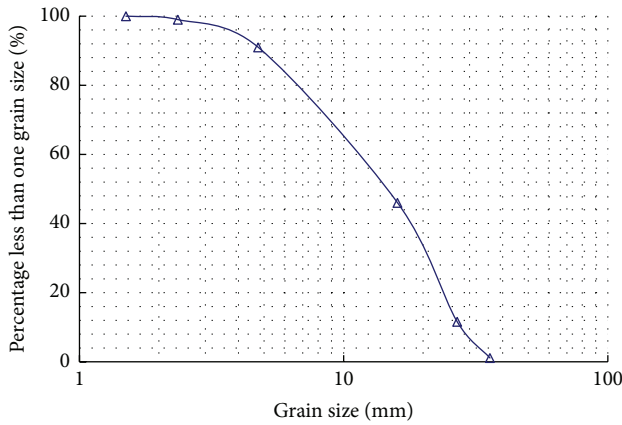
3.1. Workability of Samples with Different Mixing Amount of Iron Ore Tailings. Let the bulk density of C30 concrete be 2400 kg/m³, and let the mass ratio between iron ore tailings and natural sand be α . Here, the concrete without iron ore tailings was set as reference. On the basis of reference concrete mix, four different mixes ($\alpha = 0, 25\%, 35\%, \text{ and } 45\%$) were designed by changing the amount of iron ore tailings. The volume of each sample is 1 m³. The mixing proportion of each sample was determined by using the overall calculation method [16], as listed in Table 5. Slumps at three different positions for each series were tested. The results are shown in Figure 3.

As shown in Figure 3, the slumps and liquidity of concrete mixed with iron ore tailings decreased compared with that of normal concrete under the same condition (water, mixture ratio, admixture, etc.). This phenomenon arises because the particles of iron ore tailings are rough and occluded with coarse aggregate, so cohesion increases significantly in the tailing mixes. In addition, iron ore tailings have higher water absorption than natural sand. Therefore, the tailing mixes are weak in terms of liquidity. According to the test on the retention value of slumps for 1 h, the loss of slumps had a linear relation with the increase in the proportion of iron tail sand. The loss value of concrete with proportion of 45% for 1 h was 12%, indicating that iron tail sand concrete exhibited improved performance in agglomeration. In the experiment, cement paste easily separated with aggregate as the result of the weak liquidity of the tailing mixes. An inaccurate mix proportion would produce segregation and lead to a reduction in water retention capacity. In all the cases, the slumps are all above 150 mm and can thus be used in practice. In summary, iron tail sand could ensure the workability in transportation and pouring when the proportion is below 45%.

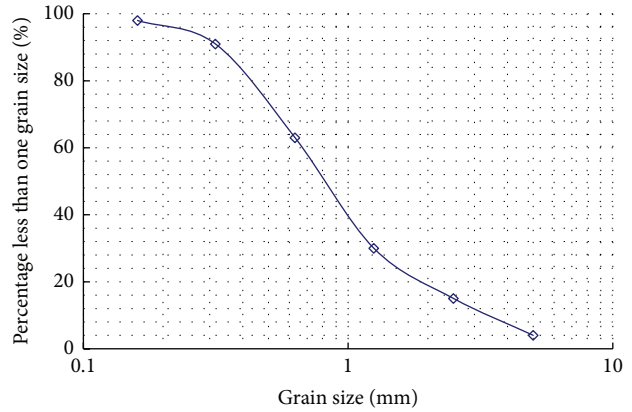
3.2. Compressive Strength of Samples with Different Mixing Amounts of Iron Ore Tailings. Mechanical properties of concrete samples with different mixing amounts of iron ore

TABLE 2: Chemical components and property indexes of ordinary Portland cement.

Proj	Chemical composition (%)				Compressive strength (MPa)				Soundness	Physical property		
	SO ₃	MgO	Loss on ignition	Cl ⁻	3 d	28 d	3 d	28 d		Specific surface (m ² /kg)	Setting time (min)	Final setting (min)
Val	1.62	3.18	3.4	0.028	3 d 29.4	28 d 49.5	3 d 5.5	28 d 8.1	Conformity	384	226	288



(a) Grading curve of crushed stone



(b) Grading curve of medium sand

FIGURE 2: Grading curve of aggregate.

TABLE 3: Chemical composition of fly ash.

Composition	SiO ₂	Al ₂ O ₃	Fe ₂ O ₃	CaO	MgO	Na ₂ O	K ₂ O	SO ₃
Content	52.38	28.42	5.47	2.57	1.38	0.36	1.84	0.56

tailings were tested in accordance with the national standard GB/T 50081-2002. As shown in Figure 4, standard compressive concrete cube specimens (150 × 150 × 150 mm³) were fabricated according to different amount of iron ore tailings. Nine test specimens were set for each type of proportion, and a total of three group experiments were conducted.

The test specimens were cured for 3 d, 7 d, and 28 d under standard conditions (20°C ± 2°C, relative humidity of 95%). Then, the compressive strength of the test specimens was tested on the electrohydraulic pressure testing machine (see Figure 5). The results are presented in Figure 6.

Compressive strength results in Figure 6 show that each group is similar. To intuitively compare the compressive properties at different replacement proportions, the average of the test values of the three groups was obtained. The change curve of compressive strength along with age is shown in Figure 7.

Comparison of Figures 6 and 7 shows that under the same experimental conditions, with the increase in the proportion of the iron ore tailings, the compressive strength of the tailing mixes at 3 d increased initially and then decreased subsequently after the first reduction. Specifically, when the replacement of natural aggregate by the tailings in the mixing concrete amount was 35%, the 3 d compressive strength was

greater than that of the control mix; the best proportions were 25%, 35%, and 45%. Similarly, with the increase in the proportion of the iron ore tailings, the compressive strength of the tailing mixes at 7 d increased and then decreased subsequently after the first reduction. However, the tailing mixes' compressive strengths of 25%, 35%, and 45% at 7 d were all less than that of the control mix because the surface activity of iron ore tailings is low. After adding iron ore tailings to concrete, more slurry was required to pad the architecture, thereby causing the tailing mixes' compressive strength at 7 d to become lower than that of the control mix. However, with the increase in time, compressive strength increased rapidly. The failure of the specimens indicates that the tailing mixes and the control mix are similar which present a wedge of upper and lower symmetry. After specimen damage, visible defects in the interior, such as the stomata, were observed. With the increase in proportion, the stomatal number increased, but the regularity was weak.

With the increase of the iron ore tailings, the compressive strength of the tailing mixes at 28 d decreased and then increased subsequently after the first reduction. Specifically, when the replacement of natural aggregate by the tailings in the concrete was 35%, the 28 d compressive strength performance was better, and the long-term compressive strength was slightly higher than that of the control mix. The compressive properties of the concrete with 45% replacement of natural aggregate by the tailings were poor mainly because excessive iron ore tailings lead to an increase in harmful voids within the concrete mixture. If mixing is insufficient, the layered bleeding phenomenon easily occurs in the concrete,

TABLE 4: Technical index of water reducing agent.

Items	Density (g/mL)	Solid content (%)	pH level	Neat paste rheology (mm)	Chloride ion content (%)	Alkali content (%)
Test result	1.05	40	7	230	0.01	1

TABLE 5: Proportion of concrete mix with iron ore tailings.

Proportion of iron ore tailings (%)	Iron ore tailings (kg)	Natural sand (kg)	Fly ash (kg)	Cement (kg)	Crushed stone (kg)	Water (kg)	Water-reducing agent (kg)
0	0	1010	94	276	806	204	10.2
25	252	758	94	276	806	204	10.2
35	352	658	94	276	806	204	10.2
45	453	557	94	276	806	204	10.2

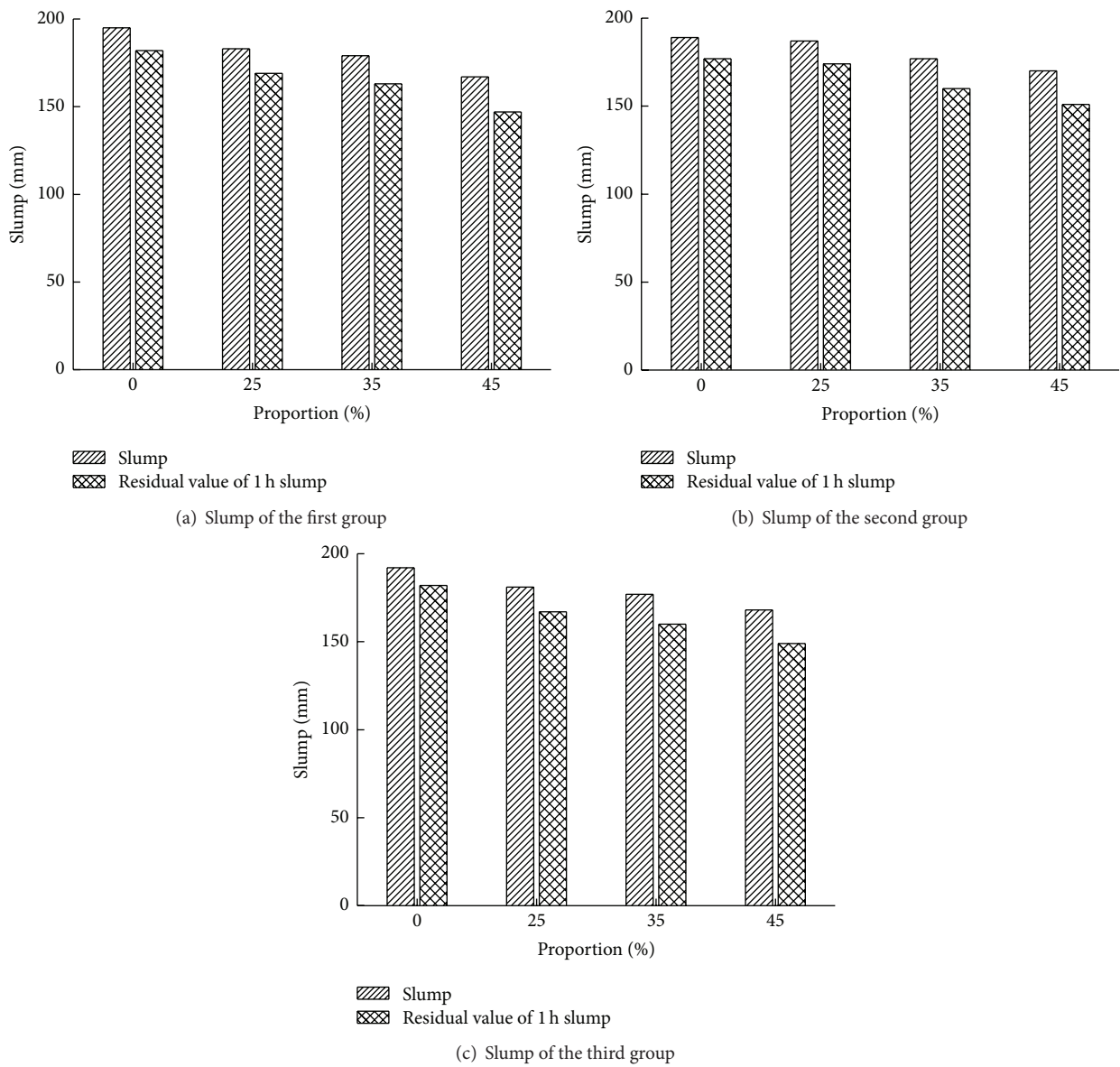


FIGURE 3: Comparison of slumps in mixture of different incorporation amounts.



FIGURE 4: Standard compression specimens.



FIGURE 5: Electrohydraulic pressure testing machine.

the development of the bond strength between the paste and aggregate is not uniform, and the overall compressive strength of concrete decreases [17].

3.3. The Optimum Mixing Amount of Iron Ore Tailings. By the comparison and analysis of the test data, the mixing amount of 35% is the most appropriate among all the proportions. When the amount of the admixture exceeded 45%, the initial strength of the tailing mixes was lower than that of the control mix, and its long-term compressive strength decreased significantly. It is thus unsuitable for use as C30 concrete in building engineering.

4. Further Durability Test on the Properties of the Concrete with Optimum Mixing Amount of Iron Ore Tailings

To evaluate the durability of the concrete mixed with 35% iron ore tailings, three tests of resistance to penetration, frost resistance, and carbonation resistance were performed.

4.1. Research on Permeability Resistance. According to the standard JGJ/T193-2009 for concrete antipenetration test,

TABLE 6: Analysis of concrete anti-infiltration test data.

Number	Water pressure during third specimen seepage	Anti-infiltration level
KS-0	0.7 MPa	6
KS-1	0.7 MPa	6
KS-2	0.7 MPa	6
KS-3	0.8 MPa	7

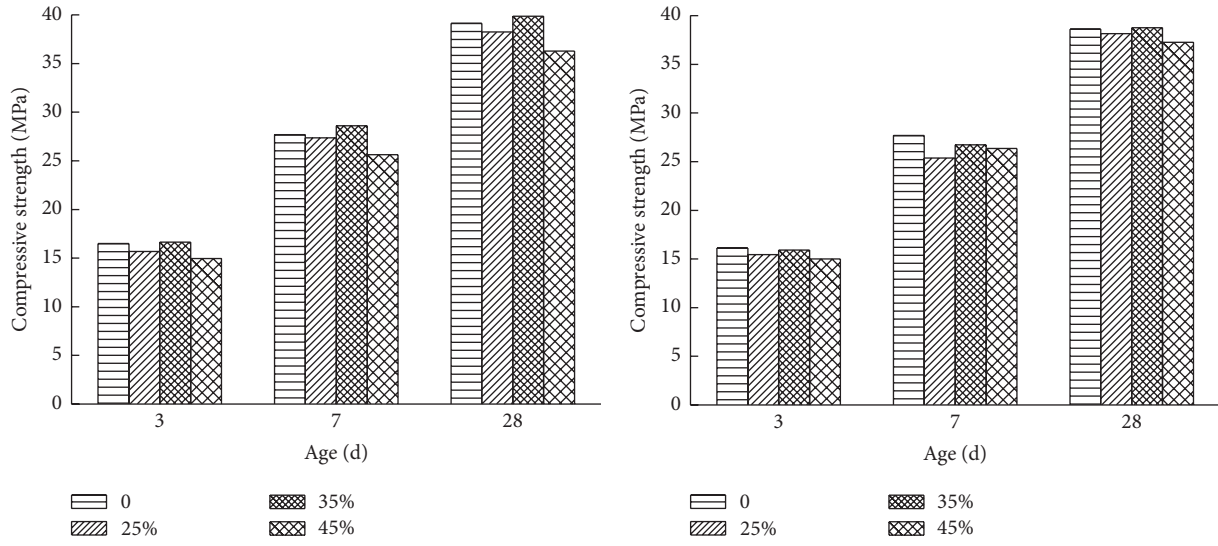
cylindrical specimens with 150 mm diameter and height were prepared. Four groups were established, and each group included six specimens. One group (KS-0), which was regarded as the control mix, was not mixed with tailings. The other three groups (KS-1, KS-2, and KS-3) were concrete with 35% iron ore tailings. As shown in Figure 8, the specimens were placed on a permeability tester for the concrete antipenetration test.

Water pressure was increased to 0.1 MPa every 8 h, until three concrete specimen surfaces exhibited seepage. Then, the test was stopped. The measured concrete anti-infiltration test data are shown in Table 6.

As revealed in Table 6, the impermeability grade of concrete with 35% iron tailings and that of natural sand concrete are basically the same. The incorporation of iron tailings did not affect the impermeability of concrete. However, the impermeability grade of concrete with the incorporation of iron tailings is not high, and its impermeability can only be used as an adjunct. In engineering application, the concrete must be added to concrete admixtures to improve impermeability.

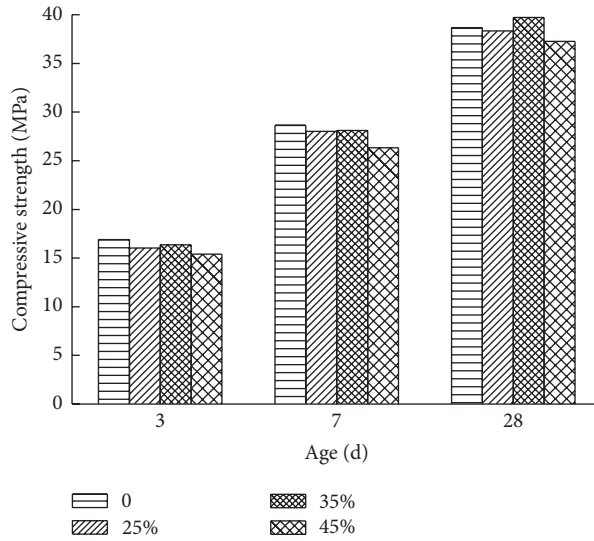
4.2. Research on Frost Resistance. The frost resistance test for long-term performance and durability of ordinary concrete was carried out based on the national standard GB/T50082-2009. Four groups of concrete cube specimens were used. Their length, width, and height were 100 mm, and each group has two specimens (one was used in the frost resistance test, and the other was used in the compression test after freezing and thawing). Similarly, one group (KD-0) was set as the reference specimen, and the other three groups (KD-1, KD-2, and KD-3) contained 35% iron tailings. The freezing-thawing test was carried out by the -40 DW/200 low temperature box (see Figure 9), and detection of quality loss was conducted every 25 freezing-thawing cycles. The quality loss curve of the four groups when the number of freezing-thawing cycles is 200 is shown in Figure 10.

Results show that the mass loss of concrete containing 35% iron ore tailings is higher than that of the reference concrete. The frost resistance of the concrete decreased to 16.2% because of the iron tailings sand. The bonding properties of certain minerals in iron tailings sand are weak at low temperatures, and some of the sand on the surface falls off. The four experimental curves show that the concrete specimens' mass increased in the early part of the freezing-thawing test because the concrete specimens exhibited micro cracks and water came in. However, as the freezing-thawing



(a) Compressive strength of the first group

(b) Compressive strength of the second group



(c) Compressive strength of the third group

FIGURE 6: Compressive strength of concrete specimens.

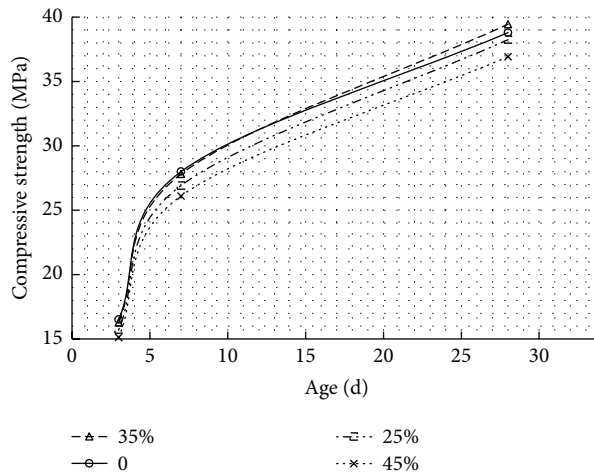


FIGURE 7: Change curve of compressive strength with age.



FIGURE 8: Antipermeability apparatus for concrete.

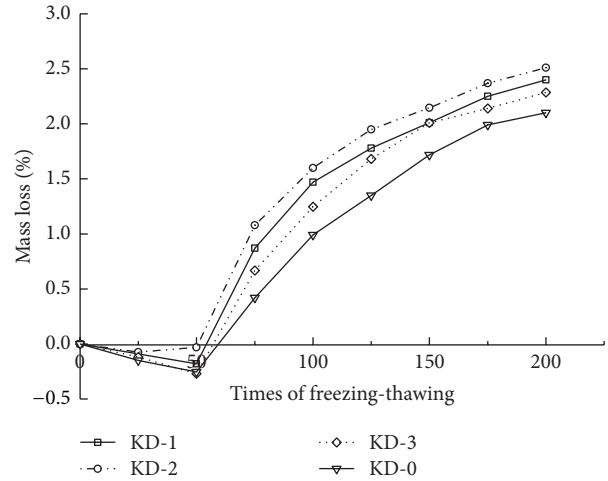


FIGURE 10: The mass loss rate varies with the number of cycles.



FIGURE 9: Low temperature box.

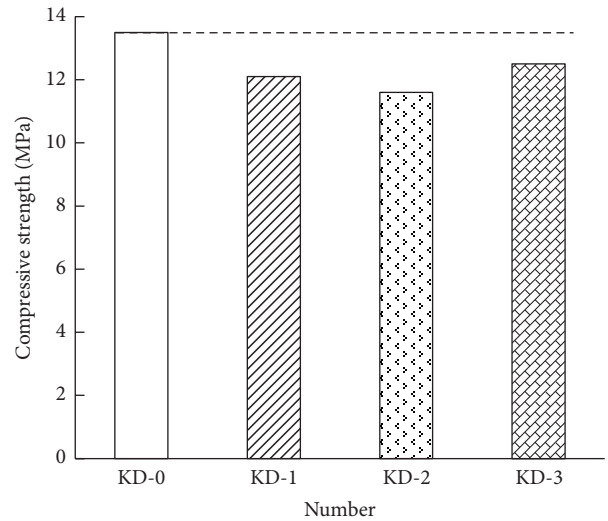


FIGURE 11: Compressive strength of concrete specimen after freezing-thawing test.

test went on, cement slurry and coarse and fine aggregates fell off from the specimens' surfaces. Then, the weight of the specimens decreased, but their mass loss was less than 3% in all the tests. A compression experiment was performed after freezing-thawing, and the results are shown in Figure 11. The compressive strength of the concrete specimens decreased by more than 60% after 200 cycles of freezing-thawing. The loss of the tailing mixes is larger than that of the control mix. The compressive strength of the concrete with iron ore tailings after freezing-thawing was approximately 90% that of the reference concrete; hence, the compressive strength of the tailing mixes after freezing-thawing had some degree of discount [18]. When used in buildings with antifreeze requirements, the concrete needs to be combined with an air-entraining agent to increase the antifreeze performance.

4.3. *Research on Carbonation Resistance.* Test code for hydraulic concrete (DL/T 5150-2001) was applied in the carbonation test. Similar to the frost resistance test, one group (KT-0) of concrete specimens was set as the reference, and three groups (KT-1, KT-2, and KT-3) of concrete specimens contained iron ore tailings. Each group has two specimens. The concrete specimens were placed in a carbonation tank at

23°C with 22% CO₂ concentration and 70% relative humidity (RH). After the concrete specimens were carbonated, we split the specimens and sprayed 1.0% phenolphthalein ethanol solution on the fracture surface. Multipoint distance was measured at each side, and the average value was regarded as the carbonation depth. The degree of carbonation of concrete at 3, 7, and 28 d is shown in Figure 11.

As shown in Figure 12, with the development of the ages of carbonation, the carbonation depth of the concrete specimens exhibited a nonlinear variation. The carbide growth rate decreased mainly because the produced CaCO₃ in the early carbonation process formed a layer of protection membrane on the surface of carbonation and prevented CO₂ from entering to a certain extent. Hence, the rate of carbonation decreased. However, after fly ash partly replaced cement, the Ca(OH)₂ generated by cement hydration reacted with SiO₂ and Al₂O₃ in fly ash and produced hydrated calcium. Therefore, late carbonation resistance of the concrete decreased

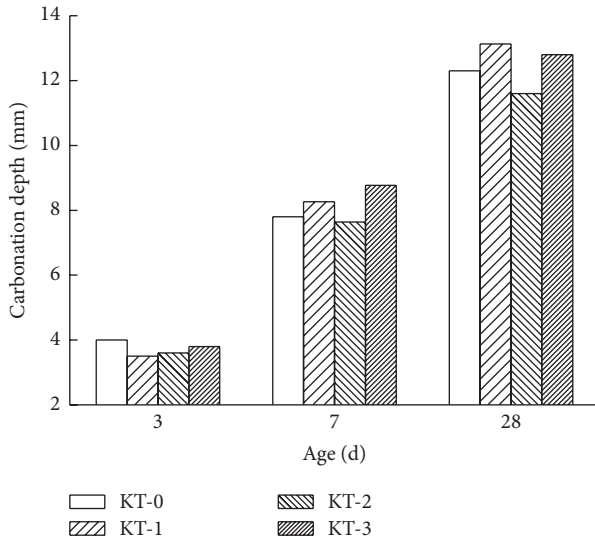


FIGURE 12: Carbonation depth change with time.

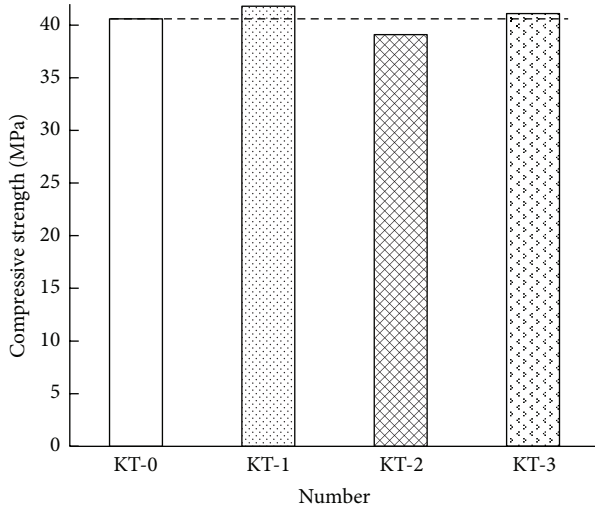


FIGURE 13: Mass loss rate change of cycles.

partly because the secondary reaction of the concrete mixed with fly ash consumed large amounts of $\text{Ca}(\text{OH})_2$ and made the pH value decrease [19]. By contrast, the carbonation speed of the tailing mixes was lower than that of the control mix in the early stage. When the carbonation age was more than 7 d, the carbonation speed of the tailing mixes was higher than that of the control mix. With the increase in time, the carbonation depth of the two groups was greater than that of the control mix. The average of the three group tests is basically equal to that of the control mix; 28 d carbonation depth was less than 20 mm. These test results show that carbonation resistance performance is good in the early stage, and replacement of natural aggregate by the tailings is not related to carbonation resistance. The tailing mixes of 35% meet the requirement for carbonation resistance in engineering design.

After the carbonation test, we used another specimen in the compressive experiment. The result is shown in Figure 13.

Compared with that in Figure 4, the compressive strength of the specimen after the carbonation experiment increased by about 5%. The main reason is that concrete absorbed CO_2 from the air in the process of carbonation and generated CaCO_3 to make the concrete surface denser. During the compression test, the ultimate deformation capacity of the specimen decreased significantly. The concrete specimen's brittleness increased after carbonation.

For plain concrete, carbonation is relatively favorable. However, for reinforced concrete, the corrosion of reinforcement is more serious because the alkalinity of concrete after carbonation is reduced. Clearly, the specification for the minimum cover thickness of steel has a regulation: when the carbonation depth is larger than the thickness of the protective layer, the strength of the steel bar in concrete decreases sharply, thereby affecting the overall strength of the reinforced concrete [20].

5. Conclusions

Based on previous studies, the modified performance of concrete with different mixing amounts of iron ore tailings was evaluated in detail in order to solve the shortage of natural sand and make full use of industrial waste. The following conclusions are reached:

- (1) Tests on workability and mechanical property of concrete specimens with different amounts of iron ore tailings were carried out. It was found that the strength development law of the tailings mixes is basically equivalent to that of natural sand concrete according to the compressive strength at 3 d, 7 d, and 28 d age. With the increasing of substitutive ratio of iron ore tailings, the mobility of mixture becomes worse, the water retention of mixture is lower than that of reference concrete, and the excreting water phenomenon may occur. The compressive strength of concrete without iron tailing reaches the highest at 7 d age, while the 35% replacement peaks at 3 d and 28 d age.
- (2) From the durability experiment on the concrete with 35% replacement of natural aggregate by ore tailings, the permeability resistance of the tailing mixes is equal to that of the control mix. Its frost resistance is slightly lower than that of the control mix, and its carbonation resistance is equivalent to that of the control mix.
- (3) Altogether, iron ore tailings can be utilized as a partial substitute for natural sand to prepare concrete. It reduces the amount of natural sand, solves the environmental pollution problem of iron ore tailings, and promotes the development of green building projects.

Competing Interests

The authors declare that they have no competing interests regarding the publication of this paper.

Acknowledgments

This work is supported by the National Natural Science Foundation of China (41472280, 51274133), the Promotive Research Fund for Excellent Young and Middle-Aged Scientists of Shandong Province (no. BS2015SF005), Qingdao Applied Basic Research Project (no. 15-9-1-33-jch), the Scientific Research Foundation of Shandong University of Science and Technology for Recruited Talents (no. 2015RCJJ042), and the Opening Project Fund of Shandong Provincial Key Laboratory of Civil Engineering Disaster Prevention and Mitigation (no. CDPM2013KF05).

References

- [1] Y. L. Tan, F. H. Yu, J. G. Ning, and T. B. Zhao, "Design and construction of entry retaining wall along a gob side under hard roof stratum," *International Journal of Rock Mechanics and Mining Sciences*, vol. 77, pp. 115–121, 2015.
- [2] Z. H. Zhao, W. M. Wang, L. H. Wang, and C. Q. Dai, "Compression-shear strength criterion of coal-rock combination model considering interface effect," *Tunnelling and Underground Space Technology*, vol. 47, pp. 193–199, 2015.
- [3] Y. L. Tan, J. G. Ning, and H. T. Li, "In situ explorations on zonal disintegration of roof strata in deep coalmines," *International Journal of Rock Mechanics and Mining Sciences*, vol. 49, pp. 113–124, 2012.
- [4] Z. H. Zhao, X. Z. Lv, W. M. Wang, and Y. L. Tan, "Damage evolution of bi-body model composed of weakly cemented soft rock and coal considering different interface effect," *SpringerPlus*, vol. 5, article 292, 2016.
- [5] Y. L. Tan, F. H. Yu, and L. Chen, "A new approach for predicting bedding separation of roof strata in underground coalmines," *International Journal of Rock Mechanics & Mining Sciences*, vol. 61, pp. 183–188, 2013.
- [6] S. Zhao, J. Fan, and W. Sun, "Utilization of iron ore tailings as fine aggregate in ultra-high performance concrete," *Construction and Building Materials*, vol. 50, pp. 540–548, 2014.
- [7] M. Alwaeli and J. Nadziakiewicz, "Recycling of scale and steel chips waste as a partial replacement of sand in concrete," *Construction and Building Materials*, vol. 28, no. 1, pp. 157–163, 2012.
- [8] K. Onoue, M. Tokitsu, M. Ohtsu, and T. A. Bier, "Fatigue characteristics of steel-making slag concrete under compression in submerged condition," *Construction and Building Materials*, vol. 70, pp. 231–242, 2014.
- [9] Z. Z. Ismail and E. A. AL-Hashmi, "Reuse of waste iron as a partial replacement of sand in concrete," *Waste Management*, vol. 28, no. 11, pp. 2048–2053, 2008.
- [10] S. Zhang, X. Xue, X. Liu et al., "Current situation and comprehensive utilization of iron ore tailing resources," *Journal of Mining Science*, vol. 42, no. 4, pp. 403–408, 2006.
- [11] J. S. Tian, *Study on Proportions and Applications of Concrete with Iron Mine Tailings*, Tsinghua University, Beijing, China, 2012.
- [12] Z. F. He, B. X. Cui, and T. Wang, "Iron gangue's application research in C60 concrete," *Chinese Journal of Concrete*, vol. 12, pp. 142–144, 2011.
- [13] M. Davraz and L. Gunduz, "Engineering properties of amorphous silica as a new natural pozzolan for use in concrete," *Cement and Concrete Research*, vol. 35, no. 7, pp. 1251–1261, 2005.
- [14] K. E. Hassan, J. G. Cabrera, and R. S. Maliehe, "Effect of mineral admixtures on the properties of high-performance concrete," *Cement and Concrete Composites*, vol. 22, no. 4, pp. 267–271, 2000.
- [15] Q. X. Zhao, W. Sun, and C. W. Miu, "Effect and mechanism of interaction between fly ash proportion and water-binder ratio on the creep characteristics of high performance concrete," *China Civil Engineering Journal*, vol. 12, no. 42, pp. 76–82, 2009.
- [16] J. K. Chen and D. M. Wang, "New mix design method for hpc—overall calculation method," *Journal of the Chinese Ceramic Society*, vol. 28, no. 4, pp. 194–198, 2000.
- [17] A. Castel and S. J. Foster, "Bond strength between blended slag and Class F fly ash geopolymer concrete with steel reinforcement," *Cement and Concrete Research*, vol. 72, pp. 48–53, 2015.
- [18] M. Arabani and S. M. Mirabdolazimi, "Experimental investigation of the fatigue behaviour of asphalt concrete mixtures containing waste iron powder," *Materials Science and Engineering: A*, vol. 528, no. 10–11, pp. 3866–3870, 2011.
- [19] J.-B. Li, J.-Z. Xiao, and Z.-P. Sun, "Properties of recycled coarse aggregate and its influence on recycled concrete," *Journal of Building Materials*, vol. 7, no. 4, pp. 390–395, 2004.
- [20] S. D. Castro and J. de Brito, "Evaluation of the durability of concrete made with crushed glass aggregates," *Journal of Cleaner Production*, vol. 41, no. 2, pp. 7–14, 2013.

Research Article

An Analysis of the Thermal Conductivity of Composite Materials (CPC-30R/Charcoal from Sugarcane Bagasse) Using the Hot Insulated Plate Technique

René Salgado-Delgado,¹ Alfredo Olarte-Paredes,¹ Areli Marlen Salgado-Delgado,¹ Zully Vargas-Galarza,¹ Teresa Lopez-Lara,² Juan Bosco Hernández-Zaragoza,² Israel Rico-Rodríguez,¹ and Gonzalo Martínez-Barrera³

¹*Division de Estudios de Posgrado e Investigación del Instituto Tecnológico de Zacatepec, Calzada Tecnológico No. 27, Col. Centro, 62780 Zacatepec, MOR, Mexico*

²*Division de Estudios de Posgrado, Facultad de Ingeniería, Universidad Autónoma de Querétaro, Cerro de las Campanas S/N, Col. de las Campanas, 76010 Querétaro, QRO, Mexico*

³*Laboratorio de Investigación y Desarrollo de Materiales Avanzados, Facultad de Química, Universidad Autónoma del Estado de México, Km 12 Toluca-Atlacomulco, 50200 San Cayetano, MEX, Mexico*

Correspondence should be addressed to René Salgado-Delgado; renesalgado@hotmail.com

Received 11 September 2015; Revised 6 February 2016; Accepted 16 February 2016

Academic Editor: Fernando Lusquiños

Copyright © 2016 René Salgado-Delgado et al. This is an open access article distributed under the Creative Commons Attribution License, which permits unrestricted use, distribution, and reproduction in any medium, provided the original work is properly cited.

The production of new thermally insulating composite materials from solid residues such as charcoal from sugarcane bagasse (CSB) is of great importance because it takes advantage of materials that might otherwise pollute the environment. Therefore, for this study, we obtained composite materials based on a portland cement (CPC-30R) matrix and CSB particles with a 4 : 1 water-cement ratio and CSB concentrations of 5%, 10%, and 15% by weight. The thermal conductivities of these materials were characterized following ASTM guideline C177, their CSB morphological properties were analyzed using scanning electron microscopy (SEM), and their compositions were determined using energy-dispersive spectrometer (EDS). The results show that the composite materials have reduced thermal conductivities. The metallic oxide percentage composition of the CSB was also determined. It was observed that there was a reduction in thermal conductivity when CSB was used as compared to 100% CPC-30R, and the influence of the CSB concentration on thermal conductivity was measured.

1. Introduction

The increasing concern about industrial pollution has forced the construction and manufacturing industries to seek innovative materials that are trustworthy and sustainable to replace the conventional synthetic fibers used as reinforcements in structural materials. Natural fibers such as sisal, jute, cotton, linen, hemp, and kenaf have been considered as possible alternatives because of their environmental friendliness and their availability in fibrous form and because they can be obtained from plant leaves at a low cost [1, 2].

Charcoal from sugarcane bagasse (CSB) is a residue generated by the bagasse burning process that has low pozzolanic reactivity due to its high porosity. This material is frequently used as a fertilizer even though it is inadequate for this use due to its high silica content (SiO_2) of more than 60% of the total metallic oxide mass. CSB has a broad and variable particle size distribution in addition to a low nutrient content. Therefore, it is important to promote other uses of CSB that generate an added value and synergistic properties for the material.

The locality of *Zacatepec*, in the Mexican state of Morelos, has a sugarcane mill. The residues generated by this industry

accumulate every year, generating a series of negative consequences for both human health and the environment. In addition, this is a waste of a potential source of products. In this study, a composite material was obtained from the agroindustrial residue CSB and used as a reinforcement and matrix for portland cement (CPC-30R).

Various studies on the characterization of composite materials based on cement and various inorganic loads that establish synergistic properties due to the volume and characteristics of the loads are reported. The fillers confer properties such as thermal insulation, light weight, and impact resistance [3, 4].

Other studies involve the use of sugarcane bagasse ash, but these differ from the charcoal from sugarcane bagasse. The use of ash does not improve the mechanical strength of the material and water permeability decreases [5].

Our material intends to use the charcoal from sugarcane bagasse to achieve thermal insulation. Bagasse coal has completely different properties to the ash. In ash the organic part is removed leaving only metal oxides.

This method is commonly employed to explain the properties of compounds even though more precise models that include the impact of the shape, size, and distribution of the particles on the elastic properties of the material have been developed [6, 7].

The thermal conductivity (λ) is a measure of a material's ability to conduct heat. It is most commonly used in Fourier's law of heat conduction. This property is very sensitive to the material's microstructure, and there are thermally conducting and insulating materials.

Fourier's law of heat transfer by conduction states that heat conduction occurs due to a temperature difference between two bodies and obeys the following equation [8]:

$$\lambda \equiv -\frac{q_x \Delta x}{A \Delta T}, \quad (1)$$

where λ is the thermal conductivity in watts per meter-degree Celsius ($\text{W}/\text{m}^\circ\text{C}$), q_x is the heat flow in the x direction in watts, Δx is the thickness of the sample in meters, ΔT is the temperature difference in $^\circ\text{C}$, and A is the area of the sample in m^2 .

The method is valid within the linear regime and allows for several material properties, including the thermal conductivity, to be calculated.

2. Experimental

2.1. Materials. We used charcoal from sugarcane bagasse (CSB) collected from the "Emiliano Zapata Salazar" sugarcane mill in Zacatepec, Morelos, fast-drying composite portland cement (CPC-30R, "Tolteca" brand), and distilled water from the company "Químicos Farmacéuticos Industriales."

2.2. Equipment. The following devices were used: a Denver Instrument digital scale with a limit of 320 g, certified to meet ISO quality guideline 9001, a Barnant Series 10 mixer, model number 700-5400, granulometry equipment from FIIC, SA de CV A CRODE SCH 0001 97 drying oven, an insulated hot plate with K-type thermocouples and an Arduino open-source hardware platform, a Thermo Haake

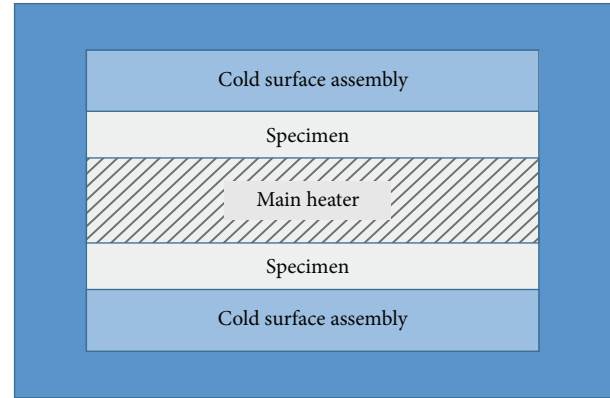


FIGURE 1: System mounting hot isolated plate by ASTM C177-97 standard.

K20 water circulation system, a PID temperature controller with a temperature range of 20 to 300°C , and JEOL/JSM-6010LA scanning electron microscope (SEM) and energy-dispersive spectroscopy (EDS).

2.3. Methods

2.3.1. Preparation of the Charcoal from Sugarcane Bagasse (CSB). To eliminate any traces of organic fiber, 250 g of CSB was placed in the drying oven for 2 hours at 400°C and then allowed to cool down. Subsequently, different sizes of CSB particles were separated using the granulometry equipment (mesh 100: 0.150 mm and mesh 200: 0.075 mm of hole opening. It is relative with ASTM E11-87).

2.3.2. Preparation of the Composite Materials. The composite materials were prepared by mixing different weight concentrations of CSB (5, 10, and 15 g) with cement (100 g) at a rate of 140 ± 5 rpm for 5 minutes. Then, water was added (40 g) and mixed at a rate of 285 ± 10 rpm for 5 minutes. The mixtures obtained were poured into $10 \times 2.5 \times 2.5$ cm metallic molds. The molds containing the mixtures were left to dry at room temperature for 72 hours. Then, the composite materials were extracted from the molds for characterization.

2.4. Characterization

2.4.1. Measurement of Thermal Conductivity. For this study, a hot plate system based on ASTM guideline C177-97 (Standard Test Method for Steady State Heat Flux Measurements and Thermal Transmission Properties by Means of the Guarded Hot Plate Apparatus) was used. Figures 1 and 2 show the experimental setup, which consists of the following elements: a hot plate, samples of the materials, two cold plates, one on each side of the system, a mounting system, an isolation chamber, and the necessary mechanisms for tuning and measurement [9].

Some of the most important specifications in the guideline are as follows: the method must be applied to materials with thermal conductivities of up to $0.62 \text{ kcal}/\text{mh}^\circ\text{C}$; the temperature during the test must be kept between -45 and

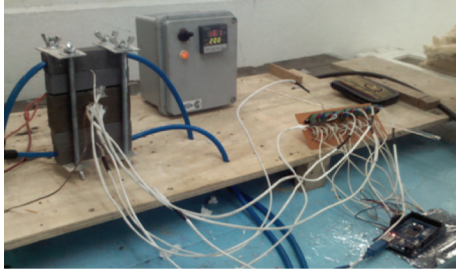


FIGURE 2: System hot insulated plate technique.

760°C; the external insulation surrounding the guard ring must have a thermal resistance of at least twice that of the material being tested; the thermocouples must be made from wire with a diameter no greater than 0.57 mm; and finally, the temperature difference between the hot and cold faces of the sample must be at least 22°C [10].

2.4.2. *Scanning Electron Microscopy (SEM) and Energy-Dispersive Spectroscopy (EDS) Analyses.* The morphology and load distribution of the composite materials were studied using the desktop SEM described in the equipment section. It was set to 3kV and to a magnification of 1000x. The EDS analysis was performed simultaneously under the same conditions to determine the elemental content and chemical composition of the CSB.

3. Results and Discussion

The composite materials were used to create a sample matrix (2 sizes × 3 weight concentrations), as shown in Table 1.

To measure the thermal conductivity, the samples were placed on the hot plate apparatus, which maintained a temperature between 30 and 230°C for 4 hours, with a flow temperature of 10°C at the cold plate. The thermal conductivities of the composite are shown in Figure 3.

The results show the behavior of the thermal conductivity as a function of temperature and the influence of the particle size and CSB concentration. At 122°C, the thermal conductivity of the pure cement matrix (CPC-30R) was high at 0.358 W/m°C.

At this temperature, all of the composite materials tested had lower thermal conductivities than the pure matrix; the values were between 0.350 and 0.300 W/m°C. Between 122 and 180°C, a decrease in the conductivity due to the CSB load was observed. For one load size (M-200 or M-100), the 10 g weight concentration marked the threshold for a minimal response because the thermal conductivity increased when the load was decreased (to 5 g) and increased (to 15 g). This may have been due to its distribution within the cement matrix. When the results of the M-200-15 g and M-100-15 g samples were compared, they showed that a larger particle size results in lower conductivity values when the load is constant. The same result was found when comparing the M-200-5 g and M-100-5 g samples. From this, we concluded that a smaller load leads to more efficient heat conduction, a finding that explains the higher conductivities obtained when the CSB particle size was increased [8].

TABLE 1: Composition of composite materials (CBC/CPC-30R/H₂O).

Mesh number	CBC (g)	CPC-30R (g)	H ₂ O (g)
M-100	15	100	40
M-100	10	100	40
M-100	5	100	40
M-200	15	100	40
M-200	10	100	40
M-200	5	100	40

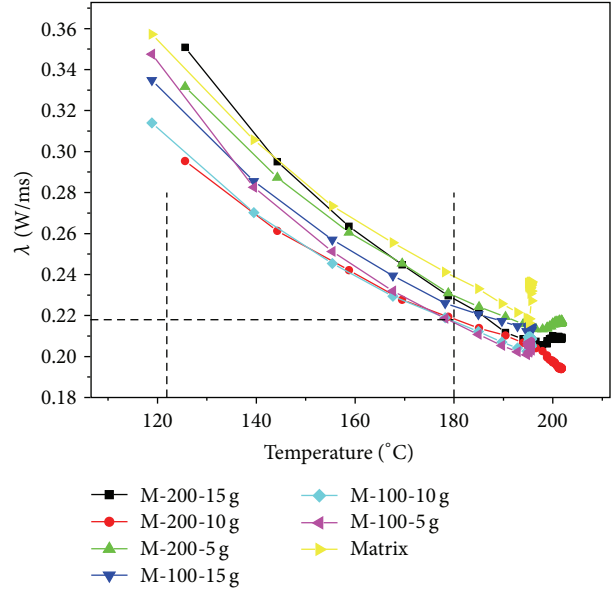


FIGURE 3: Thermal conductivity of composite materials with two sizes (M-100 and M-200) and three concentrations (15, 10, and 5 g) in the range of 120–180°C.

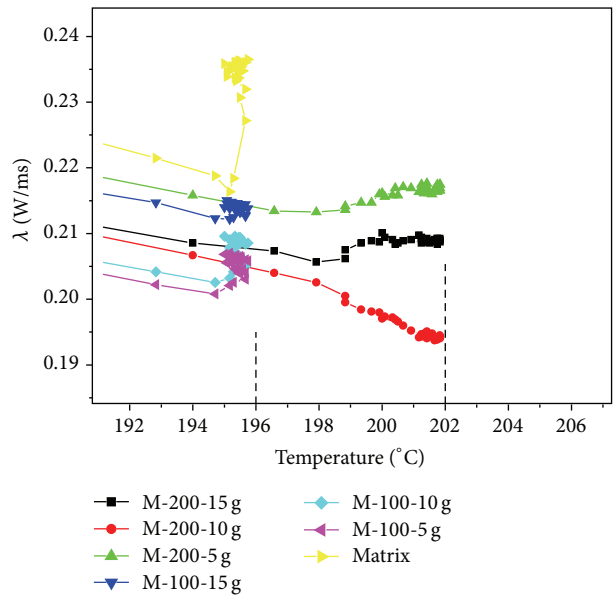


FIGURE 4: Thermal conductivity of composite materials with two sizes (M-100 and M-200) and three concentrations (15, 10, and 5 g) in the range of 194–202°C.

TABLE 2: EDS: elemental analysis of the CBC.

Chemical formula	C	Na ₂ O	MgO	Al ₂ O ₃	SiO ₂	P ₂ O ₅	SO ₃	K ₂ O	CaO	PbO
% mol	70	0.32	1.58	2.31	15.89	0.66	1.53	1.93	5.57	0.21

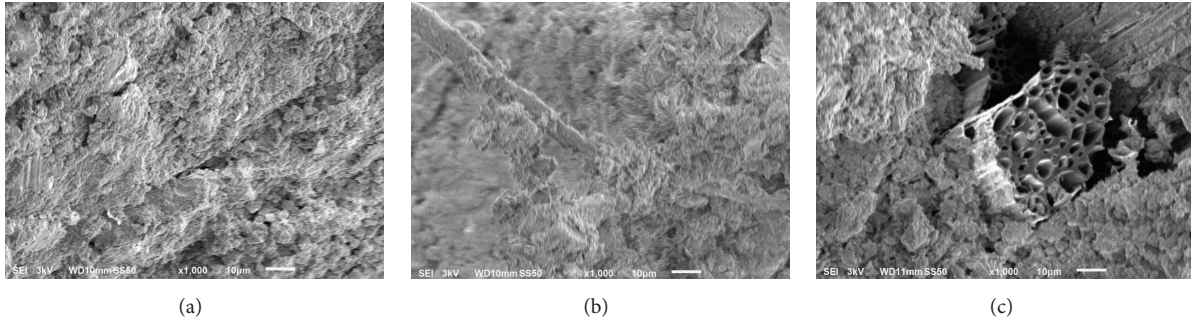
FIGURE 5: SEM micrographs (1000x) of composite materials: (a) matrix (CPC-30R/H₂O), (b) M-200-10 g, and (c) M-100-10 g.

Figure 4 shows that at 195.5°C a maximum conductivity of 0.235 W/m°C for the sample was obtained (matrix: portland cement). Samples containing charge (CSB) showed a lower thermal conductivity in the range of 0.215 to 0.205 W/m°C at this temperature (the latter being shown for M-200-10 g).

In the temperature range of 196 to 199°C the thermal conductivity decreases for all samples with CSB.

The sample M-200-10 g shows the lowest thermal conductivity of 0.194 W/m°C at a temperature of 202°C. The CSB is contributing to having a low thermal conductivity. With a concentration of 10 g CBS has the lowest income considering that this concentration is critical because by using 200-mesh distributes the load better generating sufficient space for the thermal conductivity decreases. This demonstrates that a good load distribution and a small particle size favor insulating material properties, as explained by Peña-Rodríguez et al., 2008 [8], where the thermal resistivity obtained polystyrene thermal clay loads and the same behavior is observed in the distribution and particle size.

SEM micrographs of the analysis showed that CPC-30R/H₂O ratio allows a hardening material without leaving a broken surface (Figure 5(a)). Likewise in the sample M-200-10 g good wetting of the matrix on the load can be demonstrated (see Figure 5(b)).

Figure 5(c) shows a particle load in the fracture of the composite material after undergoing strain. It can be seen that part of the load fell off the matrix suggesting a weak interaction between the filler and the matrix. It notes that the porosity of the charge also contributes to the thermal conductivity of composites decreases.

It is important to establish the composition of the CSB. We used EDS analysis, which provided evidence for the amount of carbon and oxides present in the material for that purpose. Table 2 shows the chemical composition of the CSB surface. Oxides contributed to the decrease in the thermal conductivity of the material, and here, SiO₂ was present in a greater proportion.

4. Conclusions

Composite materials were created using portland cement (CPC-30R) and charcoal from sugarcane bagasse with varying load particle sizes and concentrations. From studying these materials, we concluded that loading diminishes a composite material's thermal conductivity and that increasing the particle size reduces the thermal conductivity. This is because an increase in the particle size affects the heat conduction by decreasing the contact area. Similarly, an increase in the particle size increases the pore size, which may increase the volume of air inside the load and, therefore, reduce the thermal conductivity. The EDS analysis revealed the presence of oxides as an additional factor contributing to the diminished thermal response. The composite material with the lowest conductivity was the M-200-10 g sample (0.194 W/m°C), which behaved as a thermal insulator; it had a reduced heat transfer rate in comparison to the rest of the samples. The conductivity of the M-200-10 g sample was less than the conductivities reported by other authors for ceramic bricks and asbestos plates (0.87 and 0.36 W/m°C, resp.). The micrographs show both the porosity of the load and the load-matrix interaction at the point of fracture. In future studies, it is recommended that the effects of thermal shock on the mechanical properties of the materials should be investigated.

Competing Interests

The authors declare that they have no competing interests.

References

- [1] J. Wei and C. Meyer, "Degradation mechanisms of natural fiber in the matrix of cement composites," *Cement and Concrete Research*, vol. 73, pp. 1–16, 2015.
- [2] F. D. A. Silva, N. Chawla, and R. D. D. T. Filho, "Tensile behavior of high performance natural (sisal) fibers," *Composites Science and Technology*, vol. 68, no. 15–16, pp. 3438–3443, 2008.

- [3] M. Salas, R. Luco, and R. Ojeda, "Análisis Estructural de un Camarán de materiales compuestos," *Anales de Mecánica de la Fractura*, vol. 20, 2003.
- [4] C. S. Smith, *Design of Marine Structures in Composite Materials*, Elsevier Science, Amsterdam, The Netherlands, 1990.
- [5] Marcos De Paula Oliveira et al., "La caña de azúcarbagazo ash como material parcial- portland-cemento-reemplazo," *Dyna, Revista de la Facultad de Minas*, vol. 77, no. 163, pp. 47–54, 2010.
- [6] N. Martínez-Mateos, D. Busquets-Mataix, M. D. Salvador-Moya, and V. Amigó-Borrás, "Propiedades mecánicas de compuestos de matriz de aluminio reforzados con partículas cerámicas, obtenidos por extrusión de polvos," in *Proceedings of the VIII Congreso Nacional de Propiedades Mecánicas de Sólidos*, pp. 215–224, 2002.
- [7] G. Bao, J. W. Hutchinson, and R. M. McMeeking, "Particle reinforcement of ductile matrices against plastic flow and creep," *Acta Metallurgica et Materialia*, vol. 39, no. 8, pp. 1871–1882, 1991.
- [8] G. Peña-Rodríguez, J. Sánchez-Molina, and R. Monroy, "Efecto de la concentración de poliestireno expandido en la conductividad térmica efectiva de bloques de termoarcilla," *Revista Colombiana de Física*, vol. 40, no. 2, pp. 285–288, 2008.
- [9] M. M. Pérez-Sánchez, R. Centeno-Lara, and F. Lazcano-Serrano, "Desarrollo de un prototipo para la caracterización térmica de los materiales de construcción regionales," *Ingeniería*, vol. 6, no. 2, pp. 13–22, 2002.
- [10] ASTM C 177-97(Standard Test Method for Steady State Heat Flux Measurements and Thermal Transmission Properties by Means of the Guarded Hot plate Apparatus).

Research Article

Characterization of Various Plant-Produced Asphalt Concrete Mixtures Using Dynamic Modulus Test

Muhammad Irfan,¹ Asad S. Waraich,² Sarfraz Ahmed,¹ and Yasir Ali³

¹Military College of Engineering, National University of Sciences & Technology (NUST), Risalpur Campus, Risalpur 24080, Pakistan

²Department of Civil, Environmental, and Construction Engineering, University of Central Florida (UCF), 12800 Pegasus Drive No. 211, Orlando, FL 32816-2450, USA

³National Institute of Transportation, School of Civil and Environment Engineering, National University of Sciences & Technology, Islamabad 44000, Pakistan

Correspondence should be addressed to Muhammad Irfan; mirfan@mce.nust.edu.pk

Received 7 January 2016; Accepted 18 February 2016

Academic Editor: Osman Gencel

Copyright © 2016 Muhammad Irfan et al. This is an open access article distributed under the Creative Commons Attribution License, which permits unrestricted use, distribution, and reproduction in any medium, provided the original work is properly cited.

This research characterizes the performance of various plant-produced asphalt concrete mixtures by dynamic modulus $|E^*|$ test using asphalt mixture performance tester (AMPT). Marshall designed specimens of seven different mixtures were prepared using the Superpave gyratory compactor and subjected to sinusoidal compressive loading at various temperatures (4.4 to 54.4°C) and loading frequencies (0.1 to 25 Hz). A catalog of default dynamic modulus values for typical asphalt concrete mixtures of Pakistan was established by developing stress-dependent master curves separately, for wearing and base course mixtures. The sensitivity of temperature and loading frequency on determination of dynamic modulus value was observed by typical isothermal and isochronal curves, respectively. Also, the effects of various variables on dynamic modulus were investigated using statistical technique of two-level factorial design of experiment. Furthermore, two dynamic modulus prediction models, namely, Witczak and Hirsch, were evaluated for their regional applicability. Results indicated that both the Witczak and Hirsch models mostly underpredict the value of dynamic modulus for the selected conditions/mixtures. The findings of this study are envisaged to facilitate the implementation of relatively new performance based mechanistic-empirical structural design and analysis approach.

1. Introduction

Hot-mix asphalt (HMA) consists of the optimum combination of two basic ingredients: aggregate and asphalt binder. In order to meet the diverse and often conflicting performance parameters, for example, resistance to fatigue, deformation, cracking, and moisture damage; durability; skid resistance; and workability and economy, the mix designer generally manipulates three variables, namely, aggregates, asphalt binder, and the ratio of asphalt binder to aggregates, and thus seeks to achieve the aforementioned performance requirements. In Pakistan, the past few years have seen an increase in the premature failure due to fatigue cracking and rutting in both newly constructed and rehabilitated asphalt concrete pavements. The phenomenon of premature failure of pavement structures is attributed to the current

design procedures based on 1993 AASHTO design guide which are inherently empirical and incapable of providing adequate and reliable designs for heavy axle loads and tyre pressures in diversity of climatic regions and necessitates a more comprehensive design approach which incorporates both mechanistic and empirical aspects of design. Mechanistic-empirical pavement design guide (AASHTO Pavement ME) encompasses two parts: mechanistic (determine pavement responses) and empirical (distress prediction models/transfer functions). The success of the mechanistic-empirical structural design approach or framework lies in the accurate material characterization for predicting realistic pavement responses and ultimate performance. However, the viscoelastic nature of HMA is a challenge to be considered for its accurate characterization by the material properties. Dynamic modulus $|E^*|$ of HMA is one such material property

which reflects the loading time and temperature dependency of HMA. Dynamic modulus is considered as the stiffness property of HMA which can partially characterize its viscoelastic nature. It is the measure of the HMA's resistance to deformation under sinusoidal loading and is given by the absolute value of the complex modulus [1, 2]. Dynamic modulus of HMA has gained attention of the researchers during the past decade especially after its selection as a design input parameter for material characterization of asphalt concrete in the AASHTO Pavement ME pavement design guide and a candidate for a simple performance test to complement Superpave mix design methodology.

Several studies have been conducted in order to gain an insight into the factors affecting $|E^*|$. Bonnaure et al. [3] determined the modulus of asphalt mixtures by the application of a sinusoidal load to trapezoidal specimens and reported that the amount of aggregate and percent of air voids had a significant effect on the stiffness of the mix. Another study reported that the mixtures containing stiffer binders resulted in higher values of $|E^*|$. Furthermore, sample preparation techniques did not affect the dynamic modulus test results [4]. Kim et al. [5] reported that aggregate sources and gradation, within the North Carolina Department of Transportation, Superpave classification, did not seem to have a significant effect on dynamic modulus. This study also determined that the binder source, binder performance grade (PG), and asphalt content seemed to affect the dynamic modulus of asphalt mixtures. Flintsch et al. [6] concluded that mixes of the same type resulted in different measured $|E^*|$ values because of different constituents, that is, aggregate type, asphalt content, and percentage RAP which showed that $|E^*|$ was sensitive to mix constituents and properties. Cross et al. [7] evaluated the factors affecting $|E^*|$ and observed that the testing on lowest temperature of -10°C caused significant frost buildup on the test frame, samples, and LVDTs making it a difficult and time consuming task to determine $|E^*|$ below 0°C . Further, it was reported that the gyratory sample should be compacted to $6.0 \pm 1.0\%$ air voids in order to obtain a cored test specimen of required dimensions at $4.5 \pm 1.0\%$ air voids. PG grade in addition to test temperature and frequency was reported to have a significant effect on $|E^*|$. However, no significant effect of nominal maximum aggregate size (NMAS) or mix designation was observed. Tashman and Elangovan [8] developed a database of $|E^*|$ values of seven different job mix formulae (JMF) mixes with aggregates of different types and sources typically used in Washington state. Statistical analysis of the results revealed that use of different JMF mixes affected the dynamic modulus. However, it was also observed that the difference in $|E^*|$ due to different JMF was more significant at high temperatures and low frequencies. It was also observed that variation in the aggregate percent passing number 200 sieve did not have any effect on the dynamic modulus. Mohammad et al. [9] documented the effect of aggregate size on $|E^*|$ as a result of the study conducted for characterization of Louisiana asphalt mixtures. It was observed that NMAS had a significant effect on $|E^*|$, as the larger aggregate size combined with recycled asphalt (RAP) yielded higher values of $|E^*|$ at high temperatures. Another study developed a dynamic modulus catalog for NJDOT for

implementation of AASHTO Pavement ME structural design approach which was achieved by characterizing twenty-one different typical plant-produced HMA mixes [10]. Bonaquist [11] conducted dynamic modulus testing and reported that, for the same aggregate source mixes, dynamic modulus values were not much different from one another. Further, the aggregate sources with higher dynamic modulus values had the higher limiting minimum modulus values also when compared to other aggregate sources. Limiting minimum modulus values represents the stiffness of aggregate. A study compared the dynamic modulus of field extracted core with laboratory fabricated specimens and concluded that at 4°C dynamic modulus can be compared [12]. Laboratory evaluated dynamic modulus was related to field response and results indicated that laboratory obtained dynamic modulus was inversely proportional to the field measured pavement response of the asphalt longitudinal strains [13]. A number of recent comparative research studies characterized different HMA mixes based upon dynamic modulus test and constructed master curves in order to meet the practitioner needs [14–16].

Kim et al. [16] investigated the effect of additive (LEAD-CAP) on warm-mix asphalt using dynamic modulus, resilient modulus, and in-door accelerated pavement test (APT). The results suggested that additive is capable of producing mixture at relatively low temperature up to 30°C in comparison to conventional mixture and can be compared reasonably well with controlled hot-mix asphalt. Various researches determined the dynamic modulus of plant-produced or laboratory prepared mixes and validated the predictive ability of Witczak 1-37A model to a reasonable conformity [17–19]. El-Badawy et al. [20] in ensuing research study also calibrated the predictive equations for Idaho state mixtures. Cho et al. [21] evaluated the dynamic modulus of mixtures used in Korea and developed the $|E^*|$ predictive equation for Korean AASHTO Pavement ME and concluded that developed predictive equations were well correlated with measured values. A study was carried out in Saudi Arabia for implementation of AASHTO Ware Pavement design and evaluated two models, namely, NCHRP 1-37A and 1-40D, and concluded that NCHRP 1-37A $|E^*|$ model showed accurate and unbiased results [22]. A recent study evaluated the viscoelastic properties of a performance grade binder modified with different percentages of a wax-based warm-mix asphalt (WMA) using dynamic modulus test. This study concluded that the Hirsch model (2003) [23] provided better approximations of the $|E^*|$ values than the Witczak model [24]. In consequence of requisition of skilled personnel, time, and cost effect associated with the dynamic modulus test, researchers have been attempting for several years by using various modeling techniques to develop the prediction equations which can predict the $|E^*|$ values directly from the mix properties. The last few decades have seen the development of these predictive equations as listed in Table 1.

The most recent models listed in Table 1, that is, Andrei, Witczak, and Mirza's revised model (hereafter referred to as Witczak model) and Hirsch model of Christensen, Pellinen,

TABLE 1: List of dynamic modulus $|E^*|$ predictive models [25].

Model number	E^* predictive model	Year (published)
1	Van der Poel model	1954
2	Bonnaure model	1977
3	Shook and Kallas model	1969
4	Witczak's early model	1972
5	Witczak and Shook's model	1978
6	Witczak's model	1981
7	Witczak, Miller, and Uzan's model	1983
8	Witczak and Akhter's model	1984
9	Witczak, Leahy, Caves, and Uzan's model	1989
10	Witczak and Fonseca's model	1996
11	Andrei, Witczak, and Mirza's revised model	1999
12	Hirsch model of Christensen, Pellinen, and Bonaquist	2003

and Bonaquist (hereafter referred to as Hirsch model), have been reported to be reasonably accurate and were used to evaluate understudy HMA mixtures in this research.

The findings of studies mentioned in Table 1 indicate dynamic modulus, a key material property of HMA that better reflects the viscoelastic nature of asphalt concrete. Its significance has further been increased as a result of its selection as a material characterization design input parameter in the AASHTO Pavement ME and thus asphalt concrete mixtures need to be characterized in terms of $|E^*|$ at regional levels [20–22]. However, to the knowledge of authors, no such research study characterized locally used mixtures in Pakistan. Hence, this research study aimed to determine the dynamic modulus of plant-produced asphalt mixtures in laboratory and results obtained were employed to two-level factorial design for determination of factor affecting $|E^*|$. This research study characterizes and develops the master curves for different asphalt concrete mixes (for wearing and base course mixes), investigates the factors affecting dynamic modulus (stiffness parameter) in order to compare and rank selected asphalt concrete mixes, and validates the laboratory observed dynamic modulus values with the two dynamic modulus prediction models, namely, Witczak and Hirsch models.

2. Methodology

2.1. Objective and Scope. The objective of this study is to develop master curves for various plant-produced asphalt

concrete mixtures and rank them based on dynamic modulus. The study incorporates four wearing mixes of nominal maximum aggregate size (NMAS) of 19 mm and three base mixes of NMAS of 37.5 mm procured from different highway construction sites of Pakistan. The binder and aggregate type used for testing were penetration grade 60/70 and limestone aggregate, each from two different sources. The study variables for different selected mixtures are presented in Table 2.

2.2. Selection of Material. Seven plant-produced asphalt concrete mixtures were procured from different highway construction projects keeping in view the desired variability and availability of the plant-produced HMA in Pakistan. Representative samples of all seven mixes were collected from dump trucks at plant site, following the proper sampling techniques [26]. The mixtures used in the study were designed using Marshall method (optimum bitumen content determination) by the contractors of the selected projects pursuant to specifications of National Highway Authority (NHA) [27]. Job mix formulae and gradations of the selected asphalt mixtures are presented in Table 3.

2.3. Specimens Preparation. Representative plant-produced asphalt mix samples were subjected to testing for maximum theoretical specific gravity, asphalt content, and gradation of the aggregate. Then these samples were reheated to compaction temperature of 135°C in the laboratory and triplicate specimens for each test temperature were fabricated in accordance with ASTM 3496-99 [28] using Superpave gyratory compactor with target voids in total mix (VTM) of 4% ± 1% (after coring and/or cutting). The binders on these plant-produced mixes underwent short-term aging during their production stage; however, these binders were extracted/tested. The variation among triplicates specimens was in specified range as specified in AASHTO TP62-07 [1]. Each gyratory compacted specimen was carefully sawed up to required dimension of 100 mm diameter and 150 mm height to comply with the dynamic modulus test specimen requirements as per AASHTO TP 62-07 [1].

2.4. Laboratory Testing. The $|E^*|$ test yields phase angle and $|E^*|$ value. The phase angle (φ) is the angle by which induced axial strain lags behind the applied compressive stress. Figure 1 illustrates the sinusoidal stress and the resulting strain defined by the angular velocity which in turn are related to the loading frequency and time which implies that the phase lag represents the time dependency of HMA. AASHTO Pavement ME has three levels of input: level 1 includes determination of $|E^*|$ in laboratory (material input), whereas levels 2 and 3 encompass determination of $|E^*|$ by the use of predictive equations. Dynamic modulus has also been adopted by AASHTO as a provisional standard in AASHTO designation TP62-07 [1]. The dynamic modulus test method is a widely used laboratory test that requires application of a compressive axial stress to a cylindrical specimen of HMA and the recoverable strain is calculated from axial deformations measured at two, three, or four locations (as

TABLE 2: Project and mixtures designation—wearing and base course mixtures.

Mix course	Abbreviated name	Project name	Aggregate source	NMAS (mm)	Mix type	Bitumen source and pen. grade
Wearing course mixtures	LNLP	Lakhi-Naudero-Larkana Road	Quetta	19	Marshall	NRL 60/70
	HMW-W	Head Muhammad Wala Bridge (N-70)	Sargodha	19	Marshall	NRL 60/70
	WUP-W	Wah Underpass (N-5)	Margalla	19	Marshall	ARL 60/70
	SWB-TP	Swabi-Topi Road	Margalla	19	Marshall	ARL 60/70
Base course mixtures	JPU	Jalalpur-Pirwala-Uch Sharif Road (N-115)	Sargodha	37.5	Marshall	NRL 60/70
	HMW-B	Head Muhammad Wala Bridge (N-70)	Sargodha	37.5	Marshall	NRL 60/70
	WUP -B	Wah Underpass (N-5)	Margalla	37.5	Marshall	ARL 60/70

Note. NRL: National Refinery Limited; ARL: Attock Refinery Limited.

TABLE 3: Job mix formulae for selected asphalt mixtures.

Mix type/ name	Wearing course mixtures				Base course mixtures		
	LNLP	HMW-W	WUP-W	SWB-TP	JPU	HMW-B	WUP-B
Binder type	NRL 60/70	NRL 60/70	ARL 60/70	ARL 60/70	NRL 60/70	NRL 60/70	ARL 60/70
Binder content (%)	4.0	4.4	4.2	4.2	3.3	3.4	3.5
Air void (%)	4.0	4.0	4.0	4.0	4.0	4.0	4.0
VMA (%)	14.8	15.3	14.2	13.4	13.7	13.2	12.8
VFA (%)	66.9	63.5	66.5	59.5	58.1	59.2	58.0
Metric (US) sieve	Gradation (% passing)						
37.5 mm (1(1/2) in.)	100	100	100	100	100	100	98.8
25 mm (1 in.)	100	100	100	100	82.6	85.4	82.7
19 mm (3/4 in.)	100	99.9	99.7	100	69.7	71.0	67.4
12.5 mm (1/2 in.)	82.5	79.5	84.5	80	59.2	59.9	56.2
9.5 mm (3/8 in.)	68.7	69.4	63.4	67	52.2	53.4	43.5
4.75 mm (number 4)	49.3	48.7	46	48	41.6	35.5	35.0
2.36 mm (number 8)	30.8	35.3	30.5	33	24.5	26.4	25.1
0.3 mm (number 50)	10.5	11.8	10.3	11	9.4	10.8	7.6
0.075 mm (number 200)	5.2	5.2	5.0	4.7	5.0	4.7	4.2

required) by using linear variable differential transformers (LVDTs). Dynamic modulus is then calculated as the ratio of stress magnitude to average strain magnitude.

The dynamic modulus test was conducted at four temperatures and six frequencies for each mixture using asphalt mixture performance tester (AMPT). Specimens were conditioned for the required equilibrium in order to achieve the desired test temperatures before conducting the test. The test equipment consists of environmental chamber, which controls temperature ranging from 4 to 60°C, and confined pressure system which provides pressure up to 210 kPa. Three replicate specimens were tested at each test temperature with COV ranging from 4% to 21%. The tests were performed at the loading frequencies of 25, 10, 5, 1, 0.5, and 0.1 Hz and the temperatures used for the testing were 4.4°C, 21.1°C, 37.8°C,

and 54.4°C. The laboratory results were further cast off to develop master curves and statistical analysis.

3. Results and Discussion

The dynamic modulus exhibits stress-strain relationship under compressive sinusoidal loading. As expected, for all the tested asphalt concrete mixtures, the dynamic modulus values decreased with an increase in temperature and decrease in the loading frequency. It was observed that LNLP and WUP wearing course mixtures have relatively higher dynamic modulus values at low and high temperature variations, respectively, whereas JPU base course mix has relatively highest dynamic modulus values at both low and

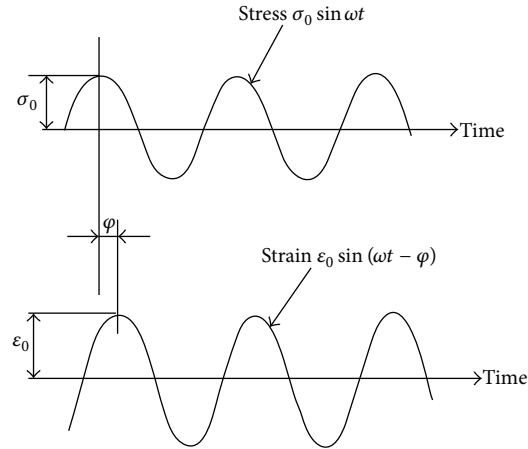


FIGURE 1: Phase lag between sinusoidal stress and recoverable strain [2].

high temperatures for the range of loading frequencies (Table 4).

The average test results/typical isothermal and isochronal curves for dynamic modulus at four different temperatures and six different loading frequencies for wearing and base mixtures tested in the study have been presented in Figures 2(a) and 2(b), respectively. It is evident from these plots that dynamic modulus decreases with increase in temperature and increases with increase in frequency. Also, sensitivity analysis reveals that, for a given loading frequency, an increase in temperature (from 21.1 to 37.8°C) translated into 57% and 55% drop in $|E^*|$ values on average for wearing and base course mixes, respectively, whereas, for a given temperature, an increase in loading frequency (from 0.1 to 25 Hz), 68% and 79% of variation in $|E^*|$ values on average, was attributed to wearing and base course mixes, respectively.

3.1. Master Curves for Dynamic Modulus. The test results obtained were used for development of master curve for subsequent use in pavement structural response and design process. The test results for the replicate specimens were averaged for each test temperature and master curves for the average values of $|E^*|$ at a reference temperature of 21°C for each mix were constructed using the time-temperature superposition principle using Microsoft® solver sheet. Also, keeping in view the testing limitation and inability of the asphalt mixture performance tester (AMPT) to conduct test at -10°C, an abbreviated approach developed in NCHRP Project 9-29 was used for construction of the stress-dependent master curves [29].

The general form of sigmoidal function used to develop a master curve is given as follows [30]:

$$\log |E^*| = \delta + \frac{\alpha}{1 + e^{\beta + \gamma(\log f_r)}}, \quad (1)$$

where $\log(|E^*|)$ is log of dynamic modulus. δ is minimum modulus value. f_r is reduced frequency, that is, $f/a(T)$, where f is actual frequency and $a(T)$ is the required shift factor at

reference temperature. α is span of modulus value (range of lowest and highest dynamic modulus values). β , γ are shape parameters of sigmoidal function.

The master curves wearing and base mixes are presented in Figure 3 which illustrates that they tend to converge at higher frequencies; however they have considerable degree of separation at lower frequencies. Higher frequency is analogous to lower temperature and vice versa in terms of temperature. It can be inferred that $|E^*|$ of LNLP wearing mix (Figure 3(a)) and JPU base mix (Figure 3(b)) are relatively better performing for given tested mixtures which is attributed to the mixtures packing arrangement with the relatively lower design asphalt content than other mixtures, thus exhibiting higher stiffness values (see Table 3).

3.2. Evaluation of Dynamic Modulus Prediction Equations.

As part of this study two prediction equations were evaluated for regional applicability in Pakistan. As there was no information available with reference to the default dynamic modulus values for commonly used mixtures in Pakistan, it was necessary to characterize the commonly used mixtures accordingly. The inputs parameters for both the equations were primarily obtained from the JMF of the mixtures. However, certain other information like viscosity and shear modulus of binder were obtained by conducting laboratory tests on the extracted binders.

3.2.1. Witczak Model. The current Witczak model used in AASHTO Pavement ME is improved version of the previous Witczak and Fonseca model in order to use a wide range of AC mixtures. The Witczak model used 205 mixtures prepared with both modified and unmodified binders having a temperature range from 0 to 54.4°C and the loading frequency ranging from 0.1 to 25 Hz. A total of 39 different aggregate types were made part of this database and the mixtures tested included both kneading and gyratory compacted specimens [31]. Input parameters of Witczak 1-37A viscosity based model (2) include bitumen viscosity, effective asphalt content, aggregate gradations, air voids, and loading frequency:

TABLE 4: Measured dynamic modulus, $|E^*|$ (MPa), and phase angle, φ .

(a) Wearing course mixes									
Temperature (°Celsius)	Freq. (Hz)	HMW-W		WUP-W		SWB-TP		LNLP	
		$ E^* $	φ						
4.4	25	23077	7.90	17395	7.85	23821	5.93	29820	6.89
	10	21360	8.15	16258	8.21	22305	6.52	27572	7.62
	5	20346	9.12	15368	8.95	21229	6.91	26028	8.29
	1	16947	9.92	13293	11.27	18712	8.82	22829	10.56
	0.5	15865	11.58	12376	12.26	17382	9.58	20815	11.49
	0.1	13279	14.21	10259	14.87	14555	11.83	16623	14.66
21.1	25	17099	12.20	14141	11.12	17306	10.61	17547	13.91
	10	14769	13.36	12679	12.41	15610	11.51	15320	15.73
	5	13348	13.87	11811	13.10	14720	12.81	13803	16.80
	1	10639	16.65	9384	16.65	11342	16.52	10108	20.25
	0.5	9315	17.90	8246	17.81	9935	17.70	8770	21.75
	0.1	6750	22.07	5819	21.41	7281	21.52	5833	26.39
37.8	25	9942	17.09	8908	19.52	11238	16.86	6322	27.98
	10	7998	19.77	9754	21.17	9494	19.38	4695	29.91
	5	7040	21.35	8580	22.23	8370	20.65	3716	30.40
	1	5047	23.83	3284	24.62	5964	23.77	2075	31.24
	0.5	4337	24.61	2732	25.17	5033	24.69	1586	30.95
	0.1	2744	26.76	1575	27.16	3054	27.23	869	29.32
54.4	25	5268	25.62	6750	22.07	5619	27.50	3323	32.50
	10	4158	26.55	5502	24.11	4413	28.50	2351	32.60
	5	3475	26.05	4675	24.78	3372	28.45	1772	32.37
	1	2158	28.46	3103	27.18	1917	28.63	917	30.97
	0.5	1717	28.58	2517	27.52	1462	28.21	676	30.29
	0.1	889	26.56	1289	29.39	731	27.42	359	27.75
(b) Base course mixes									
Temperature (°Celsius)	Freq. (Hz)	JPU		HMW-B		WUP-B			
		$ E^* $	φ	$ E^* $	φ	$ E^* $	φ		
4.4	25	31626	6.60	29068	6.72	23228		6.77	
	10	30199	7.65	27379	7.71	21801		7.92	
	5	28448	8.24	25973	8.62	20650		9.02	
	1	24387	10.97	22229	11.79	17609		12.61	
	0.5	22477	12.34	20415	13.22	16154		14.30	
	0.1	17837	16.30	16092	17.67	12569		19.19	
21.1	25	21167	11.68	19105	14.29	18699		12.41	
	10	18940	14.37	16534	16.98	16603		14.76	
	5	17037	16.15	14734	19.14	15141		16.62	
	1	12886	21.30	10432	25.55	11307		22.40	
	0.5	11156	23.33	8708	28.14	9694		24.66	
	0.1	7212	29.02	4950	34.93	5909		30.80	
37.8	25	11783	22.81	19580	22.68	12349		21.02	
	10	9336	26.83	15789	26.57	9956		24.94	
	5	7770	28.89	13190	29.11	8205		27.22	
	1	4245	33.34	7663	35.27	4744		32.26	
	0.5	2982	34.04	5669	36.78	3475		33.09	
	0.1	1299	34.33	2243	38.53	1448		32.70	

(b) Continued.

Temperature (°Celsius)	Freq. (Hz)	JPU		HMW-B		WUP-B	
		$ E^* $	φ	$ E^* $	φ	$ E^* $	φ
54.4	25	7757	28.73	3399	42.17	5392	33.94
	10	5557	32.31	2082	43.91	3544	36.05
	5	4226	33.75	1351	44.68	2434	36.59
	1	1958	35.89	462	44.44	1069	35.77
	0.5	1317	35.33	276	44.40	689	34.92
	0.1	524	31.44	110	38.61	331	30.55

$$\begin{aligned} \text{Log } E^* = & -1.249337 + 0.029232 (p_{200}) - 0.001767 (p_{200})^2 - 0.00284 (p_4) - 0.05809 V_a - 0.802208 \frac{V_{\text{beff}}}{V_{\text{beff}} + V_a} \\ & + \frac{3.871977 - 0.0021 p_4 + 0.003958 p_{38} - 0.000017 p_{(38)}^2 + 0.00547 p_{34}}{1 + e^{[-0.603313 - 0.313351 \log(f) - 0.393532 \log(\eta)]}} \end{aligned} \quad (2)$$

where E^* is dynamic modulus of mix, 10^5 psi (1 psi = 0.00689 MPa). $\dot{\eta}$ is viscosity of binder, 10^6 Poise. f is loading frequency, Hz. p_{200} is % passing number 200 sieve. p_4 is cumulative % retained on number 4 sieve. p_{38} is cumulative % retained on 3/8 in. sieve. p_{34} is cumulative % retained on 3/4 in. sieve. V_a is air voids, % by volume. V_{beff} is effective binder content, % by volume.

For evaluation purposes, values of dynamic modulus were predicted using the Witczak model at the conditions corresponding to each measured value of $|E^*|$. $|E^*|$ values were predicted using the volumetric details and aggregate gradations obtained from the JMF of the mixtures tested: loading frequency (0.1 to 25 Hz); % passing number 200 sieve (4.2 to 5.2%); cumulative % retained on number 4 sieve (35 to 49%); cumulative % retained on 3/8 in. sieve (43 to 69%); cumulative % retained on 3/4 in. sieve (67 to 100%); and air voids % by volume (3.5 to 4.5%). Results indicated that the Witczak model mostly underpredicts the values for dynamic modulus for HMA mixes of Pakistan. Figure 4(a) illustrates the comparison of measured and predicted dynamic modulus values grouped on the basis of temperature. It can be inferred from the figure that the values are distributed along the line of equality for lower temperatures. However, with an increase in temperature, the model tends to underpredict the values for dynamic modulus of the mixtures selected for the study. This implies that the said model is more relevant and significant at lower test temperatures as compared to higher temperature conditions for the tested mixtures in the study.

3.2.2. Hirsch Model. Christensen et al. [23] developed Hirsch dynamic modulus prediction equation based on law of composite mixtures. The model was developed using database of various mixtures to determine dynamic modulus using binder shear modulus, that is, G^* , and the volumetric properties of the mix, that is, voids in mineral aggregate (VMA) and voids filled with asphalt (VFA). The Hirsch model used 18 different mixtures and five different binder types to fabricate both Marshall and Superpave designed specimens. The tests

were conducted at temperature ranging from 4 to 38°C and loading frequencies of 0.1 and 5 Hz. The database used for the development of model had air voids ranging from 5.6 to 11.2%; VMA ranging from 13.7 to 21.65%; and VFA of 38.7 to 68%. However, the input parameters range used for validation purpose in this study is given in parentheses against each parameter below. Hirsch model is presented as follows:

$$\begin{aligned} |E^*| = & P_c \left[4200000 \left(1 - \frac{\text{VMA}}{100} \right) \right. \\ & \left. + 3 |G^*|_b \left(\frac{\text{VFA} \times \text{VMA}}{10000} \right) \right] \\ & + \frac{(1 - P_c)}{\left[(1 - \text{VMA}/100) / 4200000 + \text{VMA}/3 \times \text{VFA} |G^*|_b \right]} \end{aligned} \quad (3)$$

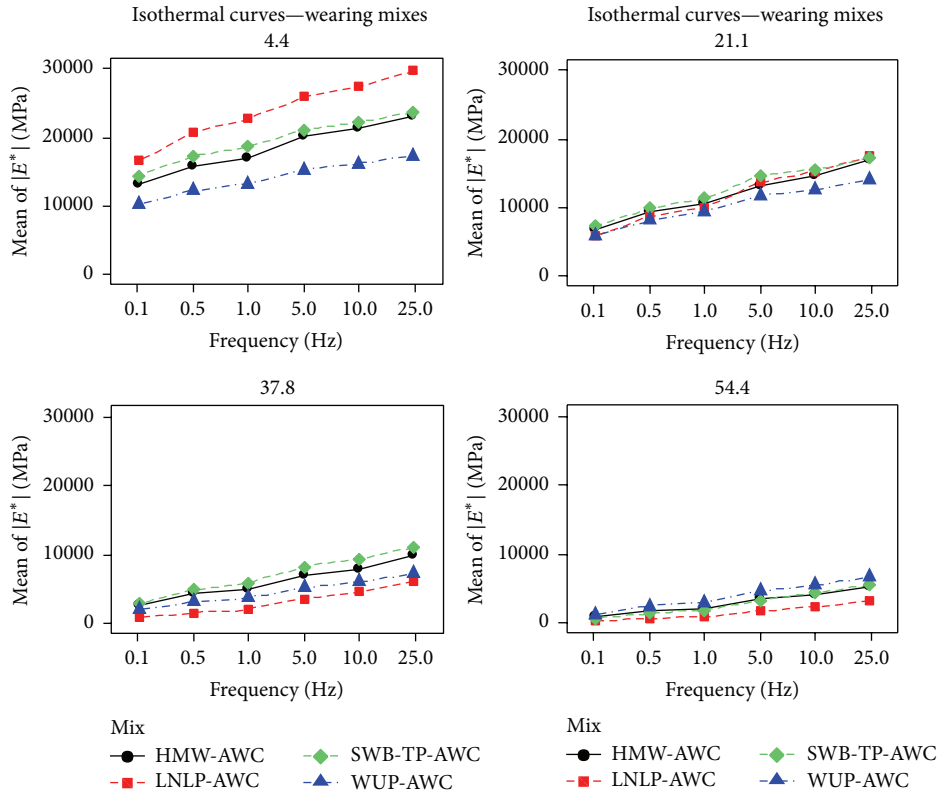
where

$$P_c = \frac{(20 + \text{VFA} \times 3 |G^*|_b / \text{VMA})^{0.58}}{650 + (\text{VFA} \times 3 |G^*|_b / \text{VMA})^{0.58}} \quad (4)$$

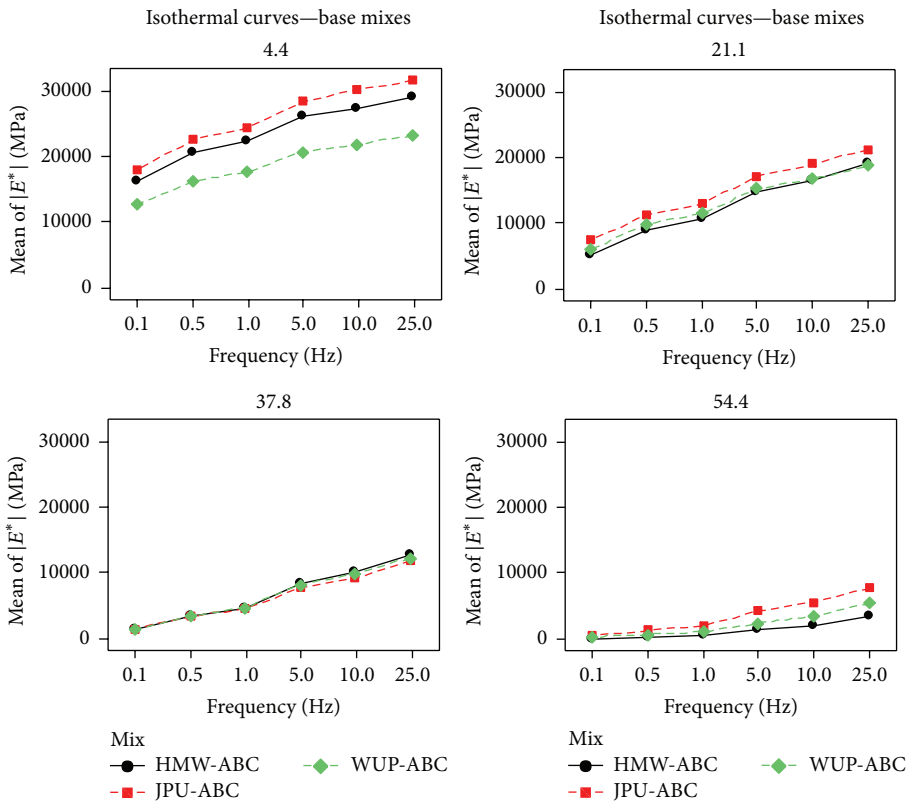
$|E^*|$ is dynamic modulus, psi (1 psi = 0.00689 MPa). VMA is voids in mineral aggregate, % (12.8 to 15.3%). VFA is voids in aggregate filled with asphalt, % (58 to 67%). $|G^*|_b$ is dynamic shear modulus of binder, psi (0.12 to 0.55 psi) or (0.83 to 3.79 kPa).

The test results obtained from laboratory testing were also used for evaluation of the Hirsch model by comparison of the measured $|E^*|$ and the predicted $|E^*|$ values. Hirsch model predictions were made using the input data, that is, VMA and VFA obtained from the JMF of each selected mix. Comparison of the results indicated that Hirsch model consistently underpredicts the dynamic modulus values for HMA mixes of Pakistan regardless of the test temperature, the frequency, or the mix selected as shown in Figure 4(b).

The underprediction of dynamic modulus values is attributed to the variation in binder and volumetric (JMF) properties used for preparation of plant-produced mixtures compared to that used for the development of Witczak



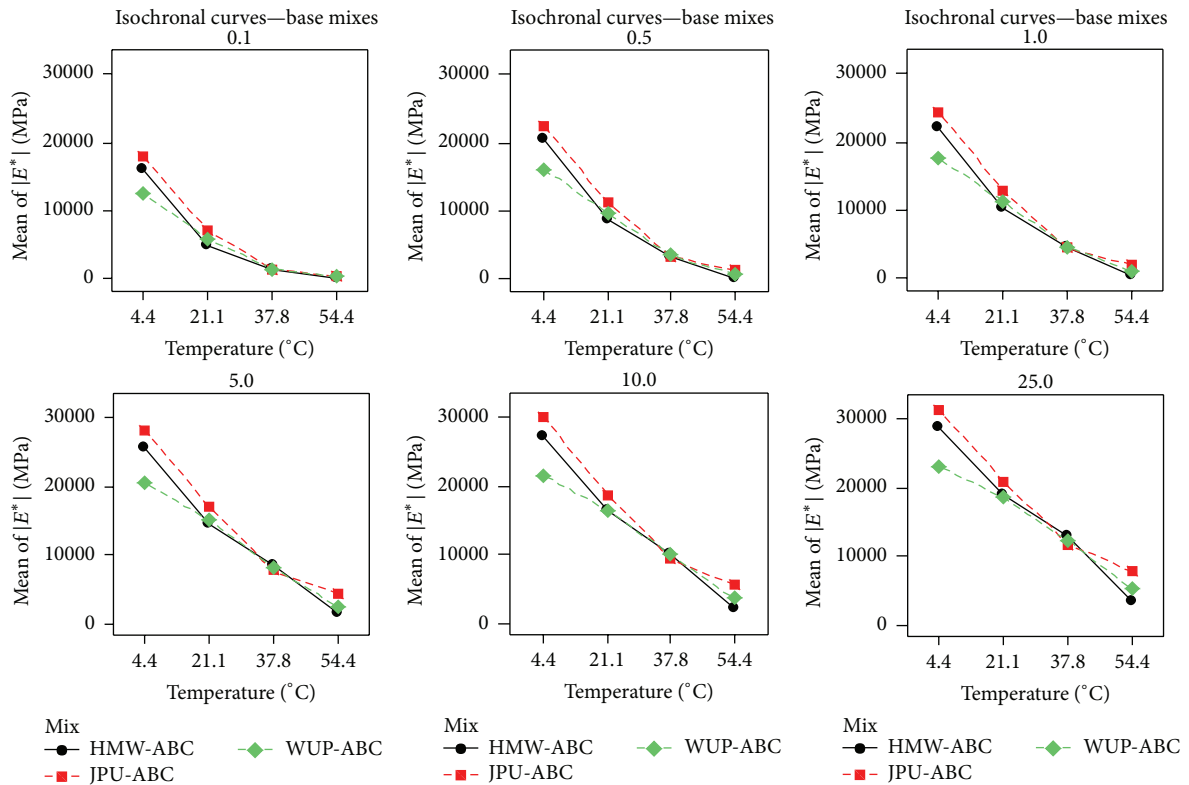
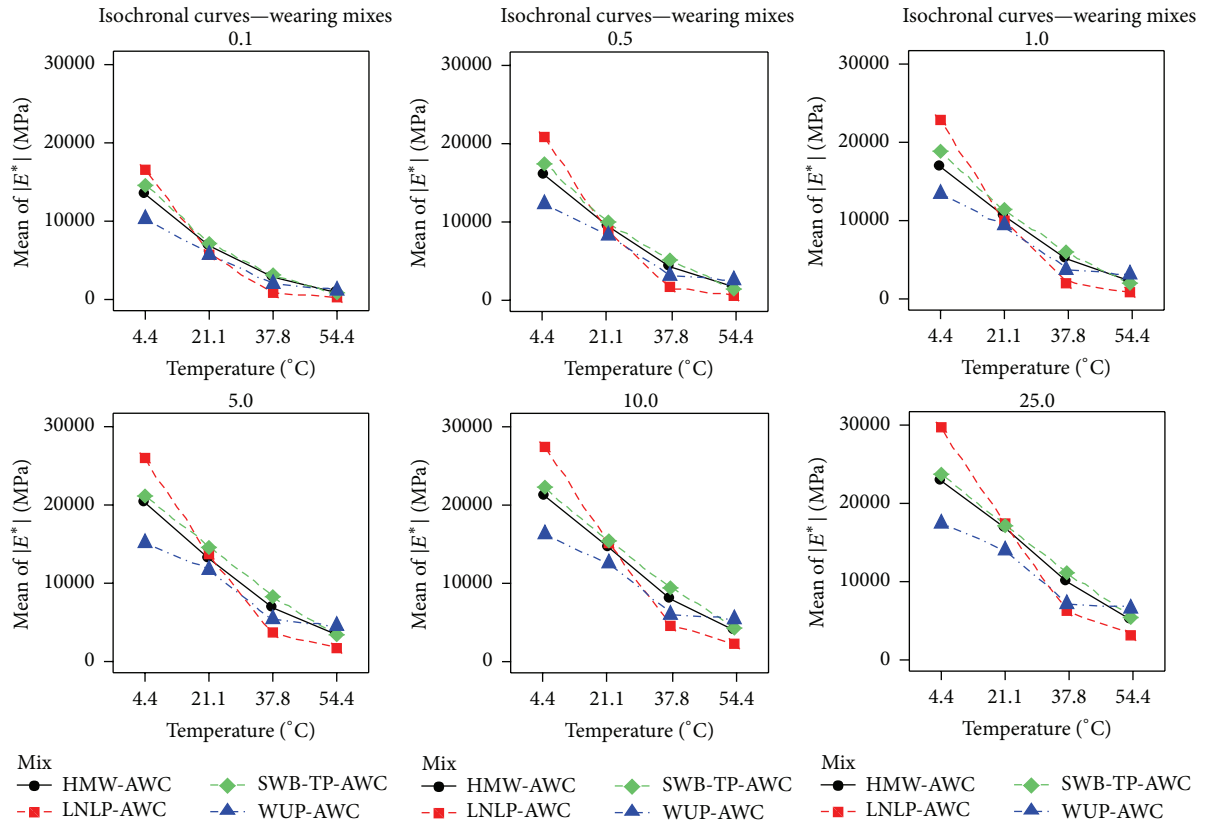
Panel variable: temperature (°C)



Panel variable: temperature (°C)

(a) Isothermal curves

FIGURE 2: Continued.



(b) Isochronal curves

FIGURE 2: Dynamic modulus test results.

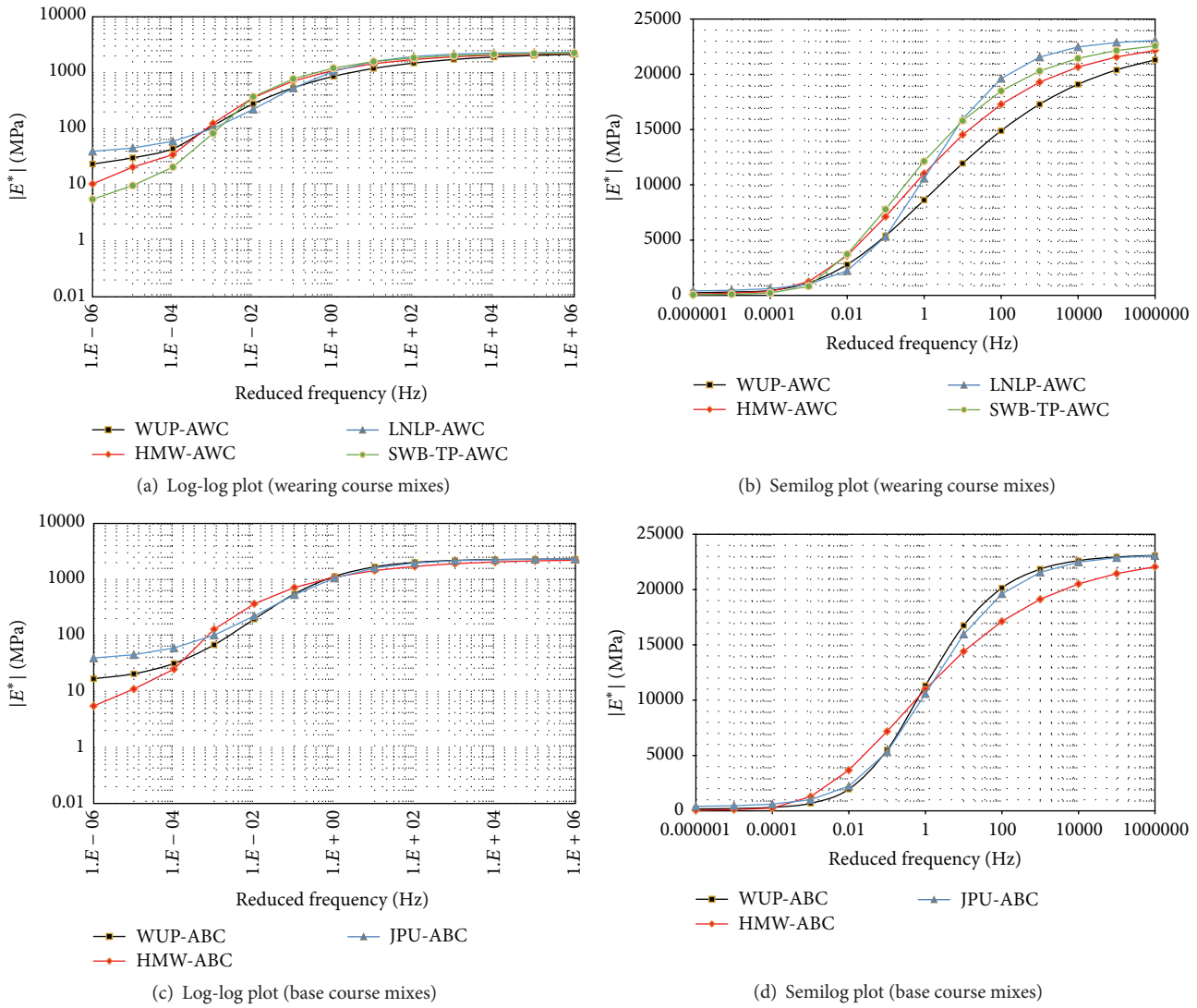


FIGURE 3: Dynamic modulus master curves for plant-produced mixtures.

and Hirsch models. The parameter values obtained from the density-void analysis on the test sample could be more accurate than JMF parameters. Also, these models were calibrated using datasets of conditions quite different from Pakistan which are quarry dependent: variation in aggregate mineralogical composition (limestone, etc.) and gradation (percent passing different sieves) and variation in binder properties and its manufacturing process and industry. Also, the underprediction of dynamic modulus values is in agreement with similar past studies conducted on the local material for calibration of these models [32, 33].

4. Conclusions

Performance evaluation of seven plant-produced HMA mixtures was carried out using dynamic modulus testing and factors influencing the dynamic modulus of HMA were evaluated. It was observed that the test temperature and loading frequency are significant factors affecting dynamic modulus

for both wearing and base course mixtures; however, VMA is marginally significant in case of base course mixtures, only. Furthermore, there was significant difference between the dynamic modulus of different mixtures based on different aggregate size, gradation, and aggregate source. At low (cold) temperatures, the parameter of viscous (or elastic) properties of the mixtures (phase angle) decreases which indicates more elastic behavior of material with high modulus values and is attributed to the dependency of binder on asphalt concrete response at lower temperatures. However, at high (warm) temperatures, the effect of aggregate skeleton/interlock starts to overpower the viscous binder effect causing the phase angle to decline. As part of this study the dynamic modulus prediction models, namely, Witczak and Hirsch, were also evaluated for their potential regional applicability. Results indicated that both models mostly underpredict the value of dynamic modulus for the selected conditions/mixtures. Nevertheless, these models could be used for evaluation purposes and for the design of low and medium traffic volumes pending future investigation of the revised prediction

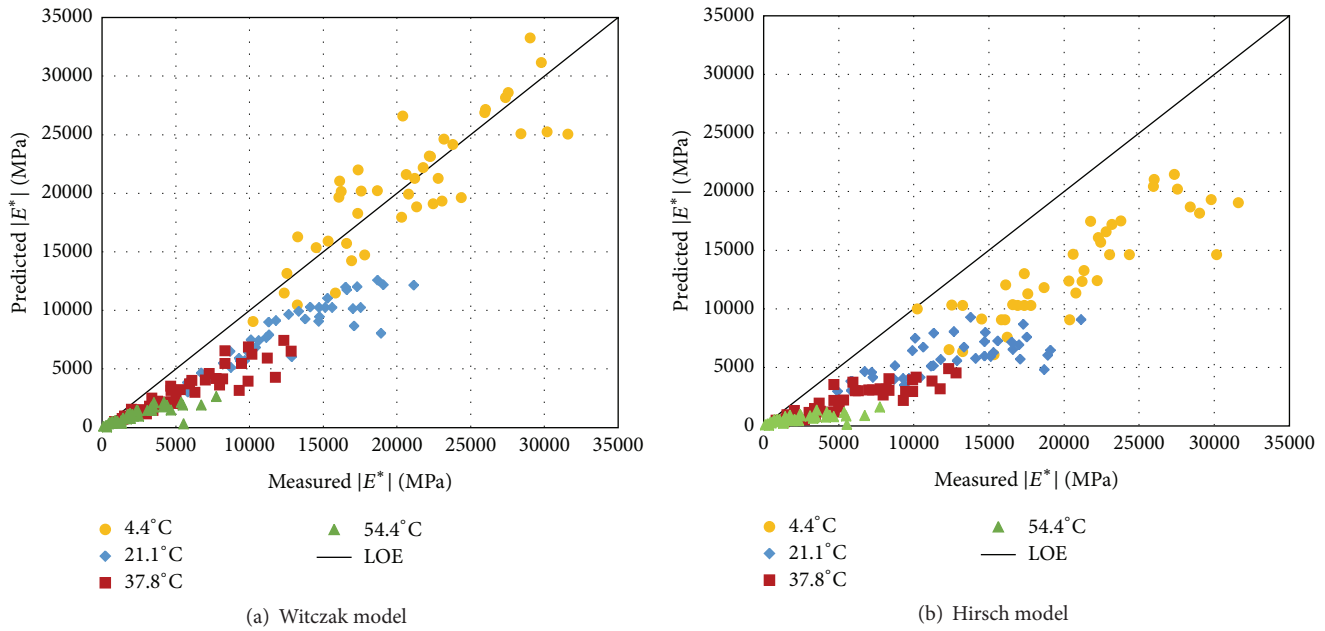


FIGURE 4: Measured versus predicted plot of dynamic modulus.

equation incorporated in the new AASHTO Pavement ME software/guide. The established default dynamic modulus values catalog for typical asphalt concrete mixtures of Pakistan at various temperatures and frequencies by developing the master curves of $|E^*|$ is the foremost effort in the country, thus facilitating the future implementation of performance based mechanistic-empirical structural design and analysis approach.

Disclosure

The content of this paper reflects the views of the authors who are responsible for the facts and the accuracy of the data and results presented herein. This is merely a technical paper for the experimental investigation of factors affecting the dynamic modulus of HMA using simple performance test. This research study does not constitute a standard, a specification, or a regulation.

Competing Interests

The authors declare that they have no competing interests.

Acknowledgments

The authors gratefully acknowledge the contribution of laboratory support staff at National Institute of Transportation, National University of Sciences and Technology (NUST), in preparing the samples for the research study.

References

- [1] AASHTO, *Standard Test Method for Determining Dynamic Modulus of Hot-Mix Asphalt (HMA)*, TP 62-07, American Association of State Highway and Transportation Officials, Washington, DC, USA, 2007.
- [2] Y. H. Huang, *Pavement Analysis and Design*, Pearson Education, New Jersey, NJ, USA, 2004.
- [3] F. Bonnaure, G. Gest, A. Gravois, and P. Uge, "A new method of predicting the stiffness of asphalt paving mixtures," in *Proceedings of the Association of Asphalt Paving Technologists*, vol. 46, pp. 64–104, San Antonio, Tex, USA, February 1977.
- [4] R. C. Timothy, L. Xingjun, O. M. Mihai, and L. S. Eugene, "Dynamic and resilient modulus of Mn/DOT asphalt mixtures," Report, Department of Civil Engineering, University of Minnesota, Minneapolis, Minn, USA, 2003.
- [5] Y. R. Kim, M. King, and M. Momen, "Typical dynamic moduli values of hot mix asphalt in North Carolina and their prediction," in *Proceedings of the 84th Annual Meeting of the Transportation Research Board*, Paper no. 05-2568, TRB, National Research Council, Washington, DC, USA, January 2005.
- [6] G. W. Flinstch, A. Loulizi, S. D. Diefenderfer, K. A. Galal, and B. K. Diefenderfer, "Asphalt materials characterization in support of implementation of the proposed mechanistic-empirical pavement design guide," Virginia Department of Transportation Final Report VTRC 07-CR10, 2007.
- [7] S. A. Cross, Y. Jakatimath, and K. C. Sumesh, *Determination of Dynamic Modulus Master Curves for Oklahoma HMA Mixtures*, FHWA Publication FHWA/OK 07 (05), US Department of Transportation, Washington, DC, USA, 2007.
- [8] L. Tashman and M. A. Elangovan, "Dynamic modulus test—laboratory investigation and future implementation in the State of Washington," Final Research Report WA-RD 704.1, Washington State Department of Transportation Final Report, 2007.
- [9] L. N. Mohammad, S. Saadeh, S. Obulareddy, and S. Cooper, "Characterization of louisiana asphalt mixtures using simple performance tests," in *Proceedings of the 86th Annual Meeting*

- of the Transportation Research Board, TRB, National Research Council, May 2007.
- [10] T. Bennert and N. Aboobaker, "Dynamic modulus of hot mix asphalt," Report FHWA-NJ-2009-011, US Department of Transportation, Washington, DC, USA, 2009.
- [11] R. F. Bonaquist, "Wisconsin mixture characterization using the asphalt mixture performance tester (AMPT) on historical aggregate structure," Wisconsin Department of Transportation Final Report WHRP 09-03, Wisconsin Department of Transportation, Pewaukee, Wis, USA, 2010.
- [12] D. S. Gedafa, M. Hossain, S. Romanoschi, and A. J. Gisi, "Field verification of superpave dynamic modulus," *Journal of Materials in Civil Engineering*, vol. 22, no. 5, Article ID 011005QMT, pp. 485–494, 2010.
- [13] A. Bayat and M. Knight, "Investigation of hot-mix asphalt dynamic modulus by means of field-measured pavement response," *Transportation Research Record*, vol. 2154, pp. 138–145, 2010.
- [14] E. Jackson, J. A. Li, I. Zofka, I. Yut, and J. Mahoney, "Establishing default dynamic modulus values for New England," New England Transportation Consortium Final Report NETCR85, 2011.
- [15] S. Goh, Z. You, R. Williams, and X. Li, "Preliminary dynamic modulus criteria of HMA for field rutting of asphalt pavements: Michigan's experience," *Journal of Transportation Engineering*, vol. 137, no. 1, pp. 37–45, 2011.
- [16] Y. Kim, J. Lee, C. Baek, S. Yang, S. Kwon, and Y. Suh, "Performance evaluation of warm- and hot-mix asphalt mixtures based on laboratory and accelerated pavement tests," *Advances in Materials Science and Engineering*, vol. 2012, Article ID 901658, 9 pages, 2012.
- [17] S. El-Badawy, A. Awed, and F. Bayomy, "Evaluation of the MEPDG dynamic modulus prediction models for asphalt concrete mixtures," in *Proceedings of the Transportation and Development Institute Congress*, pp. 576–585, Chicago, Ill, USA, March 2011.
- [18] C. Plati, K. Georgouli, and A. Loizos, "Asphalt concrete stiffness modulus estimation utilizing an algorithm approach," in *Proceedings of the Airfield and Highway Pavement*, pp. 1219–1228, Los Angeles, Calif, USA, June 2013.
- [19] K. Lee, H. Kim, and N. Kim, "Dynamic modulus of asphalt mixtures for development of korean pavement design guide," *ASTM Journal of Testing and Evaluation*, vol. 35, no. 2, pp. 28–59, 2007.
- [20] S. El-Badawy, F. Bayomy, and A. Awed, "Performance of MEPDG dynamic modulus predictive models for asphalt concrete mixtures: local calibration for Idaho," *Journal of Materials in Civil Engineering*, vol. 24, no. 12, pp. 1412–1421, 2012.
- [21] Y.-H. Cho, D.-W. Park, and S.-D. Hwang, "A predictive equation for dynamic modulus of asphalt mixtures used in Korea," *Construction and Building Materials*, vol. 24, no. 4, pp. 513–519, 2010.
- [22] A. M. Khattab, S. M. El-Badawy, A. A. Al Hazmi, and M. Elmwafi, "Evaluation of Witczak E* predictive models for the implementation of AASHTOWare-pavement ME design in the Kingdom of Saudi Arabia," *Construction and Building Materials*, vol. 64, pp. 360–369, 2014.
- [23] D. W. Christensen Jr., T. Pellinen, and R. F. Bonaquist, "Hirsch model for estimating the modulus of asphalt concrete," *Journal of the Association of Asphalt Paving Technologists from the Proceedings of the Technical Sessions*, vol. 72, pp. 97–121, 2003.
- [24] Z. Hossain and M. Zaman, "Behavior of selected warm mix asphalt additive modified binders and prediction of dynamic modulus of the mixes," *Journal of Testing and Evaluation*, vol. 41, no. 1, 2013.
- [25] J. Bari and M. W. Witczak, "Development of a new revised version of the Witczak E* predictive model for hot mix asphalt mixtures," *Journal of the Association of Asphalt Paving Technologists*, vol. 75, pp. 381–423, 2006, Proceedings of the Technical Sessions.
- [26] ASTM, *Standard Practice for Sampling Compacted Bituminous Mixtures for Laboratory Testing*, ASTM International, West Conshohocken, Pa, USA, 2014, <http://www.astm.org>.
- [27] National Highway Authority (NHA), *General Specifications*, National Highway Authority (NHA), Islamabad. Pakistan, 1998.
- [28] ASTM, "Standard practice for preparation of bituminous mixture specimens for dynamic modulus testing," Tech. Rep. ASTM 3496-99, ASTM International, West Conshohocken, Pa, USA, 2007.
- [29] R. F. Bonaquist, "Refining the simple performance tester for use in routine practice," NCHRP Report 614, Transportation Research Board, National Research Council, Washington, DC, USA, 2008.
- [30] T. K. Pellinen and M. W. Witczak, "Stress dependent master curve construction for dynamic (complex) modulus," in *Proceedings of the Annual Meeting of the Association of Asphalt Paving Technologists*, Colorado Springs, Colo, USA, March 2002.
- [31] D. Andrei, M. W. Witczak, and W. Mirza, "Appendix CC-4: development of a revised predictive model for the dynamic (complex) modulus of asphalt mixtures. Development of the 2002 guide for the design of new and rehabilitated pavement structures," Final Document NCHRP 1-37A, 1999.
- [32] S. Yousefdoost, B. Vuong, I. Rickards, P. Armstrong, and B. Sullivan, "Evaluation of dynamic modulus predictive models for typical Australian asphalt mixes," in *Proceedings of the 15th AAPA International Flexible Pavements Conference*, Brisbane, Australia, September 2013.
- [33] M. W. Witczak and O. A. Fonseca, "Revised predictive model for dynamic (complex) modulus of asphalt mixtures," *Transportation Research Record*, no. 1540, pp. 15–23, 1996.

Research Article

Utilization of Iron Ore Tailings as Raw Material for Portland Cement Clinker Production

Li Luo,¹ Yimin Zhang,^{1,2} Shenxu Bao,¹ and Tiejun Chen²

¹College of Resource and Environmental Engineering, Wuhan University of Technology, No. 122 Luoshi Road, Hongshan District, Wuhan, Hubei 430070, China

²College of Resource and Environmental Engineering, Wuhan University of Science and Technology, Wuhan, China

Correspondence should be addressed to Yimin Zhang; zym126135@126.com

Received 13 January 2016; Accepted 24 February 2016

Academic Editor: Osman Gencel

Copyright © 2016 Li Luo et al. This is an open access article distributed under the Creative Commons Attribution License, which permits unrestricted use, distribution, and reproduction in any medium, provided the original work is properly cited.

The cement industry has for some time been seeking alternative raw material for the Portland cement clinker production. The aim of this research was to investigate the possibility of utilizing iron ore tailings (IOT) to replace clay as alumina-silicate raw material for the production of Portland cement clinker. For this purpose, two kinds of clinkers were prepared: one was prepared by IOT; the other was prepared by clay as a reference. The reactivity and burnability of raw meal, mineralogical composition and physical properties of clinker, and hydration characteristic of cement were studied by burnability analysis, differential thermal analysis, X-ray diffraction, and hydration analysis. The results showed that the raw meal containing IOT had higher reactivity and burnability than the raw meal containing clay, and the use of IOT did not affect the formation of characteristic mineralogical phases of Portland cement clinker. Furthermore, the physical and mechanical performance of two cement clinkers were similar. In addition, the use of IOT was found to improve the grindability of clinker and lower the hydration heat of Portland cement. These findings suggest that IOT can replace the clay as alumina-silicate raw material for the preparation of Portland cement clinker.

1. Introduction

IOT are the solid wastes generated during the beneficiation process of iron ore concentration and are one of the main pollution concerns in the mining industry. Continuous development of the iron and steel industry has led to the increasing amount of IOT; there are over 300 million tons of IOT discharged per year, but the comprehensive utilization rate of IOT is still less than 10%; stockpiling is still the most common and cost-effective way in the management of IOT [1, 2]. However, the huge amount of stockpiled IOT brings a series of environmental and social problems. In recent years, IOT as secondary resources have received considerable attention in many countries in the world. At present, the researches about comprehensive utilization of IOT mainly focused on the recycling of useful metal and producing of building materials, among which utilizing IOT to produce the building materials is a more effective solution for resource recovery and management of IOT [3, 4]. Utilization of IOT

as raw material for building industry not only consumes large amount of IOT and realizes zero-emission of IOT wastes, but also is beneficial to protecting natural mineral resources.

Portland cement clinker production consumes large amounts of natural resources (limestone, clay, etc.), and clay has been widely used as traditional alumina-silicate raw material for good reasons [5]. Cement industry has undergone a tremendous development in the past decades, but it causes excessive exploitation of clay resource and considerable environmental damage. Now, the cement industry is facing the challenge of the insufficient supply of raw materials and environment protection, so it has for some time been seeking alternative raw materials for Portland cement clinker production. It is well known that various industrial solid wastes have been utilized as alternative raw materials in Portland cement clinker production such as steel slag, waste sludge ash, and ceramic wastes [6–9]. With the benefit of high content of silica and iron, IOT can be utilized as silicate or iron corrective material during the Portland cement clinker

TABLE 1: Chemical composition of the raw materials/wt%.

Materials	Loss	SiO ₂	Al ₂ O ₃	Fe ₂ O ₃	CaO	MgO	SO ₃
IOT	1.22	45.41	19.07	10.86	12.41	7.23	0.44
Clay	4.34	65.44	17.27	5.53	0.98	1.59	0.10
Limestone	42.97	0.49	0.16	0.05	55.78	0.35	0.12
Quartz sand	0.21	97.83	0.52	0.20	0.27	0.10	—
Iron ore	10.23	32.69	8.05	33.60	1.92	2.84	3.50

production, but the consumption of IOT is rather low. In addition, the effect of using IOT as raw material on the properties of raw meal and hydration characteristic of Portland cement has also been seldom discussed. Comparing with being used as corrective material, utilizing IOT as alumina-silicate raw material for Portland cement clinker production can consume more IOT and decrease the mining of clay; however, there is little information about IOT replacing clay as alumina-silicate raw material for the preparation of Portland cement clinker so far.

The possibility of utilizing IOT to completely replace clay as alumina-silicate raw material for Portland cement clinker production was investigated in this paper; the properties of raw meal, clinker, and cement were studied by burnability analysis, differential thermal analysis, X-ray diffraction technique, and hydration analysis. On one hand, it can solve the environment problems of IOT and improve the comprehensive utilization rate of IOT. On the other hand it can provide an alternative alumina-silicate raw material for cement industry.

2. Materials and Methods

2.1. Materials. In this study, IOT was obtained from iron ore dressing plant in Henan province. Clay was from a brick plant in Shiyang and iron ore was from Jiugang Group. Limestone and quartz sand were acquired from Huangshi XinHai Trade Co., Ltd., and Jingyou Sand Co., Ltd., respectively. IOT, clay, limestone, quartz sand, and iron ore were used as raw materials for Portland cement clinker production. Two different kinds of alumina-silicate material (clay and IOT) were used in the experiment. The calcareous material was limestone. Quartz sand and iron ore were used as corrective materials to adjust the contents of silicate and iron of raw meal, respectively.

The main chemical composition of raw materials is shown in Table 1. The chemical composition of IOT is shown in the Supplementary Material available online at <http://dx.doi.org/10.1155/2016/1596047>. The main component of IOT and clay is similar and the aluminum content of IOT is rather high, which belongs to rich-aluminum type. The hazardous substances of IOT are SO₃ and Cl, but their contents are very low. The XRD pattern (Figure 1) shows that the major mineral phases of the IOT are ferrotschermakite and anorthite while augite and clinocllore occur as minor phases. However, quartz is not detected in the XRD pattern of IOT, which is a common constituent of IOT. The SiO₂ in the amphibole and feldspar is easier to combine with

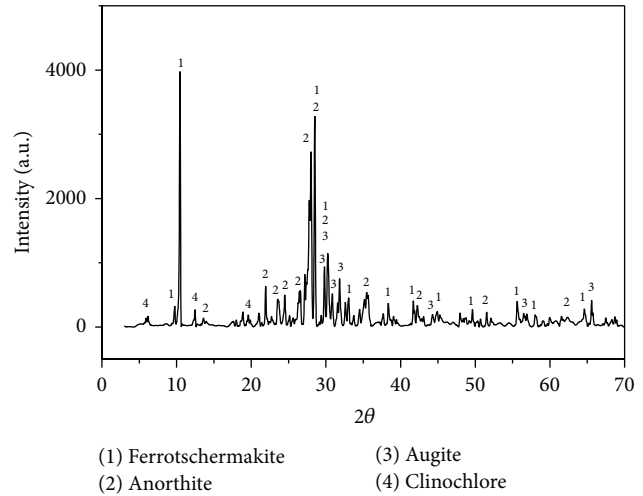


FIGURE 1: The XRD pattern of IOT.

CaO during the sintering process than in the quartz, which means that IOT has relatively high reactivity. Consequently, the IOT appears to be a suitable alternative alumina-silicate raw material for Portland cement clinker production.

2.2. Samples Preparation. Clinker modulus has always been used to control the production of Portland cement clinker. The compositional parameters of clinker modulus are listed as follows:

Lime saturation ratio (KH)

$$= \frac{(\text{CaO} - 1.65\text{Al}_2\text{O}_3 - 0.35\text{Fe}_2\text{O}_3)}{2.8\text{SiO}_2}, \quad (1)$$

$$\text{Silica modulus (SM)} = \frac{\text{SiO}_2}{(\text{Al}_2\text{O}_3 + \text{Fe}_2\text{O}_3)},$$

$$\text{Alumina modulus (IM)} = \frac{\text{Al}_2\text{O}_3}{\text{Fe}_2\text{O}_3}.$$

Two kinds of samples were prepared; one was prepared by clay as a reference (RM-1) and the other was prepared by IOT (RM-2). The clinker moduli of two samples were both adjusted to the same values (KH = 0.90, SM = 2.50, and IM = 1.50). The blend ratios of raw materials of two samples are shown in Table 2.

The quartz sand passed through a 0.08 mm sieve by grinding, because coarse quartz sand has a negative effect on the burnability of raw meal. The raw meals were shaped in small spheres with a diameter of 15 mm and then dried in an oven at 105°C for 1 h. These small spheres were burned at 1450°C for 1 h. After the sintering process, the produced clinkers were cooled rapidly to room temperature. The produced clinkers were pulverized with 5% gypsum by weight for 2 minutes in a laboratory oscillating mill to produce the Portland cement.

The cement pastes were prepared to study the hydration products of Portland cement clinker. The pastes were prepared with water to solids ratio of 0.3 and cured in standard curing box. At 3 and 28 days, the hydration of pastes was

TABLE 2: Ratio of raw materials of two samples (%).

Sample	IOT	Clay	Limestone	Quartz sand	Iron ore
RM-1	—	17.65	77.08	1.38	3.89
RM-2	17.31	—	75.07	6.31	1.31

terminated by alcohol and dried at 80°C in a vacuum oven for 24 h for the further characterization.

2.3. Testing Methods. The chemical composition of raw materials was determined by X-ray fluorescence (AXIOS).

The mineral composition of IOT, clinkers, and paste was analyzed by X-ray diffraction (D/MX-III A).

The burnability tests of cement raw meal were performed according to Chinese National Standard GB/T 26566-2011. The cement raw meals were fired at 1350°C, 1400°C, and 1450°C for 30 min, respectively. The free lime content of clinkers was analyzed by the glycerol-ethanol method.

The reactivity analysis of raw meal was carried out by the differential thermal analysis (STA 449F3).

The mechanical tests of cement were carried out according to Chinese National Standard GB/T 17671-1999.

The physical properties of cement were examined according to the Chinese National Standard GB/T 1346-2001.

The hydration heat of cement was measured by microcalorimeter (C80, SETARAM). The water-cement ratio was 0.5 and the hydration time was 3 days.

3. Result and Discussion

3.1. Characterization of the Raw Meal

3.1.1. The Reactivity of Raw Meal. The reactivity of raw meal is defined by the reaction rate of the raw materials and is related to its mineral characteristic. The reactivity of raw meal was studied by DSC analysis. The DSC heating curves of two samples are presented in Figure 2. During the sintering process, the formation of clinker minerals is accompanied with endothermic and exothermic reactions. Endothermic peak at about 830°C is attributed to thermal decomposition of the limestone. Exothermic peak between 1230°C and 1260°C is attributed to solid state reactions, which means the progressive formation of C_3A , C_4AF , and C_2S [9]. Endothermic peaks at about 1330°C are attributed to the sintering of liquid phase and the formation of C_3S . It can be seen from Figure 2 that the solid state reactions temperature of RM-2 can be up to 30°C lower than RM-1, but the decomposition temperature of limestone and the sintering temperature of liquid phase in two samples are almost the same. The results of DSC analysis indicate that using IOT as alumina-silicate material promotes the solid state reactions and improves the reactivity of raw meal while it has little effect on the processes of limestone decomposition and reducing the formation temperature of C_3S . The chemical composition of IOT that is in the Supplementary Material shows that IOT contains trace elements (CuO, TiO_2 , MnO, etc.), which can promote the solid state reaction [10].

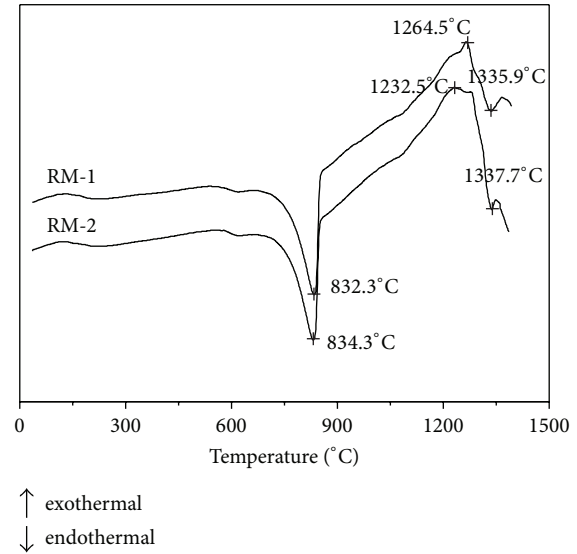


FIGURE 2: The DSC heating curves of raw meals.

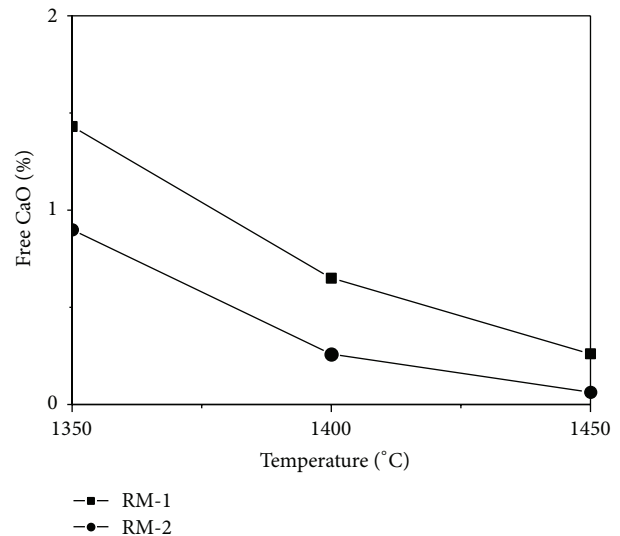


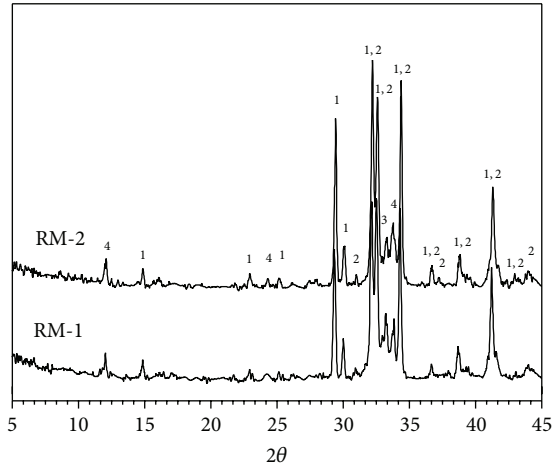
FIGURE 3: The burnability tests of raw meals.

3.1.2. The Burnability of Raw Meal. The burnability of raw meal describes the degree of difficulty of clinker formation during sintering process and is evaluated by the content of free lime in clinker. The lower the content of free lime in clinker is, the higher the raw meal burnability is. The results of burnability tests are given in Figure 3. The content of free lime in RM-2 is lower at all sintering temperatures, and the reaction of sintering process after 1350°C is mainly the formation of C_3S . The results of burnability analysis suggest that the use of IOT has improved the burnability of raw meal and promoted the formation of C_3S during the sintering process. The improvement of burnability can be attributed to the existence of trace elements and particular mineral composition of IOT.

The results of reactivity and burnability analyses show that RM-2 has higher reactivity and burnability. Comparing

TABLE 3: The physical properties of produced Portland cements.

Sample	Specific surface (m^2/kg)	Consistency/%	Setting time/min		Bending strength/MPa		Compressive strength/MPa	
			Initial time	Final time	3 d	28 d	3 d	28 d
RM-1	326.4	23.0	165	225	4.9	8.5	20.7	46.2
RM-2	355.5	23.8	160	235	4.9	8.7	20.8	48.6



- (1) C_3S -Alite
 (2) C_2S -Belite
 (3) C_3A -Aluminate
 (4) C_4AF -Ferrite

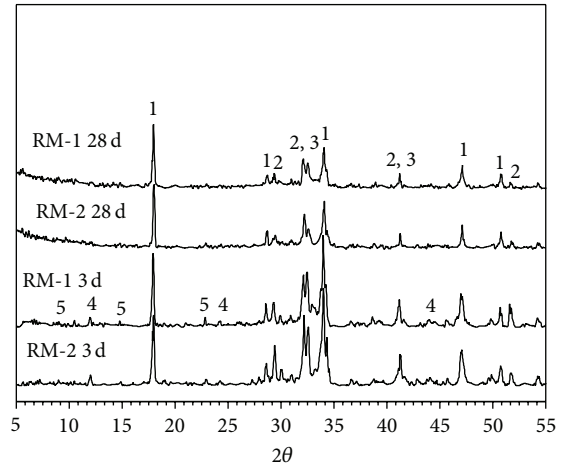
FIGURE 4: The X-ray diffraction of two produced Portland cement clinkers.

with clay, utilizing IOT as alumina-silicate raw material for Portland cement clinker production can lower the sintering temperature or reduce sintering time during sintering process, which can lower the production costs of cement industry.

3.2. Characterization of the Clinker

3.2.1. XRD Pattern of Clinker. The XRD analysis of two produced Portland cement clinkers is given in Figure 4. In both clinkers, the main mineral phases of two produced clinkers were C_3S , C_2S , C_3A , and C_4AF , which were in accord with the characteristic minerals of a typical Portland cement clinker [11]. However, there is a small difference between the two clinkers that RM-2 contains less amount of C_2S , which is related to the promotion of sintering process. Free lime content is very low in both clinkers, so it cannot be detected in the XRD pattern. The results of XRD analyses indicate that the use of IOT does not affect the formation of characteristic mineralogical phases of Portland cement clinker.

3.2.2. Physical and Mechanical Testing. Table 3 presents the physical and mechanical properties of two produced Portland cement clinkers. The results of physical tests show that the use of IOT only slightly affected the setting times of produced Portland cement. However, RM-2 cement presents greater specific surface and water demand. The greater specific surface represents better grindability and leads to the greater



- (1) $\text{Ca}(\text{OH})_2$
 (2) C_3S
 (3) C_2S
 (4) C_4AF
 (5) $\text{Ca}_6\text{Al}_2(\text{SO}_4)_3 \cdot 32\text{H}_2\text{O}$

FIGURE 5: The X-ray diffraction patterns of pastes for 3 and 28 days.

water demand. The differences in mineralogical composition of clinkers significantly impact the grindability of clinkers; C_2S is known to be the most prominent strength giving components in all clinker minerals [12]. The grindability of RM-2 clinker increases as the amount of C_2S decreases.

Portland cement sample was made by grinding the 95 wt% of clinker with 5 wt% of gypsum, and the mechanical properties of produced Portland cement sample were tested for strengths after curing for 3 and 28 days. Both mortars gave quite similar bending and compressive strengths in the same days, and the mechanical performances of two Portland cement clinkers were in agreement with those of Portland cement of 42.5 MPa strength grade, which confirmed the probability of utilizing IOT as alternative raw materials for Portland cement clinker production.

3.3. Characterization of Hydration

3.3.1. XRD Pattern of Paste. The XRD patterns of two pastes, hydrated for 3 and 28 days, are given in Figure 5. In both pastes, the hydration products of two cement clinkers are $\text{Ca}(\text{OH})_2$ and ettringite. No calcium silicate hydrate (C-S-H) was detected during the whole hydration process, presumably due to the amorphous characteristic of the calcium silicate hydrate itself [13]. The diffraction peaks of C_3S and C_2S are higher in RM-2 paste at 3 days, which indicates that the hydration velocity of calcium silicate of RM-2 cement is slower. With increasing hydration time, the peaks of C_3S , C_2S , and C_4AF decrease at 28 days.

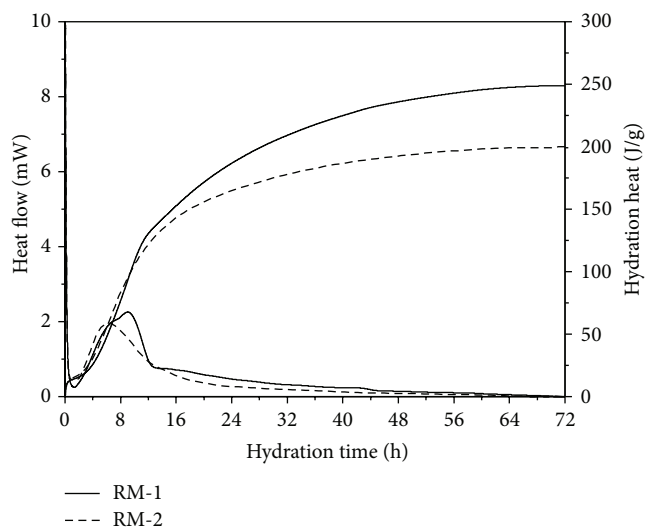


FIGURE 6: The hydration heat of two produced Portland cement clinkers.

3.3.2. Hydration Heat of Cement. The rate of heat liberation and hydration heat of two cement clinkers for 3 days is shown in Figure 6. In both cases, the heat liberation is quite intense in the first few minutes of the preinduction period. Soon thereafter, the hydration process is delayed and the rate of heat liberation decreases rapidly in the induction period. Then, a second main exothermic peak appears as a result of the formation of ettringite and hydration of C_3S [14]. And finally, the rate of heat liberation decreases gradually in the following period. It can be seen from Figure 6 that the end times of induction period of two cement clinkers are almost the same, the end times of induction period are related to the setting times of cement, and the analysis results of induction period are in good agreement with the results of physical tests. RM-2 has a weaker exothermic peak; however, the formation process of ettringite of two cement clinkers could be similar according to the results of setting time of two cement clinkers, so the weaker exothermic peak was due to the lower hydration rate of calcium silicate. The XRD analysis of two pastes also has the same results.

The hydration heat of RM-2 cement is lower in the early hydration period, which is due to the higher hydration liberation rate of RM-2 cement. The greater specific surface of RM-2 cement promotes the hydration process of cement in the initial hydration period and leads to higher hydration liberation rate of cement. As the heat liberation rate of RM-2 cement decreases faster in the following period, the hydration heat of RM-1 exceeds RM-2 after about 10 h and the gap of hydration heat of two cement clinkers gradually enlarges in the later period.

4. Conclusions

Chemical and mineralogical analysis of IOT has shown that it can be considered as a ready alumina-silicate raw material due to its high content of alumina and relatively high reactivity. Furthermore, the similar mineralogical, physical,

and mechanical properties of two produced Portland cement clinkers have confirmed that IOT can completely replace clay as an alternative alumina-silicate raw material for the production of Portland cement clinker. However, the use of IOT is found to improve the reactivity and burnability of raw meal and promote the sintering process. In addition, the Portland cement clinker prepared by IOT presents better grindability and the hydration heat of Portland cement is lower. The availability and low cost of IOT make it attractive to replace clay as alumina-silicate raw material for the production of Portland cement clinker. This will be beneficial for the management of IOT, alleviating the raw materials supply problem of the cement industry and allowing the reduction in processing costs of raw materials.

Competing Interests

The authors declare that they have no competing interests.

Acknowledgments

This research was financially supported by the National Key Science-Technology Support Programs of China (no. 2015BAB03B05) and the National Nature Science Foundation of China (no. 51404177).

References

- [1] C. Li, H. H. Sun, J. Bai, and L. T. Li, "Innovative methodology for comprehensive utilization of iron ore tailings: part 1. The recovery of iron from iron ore tailings using magnetic separation after magnetizing roasting," *Journal of Hazardous Materials*, vol. 174, no. 1-3, pp. 71-77, 2010.
- [2] Y. L. Chen, Y. M. Zhang, T. J. Chen, Y. L. Zhao, and S. X. Bao, "Preparation of eco-friendly construction bricks from hematite tailings," *Construction and Building Materials*, vol. 25, no. 4, pp. 2107-2111, 2011.
- [3] S. K. Das, S. Kumar, and P. Ramachandrarao, "Exploitation of iron ore tailing for the development of ceramic tiles," *Waste Management*, vol. 20, no. 8, pp. 725-729, 2000.
- [4] X. Y. Huang, R. Ranade, W. Ni, and V. C. Li, "Development of green engineered cementitious composites using iron ore tailings as aggregates," *Construction and Building Materials*, vol. 44, pp. 757-764, 2013.
- [5] M. Schneider, M. Romer, M. Tschudin, and H. Bolio, "Sustainable cement production—present and future," *Cement and Concrete Research*, vol. 41, no. 7, pp. 642-650, 2011.
- [6] P. E. Tsakiridis, G. D. Papadimitriou, S. Tsivilis, and C. Koroneos, "Utilization of steel slag for Portland cement clinker production," *Journal of Hazardous Materials*, vol. 152, no. 2, pp. 805-811, 2008.
- [7] K.-L. Lin and C.-Y. Lin, "Hydration characteristics of waste sludge ash utilized as raw cement material," *Cement and Concrete Research*, vol. 35, no. 10, pp. 1999-2007, 2005.
- [8] I. Vangelatos, G. N. Angelopoulos, and D. Boufounos, "Utilization of ferroalumina as raw material in the production of Ordinary Portland Cement," *Journal of Hazardous Materials*, vol. 168, no. 1, pp. 473-478, 2009.

- [9] F. Puertas, I. García-Díaz, A. Barba et al., "Ceramic wastes as alternative raw materials for Portland cement clinker production," *Cement & Concrete Composites*, vol. 30, no. 9, pp. 798–805, 2008.
- [10] K. Kolovos, S. Tsivilis, and G. Kakali, "The effect of foreign ions on the reactivity of the CaO-SiO₂-Al₂O₃-Fe₂O₃ system: part II: cations," *Cement and Concrete Research*, vol. 32, no. 3, pp. 463–469, 2002.
- [11] F. Dunstetter, M.-N. de Noirfontaine, and M. Courtial, "Polymorphism of tricalcium silicate, the major compound of Portland cement clinker: 1. Structural data: review and unified analysis," *Cement and Concrete Research*, vol. 36, no. 1, pp. 39–53, 2006.
- [12] V. C. G. de Souza, J. C. Koppe, J. F. C. L. Costa, A. L. M. Vargas, E. Blando, and R. Hübler, "The influence of mineralogical, chemical and physical properties on grindability of commercial clinkers with high MgO level," *Cement and Concrete Research*, vol. 38, no. 8-9, pp. 1119–1125, 2008.
- [13] I. Alp, H. Deveci, E. Y. Yazici, T. Türk, and Y. H. Süngün, "Potential use of pyrite cinders as raw material in cement production: results of industrial scale trial operations," *Journal of Hazardous Materials*, vol. 166, no. 1, pp. 144–149, 2009.
- [14] H. X. Li, W. Xu, X. J. Yang, and J. G. Wu, "Preparation of Portland cement with sugar filter mud as lime-based raw material," *Journal of Cleaner Production*, vol. 66, pp. 107–112, 2014.

Research Article

Properties of Self-Compacting Concrete with Recycled Coarse Aggregate

W. C. Tang,¹ P. C. Ryan,² H. Z. Cui,³ and W. Liao⁴

¹*School of Architecture and Built Environment, The University of Newcastle, Callaghan, NSW 2308, Australia*

²*College of Engineering and Informatics, National University of Ireland, Galway, Ireland*

³*Guangdong Provincial Key Laboratory of Durability for Marine Civil Engineering, Shenzhen University, China*

⁴*Department of Architecture and Civil Engineering, City University of Hong Kong, Hong Kong*

Correspondence should be addressed to W. C. Tang; patrick.tang@newcastle.edu.au

Received 7 December 2015; Revised 16 February 2016; Accepted 17 February 2016

Academic Editor: Osman Gencel

Copyright © 2016 W. C. Tang et al. This is an open access article distributed under the Creative Commons Attribution License, which permits unrestricted use, distribution, and reproduction in any medium, provided the original work is properly cited.

The utilisation of recycled concrete aggregate (RCA) in Self-Compacting Concrete (SCC) has the potential to reduce both the environmental impact and financial cost associated with this increasingly popular concrete type. However, to date limited research exists exploring the use of coarse RCA in SCC. The work presented in this paper seeks to build on the existing knowledge in this area by examining the workability, strength, and fracture properties of SCCs containing 0%, 25%, 50%, 75%, and 100% coarse RCA. The experimental programme indicated that at RCA utilisation levels of 25% to 50% little or no negative impact was observed for strength, workability, or fracture properties, with the exception of a slight reduction in Young's modulus.

1. Introduction

The importance of establishing the suitability of recycled aggregates has increased in recent years against the backdrop of a growing emphasis on sustainable building practices. As pointed out by Padmini et al. [1], the rate of building demolition is constantly increasing, making it essential to effectively reuse demolition waste to conserve nonrenewable natural resources. At present a large portion of potentially useful construction and demolition waste is disposed of in landfill sites, creating environmental problems due to scarcity of such sites, unplanned disposal, and environmental cost of transporting demolition waste [2]. The use of coarse recycled concrete aggregates (RCAs) as a replacement for natural coarse aggregates in concrete offers a sustainable solution to these problems. However, the use of RCA may potentially reduce concrete quality as coarse RCAs are generally of poorer quality than natural coarse aggregates, with greater water absorption [3, 4] and lower density [5]. This reduced quality is due to the fact that coarse RCA consists of both original aggregate and adhered mortar; thus the quality of the RCA depends not only on the original aggregate, but also on the quality and quantity of adhered mortar. The use of RCA

also affects the characteristics of the interfacial transition zones between aggregates and cement paste [6], which in turn affects the strength characteristics of concrete containing RCA. When considering the mechanical properties of concrete with RCA, most of the previous researches confirmed that the reduction in stiffness (i.e., elastic modulus) is higher than the reduction in strength [7–10].

Another important consideration is the possible reduction in workability of concretes incorporating coarse RCA, due to the increased angularity and surface roughness of RCA when compared to natural coarse aggregates [1, 4]. This is of particular importance for the increasingly popular form of concrete known as Self-Compacting Concrete (SCC) [11]. The Eurocode [12] defines SCC as concrete that is able to flow and compact under its own weight, fill formwork with its reinforcement, duct box houses, and so forth, whilst maintaining homogeneity. It is a relatively recent form of concrete construction having been developed in Japan in the mid-1980s and introduced in Europe in the mid-1990s. Despite its recent development, SCC is now widely used in industry due to the advantages of SCC which include increased on-site productivity, enhanced construction quality, and improved working conditions on-site [13, 14]. However, as pointed out

by Tuyan et al. [3], the cost of SCC is higher than traditional vibrated concretes due to the need for higher powder contents and chemical admixtures in SCC. Thus in order to allow SCC to reach its full potential in terms of industry uptake it is necessary to develop ways of making SCC more cost-effective. The use of coarse RCA as substitutes for coarse natural aggregates in SCC offers a means of reducing the cost of SCC, while reducing the carbon footprint of concrete production. Consequently, there are both business case and an environmental obligation to explore the use of RCA in SCCs.

This paper examines the use of varying proportions of coarse RCA in SCC. The work presented herein builds on the existing body of literature by examining the fresh concrete properties of SCCs containing RCA. This is an important area which has been examined by a number of researchers in recent years including [3–5, 15, 16]. The primary contribution of this paper, however, lies in the examination of the hardened properties of SCCs containing various levels of RCA and, most importantly, the examination of the fracture properties of SCC containing RCA. It is recognized that the fracture properties of concrete constitute fundamental characteristics in design and safety assessment of structures, especially large-scale structures [17, 18]. As pointed out by Bordelon et al. [19], examination of compressive strength and tensile strength alone does not give a complete picture of structural performance due to the interaction of the material behaviour, preexisting cracks, and geometry of the structure. Bordelon et al. [19] thus stated that the concrete fracture properties can provide greater insight into the potential load carrying capacity of the material in a given structural system. These fracture properties are heavily dependent on the components in the mixture [17], with fracture energy depending largely on the quality of the ITZ and the properties of the coarse aggregate [20]. Thus utilisation of coarse RCA as a replacement for natural coarse aggregate may have a notable influence on concrete fracture energy. As stated by Butler et al. [20] however, there are very few studies which examine the fracture energy of vibrated concretes containing coarse RCA [6, 19, 20]. Even less knowledge exists for SCCs, with little or no research currently available exploring the fracture energy implications of RCA use in SCCs, which have different ITZ characteristics and mix compositions to normal vibrated concretes [21, 22]. The work in this paper seeks to address this important gap in the existing literature by exploring the fracture energy of SCCs with natural coarse aggregate replaced with RCA at levels of 0% (control), 25%, 50%, 75%, and 100%. SCC strength characteristics are also examined at each of the RCA utilisation levels to enhance understanding of the effect of RCA on these properties.

2. Materials and Methods

2.1. Materials. The binder content for all the SCC mixes examined herein consisted of Ordinary Portland Cement (OPC), fly ash (FA), and silica fume (SF). The OPC used was ASTM Type I Portland cement, with a fineness of $3520 \text{ cm}^2/\text{g}$ and density of 3150 kg/m^3 . The FA and SF were used in accordance with EN 450-1:2005A [23] and ASTM

TABLE 1: Properties of natural and recycled coarse aggregates.

Type	Nominal size (mm)	Density (kg/m^3)	Water absorption (kg/m^3)
Crushed granite	10	2650	1.15
Recycled aggregate	10	2450	7.75

C 1240-11 [24], respectively. The recycled aggregate used was a crushed and unwashed recycled concrete aggregate, with a nominal size of 10 mm sourced from a construction and demolition waste recycling facility. The coarse natural aggregate consisted of crushed granite with a nominal size of 10 mm. Table 1 presents the water absorption (24 hours) and density of the natural and recycled coarse aggregates. The fine aggregate used in the study was river sand, with a fineness modulus of 2.65. The particle size distributions of all the aggregates used were in accordance with the requirements of EN 12620:2002A [25].

As mentioned in the previous section, five different SCC mixes were examined herein, with percentages of substitution of natural coarse aggregates with RCA of 0%, 25%, 50%, 75%, and 100%. Mix design details (based on aggregates being in the saturated surface dry condition) for each of these five mixes are presented in Table 2. The water/binder (w/b) ratio and superplasticizer dosage were the same for the five mixes examined. For the experimental programme described in this paper, the natural and recycled coarse aggregates were immersed in water for 24 hours and left for 1 hour in air before concrete mixing to reach surface dry condition.

2.2. Test Methods and Sample Preparations

2.2.1. Fresh Concrete Tests. The three tests used to investigate the fresh properties of the SCCs were the slump flow test, the L-box test, and the sieve segregation test, as shown in Figure 1. These three tests assess the primary characteristics of fresh SCC. The slump flow test and t_{500} time evaluate the flowability and viscosity of a SCC in the absence of any obstruction, respectively [26]. The slump flow diameter (Figure 1(a)) is the measurement required for all SCC in accordance with EN 206-9:2010 [12]. The Eurocode states that SCC should have a slump flow value of between 550 mm and 850 mm, while t_{500} times less than two seconds result in *VSI* classification, while t_{500} times greater than or equal to two seconds result in a *VS2* classification.

The L-box test, as shown in Figure 1(b), was performed in accordance with EN 12350-12350-10 [27]. This test is used to assess the passing ability of SCC. EN 206-9:2010 (2010) states that for an L-box with three reinforcement bars the blocking ratio (*B* value) should be greater than or equal to 0.80 [12]. The final workability test, the sieve segregation test (shown in Figure 1(c)), was performed in accordance with EN 12350-11:2010 [28]. The test examines resistance of SCC to segregation by measuring the mass of fresh concrete which passes through a 5 mm sieve, when poured from a height of $50 \text{ cm} \pm 5 \text{ cm}$. EN 206-9:2010 states that the percentage passing the sieve (*P*) should be less than 20% [12].

TABLE 2: Concrete mix details (1 m³ concrete).

Mix code	w/b ratio	Water (kg/m ³)	Cement (kg/m ³)	PEA (kg/m ³)	SF (kg/m ³)	10 mm aggregate (kg/m ³)	River sand (kg/m ³)	Recycled 10 mm aggregate (kg/m ³)	(%)	SP ADVA-109 (l/m ³)
Control	0.35	220	445	155	30	660	815	0	0	4.5
RCA25	0.35	220	445	155	30	495	815	152	25	4.5
RCA50	0.35	220	445	155	30	330	815	305	50	4.5
RCA75	0.35	220	445	155	30	165	815	458	75	4.5
RCA100	0.35	220	445	155	30	0	815	610	100	4.5

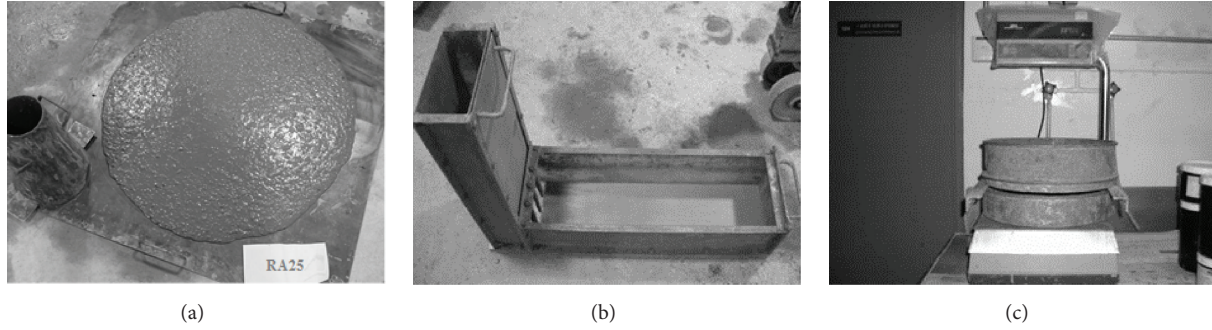


FIGURE 1: (a) Slump flow tests, (b) L-box test, and (c) sieve segregation test.

The slump flow test and L-box test were carried out at two different times for each of the SCC mixes. The first set of tests were performed directly after mixing, while the second set of tests were carried out 1 hour after mixing to evaluate any changes in the workability of the SCC over time. During the 1-hour rest period, the concrete mixture was not agitated, but the mixture was remixed for about 1 min using the initial mixing speed before the second measurements were performed.

2.2.2. Hardened Concrete Tests. Standard concrete specimens were cast to study the strength properties (compressive strength, f_c , tensile strength, f_t , and elastic modulus, E) according to the relevant British and European standards [29–31]. Notched concrete beams with the dimensions $75 \times 75 \times 250$ mm were used to study the fracture properties according to RILEM recommendations [32]. The bending tests were conducted using a servo-controlled MTS universal testing machine. Before testing the beam samples, a notch 20 mm in depth and 2 mm in thickness was saw-cut at the midsection of each beam. The test setup, including details of the notched beam, is shown in Figure 2. During the test, the crack mouth opening displacement (CMOD) was measured using a clip gauge clipped to the bottom of the beam and held in position by two steel knife edges glued to the specimen. The displacement rate was controlled at a suitable rate until the specimens failed.

The determination of the fracture energy (G_f) was based on load-deflection measurements in accordance with the RILEM standard [32] as given by

$$G_f = \frac{W_0 + m \cdot g \cdot \delta_0}{b \cdot (d - a_0)}, \quad (1)$$

where W_0 is the area under the load-deflection curve, δ_0 is the deflection when the load is zero, g is the gravity factor, m is mass of beam, b is width of beam, d is depth of beam, and a_0 is the notch depth of the beam. In order to acquire stable crack propagation in the beam during the postpeak response, the use of load-crack mouth opening displacements (load-CMOD) for evaluation of the fracture energy of concrete was suggested [33, 34]. To account for the difference in the fracture energy between load-deflection and load-CMOD variations, a correction factor was adopted by Navalurkar et al. (1999) [34]. This approach was used herein

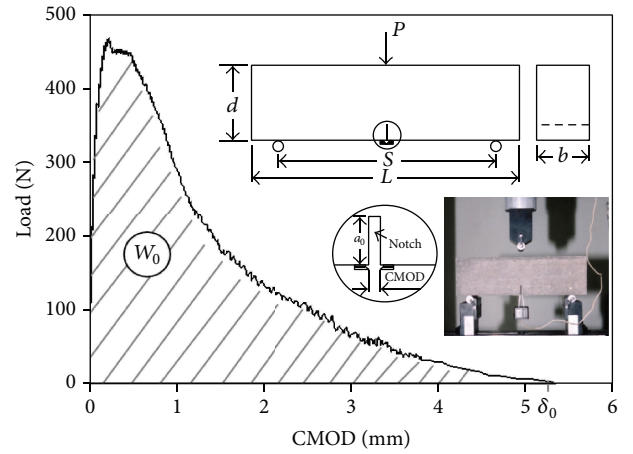


FIGURE 2: Typical experimental load-CMOD plot with testing configuration (span length = 200 mm).

with a correction factor of 0.800 as appropriate for a notch depth ratio, $a_0/d = 0.25$, and span-to-depth ratio = 2.7.

The characteristic length (l_{ch}) proposed by Hillerborg [35] in the fictitious crack model is often used to characterise the brittleness of concrete and is given by

$$l_{ch} = \frac{G_f \cdot E}{f_t^2}. \quad (2)$$

As stated by Zhou et al. [36], the smaller the value of l_{ch} , the more brittle the material. It has also been found, however, that the value of characteristic length is reduced as the compressive strength increases, leading to the development of a modified form of the characteristic length ($l_{ch,mod}$) as follows [33]:

$$l_{ch,mod} = \frac{G_f \cdot E}{f_t \cdot f_c}. \quad (3)$$

The characteristic length is calculated herein in accordance with the work of Rao and Prasad [33] using (3). It is noted that the Hillerborg method (also known as the work-of-fracture method) presented in (1) to (3) has a number of limitations. The most notable of these is the size dependency of the method, with previous researchers finding that fracture

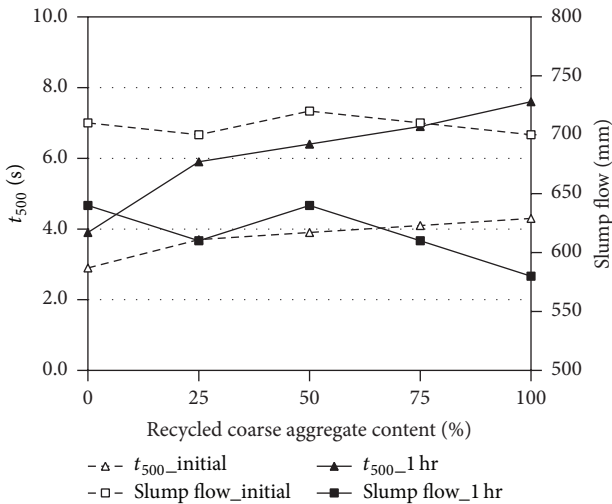


FIGURE 3: Effect of RCA content on slump flow and t_{500} times for SCC.

energy increases with test beam size [17, 18]. However, as outlined in Section 1 the purpose of the study herein is to investigate the relative performance of a control SCC and SCCs with RCA utilised at various natural coarse aggregate replacement levels. Thus the absolute values of G_f or $l_{ch,mod}$ are not of primary concern but rather the relative values obtained for the different SCCs. Thus, a single beam size was used for all test specimens herein, and the fracture energy results are presented in Section 3 of this paper in terms of the performance of the RCA SCCs relative to the control SCC (0% RCA).

3. Results and Discussion

3.1. Fresh Concrete Properties

3.1.1. Water Absorption of RCA. As can be seen in Table 1, the increased porosity of RCA, when compared to natural aggregates, results in a greater water absorption capacity in the RCA. This enhances the potential for water interchange with the surrounding paste in the RCA concretes, meaning RCA particles can have a greater role in absorbing water from or providing water to the SCC mortar. As stated by Casuccio et al. [6] this is an unwanted source of variation when comparing RCA concretes and concretes containing only natural aggregates, as RCA used in the dry condition may absorb some water from the mortar phase, and RCA used in the saturated phase may slightly increase water content.

3.1.2. Fresh Concrete Test Results. The test results of slump flow, blocking ratio, and sieve segregation for the control SCC and the SCCs with various levels of RCA utilisation are presented in Table 3 and illustrated in Figures 3–5, respectively. Firstly, considering the slump flow test results, displayed graphically, it is noted from Figure 3 that the initial measurements indicated that the addition of RCA up to 100% did not impact upon slump flow diameter; however, the t_{500} times increased with increasing RCA content. This result

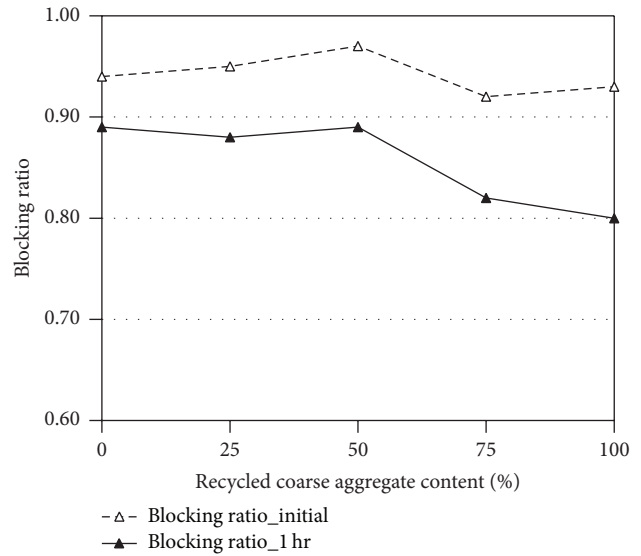


FIGURE 4: Effect of RCA content on blocking ratio of SCC mixes.

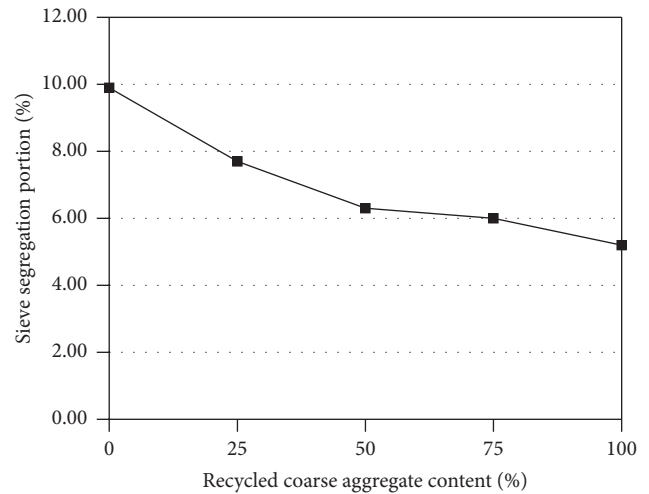


FIGURE 5: Effect of RCA content on sieve segregation resistance for SCC mixes.

indicates similar flowability across all SCCs but increased viscosity with increasing RCA content. A similar pattern was observed in the slump flow tests conducted one hour after concrete mixing; however the t_{500} times experienced a greater percentage increase with increasing RCA content; that is, from control to 100% RCA t_{500} increases by 48% at initial measurement and 94% after 1 hour (see Table 3). The one-hour slump flow diameter for the 100% RCA is also notably smaller than the control SCC. The increase in viscosity with increasing RCA content may be due to the angular shape of the RCA, while it is possible that the time dependent change in the slump flow results was caused by continued water absorption of the recycled aggregate, despite having been presoaked and dried for one hour before use. As seen in Table 1 the RCA had approximately seven times more absorption capacity than the natural aggregates, meaning

TABLE 3: Fresh concrete test results.

Mix code	Wet density (kg/m ³)	Slump flow test				L-box				
		Initial S ₀ (mm)	Initial t ₅₀₀ (s)	After 1hr S _{1hr} (mm)	After 1hr t ₅₀₀ (s)	Initial B ₀ (ratio)	After 1hr B _{1hr} (ratio)	Variation (S ₀ - S _{1hr})/S ₀ (%)	Variation (B ₀ - B _{1hr})/B ₀ (%)	Sieve segregation P (%)
Control	2380	710	2.9	640	3.9	0.94	0.89	9.86	5.32	9.90
RCA25	2360	700	3.7	610	5.9	0.95	0.88	12.86	7.37	7.70
RCA50	2350	720	3.9	640	6.4	0.97	0.89	11.11	8.25	6.30
RCA75	2330	710	4.1	610	6.9	0.92	0.82	14.08	10.87	6.00
RCA100	2320	700	4.3	580	7.6	0.93	0.80	17.14	13.98	5.20

Note: EN 206-9:2010 [12] states that SCC should have a slump flow value (S) of between 550 and 850 mm; the blocking ratio (B₀) ≥ 0.80; and sieve segregation (P) < 20%.

TABLE 4: Strength properties of control and RCAs.

Mix code	Compressive strength, f_c (MPa)	Tensile strength, f_t (MPa)	Young's modulus, E (GPa)
Control	59.4	4.1	31.5
RCA25	63.7	4.9	30.3
RCA50	65.3	4.1	29.5
RCA75	60.0	3.9	28.5
RCA100	53.8	3.8	24.5

even though both aggregate types were soaked for 24 hours and subsequently dried for 1 hour, the RCAs are likely to have had a greater capacity to absorb free water after this process.

The results of the L-box test are presented in Figure 4. As stated in the previous section this test measures the passing ability of the SCC, thus quantifying the suitability of the SCC for use in a member with congested reinforcement. From the figure it is clear that the replacement of natural coarse aggregates with coarse RCA has little impact on the initial blocking ratios, with only a very slight reduction in B_0 observed for the 75% and 100% RCA utilisation levels. However, for the L-box test carried out one hour after mixing, the difference between the control SCC and the SCCs containing 75% RCA and 100% RCA increases. For this test the reductions in the blocking ratio observed, when compared to the control SCC, are approximately 8% and 10% for the 75% and 100% RCA SCCs, respectively (see Table 3). This results in the SCC containing 100% RCA being only just inside the EN206-9:2010 [12], SCC passing ability tolerance of 0.80. As with the slump flow test results, this time dependent change in blocking ratio at the higher levels of RCA utilisation may have been caused by continued absorption of free water by the RCA after concrete mixing. Examining Figure 5, it can be seen that the segregation resistance of the SCCs increased with increasing RCA content. Again this is likely to be due to the higher water absorption capacity of the recycled concrete aggregates. All the SCCs were deemed appropriate in accordance with EN206-9:2010 [12], with each SCC mix falling into the sieve segregation resistance class SR2 (segregation portion $\leq 15\%$).

3.2. Strength Properties. The test results for concrete compressive strength, splitting tensile strength, and the static modulus of elasticity are presented in Table 4. Figure 6 facilitates the easy comparison of the control mix results and the RCA mixes results, by presenting the RCA SCC strength properties relative to the control SCC properties. Taking the RCA25 mix as an example, the compressive strength value of RCA25 was 7% greater than the compressive strength of the control mix, that is, relative compressive strength performance of 107%. Thus the RCA25 compressive strength bar in Figure 6 lies above the 100% line, representing a higher compressive strength than the control SCC.

Considering the compressive strength results from Figure 6 it is noted that the replacement of conventional aggregates with recycled concrete at percentages of 25%

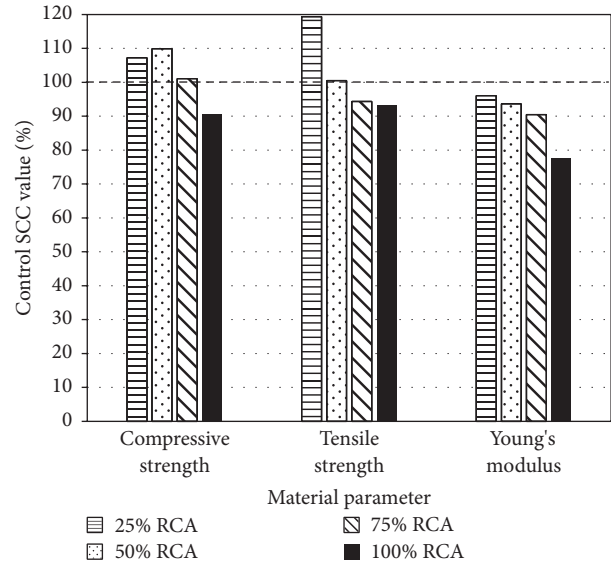


FIGURE 6: Relative comparison of RCA and control concrete strength properties.

and 50% actually increased the compressive strength by 7% and 10%, respectively. At the 75% replacement rate the compressive strength was found to be almost exactly equal to the control concrete, while 100% replacement with recycled aggregate resulted in a drop in compressive strength of 10%. Tuyan et al. [3] obtained similar findings when comparing SCC concretes containing 20%, 40%, and 60% RCA for a concrete with a w/b ratio of 0.43. These authors found the change in compressive strength to be +5%, +9%, and -2% for 20%, 40%, and 60% replacement, respectively. In an examination of high performance vibrated concretes Andreu and Miren [37] identified similar trends, although the changes for the vibrated concretes examined in the Andreu and Miren study were generally smaller.

There are a number of possible reasons for the increase in compressive strength with addition of RCA up to 50%. Hoffmann et al. [38] and Tuyan et al. [3] have both highlighted the fact that the increased surface roughness of recycled aggregates can increase cement aggregate bond. The role of the differing water absorption coefficients in recycled aggregates and conventional aggregates is also likely to have some influence. As shown herein and in other published studies, RCAs have a higher water absorption capacity than natural aggregates [4]. This increased water absorption may reduce the w/c ratio in the ITZ, increasing the strength of the cement paste in improving the bond between aggregates and cement paste [37, 39]. However, as pointed out by Tu et al. [4], if too much water is absorbed insufficient water content and poor hydration will reduce strength development in the concrete. This optimal water content balance is a possible explanation for the increase in compressive strength up to 50% RCA level, followed by the decrease in compressive strength from 50% RCA to 100% RCA, where w/b ratio remains constant at 0.35, regardless of RCA content. It is however also noted that the decrease in compressive strength

TABLE 5: Fracture properties test results.

Mix code	f_c (N/mm ²)	f_t (N/mm ²)	E (kN/mm ²)	G_f		$l_{ch,mod}$	
				(Nm-1)	(%)	(mm)	(%)
Control	59.4	4.08	31.5	170.8	100.0	22.2	100
RCA25	63.7	4.87	30.3	165.1	96.7	16.1	72.6
RCA50	65.3	4.1	29.5	164.6	96.4	18.1	81.8
RCA75	60.0	3.85	28.5	125.4	73.4	15.5	69.7
RCA100	53.8	3.81	24.5	126.2	73.9	15.1	68

Notes: f_c = compressive strength; f_t = splitting tensile strength; E = modulus of elasticity; G_f = fracture energy; $l_{ch,mod}$ = modified characteristic length.

even at 100% replacement with RCA was found to be less than 10%, indicating the suitability of RCA utilisation. Authors examining conventional vibrated concretes have identified greater reductions in compressive strength when 100% RCA is used at replacement level; however as pointed out by Tuyan et al. [3], SCCs are likely to experience a reduced effect of addition of RCA due to the reduced content of coarse aggregates in SCC mixes (which typically have an aggregate content comprising more than 50% fines).

The tensile strength results in Figure 6 exhibit a somewhat similar pattern to the compressive strength results, with the tensile strength initially increasing at the lower levels of RCA utilisation, followed by a decrease in strength beyond 50% RCA content. The tensile strength for the 25% RCA replacement is almost 20% greater than the control SCC. More subtle changes in tensile strength occur when the RCA content is greater than 25%. In similar tests Grdic et al. [15] found that the tensile strength for SCCs with 50% RCA and 100% RCA coarse aggregates resulted in approximate reductions in tensile strength of 2.5% and 14%, respectively, when compared to a control mix. Tuyan et al. [3] found that the splitting tensile strength reduced for 20%, 40%, and 60% RCA by 8.8%, 11.1%, and 16%, respectively, owing to the higher porosity and lower specific gravity of the RCA when compared to the natural aggregates. It should be noted however that, in contrast to the tests carried out herein, both Grdic et al. [15] and Tuyan et al. [3] increased water content in mix designs with increasing RCA content. Andreu and Miren [37] did not increase water content with increasing RCA content in their study of vibrated concretes containing RCA. These authors found that the use of 20% RCA increased the splitting tensile strength by between approximately 3% and 22%, a finding consistent with the results obtained herein.

Finally in terms of Figure 6, it is clear that the use of RCA at any replacement level resulted in a reduction in modulus of elasticity. The reduction in modulus of elasticity increases with increasing RCA content to a maximum of 22.2% for the 100% RCA concrete. The reduction for the 75% RCA mix is also substantial at 9.5%. As pointed out by Andreu and Miren [37], who obtained similar results for vibrated concretes containing RCA, such reductions are to be expected given that the modulus of elasticity of concrete is related to the modulus of elasticity of the coarse aggregate [40], with studies indicating that the modulus of elasticity is proportional to the square root of the aggregate density [41].

Overall considering the three strength property tests, the experimental programme indicated that the use of RCA in

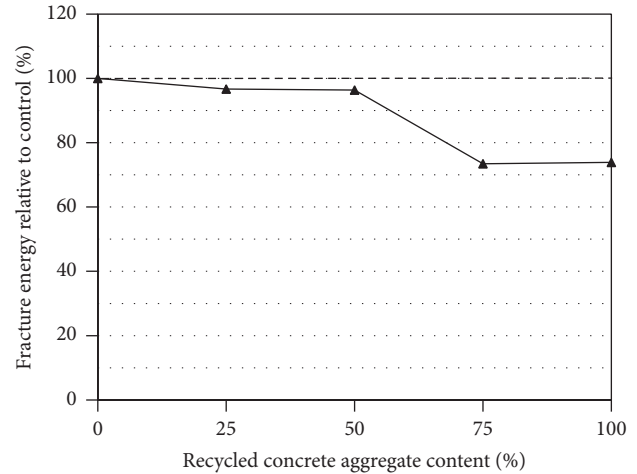


FIGURE 7: Influence of RCA coarse aggregate content on fracture energy.

proportions of 25% to 50% does not negatively impact upon the compressive and tensile strength of SCC. In fact, even up to the 100% RCA utilisation level, reductions in these parameters were less than 10% when compared to the control SCC. However, reductions in Young's modulus increased with increasing RCA utilisation across all SCCs, with the modulus of elasticity for the 100% RCA SCC 22% less than the control SCC, highlighting an issue relating to the brittleness of SCCs constructed entirely with RCA.

3.3. Fracture Properties. The fracture properties for the control concrete and the concrete mixes containing RCAs are presented in Table 5. As in the previous section, graphical presentation of the results is in the form of relative performance, with the fracture properties of the mixes containing RCA plotted, relative to the values for the control SCC. This facilitates easy visual comparison of the performance of RCA SCC mixes and the control SCC mix. Figure 7 presents the change in fracture energy with increasing RCA content.

As can be seen from the plot the fracture energy in the concrete was found to be relatively unaffected by the utilisation of 25% and 50% RCA, with these mixes having 96.7% and 96.4% of the control concrete G_f value, respectively. However, a sudden reduction in fracture energy occurs at the 75% RCA utilisation level, with 75% RCA mix and the 100% RCA mix both resulting in a 26% reduction in fracture energy. As discussed in Section 1, there is little or no existing

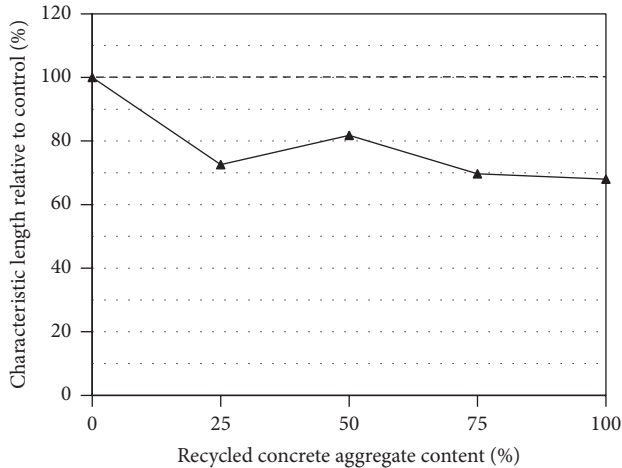


FIGURE 8: Influence of RCA coarse aggregate content on characteristic length.

literature examining fracture energy of SCC with RCAs. There are however a limited number of studies which explore fracture energy of traditional vibrated concretes containing RCA, while a number of these studies consider only 0% RCA (control) or 100% RCA [6, 20]. Bordelon et al. [19] examined a control concrete, a 50% RCA concrete, and a 100% concrete. In a similar pattern to the results obtained herein, Bordelon et al. found that, at the 50% replacement level, fracture energy was 98.8% of the control concrete; however for the 100% RCA vibrated concrete the fracture energy reduced by 35%. It is possible that the pattern of maintained fracture energy up to 50% RCA followed by stark reduction at RCA levels greater than 50% could be due to a balance of aggregate strength and aggregate bond. As discussed in the previous section aggregate-cement paste bond can be increased due to utilisation of RCA [3, 38]; however as pointed out by Butler et al. [20] and Darwin et al. [42], it is generally found that as aggregate strength decreases, fracture energy decreases. Thus, if a large portion of the total coarse aggregate volume comprises the weaker RCA (in comparison with natural granite aggregate) one might expect the fracture energy to reduce substantially. The fact that this does not occur until beyond the 50% RCA utilisation level in SCC examined herein is, however, an interesting experimental finding.

Figure 8 presents the change in characteristic length, $l_{ch,mod}$, with increasing RCA content. As stated in Section 2, $l_{ch,mod}$ parameter is a measure of brittleness derived from fracture energy, modulus of elasticity, compressive strength, and tensile strength. As can be seen from the plot the utilisation of RCA at all levels results in a notable reduction in characteristic length (increased brittleness), with relative $l_{ch,mod}$ values of 81.8% to 68.0% obtained for the RCA concretes. This is primarily due to the decrease in modulus of elasticity experienced in concretes containing RCA (discussed previously in the context of Figure 6). The low relative $l_{ch,mod}$ value for the 25% RCA mix is due to the nature of (3) and the 25% RCA mix having higher f_c and f_t values than the control concrete, as discussed in the previous section. Again, due to a lack of existing research in this area

it is not possible to compare these findings to other studies examining SCC containing RCAs; however, Casuccio et al. [6] did obtain characteristic length values for a range of vibrated concretes containing RCAs. These authors found that when compared to a control concrete, incorporation of 100% RCA across three concrete strength groups resulted in reductions in characteristic length of between 0% and 36% with an average reduction of 17%. This is in reasonable agreement with the study of SCCs and RCA herein which indicated that the use of RCAs brings about a notably more brittle concrete, with changes of 19% to 32% in characteristic length observed.

4. Conclusions

The work presented in this paper builds on the existing SCC literature by investigating the effect of incorporating various levels of RCA on workability, strength characteristics, and most importantly fracture properties. The workability tests revealed that the viscosity of the SCCs increased with increasing RCA content, as did sieve segregation resistance. The passing ability of the SCC was found to notably reduce for RCA utilisation greater than 50%; however, the 75% RCA and 100% RCA SCCs were still within allowable passing ability limits.

Experimental investigation into the strength characteristics of the SCCs, namely, f_c , f_t , and E , indicated that the use of coarse RCA in proportions of 25% to 75% did not notably impact upon the strength of SCC. However, the modulus of elasticity for the 100% RCA SCC was found to be notably reduced when compared to the control SCC, highlighting a possible issue with brittleness of SCCs constructed entirely with RCA.

The fracture energy was found to remain relatively constant from control SCC to 25% RCA SCC to 50% RCA. However, a significant reduction in fracture energy was observed for the 75% RCA and 100% RCA utilisation levels. This sudden reduction in the fracture energy beyond the 50% RCA utilisation is an interesting finding in the context of the lack of information in the literature in this area. Overall the experimental test results obtained herein indicate that the environmental and economic aspects of SCC could be improved, without impact upon workability, strength characteristics, or fracture properties, through utilisation of 25 to 50% RCA. However, even at this lower level of replacement, some increase in concrete brittleness is likely to occur.

Conflict of Interests

The authors declare that there is no conflict of interests regarding the publication of this paper.

Acknowledgments

The work described in this paper was supported by the Australian Research Council Discovery Project (no. G1500225) and Faculty Strategic Pilot Grant and the Centre for

Interdisciplinary Built Environment Research, the University of Newcastle, Australia.

References

- [1] A. K. Padmini, K. Ramamurthy, and M. S. Mathews, "Influence of parent concrete on the properties of recycled aggregate concrete," *Construction and Building Materials*, vol. 23, no. 2, pp. 829–836, 2009.
- [2] M. D. Safiuddin, U. J. Alengaram, M. A. Salam, M. Z. Jumaat, F. F. Jaafar, and H. B. Saad, "Properties of high-workability concrete with recycled concrete aggregate," *Materials Research*, vol. 14, no. 2, pp. 248–255, 2011.
- [3] M. Tuyan, A. Mardani-Aghabaglou, and K. Ramyar, "Freeze-thaw resistance, mechanical and transport properties of self-consolidating concrete incorporating coarse recycled concrete aggregate," *Materials and Design*, vol. 53, pp. 983–991, 2014.
- [4] T.-Y. Tu, Y.-Y. Chen, and C.-L. Hwang, "Properties of HPC with recycled aggregates," *Cement and Concrete Research*, vol. 36, no. 5, pp. 943–950, 2006.
- [5] S. C. Kou and C. S. Poon, "Properties of self-compacting concrete prepared with recycled glass aggregate," *Cement and Concrete Composites*, vol. 31, no. 2, pp. 107–113, 2009.
- [6] M. Casuccio, M. C. Torrijos, G. Giaccio, and R. Zerbino, "Failure mechanism of recycled aggregate concrete," *Construction and Building Materials*, vol. 22, no. 7, pp. 1500–1506, 2008.
- [7] J. Xiao, J. Li, and C. Zhang, "Mechanical properties of recycled aggregate concrete under uniaxial loading," *Cement and Concrete Research*, vol. 35, no. 6, pp. 1187–1194, 2005.
- [8] RILEM Recommendation 121-DRG Guidance for Demolition and Reuse of Concrete and Masonry, "Specifications for concrete with recycled aggregates," *Materials and Structures*, vol. 27, no. 9, pp. 557–559, 1994.
- [9] ACI Committee 555, "Removal and reuse of hardened concrete," *ACI Materials Journal*, vol. 99, no. 3, pp. 300–325, 2002.
- [10] A. Katz, "Properties of concrete made with recycled aggregate from partially hydrated old concrete," *Cement and Concrete Research*, vol. 33, no. 5, pp. 703–711, 2003.
- [11] P. C. Ryan and A. O'Connor, "Examination of self-compacting concrete options for marine bridge applications," *Journal of Bridge Engineering*, vol. 19, no. 9, Article ID 04014032, 2014.
- [12] Centre Europeen de Normalisation (CEN), *EN 206-9: 2010 Additional Rules for Self Compacting Concrete*, 2010.
- [13] W. Zhu and P. J. M. Bartos, "Permeation properties of self-compacting concrete," *Cement and Concrete Research*, vol. 33, no. 6, pp. 921–926, 2003.
- [14] P. C. Ryan and A. J. O'Connor, "Probabilistic modeling of reinforced concrete bridge repair deterioration in marine environments," in *Proceedings of the 6th International Conference on Bridge Maintenance, Safety and Management (IABMAS '12)*, pp. 3776–3783, Taylor & Francis Publishers, Stresa, Italy, July 2012.
- [15] Z. J. Grdic, G. A. Toplicic-Curcic, I. M. Despotovic, and N. S. Ristic, "Properties of self-compacting concrete prepared with coarse recycled concrete aggregate," *Construction and Building Materials*, vol. 24, no. 7, pp. 1129–1133, 2010.
- [16] C. G. Fakitsas, P. E. A. Papakonstantinou, P. D. Kiousis, and A. Savva, "Effects of recycled concrete aggregates on the compressive and shear strength of high-strength self-consolidating concrete," *Journal of Materials in Civil Engineering*, vol. 24, no. 4, pp. 356–361, 2012.
- [17] M. H. A. Beygi, M. T. Kazemi, I. M. Nikbin, and J. V. Amiri, "The effect of water to cement ratio on fracture parameters and brittleness of self-compacting concrete," *Materials & Design*, vol. 50, pp. 267–276, 2013.
- [18] Z. P. Bazant and J. Planas, *Fracture and Size Effect in Concrete and Other Quasibrittle Materials*, CRC Press, Boca Raton, Fla, USA, 1998.
- [19] A. Bordelon, V. Cervantes, and J. R. Roesler, "Fracture properties of concrete containing recycled concrete aggregates," *Magazine of Concrete Research*, vol. 61, no. 9, pp. 665–670, 2009.
- [20] L. Butler, J. S. West, and S. L. Tighe, "Effect of recycled concrete coarse aggregate from multiple sources on the hardened properties of concrete with equivalent compressive strength," *Construction and Building Materials*, vol. 47, pp. 1292–1301, 2013.
- [21] A. Leemann, R. Loser, and B. Münch, "Influence of cement type on ITZ porosity and chloride resistance of self-compacting concrete," *Cement and Concrete Composites*, vol. 32, no. 2, pp. 116–120, 2010.
- [22] M. Valcuende and C. Parra, "Bond behaviour of reinforcement in self-compacting concretes," *Construction and Building Materials*, vol. 23, no. 1, pp. 162–170, 2009.
- [23] Centre Europeen de Normalisation (CEN), *EN 450-1:2005+AI:2007 Fly Ash for Concrete. Definition, Specifications and Conformity Criteria*, 2007.
- [24] ASTM, "Standard specification for silica fume used in cementitious mixtures," ASTM C1240-11, ASTM International, West Conshohocken, Pa, USA, 2011.
- [25] Centre Europeen de Normalisation (CEN), *BS EN 12620:2002+AI:2008 Aggregates for Concrete*, 2002.
- [26] Centre Europeen de Normalisation (CEN), *EN 12350-8: 2010, Testing Fresh Concrete Part 8: Self-Compacting Concrete—Slumpflow Test*, 2010.
- [27] Centre Europeen de Normalisation (CEN), *EN 12350-10: 2010, Testing Fresh Concrete Part 10: Self-Compacting Concrete—L-Box Test*, 2010.
- [28] Centre Europeen de Normalisation CEN, "Self compacting concrete—sieve segregation test," EN 12350-11:2010, 2010.
- [29] Centre Europeen de Normalisation (CEN), *EN 12390-3:2009 Testing Hardened Concrete. Compressive Strength of Test Specimens*, 2009.
- [30] Centre Europeen de Normalisation CEN, "Testing hardened concrete. Tensile splitting strength of test specimens," EN 12390-6:2000, 2000.
- [31] British Standards Institution, "Testing concrete. Method for determination of static modulus of elasticity in compression," BS 1881-121:1983, HMSO, London, UK, 1981.
- [32] RILEM, "Determination of the fracture energy of mortar and concrete by means of three-point bend tests on notched beams," *Materials and Structures*, vol. 18, no. 4, pp. 285–290, 1985.
- [33] G. A. Rao and B. K. R. Prasad, "Fracture energy and softening behavior of high-strength concrete," *Cement and Concrete Research*, vol. 32, no. 2, pp. 247–252, 2002.
- [34] R. K. Navalurkar, C.-T. T. Hsu, S. K. Kim, and M. Wecharatana, "True fracture energy of concrete," *ACI Materials Journal*, vol. 96, no. 2, pp. 213–225, 1999.
- [35] A. Hillerborg, "Analysis of one single crack," in *Fracture Mechanics of Concrete*, Developments in Civil Engineering, pp. 223–249, Lund University Publications, Lund, Sweden, 1983.
- [36] F. P. Zhou, B. I. G. Barr, and F. D. Lydon, "Fracture properties of high strength concrete with varying silica fume content and

- aggregates,” *Cement and Concrete Research*, vol. 25, no. 3, pp. 543–552, 1995.
- [37] G. Andreu and E. Miren, “Experimental analysis of properties of high performance recycled aggregate concrete,” *Construction and Building Materials*, vol. 52, pp. 227–235, 2014.
- [38] C. Hoffmann, S. Schubert, A. Leemann, and M. Motavalli, “Recycled concrete and mixed rubble as aggregates: influence of variations in composition on the concrete properties and their use as structural material,” *Construction and Building Materials*, vol. 35, pp. 701–709, 2012.
- [39] M. Etxeberria, E. Vázquez, and A. Mari, “Microstructure analysis of hardened recycled aggregate concrete,” *Magazine of Concrete Research*, vol. 58, no. 10, pp. 683–690, 2006.
- [40] A. M. Neville, *Properties of Concrete*, Longman, Harlow, UK, 4th edition, 1995.
- [41] F. D. Lydon and R. V. Balendran, “Some observations on elastic properties of plain concrete,” *Cement and Concrete Research*, vol. 16, no. 3, pp. 314–324, 1986.
- [42] D. Darwin, S. Barham, R. Kozul, and S. Luan, “Fracture energy of high-strength concrete,” *ACI Materials Journal*, vol. 98, no. 5, pp. 410–417, 2001.

Research Article

Dye Sensitized Solar Cells with Low Cost Carbon Nanotubes Electrodes

F. M. Al-Marzouki, S. Abdalla, and S. Al-Ameer

Department of Physics, Faculty of Science, King Abdulaziz University Jeddah, P.O. Box 80203, Jeddah 21589, Saudi Arabia

Correspondence should be addressed to S. Abdalla; smabdullah@kau.edu.sa

Received 20 October 2015; Revised 24 December 2015; Accepted 3 January 2016

Academic Editor: Gonzalo Martínez-Barrera

Copyright © 2016 F. M. Al-Marzouki et al. This is an open access article distributed under the Creative Commons Attribution License, which permits unrestricted use, distribution, and reproduction in any medium, provided the original work is properly cited.

Dye sensitized solar cells (DSSCs) are very sensitive to electrodes, due to either high cost or easy corrosion problems. To minimize these factors, we present DSSCs with cheap carbon nanotubes as counter electrodes. In addition, we suggest replacing the electrolyte (in typical DSSCs) with a solid film of powdered CsSnI_3 . The electrical behavior (I - V characteristics) of the proposed device has been measured for different shading conditions. In the light of a theoretical model based on the presence of two diodes, the experimental data have been explained, taking into account a new equivalent circuit for the DSSC. These DSSCs may receive different levels of sun radiation, which stimulates the study of partial shading; so, we have studied the effect of different shadow rates on the solar conversion efficiency of a unit of 4-W-connected DSSCs. The validity of the present model has been examined by fitting it into I - V characteristics at different shading rates.

1. Introduction

Due to the enormous acceleration of modern civilization and the developments in all domains all over the world, the increase in the rate of energy consumption is a characteristic of this civilization, and a dire need for energy is always present. However, the exhausted energy sources, such as mineral and animal traces, are inevitably disappearing, and solar energy has become an increasingly hot topic, particularly over the recent years. For example, an enormous quantity of energy is supplied each second, to the earth's surface (about 9.5×10^{16} Joule/second [1]). In their pioneer work, O'Regan and Grätzel [2] have initiated the principals of dye sensitized solar cells (DSSCs). Since 1990s, DSSCs have continuously augmented by time as it is illustrated in Figure 1. In this figure, the number of publications of CNTs has been reported and CNTs have been extensively used as counter electrode. Due to the high rate of publications, several huge companies have commercialized these solar cells. As a consequence, the fabrication methods for CNT films and photoelectrode materials have been developed. Table 1 shows the different fabrication methods of DSSCs.

Grätzel has reported that this quantity of energy is ten thousand times more than mankind needs, nowadays.

This means that only a slim part of the global surface area, which is about 0.1%, with a solar efficiency of about 10%, would be totally enough to cover our energy needs. Consequently, the solar energy cells have received increasing attention over the last three decades. They have passed through several substantial steps, starting with simple solar cell [3], to a second main step, solar cells based on thin film solar cells (SCs) [4, 5] and the present third generation which uses organic-SC and dye sensitized solar cells [5–8]. In addition, the third generation has more compatibility with flexible substrate and relatively low cost of basic materials.

Furthermore, nanotechnology launches several axes of research, particularly in nanoenergy. For example, it is now easy to prepare a suitable nanomaterial with different nanostructures, using the dye sensitized solar cells to get the optimum converted energy. Moreover, one can paint a glass slide with carbon nanotubes (CNTs) and consider it as an active electrode (working electrode), which is placed against another similar glass slide which represents a counter electrode. This is illustrated in Figure 2, where the space

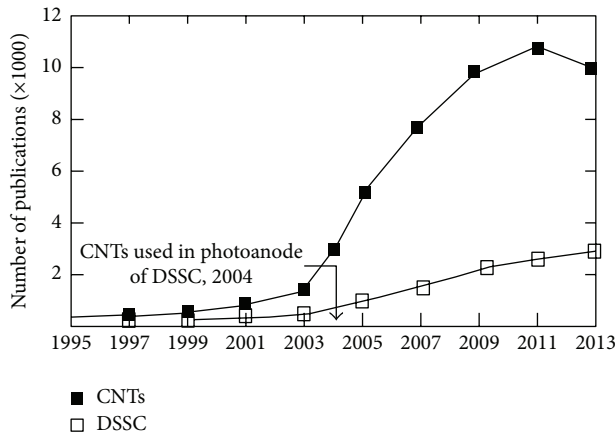


FIGURE 1: Rise of publications number, concerning nanotubes and DSSCs, with time.

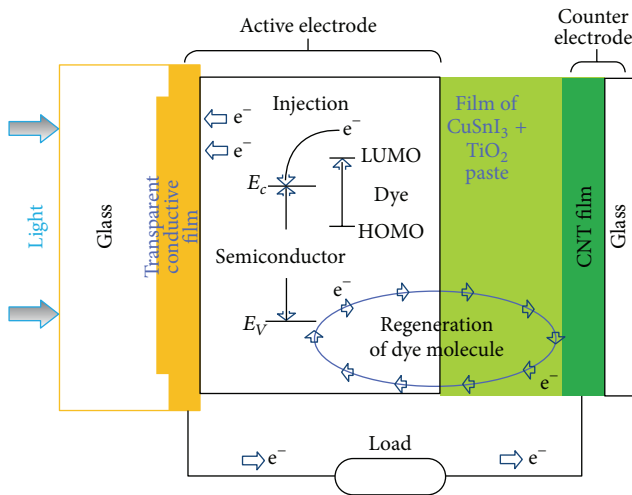


FIGURE 2: Schematic illustration shows the proposed dye sensitized solar cells.

between these electrodes lies in the micron scale $\sim 40 \mu\text{m}$, and it contains solid electrolyte acting as a high conductance medium. This illustration makes the active electrode irradiate photons which are transferred to the transparent electrode, and they arrive at the photoanode, where they will be absorbed by the sensitive-dye molecules.

The electron transition from the Highest Occupied Molecular Orbitals (HOMO) to the Lowest Unoccupied Molecular Orbitals (LUMO) is due to the optical absorption which occurs in the dye molecule [6]. These photogenerated electrons are transferred from the dye molecule towards the oxide and then spread out towards the counter electrode, where the cell is directly connected to the output load resistance. The dye molecules collect photons from the incident light, in a manner similar to the role of an antenna. This opens the doors for more progression of this technique, and for the development of more different organic dyes [9–11]. Photons, with energy $E = h\nu$, stimulate an electron from the dye to the LUMO of the semiconductor, where it reaches the

bottom electrode. The electrolyte reduces the dye molecules, which create tri-iodide ions I_3^- as follows: $3\text{I}^- \rightarrow \text{I}_3^- + 2\text{e}^-$. The external load will then absorb the energy of the electron via electrons transfer, through the wires of the external circuit. The tri-iodine ions (I_3^-) pass through the solution to the corresponding electrode where it will be reduced and thus complete the electrical circuit. Here, the semiconductor is nanoporous TiO_2 , which has a relatively high surface area. This large area increases the activity of dye molecules, but, at the same time, it reduces the rate of electron migration. Different semiconductors have been investigated, in order to get higher mobility of current carriers [12, 13]. In manufacturing DSSCs, several materials and techniques have been used: engineered semiconductor quantum dots, metal-free organic dyes, C60, and different materials. Using recent techniques with carbon nanotubes (CNTs) [14, 15], an alternative (and cheaper) to these techniques and materials has been offered. These tubes are highly conductive, photoactive, and mechanically strong, if well-prepared using different methods. For example, CNTs prepared by CVD are chemically inactive. CNTs show favorable features as counter electrodes [16].

Despite offering relatively high conversion efficiency, serious problems of life duration are strongly associated with the use of typical dye sensitized solar cells. First, problems associated with the electrodes result from the use of organic liquids ionic solutions with I^-/I_3^- , which reacts with the electrode leading to strong corrosion, in addition to the problems of solution loss by leakage process. Second, DSSCs should not rely on dyes, because they are weakened by time (bleaching effect of time), which limits the technical use of this technology. Third, platinum, which is often used as a counter electrode, has been inconvenient for use as a noble metal.

This largely inhibits the use of DSSCs on a commercial scale. Fourth, the rare indium is an undesired metal on the commercial scale. So, to minimize or even to overcome these factors that resist the large application of DSSCs, in this research work, we suggest that the extraordinary properties of carbon nanotubes should be used to build a commercial solar cell with relatively high conversion efficiency. In addition, we suggest replacing the electrolyte with a solid film of powdered CsSnI_3 “diffused” into TiO_2 (below the painted glass), as shown in Section 2. This replacement will eliminate the problem of using electrolyte as iodine ions.

Till now, only few papers have dealt with data concerning solar illumination, with different shadow rates on DSSCs conversion efficiency. In these papers, the forward bias electrical I - V characteristics are shown, taking into account the charge neutrality (via the continuity equation), through the semiconductors of the cell. But, on the contrary, the well known model of Butler-Volmer (BVM) takes into consideration the reverse bias, when polarizing the solar cell. Moreover, BVM was adopted by Chen et al. [17] and De Marco et al. [18]; however, the experimental data of partially or totally shadowed I - V characteristics are not completely fitted with one of these two models or even by some accord between these two models. Taking these points into account, this research work will deal with the elaboration of an

TABLE 1: Developments of different fabrication methods of DSSCs.

Production method	Advantage	Disadvantage	Year	Reference
Aerosol depositing (Wet Route)	Performance films and mass production	High cost, high temperature, complicated processes	2011	[26]
Array-drawing (Wet Route)	High efficient cells	Small production and difficult to control	2010	[27]
Transfer printing (Dry Route)	High performance, low cost, and simple method	Limitation of film size, limitation to control the manufacturing method	2006	[28]
Dip-coating (Dry Route)	Cheap and simple method	Hard to control film thickness	2012	[29]
Spin-coating (Dry Route)	Mass production, cheap and simple method	Loss of CNTs through fabrication and creation of inhomogeneous films	2010	[30]
Spray-coating (Dry Route)	Rapid process, mass production, cheap and simple method	Creation of rude surfaces with possible aggregation of CNTs	2010	[31]
EPD (Dry Route)	Cheap, rapid, and large area films	Hard to control the film thickness and limited substrate	2008	[32]
Printing (Dry Route)	Possibility of using different substrates, simple and fast	Hard to control the film thickness	2009	[33]
Brush painting (Dry Route)	Mass production, cheap and rapid deposition	Hard to control the film thickness	2014	[34]

adequate model to explain clearly the electrical behavior and I - V characteristics of DSSCs with partly or completely shadowing conditions. So, we will modify the well known one-diode model of a photovoltaic cell, using another diode. Thus, the cell will be represented by two diodes: one accounts for the forward bias and the other accounts for the reverse bias. The presented model is, thus, adopted to investigate the different illumination effects on a DSSC, made of 4 series-connected elements.

Finally, Slonczewski and Weiss [19] compared the ratio of energy produced per dollar, to the cost of installation and manufacturing, and they discovered that the use of graphite was an excellent solution in producing low cost cells [19] with relatively high efficiency which we took into account when we replaced them with CNTs, instead of graphite.

The literature is not poor in the application of CNTs as the counter component of the counter electrode of DSSCs [20–23]. Mixing aerosol with chemical evaporation deposition, Aitola et al. [21] have produced single-walled carbon nanotubes and have deposited film on polyethylene terephthalate substrate. Their plastic films have surface electrical resistance about 60 ohms sq^{-1} when using CNT film as transparent conducting film (TCF) for DSSC. Their data have given 0.74% solar conversion efficiency at an intensity 100 mW/cm^2 which is by far inferior to the reference cell (4.4%). Experimental data [24] have improved the efficiency of DSSCs using Pt-free

and transparent conductive oxide-free counter electrode and N-doped CNTs. The use of this doping on carbon nanotubes creates an extra free electron which can be used in reduction of electrolyte at high rate leading to increase of the efficiency. This efficiency has been improved to reach 1.5% [21]. Carbon nanotubes have been, also, used as an alternative to transparent conducting oxide materials in the Pt-based counter electrode of DSSC [25].

2. Materials and Methods

2.1. Cell Assembling (Figure 3). First, a comparison between the structure of a typical DSSC and a solid dye sensitized solar cell with carbon nanotubes is suggested. The enriched carbon nanotube solar cell (CNTSC) consists of the following:

- (1) A mixture of 90% semiconducting nanotubes and 10% metallic nanotubes, “South/West Nano Technologies,” with a length of about $2.4 \mu\text{m}$ and diameter of about 1.5 nm was used.
- (2) A thick film of powdered CsSnI_3 “diffused” into TiO_2 (below the painted glass). This thick film was prepared, using the method described by Chung et al. [35]. The advantage of using CsSnI_3 was the diffusion of SC into nanoporous TiO_2 and it could be stabilized at a solid phase inside TiO_2 [35]. In their

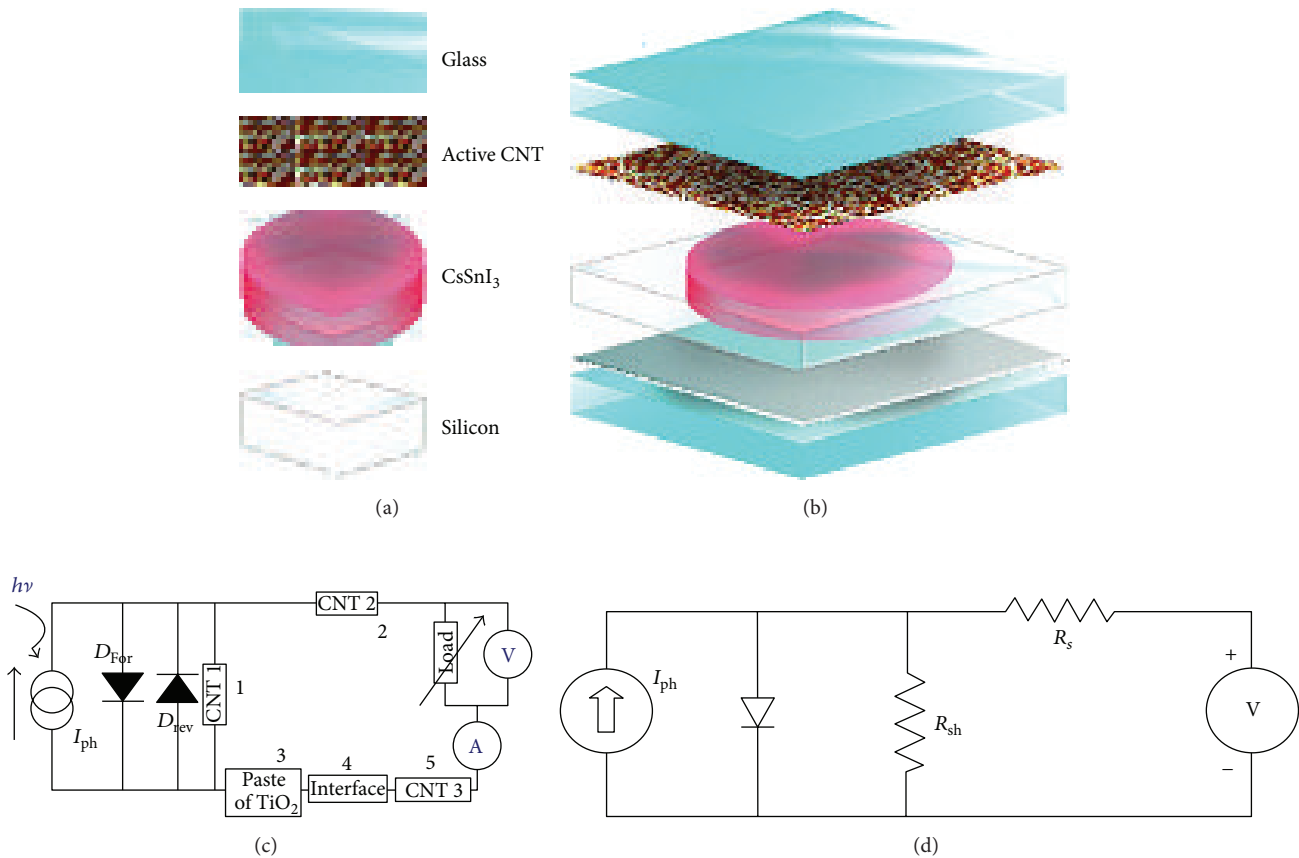


FIGURE 3: Schematic design of carbon nanotube solar cells (CNTSCs) and their equivalent electronic-circuits using the model of [36]. Figures 3(a) and 3(b) represent a CNTSCs construction where a glass slide (bluish-green) is followed by an active CNT film then film of CsSnI₃ with porous TiO₂ paste (red) followed by silicon insulator and CNT counter electrode (black) deposited on glass slide (bluish-green). Figure 3(c) shows the equivalent circuit of CNTSCs where the numbers stand for 1- Carbon nanotube film-1, 2- Carbon nanotube film-2, 3- Paste 4- interface 5- Carbon nanotube film-3 and 6- electric resistance load. The last part represents a typical “one-diode” equivalent circuit for a dye sensitized solar cell (DSSC). Figure 3(d) represents the equivalent circuit of typical one-diode circuit.

method, there were no by-products and consequently the compound was not only stable against high temperatures, but also strong against chemical reactions, in contrast to the most known solar cells [35]. This study showed that carbon nanotubes (CNTs) could replace the counter electrode. This presented it as a useful utility because the CNTs were chemically inert and corrosion of electrodes was very difficult with these tubes.

- (3) A film of semiconducting nanotubes (instead of the indium oxide in DSSCs) was used.
- (4) A film of CsSnI₃ with a porous TiO₂ paste (instead of the electrolyte in DSSCs) was used.
- (5) For photoconversion, semiconducting carbon nanotubes were used (instead of the dye in DSSCs).
- (6) A film of Mixed Carbon Nanotubes (MCNTs) was used as a counter electrode (instead of the platinum electrode in DSSCs), “South/West Nano Technologies,” with a length of about 2.4 μm and diameter of about 1.5 nm.

- (7) MCNTs were composed of mixtures of 66% semi-conducting nanotubes and 33% metallic nanotubes (Carbon Nanotechnologies, “UNIDYM® Inc.”).

Dispersion of CNTs was carried out, using ultrasound agitation in 1,2-dichloroethane for about one hour for the regular mixture and for about four hours for the enriched mixture. Using spray paint technique, the dispersion was dyed (using a technique of airbrush) onto a glass substrate. In a regular manner, the painted glass slides were rotated while spraying, in order to obtain a homogeneous painting. The glass slides were heated on a hot plate, in order to get rid of what they might present to the solvents. The exposed surface area of about 4.8 mm² resulted from the obtained solar cell, with an interelectrode distance of about 2.5 mm. The glass slides were about one mm thick.

2.2. Production of Solar Energy. The cell was connected to a resistor (R_L). The latter varied in the range of $0 < R_L < 10 \text{ M}\Omega$ and was connected to a current amplifier. The current I (and the voltage V across R_L) was measured, as a function of the load resistor R_L . The cell was subjected to solar radiation with

an average flux of about 890 W/m². We used a vast range of CNTs concentrations to build up DSSCs.

3. Model

3.1. Theoretical Aspects. The driving forces acting on the photogenerated electrons transportation in TiO₂ occur due to the diffusion mechanism, rather than due to the action of the electric field [37] (the same applies to the holes in the paste). In fact, the miniscule volume of TiO₂ nanoparticles (from 20 nm to 70 nm) creates an important space charge layer. Also, O'Regan et al. [38] and Grätzel [39] have shown that the sintered particles are usually surrounded by an excess of charges from the paste that screens any electric field in the region. Sodergerm et al. [40] used the recombination, generation, and electron transport rates, to estimate the electron collection efficiency of the nanostructured photoactive electrode. While developing our model, their model [40] was taken into account.

Here, one can describe the neutrality of charges as

$$\frac{\partial n}{\partial t} = D \frac{\partial^2 n}{\partial x^2} - \frac{n - n_0}{\tau} + g, \quad (1)$$

where n is the free electron density, " τ " is the electron lifetime, D is the diffusion coefficient, g is the generation rate of electrons, and n_0 is the electron density in an equilibrium state in a dark condition. Consider the following boundary conditions:

$$n|_{x=0} = n_0 \exp\left(\frac{qV}{mkT}\right), \quad (2)$$

$$\frac{\partial n}{\partial x}|_{x=d} = 0, \quad (3)$$

where V represents the photoelectrode potential, which is related to the energy variation between the electrode potential and Fermi energy (Fermi level), E_F . Consequently, the current density equation is given as

$$j = j_{sc} - j_0 \exp\left(\frac{qV}{mkT} - 1\right). \quad (4)$$

It is important to note that an ideality factor m is considered, when applying (2). Bashahu and Nkundabakura [41] identified a value of m to be about 22, from experimental data that considered only one set of current-voltage experimental data. Due to the inevitable presence of a parasitic resistance R_s , only the last equation cannot describe the electric I - V characteristics data. This resistance should be introduced as series resistance R_s to get an exact estimation of the current-voltage characteristics. In addition, this parasitic resistance R_s contains the resistive effects of the metallic contacts. Another parasitic resistance R_{sh} should also be considered, due to the presence of a parallel electric field, which is present due to the leakage path across the interface between TiO₂ and the paste. In order to understand the I - V characteristics and to simulate an equivalent circuit that described the electrical characteristics of DSSC, Halm et al. [42] developed the classic

"one-diode" model (Figure 1) that sufficiently described the following I - V characteristics:

$$I = I_{ph} - I_0 \left[\exp\left(\frac{q(V + IR_s)}{mkT}\right) - 1 \right] - \frac{V + IR_s}{R_{sh}}, \quad (5)$$

where I_0 is the current density at saturation-reversed conditions, I_{ph} is the photocurrent density of the diode as a current source, q is the electron charge, k is Boltzmann constant, T is the absolute temperature, and R_{sh} is a parallel electric resistance connected to the cell. Considering this with $I = 0$, the open circuit voltage V_{OC} can be given as

$$V_{OC} = \frac{mkT}{q} \ln\left(\frac{I_{ph}}{I_0} + 1\right). \quad (6)$$

This last equation gives the reason why V_{OC} corresponds with the high growing current of the short circuit. But the finely built current of the dye cells is not too simple to be described by only one diode, because it will be poorly described and it cannot be used to explain the electrical behavior of DSSC. Another important factor is that the parasitic resistances R_s and R_{sh} are considered to be independent of the voltage, which is not the real case. However, these fitting parameters represent an effective tool that is used to have a first sight interpretation of the characteristic behavior of the I - V [43].

3.2. Reverse Behavior through Dye Sensitized Solar Cells. Sastrawan et al. [44] and Chen et al. [17] have shown that the generated photocurrent produced when cells are collected together makes the shaded cell operate in reverse bias. The counter electrode (platinum or else) supplies electrons to the paste, which facilitates possible and easier ways of injecting electrons from the paste, and thus the charges will transfer from the corresponding electrode (I^-) directly to the porous TiO₂, and the oxidation of the electrode (I^-) allows one to consider the reverse current passage making a possible introduction to a reverse diode, in addition to the forward one (Figure 3).

Wolf and Rauschenbach [45] have shown that the charge transfer is mainly due to a reduction in the oxidation reaction (in the shadowed cell), and the recombination via the substrate. Following this, the net flow of charges yielded a current given by BVM and it was written in terms of overvoltage as

$$j = j_0 \left[\exp\left(\frac{\beta(qn)V}{kT}\right) - \exp\left(\frac{-(1-\beta)(qn)V}{kT}\right) \right], \quad (7)$$

where β is the cathodic transfer coefficient, j_0 is the exchange current density, and n is the number of transferred electrons. Both (I^-) and (I^-)₃ affected the current density (which was going to the cathode) via the concentrations and the reaction area. Here, the first term, in (7), is a linear function of the current, but the other term is a linear function of the current going to the anode. Moreover, the direct relationship between the two currents going to the anode and cathode resulted in the exchange current j_0 . In fact, BVM gave the reasons about the homogeneity of the electric field around the electrodes

[46]. Some limitations, however, arose, because of a small correction of the overpotential at the counter electrode, which was essential for fitting current-voltage characteristics in an effective way [47]. Chen et al. [17] introduced the idea of R_s of the transparent conductive oxide layers of the BVM, which improved the fitting process of the cell's electrical characteristics.

3.3. Electrical Behavior of DSSC. In the equivalent circuit, the rectification behavior of the diode explained the electrical behavior of DSS at the reverse polarization conditions. We proposed another parallel-diode with the current generator, in order to represent the rectifying behavior. The presence of the second diode prevented the recourse of the electrochemical variables, when the transfer of charges occurred at the paste. We schematically present the two-diode model in Figure 3. Applying the conservation of energy principal (via Kirchhoff equation), the characteristic equation of the circuit in Figure 3 can be described as

$$I = I_{ph} - I_{0-For} \left[\exp \left(\frac{q(V + IR_s)}{m_{For}kT} \right) - 1 \right] + I_{0-rev} \left[\exp \left(\frac{-q(V + IR_s)}{m_{rev}kT} \right) - 1 \right] - \frac{V + IR_s}{R_{sh}} \quad (8)$$

In dark conditions, it can be understood that, at reverse polarization, only the third term in (8) remained, while in the illumination conditions with forward polarization, the "one-diode" based model was equivalent to the two-diode based model. The values of R_s were taken to be constant in our model, in both forward and reverse bias. As a first approximation, we considered $R_{s-For} = R_{s-rev}$; that is, we considered the fact that they would have the same magnitude in both conditions. On the contrary, the physical meaning of the exponential term was controlled by the ideality-factor value, which depended on the operative conditions and was not equal. This means that the difference between the ideality factors in forward and reverse bias is a function of the condition of active working (temperature, illumination intensity, effective surface area, etc.).

4. Results

4.1. Characterization of Obtained Cell

4.1.1. Raman Scattering Spectra. At different excitation light, 514.5 nanometers, 676.4 nanometers, and 1064.0 nanometers, the main surface enhanced Raman scattering spectra characteristics of carbon nanotubes have been taken and are illustrated in Figure 4.

This figure shows characteristics of samples with different nanoropes of about 18 up to 99 separated CNTs which are in good agreement with published data [48]. As seen, the spectra of ropes are strongly depending on the excitation wavelength.

4.1.2. XPS Spectra. XPS spectra have been taken with SSX-100 ESCA spectrometer using 1486.6 eV Al-K α radiation. Figure 5 illustrates XPS spectra with two different resolutions: (a) low

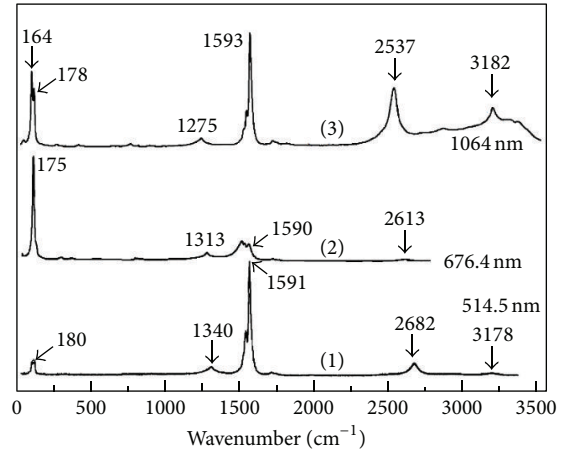


FIGURE 4: Surface enhanced Raman scattering spectra at different wave excitation lengths: (1) $\lambda_1 = 514.5$ nm, (2) $\lambda_2 = 676.4$ nm, and (3) $\lambda_3 = 1064$ nm of CNTs deposited on gold support.

and (b) high. The high resolution illustration shows the presence of C-C bond at 285 eV, in addition to some carbonyl moiety in harmony with carboxylated groups at 288 eV. The low-resolution XPS spectrum shows a net peak at 284.8 eV which is due to carbon 1s.

Mialhe et al. [49] and Ishibashi et al. [50] have shown that studying the effect of each variable on the different parts of the current-voltage curves (where some of these parameters could be neglected at certain parts of the I - V characteristics) is the best way to understand the electrical behavior of the DSSCs. Models with one diode can be used to get an accurate estimation of the DSSCs physical parameters; that is, the application of (8) to the experimental data can give the cell parameters when extrapolating numerical calculations which could be obtained either from extrapolating experimental results [51] or from using the spectral and electrochemical studies with the help of a suitable equivalent circuit of DSSC (single cell). We carried out our analysis in two successive steps. First, an initial group of fitting parameters were extracted using experimental data; then, second, they were, iteratively, refined out using "Levenberg Marquardt," an algorithmic procedure that is used for nonlinear curve fitting [52]. In the analysis, we reported a detailed procedure for the estimation of the initial parameters:

- I_{ph} was considered to be coincident with the short circuit photocurrent, I_{sc} .
- From the slope of current-voltage curves, we were able to estimate the shunt resistant R_{sh} when $I = I_{sc}$:

$$-\left. \frac{dV}{dI} \right|_{I=I_{sc}} = R_{sh} \quad (9)$$

The value of R_{sh} , in our device, was about $1.1 \times 10^5 \Omega$, which was a remarkably high value. Accordingly, when we took into account the photocurrent values of about some milliamperes, then, we can consider R_{sh} to tend to infinite values. Moreover, O'Regan et al. [53] reported that *rash* usually

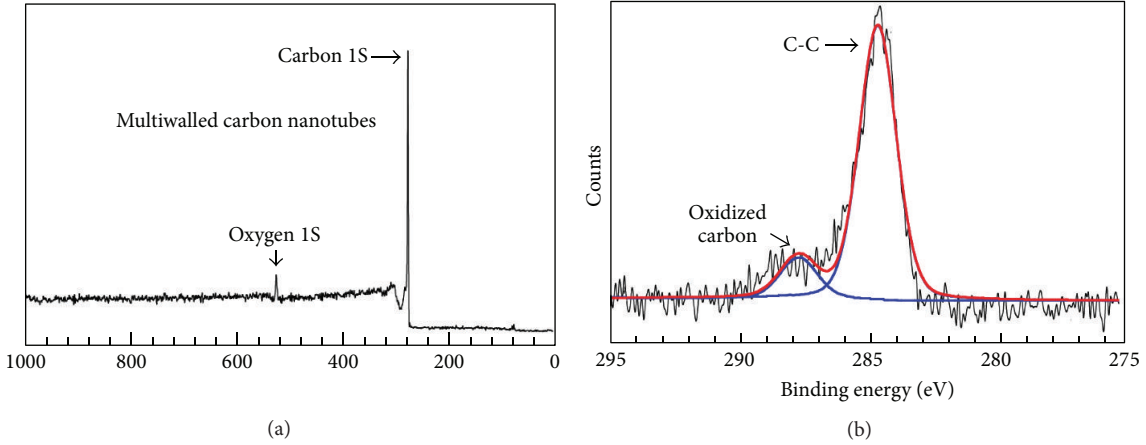


FIGURE 5: XPS spectra of carbon nanotubes (of C1s) with two different resolutions: (a) low and (b) high.

increased, when illumination decreased. Thus, we kept it as a constant factor.

- (c) Following Han et al. [36], in forward bias, the series resistance R_{s-For} could be obtained by direct application of the well known curves of $\epsilon' - \epsilon''$ because of the addition of several different resistances: contact resistance, substrate sheet resistance, electrical resistance of the paste, and resistance of all wires of the cell.
- (d) Then, we were able to estimate the exact potential through the cell V_F , by using the forward bias resistance, R_{s-For} as

$$V_F = V_{appl} - V_s = V_{appl} - IR_{s-For}. \quad (10)$$

- (e) The value of the recombination resistance was then estimated from the analysis of the different spectra of electrochemical impedance spectroscopy in the middle frequency region [42]:

$$R_{rec} = \frac{kT}{q\beta I_{0-For}} \exp\left(\frac{-q\beta V_F}{kT}\right). \quad (11)$$

- (f) We were able to estimate the value of the ideality factor in forward bias, using the semilog curve of the recombination resistance R_{rec} versus the potential at the SC electrode, V_F , where $m_{For} = 1/\beta$ and I_{0-For} .

With regard to the reverse-bias term in (8), the best fitting parameters of the current-voltage curves could be used to estimate several parameters of the DSSC: the reverse series resistance R_{s-rev} , the reverse series resistance R_{s-rev} , and the ideality factor m_{rev} . Here, one can easily neglect both R_{s-rev} and the current generator.

- (g) The value of recombination resistance is, then, estimated from analysis of the different spectra of electrochemical impedance spectroscopy in middle frequency region [42]:

$$R_{rec} = \frac{kT}{q\beta I_{0-For}} \exp\left(\frac{-q\beta V_F}{kT}\right). \quad (12)$$

- (h) The value of the ideality factor, in forward bias, could be estimated using semilog curve of recombination resistance R_{rec} versus the potential at the SC electrode, V_F , where $m_{For} = 1/\beta$ and I_{0-For} .

In regard to the reverse-bias term in (8), the best fitting parameters of current-voltage curves could be used to estimate several parameters of the DSSC: the reverse series resistance R_{s-rev} , the reverse series resistance R_{s-rev} , and the ideality factor m_{rev} . Here, one can easily neglect both R_{s-rev} and the current generator.

At elevated negative voltages, with the best nonlinear square fitting processes, we estimated I_{0-rev} values from its current value at zero voltage. Also, we found R_{s-rev} from the slope of the current-voltage curves, particularly, at the straight line of the current-voltage curves. The initial value of m_{rev} was considered as 1.5, to be in the range $1 < m_{rev} < 2$. Since we used the same series resistance, we assumed that $R_{s-rev} > R_{s-For}$. Systematically, the estimated R_{s-For} was highly affected by the illumination intensity (or shadow rate). Figure 6 illustrates a steep decrease of the short circuit current with a shadowing rate. The open circuit voltage decreased also, at a high shadow rate, which could be predicted from (6). But a minor increase of the fill factor was as a result of the high shadow rate. We attributed this decrease of R_s to the effect of photocurrent. The strong reduction in the R_s value was a function of the produced photocurrent. The magnitudes of R_{s-For} , at 1 sun illumination, ranged as 20Ω (complete illumination) $< R_{s-For} < 21 \Omega$ (0.75 of the complete illumination). Consequently, R_{s-For} was nearly not affected by the extent of the shaded photovoltaic region, and the values of R_{s-For} were taken as R_{s-rev} . Table 1 shows the information about the numerical coefficients.

To examine quantitatively the accuracy (including its validity) of our model for the different shadowing rates, we used "PSice" with the proposed model including the EC. By using this technique, the output power was accurately estimated after $I-V$ characteristics data. First, and for simplicity, at a complete shaded rate, we considered the module to be composed of only one single element, which would

TABLE 2: Methods to estimate the numerical parameters used to fit experimental data to (8).

Symbol	I_{ph}	I_0	m	R_s	R_{sh}
Forward direction	$\approx I_s$	Using EIS analysis	Using EIS	Using EIS	When $-(dV/dI) _{I=I_{sc}}$
Reverse direction	Using (8)	Using (8)	Using (8)	Using (8)	—

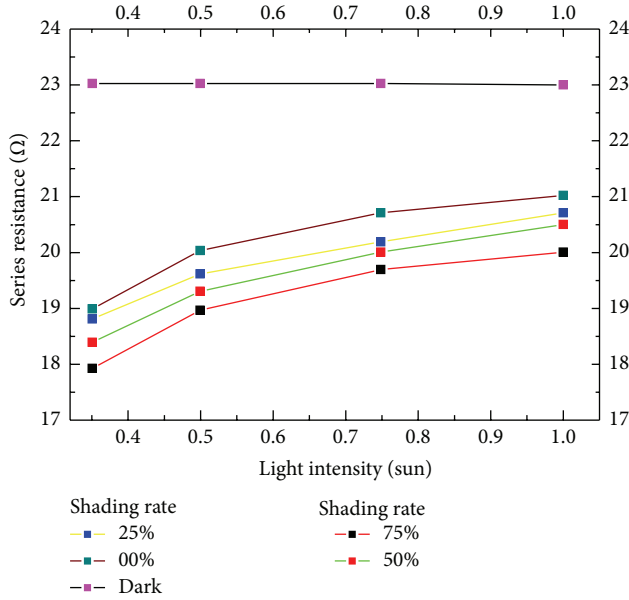


FIGURE 6: Series resistance as a function of light intensity for different shading rates.

overcome the recourse of analytical expressions. Then, we estimated the module with several elements of each solar cell, by looking for the best parameters that fit well (see (8)) with the experimental results at different rates of shadow. Fitted and experimental I - V characteristics data are reported in Figure 7 with a completely shaded cell. Because a shaded cell tends to behave in reverse bias, the data demonstrated that the reverse diode was “turned on.”

The potential that was just adequate to make the difference between the open circuit voltages of the module greater than the open circuit voltage of the shaded solar cell occurred when switching on the reverse diode. This reverse voltage V_{rev} stimulated the current to pass in a reverse direction, and this converted the cell into an electric resistor instead of being a current generator. The diminution of the potential (V_{bump}) can be estimated as

$$V_{bump} = V_{OC} + V_{rev}. \quad (13)$$

One can estimate V_{OC} directly by using (6), and V_{rev} was calculated, taking into consideration the parameters illustrated in Figure 6:

$$V_{rev} = \frac{kT}{qm_{rev}} \ln \left(\frac{I_{ph}}{I_{0-rev}} \right). \quad (14)$$

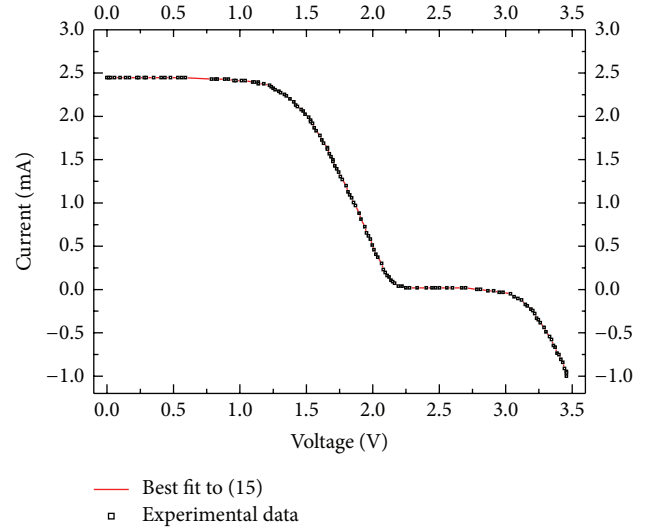
FIGURE 7: Experimental data of I - V characteristics of a four-cell module with one fully shadowed cell.

Table 2 shows the magnitudes of the physical parameters which have best fitted the experimental data to the model.

Using the principal of charge conservation, Sastrawan et al. [44] derived an expression that described the I - V characteristics of the cell in forward bias; their fitting values were not very far from ours, whereas the BVM ((7)) explained the reverse-biased behavior conduction in DSSC. One writes

$$I = I_{ph} I_{rr} \beta - A \frac{q D n_0 d}{L^2} \left[\exp \left(\frac{q(V + IR_s)}{m_{For} kT} \right) - 1 \right] \beta - A j_0 \left[\exp \left(\frac{\alpha n (V + IR_s)}{kT} \right) - \exp \left(\frac{-(1 - \alpha) n (V + IR_s)}{kT} \right) \right] - \left(\frac{V + IR_s}{R_{sh}} \right). \quad (15)$$

I_{ph} is the photocurrent, I_{rr} is the constant correlated with the irradiance parameter, β is the shadowing rate, D is the diffusion length of the electron, j_0 is the exchange current density, α is the cathodic transfer coefficient, n is the number of electrons transferred, and A is the surface of the area cell.

Equation (15) could be approximated, in reverse bias, where the first quantity could be neglected, but the second quantity has no real effect on the current density in the forward bias. The different physical parameters, described by (14), of the DSSC are reported in Table 3. Noting that I_{ph} is taken to be coincident with I_{sc} , just like Halm et al. [42],

TABLE 3: Best fitting parameters and experimental values to fit experimental data to (8).

Symbol	Parameter	Value	Units
I_{sc}	Short circuit current	2.4	mA
R_{s-For}	Series resistance	20	Ω
R_{s-rev}	Series resistance	23	Ω
I_{0-rev}	Irradiance factor	2.3×10^{-5}	mA
d	Film thickness	7×10^{-6}	m
m_{rev}	Diode ideality factor	1.1	—
m_{For}	Diode ideality factor	1.5	—
A	Area of dye sensitized solar cell	0.28	cm^2
T	Temperature	300	K

we have used the following equations to deduce the values of D and L :

$$D = \frac{d^2}{R_T C_\mu},$$

$$\tau = R_{rec} C_\mu, \quad (16)$$

$$L = \sqrt{D\tau} = d \sqrt{\frac{R_{rec}}{R_{CT}}}.$$

Moreover, just like Sastrawan et al. [44], we have calculated the cathodic transfer coefficient α and we have, also, used the work of Van De Lagemaat and Frank [52], to estimate the electron density, n_0 .

Figure 7 shows the electrical behavior of the conduction mechanism, which is a direct reflection of (15). However, the fit between the experimental data and model is not quite well demonstrated. This is because one has used the single independent measurements, to describe different physical parameters; so, some of the cell parameters have to be kept constant at certain conditions. For example, Wang et al. [54] have shown that the diffusion length L depends on the potential. The fitting parameters β and I_{rr} could be estimated, when varying the shadowing conditions of the cell. The simulated curve estimated after (8) fits the experimental data well. Thus, our model allows us to predict the values of the recombination rates (current), by following the interface between the paste and the transparent conductive oxide layer, which leads to a corresponding potential decrease, due to photovoltage drop V_{bump} . Figure 8 shows the measured and simulated current-voltage curves with the complete shadowing rate.

The presented model (two-diode model) fits well for all the 4 shadowing rates, which are seen from the simulation plots. The value of V_{bump} is doubled, when comparing it with a single cell. This is well shown after (13), when all the parameters are doubled. Similar electric results are shown with a complete shadowing rate, and with a multiplication factor of 3. This explanation is only applied, when the

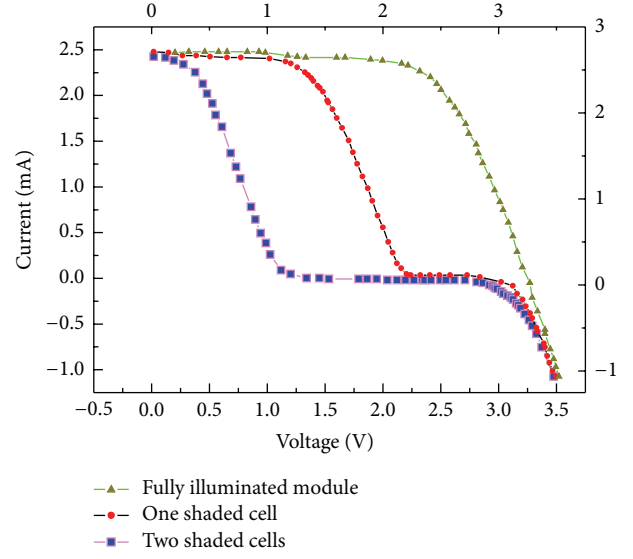


FIGURE 8: I - V characteristics experimental data for different shading rates illustrated as symbols and one shaded cell, two shaded cells, and fully illuminated module.

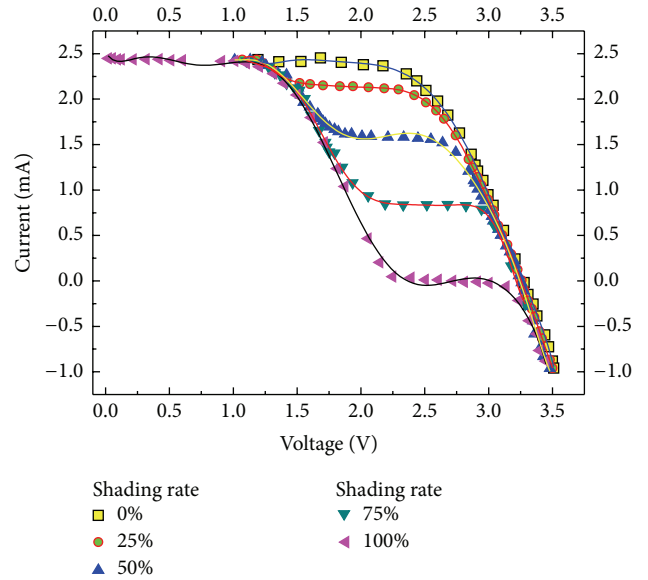


FIGURE 9: I - V characteristics experimental data for different shading rates illustrated as symbols.

four elements composed of cells with different electrical parameters, V_{rev} and V_{OC} , are determined for all the cells with different shadow rates which makes it possible to put the second term in (13) as a sum product.

Figure 9 shows that good simulation plots obtained when considering a two-diode model fit nearly perfectly for all the experimental current-voltage curves. In this figure, the simulation plots obtained by application of a 2-diode model fit nearly perfectly to the experimental data concerning all the considered shadowing rates. The reverse current passing the diode will induce the DSSC to operate as a load under potentials over 1.45 volts, if only one quart of the effective surface of

the photoelectrode is put in the dark. Consequently, the step is added to the I - V characteristics because the reverse diode is turned on suddenly. When half of the active area is shaded, the electric current arising from recombination increases more than the current generated by the photoexcitation at the unshaded photoelectrode; thus, the net output current will decrease which is shown by a plateau when reaching the critical short circuit value of the shaded cell, keeping the value of V_{bump} constant. The x -axis extension of the area lies under the influence of the photocurrent drop V_{bump} , and it does not get affected by the factor relating the illuminating active area of the photoelectrode to the obscured one as it is expected from (13).

When half of the active area is shaded, the electric current arising from recombination increases more than the current generated by the photoexcitation at the unshaded photoelectrode electrode; thus, the net output current will decrease which is shown by a plateau when reaching the critical short circuit value of the shaded cell, keeping the value of V_{bump} constant. The x -axis extension of the area lying under the influence of the photocurrent drop V_{bump} does not get affected by the factor relating illuminating active area of the photoelectrode to the obscured one as it is expected from (13). The carbon nanotubes in the present study were double-walled which are conductive materials. They can reduce the contact resistance which decreases in turn the charge transfer R_{CT} resistance with the DSSC due to fast transfer kinetics of electric charges (Table 4).

Lee et al. [55] have used carbon nanotubes as counter electrodes in DSSC and found a photovoltaic efficiency of 7.67% and the values of R_{CT} of their cell were 0.82 ohms cm^2 . Interestingly, their efficiency is comparable to the typical Pt-DSSC photovoltaic efficiency (7.83%). Experimental measurements of the present work have led to an efficiency of 5.7% and one can attribute the low value of efficiency to the nature of the impurities in the commercial carbon nanotubes and the effect of defect-rich edge planes in the bamboo-structured carbon nanotubes.

In addition, the measurements data of the present work have given relatively low values of the charge transfer resistance, about 1.05 ohms cm^2 which is lower than that of typical Pt-electrode (1.8 ohms cm^2). Our data are summarized in Table 5.

The function of DSSC is very sensitive to the number of walls of carbon nanotubes. In general, these nanotubes can be classified into single-walled carbon nanotubes, double-walled carbon nanotubes, and multiwalled carbon nanotubes. Zhang et al. [56] have compared the photovoltaic efficiency of three different DSSCs based on single-walled carbon nanotubes, double-walled carbon nanotubes, and multiwalled carbon nanotubes. They have found that the efficiencies vary in the range, 8.03% for double-walled carbon nanotubes, 7.61% for single-walled carbon nanotubes, and 7.06% for multiwalled carbon nanotubes. These efficiencies have been well matched with the charge transfer resistance; that is, $R_{\text{CT}} = 3.13$ ohms cm^2 for double-walled carbon nanotubes, $R_{\text{CT}} = 6.72$ ohms cm^2 for single-walled carbon nanotubes, and $R_{\text{CT}} = 10$ for multiwalled carbon nanotubes.

TABLE 4: Best fitting parameters and experimental values to fit experimental data to (15).

Symbol	Parameter	Value	Units
R_{sh}	Shunt resistance	1.1×10^5	Ω
R_s	Series resistance	20	Ω
I_n	Irradiance factor	$0 < I_n < 1$	—
I_{ph}	Short circuit current	2.435	mA
d	Film thickness	7×10^{-6}	m
β	Shadow's transmittance factor	$0 < \beta < 1$	—
D	Electron diffusion coefficient	5.2×10^{-5}	$\text{cm}^2 \text{s}^{-1}$
n_0	Electron density in the dark	1×10^7	cm^{-3}
D	Electron diffusion length	24.5×10^{-6}	m
j_0	Exchange current density	7×10^{-8}	mA cm^{-2}
α	Cathodic transfer coefficient	0.35	—
n	Electrons transferred	1	—
m	Diode ideality factor	1.5	—
A	Area of dye sensitized solar cell	0.28	cm^2
T	Temperature	300	K

The double-walled carbon nanotubes have larger “inner surface area” that can easily activate the charge transfer between them. However, the bamboo structure of multiwalled carbon nanotubes has more complicated “inner surface area” that strongly decrease the charge mobility and increase the corresponding charge transfer resistance. Consequently, this decreases the photovoltaic efficiency.

Carbon nanofibers have large surface area, high density of surface defects, and very thin filament size. These characteristics lead to an efficient DSSC due to their thinner thickness. As is well known, the electrical resistance of the counter electrode decreases as it gets thinner: Electrical resistance (R) = resistivity (ρ) * length (l)/area (A). For example, as the counter electrode increases from 5 micrometers, 10 micrometers, and 15 micrometers, to 20 micrometers, the net DSSC series resistance increases from 6.9 ohms cm^2 , 9.9 ohms cm^2 , 10.6 ohms cm^2 , and 11.9 ohms cm^2 . Because all factors are constant and only the counter electrode thickness decreases with the carbon nanofibers structure, the overall efficiency of DSSC with carbon nanofiber increases as a result of the reduction of counter electrode area. Table 6 shows the photovoltaic efficiency as a function of counter electrode thickness.

Comparing the experimental data recently published by Elbohy et al. [57] to the typical Pt- counter electrodes or carbon nanotubes counter electrodes, the carbon fiber SDDC has higher electrocatalytic efficiency and photovoltaic performance. This is attributed to its low electrical resistance of charge transfer and to high interfacial area. This also leads to accelerating mobility of charges which will reduce

TABLE 5: Current-voltage characteristics of DSSC with carbon nanotubes as counter electrode: measurements have been carried out under 0.75 sun illumination.

Counter electrode	R_{CT} (ohms cm^2) ± 0.4	j_{SC} (mA cm^2) ± 0.1	V_{OC} , ± 0.04 volt	FF ± 0.02	Efficiency% ± 0.2
CNTs	1.05	8.2	0.32	0.32	5.7
Pt	1.8	13.4	0.81	0.64	6.9
Bare FTO	—	1.7	0.82	0.04	0.06

R_{CT} : charge transfer resistance, j_{SC} : short circuit current, V_{OC} : open circuit voltage, and FF: fill factor. Active area of the device is 0.25 cm^2 .

TABLE 6: DSSC parameters as a function of counter electrode thickness.

Thickness, μm	R_{CT} (ohms cm^2)	j_{SC} (mA cm^2)	V_{OC} , volt	FF ± 0.02	Efficiency%
5	6.9	18.7 \pm 0.1	0.78 \pm 0.007	67	9.77 \pm 0.14
10	9.9	18.41 \pm 0.12	0.78 \pm 0.005	63	9.05 \pm 0.12
15	10.6	17.837 \pm 0.18	0.78 \pm 0.005	60	8.34 \pm 0.14
20	11.9	17.1 \pm 0.1	0.78 \pm 0.005	57	7.63 \pm 0.09

the rate of reduction and increases the performance. More studies of counter electrode thickness and charge transfer resistance will give huge steps to improving the efficiency of solar conversion.

5. Conclusions

It has been demonstrated that the addition of a second diode to the equivalent circuit explains quite well the reverse behavior of the shaded elements; and this addition fits well the forward bias I - V characteristics of the experimental data, when working in several shading conditions. It has, also, been shown that different rates of shadow affect the efficiency of a dye synthesized solar cell. When applying the 2-diode model, we found very close matching between the experimental values of I - V curves and the simulation data. Our approaches used a few amounts of fitting factors compared to the previously proposed models, which makes this model relatively flexible, effective, and more reliable.

Conflict of Interests

The authors declare that there is no conflict of interests regarding the publication of this paper.

Acknowledgments

This project was funded by the Deanship of Scientific Research (DSR), King Abdulaziz University, Jeddah, under Grant no. G-1436-130-35. The authors, therefore, acknowledge with thanks DSR technical and financial support.

References

- [1] M. Grätzel, "Solar energy conversion by dye-sensitized photovoltaic cells," *Inorganic Chemistry*, vol. 44, no. 20, pp. 6841–6851, 2005.
- [2] B. O'Regan and M. Grätzel, "Low-cost, high-efficiency solar cell based on dye-sensitized colloidal TiO_2 films," *Nature*, vol. 353, no. 6346, pp. 737–740, 1991.
- [3] U. Mehmood, S.-U. Rahman, K. Harrabi, I. A. Hussein, and B. V. S. Reddy, "Recent advances in dye sensitized solar cells," *Advances in Materials Science and Engineering*, vol. 2014, Article ID 974782, 12 pages, 2014.
- [4] A. V. Shah, H. Schade, M. Vanecek et al., "Thin-film silicon solar cell technology," *Progress in Photovoltaics: Research and Applications*, vol. 12, no. 2-3, pp. 113–142, 2004.
- [5] K. Chopra, P. Paulson, and V. Dutta, "Thin-film solar cells: an overview," *Progress in Photovoltaics: Research and Applications*, vol. 12, pp. 69–92, 2004.
- [6] M. Grätzel, "Dye-sensitized solar cells," *Journal of Photochemistry and Photobiology C: Photochemistry Reviews*, vol. 4, no. 2, pp. 145–153, 2003.
- [7] A. Hagfeldt and M. Grätzel, "Molecular photovoltaics," *Accounts of Chemical Research*, vol. 33, no. 5, pp. 269–277, 2000.
- [8] H. Hoppe and N. S. Sariciftci, "Organic solar cells: an overview," *Journal of Materials Research*, vol. 19, no. 7, pp. 1924–1945, 2004.
- [9] N. Robertson, "Optimizing dyes for dye-sensitized solar cells," *Angewandte Chemie—International Edition*, vol. 45, no. 15, pp. 2338–2345, 2006.
- [10] L. Schmidt-Mende, U. Bach, R. Humphry-Baker et al., "Organic dye for highly efficient solid-state dye-sensitized solar cells," *Advanced Materials*, vol. 17, no. 7, pp. 813–815, 2005.
- [11] D. B. Kuang, S. Ito, B. Wenger et al., "High molar extinction coefficient heteroleptic ruthenium complexes for thin film dye-sensitized solar cells," *Journal of the American Chemical Society*, vol. 128, no. 12, pp. 4146–4154, 2006.
- [12] J. B. Baxter and E. S. Aydil, "Nanowire-based dye-sensitized solar cells," *Applied Physics Letters*, vol. 86, no. 5, Article ID 053114, 2005.
- [13] M. Law, L. E. Greene, J. C. Johnson, R. Saykally, and P. Yang, "Nanowire dye-sensitized solar cells," *Nature Materials*, vol. 4, no. 6, pp. 455–459, 2005.
- [14] M. R. Karim, A. Islam, M. D. Akhtaruzzaman, L. Han, and A. Al-Ahmari, "Multiwall carbon nanotube coated with conducting polyaniline nanocomposites for quasi-solid-state dye-sensitized solar cells," *Journal of Chemistry*, vol. 2013, Article ID 962387, 5 pages, 2013.
- [15] K. T. Dembele, R. Nechache, L. Nikolova et al., "Effect of multi-walled carbon nanotubes on the stability of dye sensitized solar cells," *Journal of Power Sources*, vol. 233, pp. 93–97, 2013.

- [16] J. Balamurugan, R. Thangamuthu, and A. Pandurangan, "Growth of carbon nanotubes over transition metal loaded on Co-SBA-15 and its application for high performance dye-sensitized solar cells," *Journal of Materials Chemistry A*, vol. 1, no. 16, pp. 5070–5080, 2013.
- [17] S. Chen, J. Weng, Y. Huang et al., "Numerical model analysis of the shaded dye-sensitized solar cell module," *Journal of Physics D: Applied Physics*, vol. 43, no. 30, Article ID 305102, 2010.
- [18] L. De Marco, M. Manca, R. Giannuzzi et al., "Novel preparation method of TiO₂-nanorod-based photoelectrodes for dye-sensitized solar cells with improved light-harvesting efficiency," *Journal of Physical Chemistry C*, vol. 114, no. 9, pp. 4228–4236, 2010.
- [19] J. C. Slonczewski and P. R. Weiss, "Band structure of graphite," *Physical Review*, vol. 109, no. 2, pp. 272–279, 1958.
- [20] X. Wu, F. Li, W. Wu, and T. Guo, "Flexible white phosphorescent organic light emitting diodes based on multilayered graphene/PEDOT:PSS transparent conducting film," *Applied Surface Science*, vol. 295, pp. 214–218, 2014.
- [21] K. Aitola, A. Kaskela, J. Halme et al., "Single-walled carbon nanotube thin-film counter electrodes for indium tin oxide-free plastic dye solar cells," *Journal of the Electrochemical Society*, vol. 157, no. 12, pp. B1831–B1837, 2010.
- [22] M. S. Akhtar, Z. Y. Li, D. M. Park, D. W. Oh, D.-H. Kwak, and O.-B. Yang, "A new carbon nanotubes (CNTs)-poly acrylonitrile (PAN) composite electrolyte for solid state dye sensitized solar cells," *Electrochimica Acta*, vol. 56, no. 27, pp. 9973–9979, 2011.
- [23] M. Batmunkh, M. J. Biggs, and J. G. Shapter, "Carbonaceous dye-sensitized solar cell photoelectrodes," *Advanced Science*, vol. 2, no. 3, 2015.
- [24] X. Zheng, J. Deng, N. Wang et al., "Podlike N-doped carbon nanotubes encapsulating FeNi alloy nanoparticles: high-performance counter electrode materials for dye-sensitized solar cells," *Angewandte Chemie—International Edition*, vol. 53, no. 27, pp. 7023–7027, 2014.
- [25] C. K. Hong, H. S. Ko, E. M. Han, and K. H. Park, "Electrochemical properties of electrodeposited PEDOT counter electrode for dye-sensitized solar cells," *International Journal of Electrochemical Science*, vol. 10, pp. 5521–5529, 2015.
- [26] A. G. Nasibulin, A. Kaskela, K. Mustonen et al., "Multifunctional free-standing single-walled carbon nanotube films," *ACS Nano*, vol. 5, no. 4, pp. 3214–3221, 2011.
- [27] C. Feng, K. Liu, J.-S. Wu et al., "Flexible, stretchable, transparent conducting films made from superaligned carbon nanotubes," *Advanced Functional Materials*, vol. 20, no. 6, pp. 885–891, 2010.
- [28] L. Hu, G. Grüner, M. W. Rowell et al., "Organic solar cells with carbon nanotube network electrodes," *Applied Physics Letters*, vol. 88, Article ID 233506, 2006.
- [29] F. Mirri, A. W. K. Ma, T. T. Hsu et al., "High-performance carbon nanotube transparent conductive films by scalable dip coating," *ACS Nano*, vol. 6, no. 11, pp. 9737–9744, 2012.
- [30] J. W. Jo, J. W. Jung, J. U. Lee, and W. H. Jo, "Fabrication of highly conductive and transparent thin films from single-walled carbon nanotubes using a new non-ionic surfactant via spin coating," *ACS Nano*, vol. 4, no. 9, pp. 5382–5388, 2010.
- [31] S. Kim, J. Yim, X. Wang, D. D. C. Bradley, S. Lee, and J. C. DeMello, "Spin-and spray-deposited single-walled carbon-nanotube electrodes for organic solar cells," *Advanced Functional Materials*, vol. 20, no. 14, pp. 2310–2316, 2010.
- [32] M. D. Lima, M. J. de Andrade, C. P. Bergmann, and S. Roth, "Thin, conductive, carbon nanotube networks over transparent substrates by electrophoretic deposition," *Journal of Materials Chemistry*, vol. 18, no. 7, pp. 776–779, 2008.
- [33] B. Dan, G. C. Irvin, and M. Pasquali, "Continuous and scalable fabrication of transparent conducting carbon nanotube films," *ACS Nano*, vol. 3, no. 4, pp. 835–843, 2009.
- [34] D.-Y. Cho, K. Eun, S.-H. Choa, and H.-K. Kim, "Highly flexible and stretchable carbon nanotube network electrodes prepared by simple brush painting for cost-effective flexible organic solar cells," *Carbon*, vol. 66, pp. 530–538, 2014.
- [35] I. Chung, B. Lee, J. He, R. P. H. Chang, and M. G. Kanatzidis, "All-solid-state dye-sensitized solar cells with high efficiency," *Nature*, vol. 485, no. 7399, pp. 486–489, 2012.
- [36] L. Han, N. Koide, Y. Chiba, A. Islam, and T. Mitate, "Modeling of an equivalent circuit for dye-sensitized solar cells: improvement of efficiency of dye-sensitized solar cells by reducing internal resistance," *Comptes Rendus Chimie*, vol. 9, no. 5-6, pp. 645–651, 2006.
- [37] A. Marchioro, J. Teuscher, D. Friedrich et al., "Unravelling the mechanism of photoinduced charge transfer processes in lead iodide perovskite solar cells," *Nature Photonics*, vol. 8, no. 3, pp. 250–255, 2014.
- [38] B. O'Regan, J. Moser, M. Anderson, and M. Grätzel, "Vectorial electron injection into transparent semiconductor membranes and electric field effects on the dynamics of light-induced charge separation," *Journal of Physical Chemistry*, vol. 94, no. 24, pp. 8720–8726, 1990.
- [39] M. Grätzel, *Heterogeneous Photochemical Electron Transfer*, vol. 89, CRC Press, Boca Raton, Fla, USA, 1989.
- [40] S. Sodergern, A. Hagfeldt, J. Olsson, and S. Lindquist, "Theoretical models for the action spectrum and the current-voltage characteristics of microporous semiconductor films in photoelectrochemical cells," *The Journal of Physical Chemistry*, vol. 98, no. 21, pp. 5552–5556, 1994.
- [41] M. Bashahu and P. Nkundabakura, "Review and tests of methods for the determination of the solar cell junction ideality factors," *Solar Energy*, vol. 81, no. 7, pp. 856–863, 2007.
- [42] J. Halm, P. Vaherma, K. Miettunen, and P. Lund, "Device physics of dye solar cells," *Advanced Materials*, vol. 22, no. 35, pp. E210–E234, 2010.
- [43] E. M. Barea, C. Zafer, B. Gultekin et al., "Quantification of the effects of recombination and injection in the performance of dye-sensitized solar cells based on N-substituted carbazole dyes," *Journal of Physical Chemistry C*, vol. 114, no. 46, pp. 19840–19848, 2010.
- [44] R. Sastrawan, J. Renz, C. Prahl, J. Beier, A. Hinsch, and R. Kern, "Interconnecting dye solar cells in modules-I-V characteristics under reverse bias," *Journal of Photochemistry and Photobiology A: Chemistry*, vol. 178, no. 1, pp. 33–40, 2006.
- [45] M. Wolf and H. Rauschenbach, "Series resistance effects on solar cell measurements," *Advanced Energy Conversion*, vol. 3, no. 2, pp. 455–479, 1963.
- [46] A. Hauch and A. Georg, "Diffusion in the electrolyte and charge-transfer reaction at the platinum electrode in dye-sensitized solar cells," *Electrochimica Acta*, vol. 46, no. 22, pp. 3457–3466, 2001.
- [47] P. J. Cameron, L. M. Peter, S. M. Zakeeruddin, and M. Grätzel, "Electrochemical studies of the Co(III)/Co(II)(dbbip)₂ redox couple as a mediator for dye-sensitized nanocrystalline solar cells," *Coordination Chemistry Reviews*, vol. 248, no. 13-14, pp. 1447–1453, 2004.
- [48] A. Thess, R. Lee, P. Nikolaev et al., "Crystalline ropes of metallic carbon nanotubes," *Science*, vol. 273, no. 5274, pp. 483–487, 1996.

- [49] P. Mialhe, A. Khoury, and J. P. Charles, "A review of techniques to determine the series resistance of solar cells," *Physica Status Solidi (A)*, vol. 83, no. 1, pp. 403–409, 1984.
- [50] K.-I. Ishibashi, Y. Kimura, and M. Niwano, "An extensively valid and stable method for derivation of all parameters of a solar cell from a single current voltage characteristic," *Journal of Applied Physics*, vol. 103, no. 9, Article ID 094507, 2008.
- [51] K. Levenberg, "A method for the solution of certain non-linear problems in least squares," *Quarterly of Applied Mathematics*, vol. 2, pp. 164–168, 1944.
- [52] J. Van De Lagemaat and A. J. Frank, "Effect of the surface-state distribution on electron transport in dye-sensitized TiO₂ solar cells: nonlinear electron-transport kinetics," *The Journal of Physical Chemistry B*, vol. 104, no. 18, pp. 4292–4294, 2000.
- [53] B. O'Regan, F. Lenzmann, R. Muis, and J. Wienke, "A solid-state dye-sensitized solar cell fabricated with pressure-treated P₂O₅-TiO₂ and CuSCN: analysis of pore filling and IV characteristics," *Chemistry of Materials*, vol. 14, no. 12, pp. 5023–5029, 2002.
- [54] Q. Wang, S. Ito, M. Grätzel et al., "Characteristics of high efficiency dye-sensitized solar cells," *The Journal of Physical Chemistry B*, vol. 110, no. 50, pp. 25210–25221, 2006.
- [55] W. J. Lee, E. Ramasamy, D. Y. Lee, and J. S. Song, "Efficient dye-sensitized solar cells with catalytic multiwall carbon nanotube counter electrodes," *ACS Applied Materials and Interfaces*, vol. 1, no. 6, pp. 1145–1149, 2009.
- [56] D. Zhang, X. Li, S. Chen, Z. Sun, X. J. Yin, and S. Huang, "Performance of dye-sensitized solar cells with various carbon nanotube counter electrodes," *Microchimica Acta*, vol. 174, no. 1-2, pp. 73–79, 2011.
- [57] H. Elbohy, A. Aboagye, S. Sigdel et al., "Graphene-embedded carbon nanofibers decorated with Pt nanoneedles for high efficiency dye-sensitized solar cells," *Journal of Materials Chemistry A*, vol. 3, no. 34, pp. 17721–17727, 2015.

Research Article

Properties of Reactive Powder Concrete and Its Application in Highway Bridge

Junwei Song^{1,2} and Shuhua Liu^{1,2}

¹Nanchang Key Laboratory of Material and Structure Detection, Jiangxi University of Technology, Nanchang 330098, China

²State Key Laboratory of Water Resources and Hydropower Engineering Science, Wuhan University, Wuhan 430072, China

Correspondence should be addressed to Shuhua Liu; shliu@whu.edu.cn

Received 26 October 2015; Revised 4 January 2016; Accepted 11 January 2016

Academic Editor: Osman Gencel

Copyright © 2016 J. Song and S. Liu. This is an open access article distributed under the Creative Commons Attribution License, which permits unrestricted use, distribution, and reproduction in any medium, provided the original work is properly cited.

A high-performance reactive powder concrete (RPC) was prepared with river sand, and the maximum particle size is 1.25 mm, under the 80°C steam curing condition. It is tested completely in terms of strength, uniaxial compressive stress-strain relation, flexural load-deflection relation, and frost resisting durability, and the results indicate that the concrete is suitable to RPC200. The uniaxial compressive stress-strain curve shows a linear-elastic behaviour up to explosive failure, which is different from that of conventional concrete. High postpeak load carrying capacity shows high toughness and reinforcing effect of the steel fibers. The RPC has not only much higher limit strain than conventional concrete, but also excellent frost resisting durability at the fifth day of age exceeding F300. Furthermore, the RPC satisfactorily meets the requirement of practical application for Xialouzi Bridge built with the RPC totally according to the calculation with finite element analysis software MIDAS/Civil. And the static loading testing result suggests that design of the bridge meets the utilization requirements.

1. Introduction

In 1993, French Corporation BOUYGUES firstly developed a new type of ultra-high-performance cement based composite material—reactive powder concrete (RPC) [1–3]. Though it has not been long since its advent, RPC has already been successfully applied in engineering construction field in a few years, due to its high mechanical properties and excellent durability. The first footbridge made of RPC in the world locates in Sherbrooke, Québec Province, Canada. It adopts truss structure of RPC steel tube in 60 m width. Stainless steel tube loaded with RPC200 is used to make the web member of the truss structure. The lower chord is RPC twin beams. Each of the prefabricated sections is 10 m long and 3 m high and they are assembled together through posttensioned prestressing after being transported to the site [4]. The use of RPC not only mitigates weight greatly but also improves the structure's durability to resist the frequent corrosion from the deicing salt and damage due to the freezing and thawing cycle under environments with high humidity. RPC is a kind of ultra-high-performance concrete with high strength,

high tenacity, and low porosity. Enhancing the components' fineness and activity and abandoning coarse aggregate to minimize the material's internal defect (pore space and microcrack) are main basic preparation principles to attain ultra-high strength and durability [5–10].

RPC possesses very high strength: it is usually divided into two grades: RPC200 and RPC800. The former's compressive strength and tensile strength are 170–230 MPa and 20–50 MPa, respectively, and those of the latter are 500–800 MPa and 45–140 MPa, respectively [4]. As for the good tenacity, incorporating steel fiber could increase the RPC's fracture energy to 20000–40000 J/m². In comparison with ordinary concrete, the rupture strength of RPC is an order of magnitude higher, and the fracture energy is more than two orders of magnitude higher [11–13]. Moreover, its low w/b ratio producing good pore structure and low porosity contributes to RPC's excellent durability [14, 15].

RPC is soon widely spread in European and American countries for its excellent properties in the last two decades. The Mars Hill Bridge in Iowa, USA, built by Lafarge Corporation using Ductal® material is a successful example. Completely

constructed by using RPC, the bridge won The Tenth Bridge Competition Award held by American PCI Association and was honored to be “The future bridge” [4].

But, there are many limits in these mentioned bridges. The first RPC bridge of Sherbrooke is a pedestrian bridge, and the load-bearing capability of these pedestrian bridges is very low. What is more, most of the highway RPC bridges were built with reinforced or even prestressed RPC, and the reinforcement ratio reduces little, which does not make the best of its advantages of ultra-high strength and high toughness.

According to Xialouzi Bridge engineering project, RPC200 was prepared. Its strength, compressive stress-strain behaviour, flexure load-deflection character, and durability were tested. The bridge was built with plain RPC and without any reinforcement to take full advantage of its ultra-high strength, toughness, and durability. The RPC satisfactorily meets the requirement of practical application for Xialouzi Bridge built by RPC totally according to the calculation with finite element analysis software MIDAS/Civil.

2. Experimental

P.O 42.5 ordinary Portland cement, ultrafine active silica fume, river sand (the maximum particle diameter is 1.25 mm), superplasticizer, steel fiber (12–15 mm long, the diameter is 0.2–0.25 mm, and tensile strength exceeds 2850 MPa), and tap water were used. Table 1 shows the mix proportion of RPC200.

A forced mixer is the mixing machine for RPC preparation. Mix the sand, cement, and silica fume for 2 minutes under dry condition; pour the superplasticizer and water and mix for 5 minutes; finally add the steel fiber and mix for 3–6 minutes. Cast RPC into the mould for 24 hours. Then remove the mould and put RPC in the curing box under 80°C steam curing condition for 72 hours. After that, let them cool naturally in the curing box for 24 hours and conduct performance test. The whole period lasts five days after adding the mixing water.

3. Properties of RPC200

3.1. Strength. Prepare RPC according to the above mix proportion and test its compressive strength, flexure strength, elastic module, splitting tensile strength, and shear strength. Table 2 lists the test results. There are three various kinds of specimen size for the compressive strength test: 40 × 40 × 40 mm, 100 × 100 × 100 mm, and 100 × 100 × 300 mm, marked with 4, 10, and 10 prismoids, respectively; specimens 4 and 10 are for flexural strength test and 10 prismoids for elastic module test, and 10 is for splitting tensile strength test and shear strength test.

As is shown in Table 2, compressive strengths of cubic RPC specimens of 4 cm size and 10 cm size are 236.8 MPa and 218.3 MPa, both meeting RPC200 requirement. In addition, tensile strength and flexure strength are so high that both are exceeding 25 MPa; the elastic module is 48.9 GPa and according to these test results, RPC200 is suitable for the bridge structure.

TABLE 1: Mix proportion of RPC200/kg·m⁻³.

Cement	Silica fume	Water	Superplasticizer	Sand	Steel fiber
884.3	221.1	148.2	27.6	1105.4	150.0

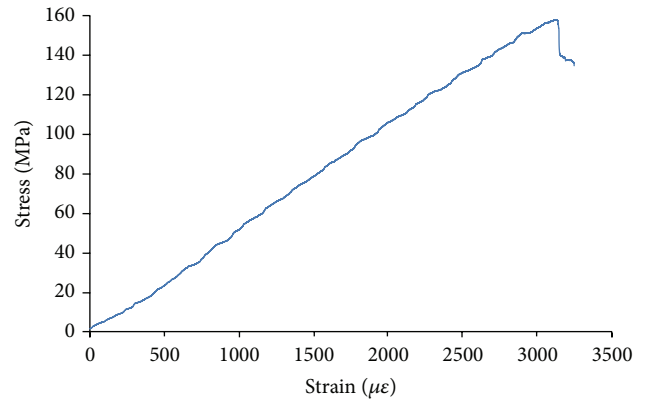


FIGURE 1: Compressive stress-strain curve of RPC200 (R).

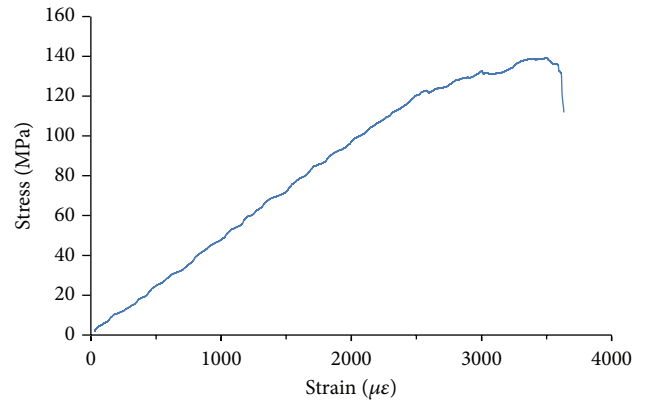


FIGURE 2: Compressive stress-strain curve of RPC200 (S).

3.2. Stress-Strain Behaviour. 100 × 100 × 300 mm prismatic specimens were tested in the compressive stress-strain curve experiment. Displacement control loading type is adopted, and the loading rates are 10⁻⁴/s (marked with “R”) and 10⁻⁵/s (marked with “S”), respectively. 100 × 100 × 400 mm prismatic specimens were tested in flexural stress-deflection curve experiment. Displacement control loading type is also adopted, and the loading rate is 10⁻⁴/s.

3.2.1. Compressive Stress-Strain Behaviour. Compressive stress-strain curves of RPC are shown as in Figures 1 and 2. It could be inferred from them that the compressive stress-strain characteristic of RPC200 displays obviously brittle failure. In both stress-strain curves of different loading rates, the stress of RPC200 increases straight as the strain increases until explosive failure so the descending stage could not be observed.

TABLE 2: Mechanical properties of RPC200.

Compressive strength/MPa			Flexural strength/MPa		Elastic module/GPa	Splitting tensile strength/Mpa	Shear strength/MPa
4	10	10 prismoids	4	10			
236.8	218.3	151.3	31.4	27.7	48.9	25.6	19.1

TABLE 3: Characteristic parameters of compressive stress-strain curves of RPC200.

Loading rate	Peak strain/ $\mu\epsilon$	Ultimate stress/MPa
$10^{-4}/s$	3129	158
$10^{-5}/s$	3508	140

Table 3 lists the characteristic parameters of compressive stress-strain curve of RPC200. Ultimate strength of the RPC under $10^{-4}/s$ loading rate is 18 MPa higher than that under $10^{-5}/s$ loading rate. The faster the loading rate, the higher the ultimate strength, which is consistent with ordinary concrete (strain ($\mu\epsilon$), stress (MPa)).

3.2.2. Flexural Load-Deflection Curve. The flexural load-deflection curve test adopted three-point bending load method and the span across the bottom pivot is 300 mm. Figure 3 displays the flexural load-deflection curve. It reveals that the flexural load-deflection curve displays favourable ductility, and the descending stage is very gentle. Extraction or tensile failure of the steel fiber should account for the curve's jumping part, but the whole still presents good ductility.

3.2.3. Constitutive Model. Unlike ordinary concrete, lack of coarse aggregate renders better uniformity of RPC for influence of the transition zone is little, and its constitutive relationship is similar to that of mortar. Judging from the previous test results and analysis, RPC is a typical elastic brittle material. In the RPC prismatic specimens' uniaxial compressive strength test, the stress-strain curve displays a linear ascent stage until the ultimate strain when the strength sharply drops, and then explosive failure occurs finally. So it is difficult to observe complete descending stage. The uniaxial compressive stress-strain relationship of RPC could be expressed as follows:

$$\begin{aligned} \sigma_c &= E_c \epsilon_c \quad (\epsilon_c \leq \epsilon_0), \\ \sigma_c &= 0 \quad (\epsilon_c > \epsilon_0). \end{aligned} \quad (1)$$

The elastic module of RPC is 40~50 GPa according to different researchers' tests. In this paper, the elastic module of RPC200 is 48.9 GPa. Elastic module of RPC relates to its matrix strength and amount of steel fiber. Besides, elastic module increases to some extent when the loading rate is fast. Compared with ordinary concrete, when strength of RPC increases a lot, its elastic module changes a little. Thus, the ultimate strain of RPC is far higher than ordinary concrete, usually 3000~5000 microstrains, and even exceeds steel's yielding strain, while that of ordinary concrete is 1500~2000.

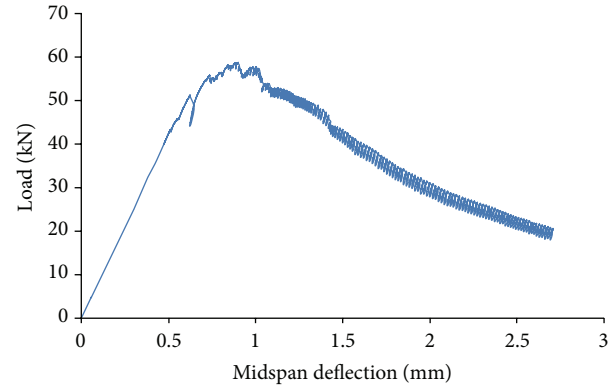


FIGURE 3: Flexural load-deflection curve of RPC200.

3.2.4. Failure Criterion. As for the ordinary concrete, the microcracks bifurcate or develop around the coarse aggregate and eventually turn into multiple cracking, which leads to the concrete's integral damage. In terms of RPC, strength of the matrix is high, and the binding capacity of steel fiber is relatively insufficient, so the crack rapidly propagates unsteadily once it happens. There are only one or several main cracks concentrated in the local area when RPC finally breaks up.

3.3. Frost Durability. Because the 3d strength of RPC under steam curing is high, frost test and strength test were simultaneously conducted; namely, both were brought forward to 5d. Moreover, owing to the excellent durability of RPC, mass loss rate and relative dynamic module were tested every 50 freezing-thawing cycles. Table 4 lists the test results. The statistics reveal that the frost resisting level of RPC exceeds F300 with low mass loss rate below 1%. The dynamic module changes little under freezing-thawing conditions. RPC, with its strong frost resistance durability, could guarantee itself good properties during its long service life.

4. Structure Calculations

RPC200 is to be used in Xialouzi Bridge reconstruction project at Xiaoying line K15 + 100 on Hubei provincial road. As is shown in Figure 4, its overall width is 13.5 m, and overall length is 18.04 m. The upper structure is 2~5.7 m rectangle slab bridge and the lower is the gravity type abutment made of mortar rubble. The design load grade is V-20, T-100. The left part of the bridge was built in 1989, and its width is 7.5 m. The concrete protective layer of the girder slab is a little thin, at the bottom of which large area of concrete spalling and steel corrosion occurred.

TABLE 4: Frost resisting durability of RPC200.

Mass loss rate (%)						Relative dynamic module (%)					
50 cycles	100 cycles	150 cycles	200 cycles	250 cycles	300 cycles	50 cycles	100 cycles	150 cycles	200 cycles	250 cycles	300 cycles
0.34	0.36	0.47	0.59	0.68	0.77	99.8	99.3	97.6	95.8	94.2	92.8

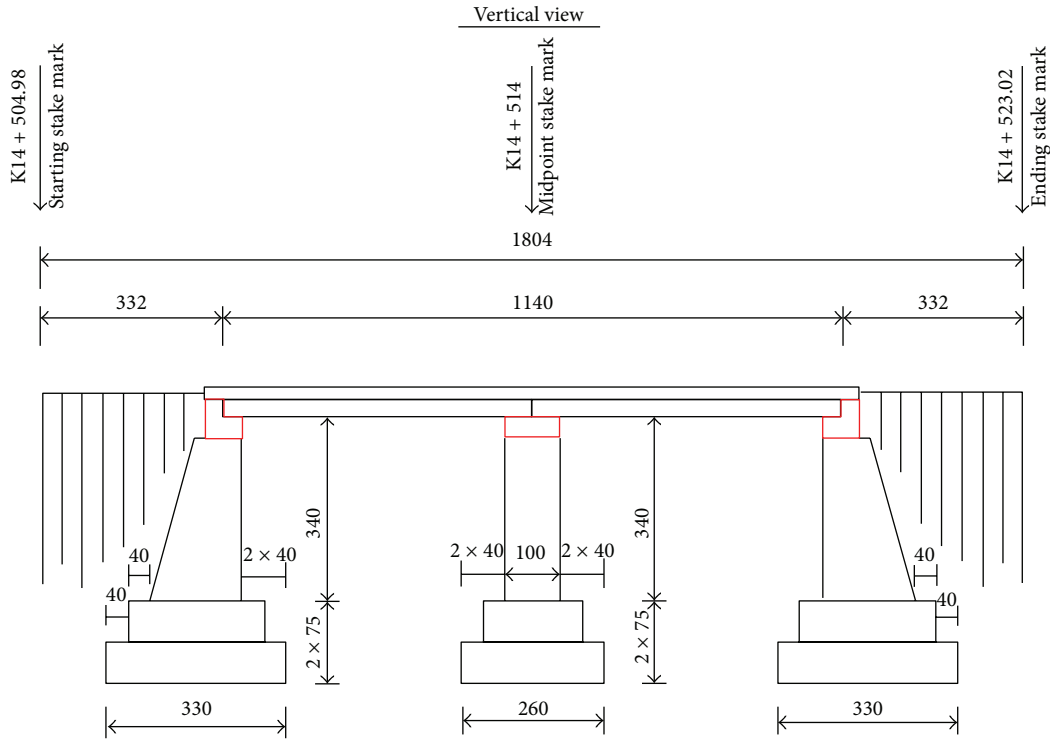


FIGURE 4: Front view of Xialouzi Bridge.

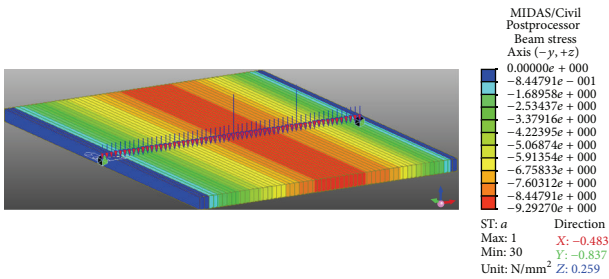


FIGURE 5: Calculation result of compressive stress.

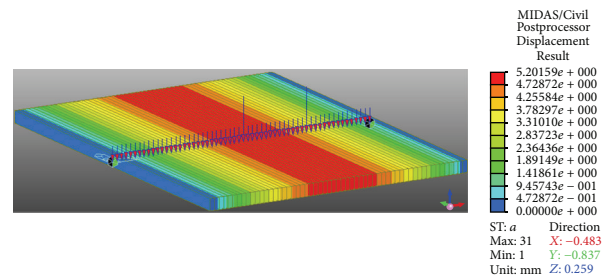


FIGURE 7: Calculation result of deflection.

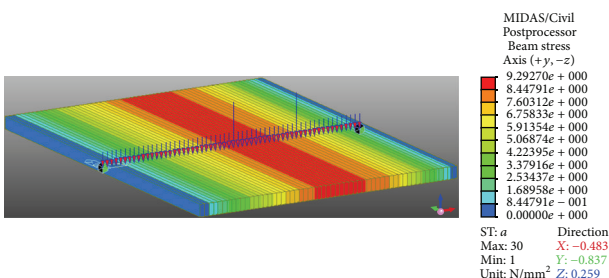


FIGURE 6: Calculation result of tensile stress.

Structure calculation is based on finite element method software MIDAS/Civil. The thickness of bridge deck slab is set to be 30 cm, expanding its length from 5.7 m to 6.0 m. Set the most unfavourable load and Figures 5–7 display the main calculation results. Based on the results, it could be concluded that the structure design of the whole slab is safe and reliable to meet all performance requirements:

- (1) On the maximum load combination condition, the maximum tensile and compressive stress value of partial cross section in the whole slab is below 14 MPa.

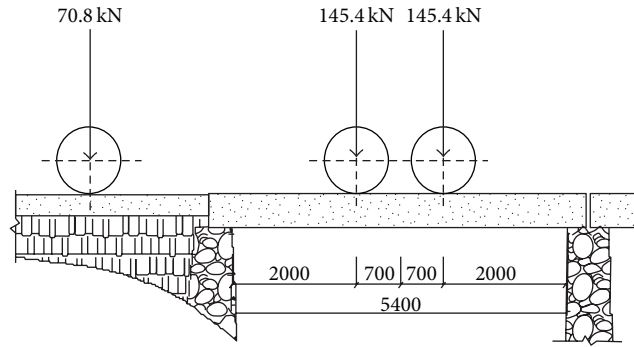


FIGURE 8: Loading trucks along the bridge's lengthways direction.

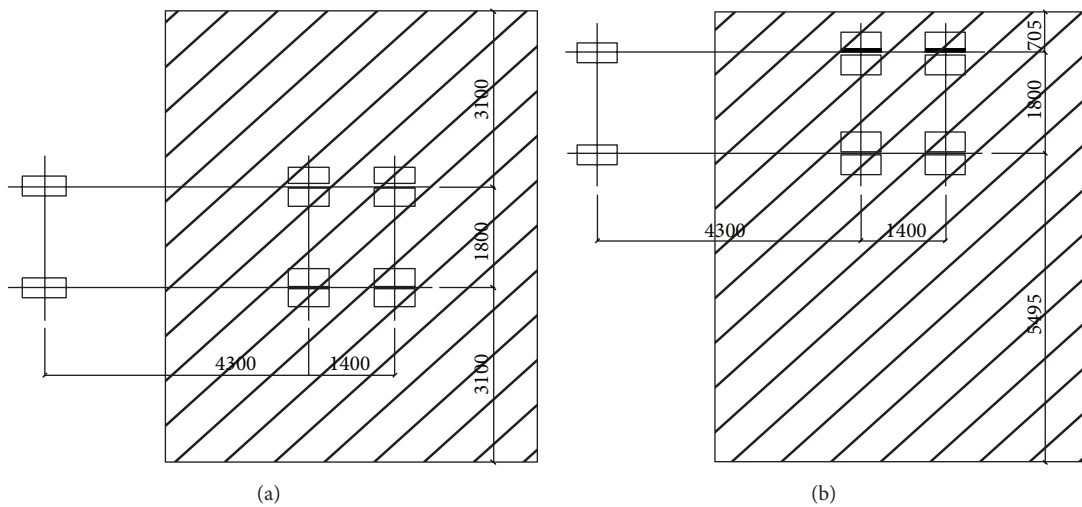


FIGURE 9: Trucks' layout of the static loading test: (a) the first condition and (b) the second condition.

Most stress values of the cross sections are below 12 MPa. Deflection of the midspan cross section is not beyond 7 mm. The overall structure possesses a certain safety stock to meet the requirements of serviceability limit state.

- (2) On the maximum load combination condition, resistances of the cross sections are all greater than the most unfavourable combination of bending moment and shearing force (absolute value). Both flexural capacity of the normal section and shear capacity of the oblique section could meet requirements of the standard.

5. Static Loading Test

In order to know actual force condition of the bridge's upper structure under the test loading, static loading test was conducted. It mainly consists of deflection, stress, and strain of the slab's midspan cross section under different test loadings. An 8 round self-discharging truck was employed. The loading trucks' layout along the bridge lengthways direction was set as

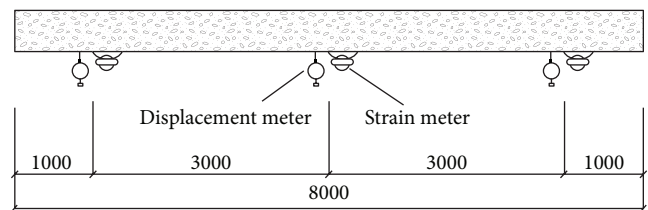


FIGURE 10: Layout of measurement points of deformation and strain on the test cross section.

shown in Figure 8 according to the worst force condition of the bridge structure considering its small span.

The upper structure of the bridge is a casting slab entirely, and the worst condition from the bridge's transverse direction is when the loading trucks locate at the center and the edge, being the first condition and second condition, respectively. Figure 9 displays specific trucks layout of each condition. Figure 10 shows the measurement points of deformation and strain on the test cross sections arrangements.

Figures 11 and 12 display the loading test results. The slab was still working in the elastic working scope under the test

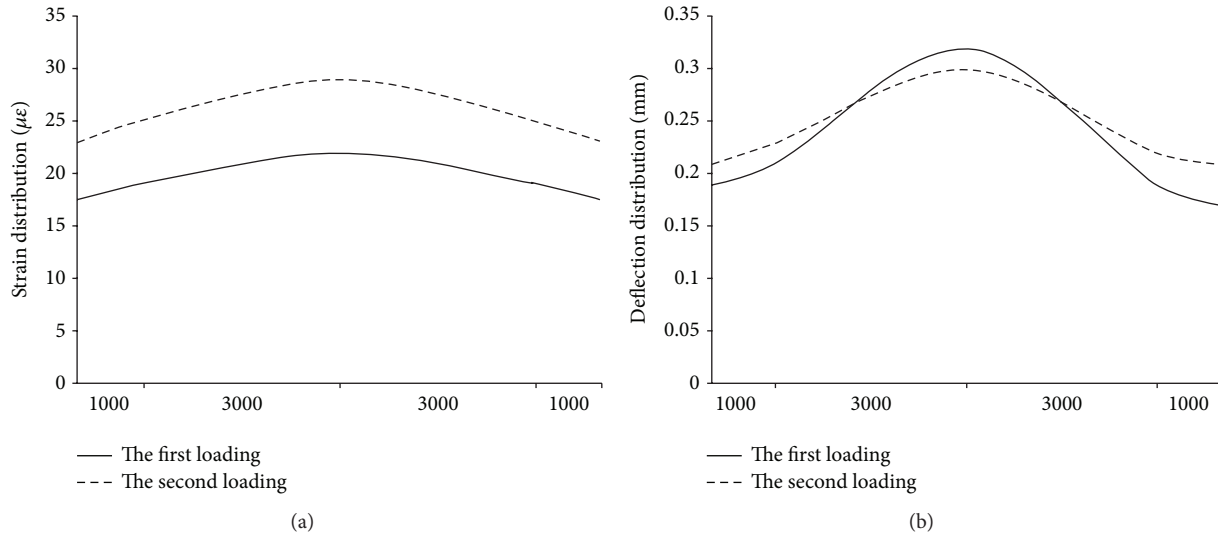


FIGURE 11: Deflection and strain distribution on the test cross section under the first condition: (a) strain distribution/ $\mu\epsilon$ and (b) deflection distribution/mm.

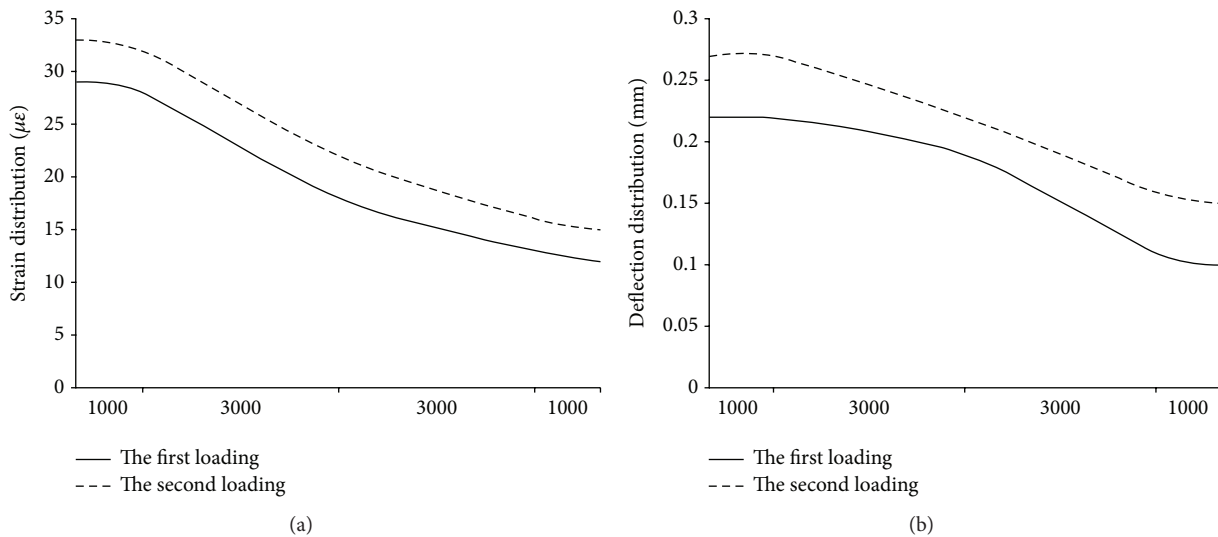


FIGURE 12: Deflection and strain distribution on the test cross section under the second condition: (a) strain distribution/ $\mu\epsilon$ and (b) deflection distribution/mm.

loadings. Differences of deflection and strain of the twice loadings under each condition were small.

The maximum deflection was 0.32 mm (under the first condition), less than the admissible values in the standard ($L/600 = 9.5$ mm). The maximum tensile strain at the bottom of slab was $30 \mu\epsilon$, strain being less than the concrete ultimate tensile strain value: $100\sim 150 \mu\epsilon$.

Under the first condition, the distributions of deflection and strain were uniform, while, under the second condition, they are conformed to the bridge mechanical characteristics, which indicated that the upper structure was still at the elastic stage. The maximum deflection of the midspan was 0.32 mm, far less than $L/600$, and its maximum tensile strain was

$30 \mu\epsilon$ far less than the concrete ultimate tensile strain. These suggest that the design of the bridge meets the utilization requirements and during the test process no crack occurred on the midspan cross section.

The Xialouzi RPC highway bridge makes full use of the advantages of ultra-high strength, toughness, and durability. The compressive and flexural strength of RPC reached up to 236.8 MPa and 31.4 MPa, respectively, and its frost resisting level exceeded F300 with very low mass loss and high dynamic module. Although the bridge was built with plain RPC, it has a high bearing capacity and a long service life. Moreover, the cost is saved because the reinforcement is cancelled and the reinforcing steel bar is not used.

6. Conclusions

Considering the engineering practice, it is necessary to amplify the size requirement in this paper. Ultra-high-performance material RPC was prepared under 80°C steam curing condition. The experiments revealed that RPC200 has high strength, tenacity, and durability. On the two stress-strain curves under different loading rates, stress of RPC200 goes linearly upward along with the increasing strain until explosive failure. Its flexural load-deflection curve shows very good ductility. The descending stage is very gentle. The extraction and tensile failure of steel fiber should account for the curve's jumping part. But as a whole the curve displays excellent tenacity. Calculation for the left of the Xialouzi Bridge, totally built by RPC, through the finite element method software MIDAS/Civil indicates that RPC is eligible to meet the requirements. Using RPC could replace the reinforcement steel bars and thus it simplifies the construction procedure. Furthermore, the excellent durability of RPC could prolong the service life of the bridge.

Conflict of Interests

The authors declare that there is no conflict of interests regarding the publication of this paper.

Acknowledgments

This project is funded by the Automobile Collaborative Innovation Project of Jiangxi University of Technology (XTCX201324), Project on Professional and Characteristic Construction of Jiangxi Province 2010 (Civil Engineering), and Project on the Planning and Construction of Disciplines in Jiangxi University of Technology (Structure Engineering).

References

- [1] P. Richard and M. Cheyrezy, "Composition of reactive powder concretes," *Cement and Concrete Research*, vol. 25, no. 7, pp. 1501–1511, 1995.
- [2] R. Yu, P. Spiesz, and H. J. H. Brouwers, "Development of an eco-friendly Ultra-High Performance Concrete (UHPC) with efficient cement and mineral admixtures uses," *Cement and Concrete Composites*, vol. 55, no. 1, pp. 383–394, 2014.
- [3] R. Yu, P. Spiesz, and H. J. H. Brouwers, "Development of Ultra-High Performance Fibre Reinforced Concrete (UHPRFC): towards an efficient utilization of binders and fibres," *Construction and Building Materials*, vol. 79, pp. 273–282, 2015.
- [4] S. H. Liu, P. Y. Yan, and J. W. Feng, "Research and application of RPC in the bridge engineering," *Highway*, vol. 58, no. 3, pp. 149–154, 2009.
- [5] M. Cheyrezy, V. Maret, and L. Frouin, "Microstructural analysis of RPC (Reactive Powder Concrete)," *Cement and Concrete Research*, vol. 25, no. 7, pp. 1491–1500, 1995.
- [6] K. Lahlou, P.-C. Aïtcin, and O. Chaallal, "Behaviour of high-strength concrete under confined stresses," *Cement and Concrete Composites*, vol. 14, no. 3, pp. 185–193, 1992.
- [7] W. Wang, J. Liu, F. Agostini, C. A. Davy, F. Skoczylas, and D. Corvez, "Durability of an Ultra High Performance Fiber Reinforced Concrete (UHPRFC) under progressive aging," *Cement and Concrete Research*, vol. 55, no. 1, pp. 1–13, 2014.
- [8] A. Beglarigale and H. Yazici, "Pull-out behavior of steel fiber embedded in flowable RPC and ordinary mortar," *Construction and Building Materials*, vol. 75, pp. 255–265, 2015.
- [9] A. Feylessoufi, F. Villiéras, L. J. Michot, P. De Donato, J. M. Cases, and P. Richard, "Water environment and nanostructural network in a reactive powder concrete," *Cement and Concrete Composites*, vol. 18, no. 1, pp. 23–29, 1996.
- [10] A. M. Soliman and M. L. Nehdi, "Effects of shrinkage reducing admixture and wollastonite microfiber on early-age behavior of ultra-high performance concrete," *Cement and Concrete Composites*, vol. 46, pp. 81–89, 2014.
- [11] L. Huynh, S. Foster, H. Valipour, and R. Randall, "High strength and reactive powder concrete columns subjected to impact: experimental investigation," *Construction and Building Materials*, vol. 78, no. 3, pp. 153–171, 2015.
- [12] S. H. Liu, G. S. Xie, and M. J. Rao, "Effect of waste glass powder on properties and microstructure of ultrahigh performance cement based materials," *Materials Research Innovations*, vol. 17, supplement 1, pp. 210–214, 2013.
- [13] R. Pierre, "Reactive powder concrete: a new ultra-high strength cementitious material," in *Proceedings of the 4th International Symposium on Utilization of High Strength/High Performance Concrete*, pp. 1343–1349, Paris, France, May 1996.
- [14] V. Matte and M. Moranville, "Durability of reactive powder composites: influence of silica fume on the leaching properties of very low water/binder pastes," *Cement and Concrete Composites*, vol. 21, no. 1, pp. 1–9, 1999.
- [15] R. Yu, P. Spiesz, and H. J. H. Brouwers, "Mix design and properties assessment of Ultra-High Performance Fibre Reinforced Concrete (UHPRFC)," *Cement and Concrete Research*, vol. 56, no. 2, pp. 29–39, 2014.

Research Article

Cost Optimization of Mortars Containing Different Pigments and Their Freeze-Thaw Resistance Properties

Sadık Alper Yıldız, ¹ Gökhan Kaplan, ² and Ali Uğur Öztürk ¹

¹Faculty of Engineering, Department of Civil Engineering, Celal Bayar University, Manisa, Turkey

²Kastamonu Vocational School of Higher Education, Kastamonu University, Kastamonu, Turkey

Correspondence should be addressed to Sadık Alper Yıldız; sadikalper.yildiz@cbu.edu.tr

Received 12 October 2015; Accepted 22 December 2015

Academic Editor: Juan J. Del Coz Díaz

Copyright © 2016 Sadık Alper Yıldız et al. This is an open access article distributed under the Creative Commons Attribution License, which permits unrestricted use, distribution, and reproduction in any medium, provided the original work is properly cited.

Nowadays, it is common to use colored concrete or mortar in prefabricated concrete and reinforced concrete construction elements. Within the scope of this study, colored mortars were obtained with the addition of brown, yellow, black, and red pigments into the white cement. Those mixtures are examined for their compressive strength, unit weight, water absorption, and freeze-thaw resistance. Subsequent to comparison of these properties, a cost optimization has been conducted in order to compare pigment costs. The outcomes showed that the pore structure in architectural mortar applications plays an important role in terms of durability. And cost optimization results show that light colored minerals can be used instead of white cements.

1. Introduction

Colored concrete is an architectural design element which is produced as a response to the unaesthetic outlook of traditional concrete. White cement and colorants are used in order to obtain colored concrete. However, it offers an aesthetical look, and colored concrete has some physical disadvantages such as efflorescence and low processability [1].

Use of colored concrete in mortar and concrete block, cement-based roofing materials, and precast concrete applications has been increasing recently. Colored concrete applications use pigments for durable color [2]. Hematite (red, orange, and purple), goethite (yellow), lepidocrocite (brown), calcite and dolomite (white), celadonite and malachite (green), quartz (white and translucent), and many others have been used as pigments since the antique ages. On the other hand, litharge (red), massicot (yellow), red lead (orange), and chrome oxide (green) are being used as synthetic pigments [3, 4].

Pigments are powdered material with finer grains compared to cement. Pigments used with cement-based composites are sieved using sieve opening number 200. Thus, it is expected for the mixtures water/pigment ratio to be higher for a specific thickness. Nevertheless, pigment's size and

surface properties also have an impact on the water/pigment ratio. Pigment's water requirement and dosage are among the important factors predicting its colour durability. Pigments also have an impact on the concrete shrinkage [5, 6]. Properties such as setting time, lightfastness, durability, mechanical properties, heat resistance, and soluble salt content gain importance in colored concrete. The cast system and the release agent used are of importance for a successful colored concrete application along with the aforementioned properties [7–11]. Cohesion of the mortar is increased when pigments are used in the mortar mixture [12] therefore reducing filler material ratio used in the mixture [13, 14].

Lee et al. [15], in a study conducted on keyed concrete blocks using iron oxide pigment as colorant, stated that the pigment/cement ratio must be less than 4%.

Bruce and Rowe [5] used inorganic pigments as colorant and found that these pigments are 10 times finer than cement. Thus, they found a decrease in the viscosity and thickness of mortars.

Jang et al. obtained colored mortars using white cement, blast-furnace slag and inorganic pigments. Viscosity of the mortar was decreased with the addition of pigments, yet it was improved with the addition of blast-furnace slag. However, addition of blast-furnace slag also alleviated the

TABLE 1: The chemical and physical properties of CEM I 52.5 R cement.

Chemical properties (%)		Physical and mechanical properties	
SiO ₂	21.6	Specific weight	3.06
Al ₂ O ₃	4.05	Specific surface (cm ² /gr)	4600
Fe ₂ O ₃	0.26	Whiteness (%)	85.5
CaO	65.7	Initial setting (min.)	100
MgO	1.30	Final setting (min.)	130
Na ₂ O	0.30	Water used for consistency (%)	30
K ₂ O	0.35	Volume constancy (mm)	1.0
SO ₃	3.30	Remnants obtained using 0.045 sieve (%)	1.0
Free CaO	1.60	Remnants obtained using 0.090 sieve (%)	0.1
Chloride (Cl)	0.01	Compressive strength for 2 days (MPa)	37.0
Insolubles	0.18	Compressive strength for 7 days (MPa)	50.0
Loss on ignition	3.20	Compressive strength for 28 days (MPa)	60.0

TABLE 2: Physical properties of the aggregate used in the mixtures.

Sieve aperture size	1 mm	710 μm	500 μm	355 μm	250 μm	180 μm	125 μm	90 μm	63 μm
Production range (%)	0	0	0	0.2	0.3	20.1	60.4	16.1	1.8
Mean grain size (μm)	140–170								
Clay content (%)	0.6–0.8								
Specific weight	2.68								
AFS value (%)	84.6								

efflorescence problem therefore increasing the long-term durability [1].

Colored mortars were obtained under laboratory conditions with the addition of brown, yellow, black, and red pigments into white cement in this study. The cement mortars obtained are examined for their compressive strength, unit weight, water absorption, and freeze-thaw resistance.

2. Material and Method

CEM I 52.5 R (White Portland Cement) manufactured by Çimsa cement manufacturing plant which complies with the TS EN 197-1 and ASTM C150 standards was preferred for the cement applications. The chemical and physical properties of CEM I 52.5 R cement are shown in Table 1. Polycarboxylate based third generation water reducer was used as the chemical agent.

Silica sand of AFS 80 to 100 (AFS is obtained by multiplying the sand grammage per sieve and DIN factor for each sieve and then division by the total grammage) was chosen as the aggregate to be used in the mixtures. Properties of the silica sand are given in Table 2.

Fe₂O₃ based 4 different pigments were used for the architectural mortar application. Technical specifications of the pigments used are given in Table 3.

Mortars obtained during the experiments were cubic samples of 5 cm × 5 cm × 5 cm dimensions. Materials used in the preparation of the mixtures are given in Table 4 (for 1 m³). Slump value was taken 4 cm for all the mixtures. For slump test, a cylindrical funnel (height: 60 mm, inner radius: 57 mm, and outer radius: 65 mm) is used. The mortar

TABLE 3: Technical specifications of pigments.

Pigment type	Brown	Yellow	Black	Red
SiO ₂ + Al ₂ O ₃ (max % 100)	4	1.2	3.2	4
Fe ₂ O ₃	96	98.8	96.8	96
Density (g/cm ³)	0.75–1.05	0.45–0.65	0.75–1.05	0.70–1.10
pH	5–8	3.2–7.5	4–8	4–7

TABLE 4: Material content of 1 m³ mortar mixture.

	Brown	Yellow	Black	Red	Reference
Pigment (g)	1250	1250	1250	1250	—
Additional water per 1 g of pigment (g)	4.5	13	4.13	4.75	—
Additional water (kg)	5.625	16.25	5.163	5.938	—
Aggregate (kg)	625	625	625	625	625
Cement (kg)	625	625	625	625	625
Superplasticizer (kg)	3.69	3.69	3.69	3.69	3.30
Water (kg)	190	190	190	190	190
Slump value (cm)	4	4	4	4	4

samples were tested for their water absorption, unit weight, and compressive strength for 1 day, 7 days, and 28 days. Nevertheless, a freeze-thaw test of 100 cycles was conducted on the mortar samples. Apart from other material mechanical test results and coefficients, F-T resistance factor has a great importance on colored aggregated concrete for preserving

TABLE 5: Mortar mixture properties.

	Reference	Brown	Yellow	Black	Red
Pigment (g)	—	1.25	1.25	1.25	1.25
Additional water per 1 g of pigment (g)	—	4.5	13	4.13	4.75
Additional water (kg)	—	5.625	16.250	5.163	5.938
Aggregate (kg)	625	625	625	625	625
Cement (kg)	625	625	625	625	625
Superplasticizer (kg)	3.3	3.69	3.69	3.69	3.69
Water (kg)	190	190	190	190	190
Slump value (cm)	4	4	4	4	4
Pigment price €/kg	—	2.58	4.32	2.28	2.58
Cost	€126.7	€131.3	€134.1	€130.8	€131.3

its initial conditions such as freezing and overheating. This type of test puts the concrete specimen through a series of extreme and rapid temperature changes it may face during the transportation and utilization processes. Following every 30 cycles, specimen dimensions and weights are checked and compared with the specimens which are not tested under dynamic temperature changes. Dynamic stability factor was calculated (ASTM C 666: $DSF = PN/M$; P : dynamic elasticity factor after n cycles; N : cycle number allowable for decreasing P ; M : total cycle number) and the results are obtained under the acceptable limits. Compression tests were also performed on the samples before and after the freeze-thaw cycle.

Aggregate, pigment, and cement were dry mixed in the coloured mortar production process with pigment addition. Dry mix procedure took approximately 30 seconds. The mixture was then stirred for 2.5 minutes following the addition of water.

3. Cost Analysis and Optimization

Cost optimization of the pigments becomes very important depending on its high costs comparing the other ingredients of the mortar. Full factorial experimental design (Minitab ver. 17 demo) was chosen due to the few test quantities. This design method is a good choice when the resources are limited. This experiment also allows the user to examine the effect of each factor on the response data. This study does not comprise the cross-sectional optimization of the final products. Further development and implementation of this approach can be taken into account for further researchers. Mixture features of the mortar using concrete pigments are shown in Table 5.

An optimization survey was conducted in order to identify the optimal pigment to be used in colored concrete production. For this purpose, 12 different functions were used and their properties are given in Table 1. These functions are maximized for strength and durability properties. Unit weight was maximized taking maximum compactness criteria into consideration. Factors such as water absorption, loss of strength, and cost were minimized.

TABLE 6: Functions used in optimization and their properties.

Number	Objective function	Property
X_1 (MPa)	Compressive strength for 1 day	Maximum
X_2 (MPa)	Compressive strength for 7 days	Maximum
X_3 (MPa)	Compressive strength for 28 days	Maximum
X_4 (kg/m ³)	Unit weight	Maximum
X_5 (%)	Water absorption	Minimum
Y_1 (MPa)	1 day, 100 F-T	Maximum
Y_2 (MPa)	7 days, 100 F-T	Maximum
Y_3 (MPa)	28 days, 100 F-T	Maximum
Z_1 (%)	1 F-T loss of strength	Minimum
Z_2 (%)	7 F-T loss of strength	Minimum
Z_3 (%)	28 F-T loss of strength	Minimum
T_1 (€)	Cost	Minimum

Four different models were created for 12 different functions as part of the optimization process. These models are summarized in Table 2. The first model involves the optimization of the concretes only by their physical properties (X). The second model involves the optimization of concretes by their physical properties (X) along with their F-T resistance (Y). The third model involves the optimization of concretes taking the loss of strength (Z) into consideration following the freeze-thaw cycles. The fourth model, on the other hand, defines the optimal mix according to the cost factor (T). The summary of the models can be shown in Table 7.

First Model. The first model involves the optimization of the concrete samples only by their physical properties. Optimization results showed that the optimal mix is the one prepared using black pigment. Table 3 compares the black pigment mix and reference mix. The results obtained from the first model are represented in Table 8.

Second Model. The second model involves the optimization of concretes samples by their physical along with their durability properties. Black pigment was found to be the optimal mix according to the second model. Table 4 compares the black pigment mix and reference mix. The results achieved from the second model can be obtained from Table 9.

Third Model. The third model involves the optimization of concretes samples by their physical properties along with their durability properties and their loss of strength. Yellow pigment was found to be the optimal mix according to the third model. Table 5 compares the yellow pigment mix and reference mix. The results obtained from the third model are represented in Table 10.

Fourth Model. The fourth model involves optimization of the concrete samples by all the functions included in the other models and also the cost function. With the inclusion of the cost function, reference mix was found to be the optimal mix. Table 6 shows the function properties of the reference sample. The results obtained from the fourth model are represented in Table 11.

TABLE 7: Summaries of the models used in optimization.

Model #	Model summary
1	Physical properties (X)
2	Physical properties-durability ($X + Y$)
3	Physical properties-durability-loss of strength ($X + Y + Z$)
4	Physical properties-durability-loss of strength-cost ($X + Y + Z + T$)

TABLE 8: Results obtained from the first model.

Function	X_1	X_2	X_3	X_4	X_5
Reference	14.31	32.28	46.21	2095	9.50
Black	15.78	33.14	47.35	2137	8.95
Difference	10.27%	2.66%	2.50%	2.00%	-5.79%

4. Results and Discussion

Compressive strength tests were conducted on the 1st, 7th, and 28th days for the mortars with and without pigment additive and the results obtained are shown in Figure 1.

Mortars obtained using brown, yellow, and black pigments delivered very high performance when compared to the reference sample in the tests conducted on the 1st, 7th, and 28th days. However, red pigment use has led to a decrease in compressive strength for the tests conducted on the 1st, 7th, and 28th days. When the compressive strength values for the 28th day were examined, it was found that the addition of black pigment has increased the compressive strength by 2.5% when compared to the reference mortar.

Coloured mortars were then subjected to 100 F-T cycles after being cured for 1 day, 7 days, and 28 days. Compressive strength values obtained after these tests are shown in Figure 2.

Mortar samples which were subjected to the F-T effect after one day of curing have shown 14.4% loss of strength for the reference sample, while this value was in a range between 16 and 20% for the samples with pigment additive. Loss of strength decreased for the samples which were cured for 7 days as the hydration process is continued. The reference sample has shown 6.4% loss of strength after the freeze-thaw cycles conducted on the 28th day. This percentage was 8% for the brown mortars, 7.2% for the yellow mortars, and 7.1% for the black mortars. Freeze-thaw results obtained from the mortar samples with red pigment additive, on the other hand, were on the contrary. Red mortars were negatively affected by the F-T process on the 1st and 7th days, yet this effect was not observable on the 28th day.

The impact of pigment type on the water absorption and unit weight is shown in Figure 3. As we can see in Figure 3, results obtained from the mortar produced using brown pigment were the closest to the reference sample. Water absorption ratio increases with the increasing pore ratio of the mortar samples. This predicts the high water absorption level and low unit weight obtained from the red mortar. However, both water absorption level and unit weight of yellow mortar were higher than the brown mortar.

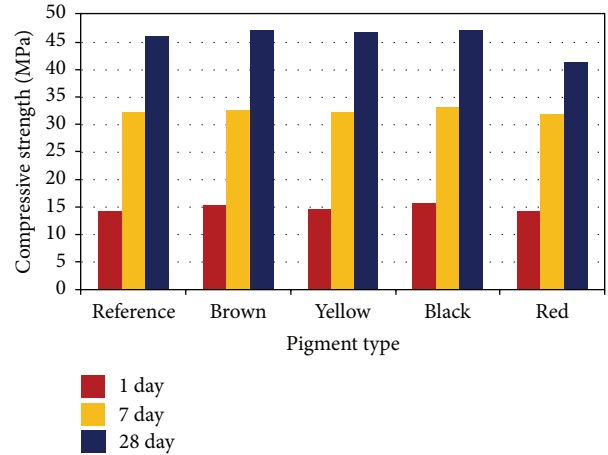


FIGURE 1: Compressive strength tests for mortars obtained using different pigments.

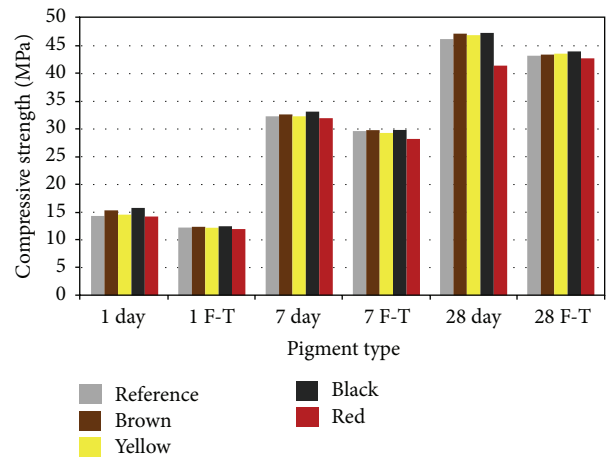


FIGURE 2: Results of the F-T tests conducted on the mortar samples.

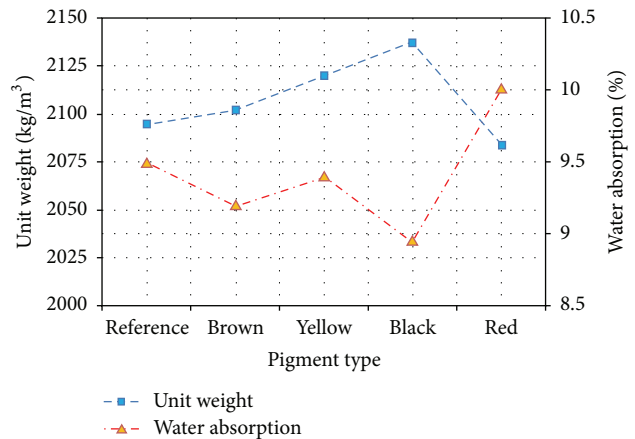


FIGURE 3: The impact of pigment type on the water absorption and unit weight.

TABLE 9: Results obtained from the second model.

Function	X_1	X_2	X_3	X_4	X_5	Y_1	Y_2	Y_3
Reference	14.31	32.28	46.21	2095	9.50	12.24	29.63	43.24
Black	15.78	33.14	47.35	2137	8.95	12.48	29.84	44.01
Difference	10.27%	2.66%	2.50%	2.00%	-5.79%	1.96%	0.71%	1.78%

TABLE 10: Results obtained from the third model.

Function	X_1	X_2	X_3	X_4	X_5	Y_1	Y_2	Y_3	Z_1	Z_2	Z_3
Reference	14.31	32.28	46.21	2095	9.50	12.24	29.63	43.24	14.47	8.21	6.43
Yellow	14.54	32.29	46.95	2120	9.40	12.20	29.31	43.58	16.09	9.23	7.18
Difference	1.60%	0.03%	1.60%	1.19%	-1.05%	-0.33%	-1.08%	0.79%	-1.62%	-1.02%	-0.75%

TABLE 11: Properties of the reference mix.

X_1	14.31
X_2	32.28
X_3	46.21
X_4	2095
X_5	9.5
Y_1	12.24
Y_2	29.63
Y_3	43.24
Z_1	14.47
Z_2	8.21
Z_3	6.43
T_1	126.7

The impact of pigment type on the F-T process (obtained from samples cured for 28 days) is shown in Figure 4.

As we can see in Figure 4, black mortar with the lowest water absorption level was the one which delivered the highest compressive strength after 100 F-T cycles. Red mortars gave the lowest compressive strength values before F-T process, yet an increase in the strength was observable after the cycles. Pore structure increases with the increasing water absorption levels while compressive strength decreases.

It was found that the impact of F-T cycles was diminished with the decreasing water absorption capacity and increasing unit weight. The findings of this study are in line with the previous experimental studies available in the literature.

Previous research suggests that strength and durability properties are negatively affected by the increasing pore structure of the mortar. The experimental study showed that the pore structure in architectural mortar applications plays an important role in terms of durability.

5. Conclusion

This study investigated the F-T resistance of architectural mortars obtained using pigments with different properties. The results obtained from this experimental study are detailed below.

It was found that brown, yellow, and black pigments contributed to the compressive strength, yet the red pigment

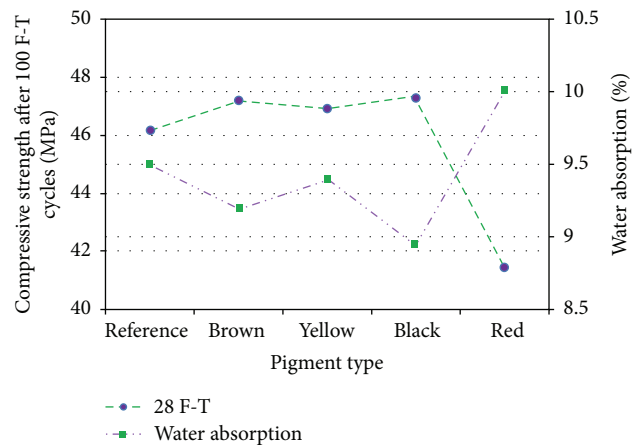


FIGURE 4: The impact of pigment type on the F-T process (samples cured for 28 days).

had an adverse effect on the compressive strength resulting in loss of resistance. Strength and durability tests showed that the black mortar has superior properties when compared to the reference sample.

Low water absorption level and high unit weight which are the characteristics of black mortar suggest that black mortar has a limited pore structure. In the light of these findings, it is clear that the use of black pigments in architectural mortar production will improve its strength and durability properties to a point superior to the mortars produced using other pigments.

The strength values of mortars produced using red pigments obtained from the 1st, 7th, and 28th days were lower than the other mortars. It was found that the addition of red pigment increases the pore ratio in the mortar according to the unit weight and water absorption analyses. The increase in the pore ratio negatively affects the strength and durability properties of the mortar.

Additional measure might be taken in order to increase the mortar strength when red pigment is used (i.e., reducing water/cement ratio). Air entrainer admixture must be preferred for freeze-thaw resistance.

It was found that the use of pigments in architectural mortar applications (except for red pigment) contributes to the strength of the mortar, therefore having an impact on the

freeze-thaw resistance of the material. When the strength loss is assessed, it would be fair to say that coloured mortars with similar properties to the reference mortar are resistant to the freeze-thaw effect.

It would be possible to obtain stronger, coloured architectural building elements with additional measures (i.e., air entrainer use) when severe freeze-thaw effect is in question. The impact of water absorption and unit weight on freeze-thaw process was found to be similar with the available literature results and proved the importance of the pore structure.

The use of yellow and black pigments has a positive effect on the strength and durability properties of concrete. Pore ratio was decreased leading to reduced water absorption values when black and yellow pigments were used. Overall, the use of any pigment has a positive effect on the strength and durability properties of concrete. Optimization results showed that the optimal pigments are black and yellow pigments. However, it was found that colored concrete cannot match the economic advantages traditional concrete offers when cost factor is brought into the equation. One of the most significant drawbacks of colored concrete is the unit price of pigment. Therefore, the use of pigments increases the unit cost of concrete having a direct impact on construction costs. Thus, the unit costs may be reduced to a point with the optimization of other material ratios. Particularly, low-cost materials such as light-colored mineral admixtures can be used instead of costly white cement.

Conflict of Interests

The authors certify that they have no affiliations with or involvement in any organization or entity with any financial interest (such as honoraria; educational grants; participation in speakers' bureaus; membership, employment, consultancies, stock ownership, or other equity interests; and expert testimony or patent-licensing arrangements) or nonfinancial interest (such as personal or professional relationships, affiliations, knowledge, or beliefs) in the subject matter or materials discussed in this paper.

References

- [1] H.-S. Jang, H.-S. Kang, and S.-Y. So, "Color expression characteristics and physical properties of colored mortar using ground granulated blast furnace slag and White Portland Cement," *KSCE Journal of Civil Engineering*, vol. 18, no. 4, pp. 1125–1132, 2014.
- [2] T. C. Patton, *Pigment Handbook*, Wiley, New York, NY, USA, 1973.
- [3] M. C. Z. Ares, E. V. González, A. I. T. Gómez, and J. M. Fernández, "An easy method to estimate the concentration of mineral pigments in colored mortars," *Dyes and Pigments*, vol. 101, pp. 329–337, 2014.
- [4] J. M. Fernández Rodríguez and J. A. Fernández Fernández, "Application of the second derivative of the Kubelka-Munk function to the semiquantitative analysis of Roman paintings," *Color Research and Application*, vol. 30, no. 6, pp. 448–456, 2005.
- [5] S. M. Bruce and G. H. Rowe, "The influence of pigments on mix designs for block paving units," in *Proceedings of the 4th International Conference on Concrete Block Paving*, vol. 2, pp. 117–124, Auckland, New Zealand, 1992.
- [6] H.-S. Lee, J.-Y. Lee, and M.-Y. Yu, "Influence of iron oxide pigments on the properties of concrete interlocking blocks," *Cement and Concrete Research*, vol. 33, no. 11, pp. 1889–1896, 2003.
- [7] M. Karagüler, "Mimarlıkta beton, mimari beton," *THBB Ready-Mix Concrete Periodical*, no. 53, p. 56, 2002.
- [8] M. Karagüler, "Mimari Beton ve Kalıp," *THBB Ready-Mix Concrete Periodical*, no. 57, p. 68, 2003.
- [9] E. Püttbach, "New pigments for the colouring of construction materials processing advantages at zero tariff," *Magazine of Concrete Precasting Plant and Technology*, no. 8, pp. 104–107, 1997.
- [10] U. Hahn, "Coloured concrete—nature has the aggregates," *Magazine of Concrete Precasting Plant and Technology*, vol. BFT 1, pp. 78–88, 1998.
- [11] E. V. D. Busken, "Innovations in concrete block paving in Belgium," in *Proceedings of the 1st International Symposium for Street Furniture*, Istanbul, Turkey, 2001.
- [12] A. López, J. M. Tobes, G. Giaccio, and R. Zerbino, "Advantages of mortar-based design for coloured self-compacting concrete," *Cement and Concrete Composites*, vol. 31, no. 10, pp. 754–761, 2009.
- [13] M. Collepardi and A. Passuelo, "The best SCC: stable, durable and colourable," in *Proceedings of the 4th International ACI/CANMET Conference on Quality of Concrete Structures and Recent Advances in Concrete Materials and Testing—Furnas Centrais Eletricas SA*, P. Helene, T. C. Holland, E. Pazzini, and R. Bittecourt, Eds., Civil Engineering Technological Center, Goibnia, Brasil, 2005.
- [14] V. Corinaldesi, S. Monosi, and M. L. Ruello, "Influence of inorganic pigments' addition on the performance of coloured SCC," *Construction and Building Materials*, vol. 30, pp. 289–293, 2012.
- [15] H.-S. Lee, J.-Y. Lee, and M.-Y. Yu, "Influence of inorganic pigments on the fluidity of cement mortars," *Cement and Concrete Research*, vol. 35, no. 4, pp. 703–710, 2005.